BEILSTEIN JOURNAL OF NANOTECHNOLOGY

Intrinsic Josephson effect and prospects of superconducting spintronics

Edited by Anatoli Sidorenko,
Vladimir Krasnov and Horst Hahn

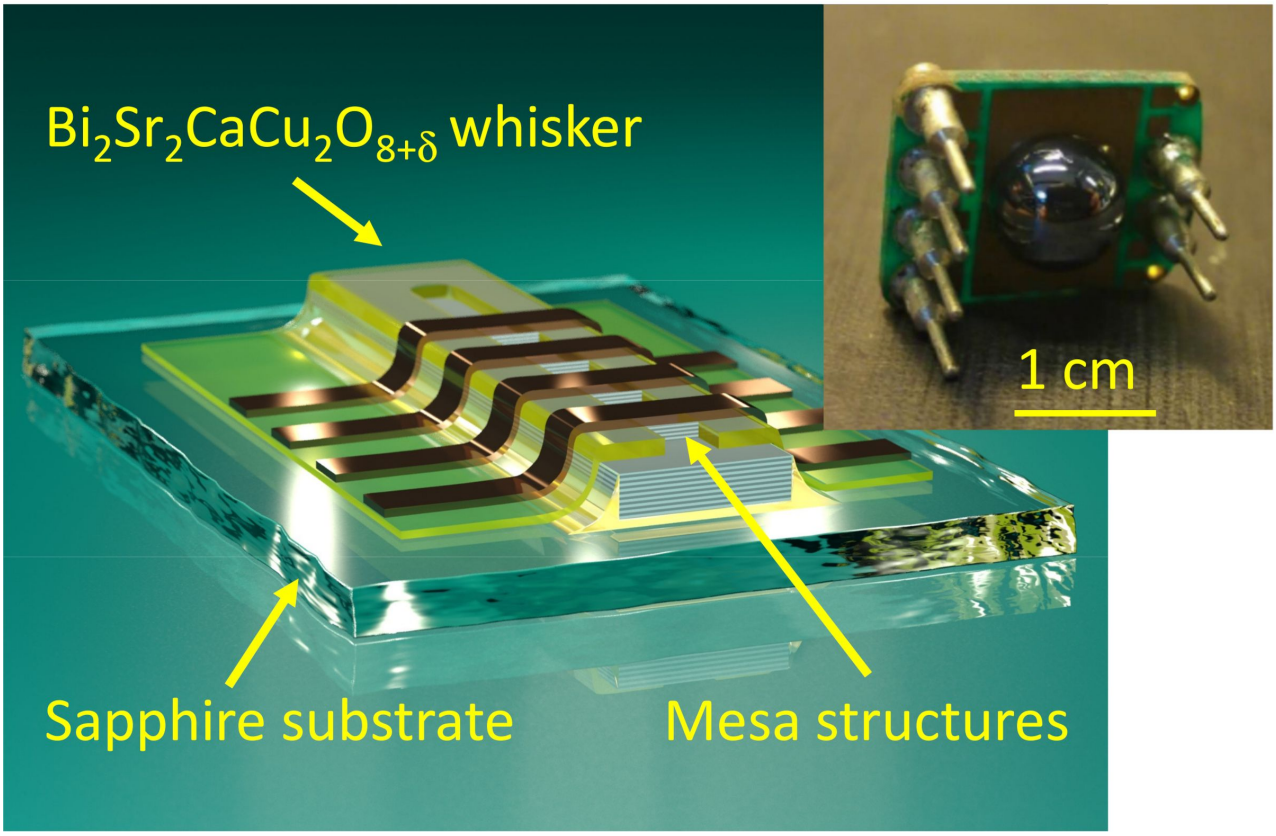

Imprint

Beilstein Journal of Nanotechnology
www.bjnano.org
ISSN 2190-4286
Email: journals-support@beilstein-institut.de

The *Beilstein Journal of Nanotechnology* is published by the Beilstein-Institut zur Förderung der Chemischen Wissenschaften.

Beilstein-Institut zur Förderung der Chemischen Wissenschaften
Trakehner Straße 7–9
60487 Frankfurt am Main
Germany
www.beilstein-institut.de

Cover image description: A superconducting THz source based on a Bi2Sr2CaCu2O8+d whisker.

BEILSTEIN JOURNAL OF NANOTECHNOLOGY

Frontiers of nanoelectronics: intrinsic Josephson effect and prospects of superconducting spintronics

Anatolie S. Sidorenko*[1,2], Horst Hahn[3,4] and Vladimir Krasnov[5]

Editorial

Open Access

Address:
[1]Institute of Electronic Engineering and Nanotechnologies of the Technical University of Moldova, Academiei 3/3, Chisinau 2028, Moldova, [2]I.S. Turgenev Orel State University, Komsomolskaya str. 95, 302026, Orel, Russia, [3]Institute of Nanotechnology, Karlsruhe Institute of Technology (KIT), D-76021 Karlsruhe, Germany, [4]Chemical, Biological and Materials Engineering, The University of Oklahoma, Norman, 73019, OK, United States and [5]Department of Physics, Stockholm University, AlbaNova University Center, SE-10691 Stockholm, Sweden

Email:
Anatolie S. Sidorenko* - sidorenko.anatoli@gmail.com

* Corresponding author

Keywords:
artificial neural networks; functional nanostructures; intrinsic Josephson effect; nanoelectronics; spintronics

Beilstein J. Nanotechnol. **2023,** *14,* 79–82.
https://doi.org/10.3762/bjnano.14.9

Received: 28 December 2022
Accepted: 03 January 2023
Published: 10 January 2023

This article is part of the thematic issue "Intrinsic Josephson effect and prospects of superconducting spintronics".

Editor-in-Chief: G. Wilde

The twenty-first century is marked by an explosive growth in the flow of information, which is necessary to process, archive, and transmit data through communication systems. For that purpose, big data centers with powerful supercomputers have been created all over the world, consuming a huge amount of electricity. For example, just one of thousands of big data centers worldwide, located in the town of Lulea, Sweden [1] consumes 9% of the electricity of the entire country. On the other hand, during the last four decades, the triumphal development of microelectronics and computers, based on traditional semiconductor chips, was enabled by the exponential growth of the number of transistors in chips and the shrinkage of the size of individual transistors, following the empirical Moore's Law, which is now showing slowing-down and failure signs [2].

It is evident that a radical reduction in energy consumption through efficiency improvement is needed and has become one of the main goals in the development of new supercomputers. For example, the powerful modern supercomputer TIANHE-2, a massive system that clocked 33.86 petaflops (i.e., 33.86 thousand trillion floating-point operations per second) has a power requirement of 17.6 MW (taking into consideration the external cooling, the power requirement is 24 MW) [3], which is comparable to the power requirement of a city.

To overcome these problems concerning increasing energy demands, a revolutionary solution is needed with two goals to be simultaneously reached: energy saving and increase in the capability of novel computers. The future of high-performance computing with low energy consumption is clearly associated with technologies with drastically lower energy dissipation.

A logical solution and the most promising candidate for radical reduction in energy consumption is the superconducting digital technology (SDT) based on Josephson junctions. The intrinsic Josephson effect, which was first reported by Reinhold Kleiner, Paul Müller, and co-workers (see [4,5] and references therein) has been investigated by many researchers [6-8]. The energy consumption of the SDT basic element is of the order of 10^{-19} J, corresponding to up to seven orders of magnitude less energy dissipation than that for their semiconductor analog, even when the energy for cryogenic cooling of superconducting circuits is considered [9-12]. Important and promising applications of the Josephson effect are its implementation in superconducting high-frequency electronics, spintronics, and nanostructures for supercomputers. In the last decade, a very rapid development in superconducting spintronics, based on functional nanostructures and Josephson junctions, has taken place [13,14]. The implementation of such devices in building blocks for quantum computers and for novel computers using non-von Neumann architecture with brain-like artificial neural networks (ANN) is a recent important development.

The main goal of this thematic issue is to highlight new research done in the field of hybrid nanostructures, including various elements using the Josephson effect and their applications in quantum electronics, spintronics, and high-frequency electronics.

The following novelties are presented in the contributed articles of this volume:

- Novel promising spintronic elements and materials with controllable switching between stable parallel, orthogonal, and antiparallel arrangements of magnetic moments of the epitaxial PdFe films and PdFe/Ag/PdFe heterostructures [15,16].

- Detection of ultrahigh frequency radiation by new devices:

  - Based on Josephson junctions with frequencies of 72–265 GHz using the Josephson grain boundary junction fabricated in YBaCuO films [17] and broad-band detectors based on YBaCuO Josephson junctions fabricated on ZrYO bicrystals with a very high responsivity at 77 K (up to 9 kV/W), low noise equivalent power (NEP) of 3×10^{-13} W/Hz$^{(1/2)}$, and with a wide power dynamic range equal to 1×10^6 [18].
  - Integrating an aluminum Josephson junction, with a size of a few micrometers, operating as a single photon counter in the microwave frequency range, switching from the superconducting to the resistive state due to absorption of a 10 GHz external signal [19].
  - Achieving a large coherent gain of the receiver, up to a factor of three, of the emitted power from two simultaneously biased arrays of Josephson junctions compared to that of the sum of the power values from two individually biased arrays. The detected phenomenon is attributed to the phase locking of Josephson junctions in different arrays via a common electromagnetic field [20].
  - Modeling of a multi-frequency receiving system based on an array of dipole antennas with cold-electron bolometers, with photon NEP of 1.1×10^{-16} W/Hz$^{(1/2)}$, achieved by replacing one of two single superconductor–insulator–normal (SIN) tunnel junctions with a single superconductor–normal (SN) contact [21].
  - Proposing a new type of cold electron bolometers with traps and hybrid superconducting/ferromagnetic absorber with a temperature reduction of the electrons in the refrigerator junctions down to 25 mK in the idle regime without an optical power load [22].

- Implementation of Josephson junctions for the design of quantum computers by analyzing the dynamics of a single-junction superconducting interferometer as an adiabatic neural cell of a perceptron artificial neural network in the quantum regime (a hybrid system whose configuration is dynamically adjusted by a quantum co-processor) [23].

- In several articles of the volume, new phenomena are predicted and investigated for promising spintronics applications, such as:

  - Plasma modes in capacitively coupled superconducting nanowires have been predicted [24]. It has been demonstrated that in the presence of inter-wire coupling plasma modes, each of the modes get split into two "new" modes propagating with different velocities across the system.
  - The magnetic proximity effect at a ferromagnetic–insulator–superconductor (FIS) interface was investigated through combined experimental and theoretical work [25].
  - Manifestations of nonlinear features in magnetic dynamics and current–voltage characteristics of the 0 Josephson junction in superconductor–ferromagnet–superconductor (SFS) structures have been predicted and calculated [26].
  - A quantitative study of the density of states (DOS) in bulk superconductor/ferromagnetic (S/F) bilayers in the diffusive limit has been presented. In addition, an analysis of the dependencies of DOS on magnetic and spin–orbit scattering times has been carried out [27].

In addition, the volume also highlights some other interesting effects in S/F functional nanostructures, which may be implemented in future spintronics devices.

The concept of this thematic issue was developed during the International SPINTECH Conference "NANO-2021: The 12th International Conference on Intrinsic Josephson Effect and Horizons of Superconducting Spintronics", which took place in September 2021 in Chisinau, Moldova. The presentations of the participants of the conference incorporating new ideas, technological approaches for the design of functional nanostructures for superconducting spintronics, quantum electronics, and novel base elements for superconducting supercomputers became the core of this volume.

The editors are convinced that this thematic issue will attract the attention of scientists, technologists, engineers, and IT experts, and will be useful for a broad readership including students wishing to extend their knowledge in this new, rapidly developing, and highly promising area.

Anatolie S. Sidorenko, Horst Hahn, and Vladimir Krasnov

Chisinau, Karlsruhe, and Stockholm, December, 2022.

Acknowledgements

We are thankful to the Production Team of the Beilstein-Institut for their professional and continuous and friendly editorial support.

Funding

A.S. thanks the EU-SPINTECH project (G.A. Nr. 810144) and the RSF project (Grant Nr. 20-62-47009) for the support.

ORCID® iDs

Anatolie S. Sidorenko - https://orcid.org/0000-0001-7433-4140
Horst Hahn - https://orcid.org/0000-0001-9901-3861

References

1. Luleå Data Center. https://www.facebook.com/LuleaDataCenter/photos/a.286677434734285/2013978478670830/ (accessed March 15, 2012).
2. Colwell, R. P. The Chip Design Game at the End of Moore's Law. In *IEEE Hot Chips 25 Symposium (HCS),* Stanford, CA, USA, Aug 25–27, 2013; IEEE, 2013; pp 1–16. doi:10.1109/hotchips.2013.7478302
3. Alba, D. China's Tianhe-2 Caps Top 10 Supercomputers: China's Tianhe-2 outflanks U.S. systems to take No. 1 spot in Top500 list. http://spectrum.ieee.org/tech-talk/computing/hardware/tianhe2-caps-top-10-supercomputers (accessed June 17, 2013).
4. Kleiner, R.; Steinmeyer, F.; Kunkel, G.; Müller, P. *Phys. Rev. Lett.* **1992,** *68,* 2394. doi:10.1103/physrevlett.68.2394
5. Kleiner, R.; Müller, P. *Phys. Rev. B* **1994,** *49,* 1327–1341. doi:10.1103/physrevb.49.1327
6. Ozyuzer, L.; Koshelev, A. E.; Kurter, C.; Gopalsami, N.; Li, Q.; Tachiki, M.; Kadowaki, K.; Yamamoto, T.; Minami, H.; Yamaguchi, H.; Tachiki, T.; Gray, K. E.; Kwok, W.-K.; Welp, U. *Science* **2007,** *318,* 1291–1293. doi:10.1126/science.1149802
7. Tafuri, F., Ed. *Fundamentals and Frontiers of the Josephson Effect,* 1st ed.; Springer Series in Materials Science, Vol. 286; Springer: Cham, Switzerland, 2019. doi:10.1007/978-3-030-20726-7_1
8. Delfanazari, K.; Klemm, R. A.; Joyce, H. J.; Ritchie, D. A.; Kadowaki, K. *Proc. IEEE* **2020,** *108,* 721–734. doi:10.1109/jproc.2019.2958810
9. Cattaneo, R.; Borodianskyi, E. A.; Kalenyuk, A. A.; Krasnov, V. M. *Phys. Rev. Appl.* **2021,** *16,* L061001. doi:10.1103/physrevapplied.16.l061001
10. Yurgens, A. A. *Supercond. Sci. Technol.* **2000,** *13,* R85–R100. doi:10.1088/0953-2048/13/8/201
11. Soloviev, I. I.; Klenov, N. V.; Bakurskiy, S. V.; Kupriyanov, M. Y.; Gudkov, A. L.; Sidorenko, A. S. *Beilstein J. Nanotechnol.* **2017,** *8,* 2689–2710. doi:10.3762/bjnano.8.269
12. Xu, Q.; Yamanashi, Y.; Ayala, C. L.; Takeuchi, N.; Ortlepp, T.; Yoshikawa, N. Design of an Extremely Energy-Efficient Hardware Algorithm Using Adiabatic Superconductor Logic. In *Proceedings of the 15th International Superconductive Electronics Conference,* ISEC 2015, Nagoya, Japan, July 6–9, 2015; P21. doi:10.1109/isec.2015.7383446
13. Sidorenko, A., Ed. *Functional Nanostructures and Metamaterials for Superconducting Spintronics;* Springer International Publishing: Cham, Switzerland, 2018. doi:10.1007/978-3-319-90481-8
14. Sidorenko, A. S. *Beilstein J. Nanotechnol.* **2020,** *11,* 1704–1706. doi:10.3762/bjnano.11.152
15. Yanilkin, I. V.; Gumarov, A. I.; Gizzatullina, G. F.; Yusupov, R. V.; Tagirov, L. R. *Beilstein J. Nanotechnol.* **2022,** *13,* 334–343. doi:10.3762/bjnano.13.28
16. Petrov, A. V.; Nikitin, S. I.; Tagirov, L. R.; Gumarov, A. I.; Yanilkin, I. V.; Yusupov, R. V. *Beilstein J. Nanotechnol.* **2022,** *13,* 836–844. doi:10.3762/bjnano.13.74
17. Revin, L. S.; Masterov, D. V.; Parafin, A. E.; Pavlov, S. A.; Pankratov, A. L. *Beilstein J. Nanotechnol.* **2021,** *12,* 1279–1285. doi:10.3762/bjnano.12.95
18. Glushkov, E. I.; Chiginev, A. V.; Kuzmin, L. S.; Revin, L. S. *Beilstein J. Nanotechnol.* **2022,** *13,* 325–333. doi:10.3762/bjnano.13.27
19. Pankratov, A. L.; Gordeeva, A. V.; Revin, L. S.; Ladeynov, D. A.; Yablokov, A. A.; Kuzmin, L. S. *Beilstein J. Nanotechnol.* **2022,** *13,* 582–589. doi:10.3762/bjnano.13.50
20. Galin, M. A.; Krasnov, V. M.; Shereshevsky, I. A.; Vdovicheva, N. K.; Kurin, V. V. *Beilstein J. Nanotechnol.* **2022,** *13,* 1445–1457. doi:10.3762/bjnano.13.119
21. Chiginev, A. V.; Blagodatkin, A. V.; Pimanov, D. A.; Matrozova, E. A.; Gordeeva, A. V.; Pankratov, A. L.; Kuzmin, L. S. *Beilstein J. Nanotechnol.* **2022,** *13,* 865–872. doi:10.3762/bjnano.13.77
22. Pimanov, D. A.; Frost, V. A.; Blagodatkin, A. V.; Gordeeva, A. V.; Pankratov, A. L.; Kuzmin, L. S. *Beilstein J. Nanotechnol.* **2022,** *13,* 896–901. doi:10.3762/bjnano.13.80
23. Bastrakova, M. V.; Pashin, D. S.; Rybin, D. A.; Schegolev, A. E.; Klenov, N. V.; Soloviev, I. I.; Gorchavkina, A. A.; Satanin, A. M. *Beilstein J. Nanotechnol.* **2022,** *13,* 653–665. doi:10.3762/bjnano.13.57
24. Latyshev, A.; Semenov, A. G.; Zaikin, A. D. *Beilstein J. Nanotechnol.* **2022,** *13,* 292–297. doi:10.3762/bjnano.13.24
25. Machon, P.; Wolf, M. J.; Beckmann, D.; Belzig, W. *Beilstein J. Nanotechnol.* **2022,** *13,* 682–688. doi:10.3762/bjnano.13.60

26. Janalizadeh, A.; Rahmonov, I. R.; Abdelmoneim, S. A.; Shukrinov, Y. M.; Kolahchi, M. R. *Beilstein J. Nanotechnol.* **2022,** *13,* 1155–1166. doi:10.3762/bjnano.13.97
27. Karabassov, T.; Pashkovskaia, V. D.; Parkhomenko, N. A.; Guravova, A. V.; Kazakova, E. A.; Lvov, B. G.; Golubov, A. A.; Vasenko, A. S. *Beilstein J. Nanotechnol.* **2022,** *13,* 1418–1431. doi:10.3762/bjnano.13.117

License and Terms

BEILSTEIN JOURNAL OF NANOTECHNOLOGY

Nonmonotonous temperature dependence of Shapiro steps in YBCO grain boundary junctions

Leonid S. Revin*[1,2], Dmitriy V. Masterov[1], Alexey E. Parafin[1], Sergey A. Pavlov[1] and Andrey L. Pankratov[1,2,3]

Full Research Paper

Open Access

Address:
[1]Institute for Physics of Microstructures of RAS, GSP-105, Nizhny Novgorod, 603950, Russia, [2]Center of Quantum Technologies, Nizhny Novgorod State Technical University, Nizhny Novgorod, Russia and [3]Lobachevsky State University of Nizhny Novgorod, Nizhny Novgorod, Russia

Email:
Leonid S. Revin* - rls@ipmras.ru

* Corresponding author

Keywords:
characteristic frequency; Shapiro steps; temperature dependence; YBaCuO Josephson junction

Beilstein J. Nanotechnol. **2021,** *12,* 1279–1285.
https://doi.org/10.3762/bjnano.12.95

Received: 08 September 2021
Accepted: 02 November 2021
Published: 23 November 2021

This article is part of the thematic issue "Intrinsic Josephson effect and prospects of superconducting spintronics".

Guest Editor: A. S. Sidorenko

Abstract

The amplitudes of the first Shapiro steps for an external signal with frequencies of 72 and 265 GHz are measured as function of the temperature from 20 to 80 K for a 6 μm Josephson grain boundary junction fabricated by YBaCuO film deposition on an yttria-stabilized zirconia bicrystal substrate. Non-monotonic dependences of step heights for different external signal frequencies were found in the limit of a weak driving signal, with the maxima occurring at different points as function of the temperature. The step heights are in agreement with the calculations based on the resistively–capacitively shunted junction model and Bessel theory. The emergence of the receiving optima is explained by the mutual influence of the varying critical current and the characteristic frequency.

Introduction

High-temperature superconducting (HTSC) Josephson junctions (JJs) are of great interest since many physical properties can be observed in dynamics during the changing the temperature within a wide range from nitrogen temperatures down to sub-kelvin, such as the phase diffusion regime [1-3], evidence for a minigap [4], and low-noise nano-junctions [5]. Such abilities raise not only fundamental interest in HTSC JJs but also an active search for ways to practically use such JJs. In recent years, the limiting characteristics of detectors and mixers based on HTSC JJs [6-11] have been actively studied. Josephson junctions have also been used for various spectroscopic applications [12]. In this area, the AC Josephson effect is utilized for the Hilbert-transform spectral analysis [13,14].

It should be noted that the simplest marker of the response level of a Josephson junction to microwave (MW) radiation is the

magnitude of Shapiro steps. In the majority of works, an increase in sensitivity at low temperatures has been demonstrated [15-17], although a part of the papers indicate the receiver's operation optimum at intermediate temperatures between the liquid nitrogen and helium temperatures [18,19]. The issue of obtaining sharp Shapiro steps is especially important for the development of HTSC Josephson voltage standards, consisting of series arrays of up to tens of thousands Josephson junctions [20,21]. Biased at frequencies in the range of $\omega/(2\pi)$ = 70–90 GHz, such arrays provide accurate quantized voltages $V_n = n\hbar\omega/(2e)$ exceeding 10 V. This accuracy is particularly determined by the magnitude of the response to external radiation. The Shapiro step observation can also be used as a clear probe to the gap symmetry of multigap superconductors [22].

The heights of the MW-induced voltage steps have been measured as a function of the MW power for various Josephson weak links fabricated from high-T_c superconductors [16,23,24]. The measured amplitudes are often smaller than those predicted by the resistively–capacitively shunted-junction (RCSJ) model [25,26], especially for measurements obtained at high temperatures. However, taking into account the effect of the YBCO junction resistance thermal noise [16] makes it possible to neutralize this difference and obtain a good agreement between the experiment and the theory.

While for low-temperature JJs the temperature dependence of the Shapiro steps is weak [27], for HTSC junctions the response to a MW signal has a general tendency to rise with decreasing temperature, but may have peculiarities for certain sample parameters [19].

In this paper, we investigate the temperature dependence of the first Shapiro step amplitude for an external signal with frequencies of 72 and 265 GHz acting on $YBa_2Cu_3O_{7-\delta}$ 6 μm Josephson grain boundary junction. The observed non-monotonous behavior of the step height in the limit of low signal power is discussed, and the measurement results are compared with the results of numerical calculations.

Experimental Setup and Numerical Model

The samples of grain boundary Josephson junctions were fabricated by on-axis dc magnetron sputtering [28-31] of $YBa_2Cu_3O_{7-\delta}$ (YBCO) film on the surface of 24°[001]-tilt $Zr_{1-x}Y_xO_2$ bicrystal substrates with modification of the substrate surface by preliminary topology masks [29,30]. The junctions with length L = 6 μm along the grain boundary and thickness 0.3 μm were integrated into a dipole antenna. The structure look follows the design from [29]. Based on the analysis of the transport properties, the best structure was selected and located at the center of a Si lens for efficient detection. The sample was mounted into a dry cryostat allowing for measurements in a wide temperature range from helium temperatures to ≈80 K. An external gigahertz signal was fed through an optical window with IR filters using a semiconductor synthesizer with a multiplier (70–78 GHz) or using a backward wave oscillator (230–370 GHz). The JJ transport properties and the response were characterized by a precise Keithley low-noise current source and nanovoltmeter using a standard 4-probe technique.

In the RCSJ model to which we compare our experimental results, the junction phase ϕ with an ideal critical current I_c, a resistance R_N and a capacitance C are described by the stochastic differential equation [32,33]

$$I = I_c \sin\phi + \frac{V}{R_N} + C\frac{dV}{dt} + I_{mw}\sin\left(2\pi F_{mw}t\right) + I_F, \quad (1)$$

where the voltage $V = d\phi/dt \times 2\pi/\Phi_0$ (Φ_0 is the magnetic flux quantum). The thermal fluctuations I_F are assumed to be a white Gaussian noise with zero mean and correlation function

$$\left\langle I_F(t) I_F(t+\tau)\right\rangle = \frac{k_B T}{\pi R_N}\delta(\tau).$$

A simple harmonic signal of the amplitude I_{mw} and the frequency $\omega_{mw} = 2\pi F_{mw}$ describes an external high-frequency radiation of the power $P_{mw} = I_{mw}^2 R_N/2$. Its effect on the Josephson system particularly depends on the characteristic frequency $\omega_c = 2eI_cR_N/\hbar$ of the JJ.

Results

First, the current–voltage characteristics (IVCs) were measured, and the value of the critical current as a function of temperature was found, see Figure 1. The $I_c(T)$ dependence is similar to the experimental observations for other such structures [34-36]. At the same time, the normal resistance of the JJ remained virtually constant, that is, R_N was 0.23–0.24 Ω within the whole studied temperature range. For the subsequent analysis of the results, we used data from the literature about similar structures of an YBCO bicrystal junction on 24°[001]-tilt $Zr_{1-x}Y_xO_2$ substrate [37] as the value of the junction capacitance $C = 3 \times 10^{-2}$ F/m^2 × 1.8 × 10^{-12} m^2 = 0.05 pF. This value, according to [35], remains almost unchanged over a wide temperature range.

It is important to understand which parameters vary in the model with the temperature. Figure 1 also shows the change in the Josephson junction characteristic length L/λ_J, where $\lambda_J = \sqrt{\Phi_0/(2\pi\mu_0 J_c d)}$ is the Josephson penetration depth,

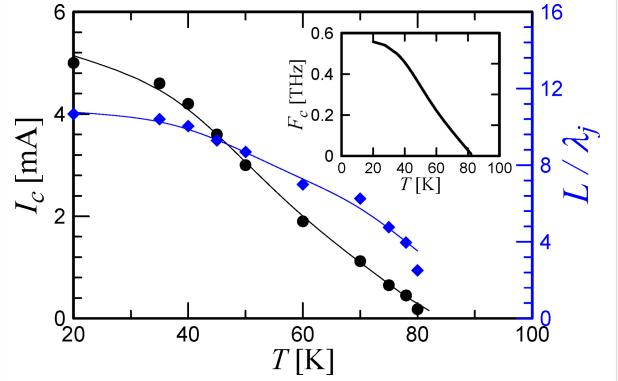

Figure 1: The dependence of the critical current (black dots) and the characteristic length of the Josephson junction (blue diamonds) on the temperature. The solid curves are spline approximations. The inset shows $F_c = \omega_c/(2\pi)$ versus T.

which determines the size of a fluxon in the junction. Here μ_0 is the vacuum permeability, J_c is the critical current density, and $d = t + 2\lambda_L$ is the effective magnetic thickness with the junction barrier thickness t = 1.5 nm and the London penetration depth λ_L = 250–150 nm [38]. It can be seen from the figure that, for nitrogen temperatures, the Josephson junction can generally be considered as a short JJ. With the decrease in the temperature, its characteristic dimension increases, and for 20 K, in the general case, Equation 1 becomes invalid, that is, the dynamics of the spatial distribution of the phase and the magnetic field inside the junction becomes important [39-41]. In the case of long JJs it is necessary to consider the sine-Gordon equation, taking into account the non-uniform distribution of currents flowing through the barrier, which is typical for bicrystal junctions [28,42,43]. However, if the junction length is of the order of the kink size and there is no external magnetic field, the long junction dynamics is close to that of a short one [39] and the used model is qualitatively adequate. This is confirmed in [40], where the escape time from the superconducting state is investigated, and it is shown that the critical length L/λ_J = 5 corresponds to the crossover between two dynamical regimes. Nevertheless, long HTSC junctions are characterized by such features as a flux creep and the change in the IVC curvature associated with the crossover from the flux flow to Josephson junction behavior [44]. That is why, as it will be shown below, in the region of low temperatures, the agreement between the experiment and the numerical calculation is not as good as in the region of high T values.

The second important parameter is the characteristic frequency ω_c (or F_c) (see the inset of Figure 1). The change of ω_c radically affects the response of the system to an external MW signal [17]. Essentially, the ω_{mw}/ω_c (or F_{mw}/F_c) ratio determines if the detection regime is optimal for the junction. This issue is discussed in more details below.

The third important parameter is the thermal noise magnitude, k_BT, which affects the smearing of the Shapiro steps, and, accordingly, the decrease in the step size in the region of low radiation power. It is not shown in Figure 1.

Figure 2 shows the IVCs for temperatures of 70 and 50 K in the absence of a high-frequency signal and in the regime of detecting external 72 or 265 GHz signals. The measurement results are in good agreement with the numerical simulations (the black curves). It should be noted that the radiation power was the same for the measurements at all temperatures. The power level of the two signals, 72 and 265 GHz, was chosen to be near the first minimum of the critical current, and, accordingly, near the first maximum of the first Shapiro step at high temperatures. This can be seen from the IVC for T = 70 K and F_{mw} = 72 GHz: the critical current is nearly zero, the amplitude of the first step is greater than the amplitude of the second and the third steps. The same picture is observed for the IVC at F_{mw} = 265 GHz. The comparison with the numerical model gives an estimate of the power absorbed by the Josephson junction: it is 0.4 μW for 72 GHz, and P_{mw} = 3 μW for 265 GHz.

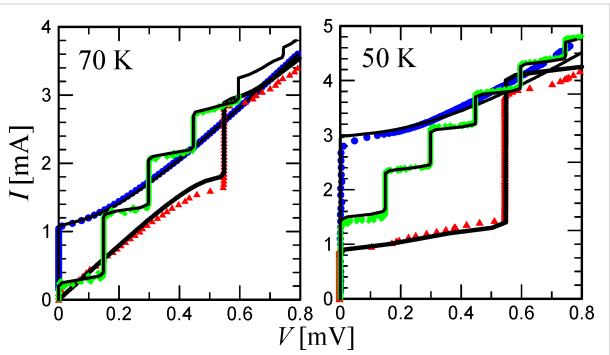

Figure 2: IVCs of a Josephson junction without an MW signal (blue dots), under the action of an external signal of 72 GHz (green diamonds) and 265 GHz (red triangles) at temperatures of 70 and 50 K. The black lines are the numerical calculations for each curve with the experimental parameters and with fitting power P_{mw}.

Figure 3, essentially the main result of the article, demonstrates the dependence of the first Shapiro step amplitude on the temperature for 72 and 265 GHz radiation at a constant power. The dependences are non-monotonic and have a maximum located at different temperature values for different MW frequencies. In addition, it can be seen that at high temperatures of approx. 80 K, the amplitudes of the steps are close, while with decreasing temperature in the case of 265 GHz radiation, the Shapiro steps become significantly higher than for 72 GHz. The numerical results (the solid curves) based on the experimental data

describe the experiment at high temperatures well and differ quantitatively at low temperatures. This may be caused by a specific dynamics arising with an increase in the characteristic length of the JJ at low temperatures. Nevertheless, the simulation qualitatively follows the experimental dependence within the entire temperature range.

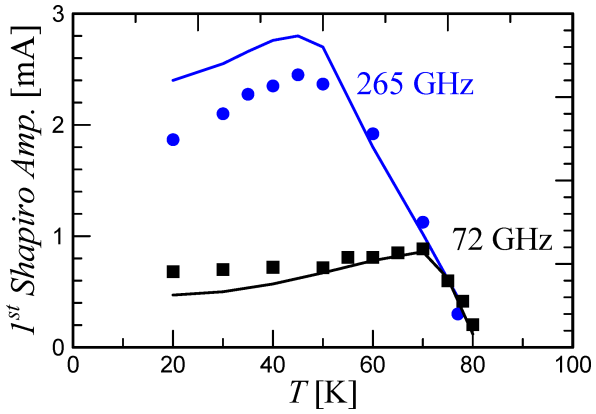

Figure 3: The dependence of the first Shapiro step amplitude on the temperature for 72 and 265 GHz radiation at a constant power. The dots are the experimental values, the lines are the theory for the temperatures at which the measurements were conducted.

The obtained effect of the optimum in the JJ response is associated with a simultaneous change of several parameters when the temperature changes. For a qualitative analysis, let us consider the expression for the first Shapiro step amplitude [33,45,46]:

$$\Delta I_1 = I_c \sum_{k=-\infty}^{+\infty} J_k(a) J_{-1-k}(a) \left| I_p \left[\left(k - \frac{1}{2} \right) \omega_{mw} \right] \right|, \quad (2)$$

where J_k and J_{-1-k} are Bessel functions at $a = \frac{I_{mw}}{2I_c\omega_{mw}/\omega_c}$, I_p is a complex function that determines the quadrature components of the supercurrent depending on the Josephson generation frequency. Although this expression is valid for a voltage-biased JJ, it is in a good agreement with measurements for the current-biased regime and RCSJ model [35]. In the case of low signal power and $\omega_{mw} \ll \omega_c$, the maximum height of the first step is proportional to

$$\max \Delta I_1 \approx I_c \omega_{mw} / \omega_c . \quad (3)$$

In the limit of $\omega_{mw} \approx \omega_c$, the expression for ΔI_1 takes the simple form:

$$\Delta I_1 \approx 2I_c \left| J_1 \left(\frac{I_{mw}}{2I_c\omega_{mw}/\omega_c} \right) \right|. \quad (4)$$

Figure 4 shows the theoretical dependence of $\max\Delta I_1$ on the frequency for various temperatures. According to Equation 3, the maximum step amplitude increases as the critical current increases and the temperature goes down. At the same time, due to the change in the critical frequency ω_c (the inset in Figure 1), the optimal signal detection regime is shifted. That is, for temperatures of 80 K and 70 K and the frequency of 72 GHz, the condition $\omega_{mw} \approx \omega_c$ is satisfied, and the step heights reach $\approx I_c$ and $\approx 0.9\ I_c$, respectively. At 50 K, $\max\Delta I_1 \approx I_c\omega_{mw}/\omega_c = I_cF_{mw}/F_c = 3$ mA × 72 GHz/330 GHz = 0.65 mA, and at 20 K, $\max\Delta I_1 \approx 5$ mA × 72 GHz/560 GHz = 0.64 mA. For 265 GHz signal, the step height almost reaches the limit $\approx I_c$ at 50 K, while at 20 K, ω_{mw} is still far from ω_c. Summarizing, for low-gigahertz radiation frequencies, lowering the temperature does not gain the response magnitude due to the non-optimal frequency of signal detection. Whereas, the closer ω_{mw} to the characteristic frequency, the greater the influence of the critical current increase with the temperature takes place.

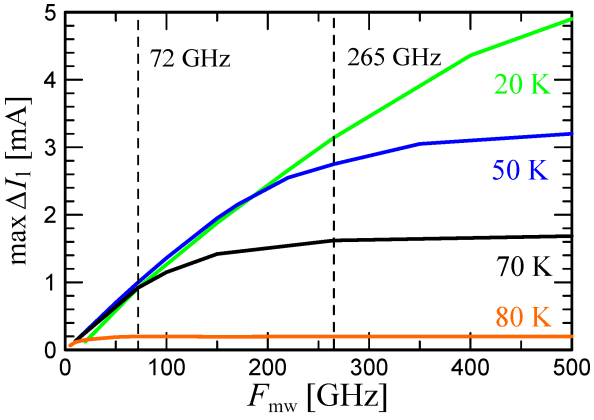

Figure 4: max ΔI_1 as function of F_{mw} at various temperatures. The dotted lines mark the position of the two frequencies used in the experiment.

In addition to the magnitude of the Shapiro step height maximum, it is important to take into account the period of the Bessel function, which, in the first approximation, determines the response of the JJ to a change in the gigahertz-signal power. Equation 4 shows that as ω_c grows, the Bessel function period increases, that is, the derivative $d\Delta I_1/dP_{mw}$ decreases. Figure 5 shows the results of the numerical calculations of the first Shapiro step height versus the external signal power at the temperatures of 70, 50, and 20 K. The upper panel of Figure 5 corresponds to the external signal frequency of 72 GHz. It can be seen that $\max\Delta I_1$ is close for all three temperatures, as explained earlier, see Figure 4. Nonetheless, due to the shift in the step maximum position in power, for small signal levels (marked with a vertical dashed line), ΔI_1 at 70 K is larger than at 50 and 20 K. The bottom panel of Figure 5 corresponds to a

265 GHz external signal. Here, for different temperatures, there is also a shift in the position of the Shapiro step maximum along the power axis, but it is smaller in comparison with the previous case, since ω_{mw}/ω_c is closer to unity. In this case, the increase in the maximum step height with temperature is also significant. Nevertheless, there is an optimum ΔI_1 in temperature due to the competition between two effects, namely an increase in $\max\Delta I_1$ with an increase in the critical current and a decrease in $d\Delta I_1/dP_{mw}$ with an increase in the critical current.

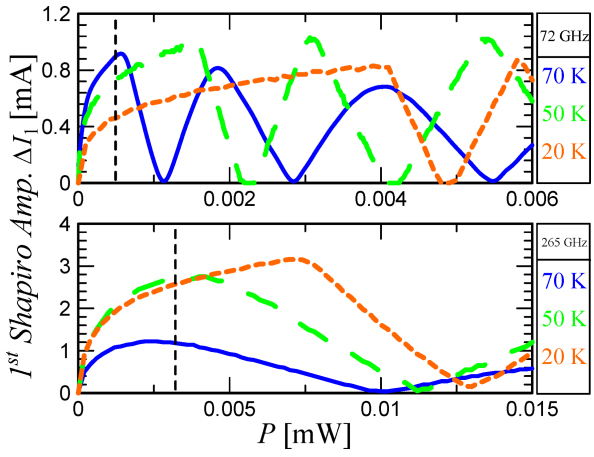

Figure 5: The first Shapiro step as function of P_{mw} at three temperatures and under a signal at 72 GHz (upper graph) and 265 GHz (lower graph). The black dashed lines indicate the power levels from the experiment.

Conclusion

The response in the form of the amplitudes of the Shapiro steps to an external signal with frequencies of 72 and 265 GHz was measured for 6 μm YBaCuO bicrystal junctions as a function of temperature in the range from 20 to 80 K. Nonmonotonic dependences of the step height were found in the region of a weak external signal with maxima at various points. The heights of the steps are consistent with calculations based on the RCSJ model and are qualitatively described by Bessel functions. The occurrence of the receiving optima is explained by the mutual influence of the varying critical current and the characteristic frequency. The maximum response to a 72 GHz signal has an optimum at 70 K, while to a 265 GHz signal – at 50 K.

For applied tasks of terahertz imaging [47], mixing [36], and Hilbert-transform spectral analysis [13] it is not possible to vary the incident power over a wide range. The power level is set there by losses, mismatch, and power absorption by the samples under study. Moreover, in applied problems one has to deal with low power levels and a linear response of detector [48]. Specifically in this area of the device operation, the effect described in the paper can be observed.

The obtained optima arise at certain JJ parameters (R_N, $I_c(T)$, C, and $\omega_c(T)$). Depending on these parameters, such maxima may appear [18,19] or not appear [17] in the measurements at an intermediate temperature. For specific purposes and operation regions, it is possible to tune JJ parameters to operate in the optimal regime [47,49]. In addition to JJ characteristics, the operating frequency or the frequency range is important. For low ω_{mw}, the change in the response of the Josephson junction will be small with the temperature [16] since at these frequencies the detection is not optimal. At the same time, at high temperatures, thermal noise will blur the step more than at low temperatures, and with increasing I_c the step height will increase. This also applies to high frequencies close or greater than the gap. Non-monotonous peculiarities in the response will occur at intermediate frequencies at, in fact, the most interesting range from a practical point of view. The same optima of the response can be achieved in the operation temperature range at a low power of the external signal with a higher normal resistance and critical current of the sample.

Therefore, lowering the temperature for the HTSC does not necessarily lead to an improvement in the detection properties of the Josephson junctions. An interesting question for further investigation is the search for an analytical expression for the optimal temperature of receiving an external signal of a given power and frequency for given JJ parameters.

Funding

The work is supported by the Russian Science Foundation (Project No. 20-79-10384).

ORCID® iDs

Leonid S. Revin - https://orcid.org/0000-0003-1645-4122
Andrey L. Pankratov - https://orcid.org/0000-0003-2661-2745

References

1. Longobardi, L.; Massarotti, D.; Stornaiuolo, D.; Galletti, L.; Rotoli, G.; Lombardi, F.; Tafuri, F. *Phys. Rev. Lett.* **2012,** *109,* 050601. doi:10.1103/physrevlett.109.050601
2. Revin, L. S.; Pankratov, A. L.; Gordeeva, A. V.; Yablokov, A. A.; Rakut, I. V.; Zbrozhek, V. O.; Kuzmin, L. S. *Beilstein J. Nanotechnol.* **2020,** *11,* 960–965. doi:10.3762/bjnano.11.80
3. Massarotti, D.; Longobardi, L.; Galletti, L.; Stornaiuolo, D.; Rotoli, G.; Tafuri, F. *Low Temp. Phys.* **2013,** *39,* 294–298. doi:10.1063/1.4795203
4. Lucignano, P.; Stornaiuolo, D.; Tafuri, F.; Altshuler, B. L.; Tagliacozzo, A. *Phys. Rev. Lett.* **2010,** *105,* 147001. doi:10.1103/physrevlett.105.147001
5. Couëdo, F.; Amari, P.; Feuillet-Palma, C.; Ulysse, C.; Srivastava, Y. K.; Singh, R.; Bergeal, N.; Lesueur, J. *Sci. Rep.* **2020,** *10,* 10256. doi:10.1038/s41598-020-66882-1
6. Yu, M.; Geng, H.; Hua, T.; An, D.; Xu, W.; Chen, Z. N.; Chen, J.; Wang, H.; Wu, P. *Supercond. Sci. Technol.* **2020,** *33,* 025001. doi:10.1088/1361-6668/ab5e13

7. Sharafiev, A.; Malnou, M.; Feuillet-Palma, C.; Ulysse, C.; Wolf, T.; Couëdo, F.; Febvre, P.; Lesueur, J.; Bergeal, N. *Supercond. Sci. Technol.* **2018,** *31,* 035003. doi:10.1088/1361-6668/aa9d48
8. Malnou, M.; Feuillet-Palma, C.; Ulysse, C.; Faini, G.; Febvre, P.; Sirena, M.; Olanier, L.; Lesueur, J.; Bergeal, N. *J. Appl. Phys.* **2014,** *116,* 074505. doi:10.1063/1.4892940
9. Gao, X.; Du, J.; Zhang, T.; Jay Guo, Y.; Foley, C. P. *J. Infrared, Millimeter, Terahertz Waves* **2017,** *38,* 1357–1367. doi:10.1007/s10762-017-0422-x
10. Gao, X.; Zhang, T.; Du, J.; Weily, A. R.; Guo, Y. J.; Foley, C. P. *Supercond. Sci. Technol.* **2017,** *30,* 095011. doi:10.1088/1361-6668/aa7cc1
11. Yu, M.; Geng, H.; Jiang, S.; Hua, T.; An, D.; Xu, W.; Chen, Z. N.; Li, J.; Wang, H.; Chen, J.; Wu, P. *Opt. Express* **2020,** *28,* 14271. doi:10.1364/oe.390997
12. Chantry, G. W. *Submillimetre Spectroscopy;* Academic Press: London and New York, 1971.
13. Snezhko, A. V.; Gundareva, I. I.; Lyatti, M. V.; Volkov, O. Y.; Pavlovskiy, V. V.; Poppe, U.; Divin, Y. Y. *Supercond. Sci. Technol.* **2017,** *30,* 044001. doi:10.1088/1361-6668/aa5ab5
14. Divin, Y.; Poppe, U.; Gubankov, V. N.; Urban, K. *IEEE Sens. J.* **2008,** *8,* 750–757. doi:10.1109/jsen.2008.923185
15. Du, J.; Smart, K.; Li, L.; Leslie, K. E.; Hanham, S. M.; Wang, D. H. C.; Foley, C. P.; Ji, F.; Li, X. D.; Zeng, D. Z. *Supercond. Sci. Technol.* **2015,** *28,* 084001. doi:10.1088/0953-2048/28/8/084001
16. Kautz, R. L.; Ono, R. H.; Reintsema, C. D. *Appl. Phys. Lett.* **1992,** *61,* 342–344. doi:10.1063/1.107931
17. Pavlovskiy, V. V.; Divin, Y. Y. *J. Commun. Technol. Electron.* **2019,** *64,* 1003–1010. doi:10.1134/s106422691908014x
18. Lyatti, M. V.; Tkachev, D. A.; Divin, Y. Y. *Tech. Phys. Lett.* **2006,** *32,* 860–863. doi:10.1134/s1063785006100130
19. Konopka, J.; Wolff, I.; Beuven, S.; Siegel, M. *IEEE Trans. Appl. Supercond.* **1995,** *5,* 2443–2446. doi:10.1109/77.403085
20. Klushin, A. M.; Prusseit, W.; Sodtke, E.; Borovitskii, S. I.; Amatuni, L. E.; Kohlstedt, H. *Appl. Phys. Lett.* **1996,** *69,* 1634–1636. doi:10.1063/1.117055
21. Sosso, A.; Andreone, D.; Lacquaniti, V.; Klushin, A. M.; He, M.; Klein, N. *IEEE Trans. Appl. Supercond.* **2007,** *17,* 874–877. doi:10.1109/tasc.2007.898581
22. Ota, Y.; Machida, M.; Koyama, T. *Phys. Rev. B* **2010,** *82,* 140509. doi:10.1103/physrevb.82.140509
23. Gao, J.; Boguslavskij, Y.; Klopman, B. B. G.; Terpstra, D.; Gerritsma, G. J.; Rogalla, H. *Appl. Phys. Lett.* **1991,** *59,* 2754–2756. doi:10.1063/1.105878
24. Siegel, M.; Heinz, E.; Seidel, P.; Hilarius, V. *Z. Phys. B: Condens. Matter* **1991,** *83,* 323–326. doi:10.1007/bf01313400
25. Russer, P. *J. Appl. Phys.* **1972,** *43,* 2008–2010. doi:10.1063/1.1661440
26. Likharev, K. K.; Semenov, V. K. *Radio Eng. Electron Phys.* **1971,** *16,* 1917–1922.
27. Baars, P.; Richter, A.; Merkt, U. *Phys. Rev. B* **2003,** *67,* 224501. doi:10.1103/physrevb.67.224501
28. Revin, L. S.; Chiginev, A. V.; Pankratov, A. L.; Masterov, D. V.; Parafin, A. E.; Luchinin, G. A.; Matrozova, E. A.; Kuzmin, L. S. *J. Appl. Phys.* **2013,** *114,* 243903. doi:10.1063/1.4856915
29. Masterov, D. V.; Parafin, A. E.; Revin, L. S.; Chiginev, A. V.; Skorokhodov, E. V.; Yunin, P. A.; Pankratov, A. L. *Supercond. Sci. Technol.* **2017,** *30,* 025007. doi:10.1088/1361-6668/30/2/025007
30. Revin, L. S.; Pankratov, A. L.; Masterov, D. V.; Parafin, A. E.; Pavlov, S. A.; Chiginev, A. V.; Skorokhodov, E. V. *IEEE Trans. Appl. Supercond.* **2018,** *28,* 1100505. doi:10.1109/tasc.2018.2844354
31. Revin, L.; Pankratov, A.; Gordeeva, A.; Masterov, D.; Parafin, A.; Zbrozhek, V.; Kuzmin, L. *Appl. Sci.* **2020,** *10,* 7667. doi:10.3390/app10217667
32. Stephen, M. J. *Phys. Rev.* **1969,** *186,* 393–397. doi:10.1103/physrev.186.393
33. Likharev, K. K. *Dynamics of Josephson Junctions and Circuits;* Gordon and Breach Science Publishers: New York, 1986.
34. Il'ichev, E.; Zakosarenko, V.; IJsselsteijn, R. P. J.; Hoenig, H. E.; Meyer, H.-G.; Fistul, M. V.; Müller, P. *Phys. Rev. B* **1999,** *59,* 11502–11505. doi:10.1103/physrevb.59.11502
35. Rosenthal, P. A.; Grossman, E. N. *IEEE Trans. Microwave Theory Tech.* **1994,** *42,* 707–714. doi:10.1109/22.285085
36. Du, J.; Weily, A. R.; Gao, X.; Zhang, T.; Foley, C. P.; Guo, Y. J. *Supercond. Sci. Technol.* **2017,** *30,* 024002. doi:10.1088/0953-2048/30/2/024002
37. Zhang, Y. Dynamics and applications of long Josephson junctions. Ph.D. Thesis, Chalmers University of Technology, Göteborg, Sweden, 1993.
38. Il'ichev, E.; Dörrer, L.; Schmidl, F.; Zakosarenko, V.; Seidel, P.; Hildebrandt, G. *Appl. Phys. Lett.* **1996,** *68,* 708–710. doi:10.1063/1.116599
39. Fedorov, K. G.; Pankratov, A. L. *Phys. Rev. B* **2007,** *76,* 024504. doi:10.1103/physrevb.76.024504
40. Fedorov, K. G.; Pankratov, A. L. *Phys. Rev. Lett.* **2009,** *103,* 260601. doi:10.1103/physrevlett.103.260601
41. Gordeeva, A. V.; Pankratov, A. L. *Phys. Rev. B* **2010,** *81,* 212504. doi:10.1103/physrevb.81.212504
42. Revin, L. S.; Pankratov, A. L.; Chiginev, A. V.; Masterov, D. V.; Parafin, A. E.; Pavlov, S. A. *Supercond. Sci. Technol.* **2018,** *31,* 045002. doi:10.1088/1361-6668/aaacc3
43. Kupriyanov, M. Y.; Khapaev, M. M.; Divin, Y. Y.; Gubankov, V. N. *JETP Lett.* **2012,** *95,* 289–294. doi:10.1134/s0021364012060069
44. Hilgenkamp, H.; Mannhart, J. *Rev. Mod. Phys.* **2002,** *74,* 485–549. doi:10.1103/revmodphys.74.485
45. Kautz, R. L. *J. Appl. Phys.* **1995,** *78,* 5811–5819. doi:10.1063/1.359644
46. Braiman, Y.; Ben-Jacob, E.; Imry, Y. *IEEE Trans. Magn.* **1981,** *17,* 784–787. doi:10.1109/tmag.1981.1060952
47. Du, J.; Hellicar, A. D.; Hanham, S. M.; Li, L.; Macfarlane, J. C.; Leslie, K. E.; Foley, C. P. *J. Infrared, Millimeter, Terahertz Waves* **2011,** *32,* 681–690. doi:10.1007/s10762-010-9650-z
48. Lyatti, M.; Divin, Y.; Volkov, O.; Pavlovskii, V.; Gubankov, V.; Urban, K. *IEEE Trans. Appl. Supercond.* **2007,** *17,* 332–335. doi:10.1109/tasc.2007.898188
49. Gundareva, I.; Divin, Y. *IEEE Trans. Appl. Supercond.* **2016,** *26,* 1100204. doi:10.1109/tasc.2016.2520465

BEILSTEIN JOURNAL OF NANOTECHNOLOGY

Design aspects of $Bi_2Sr_2CaCu_2O_{8+\delta}$ THz sources: optimization of thermal and radiative properties

Mikhail M. Krasnov[1,2], Natalia D. Novikova[1,2], Roger Cattaneo[3], Alexey A. Kalenyuk[3,4,5] and Vladimir M. Krasnov[*2,3]

Full Research Paper

Open Access

Address:
[1]Keldysh Institute of Applied Mathematics of RAS, Moscow, Russia, [2]Moscow Institute of Physics and Technology, 141700 Dolgoprudny, Russia, [3]Department of Physics, Stockholm University, AlbaNova University Center, SE-10691 Stockholm, Sweden, [4]Institute of Metal Physics of National Academy of Sciences of Ukraine, 03142 Kyiv, Ukraine and [5]Kyiv Academic University, 03142 Kyiv, Ukraine

Email:
Vladimir M. Krasnov[*] - vladimir.krasnov@fysik.su.se

* Corresponding author

Keywords:
high-temperature superconductivity; Josephson junctions; numerical modelling; terahertz sources

Beilstein J. Nanotechnol. **2021,** *12,* 1392–1403.
https://doi.org/10.3762/bjnano.12.103

Received: 30 September 2021
Accepted: 02 December 2021
Published: 21 December 2021

This article is part of the thematic issue "Intrinsic Josephson effect and prospects of superconducting spintronics".

Associate Editor: A. J. Meixner

Abstract

Impedance matching and heat management are important factors influencing the performance of terahertz sources. In this work we analyze thermal and radiative properties of such devices based on mesa structures of a layered high-temperature superconductor $Bi_2Sr_2CaCu_2O_{8+\delta}$. Two types of devices are considered containing either a conventional large single crystal or a whisker. We perform numerical simulations for various geometrical configurations and parameters and make a comparison with experimental data for the two types of devices. It is demonstrated that the structure and the geometry of both the superconductor and the electrodes play important roles. In crystal-based devices an overlap between the crystal and the electrode leads to appearance of a large parasitic capacitance, which shunts terahertz emission and prevents impedance matching with open space. The overlap is avoided in whisker-based devices. Furthermore, the whisker and the electrodes form a turnstile (crossed-dipole) antenna facilitating good impedance matching. This leads to more than an order of magnitude enhancement of the radiation power efficiency in whisker-based, compared to crystal-based, devices. These results are in good agreement with presented experimental data.

Introduction

Tunable, monochromatic, continuous-wave (CW), compact, and power-efficient terahertz (THz) sources of electromagnetic waves (EMW) are required for a broad variety of applications [1]. However, the key obstacle, colloquially known as “the THz gap” [1], is caused by a low radiation power efficiency (RPE) of THz sources. Despite a remarkable progress achieved by semi-

conducting quantum cascade lasers (QCL's) [2,3], their RPE drops well below the percent level at low THz frequencies [4-6]. Furthermore, operation of QCLs is limited by the thermal smearing of quantum levels, which becomes significant at frequencies $f \lesssim k_B T/h$, where k_B and h are the Boltzmann and the Planck constant, respectively, and T is the operation temperature. For room temperature, T = 300 K, this happens at $f \simeq 6.25$ THz. QCLs have to be cooled down in order to operate at significantly lower primary frequencies [4-6]. Although room temperature operation of QCLs at low frequencies can be achieved via mixing and down conversion of higher primary frequencies, this comes at the expense of dramatic reduction of RPE [2,3,5,7,8].

The layered high-temperature superconductor Bi-2212 ($Bi_2Sr_2CaCu_2O_{8+\delta}$) may provide an alternative possibility for the creation of cryogenic CW THz sources [9-22]. Bi-2212 represents a natural stack of atomic scale intrinsic Josephson junctions (IJJs) [23-26]. Josephson junctions have an inherently tunable oscillation frequency, $f_J = (2e/h)V$, where e is electron charge and V is the bias voltage per junction. The frequency is limited only by the superconducting energy gap, which can be in excess of 30 THz for Bi-2212 [27,28]. A broad range tunability of emission in the whole THz range 1–11 THz has been demonstrated for small Bi-2212 mesa structures [14].

The operation of Josephson emitters is limited by two primary obstacles: self-heating and impedance mismatch. Josephson devices stop operating when their temperature exceeds the superconducting critical temperature T_c. Self-heating in Bi-2212 mesa structures has been extensively studied [28-39]. Although T_c of Bi-2212 may be quite high, up to ≃95 K [28], self-heating is substantial due to the low heat conductance of superconductors. Self-heating limits the maximum bias voltage that can be reached without critical overheating of a mesa and, therefore, the maximum achievable frequency and emission power. Furthermore, as pointed out in [40], self-heating creates a general limitation for the maximal achievable emission power for any cryogenic device (not only superconducting). Taking into account the limited cooling power of compact cryorefrigerators (sub-watt at low T), a device with RPE ≈ 1% would not be able to emit significantly more than 1 mW. Therefore, larger emission power from cryogenic sources may only be achieved via enhancement of the RPE. The maximum achievable RPE is 50% in the case of perfect match between the device microwave impedance and that of open space [41]. However, the reported RPE of Bi-2212 THz sources is much smaller [14] due to a significant impedance mismatch. Therefore, improvement of THz sources requires a proper design of cooling elements, to handle self-heating, and impedance matching microwave antennas, to improve RPE.

In this work we analyze design aspects of THz sources based on Bi-2212 mesa structures. Thermal and radiative properties are studied for two types of devices containing either a conventional large single crystal or a needle-like whisker. We present numerical simulations for various geometrical configurations and parameters and make a comparison with experimental data. It is demonstrated that the structure and the geometry of both the superconductor and the electrodes play important roles. Electrodes provide an effective heat sink channel and help in the reduction of self-heating. They also influence radiative properties. However, this influence is opposite for crystal-based (worsening) and whisker-based (improvement) devices. The superconductor geometry is also crucial. Devices based on large crystals suffer from a large parasitic capacitance at the overlap between the crystal and the electrodes. It prevents good impedance matching and reduces RPE. The overlap is avoided in whisker-based devices. Moreover, the whisker itself, together with the electrodes, forms a turnstile (crossed-dipole) antenna, facilitating good impedance matching. We show that this can lead to more than an order of magnitude enhancement of RPE, compared to crystal-based devices. Those results are in good agreement with experimental data, which demonstrate that THz emission from whisker-based devices is much larger than from crystal-based devices with the same geometry.

Experimental Results

Figure 1a,b show optical images of two studied devices. They have a similar geometry and were fabricated using the same procedure. The main difference is that the device in panel (a) was made using a whisker while that in panel (b) was made using a conventional single crystal. Figure 1c shows sketches of both devices. Bi-2212 whiskers have typical aspect ratios of 100:10:1 in the a, b, and c crystallographic directions, respectively [42]. Our whiskers have typical dimensions of several hundreds of micrometers along a, 20–40 μm along b, and just a few micrometers along c. The conventional single crystal is much larger with sizes of almost a square millimeter in the ab-plane and several hundreds of micrometers in the c-direction.

The fabrication process starts by gluing a corresponding crystal on a 5 × 5 mm^2 sapphire substrate using epoxy glue. The crystal is cleaved under ambient conditions. After that the sample is immediately put into a deposition chamber and a protective gold layer of 60–80 nm is deposited to avoid surface passivation. Next, a line pattern of photoresist is written with a length of 100–200 μm and a width of 5–15 μm on a flat portion of Bi-2212 surface, followed by argon-ion etching of the unprotected parts of Au and Bi-2212, the deposition of insulating SiO_2 or CaF_2 layers and a lift-off of the photoresist at the line. The depth of Bi-2212 etching at this stage ($d_m \approx$ 200–400 nm)

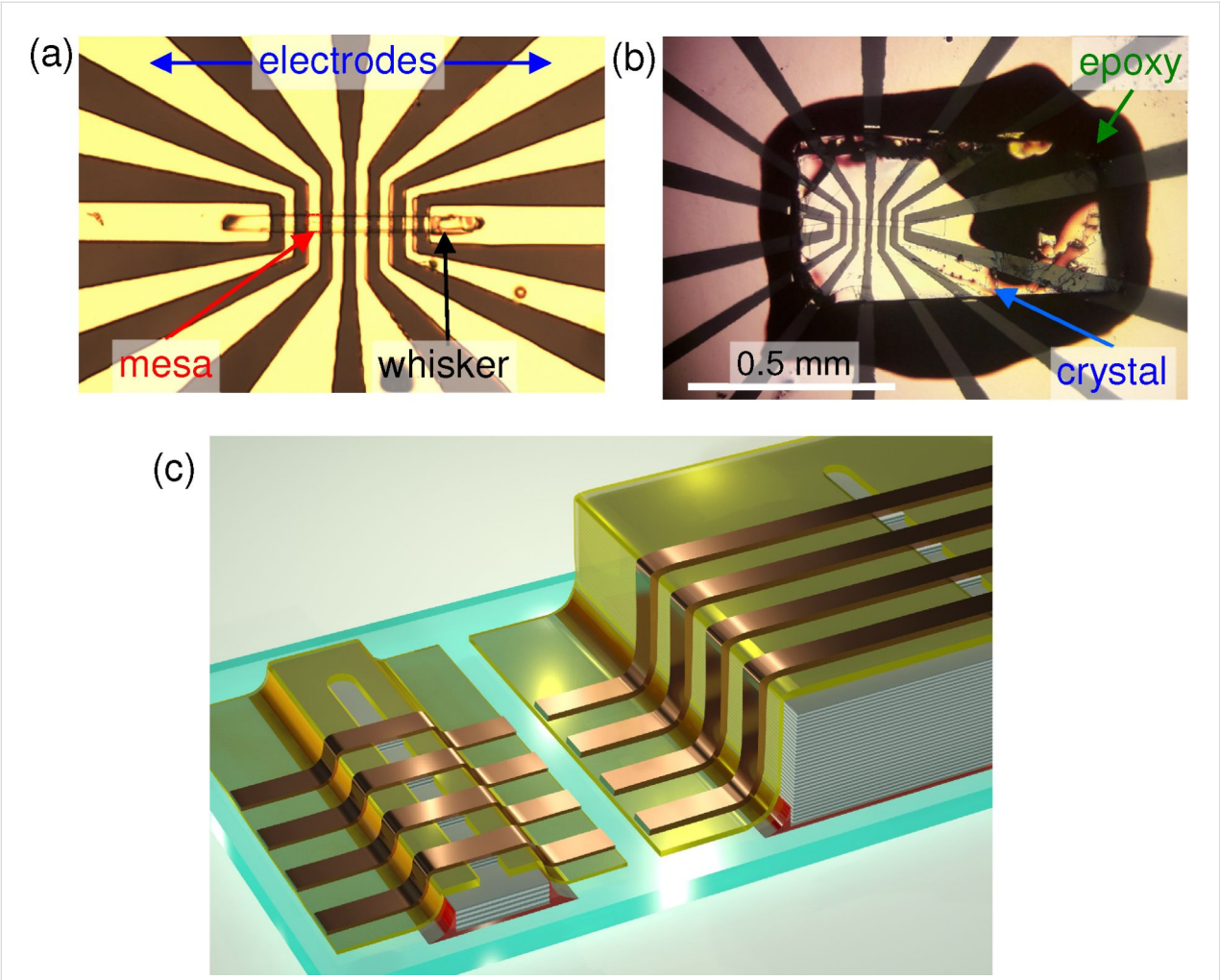

Figure 1: Optical images of (a) a whisker and (b) a crystal-based device with similar electrode geometries. (c) A sketch of both devices.

defines the height of mesas and the number of IJJ in the device, $N = d_m/s$, where $s \simeq 1.5$ nm is the interlayer spacing between double CuO_2 layers in Bi-2212. After that a top Ti/Au layer with a total thickness of approx. 200 nm is deposited. Finally, several electrodes, crossing the line in a perpendicular direction, are made by photolithography and argon-ion etching. Mesa structures are formed at the overlap between the line and the electrodes, as indicated in Figure 1a.

Figure 2a,b shows current–voltage (I–V) characteristics of mesas of whisker- and crystal-based devices, respectively. The I–V curves are fairly similar. They contain multiple branches due to one-by-one switching of IJJs from the superconducting to the resistive state. The are $N \approx 200$ and ≈300 IJJs in whisker and crystal mesas, respectively. Both the whisker and the crystal have a similar suppressed $T_c \approx 65$–70 K and low critical current densities of IJJs, $J_c \approx 100$ A/cm^2, indicating a strongly underdoped state of Bi-2212 [43].

Radiative properties of our whisker-based devices were analyzed in [40]. A significant EMW emission at $f \simeq 4.2$ THz with a record-high RPE reaching 12% was reported. The emission occurs at the step in the I–V marked in Figure 2a. In Figure 2c we show results of in situ THz generation-detection experiment on a whisker-based device. We follow the procedure developed in [14], where details of the technique can be found. We use one mesa with the I–V like in Figure 2a as a generator, and another mesa on the same device as a switching current detector. The detector mesa is biased by a small alternating current and the generator by a direct current in the same range as in Figure 2a. Figure 2c shows the ac resistance of the detector mesa, R_{det}, as a function of dissipation power in the generator mesa, $P_{gen} = I_{gen}V_{gen}$. It is anticipated that self-heating is monotonic (approximately linear) with the dissipation power, while the emission is nonmonotonic [14,40] because it occurs at certain bias voltages, corresponding to geometrical resonances in the mesa [14,16,24,26]. From

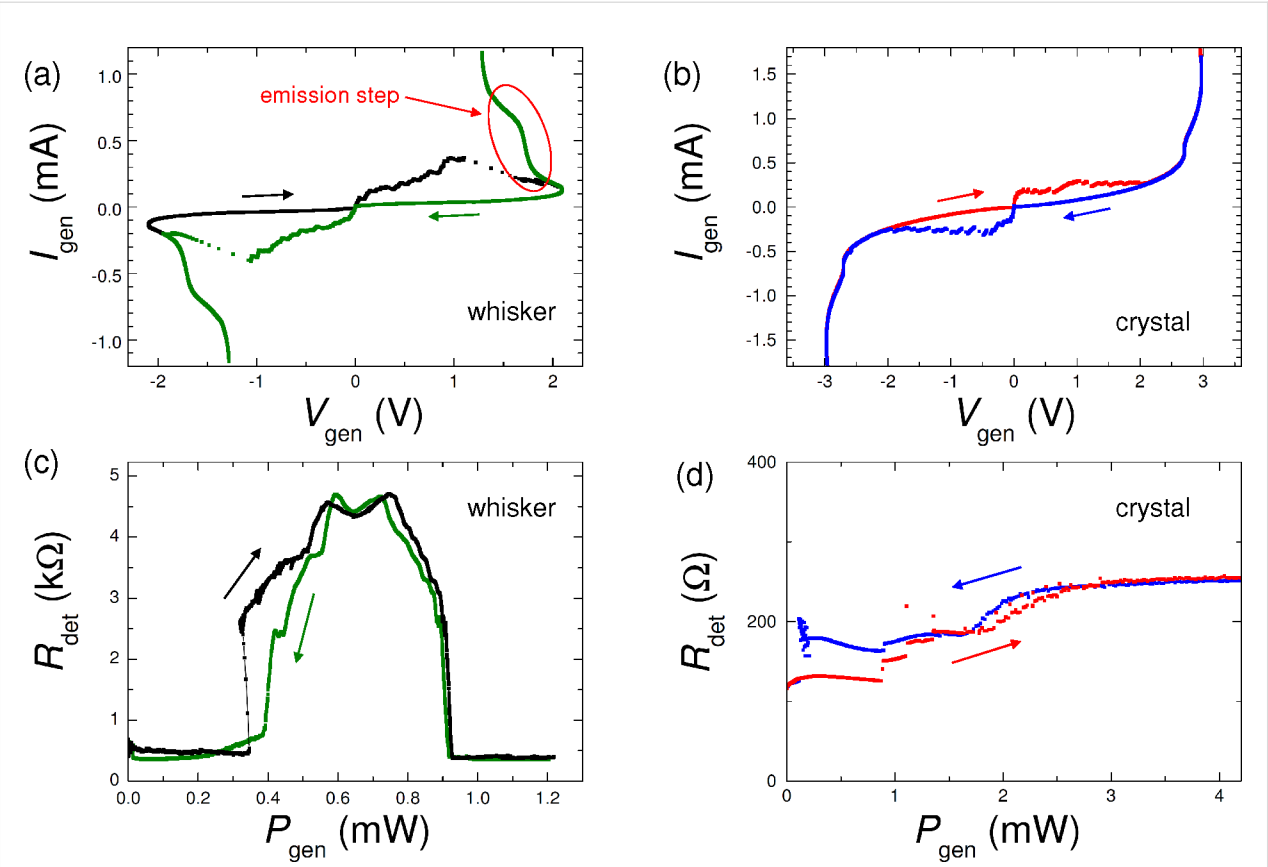

Figure 2: Current–voltage characteristics of mesa structures on (a) whisker- and (b) crystal-based devices. (c, d) On-chip generation–detection experiment for (c) whisker- and (d) crystal-based devices. Here, the ac resistance of the detector mesa is shown as function of the total dc dissipation power, P_{gen}, of the generator mesa. For the whisker-based device (c) a profound emission occurs at the step in the *I*–*V* marked in panel (a). For the crystal-based device (d) only a small monotonic increment of R_{det} vs P_{gen} is observed, caused by gradual self-heating.

Figure 2c it is seen that a profound EMW emission occurs in a whisker-based mesa, leading to more than an order of magnitude enhancement of R_{det}. The emission occurs in a specific bias range, corresponding to the step in the *I*–*V* marked in Figure 2a. To avoid repetitions we address the reader to [40] for more details.

In Figure 2d we show similar generation–detection data for the crystal-based device from Figure 1b and Figure 2b. In contrast to the whisker-based device, here we observe only a small monotonic increment of R_{det} with increasing P_{get}, which is the consequence of self-heating. On top of it there may be a small non-monotonic signal at 0.5 mW $\lesssim P_{gen} \lesssim$ 1.5 mW, which can be attributed to THz emission. This is qualitatively similar to results reported earlier for small mesas on crystal-based devices [14]. For whisker-based mesas the ratio between emission and self-heating responses is quantitatively different: The emission peak $R_{det}(P_{get})$ is much larger than the monotonic self-heating background. This indicates a much larger RPE in whisker-based devices [40].

Numerical Results

To understand the reported difference between crystal- and whisker-based devices and to suggest possible optimizations of THz sources, we performed numerical modelling using the 3D finite element software Comsol Multiphysics. Below, we present simulations of thermal and radiative properties calculated using “Heat Transfer” and “RF” modules, respectively. The presented simulations contain several simplifications and, therefore, are not aiming to self-consistently predict the extent of self-heating, ΔT, or the radiative power. Their goal is to reveal general trends and geometrical factors contributing to design aspects of Bi-2212 THz sources.

Modelling of heat transfer

Accurate analysis of self-heating in Bi-2212 mesas is a complex non-linear problem [28,30-32,36,38]. Simulations presented below are made for the base temperature T_0 = 10 K and for sizes similar to the actual devices, shown in Figure 1: substrate 5 × 5 × 0.3 mm^3, crystal 1 × 1 × 0.3 mm^3, whisker 300 × 30 × 3 μm^3 and mesa 30 × 30 × 0.3 μm^3. The thickness

of gold electrode is 200 nm. The thickness of epoxy layer, d_e, depends on the quantity of applied glue, area of the crystal, experience, and luck. For whisker devices we managed to reduce it to $d_e \lesssim 1$ μm. To do so we use a tiny amount of epoxy and also squeeze it out by pressing the whisker upon gluing. This procedure is effective for whiskers due to their small area. For large crystals, requiring more epoxy, this is more difficult and the remaining epoxy layer is usually thicker. For this reason we assume the epoxy thickness $d_e = 1$ μm for whisker and $d_e = 5$ μm for crystal-based devices.

The monocrystalline sapphire substrate has a very good thermal conductivity, κ, at low T. The substrate is thermally well anchored with the boundary condition at the bottom surface $T = T_0$. Due to the large κ, temperature variation in the substrate is negligible. Therefore, we use a constant $\kappa = 3000\ \mathrm{W{\cdot}K^{-1}{\cdot}m^{-1}}$ for the substrate, corresponding to a monocrystalline sapphire at $T \simeq 10$ K [44]. In contrast, the epoxy used for gluing Bi-2212 crystals has a poor heat conductance at low T. We do not consider its T-dependence because it acts just as a heat blocking layer, which we assume to have $\kappa_e = 0.0025\ \mathrm{W{\cdot}K^{-1}{\cdot}m^{-1}}$. However, it is necessary to take into account actual $\kappa(T)$ dependencies of the other two materials, namely Bi-2212 and polycrystalline gold electrodes. At low T both have linear $\kappa(T)$. For Bi-2212 we assume $\kappa_{ab}(T) = 0.1\ T(K)\ \mathrm{W{\cdot}K^{-1}{\cdot}m^{-1}}$ [45] with an anisotropy $\kappa_{ab}/\kappa_c = 8$ [46]. For a polycrystalline gold thin film we use $\kappa(T) = 3\ T(K)\ \mathrm{W{\cdot}K^{-1}{\cdot}m^{-1}}$ [32]. The heat is produced in the mesa volume with a total power of 1 mW and uniform density.

Figure 3 represents heat transfer simulations for a whisker without an electrode. Figure 3a,b shows sketches of the device and the x–z cross-section through the mesa (not to scale), respectively. Figure 3c–e shows the temperature distribution for the case when the sample is placed in vacuum. Figure 3c shows the top view, Figure 3d the x–z cross section through the mesa (stretched by a factor of three in the vertical direction), and Figure 3e shows the temperature distribution in the mesa (stretched by a factor of 50 in the vertical direction). In this case the heat can only sink into the substrate. As seen from Figure 3d, the epoxy layer between the substrate and the whisker blocks heat flow into the substrate and causes substantial heating of the whole whisker with the maximum temperature in the center of the mesa reaching $T_{max} = 85.2$ K.

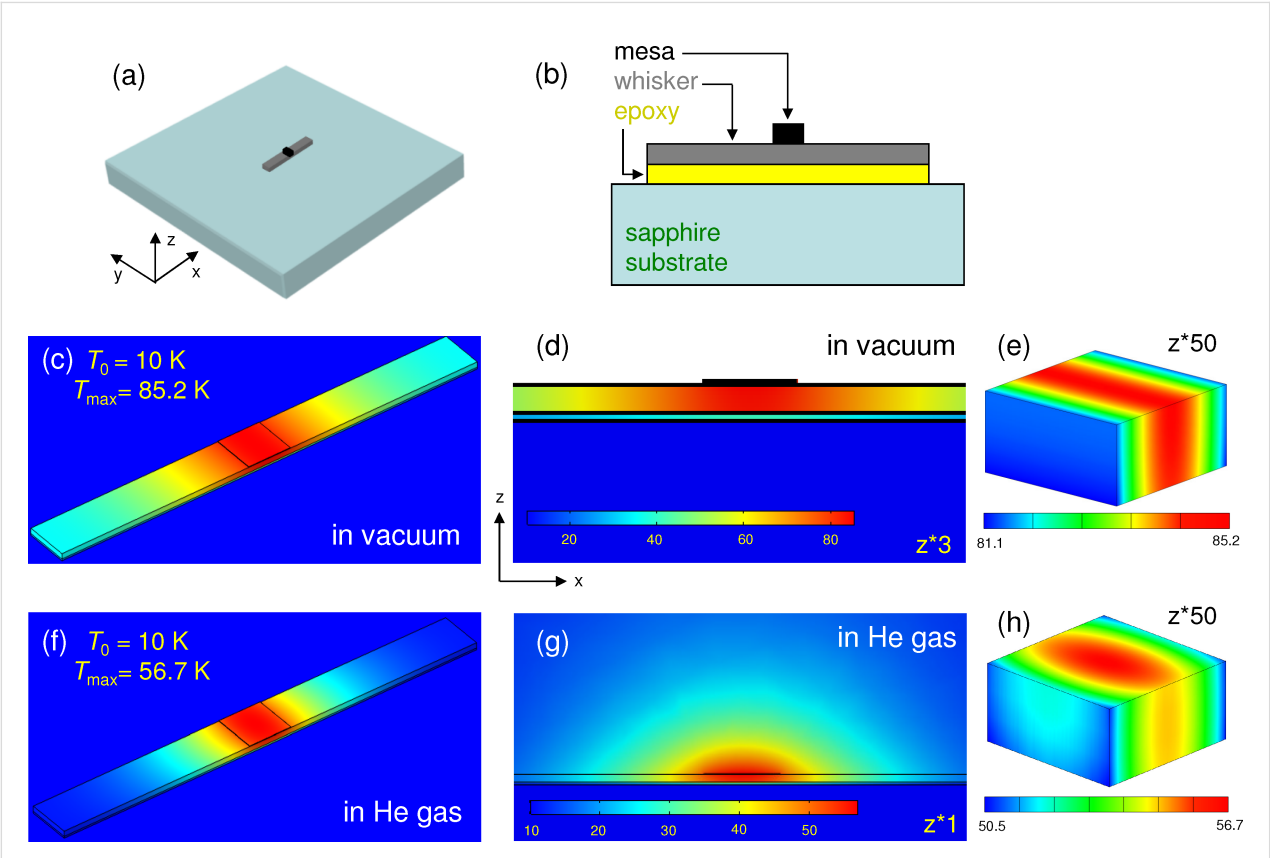

Figure 3: Heat transport in a whisker-based device without electrodes. (a) A sketch of the device and (b) a cross section through the mesa (not to scale). (c–e) Calculated temperature distribution for the device in vacuum. (f–h) The same for the device in exchange He gas.

Figure 3f–h show simulations for the same device in exchange ^{4}He gas. Clearly, it helps to cool down the device, although self-heating still remains substantial, T_{max} = 56.7 K.

Figure 4 shows simulations for the whisker-based device with a top Au electrode. Outside the whisker the electrode is in a direct contact with the sapphire substrate (no epoxy). This creates a good thermal sink and, as a result, T_{max} falls to ≈23 K. Addition of an exchange gas does not play a major role in this case because the main heat sink channel is provided by the electrode [33,34] acting as a heat spreading layer [29].

Figure 5 shows the temperature distribution in a crystal-based device in vacuum without electrodes (Figure 5a) and with electrodes (Figure 5b). The main difference is that unlike in the whisker-device, Figure 3, there is no major temperature jump in the epoxy layer between the crystal and the substrate. This occurs because the heat resistance, $R_h = d/(\kappa A)$, is inversely proportional to the area A. Due to a much larger crystal area, R_h of epoxy is negligible despite a low κ and larger d_e = 5 μm. Adding an electrode and He exchange gas further reduces self-heating, but their effect is not as profound as for the whisker-device, Figure 4, due to the effective heat sink channel into the substrate.

In many cases, self-heating is dominated by some bottlenecks. The origin of blocks to the heat flow is clearly revealed from inspection of the thermal gradients in the mesa where the heat is produced and by estimation of heat resistances of different elements. For example, from Figure 3e it is seen that for a bare mesa on a whisker the heat is flowing along the whisker. This occurs because the epoxy layer with a large R_h = 44.4 K/mW blocks direct (vertical) heat flow into the substrate. However, the maximal self-heating, ΔT = 75.2 K, is almost two times larger, implying that there is yet another bottleneck. It is caused by a small bc (yz) cross sectional area of the whisker. This additional in-plane heat resistance, $R_h \approx 30$ K/mW, corresponds to the effective length of heat spreading along the whisker comparable to the size of the mesa, as can be seen from Figure 3d. For a whisker mesa with an electrode the thermal gradient changes the direction, see Figure 4e, indicating that the heat is flowing predominantly along the electrode. For comparison, the c-axis

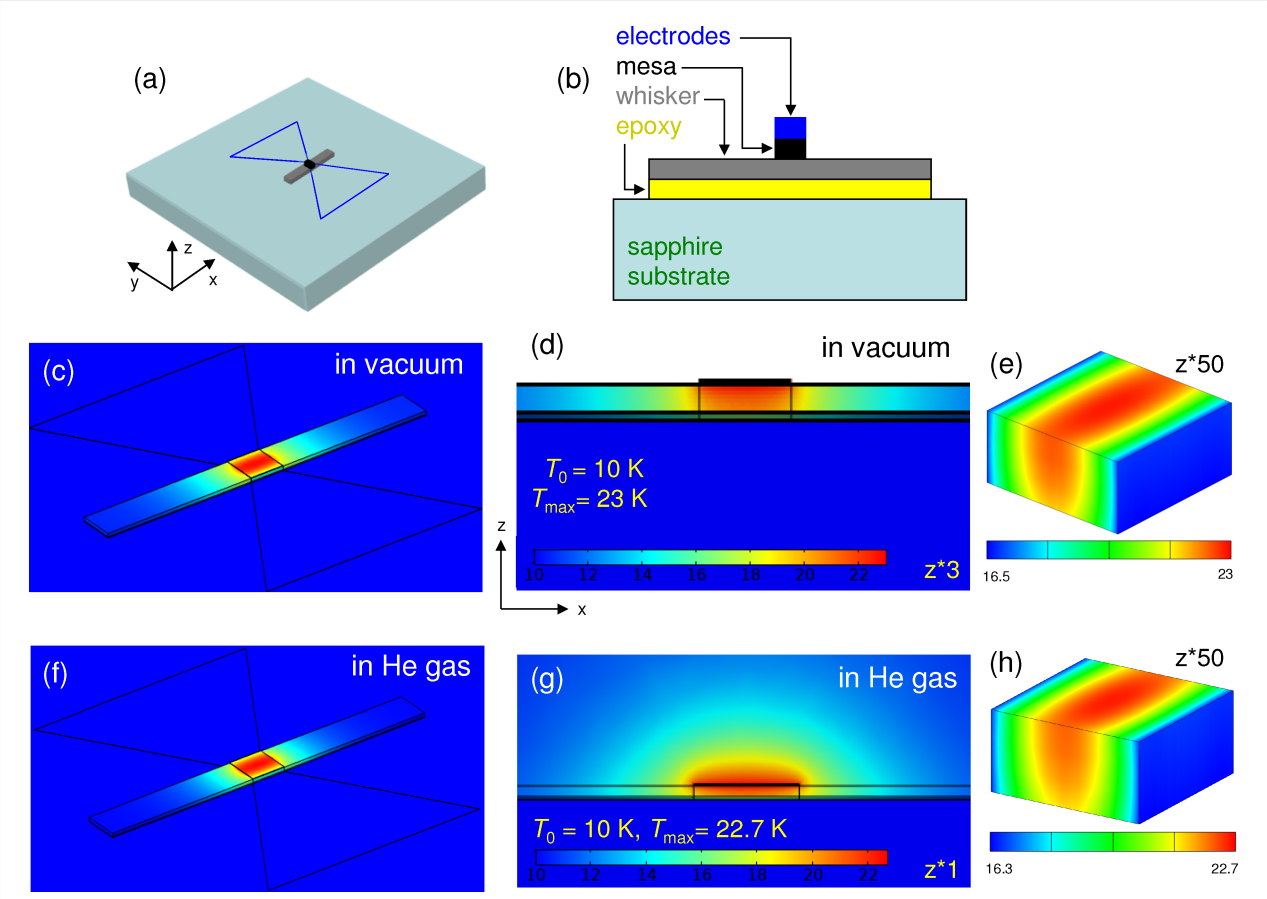

Figure 4: Heat transport in a whisker-based device with an electrode. (a) A sketch of the device and (b) a cross section through the mesa (not to scale). (c–e) Calculated temperature distribution for the device in vacuum. (f–h) The same for the device in exchange He gas.

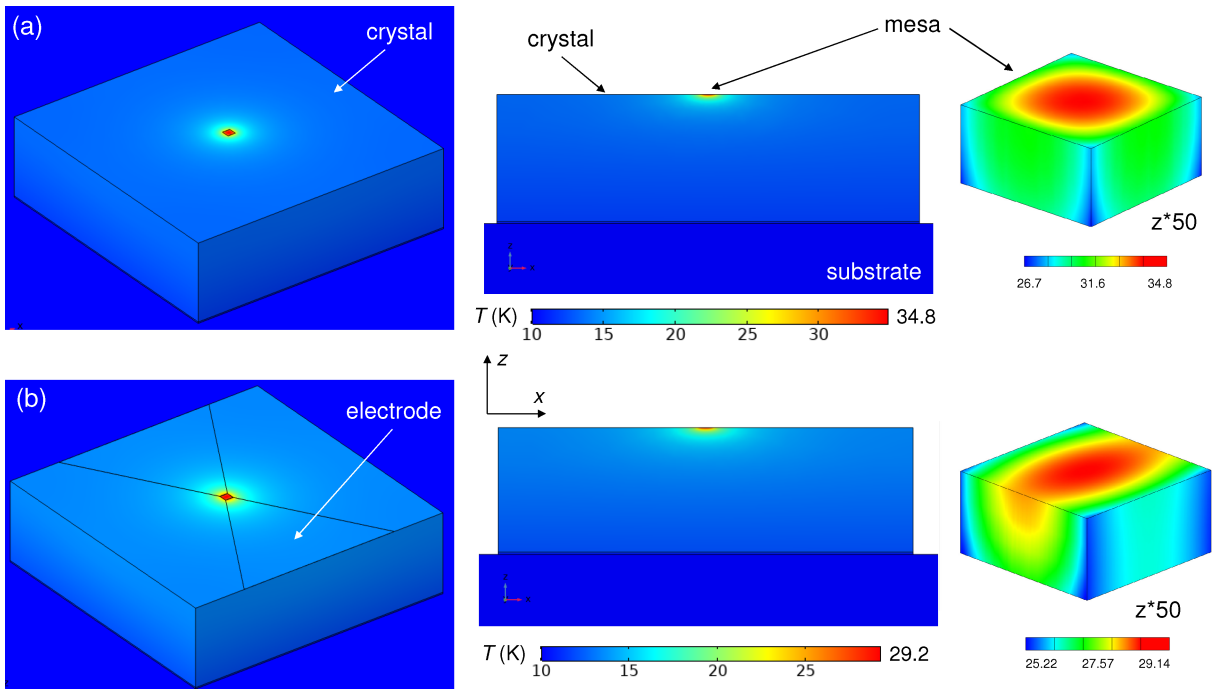

Figure 5: Heat transport in a crystal-based device in vacuum (a) without electrodes, (b) with electrodes. The left panels represent top views, the middle panels the *x*–*z* cross section through the mesa, and the right panels the mesa (expanded by factor of 50 in the *z*-direction).

heat resistance of the mesa and the whisker are only 1.3 K/mW at $T = 20$ K. This implies that a significant reduction of self-heating in whisker devices could be achieved by replacing epoxy with a better heat-conducting material, for example, by soldering [10].

For a mesa on a crystal, Figure 5, the thermal gradient is fairly spherical (taking into account the anisotropy $\kappa_{ab}/\kappa_c = 8$). In this case self-heating is dominated by the spreading heat resistance in the crystal [29,31], $R_h \simeq 1/2L\sqrt{\kappa_{ab}\kappa_c} = 23.6$ K/mW at $T = 20$ K, where $L = 30$ µm is the in-plane size of the mesa. For comparison, the heat resistance of epoxy is only 2 K/mW for $d_e = 5$ µm. Consequently, epoxy is not the major problem for crystal devices (unless it is very thick $d_e > 50$ µm). For a real device self-heating will depend on the actual geometry, thicknesses, and material parameters. However, our analysis indicates that the optimization is much more important and efficient for whisker devices. This is caused by the low intrinsic *c*-axis heat resistance of whiskers due to the small thickness.

Modelling of radiative properties

For the calculation of THz properties, a mesa (the source) is modelled as a lumped port with a fixed voltage amplitude. Unlike the heat transfer problem, this problem is linear so that the results directly scale with the source amplitude. To ease the understanding, we use an amplitude of 1 V. Simulations are made in a sphere with the radius R, which is chosen to be at least two times larger than the largest device size and the wavelength in vacuum. A perfectly matching layer with the thickness $0.1R$ is added outside the sphere to avoid reflections. We checked that the presented results do not depend on R and, therefore, properly describe far-field characteristics.

Figure 6 shows radiative characteristics for three device geometries, sketched in the leftmost panels: Figure 6a shows a mesa (red) on a large crystal (black) with an attached metallic electrode (yellow), mounted on a dielectric substrate; Figure 6b shows a mesa on a large crystal with a capping metallic layer, without electrode; Figure 6c shows a mesa on a thin whisker (black) with an attached electrode. Simulations are performed for $f = 1$ THz and the sizes are selected relative to the wavelength in vacuum, $\lambda_1 = 300$ µm: the substrate and the in-plane crystal size as well as whisker and electrode lengths are $\lambda_1/2 = 150$ µm; the substrate height is $\lambda_1/4 = 75$ µm; the in-plane mesa size, as well as whisker and electrode widths are $\lambda_1/8 = 37.5$ µm; the crystal height is $\lambda_1/10 = 30$ µm; mesa and whisker heights and the electrode thickness are $\lambda_1/100 = 3$ µm; the simulation sphere radius is $R = 2\lambda_1$ and the perfectly matching layer thickness is $0.2\lambda_1$. The sizes and parameters are chosen to be similar (but not identical) to studied samples in order to optimize the mesh size and the calculation time. Therefore, such simulations serve for a qualitative illustration of the

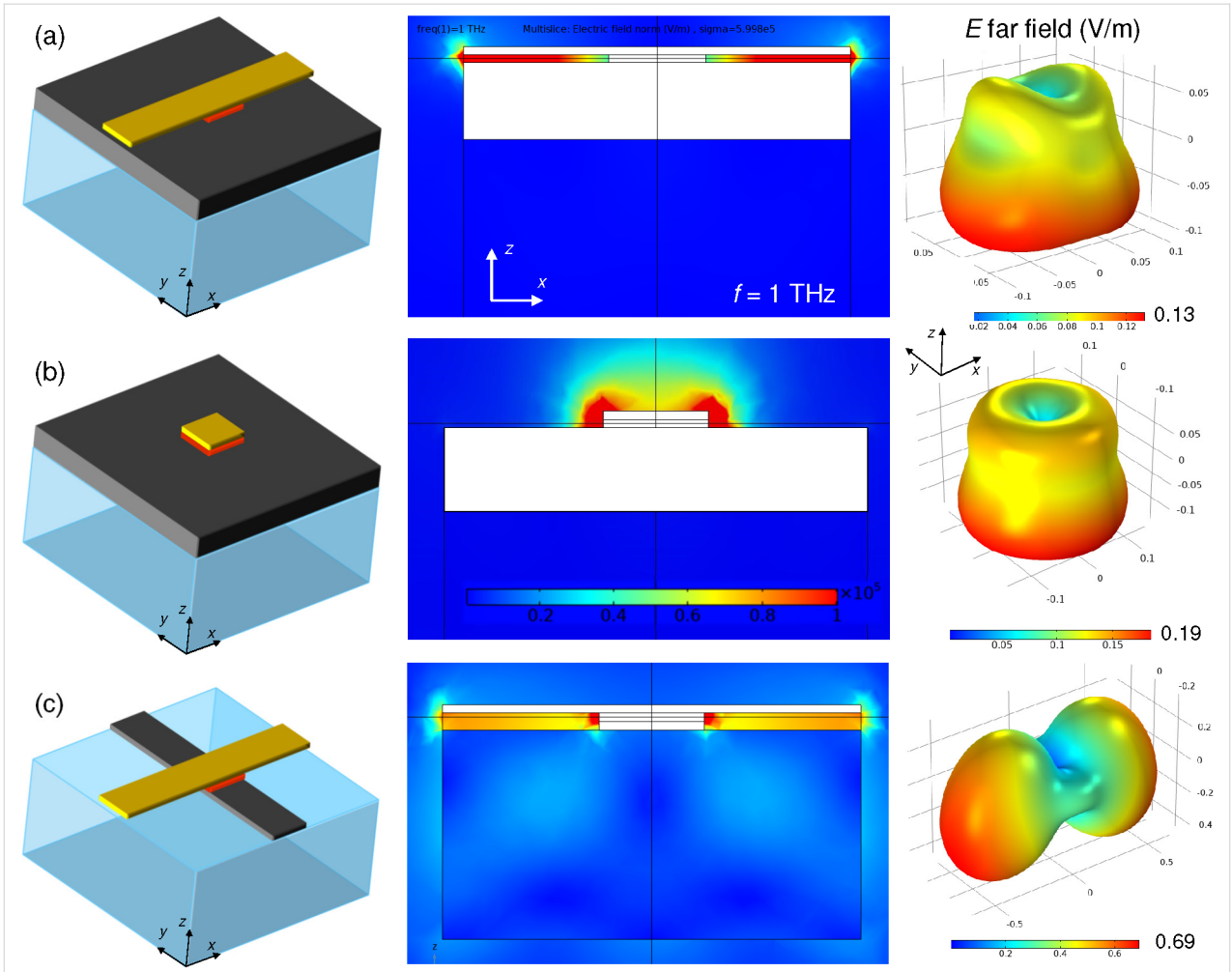

Figure 6: Simulated radiative properties at f = 1 THz for (a) crystal based device, (b) crystal-based device without electrodes, and (c) whisker-based device. Left panels show sketches of devices; middle panels – electric field amplitudes in the x-z cross-section through the mesa; right panels represent radiation patterns for the electric field amplitude in the far-field (outside the simulation sphere). Note a strong field concentration between the crystal and the electrode in (a).

difference between crystal- and whisker-based devices and the role of the electrodes. The conductivity of electrode and whisker is set to ≃6×10^5 $(\Omega{\cdot}\mathrm{m})^{-1}$ and the relative dielectric permittivity of the substrate is $\varepsilon_r = 10$. First we consider the case without dielectric losses, $\tan(\delta) = 0$. The middle panels in Figure 6 show the local distributions of electric field amplitudes in the xz crosssection through the mesa. The same color scale is used, indicated in the middle panel of Figure 6b. The rightmost panels represent far-field radiation patterns (directionality diagrams) of the electric field amplitude outside the simulation sphere.

From comparison of the middle panels in Figure 6a,b it can be seen that the electric field distribution is significantly different. In the crystal-based device the field is locked between the electrode and the crystal. This occurs because the electrode is laying on top of the crystal, forming together a parallel plate capacitor. The field is trapped inside this capacitor and goes neither in the substrate, nor into open space in the top hemisphere (with the exception of small edge fields). If we take a realistic specific capacitance of $C_\square \approx 0.1$–1 fF/μm^2 and an electrode area of 37.5×150 μm^2, we obtain for f = 1 THz that the capacitive impedance is very small $|Z_C| = 1/2\pi fC \simeq 0.03$–$0.3$ Ω, much smaller than the wave impedance of the free space, $Z_0 = \sqrt{\mu_0/\varepsilon_0} \simeq 377$ Ω. This leads to trapping of EMW in the electrode/crystal capacitance, which shunts open space and prevents emission.

To the contrary, for the whisker-based device, Figure 6c, the field goes out of the mesa as can be seen from the brighter overall tone of the pattern in the middle panel. The EMW propagation is particularly well seen in the bottom hemisphere due to formation of a standing wave pattern in the substrate. It is induced by reflections at the substrate/vacuum interfaces caused

by a significant difference in refractive indices. Emission of EMW is associated with a cross-like structure of the whisker device, as sketched in the leftmost panel of Figure 6c. It obviates direct overlap of the whisker and the electrode and prevents the appearance of the large parasitic capacitance. This cross-like structure resembles the turnstile (crossed-dipole) antenna geometry, which facilitates good impedance matching with open space.

The difference between crystal- and whisker-based devices is also reflected in the far-field characteristics, shown in the rightmost panels of Figure 6a and Figure 6c. The maximum field amplitudes, E_{max}, given in the bottom-right corners, are significantly different: 0.13 V/m for crystal- and 0.69 V/m for whisker-based device. Since the emitted power is proportional to E_{max}^2, the RPE of the whisker-based device is almost 30 times larger than that of the crystal-based device. This indicates a good impedance matching for the whisker device and a poor matching for the crystal device. To further demonstrate the detrimental role of the parasitic electrode/crystal capacitor, in Figure 6b we considered the case with a mesa on a crystal without electrode and only with a capping top layer on the mesa. Such configuration is relevant for large mesas, contacted by a bonding wire [9]. Remarkably, the far-field emission is larger, E_{max} = 0.19 V/m, in the absence of the electrode. This clearly shows that the electrode on top of the crystal does not help in impedance matching. To the contrary, it makes things worse due to formation of the large parasitic capacitance shunting the EMW.

Simulations presented in Figure 6 are made for ideal dielectrics with tan(δ) = 0. The detrimental role of the parasitic crystal/electrode capacitance becomes much more pronounced if we take into account dielectric losses, which can be significant at THz frequencies. In Figure 7 we show the variation of radiative properties of crystal-based (Figure 7a) and whisker-based devices (Figure 7b) upon increasing dielectric losses in the insulating layer between the crystal and the electrode for the crystal-based device and between substrate and electrode for the whisker-based device: tan(δ) = 0 (top), tan(δ) = 1 (middle), and tan(δ) = 2 (bottom row of panels). It is seen that for the whisker-based device dielectric losses only slightly reduce E_{max} from 0.69 V/m for tan(δ) = 0 to 0.55 V/m for tan(δ) = 2. For the crystal-based device the relative reduction is significantly larger, from 0.13 V/m for tan(δ) = 0 to 0.06 V/m for tan(δ) = 2. As a result, the ratio of RPE for whisker and crystal devices in-

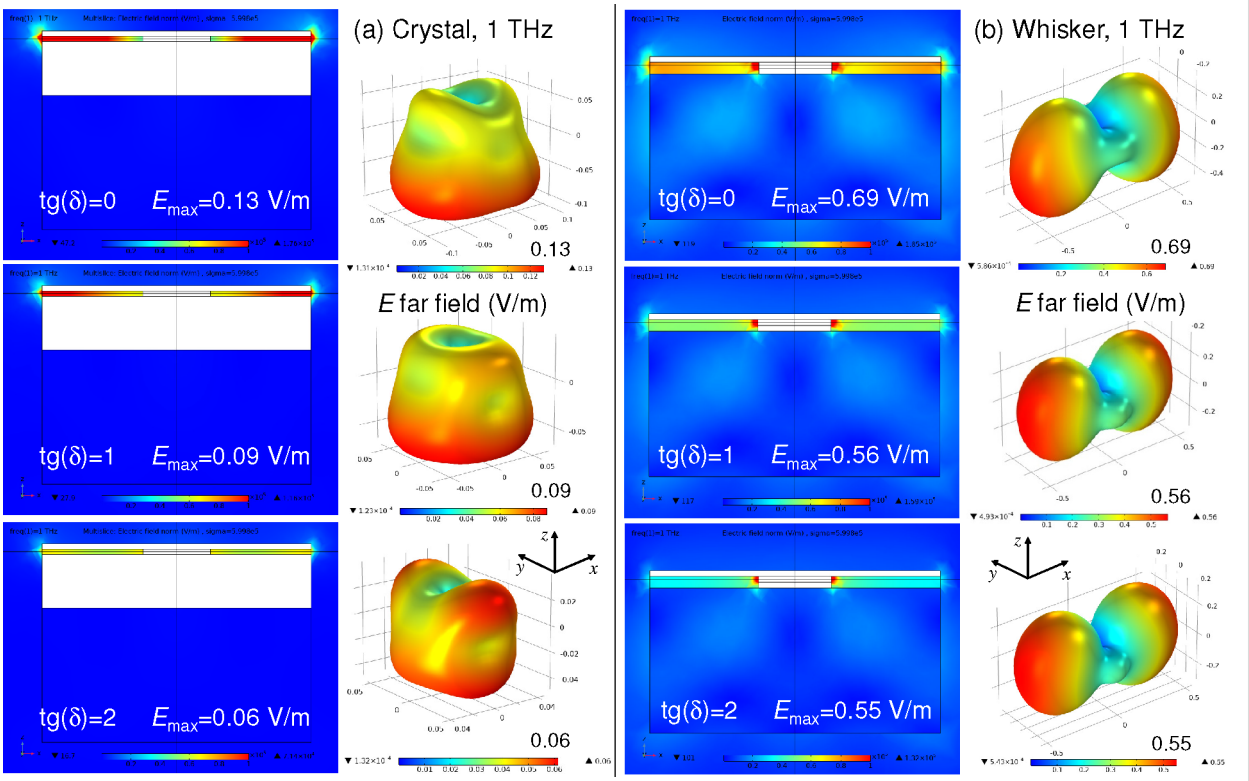

Figure 7: Variation of radiative properties with increasing dielectric losses tan(δ) = 0 (top row), 1 (middle row), and 2 (bottom row) for (a) crystal-based (two leftmost columns) and (b) whisker-based devices (two rightmost columns). Simulations are made at f = 1 THz. Note a rapid suppression of the far-field amplitudes in crystal-based devices.

creases from ≈28 for tan(δ) = 0, to ≈39 for tan(δ) = 1 and ≈84 for tan(δ) = 2. This is a direct consequence of the electric field concentration in the parasitic crystal/electrode capacitance of crystal-based devices.

Discussion

Josephson oscillators can provide unprecedented tunability in the whole THz range at a primary frequency [14]. However, being cryogenic devices, they are susceptible to self-heating, which limits both the achievable frequency range and the emission power. As pointed out in [40], the maximum emission power is limited by the cooling power of the device and the radiation power efficiency:

$$P_{\mathrm{THz}} < P_{\mathrm{cooling}} \times \mathrm{RPE}. \quad (1)$$

Enhancement of the effective cooling power requires implementation of special cooling elements in the device. Despite a significant progress in this direction [10,12,13,35,36,38,47], it is unlikely that a single emitter would be able to sustain the dissipation power above few tens of milliwatts. The tolerable dissipation power can be significantly enhanced by spreading it between several smaller emitters [10,19] because smaller mesa structures are less prone to self-heating [14,28,29,31]. Such a strategy has been successfully proved for arrays of Josephson junctions [48-50], for which coherent emission from up to 9000 synchronized junctions was reported [49]. Yet, the ultimate dissipation power is limited by the cooling power of the cryostat itself. For compact cryorefrigerators it is in the range of 100 mW. As follows from Equation 1, a source with RPE = 1% (which is good for THz sources) would not be able to emit more than P_{THz} = 1 mW. Therefore, further enhancement of the emission power requires enhancement of RPE. This, in turn, requires proper microwave design to facilitate impedance matching with open space. The maximum RPE in case of perfect matching is 50% [41], implying that up to 50 mW emitted THz power could be achieved.

Above we considered design aspects of THz sources, which contribute to obviation of self-heating and improvement of impedance matching. Several geometries of Bi-2212 devices were analyzed. It is shown that geometries of both the Bi-2212 crystal and the electrodes play important roles. Their effect, however, depends on the device type.

For crystal-based devices with large crystals of approx. 1×1 mm^2 in the *ab*-plane, see Figure 1b, the size of the crystal plays contradicting roles in device operation. On the one hand, a large *ab*-plane area helps to spread heat into the substrate and reduces self-heating of the device, as seen from Figure 5. On the other hand, it leads to a large overlap area between the crystal and the top electrode. This creates a large parasitic capacitance that shunts THz emission and suppresses RPE.

In whisker-based devices the situation is different. Here the electrode provides the main heat sink channel, as shown in Figure 4. In general, our analysis indicated that self-heating optimization is much more important and efficient for whisker devices due to the low intrinsic *c*-axis heat resistance (caused by the small thickness of the whisker). Furthermore, the cross-like geometry prevents an overlap between the whisker and the electrode, thus obviating the parasitic capacitance. Moreover, the long whisker and the electrode act as two arms of a turnstile (crossed-dipole) antenna, facilitating good impedance matching with open space. Operation of whisker-based devices [22,40] and devices based on stand-alone mesas with similar cross-like electrodes [16] has been demonstrated by several groups.

The role of the substrate is also different. In crystal-based devices the large superconducting crystal screens the EMW, so that there is practically no field in the substrate, see Figure 6a,b. In this case, the substrate does not influence radiative properties. To the contrary, for a whisker-based device a significant fraction of EMW is going into the substrate due to its larger dielectric constant. The difference of dielectric constants of the substrate and vacuum leads to internal reflections and the formation of standing waves in the substrate, see Figure 6c. Therefore, the substrate acts as a dielectric resonator and may strongly affect the radiation pattern of the device.

The presented numerical simulations provide a qualitative explanation of the reported difference in radiative properties of whisker- and crystal-based devices, shown in Figure 1a,b. They explain why the RPE of whisker-based devices is much larger (by more than an order of magnitude, as follows from Figure 7). Those conclusions are in agreement with experimentally reported RPE values, which are in the range of $\lesssim$1% for crystal-based [10,14] and up to 12% for whisker-based [40] devices.

Conclusion

To conclude, intrinsic Josephson junctions in the layered high-temperature superconductor Bi-2212 can provide an alternative technology for the creation of tunable, CW THz sources. In this work we analyzed two main phenomena that limit performance of such devices: self-heating and low RPE caused by impedance mismatch. We presented numerical simulations of thermal and radiative properties of Bi-2212 THz sources based on conventional large single crystals and needle-like whiskers. Simulations are performed for various geometrical configurations and parameters. A comparison with experimental data for crystal- and whisker-based devices is made. It is demonstrated that the structure and the geometry of both the superconductor

and the electrodes play important roles. Crystal-based devices suffer from a large parasitic capacitance due to an overlap between the crystal and the electrodes. This prevents good impedance matching and reduces RPE. The overlap is avoided in whisker-based devices. Moreover, the whisker and the electrodes form a turnstile (crossed-dipole) antenna facilitating good impedance matching with open space. Our simulations demonstrate that this may enhance the radiation power efficiency in whisker-based devices by more than an order of magnitude compared to crystal-based devices, which is consistent with experimental data.

Acknowledgements

We are grateful to A. Agostino and M. Truccato for assistance with whisker preparation and to A. Efimov and K. Shiianov for assistance in experiment.

Funding

The work was supported by the Russian Science Foundation Grant No. 19-19-00594. The manuscript was written during a sabbatical semester of V. M. K. at MIPT, supported by the Faculty of Sciences at SU.

ORCID® iDs

Mikhail M. Krasnov - https://orcid.org/0000-0001-7988-6323
Natalia D. Novikova - https://orcid.org/0000-0002-3896-2956
Roger Cattaneo - https://orcid.org/0000-0002-5935-7165
Vladimir M. Krasnov - https://orcid.org/0000-0002-3131-8658

Preprint

A non-peer-reviewed version of this article has been previously published as a preprint: https://doi.org/10.3762/bxiv.2021.71.v1

References

1. Tonouchi, M. *Nat. Photonics* **2007,** *1,* 97–105. doi:10.1038/nphoton.2007.3
2. Razeghi, M.; Lu, Q. Y.; Bandyopadhyay, N.; Zhou, W.; Heydari, D.; Bai, Y.; Slivken, S. *Opt. Express* **2015,** *23,* 8462–8475. doi:10.1364/oe.23.008462
3. Belkin, M. A.; Capasso, F. *Phys. Scr.* **2015,** *90,* 118002. doi:10.1088/0031-8949/90/11/118002
4. Wang, X.; Shen, C.; Jiang, T.; Zhan, Z.; Deng, Q.; Li, W.; Wu, W.; Yang, N.; Chu, W.; Duan, S. *AIP Adv.* **2016,** *6,* 075210. doi:10.1063/1.4959195
5. Curwen, C. A.; Reno, J. L.; Williams, B. S. *Nat. Photonics* **2019,** *13,* 855–859. doi:10.1038/s41566-019-0518-z
6. Walther, C.; Fischer, M.; Scalari, G.; Terazzi, R.; Hoyler, N.; Faist, J. *Appl. Phys. Lett.* **2007,** *91,* 131122. doi:10.1063/1.2793177
7. Vijayraghavan, K.; Jiang, Y.; Jang, M.; Jiang, A.; Choutagunta, K.; Vizbaras, A.; Demmerle, F.; Boehm, G.; Amann, M. C.; Belkin, M. A. *Nat. Commun.* **2013,** *4,* 2021. doi:10.1038/ncomms3021
8. Rösch, M.; Scalari, G.; Beck, M.; Faist, J. *Nat. Photonics* **2015,** *9,* 42–47. doi:10.1038/nphoton.2014.279
9. Ozyuzer, L.; Koshelev, A. E.; Kurter, C.; Gopalsami, N.; Li, Q.; Tachiki, M.; Kadowaki, K.; Yamamoto, T.; Minami, H.; Yamaguchi, H.; Tachiki, T.; Gray, K. E.; Kwok, W.-K.; Welp, U. *Science* **2007,** *318,* 1291–1293. doi:10.1126/science.1149802
10. Benseman, T. M.; Gray, K. E.; Koshelev, A. E.; Kwok, W.-K.; Welp, U.; Minami, H.; Kadowaki, K.; Yamamoto, T. *Appl. Phys. Lett.* **2013,** *103,* 022602. doi:10.1063/1.4813536
11. Welp, U.; Kadowaki, K.; Kleiner, R. *Nat. Photonics* **2013,** *7,* 702–710. doi:10.1038/nphoton.2013.216
12. Kashiwagi, T.; Yamamoto, T.; Minami, H.; Tsujimoto, M.; Yoshizaki, R.; Delfanazari, K.; Kitamura, T.; Watanabe, C.; Nakade, K.; Yasui, T.; Asanuma, K.; Saiwai, Y.; Shibano, Y.; Enomoto, T.; Kubo, H.; Sakamoto, K.; Katsuragawa, T.; Marković, B.; Mirković, J.; Klemm, R. A.; Kadowaki, K. *Phys. Rev. Appl.* **2015,** *4,* 054018. doi:10.1103/physrevapplied.4.054018
13. Zhou, X.; Zhu, Q.; Ji, M.; An, D.; Hao, L.; Sun, H.; Ishida, S.; Rudau, F.; Wieland, R.; Li, J.; Koelle, D.; Eisaki, H.; Yoshida, Y.; Hatano, T.; Kleiner, R.; Wang, H.; Wu, P. *Appl. Phys. Lett.* **2015,** *107,* 122602. doi:10.1063/1.4931623
14. Borodianskyi, E. A.; Krasnov, V. M. *Nat. Commun.* **2017,** *8,* 1742. doi:10.1038/s41467-017-01888-4
15. Sun, H.; Wieland, R.; Xu, Z.; Qi, Z.; Lv, Y.; Huang, Y.; Zhang, H.; Zhou, X.; Li, J.; Wang, Y.; Rudau, F.; Hampp, J. S.; Koelle, D.; Ishida, S.; Eisaki, H.; Yoshida, Y.; Jin, B.; Koshelets, V. P.; Kleiner, R.; Wang, H.; Wu, P. *Phys. Rev. Appl.* **2018,** *10,* 024041. doi:10.1103/physrevapplied.10.024041
16. Kashiwagi, T.; Yuasa, T.; Tanabe, Y.; Imai, T.; Kuwano, G.; Ota, R.; Nakamura, K.; Ono, Y.; Kaneko, Y.; Tsujimoto, M.; Minami, H.; Yamamoto, T.; Klemm, R. A.; Kadowaki, K. *J. Appl. Phys.* **2018,** *124,* 033901. doi:10.1063/1.5033914
17. Zhang, H.; Wieland, R.; Chen, W.; Kizilaslan, O.; Ishida, S.; Han, C.; Tian, W.; Xu, Z.; Qi, Z.; Qing, T.; Lv, Y.; Zhou, X.; Kinev, N.; Ermakov, A. B.; Dorsch, E.; Ziegele, M.; Koelle, D.; Eisaki, H.; Yoshida, Y.; Koshelets, V. P.; Kleiner, R.; Wang, H.; Wu, P. *Phys. Rev. Appl.* **2019,** *11,* 044004. doi:10.1103/physrevapplied.11.044004
18. Kuwano, G.; Tsujimoto, M.; Kaneko, Y.; Imai, T.; Ono, Y.; Nakagawa, S.; Kusunose, S.; Minami, H.; Kashiwagi, T.; Kadowaki, K.; Simsek, Y.; Welp, U.; Kwok, W.-K. *Phys. Rev. Appl.* **2020,** *13,* 014035. doi:10.1103/physrevapplied.13.014035
19. Tsujimoto, M.; Fujita, S.; Kuwano, G.; Maeda, K.; Elarabi, A.; Hawecker, J.; Tignon, J.; Mangeney, J.; Dhillon, S. S.; Kakeya, I. *Phys. Rev. Appl.* **2020,** *13,* 051001. doi:10.1103/physrevapplied.13.051001
20. Saiwai, Y.; Kashiwagi, T.; Nakade, K.; Tsujimoto, M.; Minami, H.; Klemm, R. A.; Kadowaki, K. *Jpn. J. Appl. Phys.* **2020,** *59,* 105004. doi:10.35848/1347-4065/abb8f1
21. Delfanazari, K.; Klemm, R. A.; Joyce, H. J.; Ritchie, D. A.; Kadowaki, K. *Proc. IEEE* **2020,** *108,* 721–734. doi:10.1109/jproc.2019.2958810
22. Saito, Y.; Adachi, S.; Matsumoto, R.; Nagao, M.; Fujita, S.; Hayama, K.; Terashima, K.; Takeya, H.; Kakeya, I.; Takano, Y. *Appl. Phys. Express* **2021,** *14,* 033003. doi:10.35848/1882-0786/abe166
23. Kleiner, R.; Müller, P. *Phys. Rev. B* **1994,** *49,* 1327–1341. doi:10.1103/physrevb.49.1327
24. Krasnov, V. M.; Mros, N.; Yurgens, A.; Winkler, D. *Phys. Rev. B* **1999,** *59,* 8463–8466. doi:10.1103/physrevb.59.8463
25. Katterwe, S. O.; Krasnov, V. M. *Phys. Rev. B* **2009,** *80,* 020502. doi:10.1103/physrevb.80.020502

26. Katterwe, S. O.; Rydh, A.; Motzkau, H.; Kulakov, A. B.; Krasnov, V. M. *Phys. Rev. B* **2010,** *82,* 024517. doi:10.1103/physrevb.82.024517
27. Krasnov, V. M.; Yurgens, A.; Winkler, D.; Delsing, P.; Claeson, T. *Phys. Rev. Lett.* **2000,** *84,* 5860–5863. doi:10.1103/physrevlett.84.5860
28. Krasnov, V. M. *Phys. Rev. B* **2009,** *79,* 214510. doi:10.1103/physrevb.79.214510
29. Krasnov, V. M.; Yurgens, A.; Winkler, D.; Delsing, P. *J. Appl. Phys.* **2001,** *89,* 5578. doi:10.1063/1.1367880
30. Krasnov, V. M. *Phys. C (Amsterdam, Neth.)* **2002,** *372-376,* 103–106. doi:10.1016/s0921-4534(02)00856-0
31. Krasnov, V. M.; Sandberg, M.; Zogaj, I. *Phys. Rev. Lett.* **2005,** *94,* 077003. doi:10.1103/physrevlett.94.077003
32. Yurgens, A. *Phys. Rev. B* **2011,** *83,* 184501. doi:10.1103/physrevb.83.184501
33. Kakeya, I.; Omukai, Y.; Yamamoto, T.; Kadowaki, K.; Suzuki, M. *Appl. Phys. Lett.* **2012,** *100,* 242603. doi:10.1063/1.4727899
34. Tsujimoto, M.; Kambara, H.; Maeda, Y.; Yoshioka, Y.; Nakagawa, Y.; Kakeya, I. *Phys. Rev. Appl.* **2014,** *2,* 044016. doi:10.1103/physrevapplied.2.044016
35. Asai, H.; Kawabata, S. *Appl. Phys. Lett.* **2014,** *104,* 112601. doi:10.1063/1.4868219
36. Rudau, F.; Tsujimoto, M.; Gross, B.; Judd, T. E.; Wieland, R.; Goldobin, E.; Kinev, N.; Yuan, J.; Huang, Y.; Ji, M.; Zhou, X. J.; An, D. Y.; Ishii, A.; Mints, R. G.; Wu, P. H.; Hatano, T.; Wang, H. B.; Koshelets, V. P.; Koelle, D.; Kleiner, R. *Phys. Rev. B* **2015,** *91,* 104513. doi:10.1103/physrevb.91.104513
37. Benseman, T. M.; Koshelev, A. E.; Vlasko-Vlasov, V.; Hao, Y.; Kwok, W.-K.; Welp, U.; Keiser, C.; Gross, B.; Lange, M.; Kölle, D.; Kleiner, R.; Minami, H.; Watanabe, C.; Kadowaki, K. *Phys. Rev. Appl.* **2015,** *3,* 044017. doi:10.1103/physrevapplied.3.044017
38. Rudau, F.; Wieland, R.; Langer, J.; Zhou, X. J.; Ji, M.; Kinev, N.; Hao, L. Y.; Huang, Y.; Li, J.; Wu, P. H.; Hatano, T.; Koshelets, V. P.; Wang, H. B.; Koelle, D.; Kleiner, R. *Phys. Rev. Appl.* **2016,** *5,* 044017. doi:10.1103/physrevapplied.5.044017
39. Oikawa, D.; Mitarai, H.; Tanaka, H.; Tsuzuki, K.; Kumagai, Y.; Sugiura, T.; Andoh, H.; Tsukamoto, T. *AIP Adv.* **2020,** *10,* 085113. doi:10.1063/5.0018989
40. Cattaneo, R.; Borodianskyi, E. A.; Kalenyuk, A. A.; Krasnov, V. M. *Phys. Rev. Appl.* **2021,** *16,* L061001. doi:10.1103/physrevapplied.16.l061001
41. Krasnov, V. M. *Phys. Rev. B* **2010,** *82,* 134524. doi:10.1103/physrevb.82.134524
42. Matsubara, I.; Kageyama, H.; Tanigawa, H.; Ogura, T.; Yamashita, H.; Kawai, T. *Jpn. J. Appl. Phys., Part 1* **1989,** *28,* L1121–L1124. doi:10.1143/jjap.28.l1121
43. Jacobs, T.; Simsek, Y.; Koval, Y.; Müller, P.; Krasnov, V. M. *Phys. Rev. Lett.* **2016,** *116,* 067001. doi:10.1103/physrevlett.116.067001
44. Dobrovinskaya, E. R.; Lytvynov, L. A.; Pishchik, V. Properties of Sapphire. *Sapphire. Materials, Manufacturing, Applications;* Springer Science + Business Media: New York, NY, USA, 2009; pp 109–114.
45. Zavaritsky, N. V.; Samoilov, A. V.; Yurgens, A. A. *Phys. C (Amsterdam, Neth.)* **1991,** *180,* 417–425. doi:10.1016/0921-4534(91)90556-e
46. Crommie, M. F.; Zettl, A. *Phys. Rev. B* **1991,** *43,* 408–412. doi:10.1103/physrevb.43.408
47. Ji, M.; Yuan, J.; Gross, B.; Rudau, F.; An, D. Y.; Li, M. Y.; Zhou, X. J.; Huang, Y.; Sun, H. C.; Zhu, Q.; Li, J.; Kinev, N.; Hatano, T.; Koshelets, V. P.; Koelle, D.; Kleiner, R.; Xu, W. W.; Jin, B. B.; Wang, H. B.; Wu, P. H. *Appl. Phys. Lett.* **2014,** *105,* 122602. doi:10.1063/1.4896684
48. Barbara, P.; Cawthorne, A. B.; Shitov, S. V.; Lobb, C. J. *Phys. Rev. Lett.* **1999,** *82,* 1963–1966. doi:10.1103/physrevlett.82.1963
49. Galin, M. A.; Borodianskyi, E. A.; Kurin, V. V.; Shereshevskiy, I. A.; Vdovicheva, N. K.; Krasnov, V. M.; Klushin, A. M. *Phys. Rev. Appl.* **2018,** *9,* 054032. doi:10.1103/physrevapplied.9.054032
50. Galin, M. A.; Rudau, F.; Borodianskyi, E. A.; Kurin, V. V.; Koelle, D.; Kleiner, R.; Krasnov, V. M.; Klushin, A. M. *Phys. Rev. Appl.* **2020,** *14,* 024051. doi:10.1103/physrevapplied.14.024051

License and Terms

BEILSTEIN JOURNAL OF NANOTECHNOLOGY

Plasma modes in capacitively coupled superconducting nanowires

Alex Latyshev[1,2], Andrew G. Semenov[1,3] and Andrei D. Zaikin[*1,4]

Full Research Paper

Open Access

Address:
[1]I.E. Tamm Department of Theoretical Physics, P.N. Lebedev Physical Institute, 119991 Moscow, Russia, [2]National Research University Higher School of Economics, 101000 Moscow, Russia, [3]Department of Physics, Moscow Pedagogical State University, 119435 Moscow, Russia and [4]Institute for Quantum Materials and Technologies, Karlsruhe Institute of Technology (KIT), 76021 Karlsruhe, Germany

Email:
Andrei D. Zaikin[*] - andrei.zaikin@kit.edu

* Corresponding author

Keywords:
plasma modes; quantum fluctuations, quantum phase slips; superconducting nanowires

Beilstein J. Nanotechnol. **2022,** *13,* 292–297.
https://doi.org/10.3762/bjnano.13.24

Received: 29 November 2021
Accepted: 03 February 2022
Published: 04 March 2022

This article is part of the thematic issue "Intrinsic Josephson effect and prospects of superconducting spintronics".

Guest Editor: A. S. Sidorenko

Abstract

We investigate plasma oscillations in long electromagnetically coupled superconducting nanowires. We demonstrate that in the presence of inter-wire coupling plasma modes in each of the wires get split into two “new” modes propagating with different velocities across the system. These plasma modes form an effective dissipative quantum environment interacting with electrons inside both wires and causing a number of significant implications for the low-temperature behavior of the systems under consideration.

Introduction

Physical properties of ultrathin superconducting nanowires differ strongly from those of bulk superconductors owing to a prominent role of fluctuation effects in a reduced dimension [1-3]. Such fluctuations cause a reduction of the superconducting critical temperature [4] and yield a negative correction to the mean field value of the order parameter Δ_0. In particular, at $T\to 0$ for the absolute value of the order parameter $|\Delta|$ in superconducting nanowires one finds [5]:

$$|\Delta| = \Delta_0 - \delta\Delta_0, \quad \frac{\delta\Delta_0}{\Delta_0} \sim \frac{R_\xi}{R_q}, \tag{1}$$

where R_ξ is the normal-state resistance of the wire segment of length equal to the superconducting coherence length ξ and $R_q = 2\pi/e^2 \simeq 25.8\ \mathrm{k\Omega}$ is the quantum resistance unit. For generic metallic nanowires one typically has $R_\xi \ll R_q$, implying that

fluctuation correction to the mean value of the superconducting order parameter (Equation 1) remains weak and in the majority of cases can be neglected.

Is the condition $R_\xi/R_q \ll 1$ sufficient to disregard fluctuation effects in superconducting nanowires? The answer to this question is obviously negative since even in this limit fluctuations of the phase $\varphi(x,t)$ of the order parameter $\Delta = |\Delta|\exp(i\varphi)$ survive being essentially decoupled from those of the absolute value $|\Delta|$. Such phase fluctuations are intimately related to sound-like plasma modes [6,7] (the so-called Mooij–Schön modes), which can propagate along the wire playing the role of an effective quantum dissipative environment for electrons inside the wire. The frequency spectrum of this effective environment is similar to that of the celebrated Caldeira–Leggett model [8], which is widely employed in order to account for both quantum dissipation and quantum decoherence in normal [9,10] and superconducting [11,12] metallic structures, see also the book [1] for an extensive review on this issue.

The presence of Mooij–Schön plasma modes is an important feature inherent to long superconducting nanowires that leads to a number of interesting effects. One of them is the theoretically predicted [13,14] and experimentally observed [15,16] smearing of the square-root singularity in the density of states (DOS) near the superconducting gap accompanied by a non-vanishing tail in DOS at subgap energies. Mooij–Schön plasmons also mediate the interaction between quantum phase slips (QPS) [1,2,17,18] causing Berezinskii–Kosterlitz–Thouless-like [17] and Schmid-like [19-21] quantum phase transitions in structures involving superconducting nanowires.

In this work we are going to investigate propagation of plasma modes in a system of two long capacitively coupled superconducting nanowires. We are going to demonstrate that in the presence of electromagnetic interaction between the wires their plasma modes get split into a pair of "new" modes propagating along the system with two different velocities. This effect may have various implications for the low-temperature behavior of the structures under consideration.

Results and Discussion

Consider a system composed of two long parallel to each other superconducting nanowires. This structure is schematically depicted in Figure 1. The wires are characterized by kinetic inductances $\mathcal{L}_1$ and $\mathcal{L}_2$ (times unit wire length) and geometric capacitances C_1 and C_2 (per unit length). In the absence of any interaction between the wires they represent two independent transmission lines where low-energy plasma excitations propagate with velocities $v_1 = 1/\sqrt{\mathcal{L}_1 C_1}$ and $v_2 = 1/\sqrt{\mathcal{L}_2 C_2}$, respectively, in the first and the second wires.

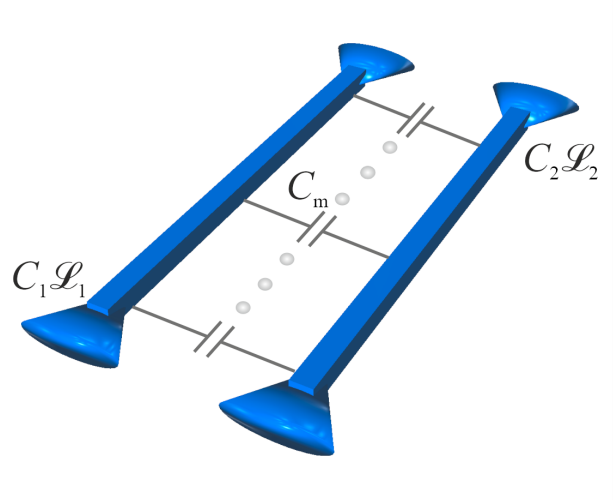

Figure 1: The system of two capacitively coupled superconducting nanowires.

Note that the wires can be treated as independent only provided that they are located far from each other. If, on the contrary, the distance between the wires becomes sufficiently short they develop electromagnetic coupling even though there exists no direct electric contact between them. In this case each fluctuation associated with an electromagnetic pulse in the first wire induces an electromagnetic perturbation in the second one and vice versa. Accordingly, propagation of plasma modes along the wires gets modified and is not anymore described by two independent velocities v_1 and v_2. The task at hand is to investigate the effect of electromagnetic coupling on plasma excitations in the system of two superconducting nanowires.

To this end, we will routinely model electromagnetic coupling between the wires by introducing mutual geometric inductance $\mathcal{L}_m$ and capacitance C_m for these wires. All geometric inductances for ultrathin superconducting wires are typically much smaller than kinetic ones and, hence, $\mathcal{L}_m$ can be safely neglected as compared to $\mathcal{L}_{1,2}$. On the contrary, the mutual capacitance C_m can easily reach values comparable with $C_{1,2}$ and for this reason it needs to be explicitly accounted for within the framework of our consideration.

As a result, making use of the microscopic effective action analysis [17,18,22] we arrive at the following Hamiltonian that includes both electric and magnetic energies of our superconducting nanowires [23,24]

$$\hat{H}_{EM} = \frac{1}{2}\sum_{i,j=1,2}\int dx\Big[\mathcal{L}_{ij}^{-1}\hat{\Phi}_i(x)\hat{\Phi}_j(x) + \left(1/\Phi_0^2\right)C_{ij}^{-1}\left(\nabla\hat{\chi}_i(x)\nabla\hat{\chi}_j(x)\right)\Big], \tag{2}$$

where x denotes the coordinate along the nanowires,

$$\check{\mathcal{L}}=\begin{bmatrix}\mathcal{L}_1 & 0\\ 0 & \mathcal{L}_2\end{bmatrix},\ \check{C}=\begin{bmatrix}C_1 & C_\mathrm{m}\\ C_\mathrm{m} & C_2\end{bmatrix} \tag{3}$$

($C_\mathrm{m} < C_{1,2}$) are the inductance and capacitance matrices and $\Phi_0 = \pi/e$ is the superconducting flux quantum (here and below we set Planck constant $\hbar$, speed of light c and Boltzmann constant k_B equal to unity).

The Hamiltonian in Equation 2 is expressed in terms of the dual operators $\hat{\chi}(x)$ and $\hat{\Phi}(x)$ [25] obeying the canonical commutation relation

$$\left[\hat{\Phi}(x),\hat{\chi}(x')\right]=-i\Phi_0\delta(x-x') \tag{4}$$

and are linked to the charge density and the phase operators $\hat{Q}(x)$ and $\hat{\varphi}(x)$ as

$$\hat{Q}(x)=\frac{1}{\Phi_0}\nabla\hat{\chi}(x),\quad \hat{\varphi}=2e\int_0^x \mathrm{d}x'\hat{\Phi}(x'). \tag{5}$$

Physically, $\hat{\Phi}_i(x)$ represents the magnetic flux operator, while the operator $\hat{\chi}_i(x)$ is proportional to that for the total charge $\hat{q}_i(x)$ that has passed through the point x of the i-th wire up to the same time moment t, that is, $\hat{q}_i(x)=-\hat{\chi}_i(x)/\Phi_0$.

As we already pointed out above, in the case of two capacitively coupled wires any perturbation that occurs in one of the wires generates charge redistribution and voltage pulses in both wires. The corresponding voltage drop in these wires $\hat{V}_{1,2}$ can be expressed in terms of the local charge operators by means of the following equation [23]:

$$\hat{V}_i(t)=\frac{1}{\Phi_0}\sum_{j=1,2}C_{ij}^{-1}\left(\nabla\hat{\chi}_j(x_1,t)-\nabla\hat{\chi}_j(x_2,t)\right),\quad i,j=1,2. \tag{6}$$

In what follows, it will be convenient for us to go over to the phase representation and to express the equation of motion for the phase perturbations $\varphi_{1,2}$ in both wires in the form of

$$\left(\check{1}\partial_t^2-\check{\mathcal{V}}^2\partial_x^2\right)\begin{bmatrix}\varphi_1(x,t)\\ \varphi_2(x,t)\end{bmatrix}=0 \tag{7}$$

that follows directly from the Hamiltonian for our structure (Equation 2). Here $\check{\mathcal{V}}=\left(\check{C}\check{\mathcal{L}}\right)^{-1/2}$ is the velocity matrix that accounts for plasma modes propagating along the wires.

In order to evaluate the velocities of plasma modes in the presence of electromagnetic coupling between the wires it is necessary to diagonalize the velocity matrix $\check{\mathcal{V}}$ and to determine its eigenvalues $v_\pm$. Making use of Equation 3 after a trivial algebra we obtain

$$v_\pm=\frac{1}{2\kappa}\left[\sqrt{v_1^2+v_2^2+2v_1v_2\kappa}\pm\frac{\sqrt{\left(v_1^2-v_2^2\right)^2+\dfrac{4C_\mathrm{m}^2v_1^2v_2^2}{C_1C_2}}}{\sqrt{v_1^2+v_2^2+2v_1v_2\kappa}}\right], \tag{8}$$

where we defined $\kappa=\sqrt{1-C_\mathrm{m}^2/(C_1C_2)}$.

Equation 8 represents the central result of our present work. It demonstrates that in the presence of electromagnetic coupling plasma modes in each of the wires are split into two "new" modes being common for both wires and propagating along them with velocities $v_\pm$. As we expected, no independent plasma modes in each of the wires could exist in this case. Only in the absence of inter-wire interaction (i.e., for $\kappa = 1$) Equation 8 yields $v_+ = v_1$ and $v_- = v_2$.

In the case of identical wires with $C_1 = C_2 = C$, $\mathcal{L}_1 = \mathcal{L}_2 = \mathcal{L}$ and $v_1 = v_2 = v$ the result (Equation 8) reduces to a particularly simple form

$$v_\pm=1/\sqrt{\mathcal{L}\left(C\mp C_\mathrm{m}\right)}\equiv v/\sqrt{1\mp C_\mathrm{m}/C}\,. \tag{9}$$

Provided the parameters of both wires differ in such a way that one of the unperturbed velocities strongly exceeds the other one, $v_1 \gg v_2$, Equation 8 yields

$$v_+\simeq v_1/\kappa,\qquad v_-\simeq v_2. \tag{10}$$

Equation 8–Equation 10 demonstrate that one of the plasma modes may propagate much faster than any of such modes in the absence of inter-wire interaction. This situation can be realized provided the wires are located close enough to each other in which case the cross-capacitance C_m may become of the same order as $C_{1,2}$ implying $\kappa \ll 1$.

Provided the wires are thick enough, the low-energy Hamiltonian in Equation 2 is sufficient. However, for thinner wires one should also take into account the effect of quantum phase slips [1,2,17,18], which correspond to a fluctuation-induced local temporal suppression of the superconducting order parameter inside the wire accompanied by the phase slippage process and quantum fluctuations of the voltage in the form of pulses. Here, it will be sufficient for our purposes to account for QPS

effects only in the first wire and ignore these effects in the second one. In this case, the Hamiltonian in Equation 2 should be replaced by that for an effective sine-Gordon model [25]

$$\hat{H} = \hat{H}_{\mathrm{EM}} - \gamma_1 \int \mathrm{d}x \cos\left(\hat{\chi}_1(x)\right), \tag{11}$$

where the last term describes QPS effects in the first wire and γ_1 defines the QPS amplitude (per unit wire length) in this wire. In simple terms, the last term in Equation 11 can be treated as a linear combination of creation ($e^{i\hat{\chi}_1}$) and annihilation ($e^{-i\hat{\chi}_1}$) operators for the flux quantum Φ_0 and accounts for tunneling of such flux quanta Φ_0 across the first wire.

It is well known that any QPS event causes redistribution of charges inside the wire and generates a pair of voltage pulses propagating simultaneously in opposite directions along the wire. Assume that a QPS event occurs at the initial time moment $t = 0$ at the point $x = 0$ inside the first wire. This event corresponds to the phase jump by 2π, as it is shown in Figure 2. Provided the first wire is electromagnetically decoupled from the second one, at $t > 0$, voltage pulses originating from this QPS event will propagate with the velocity $v_1 = 1/\sqrt{\mathcal{L}_1 C_1}$ along the first wire, see Figure 2. Obviously, the second wire remains unaffected.

Let us now "turn on" capacitive coupling between the wires. In this case, quantum phase slips in one of the wires generate voltage pulses already in both wires. Resolving Equation 7 together with proper initial conditions corresponding to a QPS event, we arrive at the following picture, summarized in Figure 3 and Figure 4. In the first wire each of the two voltage pulses propagating in opposite directions is now, in turn, split into two pulses of the same sign moving with different velocities v_+ and v_-, as it is illustrated in Figure 3. Voltage pulses generated in the second wire by a QPS event in the first one have a different form. There are also two pairs of pulses propagating in opposite directions with velocities v_+ and v_- along the second wire. However, the signs of voltage pulses moving in the same direction are now opposite to each other, cf. Figure 4. This result clearly illustrates specific features of voltage fluctuations induced in the second wire by a QPS event in the first wire: Such fluctuations are characterized by zero average voltage and non-vanishing voltage noise [24].

Conclusion

In this work we have investigated plasma oscillations in capacitively coupled superconducting nanowires. We have shown that in such structures there exist two plasma modes propagating with different velocities along the wires. We have explicitly evaluated these velocities and demonstrated that these plasma

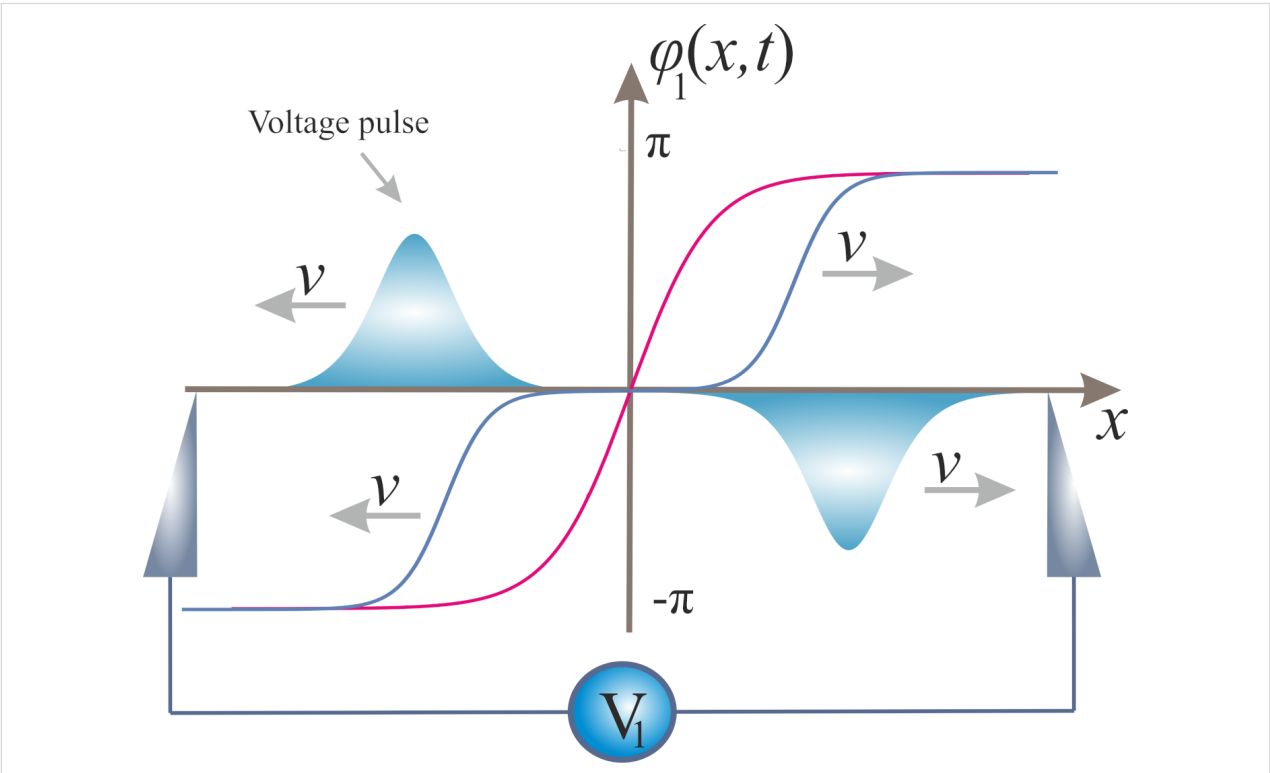

Figure 2: Time-dependent phase configurations describing a QPS event at $t = 0$ (red) and $t > 0$ (blue) together with propagating voltage pulses generated by this QPS event in a single superconducting nanowire.

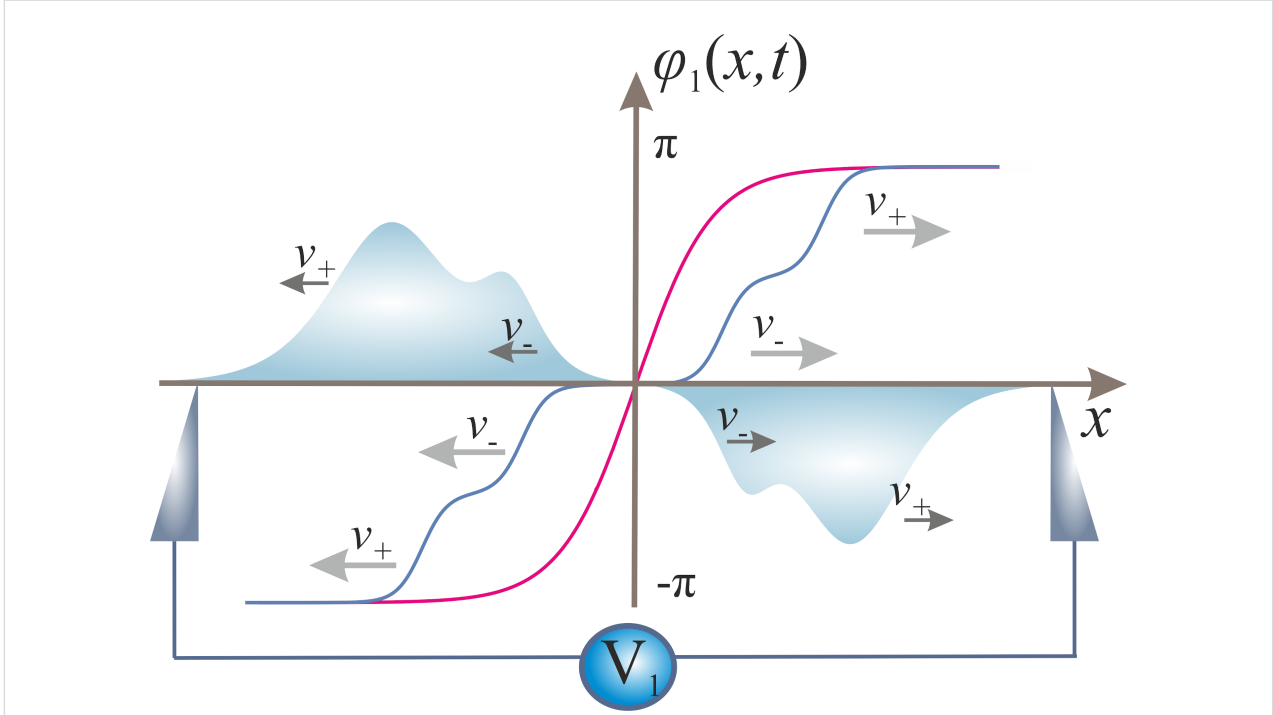

Figure 3: The same as in Figure 1 in the first of the two capacitively coupled superconducting nanowires. Each of the voltage pulses is split into two propagating with different velocities $v_{\pm}$.

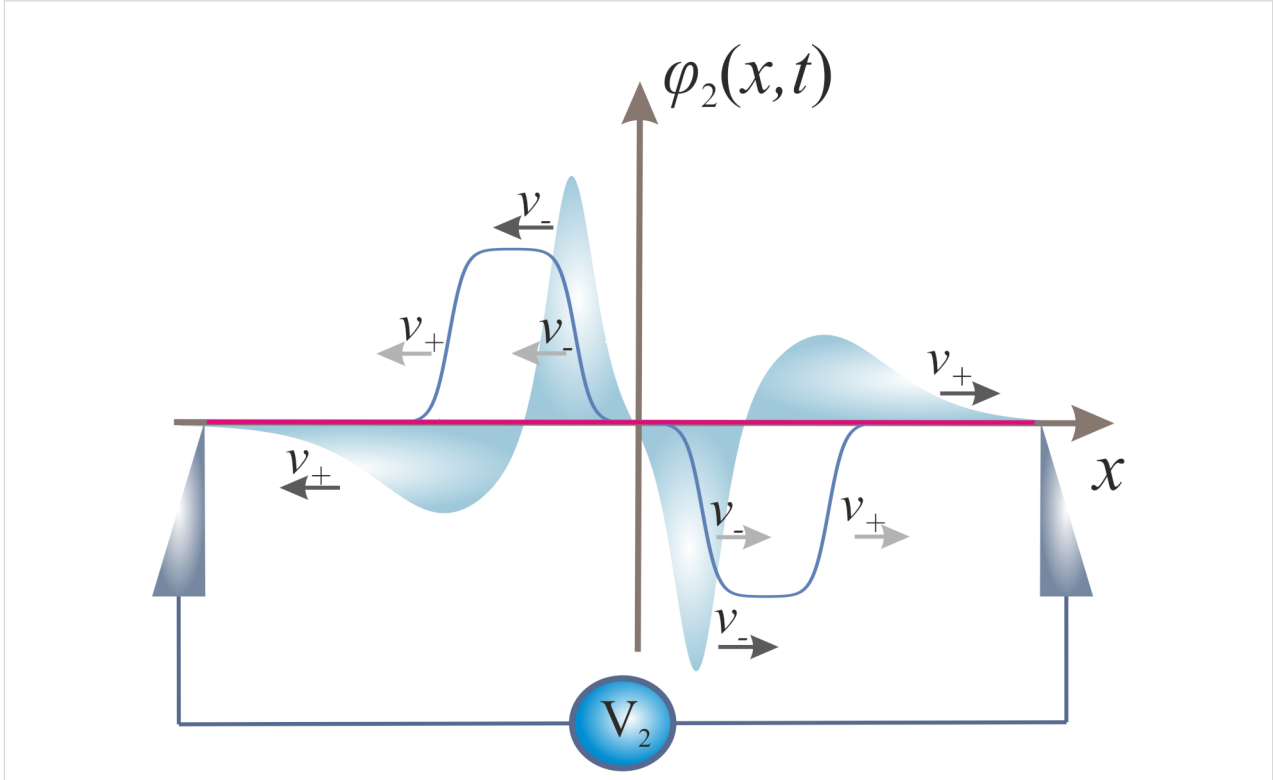

Figure 4: Time-dependent phase configurations at $t = 0$ (red) and $t > 0$ (blue) together with propagating voltage pulses in the second of the two capacitively coupled superconducting nanowires generated by a QPS event in the first one.

modes are the same for both wires forming a single effective dissipative quantum environment interacting with electrons inside the structure. Our results might have significant implications for the low-temperature behavior of coupled superconducting nanowires. For instance, electron DOS in each of the wires can be affected by fluctuations in a somewhat different manner as compared to the noninteracting case [13-16]. Likewise, the logarithmic interaction between different quantum phase slips mediated by such plasma modes gets modified, implying a shift of the superconductor–insulator quantum phase transition in a way to increase the tendency towards localization of Cooper pairs [23]. Further interesting effects are expected that can be related to the correlated behavior of quantum phase slips in different superconducting nanowires. This problem, however, goes beyond the scope of the present paper and will be studied elsewhere.

Funding

AGS acknowledges support by the Russian Science Foundation (project No. 19-72-10101). AL acknowledges support by the Russian Foundation for Basic Research (Project No.18-29-20033).

ORCID® iDs

Alex Latyshev - https://orcid.org/0000-0001-6717-7044
Andrew G. Semenov - https://orcid.org/0000-0002-6992-7862
Andrei D. Zaikin - https://orcid.org/0000-0001-8744-3792

Preprint

A non-peer-reviewed version of this article has been previously published as a preprint: https://doi.org/10.3762/bxiv.2021.82.v1

References

1. Zaikin, A. D.; Golubev, D. S. *Dissipative Quantum Mechanics of Nanostructures;* Jenny Stanford Publishing: New York City, NY, U.S.A., 2019. doi:10.1201/9780429298233
2. Arutyunov, K. Y.; Golubev, D. S.; Zaikin, A. D. *Phys. Rep.* **2008,** *464,* 1–70. doi:10.1016/j.physrep.2008.04.009
3. Bezryadin, A. *Superconductivity in Nanowires;* Wiley-VCH Verlag GmbH: Weinheim, Germany, 2012. doi:10.1002/9783527651931
4. Oreg, Y.; Finkel'stein, A. M. *Phys. Rev. Lett.* **1999,** *83,* 191–194. doi:10.1103/physrevlett.83.191
5. Golubev, D. S.; Zaikin, A. D. *Phys. Rev. B* **2008,** *78,* 144502. doi:10.1103/physrevb.78.144502
6. Mooij, J. E.; Schön, G. *Phys. Rev. Lett.* **1985,** *55,* 114–117. doi:10.1103/physrevlett.55.114
7. Camarota, B.; Parage, F.; Balestro, F.; Delsing, P.; Buisson, O. *Phys. Rev. Lett.* **2001,** *86,* 480–483. doi:10.1103/physrevlett.86.480
8. Caldeira, A. O.; Leggett, A. J. *Phys. Rev. Lett.* **1981,** *46,* 211–214. doi:10.1103/physrevlett.46.211
9. Golubev, D. S.; Zaikin, A. D. *Phys. B (Amsterdam, Neth.)* **1998,** *255,* 164–178. doi:10.1016/s0921-4526(98)00464-5
10. Golubev, D. S.; Zaikin, A. D.; Schön, G. *J. Low Temp. Phys.* **2002,** *126,* 1355–1376. doi:10.1023/a:1013800304448
11. Semenov, A. G.; Zaikin, A. D.; Kuzmin, L. S. *Phys. Rev. B* **2012,** *86,* 144529. doi:10.1103/physrevb.86.144529
12. Semenov, A. G.; Zaikin, A. D. *Phys. Rev. B* **2015,** *91,* 024505. doi:10.1103/physrevb.91.024505
13. Radkevich, A.; Semenov, A. G.; Zaikin, A. D. *Phys. Rev. B* **2017,** *96,* 085435. doi:10.1103/physrevb.96.085435
14. Radkevich, A. A.; Semenov, A. G.; Zaikin, A. D. *Eur. Phys. J.: Spec. Top.* **2019,** *227,* 2289–2295. doi:10.1140/epjst/e2018-800046-x
15. Arutyunov, K. Y.; Lehtinen, J. S.; Radkevich, A. A.; Semenov, A. G.; Zaikin, A. D. *J. Magn. Magn. Mater.* **2018,** *459,* 356–358. doi:10.1016/j.jmmm.2017.08.026
16. Arutyunov, K. Y.; Lehtinen, J. S.; Radkevich, A.; Semenov, A. G.; Zaikin, A. D. *Commun. Phys.* **2021,** *4,* 146. doi:10.1038/s42005-021-00648-7
17. Zaikin, A. D.; Golubev, D. S.; van Otterlo, A.; Zimányi, G. T. *Phys. Rev. Lett.* **1997,** *78,* 1552–1555. doi:10.1103/physrevlett.78.1552
18. Golubev, D. S.; Zaikin, A. D. *Phys. Rev. B* **2001,** *64,* 014504. doi:10.1103/physrevb.64.014504
19. Hekking, F. W. J.; Glazman, L. I. *Phys. Rev. B* **1997,** *55,* 6551–6558. doi:10.1103/physrevb.55.6551
20. Radkevich, A.; Semenov, A. G.; Zaikin, A. D. *Phys. Rev. B* **2019,** *100,* 014520. doi:10.1103/physrevb.100.014520
21. Radkevich, A.; Semenov, A. G.; Zaikin, A. D. *J. Supercond. Novel Magn.* **2020,** *33,* 2335–2339. doi:10.1007/s10948-019-05381-5
22. van Otterlo, A.; Golubev, D. S.; Zaikin, A. D.; Blatter, G. *Eur. Phys. J. B* **1999,** *10,* 131–143. doi:10.1007/s100510050836
23. Latyshev, A.; Semenov, A. G.; Zaikin, A. D. *Beilstein J. Nanotechnol.* **2020,** *11,* 1402–1408. doi:10.3762/bjnano.11.124
24. Latyshev, A.; Semenov, A. G.; Zaikin, A. D. *J. Supercond. Novel Magn.* **2020,** *33,* 2329–2334. doi:10.1007/s10948-019-05402-3
25. Semenov, A. G.; Zaikin, A. D. *Phys. Rev. B* **2013,** *88,* 054505. doi:10.1103/physrevb.88.054505

License and Terms

BEILSTEIN JOURNAL OF NANOTECHNOLOGY

A broadband detector based on series YBCO grain boundary Josephson junctions

Egor I. Glushkov[1,2], Alexander V. Chiginev[1,2], Leonid S. Kuzmin[2,3] and Leonid S. Revin[*1,2]

Full Research Paper

Open Access

Address:
[1]Institute for Physics of Microstructures of RAS, GSP-105, Nizhny Novgorod, 603950, Russia, [2]Nizhny Novgorod State Technical University n.a. R. E. Alekseev, GSP-41, Nizhny Novgorod, 603950, Russia and [3]Chalmers University of Technology, SE-41296 Gothenburg, Sweden

Email:
Leonid S. Revin[*] - rls@ipmras.ru

* Corresponding author

Keywords:
array; electromagnetic modeling; log-periodic antenna; RCSJ model; series Josephson junctions; YBaCuO Josephson junction

Beilstein J. Nanotechnol. **2022,** *13,* 325–333.
https://doi.org/10.3762/bjnano.13.27

Received: 22 December 2021
Accepted: 16 March 2022
Published: 28 March 2022

This article is part of the thematic issue "Intrinsic Josephson effect and prospects of superconducting spintronics".

Guest Editor: A. S. Sidorenko

Abstract

Modeling of a broadband receiving system based on a meander series of Josephson YBaCuO grain boundary junctions integrated into a log-periodic antenna was carried out. The electromagnetic properties of the system, namely amplitude–frequency characteristic, beam pattern, and fraction of the absorbed power in each Josephson junction were investigated. Based on the obtained results, a numerical simulation of one-dimensional arrays was carried out. The dc characteristics of the detector were calculated, that is, current–voltage characteristic, responsivity, noise, and noise-equivalent power (NEP) for a 250 GHz external signal. The optimal number of junctions to obtain the minimum NEP was found. The use of a series of junctions allows one to increase the responsivity by a factor of 2.5, the NEP value by a factor of 1.5, and the power dynamic range by a factor of 5. For typical YBaCuO Josephson junctions fabricated on a ZrYO bicrystal substrate by magnetron deposition, the following parameters were obtained at a temperature of 77 K: responsivity = 9 kV/W; NEP = $3{\cdot}10^{-13}$ W/Hz$^{(1/2)}$; power dynamic range = $1{\cdot}10^{6}$.

Introduction

High-temperature superconducting (HTSC) Josephson junctions (JJs) have great potential as promising materials for creating high-frequency devices, such as microwave generators [1,2], sensitive detectors or mixers [3,4], and voltage standards [5-7]. Recent impressive developments in this area make this possible [8-10].

The advantage of HTSCs lies not only in the ability to operate at liquid-nitrogen temperature, but also in a wide temperature range. For instance, an YBaCuO Josephson detector was applied to detect a small signal from a BiSrCaCuO mesa structure at an operating temperature of 25 K [11]. A HTSC JJ has also analyzed pulsed terahertz radiation from quantum cascade

lasers located in the same cryogenic environment at 50 K [12]. Another important advantage of HTSCs is a wide frequency range from tens of gigahertz to several terahertz [13,14], which exceeds the gap limitation of low-T_c detectors. So, in [12] the spectrum of a quantum cascade laser emission has been recovered by an YBaCuO detector at a central frequency around 2.2 THz.

However, for some applications the performance of the HTSC devices is limited by the fairly low impedance of the JJ. It leads to moderate conversion efficiency in Josephson mixers [15,16] and reduced absorbed power in JJ detectors [17]. One possible way to solve this problem is to replace a single JJ by a chain or an array of JJs combined with planar coupling structures. The task of developing and calculating such systems is quite complex and faced with obscures such as unresolved Shapiro steps [18,19] and parasitic resonances [3].

To effectively match JJs with open space and the incoming external signal, dipole antennas for each junction can be used [20], but the development of a broadband detector requires the use of spiral [4], log-periodic [3], or other types of broadband antennas. In this case JJs are integrated into the single receiving system. This is the case considered in our article.

The aim of this work is the electromagnetic analysis and numerical simulation of the broadband detector based on a series of HTSC bicrystal Josephson junctions to maximize response, power dynamic range, and noise-equivalent power.

Electromagnetic Simulation

Figure 1a–c shows options for the geometry of a log-periodic antenna. Its main advantage is a wide frequency band. The basic formulas and parameters that define this type of antenna are the angles α and β, determining the length of the teeth, the number of teeth n and their radii [21,22]:

$$R_n = \tau^{\left(n-\frac{1}{2}\right)} r_1, \qquad r_{n+1} = \tau^n r_1. \tag{1}$$

For the geometry in Figure 1c with a sinuous modulation of the antenna edges, additional expressions were used [23].

The tool used for the simulation was time domain solver of CST Microwave Studio. Two methods for calculating the receiving characteristics of the antenna were used. In the first method, microwave (MW) currents and voltages excited in each receiving element (port) were calculated for the case that a plane wave was incident on the structure through the lens. In the second method, the full matrix of the antenna input impedance Z was calculated for all ports in the emission regime. The first calculation method is well applicable for low frequencies, while for high frequencies the duration of calculations increases sig-

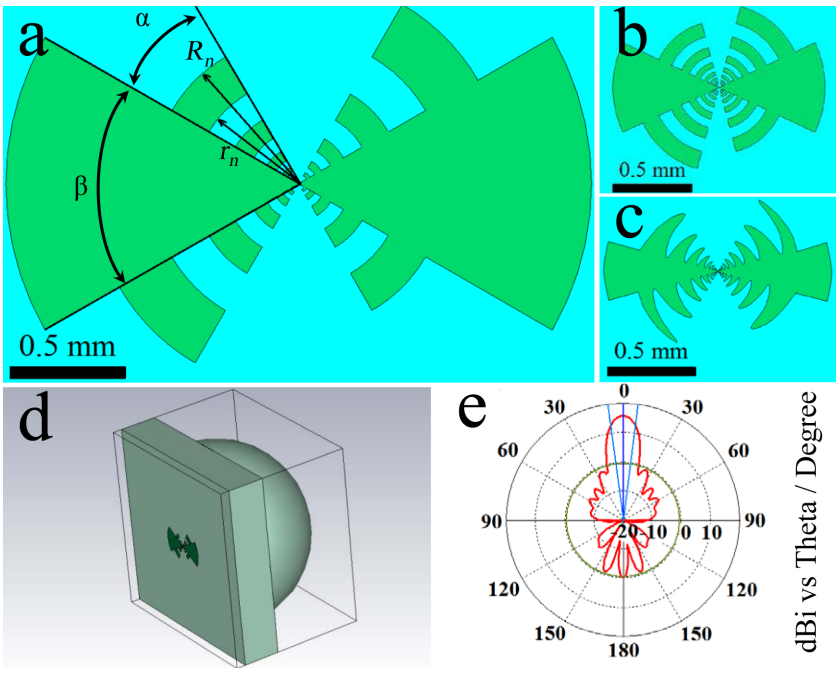

Figure 1: (a–c) Three log-periodic antennas of various geometries; (d) system with a lens (d) and (e) beam pattern at 250 GHz.

nificantly with a decrease in the step of the computation grid. The second method works well for a small number of ports; with an increase in the number of receiving elements, the computation time for the complete Z-matrix increases. Both methods give similar results with acceptable accuracy.

Figure 1 shows a complete modeling system with lens (Figure 1d) and calculated beam pattern at 250 GHz (Figure 1e). The obtained values of 15.7 dBi main lobe magnitude with 15° angular width demonstrate good receiving characteristics. A port with an impedance of 5 Ω was used as an element simulating the Josephson junction. It is known [17,24] that the impedance of the HTSC JJ is low, which makes the development of HTSC detectors and mixers difficult in comparison with low-temperature superconductor Josephson junction analogues. Figure 2 shows the dependence of the received power $P_{absorbed}/P_{incident}$ as function of the frequency for the three different antenna geometries from Figure 1. It can be seen that this value does not reach 1 due to the mismatch of the antenna impedance (about 50 Ω) and the port impedance. The differences in the results for the three antenna geometries are explained by the influence of the antenna parameters on the S-parameters. τ affects the frequency distance between resonances, and the length of the teeth (combination of α and β) affects the depth of the resonances. For the antennas in Figure 1b,c τ is smaller than for the antenna in Figure 1a. Therefore, more resonances are within the range of 50 to 800 GHz. In addition, the teeth for these two designs are longer, so the maxima of the absorbed power at the resonant frequencies are greater. At the same time, the power drops at non-resonant frequencies increase, making the amplitude–frequency characteristic (AFC) less smooth. Since the purpose of the current work was to develop a broadband system, for further consideration we chose an antenna with the most uniform AFC, sacrificing the maximum absorbed power in resonances. This is the antenna in Figure 1a with the parameters α = 30°, β = 60°, r_1 = 28 μm, τ = 2, and n = 5.

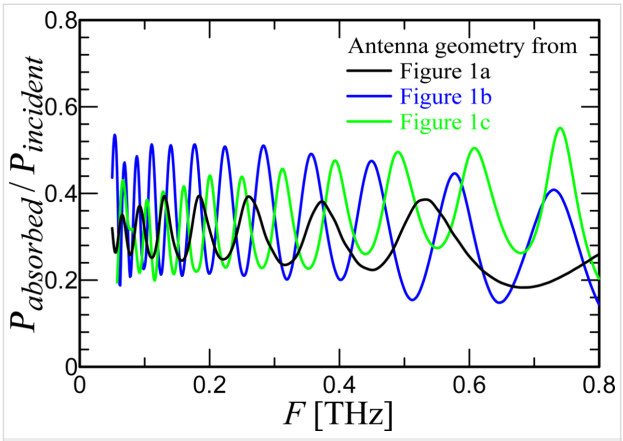

Figure 2: Normalized level of absorbed power in the port for the three antenna geometries in Figure 1.

To improve the match between receiving system and antenna, designs with series of up to eleven Josephson junctions were considered. In this case, there are two possible ways to implement the geometry (Figure 3a,b). The fabrication of bicrystal

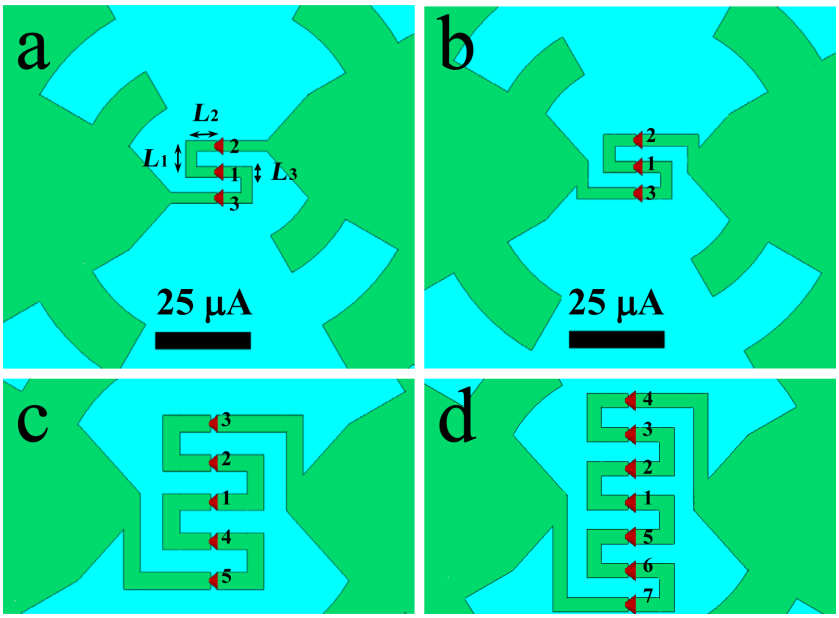

Figure 3: Geometry of log-periodic antennas with a meander series of Josephson YBaCuO grain boundary junctions. (a) Displaced geometry with three ports; (b) unchanged antenna with long meander and three ports; (c, d) antennas with five and seven ports, respectively.

junctions requires the use of a meander-type microstrip since, for the formation of a weak link, it is necessary for the superconducting film to cross the grain boundary. In the first case implemented in [3], the length of the meander is minimal (Figure 3a). To minimize this length, the two parts of the antenna are displaced vertically relative to each other. The disadvantage of this approach is that with an increase in the number of ports and, accordingly, an increase in the meander length, the vertical displacement of the antenna parts becomes noticeable, which is detrimental to its receiving properties. In the case of the geometry in Figure 3b, the antenna itself remains unchanged, and the meander becomes longer compared with the first case. This design will not violate the concept of a log-periodic antenna, but due to the proximity of the meander microstripes to the tooth with $n = 1$, it may lead to distortion of the AFC at high frequencies. Figure 3c,d shows antennas with five and seven ports, respectively. Due to the central symmetry of such a geometry, the receiving properties of the ports above and below the central one will be the same, thus, ports 2 and 3 in a three-port antenna will be equally excited. For an antenna with five ports, $S_{22} = S_{44}$, $S_{33} = S_{55}$ and so on.

Figure 4 shows a comparison of the simulation results for one receiving element and three receiving elements in series. It can be seen that the integral power absorbed in three ports (blue curve) is greater than the power absorbed in one port (black curve). For low frequencies, the power received by three ports with an impedance of 5 Ω is equal to the power received by one port in the antenna with an impedance of $5 \times 3 = 15$ Ω since for these wavelengths three ports "act" like one. For higher frequencies, the geometry of the meander begins to influence the AFC and to distort it. It is obvious that a decrease in the meander dimensions L_1, L_2, and L_3 leads to a decrease in the described effect. But, in our case, these dimensions were chosen based on the maximum resolution of the standard technology of alignment and magnetron deposition of YBaCuO films on a bicrystal substrate [25]. This problem can be mitigated by using ion irradiation [4,18,26] or step-edge junction technology [19], which will significantly increase the receiving properties and efficiency of the JJ series at high frequencies. While the integral received power of the three-port configuration increases due to better antenna matching, each individual port in the array receives less power than in the case of a single port in the antenna. Due to the serial connection of the JJs into a common receiving system, the elements share the power among them. The more elements there are, the less power goes to each individual port.

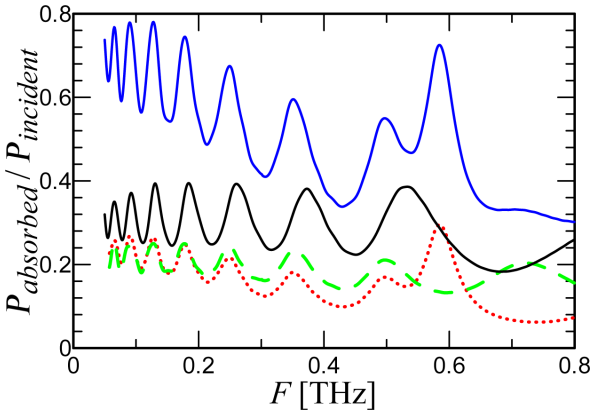

Figure 4: Integral absorbed power for two different cases. Black curve: a single port in an antenna; blue curve: three ports in series. Green dashed line: $P_{absorbed}$ in the central port of the three-port configuration. Red dotted line: $P_{absorbed}$ in port 2 and port 3.

Table 1 shows the proportion of absorbed power for each element and the total value depending on the number of junctions in the antenna for a frequency of 250 GHz. Note that the port numbering such that port number 1 is always assigned to the central port and ascending port numbers correspond to ports with increasing distance from the center (see Figure 3). The table shows values for only half of the ports plus the center one because, as discussed earlier, the result for the rest of the ports are identical.

Table 1: Absorbed power for different configurations of JJs series integrated into the same log-periodic antenna.

Total number of ports in series	Total absorbed power/incident power	Power absorbed in each port/incident power, p_i					
		p_1	p_2	p_3	p_4	p_5	p_6
1	0.36	0.36					
3	0.65	0.24	0.20				
5	0.81	0.16	0.18	0.14			
7	0.82	0.13	0.11	0.12	0.10		
9	0.75	0.08	0.09	0.08	0.09	0.07	
11	0.70	0.08	0.06	0.07	0.06	0.07	0.05

It can be shown that for the case of a strong mismatch between the impedance of the antenna and the receiving elements, an increase in the series ports number leads to an increase in the total absorbed power as $P_{total} \approx NP_{per\_port}$, while the power per port P_{per_port} remains constant. For the case of matched impedances with an increase in the number of JJs, the total power P_{total} remains constant and is divided between all elements such that $P_{per\_port} \approx P_{total}/N$. The situation considered in this work is in the middle between the two cases, that is, the total absorbed power increases with the number of junctions, but P_{per_port} decreases. Starting from five JJs in series, P_{total} reaches saturation with a level below 1. This is due to the fact that the length of the meander becomes so large that it begins to affect the absorption at a given frequency and cross resonances reduce the receiving properties of the system.

Numerical Modeling

Let us now consider a model of an underdamped Josephson junction series array shunted by a load with inductance L_L, resistance R_L, and capacitance C_L and exposed to an external high-frequency radiation with power $P_{MW} = I_{MW}^2 \cdot R_N/2$ and frequency $F_{MW} = \omega_{MW}/2\pi$. This model consists of a circuit in which there are N junctions connected in series one after another with a common load in parallel to all junctions (see Figure 5, left). The circuit equations describing the current–voltage relation are [27-29]:

$$I + A_i I_{MW} \sin(\omega_{MW} t) = \frac{C\hbar}{2e}\ddot{\phi}_i + \frac{\hbar}{2eR_N}\dot{\phi}_i + I_c \sin\phi_i + I_F + \dot{Q}, \quad \text{with } i = 1,\ldots,N$$
$$V = \sum_{k=1}^{N} \frac{\hbar}{2e}\dot{\phi}_k. \tag{2}$$

where ϕ_i is the Josephson phase in the i-th junction, and the overdot denotes differentiation with respect to time. I is the dc current through the junctions, and V is the voltage drop across the entire array of series junctions. The amplitude I_{MW} of a simple harmonic signal describes the external high-frequency radiation. This signal is multiplied by the coefficient $A_i = \sqrt{p_i}$, which determines how much of the power received by the antenna is absorbed in a particular JJ (according to Table 1). In Equation 2, the first three terms on the right represent, respectively, the displacement current, the normal current, and the supercurrent with junction critical current I_c, capacitance C, and normal resistance R_N set the same for all JJs in series. Thermal fluctuations I_F are treated as white Gaussian noise with zero mean and the correlation function

$$\langle I_F(t) I_F(t+\tau)\rangle = \frac{k_B T}{\pi R_N}\delta(\tau).$$

Q is the charge on the load capacitor calculated from the equation for the oscillatory circuit:

$$L_L\ddot{Q} + R_L\dot{Q} + Q/C_L = V. \tag{3}$$

The described model is not complete. To simulate a log-periodic antenna, it is necessary to use an additional system of K equations, where K is the number of antenna resonances in the frequency range under consideration [30]. Nevertheless, in the described model, the Josephson junctions are connected to each other through the resonant circuit while the electrodynamics is taken into account through the amplitudes of the external signal A_i followed from the previous section. A complete model of the antenna interacting with the nonlinear resonance circuit (Josephson junction) through the Y-matrix is currently being developed. This model will allow one to dynamically calculate the MW current flowing in each of the junctions at a given total high-frequency current in the antenna.

As previously mentioned, the junctions parameters were set the same for all JJs. Although there is always a parameter spread in fabrication, for high temperatures of the order of 70 K this difference is insignificant [3]. Thus, the parameters of the junctions were chosen as typical for bicrystal JJs fabricated by magnetron deposition [24,25,31-33]: I_c = 100 μA, R_N = 5 Ω, C = 0.02 pF. The antenna parameters were chosen based on the impedance calculation using the relations Re(Z) = R_L, dIm(Z)/dω = 2L_L, and $F = 1/(2\pi\sqrt{L_L C_L})$. For the serial resonance at 250 GHz, R_L = 43 Ω, L_L = 500 pH, and C_L = 0.8 fF.

Figure 5, right, shows the current–voltage characteristics (IVCs) of a single junction with the antenna under the influence of an

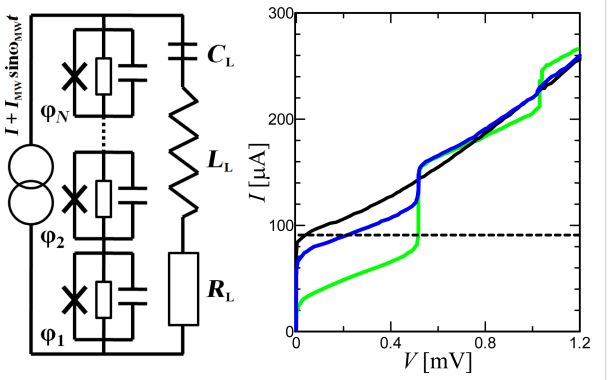

Figure 5: Left: circuit schematic of JJs in a series array interacting via a common RLC load. Right: current–voltage characteristics of a single junction in the absence and under the influence of an external 250 GHz signal, from bottom to top: P_{MW} = 250, 50, and 0 nW. The dotted line is the optimal bias current.

external signal. A bias current regime with the optimum operating point near the critical current (dashed line) is selected for broadband detection. The response is determined by the voltage, which increases with increasing power until it reaches the voltage $V = \hbar\omega_{MW} / 2e$ at the Shapiro step. For this regime, the use of serial JJs can be beneficial since the total voltage increases in proportion to the number of junctions.

The first important feature for the characterization of a Josephson junction as a direct detector is the voltage response ΔV, that is, the voltage difference between the absence and the presence of an external signal. Figure 6a shows the response as function of the bias current for several power levels P_{MW}. Qualitatively, the response dependencies coincide with the measured ones in [17]. The dependencies have two maxima, which merge into one with increasing power. The right peak corresponds to the frequency-selective response at a constant voltage of the Shapiro step. The left peak is a classical response with a bias current near the critical one. The inset of Figure 6a shows the $\Delta V(P_{MW})$ dependence at the optimal bias I = 98 μA. The response amplitude is a linear function of the radiation power at low values of P_{MW} and saturates for $P_{MW} = 10^{-7}$ W [17,33,34]. The responsivity r_V, which is a derivative of the $\Delta V(P_{MW})$ dependence, will be discussed later.

The second important parameter is the output voltage noise δV. The theoretical estimation of δV according to the Nyquist formula gives a discrepancy with the experimental values by two orders of magnitude [34,35]. It does not take into account the increase in output noise due to the influence of low-frequency noise spectra of the critical current fluctuations δI_c and normal resistance fluctuations δR_N associated with the transport mechanisms of the Cooper pairs and quasiparticles, respectively [36,37]. For a Josephson junction having a non-hysteretic IVC, the output voltage spectrum at a fixed bias current is defined as [38]:

$$S_V(F) = (V - R_d I)^2 S_I(F) + V^2 S_R(F), \qquad (4)$$

where R_d is the differential resistance; $S_I = |\delta I_c / I_c|^2$ and $S_R = |\delta R_N / R_N|^2$ depend on the nature of the junction barrier. For the considered structures, $S_I = 10^{-12}$ was chosen as a typical value of the current fluctuations at a frequency of 100 Hz [39,40]. For fluctuations of bicrystal YBCO junctions, δR_N are mostly insignificant [31,41,42]. In the considered case of the operating point near zero voltage, they do not play a role and are assumed equal to zero $S_R = 0$. The model also takes into account the amplifier noise, which has a typical value of $\delta V_{amp} = 2\,\text{nV}/\sqrt{\text{Hz}}$ [43]. Thus, the total output noise for N Josephson junctions is

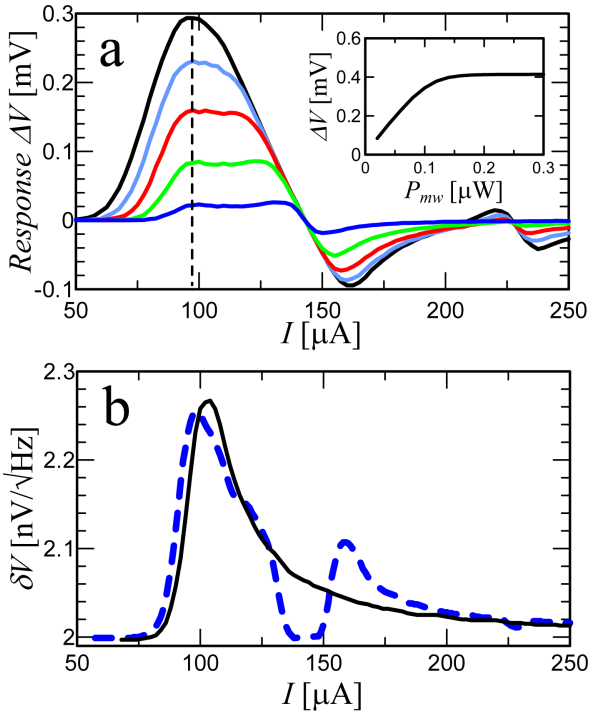

Figure 6: (a) Response ΔV versus dc current I for different MW signals, from bottom to top: P_{MW} = 5, 20, 40, 60, and 80 nW. The dotted line represents the optimal detection regime for the bias current I = 98 μA. The inset shows the dependence of the response at the operating point on the magnitude of the external signal. (b) Total output voltage noise of the Josephson junction versus bias current for P_{MW} = 0 W (solid curve) and P_{MW} = 10 nW (dashed curve).

$$\delta V = \sqrt{\delta V_{amp}{}^2 + N \cdot S_V}, \qquad (5)$$

and the $\delta V(I)$ dependence is shown in Figure 6b for two power levels.

Now let us consider the receiving characteristics of structures depending on the number of JJs. Figure 7a shows the current–voltage characteristics for a signal power level P_{MW} = 3 μW and different numbers of junctions in series. With an increase in the number of junctions, the Shapiro steps are blurred. This is due to an increase in the spread of the amplitudes A_i in different junctions according to Table 1.

As discussed earlier, the Josephson junction has a constant responsivity for low signal levels. Figure 7b shows the dependence of $r_V = dV/dP_{MW}$ on the power for the optimal operating current. For a single junction (bottom blue curve) r_V reaches the typical 4000 V/W [34,43,44]. The voltage responsivity can be approximately expressed as [43]

$$r_V = R_d \cdot A_1{}^2 \Big/ \left(2 I_c R_N \Omega^2\right), \qquad (6)$$

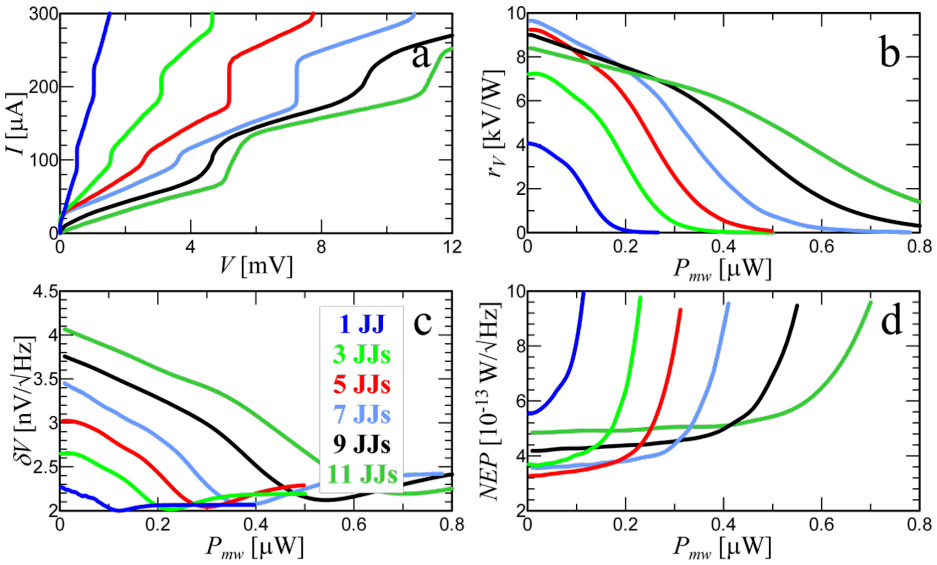

Figure 7: (a) IVCs for different numbers of JJs from one to eleven under a MW signal with power P_{MW} = 3 μW and frequency F_{MW} = 250 GHz. (b) Responsivity, (c) output voltage noise, and (d) NEP are shown depending on the power of the external signal at an operating point I = 98 μA.

where Ω is the normalized frequency, $\Omega = F_{MW} / (I_c R_N \cdot 2e/\hbar)$. For a single junction with R_d = 12 Ω, $A_1{}^2$ = 0.36 (Table 1), Ω = 1.04 the approximate value r_V = 4025 V/W is close to the numerical one. It is also possible to estimate the response for N Josephson junctions according to the additive law:

$$r_V = R_d \sum_{k=1}^{N} A_k{}^2 \Big/ \left(2 I_c R_N \Omega^2\right) \approx N R_d \left\langle A^2 \right\rangle \Big/ \left(2 I_c R_N \Omega^2\right).$$

The $\delta V(P_{MW})$ dependence in Figure 7c, which is proportional to R_d^2 (Equation 4), has a maximum for the highest responsivity and falls to the minimum noise level at the Shapiro step. The receiving system is most comprehensively characterized by the noise-equivalent power

$$\mathrm{NEP} = \delta V / r_V \,. \tag{7}$$

Its value (Figure 7d) for a single JJ of about $5 \cdot 10^{-13}$ W / $\sqrt{\mathrm{Hz}}$ is in agreement with the experimental values [17,34,43,44]. For a configuration of three JJs in series, the responsivity increased by 1.8 times compared to a single junction, and the noise increased by 1.2 times. As a result, the NEP fell by 1.5 times. Note that despite the fact that the responsivity decreases with increasing power, the NEP remains almost unchanged over a wide range of P_{MW}.

Another important characteristic is the power dynamic range $D = P_S/P_0$. Here P_S is the upper limit for which the detector response deviates from linearity. The 3 dB criterion is also used as a definition, that is, P_S is the level of input radiation power, at which the detector responsivity decreases by a factor of two. P_0 is the bottom limit determined by the noise equivalent power and the frequency band ΔF of the detection system, $P_0 = \mathrm{NEP}\sqrt{\Delta F}$. For a single junction the upper limit of the power dynamic range is P_S = 110 nW. For eleven JJs in series P_S = 555 nW. That is, the Josephson junctions in series share the total power among themselves and do not saturate. The power dynamic range D increases with an increase in the number of junctions. For 11 JJs, D increased by 5.6 times compared to a single junction. This is possible due to the mismatch of the impedances of JJs and antenna. As a result, with an increase in the number of junctions in a chain, the total absorbed power increases and is divided between the JJs.

Conclusion

The technique for calculating the receiving properties of JJs in the broadband detection regime was developed and applied. At the first stage, electromagnetic modeling of several geometries of antennas was carried out for effective receiving in the frequency range of 50–800 GHz. The electromagnetic properties of the systems were investigated, namely the amplitude–frequency characteristic and the beam pattern. For the chosen antenna geometry, different cases of a series of junctions integrated as a receiving element were considered; the fraction of the absorbed power in each JJ was investigated and it was shown that the use of seven junctions makes it possible to increase the total absorbed power at a fixed frequency of 250 GHz by a factor of 2.3. At the second stage, by solving a system of second-order differential equations related through

the equation for the antenna, the characteristics of the detector in the bias current regime were calculated, namely current–voltage characteristic, responsivity, voltage noise, and noise equivalent power. It was shown that the use of a series chain of junctions improves the responsivity by a factor of 2.5, the NEP value by a factor of 1.5, and the dynamic range by a factor of 5. As a result, for the standard technology of YBaCuO magnetron sputtering on a bicrystal substrate for a temperature of 77 K, a NEP in the region of $3 \cdot 10^{-13}$ W / $\sqrt{\text{Hz}}$ can be obtained.

It is possible to improve the match between the Josephson junction chain and the antenna of the receiving system by reducing the size of the JJs and the meander-type microstrip. This will avoid the observed effect of a decrease in the absorbed power in each junction at high frequencies. In addition, reducing the current noise of JJs can improve NEP and increase the benefit from linking junctions into a series chain. For this it is necessary, first, to perform synchronous detection at frequencies higher than 100 Hz, where the noise falls [45], and second, to reduce the noise by annealing the YBCO bicrystal junction in atomic oxygen [39].

Funding

The work is supported by the Russian Science Foundation (Project No. 20-79-10384).

ORCID® iDs

Alexander V. Chiginev - https://orcid.org/0000-0002-6676-9141
Leonid S. Revin - https://orcid.org/0000-0003-1645-4122

References

1. Reuter, W.; Siegel, M.; Herrmann, K.; Schubert, J.; Zander, W.; Braginski, A. I.; Müller, P. *Appl. Phys. Lett.* **1993,** *62,* 2280–2282. doi:10.1063/1.109395
2. Revin, L.; Pankratov, A.; Gordeeva, A.; Masterov, D.; Parafin, A.; Zbrozhek, V.; Kuzmin, L. *Appl. Sci.* **2020,** *10,* 7667. doi:10.3390/app10217667
3. Yu, M.; Geng, H.; Hua, T.; An, D.; Xu, W.; Chen, Z. N.; Chen, J.; Wang, H.; Wu, P. *Supercond. Sci. Technol.* **2020,** *33,* 025001. doi:10.1088/1361-6668/ab5e13
4. Sharafiev, A.; Malnou, M.; Feuillet-Palma, C.; Ulysse, C.; Wolf, T.; Couëdo, F.; Febvre, P.; Lesueur, J.; Bergeal, N. *Supercond. Sci. Technol.* **2018,** *31,* 035003. doi:10.1088/1361-6668/aa9d48
5. Benz, S. P.; Hamilton, C. A. *Appl. Phys. Lett.* **1996,** *68,* 3171–3173. doi:10.1063/1.115814
6. Klushin, A. M.; Prusseit, W.; Sodtke, E.; Borovitskii, S. I.; Amatuni, L. E.; Kohlstedt, H. *Appl. Phys. Lett.* **1996,** *69,* 1634–1636. doi:10.1063/1.117055
7. Sosso, A.; Andreone, D.; Lacquaniti, V.; Klushin, A. M.; He, M.; Klein, N. *IEEE Trans. Appl. Supercond.* **2007,** *17,* 874–877. doi:10.1109/tasc.2007.898581
8. Du, J.; Weily, A. R.; Gao, X.; Zhang, T.; Foley, C. P.; Guo, Y. J. *Supercond. Sci. Technol.* **2017,** *30,* 024002. doi:10.1088/0953-2048/30/2/024002
9. Snezhko, A. V.; Gundareva, I. I.; Lyatti, M. V.; Volkov, O. Y.; Pavlovskiy, V. V.; Poppe, U.; Divin, Y. Y. *Supercond. Sci. Technol.* **2017,** *30,* 044001. doi:10.1088/1361-6668/aa5ab5
10. Du, J.; Pegrum, C. M.; Gao, X.; Weily, A. R.; Zhang, T.; Guo, Y. J.; Foley, C. P. *IEEE Trans. Appl. Supercond.* **2017,** *27,* 1500905. doi:10.1109/tasc.2016.2636081
11. An, D. Y.; Yuan, J.; Kinev, N.; Li, M. Y.; Huang, Y.; Ji, M.; Zhang, H.; Sun, Z. L.; Kang, L.; Jin, B. B.; Chen, J.; Li, J.; Gross, B.; Ishii, A.; Hirata, K.; Hatano, T.; Koshelets, V. P.; Koelle, D.; Kleiner, R.; Wang, H. B.; Xu, W. W.; Wu, P. H. *Appl. Phys. Lett.* **2013,** *102,* 092601. doi:10.1063/1.4794072
12. Volkov, O.; Pavlovskiy, V.; Gundareva, I.; Khabibullin, R.; Divin, Y. *IEEE Trans. Terahertz Sci. Technol.* **2021,** *11,* 330–338. doi:10.1109/tthz.2020.3034815
13. Pavlovskiy, V. V.; Gundareva, I. I.; Volkov, O. Y.; Divin, Y. Y. *Appl. Phys. Lett.* **2020,** *116,* 082601. doi:10.1063/1.5142400
14. Chen, J.; Kurigata, Y.; Wang, H.; Nakajima, K.; Yamashita, T.; Wu, P. *IEEE Trans. Appl. Supercond.* **2003,** *13,* 1143–1146. doi:10.1109/tasc.2003.814176
15. Malnou, M.; Luo, A.; Wolf, T.; Wang, Y.; Feuillet-Palma, C.; Ulysse, C.; Faini, G.; Febvre, P.; Sirena, M.; Lesueur, J.; Bergeal, N. *Appl. Phys. Lett.* **2012,** *101,* 233505. doi:10.1063/1.4769441
16. Malnou, M.; Feuillet-Palma, C.; Ulysse, C.; Faini, G.; Febvre, P.; Sirena, M.; Olanier, L.; Lesueur, J.; Bergeal, N. *J. Appl. Phys.* **2014,** *116,* 074505. doi:10.1063/1.4892940
17. Gundareva, I.; Pavlovskiy, V.; Divin, Y. *IEEE Trans. Appl. Supercond.* **2018,** *28,* 1800105. doi:10.1109/tasc.2018.2822800
18. Kasaei, L.; Melbourne, T.; Li, M.; Manichev, V.; Qin, F.; Hijazi, H.; Feldman, L. C.; Gustafsson, T.; Davidson, B. A.; Xi, X.; Chen, K. *IEEE Trans. Appl. Supercond.* **2019,** *29,* 1102906. doi:10.1109/tasc.2019.2903418
19. Du, J.; Lazar, J. Y.; Lam, S. K. H.; Mitchell, E. E.; Foley, C. P. *Supercond. Sci. Technol.* **2014,** *27,* 095005. doi:10.1088/0953-2048/27/9/095005
20. Tarasov, M.; Stepantsov, E.; Lindström, T.; Kalabukhov, A.; Ivanov, Z.; Claeson, T. *Phys. C (Amsterdam, Neth.)* **2002,** *372-376,* 355–359. doi:10.1016/s0921-4534(02)00668-8
21. Semenov, A. D.; Richter, H.; Hübers, H.-W.; Günther, B.; Smirnov, A.; Il'in, K. S.; Siegel, M.; Karamarkovic, J. P. *IEEE Trans. Microwave Theory Tech.* **2007,** *55,* 239–247. doi:10.1109/tmtt.2006.889153
22. Huo, Y.; Taylor, G. W.; Bansal, R. *Int. J. Infrared Millimeter Waves* **2002,** *23,* 819–839. doi:10.1023/a:1015738932198
23. Volkov, O. Yu.; Divin, Yu. Ya.; Gubankov, V. N.; Gundareva, I. I.; Pavlovskiy, V. V. *J. Commun. Technol. Electron.* **2009,** *54,* 1310. doi:10.1134/s1064226909110114
24. Zhang, Y. Dynamics and applications of long Josephson junctions. Ph.D. Thesis, Chalmers University of Technology, Göteborg, Sweden, 1993.
25. Masterov, D. V.; Parafin, A. E.; Revin, L. S.; Chiginev, A. V.; Skorokhodov, E. V.; Yunin, P. A.; Pankratov, A. L. *Supercond. Sci. Technol.* **2017,** *30,* 025007. doi:10.1088/1361-6668/30/2/025007
26. Bergeal, N.; Lesueur, J.; Sirena, M.; Faini, G.; Aprili, M.; Contour, J. P.; Leridon, B. *J. Appl. Phys.* **2007,** *102,* 083903. doi:10.1063/1.2796105
27. Wiesenfeld, K. *J. Phys. A: Math. Theor.* **2020,** *53,* 064002. doi:10.1088/1751-8121/ab5e4e

28. Ray, A.; Mishra, A.; Ghosh, D.; Kapitaniak, T.; Dana, S. K.; Hens, C. *Phys. Rev. E* **2020,** *101,* 032209. doi:10.1103/physreve.101.032209
29. Domínguez, D.; Cerdeira, H. A. *Phys. Rev. B* **1995,** *52,* 513–526. doi:10.1103/physrevb.52.513
30. Gundareva, I. I.; Volkov, O. Y.; Lyatti, M. V.; Divin, Y. Y.; Gubankov, V. N.; Pavlovskiy, V. V. *IEEE Trans. Appl. Supercond.* **2011,** *21,* 147–150. doi:10.1109/tasc.2010.2101030
31. Tarasov, M.; Golubev, D.; Shumeiko, V.; Ivanov, Z.; Stepantsov, E.; Harnak, O.; Claeson, T. *J. Exp. Theor. Phys. Lett.* **1998,** *68,* 454–459. doi:10.1134/1.567889
32. Tarasov, M. A.; Stepantsov, E. A.; Naito, M.; Tsukada, A.; Winkler, D.; Kalabukhov, A. S.; Kupriyanov, M. Y. *J. Exp. Theor. Phys.* **2007,** *105,* 636–641. doi:10.1134/s106377610709021x
33. Lyatti, M.; Divin, Y.; Volkov, O.; Pavlovskii, V.; Gubankov, V.; Urban, K. *IEEE Trans. Appl. Supercond.* **2017,** *17,* 332–335. doi:10.1109/tasc.2007.898188
34. Lyatti, M. V.; Tkachev, D. A.; Divin, Yu. Ya. *Tech. Phys. Lett.* **2006,** *32,* 860–863. doi:10.1134/s1063785006100130
35. Pavlovskiy, V. V.; Divin, Y. Y. *J. Commun. Technol. Electron.* **2019,** *64,* 1003–1010. doi:10.1134/s106422691908014x
36. Ambegaokar, V.; Halperin, B. I. *Phys. Rev. Lett.* **1969,** *22,* 1364–1366. doi:10.1103/physrevlett.22.1364
37. Kawasaki, M.; Chaudhari, P.; Gupta, A. *Phys. Rev. Lett.* **1992,** *68,* 1065–1068. doi:10.1103/physrevlett.68.1065
38. Gustafsson, D.; Lombardi, F.; Bauch, T. *Phys. Rev. B* **2011,** *84,* 184526. doi:10.1103/physrevb.84.184526
39. Lyatti, M. V.; Poppe, U.; Divin, Y. Y. *IEEE Trans. Appl. Supercond.* **2007,** *17,* 314–317. doi:10.1109/tasc.2007.898674
40. Tarasov, M.; Stepantsov, E.; Kalabukhov, A.; Kupriyanov, M.; Winkler, D. *J. Exp. Theor. Phys. Lett.* **2008,** *86,* 718–720. doi:10.1134/s0021364007230075
41. Tarasov, M.; Shul'man, A.; Polyanskii, O.; Vystavkin, A.; Kosarev, E.; Golubev, D.; Stepantsov, E.; Darula, M.; Harnack, O.; Ivanov, Z. *J. Exp. Theor. Phys. Lett.* **1999,** *70,* 340–345. doi:10.1134/1.568177
42. Tarasov, M.; Stepantsov, E.; Golubev, D.; Ivanov, Z.; Claeson, T.; Harnack, O.; Darula, M.; Beuven, S.; Kohlstedt, H. *IEEE Trans. Appl. Supercond.* **1999,** *9,* 3761–3764. doi:10.1109/77.783846
43. Du, J.; Smart, K.; Li, L.; Leslie, K. E.; Hanham, S. M.; Wang, D. H. C.; Foley, C. P.; Ji, F.; Li, X. D.; Zeng, D. Z. *Supercond. Sci. Technol.* **2015,** *28,* 084001. doi:10.1088/0953-2048/28/8/084001
44. Ovsyannikov, G. A.; Borisenko, I. V.; Constantinian, K. Y.; Kislinski, Y. V.; Hakhoumian, A. A.; Pogosyan, N. G.; Zakaryan, T.; Pedersen, N. F.; Mygind, J.; Uzunoglu, N.; Karagianni, E. *IEEE Trans. Appl. Supercond.* **2005,** *15,* 533–536. doi:10.1109/tasc.2005.849902
45. Horng, H. E.; Yang, S. Y.; Jeng, J. T.; Wu, J. M.; Chen, J. H.; Yang, H. C. *IEEE Trans. Appl. Supercond.* **1999,** *9,* 3986–3989. doi:10.1109/77.783901

License and Terms

BEILSTEIN JOURNAL OF NANOTECHNOLOGY

Controllable two- and three-state magnetization switching in single-layer epitaxial $Pd_{1-x}Fe_x$ films and an epitaxial $Pd_{0.92}Fe_{0.08}$/Ag/$Pd_{0.96}Fe_{0.04}$ heterostructure

Igor V. Yanilkin*[1], Amir I. Gumarov[1,2], Gulnaz F. Gizzatullina[1], Roman V. Yusupov[1] and Lenar R. Tagirov[2]

Full Research Paper

Open Access

Address:
[1]Institute of Physics, Kazan Federal University, Kremlyovskaya Str. 18, 420008 Kazan, Russia and [2]Zavoisky Physical-Technical Institute, FRC Kazan Scientific Centre of RAS, 420029 Kazan, Russia

Email:
Igor V. Yanilkin* - yanilkin-igor@yandex.ru

* Corresponding author

Keywords:
anisotropic magnetoresistance; magnetization reversal; Pd–Fe alloy; thin epitaxial film

Beilstein J. Nanotechnol. **2022,** *13,* 334–343.
https://doi.org/10.3762/bjnano.13.28

Received: 27 December 2021
Accepted: 16 March 2022
Published: 30 March 2022

This article is part of the thematic issue "Intrinsic Josephson effect and prospects of superconducting spintronics".

Guest Editor: A. S. Sidorenko

Abstract

We have investigated the low-temperature magnetoresistive properties of a thin epitaxial $Pd_{0.92}Fe_{0.08}$ film at different directions of the current and the applied magnetic field. The obtained experimental results are well described within an assumption of a single-domain magnetic state of the film. In a wide range of the appled field directions, the magnetization reversal proceeds in two steps via the intermediate easy axis. An epitaxial heterostructure of two magnetically separated ferromagnetic layers, $Pd_{0.92}Fe_{0.08}$/Ag/$Pd_{0.96}Fe_{0.04}$, was synthesized and studied with dc magnetometry. Its magnetic configuration diagram has been constructed and the conditions have been determined for a controllable switching between stable parallel, orthogonal, and antiparallel arrangements of magnetic moments of the layers.

Introduction

The generation of the long-range triplet component of the superconducting pairing at noncollinear orientations of magnetization in ferromagnetic layered systems is extensively studied in the framework of magnetic Josephson junctions (MJJs) ([1-3] for early works, and [4,5] for very recent papers), and superconductive spin valves (SSVs) [6-9]. The key points of the underlying physics are non-uniform magnetic configurations in the system that mix singlet and triplet superconducting pairing channels. As a result, at collinear magnetic configurations, short-range singlet and zero-spin-projection triplet pairings

carry the Josephson supercurrent in MJJs. At non-collinear magnetic configurations, on the contrary, long-range equal-spin pairings can conduct the supercurrent in MJJs with much thicker or long narrow weak links. This gives additional degrees of freedom to control the critical current of MJJs [10] or SSVs [6], or current–phase relations in MJJs [11,12]. In particular, the spin-valve structure embedded into a MJJ can serve as an actuator for switching the MJJ between critical current modes or flipping its current–phase relation, thus, extending its functionality.

Palladium–iron alloys $Pd_{1-x}Fe_x$ with $x < 0.10$ are of strong practical interest for such MJJ and SSV structures [13-17] as a material for weak ferromagnetic links with tunable magnetic properties [18]. Epitaxial films of $Pd_{1-x}Fe_x$ alloys with low iron content x are easy-plane ferromagnets with four-fold anisotropy in the film plane [18,19]. Our conjecture is a possibility to switch the magnetic moment of a $Pd_{1-x}Fe_x$ alloy film between the steady directions (90° apart) as it had been done with epitaxial iron films [20-22]. To realize this idea, it is necessary to find the particular angle of the applied magnetic field direction with respect to the in-plane four-fold easy axes. Once the conditions of magnetization rotation by 90° are found, the addition of the second, magnetically more hard ferromagnetic layer with properly aligned in-plane easy axes makes it possible to achieve parallel, orthogonal, and antiparallel configurations of their magnetic moments. Such a heterostructure can serve as a magnetic actuator for switching the MJJ from the singlet conduction mode to the triplet conduction mode and vice versa.

The experimental rotation of the magnetic moment by 90° in epitaxial $Pd_{1-x}Fe_x$ films has not been yet explored. In [18,19], based on magnetometry data, it was assumed that magnetization reversal occurs as a result of the coherent rotation of the magnetic moment by 180°; and in the study of the $Pd_{0.96}Fe_{0.04}$/VN/$Pd_{0.92}Fe_{0.08}$ structure [23], stable parallel and antiparallel configurations of magnetic moments were obtained. However, the maximum amplitude of the triplet pairing component in the PdFe1/N/PdFe2 bilayer structure is achieved near the orthogonal magnetic configuration of the ferromagnetic layers PdFe1 and PdFe2 [6]. Therefore, it is instructive to investigate the switching properties of $Pd_{1-x}Fe_x$ films and heterostructures based on this alloy targeting the controllable non-collinear magnetic configurations in the bilayer structure.

Experimental

An epitaxial film of the $Pd_{0.92}Fe_{0.08}$ alloy with a thickness of 20 nm and an epitaxial thin-film heterostructure $Pd_{0.92}Fe_{0.08}$(20 nm)/Ag(20 nm)/$Pd_{0.96}Fe_{0.04}$(20 nm) were grown in an ultrahigh-vacuum (UHV) apparatus (SPECS, Germany) by molecular beam deposition. Epi-polished MgO(100) single-crystal plates (Crystal GmbH, Germany) were used as substrates. The deposition routine and structural studies of similar films are described in [24], the magnetic properties measured by ferromagnetic resonance (FMR) and vibrating sample magnetometry (VSM) in magnetic fields along the easy and hard magnetic axes are presented in [18,19].

In this paper, the magnetization reversal in the $Pd_{0.92}Fe_{0.08}$ film at different in-plane orientations of the magnetic field was studied by measuring the anisotropic magnetoresistance (AMR) using the four-probe method. For this purpose, the $Pd_{0.92}Fe_{0.08}$ film was cut with a diamond saw into stripe-like pieces. In the first sample the current flowed along the ⟨100⟩ direction of the $Pd_{0.92}Fe_{0.08}$ film (sample S00), in the second sample at an angle of 25° with respect to the ⟨100⟩ direction (sample S25). The current contacts were ultrasonically welded at several locations in a line across the width of the sample to ensure a uniform current distribution throughout the core part of the sample supplied with the potential terminals.

The magnetic hysteresis loops for the $Pd_{0.92}Fe_{0.08}$(20 nm)/Ag(20 nm)/$Pd_{0.96}Fe_{0.04}$(20 nm) heterostructure were obtained via vibrational sample magnetometry since the AMR measurement for this system is useless due to a short cut by the silver layer. All AMR and VSM experiments were carried out with the PPMS-9 system (Quantum Design).

Results

Current along the [100] direction

We start with the presentation of the results for a sample S00 of the $Pd_{0.92}Fe_{0.08}$ film where the electrical current flowed along the [100] direction of the film (and the substrate). The reference frame orientation with respect to the sample is shown in the insets in Figure 1. When measuring the magnetoresistance, the magnetic field was applied at different angles in three main planes as shown in Figure 1. At any orientation, on approaching zero field, the resistivity returns to a common value of approx. 15.8 μΩ·cm, corresponding to the magnetic moment along the easy axes (see more details below). The resistivities hierarchy for the magnetic moment oriented along the *X*-, *Y*-, and *Z*-axes, $\rho_x > \rho_y > \rho_z$, is typical for ferromagnetic films of comparable thickness [25]. The difference in resistances ρ_x and ρ_z (magnetic field perpendicular to the current) is usually associated with the geometrical size effect [26]. A detailed study of the size effect for the $Pd_{0.92}Fe_{0.08}$ film is beyond the scope of this study.

In addition to the anisotropic magnetoresistance associated with the mutual orientations of the magnetic moment and the direction of the current, there is a resistance drop with an increase of the magnetic field strength, that is, the negative magnetoresistance. The latter effect is related to a decrease in electron-

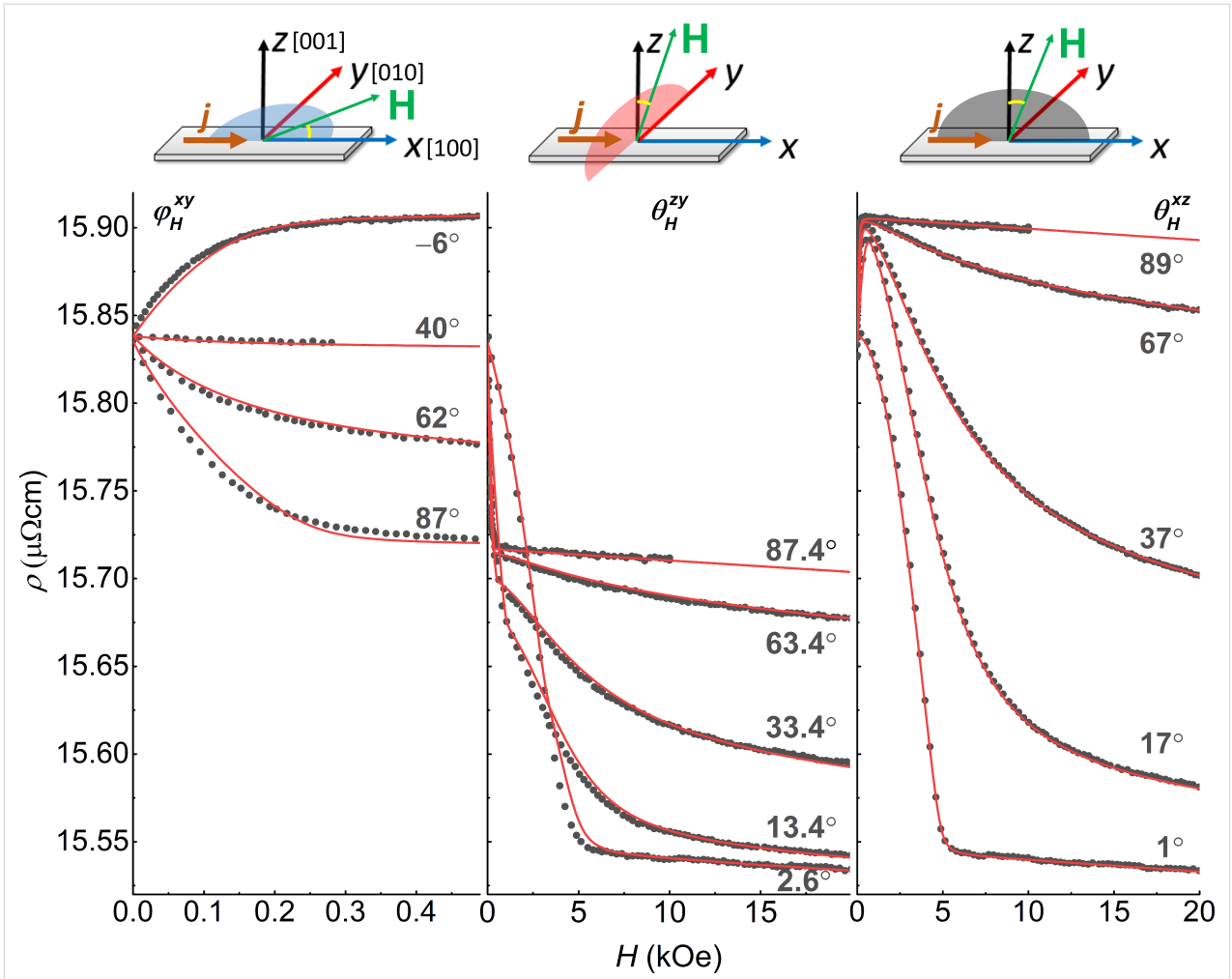

Figure 1: Dependence of the resistivity on the magnetic field at its different orientations, T = 5 K. The field is varied from its maximum value to zero. Circles indicate the experimental data, lines indicate the results of the modeling following Equation 2.

magnon scattering due to the suppression of spin waves in high magnetic fields [27]. At low temperatures, this effect is usually small, and a positive magnetoresistance caused by the action of the Lorentz force dominates [27,28]. However, in the $Pd_{0.92}Fe_{0.08}$ epitaxial film, the electron mean free path is small even at low temperatures and is determined by the mean distance between the iron atoms. Therefore, the Lorentzian contribution is small, and even at 5 K, the negative magnetoresistance is observed. As the temperature is increased, the number of magnons grows, thereby leading to a larger negative slope $\Delta\rho/\Delta H$ (Figure 2a). A theoretical description of this process for elemental 3d ferromagnets was proposed in [27]. The dependence of the resistance on a magnetic field up to 100 T is described by the expression:

$$\Delta\rho_m = \rho_m(T,B) - \rho_m(T,0) \approx \frac{BT}{D(T)} \ln\left(\frac{\mu_B B}{kT}\right), \quad (1)$$

where $D(T) \approx D_0 - AT^2$ determines the increase in the effective mass of magnons with increasing the temperature. The dependence $\Delta\rho_z(H) = \Delta\rho_{AMR} + \Delta\rho_m$ is shown in Figure 2a, where $\Delta\rho_{AMR}$ is the contribution from the anisotropic magnetoresistance. It is seen that Equation 1 describes the experimental results quite well. In the inset of Figure 2a, the variation of the slope of $\Delta\rho_x$ with temperature is shown. It reaches the maximum value at the Curie temperature $T_C \approx 230$ K according to the magnetometry data.

At a fixed magnetic field and temperature, the resistance value reflects the direction of the magnetic moment in space. In a spherical coordinate system, the resistance is described by the following expression [29]:

$$\rho(\varphi_M, \theta_M, H) = \left(\rho_x \cos^2\varphi_M + \rho_y \sin^2\varphi_M\right)\sin^2\theta_M + \rho_z \cos^2\theta_M + \Delta\rho_m(H), \quad (2)$$

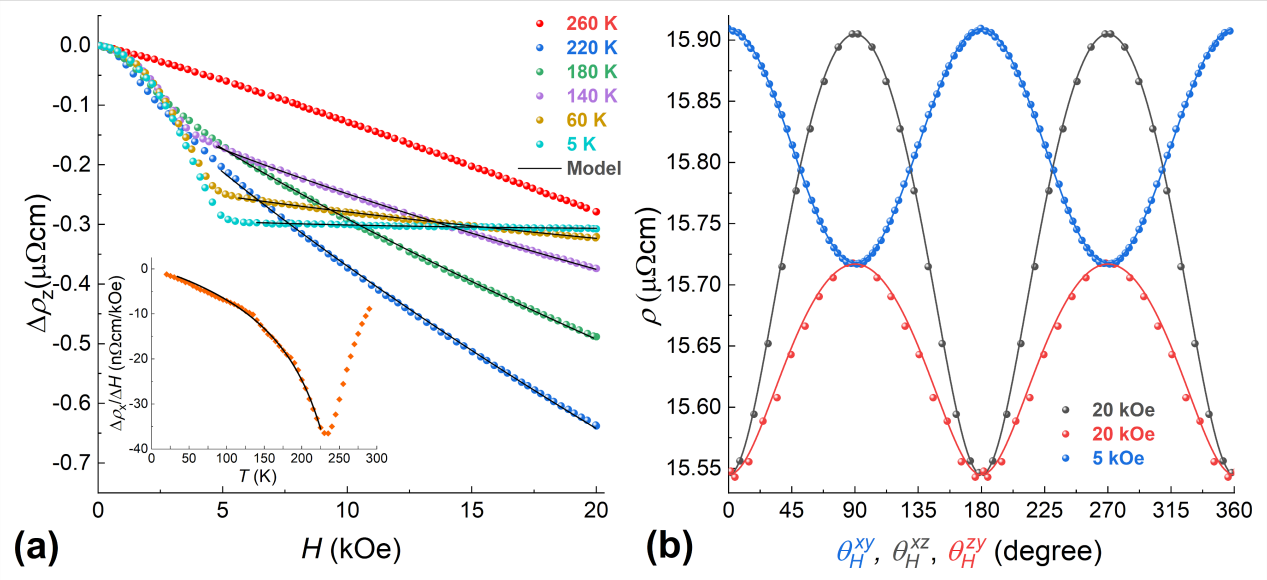

Figure 2: (a) Dependence of the resistivity $\Delta\rho_z$ on the magnetic field strength at different temperatures. Inset: a variation of the (ρ_x(10 kOe) – ρ_x(0.5 kOe))/9.5 kOe slope with temperature. Lines are drawn using the model of Equation 1. (b) Dependence of the resistance on the orientation of the magnetic field at T = 5 K. The contribution from the electron–magnon scattering is subtracted. Lines are drawn using the model of Equation 2.

where ρ_x, ρ_y, and ρ_z are the resistivities for the cases of the magnetic moment oriented along the X-, Y-, and Z-axes, respectively. The contribution from the electron–magnon scattering is subtracted for each of ρ_x, ρ_y, and ρ_z. Angles θ_M and φ_M are referenced relative to the [001] and [100] axes, respectively.

For a theoretical description of the dependencies $\rho(H)$, $\rho(\varphi_H, \theta_H)$ presented in Figure 1 and Figure 2b, we used an approach similar to the Stoner–Wolfarth one for a single-domain magnetic system. According to [18], the $Pd_{0.92}Fe_{0.08}$ epitaxial film is the easy-plane system; the magnetocrystaline energy of the film can be written in terms of the cubic anisotropy with small tetragonal distortion. In addition, based on the guess simulations, an importance of the uniaxial anisotropy in the film plane became obvious:

$$E = -\mathbf{M}\cdot\mathbf{H} + 2\pi M_s^2\alpha_3^2 - K_p\alpha_3^2 - K_u\alpha_u^2 - \frac{1}{2}K_1\left(\alpha_1^4+\alpha_2^4+\alpha_3^4\right) - \frac{1}{2}K_2\alpha_3^4, \quad (3)$$

where α_i are directional cosines for the magnetic M with respect to crystallographic axes [100], [010], [001] of the film, α_u is the cosine of the angle between M and the direction of the uniaxial anisotropy axis, K_u is the in-plane uniaxial anisotropy constant. As a result of the parameter adjustment, a good agreement of the theoretical dependences with the experimental data was achieved (Figure 1 and Figure 2b), indicating correctness of the models, Equation 2 and Equation 3. The values of the anisotropy constants, obtained by the fitting, are K_p = −190 kerg/cm^3 for the perpendicular anisotropy term, K_1 = −20 kerg/cm^3 for the cubic term, and K_2 = −20 kerg/cm^3 for the tetragonal term, in good agreement with the values obtained from the FMR data analysis [18]. The uniaxial anisotropy is directed along [100], and its magnitude is K_u = 5 kerg/cm^3. It should be noted that the occurrence of uniaxial anisotropy is not related to the shape of the samples. We further explored this by measuring the AMR and FMR of different square $Pd_{0.92}Fe_{0.08}$ samples and obtained the uniaxial anisotropy both along the [100] and [−110] axes. The origin of the uniaxial anisotropy term is not clear at the moment. Based on the values of the anisotropy constants, we can conclude that our film is a system with easy axes lying in the plane of the film and close to [110] (⟨110⟩) (approx. 38° relative to [100], see Figure 3b).

In the following, we denote the measured resistivity by ρ_{xy}, ρ_{xz}, and ρ_{yz}, with the magnetic field applied in the XY-, XZ-, and YZ-planes, respectively. The angles are defined in the top insets in Figure 1. Let us consider in more detail the dependence of ρ_{xy} on the magnetic field applied at φ_H = 6° (Figure 3a). The measurement started from the saturation in the positive direction of the field (not shown). This direction is close to the hard axis; therefore, on the field value decrease, at its certain value of approx. 300 Oe, the magnetic moment starts to rotate coherently from the direction of the field towards the easy axis (see Figure 3a,b). At zero field, the moment is oriented along the easy axis. At small negative fields, the resistance experiences two abrupt jumps at −20 Oe and at −67 Oe. Such double jumps were observed in the $\rho_{xy}(H)$ dependence for a wide range of angles φ_H of the applied magnetic field. The magnitude of the magnetic field, at which the jumps occur, depends on the direc-

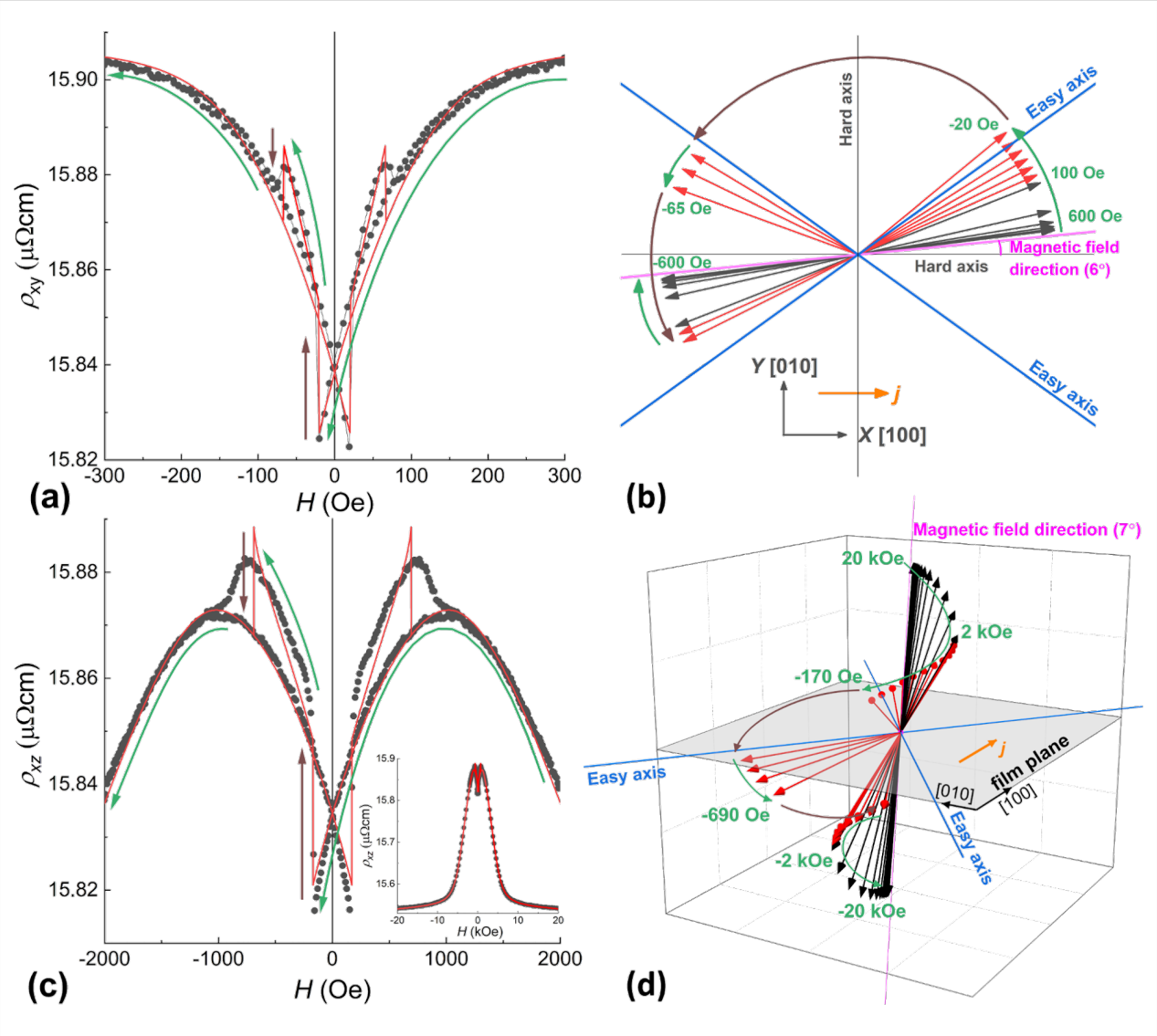

Figure 3: Dependences of the resistivity on the applied magnetic field for (a) $\varphi_H = 6°$, $\theta_H = 90°$ and (c) $\varphi_H = 0°$, $\theta_H = 7°$; points: experimental data, lines: results of the modelling with Equation 2 and Equation 3. (b) Rotation of the magnetic moment of the film (within the same model) for $\varphi_H = 6°$, $\theta_H = 90°$; the vectors show the direction of the moment at different values of the magnetic field (for the black vectors, the step is 100 Oe, while for the red ones it is –20 Oe); insert: the geometry of the experiment. (d) Rotation of the magnetic moment of the film (within the model) in space at $\varphi_H = 0°$, $\theta_H = 7°$; (for the black vectors the step is 2 kOe, while for the red ones –0.2 kOe). Green arrows in all figures denote a smooth change in the direction of the magnetic moment, brown: magnetization direction jumps.

tion of the field. Modeling of such a scenario (Figure 3a) brings us to the conclusion that these jumps in $\rho_{xy}(H)$ originate from two successive turns between the directions adjacent to the easy axes, as shown in Figure 3b.

The double jump also manifests itself in the dependences of $\rho_{xz}(H)$ and $\rho_{yz}(H)$. As an example, the dependence of ρ_{xz} on the magnetic field applied at $\theta_H = 7°$ and a modelled process of the magnetization reversal are shown in Figure 3c and 3d, respectively. Since the projection of the magnetic field onto the film plane is small ($H_x \approx 0.12H_{xz}$), the coercive field values are increased and the double jumps becomes smeared.

Current at an angle to [100] direction, field H in the *XY* plane

For the sample S25, with a current directed at an angle of approx. 25° to the [100] axis, the double jumps are manifested much brighter (Figure 4a), since in this case, the easy axes are not equivalent in terms of the measured resistance. At the same time, the relative magnitude of the AMR effect $(\Delta\rho_{xy}/\rho_{xy})\cdot 100\%$ turns out to be less pronounced than with the current along the hard axis [100], that is, 0.45% and 1.22%, respectively. This is in a qualitative agreement with the experiments on AMR of epitaxial iron films, where the AMR effect was also maximal when the current direction was along the hard axis [30].

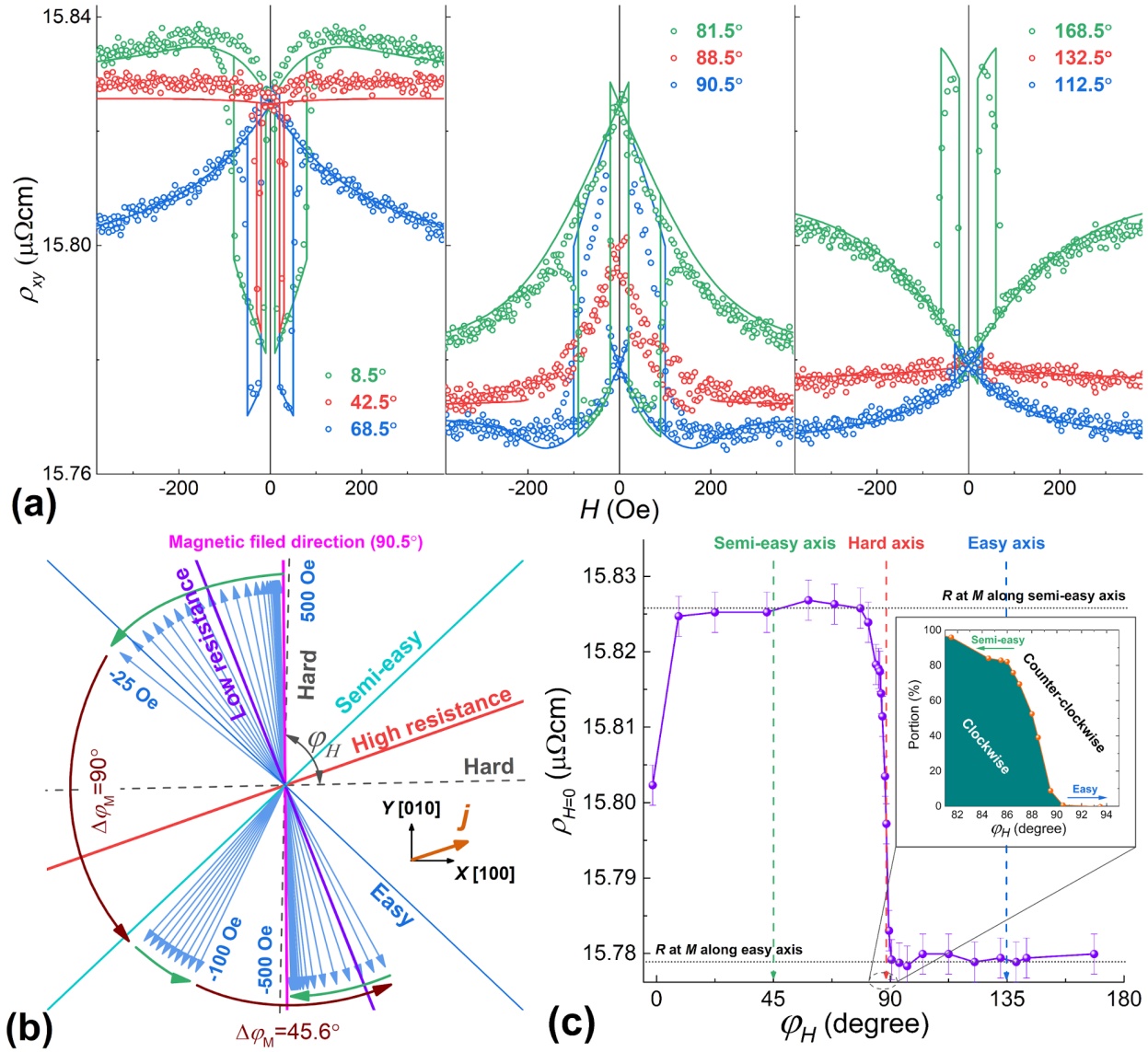

Figure 4: (a) Dependences of the resistivity ρ_{xy} on the applied magnetic field for different angles φ_H (measured from [100]) at T = 5 K; points: experimental data, lines: results of the modelling with Equation 2 and Equation 3. (b) Rotation (within the model) of the magnetic moment of the film with a step of 20 Oe for φ_H = 90.5° under the field variation from +500 Oe to –500 Oe; insert: the geometry of the experiment. (c) Dependence of the resistance at zero fields on the direction of the applied field; insert: the calculated fraction of the film material with the magnetic moment rotated clockwise to a semi-easy axis.

For the theoretical description of the $\rho_{xy}(H)$ dependences, the constant of the in-plane uniaxial anisotropy K_u and its direction were adjusted (leaving all the other parameters the same as for the previous sample). The easy axis of the uniaxial anisotropy was found along the [−110] direction (see the inset to Figure 4b) with K_u = 1 kerg/cm^3. The model of the single-domain equilibrium state of the system describes well the experimental $\rho_{xy}(H)$ dependences (Figure 4a), except for the angles adjacent to the hard axis (see more details below). A superimposed uniaxial anisotropy makes the [−110] direction easier than the [110] one. Therefore we call the latter the semi-easy axis. This significantly modifies the process of the magnetization reversal (compared with the first sample, where the easy axes were equivalent) when the magnetic field is applied along the easy axes. If the field is applied along the semi-easy axis, the magnetization reversal occurs in two jumps (Figure 4a, φ_H = 42.5°), in the other case, the magnetization reversal occurs in one jump (Figure 4a, φ_H = 132.5°). Recall that for AMR, the

magnetic moment rotation by 180° does not lead to any change in resistance, therefore, a one-jump magnetization reversal manifests itself in an absence or only a small drop in resistance.

By measuring the residual resistance (after field removal), it is possible to realize which easy axis was chosen by a system (Figure 4c). Near the direction of the heavy axis, there is a transition from the counter-clockwise rotation to the clockwise one. This transition spans over a notable range of angles. For example, within the angle range of 82–90°, in the course of the magnetization reversal, one fraction of the film rotates its moment clockwise, while the other rotates counter-clockwise (Figure 4c, inset).

As follows from Figure 4a, the coercive fields corresponding to the first step of the reversal (H_{c1}) and, especially, to the second one (H_{c2}) depend significantly on the direction of the applied field. Figure 5a illustrates this relationship. A detailed explanation of this behavior was proposed in [21]. It suggested the successive movements of two 90° domain walls. The values of the coercive fields are determined by the conditions when the energy gain due to a moment rotation overcomes the wall pinning energy:

$$H_{c1,c2} = \frac{\varepsilon_{90\,deg} \pm K_u}{M\left(\pm\cos\left(\varphi_H - \frac{\pi}{4}\right) \pm \sin\left(\varphi_H - \frac{\pi}{4}\right)\right)} \qquad (4)$$

For the $Pd_{0.92}Fe_{0.08}$ film, this model describes well the dependence of $H_{c1}(\varphi_H)$ at $\varepsilon_{90deg} \approx 6$ kerg/cm^3. However, for the values of H_{c2}, the 90° domain wall model is not suitable. This is because at the second jump the domain wall, in fact, is not the 90° type, the difference in the angles in the wall $\Delta\varphi_M$ is much smaller than 90° (see Figure 4b). Moreover, it depends on the angle of the applied field. Based on the experimental data for $H_{c2}(\varphi_H)$, this dependence can be calculated. Figure 5b shows the obtained dependences $\Delta\varphi_M(\varphi_H)$. It can be seen that as the hard axis is approached, the amplitude of the rotation angle of the moment in the domain wall decreases. In this situation, it is no longer possible to assert that the pinning energy is constant since it decreases with decreasing the angle difference in the domain wall.

For the field directions close to the hard axis (for example, at φ_H = 87–90°), it is generally difficult to describe the magnetization reversal, since the volume of the material is divided into two fractions that rotate their moments in opposite directions. In addition, at the field strengths of the second jump in magnetization, the height of the barrier for the coherent rotation also becomes insignificant. Therefore, in this range of angles, magnetization reversal is potentially possible by the macroscopic coherent rotation of the magnetic moment of the film.

Discussion

The dependences of $H_{c1,c2}(\varphi_H)$ obtained in this work for the $Pd_{0.92}Fe_{0.08}$ film confirm the conjecture that three steady magnetic configurations, parallel (P), anti-parallel (AP), and orthogonal (OG) can be realized in the epitaxial PdFe1/N/PdFe2 heterostructure by choosing the appropriate magnetic field direction and varying the applied magnetic field pulse amplitude. An important condition for this is an absence of a substantial magnetic interaction between the PdFe1 and PdFe2 layers. It is achieved by introducing the non-magnetic spacer layer N of

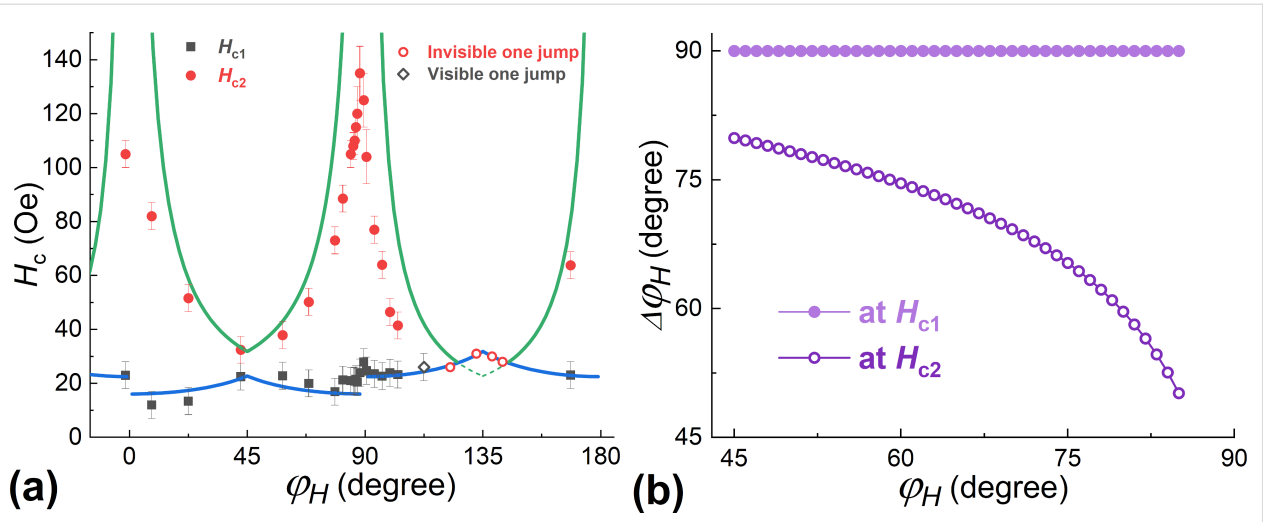

Figure 5: (a) Dependences of the coercive fields of the two jumps (H_{c1} and H_{c2}) on the direction of the applied magnetic field at T = 5 K; lines: the model of Equation 4. (b) Dependence of the magnetic moment rotation angle within the particular jump on the direction of the applied field.

silver satisfying the epitaxial growth conditions. The different coercive fields were obtained choosing the $Pd_{0.92}Fe_{0.08}$ and $Pd_{0.96}Fe_{0.04}$ compositions for the ferromagnetic PdFe1 and PdFe2 layers [18]. Figure 6 shows magnetic hysteresis loops of the $Pd_{0.92}Fe_{0.08}$/Ag/$Pd_{0.96}Fe_{0.04}$ heterostructure for magnetic field angles of 40°, 30°, and −30° degrees relative to the [100] direction. For an angle of 40°, the minor loops show the switching sequence of P → OG → AP, for 30°, P → OG, and for −30°, P → AP. The analysis of the magnetic hysteresis loops at different angles of the applied magnetic field makes it possible to build a magnetic configuration diagram for this heterostructure (Figure 7a). As one can see, there are quite large regions of various stable P, OG, and AP states.

An analysis of the angular dependences of $H_c(\varphi_H)$, Figure 7a, allows us to conclude that the pinning energy for the $Pd_{0.94}Fe_{0.04}$ film is much lower (about $\varepsilon_{90deg} \approx 1.8$ kerg/cm^3) than for the $Pd_{0.92}Fe_{0.08}$ film ($\varepsilon_{90deg} \approx 6$ kerg/cm^3). Moreover,

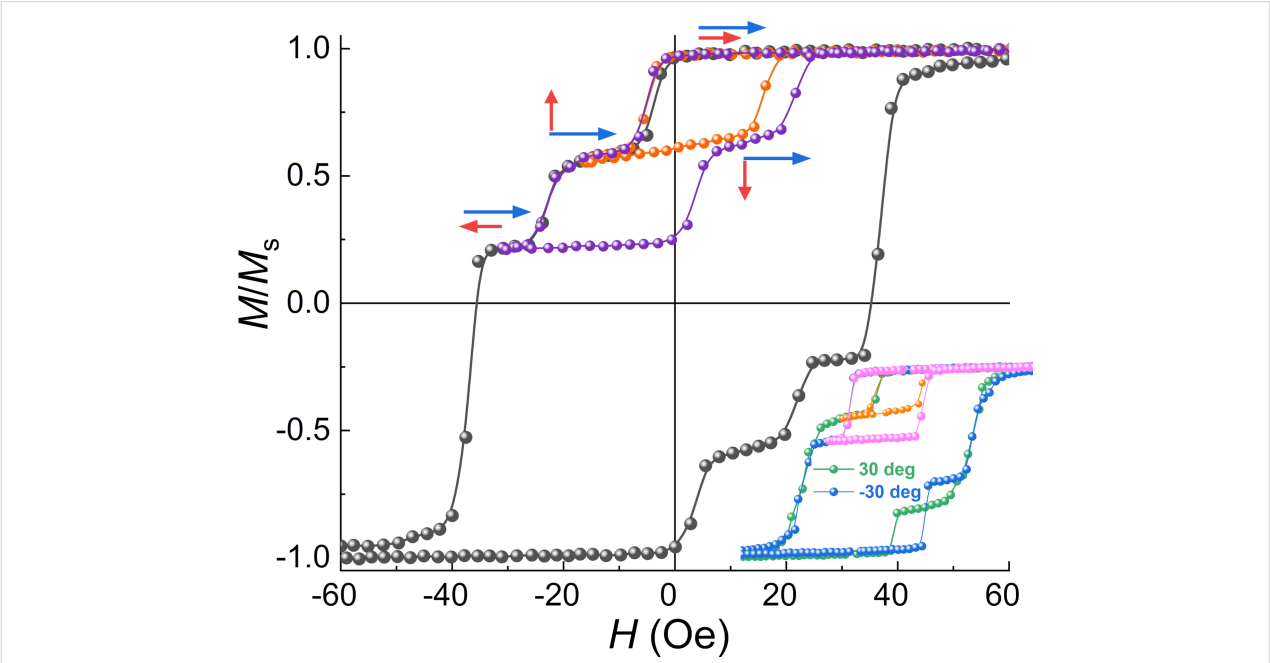

Figure 6: Magnetic hysteresis loops for the $Pd_{0.92}Fe_{0.08}$/Ag/$Pd_{0.96}Fe_{0.04}$ heterostructure at T = 5 K at an angle of 40° with respect to [100] (inset: the same for angles of 30° and −30°).

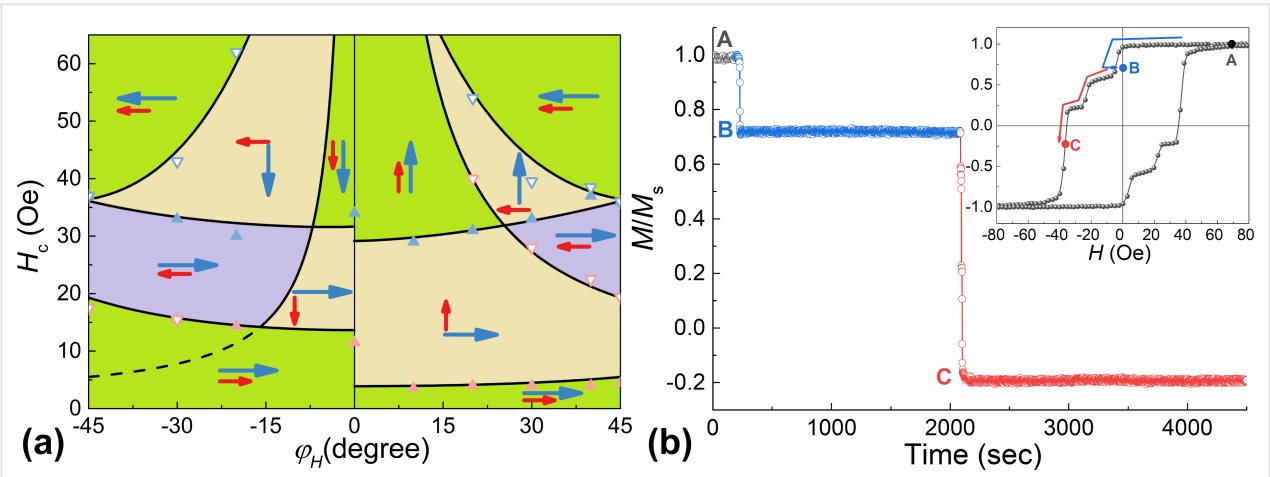

Figure 7: (a) Dependences of the coercive fields of the $Pd_{0.92}Fe_{0.08}$/Ag/$Pd_{0.96}Fe_{0.04}$ heterostructure on the angle of the applied magnetic field relative to the [100] axis at T = 5 K. The symbols are experimental values (red: $Pd_{0.96}Fe_{0.04}$, blue: $Pd_{0.92}Fe_{0.08}$, solid: H_{c1}, open: H_{c2}), the lines represent the calculations. (b) Time dependence of the reduced moment for a magnetic field at an angle of 40° to [100]; arrows in the inset show the path from point A (P) to points B (OG) further to C (mixed AP+OG).

in our $Pd_{0.92}Fe_{0.08}$/Ag/$Pd_{0.96}Fe_{0.04}$ heterostructure, the $Pd_{0.96}Fe_{0.04}$ layer has a significant uniaxial anisotropy ($K_u \approx 1$ kerg/cm^3) along the [−110] direction, while in the $Pd_{0.92}Fe_{0.08}$ layer it is practically absent.

Low temperatures and single-domain state (or bi-domain at magnetization reversal along a hard axis) of the magnetic film ensure the stability of the obtained magnetic configurations. Figure 7b shows the time evolution of the reduced moment depending on the history of the evolution of the applied magnetic field (inset to Figure 7b). The system was brought to point B (OG state) by sweeping the magnetic field in the following order: 50 Oe → −5 Oe → 0 Oe; to point C (mixed AP+OG state): 0 Oe → −36 Oe. In both cases, on a time scale of approx. 1000 s, there are no noticeable changes in the magnetic moment of the steady states of the heterostructure. This is fundamentally different from the dynamics of the magnetization of the polycrystalline $Pd_{0.99}Fe_{0.01}$ film, in which significant demagnetization occurred on a time scale of approx. 100 s [31].

Conclusion

Detailed measurements of the magnetoresistance have shown that the $Pd_{0.92}Fe_{0.08}$ epitaxial film, being an easy-plane ferromagnet with a pronounced in-plane anisotropy, undergoes magnetization switching between two (with collinear magnetization directions) or three (including orthogonal to the previously indicated two directions) single-domain states depending on the direction of the applied magnetic field. In the latter case, the magnetization reversal proceeds in two distinct stages, the first stage being the motion of the 90° domain wall, and the second one is the motion of the angle-φ domain wall, where the angle φ depends on the angle of the applied field relative to crystallographic axes. The pinning energy of the 90° domain wall is approx. 6 kerg/cm^3 for the $Pd_{0.92}Fe_{0.08}$ film, and approx. 1.8 kerg/cm^3 for the $Pd_{0.96}Fe_{0.04}$ film. The use of two magnetic layers PdFe1 and PdFe2 with different coercive fields, separated by a nonmagnetic spacer N, makes it possible to realize parallel, orthogonal, and antiparallel configurations of magnetic moments. It has been experimentally demonstrated that the $Pd_{0.92}Fe_{0.08}$/Ag/$Pd_{0.96}Fe_{0.04}$ heterostructure can switch between P, OG, and AP steady magnetic configurations in the film plane by rotating the magnetic moment of the soft magnetic layer with respect to the magnetically harder layer.

Funding

YIV, GAI, and YRV acknowledge the subsidy allocated to Kazan Federal University for the state assignment in the sphere of scientific activities No. FZSM-2020-0050. LRT thanks the support by a state assignment no. AAAA-A18-118030690040-8 to the Federal Research Center of Kazan Scientific Center of the Russian Academy of Sciences.

ORCID® iDs

Igor V. Yanilkin - https://orcid.org/0000-0002-8879-8904
Amir I. Gumarov - https://orcid.org/0000-0002-7250-4377
Roman V. Yusupov - https://orcid.org/0000-0002-7516-2392
Lenar R. Tagirov - https://orcid.org/0000-0002-1549-7940

Preprint

A non-peer-reviewed version of this article has been previously published as a preprint: https://doi.org/10.3762/bxiv.2021.93.v1

References

1. Eschrig, M. *Phys. Today* **2011,** *64* (1), 43. doi:10.1063/1.3541944
2. Eschrig, M. *Rep. Prog. Phys.* **2015,** *78,* 104501. doi:10.1088/0034-4885/78/10/104501
3. Linder, J.; Robinson, J. W. A. *Nat. Phys.* **2015,** *11,* 307–315. doi:10.1038/nphys3242
4. Kapran, O. M.; Iovan, A.; Golod, T.; Krasnov, V. M. *Phys. Rev. Res.* **2020,** *2,* 013167. doi:10.1103/physrevresearch.2.013167
5. Bhatia, E.; Srivastava, A.; Devine-Stoneman, J.; Stelmashenko, N. A.; Barber, Z. H.; Robinson, J. W. A.; Senapati, K. *Nano Lett.* **2021,** *21,* 3092–3097. doi:10.1021/acs.nanolett.1c00273
6. Fominov, Y. V.; Golubov, A. A.; Karminskaya, T. Y.; Kupriyanov, M. Y.; Deminov, R. G.; Tagirov, L. R. *JETP Lett.* **2010,** *91,* 308–313. doi:10.1134/s002136401006010x
7. Leksin, P. V.; Garif'yanov, N. N.; Garifullin, I. A.; Fominov, Y. V.; Schumann, J.; Krupskaya, Y.; Kataev, V.; Schmidt, O. G.; Büchner, B. *Phys. Rev. Lett.* **2012,** *109,* 057005. doi:10.1103/physrevlett.109.057005
8. Zdravkov, V. I.; Kehrle, J.; Obermeier, G.; Lenk, D.; Krug von Nidda, H.-A.; Müller, C.; Kupriyanov, M. Y.; Sidorenko, A. S.; Horn, S.; Tidecks, R.; Tagirov, L. R. *Phys. Rev. B* **2013,** *87,* 144507. doi:10.1103/physrevb.87.144507
9. Kamashev, A. A.; Garif'yanov, N. N.; Validov, A. A.; Schumann, J.; Kataev, V.; Büchner, B.; Fominov, Y. V.; Garifullin, I. A. *Beilstein J. Nanotechnol.* **2019,** *10,* 1458–1463. doi:10.3762/bjnano.10.144
10. Houzet, M.; Buzdin, A. I. *Phys. Rev. B* **2007,** *76,* 060504. doi:10.1103/physrevb.76.060504
11. Golubov, A. A.; Kupriyanov, M. Y.; Il'ichev, E. *Rev. Mod. Phys.* **2004,** *76,* 411–469. doi:10.1103/revmodphys.76.411
12. Soloviev, I. I.; Klenov, N. V.; Bakurskiy, S. V.; Kupriyanov, M. Y.; Gudkov, A. L.; Sidorenko, A. S. *Beilstein J. Nanotechnol.* **2017,** *8,* 2689–2710. doi:10.3762/bjnano.8.269
13. Larkin, T. I.; Bol'ginov, V. V.; Stolyarov, V. S.; Ryazanov, V. V.; Vernik, I. V.; Tolpygo, S. K.; Mukhanov, O. A. *Appl. Phys. Lett.* **2012,** *100,* 222601. doi:10.1063/1.4723576
14. Ryazanov, V. V.; Bol'ginov, V. V.; Sobanin, D. S.; Vernik, I. V.; Tolpygo, S. K.; Kadin, A. M.; Mukhanov, O. A. *Phys. Procedia* **2012,** *36,* 35–41. doi:10.1016/j.phpro.2012.06.126
15. Vernik, I. V.; Bol'ginov, V. V.; Bakurskiy, S. V.; Golubov, A. A.; Kupriyanov, M. Y.; Ryazanov, V. V.; Mukhanov, O. A. *IEEE Trans. Appl. Supercond.* **2013,** *23,* 1701208. doi:10.1109/tasc.2012.2233270
16. Niedzielski, B. M.; Diesch, S. G.; Gingrich, E. C.; Wang, Y.; Loloee, R.; Pratt, W. P., Jr.; Birge, N. O. *IEEE Trans. Appl. Supercond.* **2014,** *24,* 1800307. doi:10.1109/tasc.2014.2311442

17. Glick, J. A.; Loloee, R.; Pratt, W. P.; Birge, N. O. *IEEE Trans. Appl. Supercond.* **2017,** *27,* 1–5. doi:10.1109/tasc.2016.2630024
18. Esmaeili, A.; Yanilkin, I. V.; Gumarov, A. I.; Vakhitov, I. R.; Gabbasov, B. F.; Yusupov, R. V.; Tatarsky, D. A.; Tagirov, L. R. *Sci. China Mater.* **2021,** *64,* 1246–1255. doi:10.1007/s40843-020-1479-0
19. Esmaeili, A.; Vakhitov, I. R.; Yanilkin, I. V.; Gumarov, A. I.; Khaliulin, B. M.; Gabbasov, B. F.; Aliyev, M. N.; Yusupov, R. V.; Tagirov, L. R. *Appl. Magn. Reson.* **2018,** *49,* 175–183. doi:10.1007/s00723-017-0946-1
20. Cowburn, R. P.; Gray, S. J.; Ferré, J.; Bland, J. A. C.; Miltat, J. *J. Appl. Phys.* **1995,** *78,* 7210–7219. doi:10.1063/1.360431
21. Zhan, Q.-f.; Vandezande, S.; Temst, K.; Van Haesendonck, C. *New J. Phys.* **2009,** *11,* 063003. doi:10.1088/1367-2630/11/6/063003
22. Mallik, S.; Chowdhury, N.; Bedanta, S. *AIP Adv.* **2014,** *4,* 097118. doi:10.1063/1.4895803
23. Yanilkin, I. V.; Mohammed, W. M.; Gumarov, A. L.; Kiiamov, A. C.; Yusupov, R. V.; Tagirov, L. R. *Nanomaterials* **2021,** *11,* 64. doi:10.3390/nano11010064
24. Esmaeili, A.; Yanilkin, I. V.; Gumarov, A. I.; Vakhitov, I. R.; Gabbasov, B. F.; Kiiamov, A. G.; Rogov, A. M.; Osin, Y. N.; Denisov, A. E.; Yusupov, R. V.; Tagirov, L. R. *Thin Solid Films* **2019,** *669,* 338–344. doi:10.1016/j.tsf.2018.11.015
25. Jia, M.; Zeng, F.; Xiao, X.; Zhou, C.; Hu, X.; Wu, Y. *J. Magn. Magn. Mater.* **2020,** *508,* 166863. doi:10.1016/j.jmmm.2020.166863
26. Gil, W.; Görlitz, D.; Horisberger, M.; Kötzler, J. *Phys. Rev. B* **2005,** *72,* 134401. doi:10.1103/physrevb.72.134401
27. Raquet, B.; Viret, M.; Sondergard, E.; Cespedes, O.; Mamy, R. *Phys. Rev. B* **2002,** *66,* 024433. doi:10.1103/physrevb.66.024433
28. van Gorkom, R. P.; Caro, J.; Klapwijk, T. M.; Radelaar, S. *Phys. Rev. B* **2001,** *63,* 134432. doi:10.1103/physrevb.63.134432
29. Kachlon, Y.; Kurzweil, N.; Sharoni, A. *J. Appl. Phys.* **2014,** *115,* 173911. doi:10.1063/1.4874217
30. Tondra, M.; Lottis, D. K.; Riggs, K. T.; Chen, Y.; Dahlberg, E. D.; Prinz, G. A. *J. Appl. Phys.* **1993,** *73,* 6393–6395. doi:10.1063/1.352607
31. Uspenskaya, L. S.; Khlyustikov, I. N. *J. Exp. Theor. Phys.* **2017,** *125,* 875–878. doi:10.1134/s1063776117100090

License and Terms

BEILSTEIN JOURNAL OF NANOTECHNOLOGY

Tunable superconducting neurons for networks based on radial basis functions

Andrey E. Schegolev[1,2], Nikolay V. Klenov[*3,4], Sergey V. Bakurskiy[1,5], Igor I. Soloviev[1], Mikhail Yu. Kupriyanov[1], Maxim V. Tereshonok[2] and Anatoli S. Sidorenko[6,7]

Full Research Paper

Open Access

Address:
[1]Skobeltsyn Institute of Nuclear Physics, Lomonosov Moscow State University, 119991 Moscow, Russia, [2]Moscow Technical University of Communication and Informatics (MTUCI), 111024 Moscow, Russia, [3]Faculty of Physics, Lomonosov Moscow State University, 119991 Moscow, Russia, [4]Lobachevsky State University of Nizhni Novgorod Faculty of Physics, 603950 Nizhny Novgorod, Russia, [5]Dukhov All-Russia Research Institute of Automatics, 101000 Moscow, Russia, [6]Institute of Electronic Engineering and Nanotechnologies ASM, MD2028 Kishinev, Moldova and [7]Laboratory of Functional Nanostructures, Orel State University named after I.S. Turgenev, 302026, Orel, Russia

Email:
Nikolay V. Klenov[*] - nvklenov@gmail.com

* Corresponding author

Keywords:
networks on radial basis functions; Josephson circuits; radial basis functions (RBFs); spintronics; superconducting electronics; superconducting neural network

Beilstein J. Nanotechnol. **2022,** *13,* 444–454.
https://doi.org/10.3762/bjnano.13.37

Received: 17 March 2022
Accepted: 05 May 2022
Published: 18 May 2022

This article is part of the thematic issue "Intrinsic Josephson effect and prospects of superconducting spintronics".

Associate Editor: J. M. van Ruitenbeek

Abstract

The hardware implementation of signal microprocessors based on superconducting technologies seems relevant for a number of niche tasks where performance and energy efficiency are critically important. In this paper, we consider the basic elements for superconducting neural networks on radial basis functions. We examine the static and dynamic activation functions of the proposed neuron. Special attention is paid to tuning the activation functions to a Gaussian form with relatively large amplitude. For the practical implementation of the required tunability, we proposed and investigated heterostructures designed for the implementation of adjustable inductors that consist of superconducting, ferromagnetic, and normal layers.

Introduction

For modern telecommunications, probabilistic identification of various sources in a broadband group signal is extremely important. Also, probabilistic analysis is used in the consideration of stochastic processes [1-4], as a popular machine learning method for spatial interpolation of non-stationary and non-Gaussian data [5], as a central part of a compensation block to

enhance the tracking performance in control systems for a class of nonlinear and non-Gaussian stochastic dynamic processes [6].

An important example for this work is the cognitive radio, which is able to receive information about the features of the "radio environment" and adjust its operating parameters based on this data [7-13]. Similar problems arise nowadays when reading data in superconducting noisy intermediate-scale quantum (NISQ) computers [14-17]. Here again, we need real-time identification and classification of varying signals from multiple sources (qubits) in a narrow frequency range. When working with large data, it is necessary to create specialized neural networks at the hardware level to effectively solve such problems.

Josephson digital circuits and analog receivers have been used for a long time to create software-defined radio-systems [18-25] as well as read-out circuits for quantum computing [26-33]. They realize a unique combination of a wide dynamic range and high sensitivity when receiving signals, with high performance and energy efficiency at the stage of the processing. It seems reasonable to implement additional processing of incoming data inside the cryosystem using the capabilities of neural network computing [34-43]. The creation of an extremely low-dissipating element base for such systems is a very actual scientific and technical task, which requires theoretical and experimental studies of the features of macroscopic quantum interference in the complex Josephson circuits.

The direct use of the previously proposed superconducting adiabatic neural network (ANN) based on the perceptron [44-48] for probabilistic identification is not possible. In particular, during the formation of the output signal in the ANN, the so-called global approximation of the input signal is implemented [11,12], in which almost all neurons are included in signal processing. In addition, the perceptron is a fully connected network, which means an abundance of synaptic connections between neurons. These circumstances suppose a highly resource-intensive learning of the network for signal analysis. There is an alternative approach with a representation of the input set of data into the set of output values by using only one hidden layer of neurons. Each of these neurons is responsible for its own area of the parameter space of incoming data. This is the probabilistic or Bayesian approach, where radial basis functions (for example, Gaussian-like functions) are used as neuron activation functions.

The most common networks operating on this principle are radial basis function networks (RBFNs) (also known as Bayesian networks). When using such a network, objects are classified on the basis of assessments of their proximity to neighboring samples. For each sample, a decision can be made based on the selection of the most likely class from those to which the sample could belong. Such a solution requires an estimate of the probability density function for each class. This score is obtained by consideration of training data. The formal rule is that the class with the tightest distribution in the scope of the unknown instance will take precedence over other classes. The traditional approach for estimating the probability density for each class is to assume that the density has some definite form. The normal distribution is the most preferred since it allows one to estimate such parameters of the model as the mean and standard deviation analytically. The superconducting implementation of the key elements of the discussed neural networks is the focus of this work.

Results and Discussion

Model of tunable Gauss-neuron: numerical simulations

A common architecture of the considered RBFNs [49] is presented in Figure 1a. These networks have only one hidden layer of neurons on which components of the input vector x are fed. Every neuron of the hidden layer calculates the values of the 1D function $h_k(x)$.

$$h_k\left(\vec{x}\right) = \exp\left\{-\frac{\left(\left\|x - x_k\right\|\right)^2}{2\sigma_k^2}\right\}, \tag{1}$$

where x_k is the k-th reference point and σ_k is the scattering parameter for the one-dimensional function $h_k(\vec{x})$.

In this paper, we propose a modified tunable neuron circuit [44] for RBFNs (see Figure 1b), with a Gaussian-like activation function. It consists of two identical Josephson junctions JJ_1 and JJ_2 in the shoulders with input inductances, L, and output inductance L_{out}. It is also used to set an additional bias magnetic flux, Φ_b. Flux biasing is used to provide a suitable transfer function for asynchronous circulation of currents in the connected circuits. In the following, we will call such a cell a "Gauss-neuron" or a "G-cell/neuron".

Hereinafter, we use normalized values for typical parameters of the circuit. All fluxes (input Φ_{in} and output Φ_{out}, and bias Φ_b) are normalized to the flux quantum Φ_0; currents are normalized to the critical current of the Josephson junctions I_C; inductances are normalized to the characteristic inductance $2\pi LI_C/\Phi_0$, times are normalised to the characteristic time $t_C = \Phi_0/(2\pi V_C)$ (V_C is the characteristic voltage of a Josephson junction).

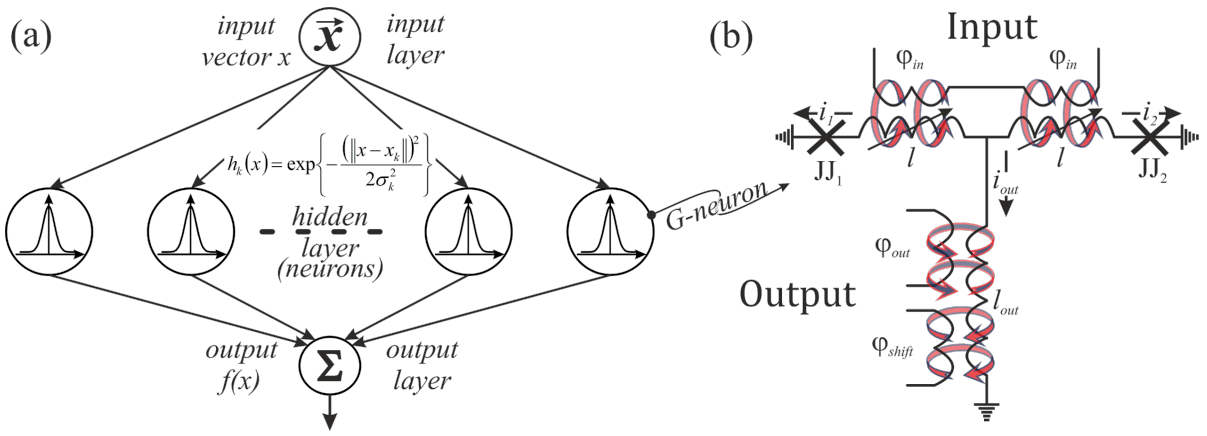

Figure 1: (a) Schematic illustration of a RBF network. (b) Schematic representation of a Gauss-neuron ensuring a Gauss-like transfer function.

Equations of motion were obtained in terms of half-sum and half-difference of Josephson phases φ_1, φ_2 ($\theta = (\varphi_1 + \varphi_2)/2$ and $\psi = (\varphi_1 - \varphi_2)/2$), a detailed derivation of the equations is given in the Appendix section:

$$\dot{\theta} = \frac{\varphi_b - \theta}{l + 2l_{out}} - \sin\theta\cos\psi, \tag{2}$$

$$\dot{\psi} = -\frac{\varphi_{in} + \psi}{l} - \sin\psi\cos\theta. \tag{3}$$

The output magnetic flux obeys the following equation:

$$\varphi_{out} = \frac{2l_{out}}{l + 2l_{out}} \cdot (\theta - \varphi_b). \tag{4}$$

Figure 2a,b shows the families of transfer functions of a Gauss-neuron at different bias fluxes. They are compared with the radial basis function taken in the form $g(x) = \exp(-x^2/(2\sigma^2))$ (dashed line). All transfer functions were normalized to their maximum value, since at the first stage we were interested in the shape of the curve itself. It can be seen that the shape of the response meets the requirements; in addition, it can be adjusted using a bias magnetic flux φ_b. An important feature of the system is that it also allows for non-volatile tuning with memory using tunable inductances l and l_{out}, see Figure 2c–e. Estimations for different values of φ_b show that the best match (with Gauss-like radial basis function) can be achieved with $\varphi_b = 0.05\pi$ and inductance values of $l = 0.1$ and $l_{out} = 0.1$. Also the investigation of the full width at half maximum (FWHM) and of the amplitude of the transfer functions of the Gauss-neuron was carried out for different values of φ_b (Figure 2c,d) and inductance l (Figure 2e). It can be seen that an increase in the value of the inductance l decreases the FWHM of the transfer function and increases its amplitude. The bias flux is a convenient adjustment of the transfer function of the tunable Gauss-neuron; the bias flux should vary in the $[0\ldots0.5]\pi$ range to save the proper form of the transfer function. The mean of the transfer function can be controlled by an additional constant component in the input flux. By selecting the parameters of a configurable G-neuron, we can make the effective field period for the activation function (resulting from the Φ_0-periodicity of all flux dependencies for the interferometer-based structures) large enough for practical use in real neural networks (Figure 2e).

We calculated the standard deviation (SD) of the transfer function from the Gaussian-like function $g(x)$ with fixed amplitude. The obtained results are presented in the $\{l, l_{out}\}$ plane. This visualization allows one to find the most proper operating parameters for the considered element. The magnitude of the amplitude of the transfer function is also presented (Figure 3a,b). The optimal values of inductance corresponding to the minimum of SD lies in the hollow of the surface, see Figure 3b. The minimum SD value is reached at $l = 0.1$, $l_{out} = 0.1$. The position of the hollow in Figure 3b could be expressed as $(l_{out})_{SD} \approx 0.8 - 0.55(l)_{SD}$. At the same time, for relatively small φ_b, the transfer function amplitude increases with increase of the output and shoulder inductances, l_{out} and l. Thus, the choice between the proximity of the transfer function to a Gaussian-like form and the maximization of the response amplitude is determined by the specifics of the network when solving a specific problem. Once again, we emphasize that variations in the parameters of the circuit within a fairly wide range allow one to change the amplitude and width of the activation function, while maintaining its Gaussian-like shape.

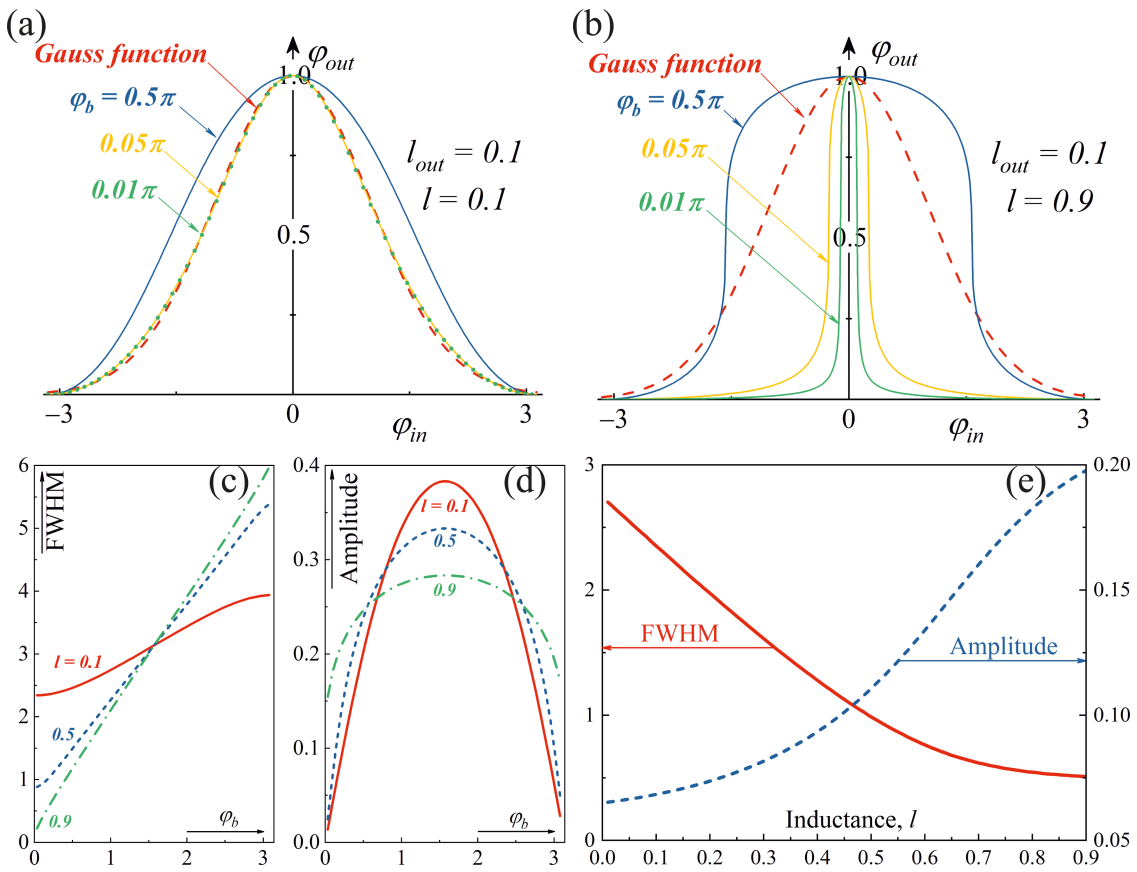

Figure 2: Transfer functions (normalized) and their main characteristics for the Gauss-neuron. (a, b) Families of the normalised transfer functions depending on the magnitude of the bias flux φ_b for various pairs of inductances l and l_{out}: (a) l = 0.1, l_{out} = 0.1; (b) l = 0.9, l_{out} = 0.1. (c) Dependencies of FWHM and amplitude on the bias flux φ_b of transfer functions for l = 0.1, 0.5, and 0.9 with l_{out} = 0.1. (d) Dependencies of FWHM and amplitude on the inductance l for transfer functions of the Gauss-neuron at l_{out} = 0.1 and $\varphi_b = 0.05\pi$.

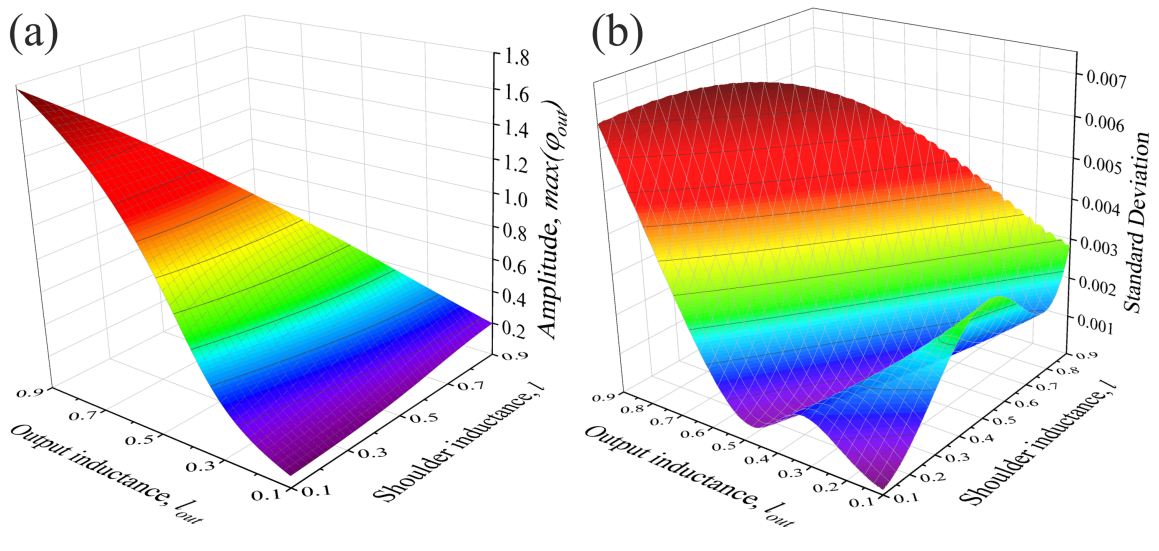

Figure 3: (a) Amplitude of the transfer function and (b) its standard deviation from the Gaussian-like function depending on the inductances l and l_{out} of the G-cell. The bias flux is equal to 0.05π.

The dynamic transfer functions (i.e., the dependencies of the output current on the time-varying input flux) were also calculated, see Figure 4a. The input magnetic signal is a smoothed trapezoidal function of time with a rise/fall time t_{RF}, see the inset in Figure 4b. It can be seen that the dynamic activation function of the required type without hysteresis can be obtained with adiabatic operation of the cell (t_{RF} up to $8000t_C$, where t_C is the characteristic time for the Josephson junction). The dissipation during the operation of the Gauss-neuron remains small, which justifies classifying the proposed cell as adiabatic (Figure 4b).

Realization of tunability: adjustable kinetic inductance

For neural networks based on the considered G-neurons, tunable elements with linear current-to-flux transformation (linear inductors) and memory properties are extremely important [50,51]. Tunability of the inductance l in Figure 1b allows for an in situ switching between operating modes directly on the chip.

In thin layers of superconductors used to create parts of a neuron, the kinetic inductance is relatively large compared to the geometric one [52]. This is important for us since one can change the kinetic inductance relatively simply by controlling the concentration of superconducting charge carriers (Cooper pairs or superconducting correlations). This approach is the basis of the concept of our tunable in situ Gauss-neuron. A similar idea is used in kinetic inductance devices, which are based on thin superconducting strips [53,54]. They are commonly used for the design of photon detectors and parametric amplifiers. But these devices use nonlinear properties of thin superconducting films at large values of carrying currents comparable to the critical current. However, for our purposes, linear inductors are required. So we consider only the case of a small current in comparison with the depairing current of the superconductor.

In this paper, we propose a tunable kinetic inductance with integrated spin-valve structure [46]. A superconducting spin valve is a device that can control the propagation of the superconducting charge carriers, induced from the superconducting layer via the proximity effect. The typical spin valve [55-57] is a hybrid structure containing at least a pair of ferromagnetic (FM) layers with different coercive forces. Variations in the relative orientation of their magnetizations change the spatial distribution of the superconducting order parameter. In the case of parallel magnetization of the FM layers the Cooper pairs are effectively depairing inside them (closed spin valve). For the antiparallel orientation, the effective exchange energy of the magnetic layers is averaged and suppression of the superconducting order parameter is weaker (open spin valve), providing a propagation of Cooper pairs to the outlying layers of the hybrid structure. The switching between the open and closed states of the valve leads to a noticeable change in the spatial distribution of Cooper pairs. The implementation of a thin superconducting spacer (s) between the FM layers supports the superconducting order parameter and increases the efficiency of the spin valve effect [58]. Here, we propose a development of this approach, allowing one to significantly increase the effective variations in the kinetic inductance.

We study proximity effect and electronic transport in the multilayer hybrid structures in the frame of Usadel equations [59]:

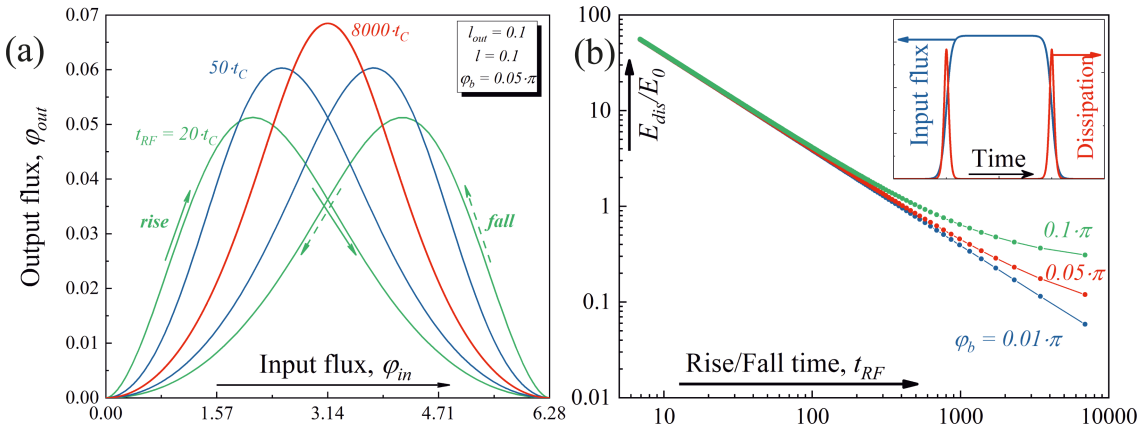

Figure 4: (a) Dynamic transfer function of a Gauss-neuron for a trapezoidal external signal for different values of the rise/fall times of the signal t_{RF} and (b) energy dissipation, normalised to the characteristic energy $E_0 = \Phi_0 I_C/2\pi$, as function of the rise/fall time of the input signal for different bias fluxes: $\varphi_b = \{0.01, 0.05, 0.1\}\pi$. The insert demonstrates the form of temporal dynamic for input flux and dissipation. If the critical current for Josephson junctions I_C is equal to 100 μA and $\varphi_b = 0.05\pi$ than $E_{dis} \approx 0.01$ aJ for $t_{RF} = 6$ ns (corresponds to approx. $1700t_C$).

$$\pi k_B T_C \xi^2 \left(G\frac{d^2F}{dx^2} - F\frac{d^2G_p}{dx^2} \right) - \tilde{\omega}F = -G\Delta,\ G_\omega^2 + F_\omega F_{-\omega}^* = 1, \quad (5)$$

$$\Delta \ln\frac{T}{T_C} + \pi k_B T \sum_{\omega=-\infty}^{\infty} \left(\frac{\Delta}{|\omega|} - F \right) = 0, \quad (6)$$

with Kupriyanov–Lukichev boundary conditions [60],

$$\gamma_B \xi_l \left(\frac{dF_l}{dx} - \frac{F_l}{G_l}\frac{dG_l}{dx} \right) = F_r - F_l\frac{G_r}{G_l}, \quad (7)$$

at the S/FM interfaces. Here G and F are normal and anomalous Green's functions, Δ is a pair potential (superconducting order parameter), $\omega = \pi k_B T\,(2n + 1)$, where n is a natural number, T is the temperature, k_B is Boltzmann's constant, $\tilde{\omega} = \omega + iH$, where H is the exchange energy ($H = 0$ in S and N layers). The indexes "l" and "r" denote the materials at, respectively, the left and right side of an interface, ξ is the coherence length, ρ is the resistivity of the material (in the following, ξ and ρ will also will be mentioned with indexes that denote the layer of these parameters), T_C is the critical temperature of the superconductor, and $\gamma_B = (R_B A)/(\rho_l \xi_l)$ is the interface parameter, where $R_B A$ is the resistance per square of the interface

The calculated distribution of the anomalous Green function, F, permits one to estimate the ability to influence the propagation of the superconducting correlations (screening properties) for the hybrid structure. The spatial distribution of the screening length $\lambda(x)$ directly depends on the proximization of the superconducting order parameter in the system [61,62]:

$$\lambda(x)^{-2} = \lambda_0^{-2}\frac{T}{T_C}\sum_{\omega>0}\mathrm{Re}\left(F(x)^2\right); \quad \lambda_0^{-2} = \frac{2\pi\mu_0 k_B T_C}{\rho_S \hbar}, \quad (8)$$

where ρ_S is the resistivity of the superconducting material, μ_0 is the vacuum permeability and $\hbar$ is Planck's constant. For instance, for a homogeneous niobium film, the estimate for the constant λ_0 is around 100 nm, while experimentally measured values of the screening length λ at $T = 4.2$ K are around 150 nm. The expression for the kinetic inductance of the structure is directly correlated with screening length [52,63],

$$L_K = \frac{\mu_0 X}{W}\left[\int_0^d \left[\lambda(x)\right]^{-2} dx\right]^{-1}, \quad (9)$$

where X is the length of the strip, W is the width, and d is the thickness of the multilayer. In our calculations, we assume that the currents in the system are weak, and the structure thickness is much smaller than the screening length.

We propose a hybrid structure (see Figure 5) consisting of three parts, namely a pairing source, a spin valve, and a current-carrying layer of normal metal with low-resistivity. The general principle of operation is the following: The pairing source generates Cooper pairs and the spin valve controls their propagation to the layer von low inductance. If the valve is open

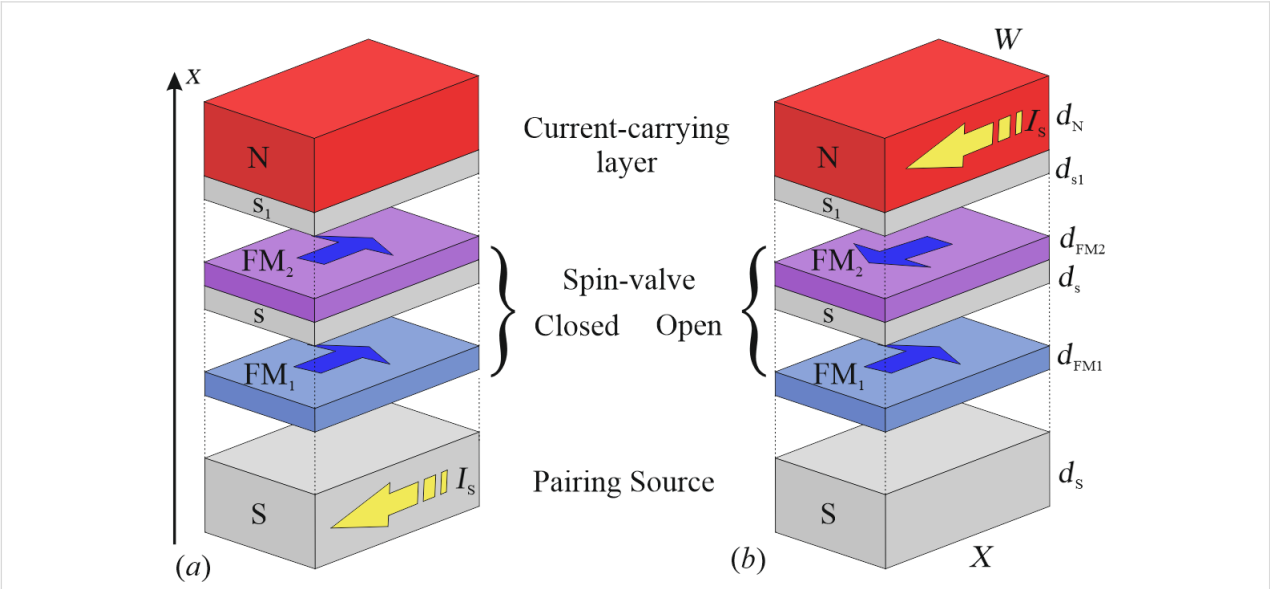

Figure 5: Sketch of the tunable kinetic inductance based on multilayer structure in the (a) closed and (b) open states. Blue solid arrows reveal magnetization orientation of FM_1 and FM_2 layers, and dashed yellow arrows demonstrate direction and localization of the supercurrent I_S.

(Figure 5b), the normal metal is repleted with Cooper pairs, and the biggest part of the supercurrent I_S is flowing along the structure through the metallic layer (N) with relatively low inductance. In the case of the closed valve (Figure 5a), pairs are locked up in the source layer, and the supercurrent I_S is limited to this highly inductive part of the structure. The redistribution of the current flowing along the multilayer is associated with a change of the total kinetic inductance.

For a quantitative model, we choose the following components of the structure: The pairing source is a superconductor layer slightly thicker than the critical value at which the pair potential appears. During calculations we suppose its thickness $d_S = 3\xi_S$.

The spin valve can be implemented as a multilayer structure FM_1–s–FM_2–s–FM_1–s–FM_2 with several ferromagnetic layers FM_1 and FM_2 of different thicknesses $d_{FM1,2}$ ($d_{FM1} = 0.15\xi$, $d_{FM2} = 0.1\xi$, exchange energy $H = 100\ k_BT_C$ in calculations, separated by thin spacers of a superconductor or normal metal (N) ($d_s = 0.5\xi$ for example).

The control of the spin valve is operated by turning the FM layers into states with parallel (P) and antiparallel (AP) mutual orientations of their magnetizations. This process can be realized by application of the finite external magnetic field or by injection of the spin current due to the spin torque effect [56]. For the proposed design of the Gauss-neuron, it is suitable to change magnetizations in the tunable inductance l with the control currents in the input circuits, see Figure 1b. Earlier we experimentally demonstrated [58] that for such a control it is sufficient to create a magnetic field strength of the order of 30 Oe. Note that after the control current is turned off, the valve remains in the open/closed state, since the direction of magnetizations in the FM layers is preserved.

The current-carrying layer is a thin strip of normal metal with thickness $d_N = 2\xi$ and small resistivity $\rho_N \ll \rho_S$, which ensures its lower kinetic inductance relative to the rest of the structure. This leads to a flow of the current mostly through this layer in the case of the open valve.

Figure 6a shows the spatial distributions of the pairing amplitude $F(x)$ in the cross section of this structure for parallel (blue solid line) and antiparallel (red dashed line) orientations of the magnetization of the FM_1 and FM_2 layers. The pairing amplitude F significantly drops in the spin valve region for both cases. However, the residual level of proximization (value of F) in the N layer is five times larger for the AP orientation than for the P orientation.

To enhance the effect, we propose to add an additional superconductor layer s_1 (Figure 6b). In the case of the closed valve, the s_1 layer is in the normal state, and the superconducting correlations in the N layer are negligible. If the valve is open, the s_1 layer goes into a superconducting state with an increase of the pairing amplitude F in the N layer up to two times (see Figure 6a).

Figure 7 demonstrates the dependence of the kinetic inductance of the structure shown in Figure 6b versus as a function of the thickness of the intermediate s or n layers. At large thicknesses of the intermediate layers, the valve loses efficiency. In the case of normal spacers, the transition occurs to a completely normal state, where the kinetic inductance of the entire structure coincides with the kinetic inductance of the source layer S. With a

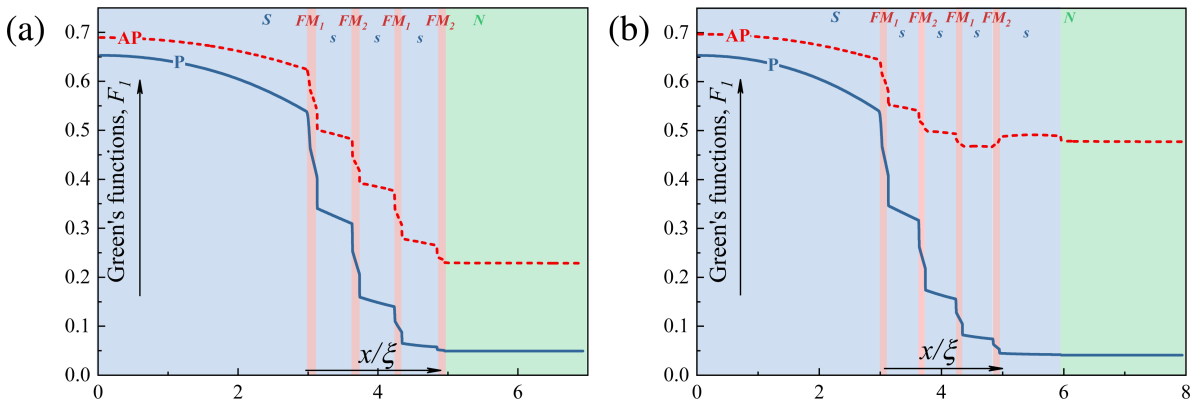

Figure 6: Spatial distribution of the pair amplitude F in the hybrid structures (a) S–FM_1–s–FM_2–s–FM_1–s–FM_2–N without additional s_1 layer and (b) S–FM_1–s–FM_2–s–FM_1–s–FM_2–s_1–N with an additional superconducting layer for parallel (blue solid line) and antiparallel (red dashed line) mutual orientations of magnetization between FM_1 and FM_2 layers.

large thickness of superconducting spacers s, the valve system also loses efficiency, transferring the entire structure to a completely superconducting state. However, at thicknesses of the order of (0.5…1)ξ, the maximum spin-valve effect appears, and the total kinetic inductance of the structure changes several times during switching between states with parallel and antiparallel magnetization orientations.

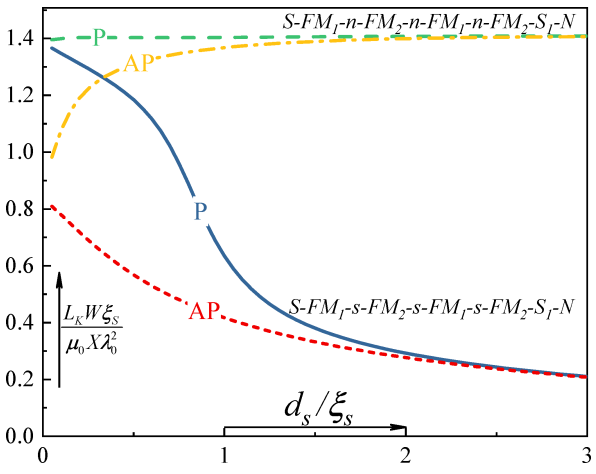

Figure 7: Kinetic inductance of the hybrid structures S–FM_1–s–FM_2–s–FM_1–s–FM_2–s–N and S–FM_1–n–FM_2–n–FM_1–n–FM_2–s_1–N for parallel (dark blue solid line and long dashed green line) and antiparallel (red dashed line and orange dash–dot line) mutual orientations of magnetization between FM_1 and FM_2 layers as functions of the spacer thickness.

We also made some estimates for the quantitative value of the kinetic inductance of the structure shown in Figure 7 based on niobium technology. The inductance of the strip with width W = 100 nm, length X = 1 μm, and total thickness d = 80 nm (this corresponds to the spacer thickness d_s =5 nm) the estimated kinetic inductance is about 7 pH in the closed state and about 15 pH in the open state. For comparison, the geometric inductance of such a strip is of the order of 1 pH.

Conclusion

We have considered a basic cell for superconducting signal neurocomputers designed for the fast processing of a group signal with extremely low energy dissipation. It turned out that for this purpose it is possible to modify the previously discussed element of adiabatic superconducting neural networks. The ability to adjust the parameters of the studied Gauss-cell (with Gaussian-like activation function) is very important for in situ switching between operating modes. Using microscopic modeling, we have shown that the desired compact tunable passive element can be implemented in the form of a controllable kinetic inductance. An example is a multilayer structure consisting of a superconducting "source", a current-carrying layer and a spin valve with at least two magnetic layers with different thicknesses. The proposed tunable inductance does not require suppression of superconductivity in the source layer. In this case, the spin-valve effect determines the efficiency of penetration of superconducting correlations into the current-carrying layer, which is the reason for the change in inductance.

Appendix

We present the derivation of Equation 2–Equation 4 in the framework of the resistively shunted junction (RSJ) model. A typical approach to obtain the equations of motion for Josephson systems is to write the Kirchhoff and phase constraints. From Figure 1b), it follows:

$$\begin{cases} i_1 + i_2 + i_{\text{out}} = 0, \\ \varphi_1 + i_1 \cdot l + \varphi_{\text{in}} = i_{\text{out}} \cdot l_{\text{out}} + \varphi_{\text{b}}, \\ \varphi_2 + i_2 \cdot l - \varphi_{\text{in}} = i_{\text{out}} \cdot l_{\text{out}} + \varphi_{\text{b}}. \end{cases} \tag{10}$$

Let us sum up the second and third equations of the system in Equation 10, taking into account the first equation, and dividing the left and right sides by 2:

$$\theta + \frac{i_1 + i_2}{2} \cdot \left(l + 2 l_{\text{out}} \right) = \varphi_{\text{b}}. \tag{11}$$

As the current through the Josephson junction has a form $i_{\text{JJ}} = \dot{\varphi} + \sin\varphi$, Equation 11 gives us the first equation of motion (Equation 2) for the Gauss-neuron:

$$\dot{\theta} = \frac{\varphi_{\text{b}} - \theta}{l + 2 l_{\text{out}}} - \sin\theta \cos\psi. \tag{12}$$

Similar operations should be conducted for the difference between the second and third equations of the system in Equation 10:

$$\psi + \frac{i_1 - i_2}{2} \cdot l = -\varphi_{\text{in}}, \tag{13}$$

and the second equation of motion (Equation 3) for the system is obtained:

$$\dot{\psi} = -\frac{\varphi_{\text{in}} + \psi}{l} - \sin\psi \cos\theta. \tag{14}$$

To obtain Equation 4, we have to convert Equation 11 according to the expression $i_1 + i_2 = -i_{\text{out}} = -(\varphi_{\text{out}}/l_{\text{out}})$:

$$\varphi_{\text{out}} = \frac{2l_{\text{out}}}{l + l_{\text{out}}} \cdot \left(\theta - \varphi_{\text{b}}\right). \quad (15)$$

Funding

G-neuron and tunable inductance were developed with the support of the Russian Science Foundation (project no. 20-69-47013). The numerical simulations were supported within the framework of the strategic academic leadership program of UNN.

ORCID® iDs

Andrey E. Schegolev - https://orcid.org/0000-0002-5381-3297
Nikolay V. Klenov - https://orcid.org/0000-0001-6265-3670
Mikhail Yu. Kupriyanov - https://orcid.org/0000-0003-1204-9664
Maxim V. Tereshonok - https://orcid.org/0000-0003-1330-281X

Preprint

A non-peer-reviewed version of this article has been previously published as a preprint: https://doi.org/10.3762/bxiv.2022.16.v1

References

1. Turchetti, C.; Crippa, P.; Pirani, M.; Biagetti, G. *IEEE Trans. Neural Networks* **2008,** *19,* 1033–1060. doi:10.1109/tnn.2007.2000055
2. Groth, C.; Costa, E.; Biancolini, M. E. *Aircr. Eng. Aerosp. Technol.* **2019,** *91,* 620–633. doi:10.1108/aeat-07-2018-0178
3. Zhang, J.; Li, H.; Hu, B.; Min, Y.; Chen, Q.; Hou, G.; Huang, C. Modelling of SFR for Wind-Thermal Power Systems via Improved RBF Neural Networks. In *CISC 2020: Proceedings of 2020 Chinese Intelligent Systems Conference,* 2020; pp 630–640.
4. Xie, S.; Xie, Y.; Huang, T.; Gui, W.; Yang, C. *IEEE Trans. Ind. Electron.* **2019,** *66,* 1192–1202. doi:10.1109/tie.2018.2835402
5. Shi, C.; Wang, Y. *Geosci. Front.* **2021,** *12,* 339–350. doi:10.1016/j.gsf.2020.01.011
6. Zhou, Y.; Wang, A.; Zhou, P.; Wang, H.; Chai, T. *Automatica* **2020,** *112,* 108693. doi:10.1016/j.automatica.2019.108693
7. Abidi, A. A. *IEEE J. Solid-State Circuits* **2007,** *42,* 954–966. doi:10.1109/jssc.2007.894307
8. Ulversoy, T. *IEEE Commun. Surv. Tutorials* **2010,** *12,* 531–550. doi:10.1109/surv.2010.032910.00019
9. Wang, B.; Liu, K. J. R. *IEEE J. Sel. Top. Signal Process.* **2011,** *5,* 5–23. doi:10.1109/jstsp.2010.2093210
10. Macedo, D. F.; Guedes, D.; Vieira, L. F. M.; Vieira, M. A. M.; Nogueira, M. *IEEE Commun. Surv. Tutorials* **2015,** *17,* 1102–1125. doi:10.1109/comst.2015.2402617
11. Adjemov, S. S.; Klenov, N. V.; Tereshonok, M. V.; Chirov, D. S. *Moscow Univ. Phys. Bull. (Engl. Transl.)* **2015,** *70,* 448–456. doi:10.3103/s0027134915060028
12. Adjemov, S. S.; Klenov, N. V.; Tereshonok, M. V.; Chirov, D. S. *Program. Comput. Software* **2016,** *42,* 121–128. doi:10.1134/s0361768816030026
13. Ahmad, W. S. H. M. W.; Radzi, N. A. M.; Samidi, F. S.; Ismail, A.; Abdullah, F.; Jamaludin, M. Z.; Zakaria, M. N. *IEEE Access* **2020,** *8,* 14460–14488. doi:10.1109/access.2020.2966271
14. Córcoles, A. D.; Magesan, E.; Srinivasan, S. J.; Cross, A. W.; Steffen, M.; Gambetta, J. M.; Chow, J. M. *Nat. Commun.* **2015,** *6,* 6979. doi:10.1038/ncomms7979
15. Arute, F.; Arya, K.; Babbush, R.; Bacon, D.; Bardin, J. C.; Barends, R.; Biswas, R.; Boixo, S.; Brandao, F. G. S. L.; Buell, D. A.; Burkett, B.; Chen, Y.; Chen, Z.; Chiaro, B.; Collins, R.; Courtney, W.; Dunsworth, A.; Farhi, E.; Foxen, B.; Fowler, A.; Gidney, C.; Giustina, M.; Graff, R.; Guerin, K.; Habegger, S.; Harrigan, M. P.; Hartmann, M. J.; Ho, A.; Hoffmann, M.; Huang, T.; Humble, T. S.; Isakov, S. V.; Jeffrey, E.; Jiang, Z.; Kafri, D.; Kechedzhi, K.; Kelly, J.; Klimov, P. V.; Knysh, S.; Korotkov, A.; Kostritsa, F.; Landhuis, D.; Lindmark, M.; Lucero, E.; Lyakh, D.; Mandrà, S.; McClean, J. R.; McEwen, M.; Megrant, A.; Mi, X.; Michielsen, K.; Mohseni, M.; Mutus, J.; Naaman, O.; Neeley, M.; Neill, C.; Niu, M. Y.; Ostby, E.; Petukhov, A.; Platt, J. C.; Quintana, C.; Rieffel, E. G.; Roushan, P.; Rubin, N. C.; Sank, D.; Satzinger, K. J.; Smelyanskiy, V.; Sung, K. J.; Trevithick, M. D.; Vainsencher, A.; Villalonga, B.; White, T.; Yao, Z. J.; Yeh, P.; Zalcman, A.; Neven, H.; Martinis, J. M. *Nature* **2019,** *574,* 505–510. doi:10.1038/s41586-019-1666-5
16. Babukhin, D. V.; Zhukov, A. A.; Pogosov, W. V. *Phys. Rev. A* **2020,** *101,* 052337. doi:10.1103/physreva.101.052337
17. Vozhakov, V.; Bastrakova, M. V.; Klenov, N. V.; Soloviev, I. I.; Pogosov, W. V.; Babukhin, D. V.; Zhukov, A. A.; Satanin, A. M. *Phys.-Usp.* **2022,** in press. doi:10.3367/ufne.2021.02.038934
18. Fujimaki, A.; Katayama, M.; Hayakawa, H.; Ogawa, A. *Supercond. Sci. Technol.* **1999,** *12,* 708–710. doi:10.1088/0953-2048/12/11/305
19. Fujimaki, A.; Nakazono, K.; Hasegawa, H.; Sato, T.; Akahori, A.; Takeuchi, N.; Furuta, F.; Katayama, M.; Hayakawa, H. *IEEE Trans. Appl. Supercond.* **2001,** *11,* 318–321. doi:10.1109/77.919347
20. Brock, D. K.; Mukhanov, O. A.; Rosa, J. *IEEE Commun. Mag.* **2001,** *39,* 174–179. doi:10.1109/35.900649
21. Vernik, I. V.; Kirichenko, D. E.; Filippov, T. V.; Talalaevskii, A.; Sahu, A.; Inamdar, A.; Kirichenko, A. F.; Gupta, D.; Mukhanov, O. A. *IEEE Trans. Appl. Supercond.* **2007,** *17,* 442–445. doi:10.1109/tasc.2007.898613
22. Gupta, D.; Filippov, T. V.; Kirichenko, A. F.; Kirichenko, D. E.; Vernik, I. V.; Sahu, A.; Sarwana, S.; Shevchenko, P.; Talalaevskii, A.; Mukhanov, O. A. *IEEE Trans. Appl. Supercond.* **2007,** *17,* 430–437. doi:10.1109/tasc.2007.898255
23. Gupta, D.; Kirichenko, D. E.; Dotsenko, V. V.; Miller, R.; Sarwana, S.; Talalaevskii, A.; Delmas, J.; Webber, R. J.; Govorkov, S.; Kirichenko, A. F.; Vernik, I. V.; Tang, J. *IEEE Trans. Appl. Supercond.* **2011,** *21,* 883–890. doi:10.1109/tasc.2010.2095399
24. Kornev, V. K.; Soloviev, I. I.; Sharafiev, A. V.; Klenov, N. V.; Mukhanov, O. A. *IEEE Trans. Appl. Supercond.* **2013,** *23,* 1800405. doi:10.1109/tasc.2012.2232691
25. Mukhanov, O.; Prokopenko, G.; Romanofsky, R. *IEEE Microwave Mag.* **2014,** *15,* 57–65. doi:10.1109/mmm.2014.2332421
26. Pankratov, A. L.; Gordeeva, A. V.; Kuzmin, L. S. *Phys. Rev. Lett.* **2012,** *109,* 087003. doi:10.1103/physrevlett.109.087003
27. Soloviev, I. I.; Klenov, N. V.; Pankratov, A. L.; Il'ichev, E.; Kuzmin, L. S. *Phys. Rev. E* **2013,** *87,* 060901. doi:10.1103/physreve.87.060901
28. Soloviev, I. I.; Klenov, N. V.; Bakurskiy, S. V.; Pankratov, A. L.; Kuzmin, L. S. *Appl. Phys. Lett.* **2014,** *105,* 202602. doi:10.1063/1.4902327
29. Soloviev, I. I.; Klenov, N. V.; Pankratov, A. L.; Revin, L. S.; Il'ichev, E.; Kuzmin, L. S. *Phys. Rev. B* **2015,** *92,* 014516. doi:10.1103/physrevb.92.014516

30. McDermott, R.; Vavilov, M. G.; Plourde, B. L. T.; Wilhelm, F. K.; Liebermann, P. J.; Mukhanov, O. A.; Ohki, T. A. *Quantum Sci. Technol.* **2018,** *3,* 024004. doi:10.1088/2058-9565/aaa3a0
31. Opremcak, A.; Pechenezhskiy, I. V.; Howington, C.; Christensen, B. G.; Beck, M. A.; Leonard, E., Jr.; Suttle, J.; Wilen, C.; Nesterov, K. N.; Ribeill, G. J.; Thorbeck, T.; Schlenker, F.; Vavilov, M. G.; Plourde, B. L. T.; McDermott, R. *Science* **2018,** *361,* 1239–1242. doi:10.1126/science.aat4625
32. Howington, C.; Opremcak, A.; McDermott, R.; Kirichenko, A.; Mukhanov, O. A.; Plourde, B. L. T. *IEEE Trans. Appl. Supercond.* **2019,** *29,* 1700305. doi:10.1109/tasc.2019.2908884
33. Leonard, E., Jr.; Beck, M. A.; Nelson, J.; Christensen, B. G.; Thorbeck, T.; Howington, C.; Opremcak, A.; Pechenezhskiy, I. V.; Dodge, K.; Dupuis, N. P.; Hutchings, M. D.; Ku, J.; Schlenker, F.; Suttle, J.; Wilen, C.; Zhu, S.; Vavilov, M. G.; Plourde, B. L. T.; McDermott, R. *Phys. Rev. Appl.* **2019,** *11,* 014009. doi:10.1103/physrevapplied.11.014009
34. Chiarello, F.; Carelli, P.; Castellano, M. G.; Torrioli, G. *Supercond. Sci. Technol.* **2013,** *26,* 125009. doi:10.1088/0953-2048/26/12/125009
35. Segall, K.; LeGro, M.; Kaplan, S.; Svitelskiy, O.; Khadka, S.; Crotty, P.; Schult, D. *Phys. Rev. E* **2017,** *95,* 032220. doi:10.1103/physreve.95.032220
36. Schneider, M. L.; Donnelly, C. A.; Russek, S. E.; Baek, B.; Pufall, M. R.; Hopkins, P. F.; Dresselhaus, P. D.; Benz, S. P.; Rippard, W. H. *Sci. Adv.* **2018,** *4,* e1701329. doi:10.1126/sciadv.1701329
37. Shainline, J. M.; Buckley, S. M.; McCaughan, A. N.; Chiles, J.; Jafari-Salim, A.; Mirin, R. P.; Nam, S. W. *J. Appl. Phys.* **2018,** *124,* 152130. doi:10.1063/1.5038031
38. Shainline, J. M.; Buckley, S. M.; McCaughan, A. N.; Chiles, J. T.; Jafari Salim, A.; Castellanos-Beltran, M.; Donnelly, C. A.; Schneider, M. L.; Mirin, R. P.; Nam, S. W. *J. Appl. Phys.* **2019,** *126,* 044902. doi:10.1063/1.5096403
39. Cheng, R.; Goteti, U. S.; Hamilton, M. C. *IEEE Trans. Appl. Supercond.* **2019,** *29,* 1300505. doi:10.1109/tasc.2019.2892111
40. Toomey, E.; Segall, K.; Berggren, K. K. *Front. Neurosci.* **2019,** *13,* 933. doi:10.3389/fnins.2019.00933
41. Toomey, E.; Segall, K.; Castellani, M.; Colangelo, M.; Lynch, N.; Berggren, K. K. *Nano Lett.* **2020,** *20,* 8059–8066. doi:10.1021/acs.nanolett.0c03057
42. Ishida, K.; Byun, I.; Nagaoka, I.; Fukumitsu, K.; Tanaka, M.; Kawakami, S.; Tanimoto, T.; Ono, T.; Kim, J.; Inoue, K. *IEEE Micro* **2021,** *41,* 19–26. doi:10.1109/mm.2021.3070488
43. Feldhoff, F.; Toepfer, H. *IEEE Trans. Appl. Supercond.* **2021,** *31,* 1800505. doi:10.1109/tasc.2021.3063212
44. Schegolev, A. E.; Klenov, N. V.; Soloviev, I. I.; Tereshonok, M. V. *Beilstein J. Nanotechnol.* **2016,** *7,* 1397–1403. doi:10.3762/bjnano.7.130
45. Soloviev, I. I.; Schegolev, A. E.; Klenov, N. V.; Bakurskiy, S. V.; Kupriyanov, M. Y.; Tereshonok, M. V.; Shadrin, A. V.; Stolyarov, V. S.; Golubov, A. A. *J. Appl. Phys.* **2018,** *124,* 152113. doi:10.1063/1.5042147
46. Bakurskiy, S.; Kupriyanov, M.; Klenov, N. V.; Soloviev, I.; Schegolev, A.; Morari, R.; Khaydukov, Y.; Sidorenko, A. S. *Beilstein J. Nanotechnol.* **2020,** *11,* 1336–1345. doi:10.3762/bjnano.11.118
47. Schegolev, A.; Klenov, N.; Soloviev, I.; Tereshonok, M. *Supercond. Sci. Technol.* **2021,** *34,* 015006. doi:10.1088/1361-6668/abc569
48. Schneider, M.; Toomey, E.; Rowlands, G.; Shainline, J.; Tschirhart, P.; Segall, K. *Supercond. Sci. Technol.* **2022,** *35,* 053001. doi:10.1088/1361-6668/ac4cd2
49. Park, J.; Sandberg, I. W. *Neural Comput.* **1991,** *3,* 246–257. doi:10.1162/neco.1991.3.2.246
50. Splitthoff, L. J.; Bargerbos, A.; Grünhaupt, L.; Pita-Vidal, M.; Wesdorp, J. J.; Liu, Y.; Kou, A.; Andersen, C. K.; van Heck, B. *arXiv* **2022,** No. 2202.08729. doi:10.48550/arxiv.2202.08729
51. Jué, E.; Iankevich, G.; Reisinger, T.; Hahn, H.; Provenzano, V.; Pufall, M. R.; Haygood, I. W.; Rippard, W. H.; Schneider, M. L. *J. Appl. Phys.* **2022,** *131,* 073902. doi:10.1063/5.0080841
52. Annunziata, A. J. Single-photon detection, kinetic inductance, and non-equilibrium dynamics in niobium and niobium nitride superconducting nanowires. Ph.D. Thesis, Yale University, New Haven, CT, USA, 2010.
53. Annunziata, A. J.; Santavicca, D. F.; Frunzio, L.; Catelani, G.; Rooks, M. J.; Frydman, A.; Prober, D. E. *Nanotechnology* **2010,** *21,* 445202. doi:10.1088/0957-4484/21/44/445202
54. Bockstiegel, C.; Wang, Y.; Vissers, M. R.; Wei, L. F.; Chaudhuri, S.; Hubmayr, J.; Gao, J. *Appl. Phys. Lett.* **2016,** *108,* 222604. doi:10.1063/1.4953209
55. Fominov, Y. V.; Golubov, A. A.; Karminskaya, T. Y.; Kupriyanov, M. Y.; Deminov, R. G.; Tagirov, L. R. *JETP Lett.* **2010,** *91,* 308–313. doi:10.1134/s002136401006010x
56. Leksin, P. V.; Garif'yanov, N. N.; Garifullin, I. A.; Fominov, Y. V.; Schumann, J.; Krupskaya, Y.; Kataev, V.; Schmidt, O. G.; Büchner, B. *Phys. Rev. Lett.* **2012,** *109,* 057005. doi:10.1103/physrevlett.109.057005
57. Lenk, D.; Morari, R.; Zdravkov, V. I.; Ullrich, A.; Khaydukov, Y.; Obermeier, G.; Müller, C.; Sidorenko, A. S.; von Nidda, H.-A. K.; Horn, S.; Tagirov, L. R.; Tidecks, R. *Phys. Rev. B* **2017,** *96,* 184521. doi:10.1103/physrevb.96.184521
58. Klenov, N.; Khaydukov, Y.; Bakurskiy, S.; Morari, R.; Soloviev, I.; Boian, V.; Keller, T.; Kupriyanov, M.; Sidorenko, A.; Keimer, B. *Beilstein J. Nanotechnol.* **2019,** *10,* 833–839. doi:10.3762/bjnano.10.83
59. Usadel, K. D. *Phys. Rev. Lett.* **1970,** *25,* 507–509. doi:10.1103/physrevlett.25.507
60. Kuprianov, M. Y.; Lukichev, V. *Sov. Phys. JETP* **1988,** *67,* 1163.
61. Houzet, M.; Meyer, J. S. *Phys. Rev. B* **2009,** *80,* 012505. doi:10.1103/physrevb.80.012505
62. Mironov, S.; Mel'nikov, A. S.; Buzdin, A. *Appl. Phys. Lett.* **2018,** *113,* 022601. doi:10.1063/1.5037074
63. Marychev, P. M.; Vodolazov, D. Y. *J. Phys.: Condens. Matter* **2021,** *33,* 385301. doi:10.1088/1361-648x/ac1153

BEILSTEIN JOURNAL OF NANOTECHNOLOGY

Approaching microwave photon sensitivity with Al Josephson junctions

Andrey L. Pankratov[1,2,3], Anna V. Gordeeva[*1,2], Leonid S. Revin[1,2], Dmitry A. Ladeynov[1,2,3], Anton A. Yablokov[1,2] and Leonid S. Kuzmin[1,4]

Full Research Paper

Open Access

Address:
[1]Nizhny Novgorod State Technical University n.a. R.E. Alekseev, GSP-41, Nizhny Novgorod, 603950, Russia, [2]Institute for Physics of Microstructures of RAS, GSP-105, Nizhny Novgorod, 603950, Russia, [3]Lobachevsky State University of Nizhny Novgorod, 603950, Nizhny Novgorod, Russia and [4]Chalmers University of Technology, 41296, Gothenburg, Sweden

Email:
Anna V. Gordeeva[*] - a.gordeeva@nntu.ru

* Corresponding author

Keywords:
Josephson junction; microwave photons; single photon counter; thermal activation

Beilstein J. Nanotechnol. **2022,** *13,* 582–589.
https://doi.org/10.3762/bjnano.13.50

Received: 29 March 2022
Accepted: 10 June 2022
Published: 04 July 2022

This article is part of the thematic issue "Intrinsic Josephson effect and prospects of superconducting spintronics".

Guest Editor: A. S. Sidorenko

Abstract

Here, we experimentally test the applicability of an aluminium Josephson junction of a few micrometers size as a single photon counter in the microwave frequency range. We have measured the switching from the superconducting to the resistive state through the absorption of 10 GHz photons. The dependence of the switching probability on the signal power suggests that the switching is initiated by the simultaneous absorption of three and more photons, with a dark count time above 0.01 s.

Introduction

The development of a single photon counter (SPC) for microwave frequencies of tens of gigahertz has been required for several applications at least for the last two decades. The difficulty of this development is in the small energy scale: The energy of a photon of 10 GHz is just 7 yoctojoule (7×10^{-24} J). To realize the detection, the photon must trigger a process whose energy is of the order of this value (the difference between initial and excited states). There are not many examples in solid-state physics with such energy scales. Another difficulty is that a spontaneous change of the state must be significantly less probable so that the detector could be in a waiting mode for a significant amount of time.

Superconductor–insulator–superconductor (SIS) junctions have not been seriously considered previously for the role of detectors of single photons in the microwave range, despite sporadic works showing such a possibility [1-7]. Recently, the interest in microwave SPCs has been increased [8,9] due to new experi-

ments of dark matter search [10-12] and the corresponding program initiated by INFN in Italy [13-22].

Our experiments show that typical aluminium Josephson junctions (JJs) can indeed have a few-photon sensitivity in the microwave frequency range, and a photon counter can be made on their basis. We use the metastable quasi-equilibrium state of a Josephson junction, which, at low temperatures, is stable enough for thermal fluctuations and quantum tunneling, but can be easily destroyed by absorption of a single photon. We demonstrate few-photon sensitivity of our samples in a single-shot regime and outline the junction parameter range where approaching single photon sensitivity is possible.

Results and Discussion

In this section, we describe our experimental setup, as well as the measurement results and comparison with theory. To study the dynamics of a SIS tunnel junction, we have thermally anchored the sample to the mixing chamber of a He3/He4 dilution refrigerator Triton 200 from Oxford Instruments. A block diagram of the experimental setup, including filtering and room-temperature electronics, is shown in Figure 1a. The sample (Figure 1b) was mounted in an RF-tight box with a superconducting shielding on the coldest plate. The dc bias wires were filtered with feedthrough capacitors at room temperature and RC filters at the 10 mK cryostat plate, minimizing the effect of unwanted low-frequency noise.

For an experiment with microwave radiation, we used phosphor bronze twisted pairs with an attenuation of −15 dB/m at 10 GHz to provide the radiation to the sample in the cryostat. The twisted pair ended with a loop antenna near the JJ, see [7,23] for the setup description. As any in-stock microwave synthesizer would produce a far too powerful signal, in our setup, we used constant attenuators from 2 dB to 30 dB and a voltage-controlled room-temperature attenuator, preliminarily

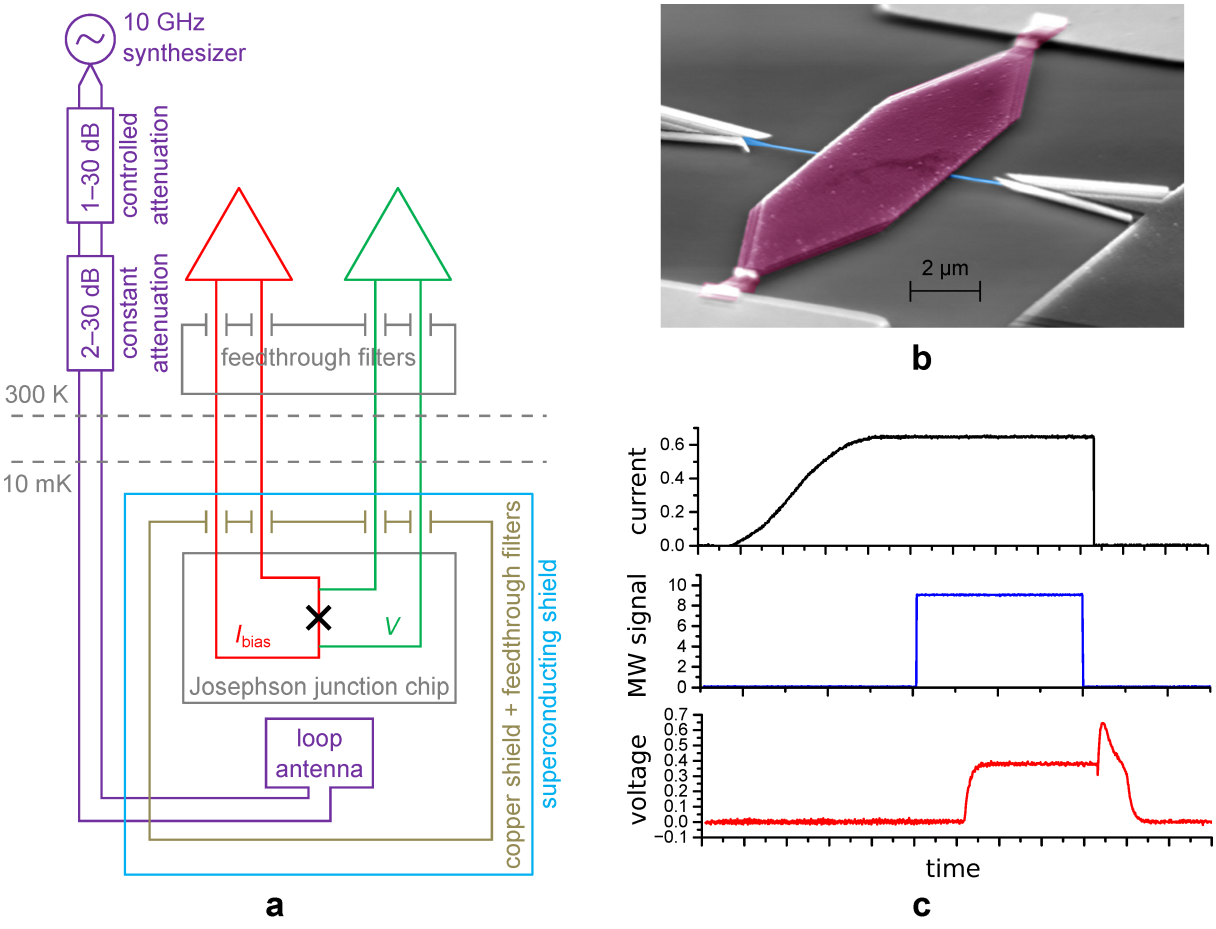

Figure 1: (a) Scheme of the measurement electronics with thermal anchoring and various filtering stages. (b) SEM image of the SIS junction. The top electrode is highlighted in magenta color, the bottom electrode (blue color) has the same shape as the top one in the area of the tunnel barrier. (c) Time diagram of the channels: current through the JJ, initial pulse modulation of the microwave signal (assuming front smoothing due to twisted pairs) and voltage across the JJ.

calibrated with a spectrum analyzer. We altered the power of the signal from high power, at which the photon-assisted tunneling steps are well pronounced in the I/V curve [23], to low power, whose presence can be observed only in the switching distributions and in the shorter lifetime of the superconducting state.

The used experimental setup is the same as in [7], except for the measured sample. In [7], the critical current of the sample was very low, and the phase diffusion regime was noticeably pronounced. The sample considered here has a much higher critical current, and the phase diffusion does not appear. As a result, the theoretical estimates based on the BCS theory for critical currents and Kramers' theory for escape times are well applicable. Furthermore, the analysis of the experiment is done with a more general theory, which considers the absorption probabilities of different numbers of photons.

The time traces of setting a current and an external microwave signal to measure the switching probability as a function of power are shown in Figure 1c. First, the current through the junction is increased up to the required value by a $\sin^2$ law [24] to realize a quasi-adiabatic ramping, then the microwave signal is turned on for a fixed time slot, assuming significant smoothing of pulse fronts due to transfer via twisted pairs. Due to strong attenuation of the harmonic signal, the microwave pulse represents a sequence of single photons, pairs, triples, and so on, which obey a Poisson distribution [25,26]. After turning off the signal, the state of the JJ is checked. Depending on whether the JJ is in the resistive or superconducting state, unity or zero is added to the switching probability, respectively.

We begin our consideration of the Josephson junction as a photon counter with its current–voltage characteristic (see Figure 2a) and the determination of the critical current. All further analysis of experimental results and understanding of the energy relations of the JJ in comparison with the energy of photons (see Figure 2b) depends on the accuracy of determining the critical current. An area of 60 μm^2 and a critical current $I_c \approx 8.6$ μA have been measured for the Al JJ, see the SEM image of the sample in Figure 1b. Due to rather low-noise measuring environment, used before for terahertz receiver ap-

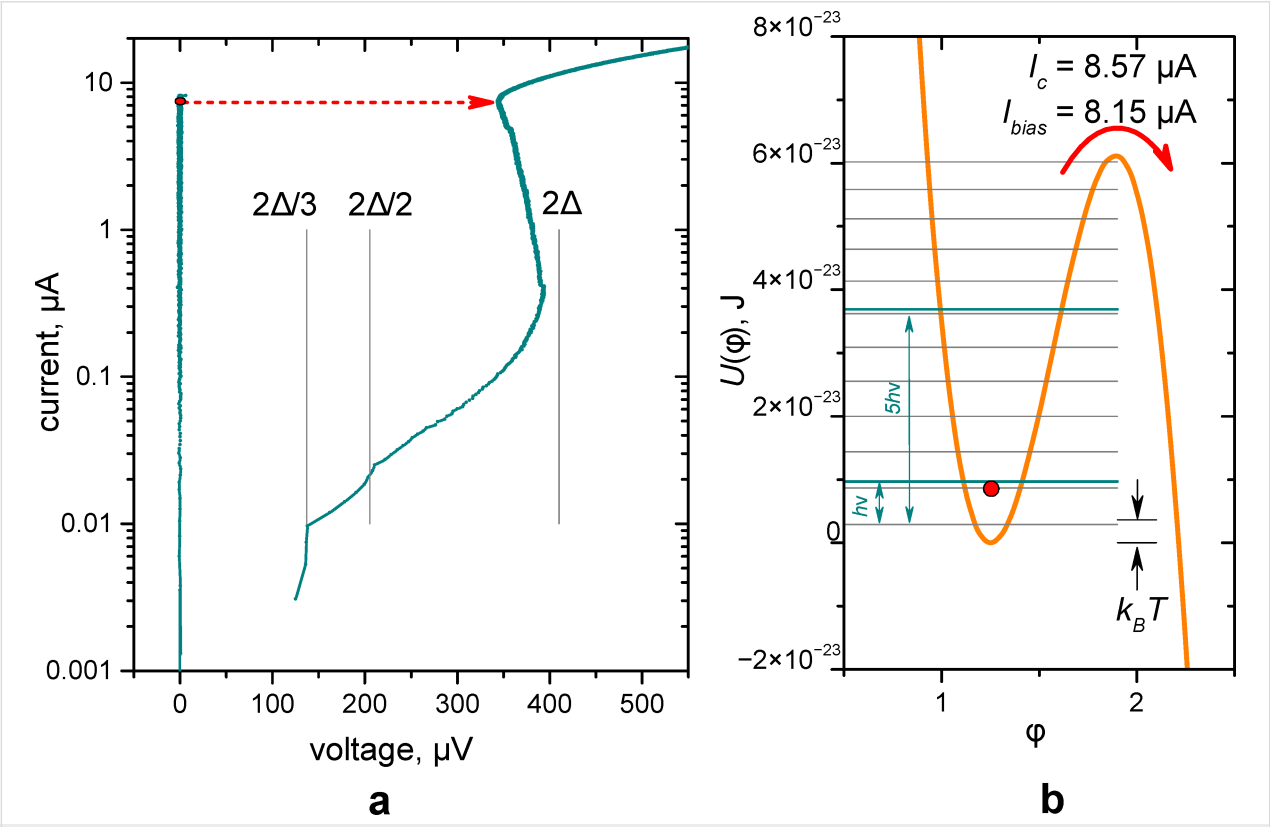

Figure 2: (a) The current–voltage characteristics of the Josephson junction with $I_c = 8.6$ μA at 50 mK. The red point indicates the state of JJ in a "waiting" mode, the arrow shows a jump to the resistive state after absorption of photons. (b) The potential profile at the bias current of 8.15 μA. The energies of one and five photons are shown by lines relative to the minimum energy level. Under these conditions, the JJ switches with a probability of 1 when five photons are absorbed simultaneously ($q[5] = 1$), and with a probability of 0.13 when four photons are absorbed ($q[4] = 0.13$). These probabilities are obtained from fitting experimental data, see Figure 5 below. The scale of the effective thermal fluctuation energy is given by black arrows for $T = 265$ mK (see the main text).

plications [27,28], in Figure 2a one can see a typical current–voltage characteristics (IVC) with the critical current close to the theoretical value [29]. Besides, a subgap structure is visible at the inverse branch of the IVC. Such a structure with peculiarities in the differential resistance at voltages $2\Delta/n$ was calculated theoretically for normal metal links between two superconductors as multiple Andreev reflections [30] and observed in experiment both for superconductor–normal metal–superconductor and SIS junctions [31].

In contrast to smaller junctions [7], where the phase-diffusion regime is possible [32-37], the analyzed junction demonstrates a typical behavior [4,38], that is, a monotonic increase in the switching current distribution width with the rise of the temperature, see Figure 3. For the switching current measurements, the bias current of the junction was ramped up at a constant rate. The voltage was measured using a low-noise room-temperature differential amplifier AD745 and was fed to a high-speed NI ADC card. The switching current histograms were collected in the temperature range between 1 K and 30 mK. The dependence of their width on the temperature is shown in Figure 3. It is interesting to note the crossover temperature to the quantum regime of about 250 mK, which is somewhat lower than in [38] for junctions with larger critical currents.

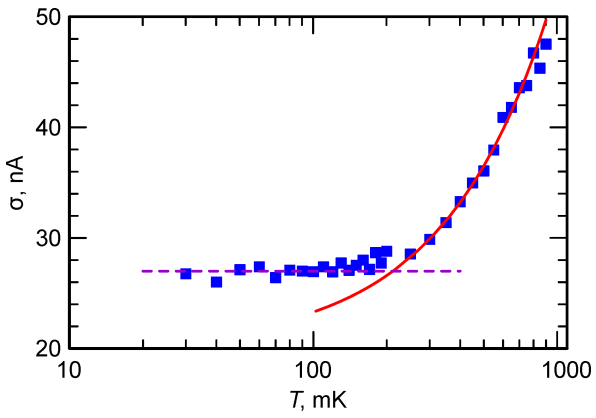

Figure 3: Width of the switching current distribution of the Josephson junction. One can see a standard behavior when the distribution width grows monotonically with increase of the temperature. Here, the violet dashed line shows the quantum regime and the red solid curve shows the thermal activation regime.

The switching current to the resistive state depends on the sweep rate. Therefore, its value is underestimated in dc measurements. The upper limit is given by the BCS expression $1.75kT_c/(eR_N)$ [29], which depends on the critical temperature of the electrodes and the normal resistance of the tunnel barrier only. This maximum possible critical current is difficult to achieve in real junctions. In our opinion, the most reliable way to determine the critical current is to compare the experimental lifetime as a function of the current with the lifetime calculated using numerical simulations [39-41] in the frame of the resistively–capacitively shunted junction (RCSJ) model with additive noise [29]. It is important to use the RCSJ model in the temperature range in which it is valid, that is, above the crossover temperature in the quantum regime.

The lifetime (dark count time) measurements are organized as follows. The current through the junction is quasi-adiabatically ramped up to a given value. After reaching the required bias current, the countdown of lifetimes begins until the moment of jumping to the resistive branch. This cycle is repeated 100–200 times to collect statistics, after which the average value of the switching time and its standard deviation are calculated.

Since the considered Josephson junction is standard and there is no phase-diffusion regime observed (see Figure 3), there is no mixed mode of operation, in which a part of the time there are short voltage pulses due to escapes to the adjacent potential minima and a part of the time the voltage is zero. This makes it easier to determine the lifetime in the numerical model. In this case, the JJ is considered to be switched if the phase exceeds a certain threshold value, usually chosen to the right of the position of the nearest maximum of the potential for a given bias current.

There is a need to use numerical simulations since, in the experiment, we are limited by the time constant of the filters that provide suppression of external interferences. As a result, we cannot measure switching times faster than the time constant, which in our case is about 1 ms. To obtain shorter times, we numerically solve the Langevin equation with noise source [39,40] in the frame of the RCSJ model, which has been proven for classical JJs in the thermal regime [29]. Its applicability is also confirmed for our case by a good overlap with the experimental data.

It is seen from Figure 4 that the experimental points at 300 and 600 mK agree well with the simulation results if the parameters for numerical calculations are 401 mK, I_c = 8.536 μA and 575 mK, I_c = 8.51 μA, respectively. The normal resistance and the capacitance are R_N = 29 Ω and C = 2700 fF.

It is interesting to note that even the curve for 50 mK is well-fitted if the critical current is set to 8.586 μA and the temperature is 265 mK, which is close to the crossover temperature deduced from Figure 3. For the same parameters, the lifetime was calculated with the well-known Kramers' formula [42-47], modified for intermediate damping values [48,49]:

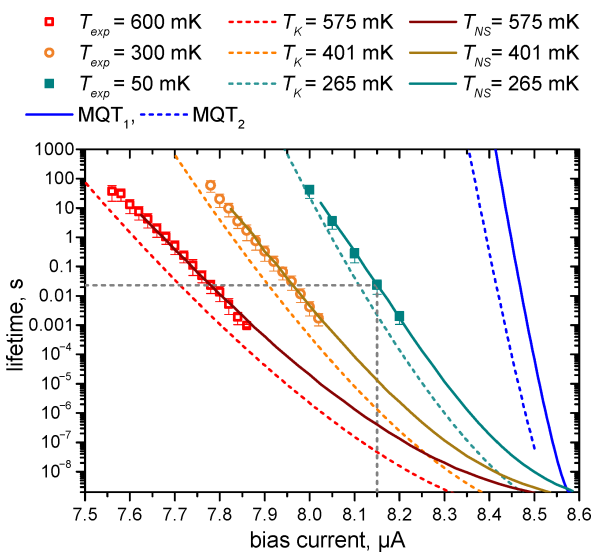

Figure 4: The lifetime of the junction as a function of the bias current at temperatures of 50 mK (green), 300 mK (orange), 600 mK (red). Here, fitting is performed using the approximate Kramers' formula in Equation 1 (dashed curve) and using the numerical solution of the Langevin equation with noise (solid curve). In the latter case, the agreement is rather good.

$$\tau = \frac{a_t \exp(\Delta u/\gamma)}{\left(1-i^2\right)^{1/4}}, \quad a_t = 4\left(\sqrt{1+\frac{\alpha\gamma}{3.6\sqrt{1-i^2}}}+1\right)^{-2} \tag{1}$$

The used notations are the following: $i = I_{bias}/I_c$ is the dimensionless bias current with the bias current I_{bias} and the critical current I_c, $\Delta u = 2\sqrt{1-i^2} + 2i\left(\arcsin(i) - \pi/2\right)$ is the potential barrier height, $\gamma = I_T/I_c$ is the noise intensity, and $I_T = 2ekT/\hbar$ is the fluctuational current which can be calculated as: I_T [μA] = 0.042 T [K] [29] for a given temperature T. Note that, the thermal current is 2.1 nA for 50 mK and 21 nA for 500 mK, respectively.

The investigated junction also demonstrates a typical Kramers' dependence of the lifetime, see Figure 4, but the analytical estimates from Equation 1 give an underestimated lifetime compared to a more accurate numerical calculation.

Thus, the critical current at a temperature of 50 mK was determined as 8.586 μA. For this I_c value, the tunneling time as a function of the bias current was calculated, which is believed to be the reason that, below the crossover temperature, the lifetime stops changing. The results are shown as a solid blue curve if the tunneling occurs from the minimum of the potential profile [49], and as a dotted blue curve if it occurs from the zero-energy level [50]. As can be seen, these curves have a steeper slope than the experimental lifetime at 50 mK. This may indicate that we do not reach the true quantum regime, and the lifetime stops changing with decreasing temperature due to either residual low-frequency interference or overheating. Additional experiments are planned to determine this issue.

The absorption of a photon increases the energy of a JJ by a certain value and may result in switching into the resistive state. Several frequency ranges of effective detection may exist [39] due to resonant activation, and the most efficient switching occurs at signal frequencies of 0.6 from $\omega_p = (2eI_c/\hbar C)^{1/2}$ [40], which is fully consistent with the parameters of the considered experiment. In the current work, we measure the probability of switching initiated by a 10 GHz signal with a fixed duration t_{sw} = 0.05 s. The plasma frequency of the junction is 15.6 GHz, while at the bias current of 815 μA, where we presumably see three-photon sensitivity, the resonant frequency ω_r of the Josephson junction oscillation circuit $\omega_r = \omega_p(1 - i^2)^{1/4}$ is 8.8 GHz.

The statistics of switching as function of the absorbed power is illustrated in Figure 5a,b for several bias currents and temperatures of 50 and 500 mK, respectively. Each curve in Figure 5 has been collected with (200 to 10^4) averages of switching events.

The experimental results in Figure 5a,b can be reproduced using the Poisson distribution of photons and the fitting procedure from [23]. To take into account that there may be several switching attempts during the pulse, for the fitting procedure, the signal with duration t_{sw} is divided into M shorter pulses δt, each of which contains only one group of photons, and we can assume only one switching attempt. The average number of photons N in each group is determined by the Poisson distribution. The switching probability in δt is the sum of the products of the Poisson distributions that photons are contained in the signal and the switching probabilities $q[i]$ due to absorption of i photons. The switching probability p_{sw} is the result of M switching attempts over time δt:

$$p_{sw} = 1 - \left(1 - p_{\delta t}\right)^M,$$
$$p_{\delta t} = e^{-N}\left(q[0] + q[1]N + q[2]\frac{N^2}{2!} + q[3]\frac{N^3}{3!} + \ldots\right), \tag{2}$$

where $q[0]$ is the probability of the erroneous detection without a photon, and $q[1]$, $q[2]$, $q[3]$, … are the detection efficiencies for one, two, three, … photons, respectively.

The slope of the fitting curves is set by the number of photons, triggering the switching. The position on the power axis is determined by the effective system response time δt and by the

efficiency of switching q. The fitting curves in Figure 5a are obtained with δt = 0.3 ns for slope 3 and δt = 5.7 ns for slope 15.

The curve with slope 3 fits the experimental data for the bias current of 8.15 μA quite well if the q-array is [5×10^{-10}, 5×10^{-10}, 5×10^{-10}, 0.002, 0.13, 1, 1, …]. Therefore, the probability of switching due to the absorption of 3 photons is 0.002. In Figure 2b the barrier height is compared with the energy of one photon. The potential profile is calculated for the critical current of 8.586 μA. Photon frequency and energy are, respectively, 10 GHz and 6.8×10^{-24} J. The energies of three and even five photons are smaller than the barrier height. However, switching may still occur due to either resonant tunneling or resonant activation effects [22,39,40,49,51].

With the critical current of 8.586 μA, the barrier height for bias currents in the range of 7.5–8.08 μA equals to the energy of 35 to 11 photons. This number is quite close to the number we get from the fit of probability versus power slopes, that is, 15 to 3. Even if the total energy of absorbed photons is less than the barrier height, the probability to switch to the resistive state by tunneling increases significantly.

In Figure 5, one can see how the switching probability evolves with increasing temperature from 50 to 500 mK. The difference is not very large because at 50 mK the effective temperature was rather 265 mK, according to numerical simulations, and the thermal current at 500 mK is much smaller than the critical current. There is still three-photon sensitivity with efficiency 0.01, but for a slightly lower bias current of 8 μA. Curves for other bias currents can be fitted with slopes 4, 5, 6, 9, and 12.

The small difference between the results at 50 mK (265 mK) and 500 mK can be understood from Figure 2b. The superconducting gap decreases by a few percent due to the temperature increase from 265 to 500 mK according to the BCS model. It leads to a minor decrease in the JJ critical current. Thus, the qualitative picture remains the same for 265 and 500 mK: The height of the potential barrier is still several times larger than the thermal energy and the energy of a single 10 GHz photon.

Conclusion

We have presented an experimental study of a Josephson junction with an area of 60 μm^2 and a critical current of 8.6 μA for application as a single photon counter in the microwave frequency range. Using a strongly attenuated 10 GHz harmonic signal with Poisson distribution of photons as the photon source, three-photon sensitivity with an efficiency of 0.002 and a dark count time of 0.02 s has been shown.

From the analysis of the lifetime, we see that there is a room for improvement of the sensitivity if residual low-frequency noise or overheating of the junction could be decreased. The source of the issue and the way of its suppression need to be investigated in further experiments.

Comparing the obtained results for the considered sample with other small-area junctions [7,23], we can conclude that the

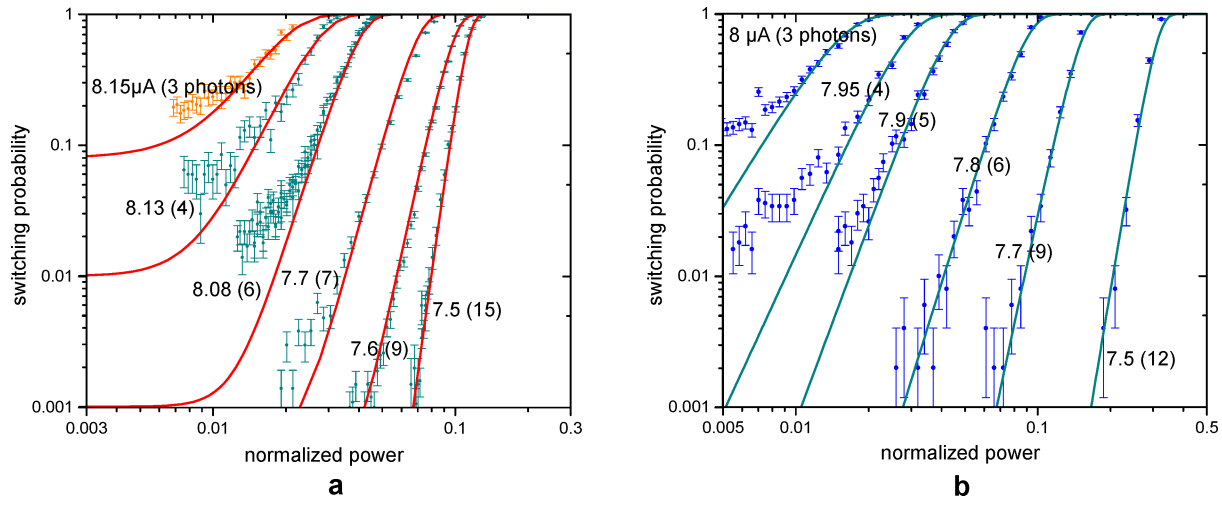

Figure 5: The switching probability of the JJ as a function of the power of the signal (with duration 50 ms) for different bias currents. The dots with error bars are experimental data. For each switching event, the system was first prepared in the initial state by quasi-adiabatically ramping the bias current over 50 ms. If the microwave signal caused a switching to the finite-voltage state during the driving pulse, such event was counted as 1, and 0 otherwise. (a) T = 50 mK. The orange dots represent a bias of 8.15 μA. The red fit curves are obtained with the formula in Equation 2. (b) T = 500 mK. The green fit curves are obtained with the formula in Equation 2.

optimal critical current range, allowing for improvement of both sensitivity and dark count time, is about hundreds of nanoamperes as predicted in [6]. Such junctions are currently being measured.

Acknowledgements

The samples were fabricated in the Chalmers Nanotechnology Center. The measurements were performed using the facilities of the Laboratory of Superconducting Nanoelectronics of NNSTU. The SEM image of the sample was obtained using the Common Research Center "Physics and technology of micro- and nanostructures" of IPM RAS.

Funding

The work is supported by the Russian Science Foundation (Project No. 19-79-10170).

ORCID® iDs

Andrey L. Pankratov - https://orcid.org/0000-0003-2661-2745
Anna V. Gordeeva - https://orcid.org/0000-0001-6948-3950
Leonid S. Revin - https://orcid.org/0000-0003-1645-4122
Dmitry A. Ladeynov - https://orcid.org/0000-0001-6856-7079
Anton A. Yablokov - https://orcid.org/0000-0002-9004-7069

Preprint

A non-peer-reviewed version of this article has been previously published as a preprint: https://doi.org/10.3762/bxiv.2022.19.v1

References

1. Wallraff, A.; Duty, T.; Lukashenko, A.; Ustinov, A. V. *Phys. Rev. Lett.* **2003,** *90,* 037003. doi:10.1103/physrevlett.90.037003
2. Chen, Y.-F.; Hover, D.; Sendelbach, S.; Maurer, L.; Merkel, S. T.; Pritchett, E. J.; Wilhelm, F. K.; McDermott, R. *Phys. Rev. Lett.* **2011,** *107,* 217401. doi:10.1103/physrevlett.107.217401
3. Poudel, A.; McDermott, R.; Vavilov, M. G. *Phys. Rev. B* **2012,** *86,* 174506. doi:10.1103/physrevb.86.174506
4. Oelsner, G.; Revin, L. S.; Il'ichev, E.; Pankratov, A. L.; Meyer, H.-G.; Grönberg, L.; Hassel, J.; Kuzmin, L. S. *Appl. Phys. Lett.* **2013,** *103,* 142605. doi:10.1063/1.4824308
5. Oelsner, G.; Andersen, C. K.; Rehák, M.; Schmelz, M.; Anders, S.; Grajcar, M.; Hübner, U.; Mølmer, K.; Il'ichev, E. *Phys. Rev. Appl.* **2017,** *7,* 014012. doi:10.1103/physrevapplied.7.014012
6. Kuzmin, L. S.; Sobolev, A. S.; Gatti, C.; Di Gioacchino, D.; Crescini, N.; Gordeeva, A.; Ilichev, E. *IEEE Trans. Appl. Supercond.* **2018,** *28,* 2400505. doi:10.1109/tasc.2018.2850019
7. Revin, L. S.; Pankratov, A. L.; Gordeeva, A. V.; Yablokov, A. A.; Rakut, I. V.; Zbrozhek, V. O.; Kuzmin, L. S. *Beilstein J. Nanotechnol.* **2020,** *11,* 960–965. doi:10.3762/bjnano.11.80
8. Kokkoniemi, R.; Girard, J.-P.; Hazra, D.; Laitinen, A.; Govenius, J.; Lake, R. E.; Sallinen, I.; Vesterinen, V.; Partanen, M.; Tan, J. Y.; Chan, K. W.; Tan, K. Y.; Hakonen, P.; Möttönen, M. *Nature* **2020,** *586,* 47–51. doi:10.1038/s41586-020-2753-3
9. Lee, G.-H.; Efetov, D. K.; Jung, W.; Ranzani, L.; Walsh, E. D.; Ohki, T. A.; Taniguchi, T.; Watanabe, K.; Kim, P.; Englund, D.; Fong, K. C. *Nature* **2020,** *586,* 42–46. doi:10.1038/s41586-020-2752-4
10. Barbieri, R.; Braggio, C.; Carugno, G.; Gallo, C. S.; Lombardi, A.; Ortolan, A.; Pengo, R.; Ruoso, G.; Speake, C. C. *Phys. Dark Universe* **2017,** *15,* 135–141. doi:10.1016/j.dark.2017.01.003
11. Crescini, N.; Alesini, D.; Braggio, C.; Carugno, G.; D'Agostino, D.; Di Gioacchino, D.; Falferi, P.; Gambardella, U.; Gatti, C.; Iannone, G.; Ligi, C.; Lombardi, A.; Ortolan, A.; Pengo, R.; Ruoso, G.; Taffarello, L. *Phys. Rev. Lett.* **2020,** *124,* 171801. doi:10.1103/physrevlett.124.171801
12. McAllister, B. T.; Flower, G.; Ivanov, E. N.; Goryachev, M.; Bourhill, J.; Tobar, M. E. *Phys. Dark Universe* **2017,** *18,* 67–72. doi:10.1016/j.dark.2017.09.010
13. Alesini, D.; Babusci, D.; Barone, C.; Buonomo, B.; Beretta, M. M.; Bianchini, L.; Castellano, G.; Chiarello, F.; Di Gioacchino, D.; Falferi, P.; Felici, G.; Filatrella, G.; Foggetta, L. G.; Gallo, A.; Gatti, C.; Giazotto, F.; Lamanna, G.; Ligabue, F.; Ligato, N.; Ligi, C.; Maccarrone, G.; Margesin, B.; Mattioli, F.; Monticone, E.; Oberto, L.; Pagano, S.; Paolucci, F.; Rajteri, M.; Rettaroli, A.; Rolandi, L.; Spagnolo, P.; Toncelli, A.; Torrioli, G. *J. Low Temp. Phys.* **2020,** *199,* 348–354. doi:10.1007/s10909-020-02381-x
14. Alesini, D.; Babusci, D.; Barone, C.; Buonomo, B.; Beretta, M. M.; Bianchini, L.; Castellano, G.; Chiarello, F.; Di Gioacchino, D.; Falferi, P.; Felici, G.; Filatrella, G.; Foggetta, L. G.; Gallo, A.; Gatti, C.; Giazotto, F.; Lamanna, G.; Ligabue, F.; Ligato, N.; Ligi, C.; Maccarrone, G.; Margesin, B.; Mattioli, F.; Monticone, E.; Oberto, L.; Pagano, S.; Paolucci, F.; Rajteri, M.; Rettaroli, A.; Rolandi, L.; Spagnolo, P.; Toncelli, A.; Torrioli, G. *J. Phys.: Conf. Ser.* **2020,** *1559,* 012020. doi:10.1088/1742-6596/1559/1/012020
15. Guarcello, C.; Braggio, A.; Solinas, P.; Giazotto, F. *Phys. Rev. Appl.* **2019,** *11,* 024002. doi:10.1103/physrevapplied.11.024002
16. Guarcello, C.; Braggio, A.; Solinas, P.; Pepe, G. P.; Giazotto, F. *Phys. Rev. Appl.* **2019,** *11,* 054074. doi:10.1103/physrevapplied.11.054074
17. Pountougnigni, O. V.; Yamapi, R.; Tchawoua, C.; Pierro, V.; Filatrella, G. *Phys. Rev. E* **2020,** *101,* 052205. doi:10.1103/physreve.101.052205
18. Piedjou Komnang, A. S.; Guarcello, C.; Barone, C.; Gatti, C.; Pagano, S.; Pierro, V.; Rettaroli, A.; Filatrella, G. *Chaos, Solitons Fractals* **2021,** *142,* 110496. doi:10.1016/j.chaos.2020.110496
19. Piedjou Komnang, A. S.; Guarcello, C.; Barone, C.; Pagano, S.; Filatrella, G. Analysis of Josephson Junction Lifetimes for the Detection of Single Photons in a Thermal Noise Background. *2021 IEEE 14th Workshop on Low Temperature Electronics (WOLTE);* Institute of Electrical and Electronics Engineers, 2021; pp 1–4. doi:10.1109/wolte49037.2021.9555447
20. Guarcello, C.; Piedjou Komnang, A. S.; Barone, C.; Rettaroli, A.; Gatti, C.; Pagano, S.; Filatrella, G. *Phys. Rev. Appl.* **2021,** *16,* 054015. doi:10.1103/physrevapplied.16.054015
21. Grimaudo, R.; Valenti, D.; Spagnolo, B.; Filatrella, G.; Guarcello, C. *Phys. Rev. D* **2022,** *105,* 033007. doi:10.1103/physrevd.105.033007
22. Chiarello, F.; Alesini, D.; Babusci, D.; Barone, C.; Beretta, M. M.; Buonomo, B.; D'Elia, A.; Di Gioacchino, D.; Felici, G.; Filatrella, G.; Foggetta, L. G.; Gallo, A.; Gatti, C.; Ligi, C.; Maccarrone, G.; Mattioli, F.; Pagano, S.; Piersanti, L.; Rettaroli, A.; Tocci, S.; Torrioli, G. *IEEE Trans. Appl. Supercond.* **2022,** *32,* 1100305. doi:10.1109/tasc.2022.3148693

23. Pankratov, A. L.; Revin, L. S.; Gordeeva, A. V.; Yablokov, A. A.; Kuzmin, L. S.; Il'ichev, E. *npj Quantum Inf.* **2022,** *8,* 61. doi:10.1038/s41534-022-00569-5
24. Revin, L. S.; Pankratov, A. L. *Appl. Phys. Lett.* **2011,** *98,* 162501. doi:10.1063/1.3582615
25. Gol'tsman, G. N.; Okunev, O.; Chulkova, G.; Lipatov, A.; Semenov, A.; Smirnov, K.; Voronov, B.; Dzardanov, A.; Williams, C.; Sobolewski, R. *Appl. Phys. Lett.* **2001,** *79,* 705–707. doi:10.1063/1.1388868
26. Fox, M. *Quantum Optics: An Introduction;* Oxford University Press, 2006; Vol. 15.
27. Gordeeva, A. V.; Zbrozhek, V. O.; Pankratov, A. L.; Revin, L. S.; Shamporov, V. A.; Gunbina, A. A.; Kuzmin, L. S. *Appl. Phys. Lett.* **2017,** *110,* 162603. doi:10.1063/1.4982031
28. Kuzmin, L. S.; Pankratov, A. L.; Gordeeva, A. V.; Zbrozhek, V. O.; Shamporov, V. A.; Revin, L. S.; Blagodatkin, A. V.; Masi, S.; de Bernardis, P. *Commun. Phys.* **2019,** *2,* 104. doi:10.1038/s42005-019-0206-9
29. Likharev, K. K. *Dynamics of Josephson junctions and circuits;* Gordon and Breach Science Publishers: New York, NY, USA, 1986.
30. Klapwijk, T. M.; Blonder, G. E.; Tinkham, M. *Physica B+C (Amsterdam)* **1982,** *109–110,* 1657–1664. doi:10.1016/0378-4363(82)90189-9
31. Kleinsasser, A. W.; Miller, R. E.; Mallison, W. H.; Arnold, G. B. *Phys. Rev. Lett.* **1994,** *72,* 1738–1741. doi:10.1103/physrevlett.72.1738
32. Martinis, J. M.; Kautz, R. L. *Phys. Rev. Lett.* **1989,** *63,* 1507–1510. doi:10.1103/physrevlett.63.1507
33. Vion, D.; Götz, M.; Joyez, P.; Esteve, D.; Devoret, M. H. *Phys. Rev. Lett.* **1996,** *77,* 3435–3438. doi:10.1103/physrevlett.77.3435
34. Kivioja, J. M.; Nieminen, T. E.; Claudon, J.; Buisson, O.; Hekking, F. W. J.; Pekola, J. P. *Phys. Rev. Lett.* **2005,** *94,* 247002. doi:10.1103/physrevlett.94.247002
35. Koval, Y.; Fistul, M. V.; Ustinov, A. V. *Phys. Rev. Lett.* **2004,** *93,* 087004. doi:10.1103/physrevlett.93.087004
36. Longobardi, L.; Massarotti, D.; Stornaiuolo, D.; Galletti, L.; Rotoli, G.; Lombardi, F.; Tafuri, F. *Phys. Rev. Lett.* **2012,** *109,* 050601. doi:10.1103/physrevlett.109.050601
37. Lisitskiy, M.; Massarotti, D.; Galletti, L.; Longobardi, L.; Rotoli, G.; Russo, M.; Tafuri, F.; Ruggiero, B. *J. Appl. Phys.* **2014,** *116,* 043905. doi:10.1063/1.4890317
38. Wallraff, A.; Lukashenko, A.; Coqui, C.; Kemp, A.; Duty, T.; Ustinov, A. V. *Rev. Sci. Instrum.* **2003,** *74,* 3740–3748. doi:10.1063/1.1588752
39. Yablokov, A. A.; Mylnikov, V. M.; Pankratov, A. L.; Pankratova, E. V.; Gordeeva, A. V. *Chaos, Solitons Fractals* **2020,** *136,* 109817. doi:10.1016/j.chaos.2020.109817
40. Yablokov, A. A.; Glushkov, E. I.; Pankratov, A. L.; Gordeeva, A. V.; Kuzmin, L. S.; Il'ichev, E. V. *Chaos, Solitons Fractals* **2021,** *148,* 111058. doi:10.1016/j.chaos.2021.111058
41. Guarcello, C. *Chaos, Solitons Fractals* **2021,** *153,* 111531. doi:10.1016/j.chaos.2021.111531
42. Kramers, H. A. *Physica (Amsterdam)* **1940,** *7,* 284–304. doi:10.1016/s0031-8914(40)90098-2
43. Hänggi, P.; Talkner, P.; Borkovec, M. *Rev. Mod. Phys.* **1990,** *62,* 251–341. doi:10.1103/revmodphys.62.251
44. Malakhov, A. N.; Pankratov, A. L. *Phys. A (Amsterdam, Neth.)* **1996,** *229,* 109–126. doi:10.1016/0378-4371(95)00395-9
45. Malakhov, A. N.; Pankratov, A. L. *Phys. C (Amsterdam, Neth.)* **1996,** *269,* 46–54. doi:10.1016/0921-4534(96)00426-1
46. Malakhov, A. N. *Chaos* **1997,** *7,* 488–504. doi:10.1063/1.166220
47. Blackburn, J. A.; Cirillo, M.; Grønbech-Jensen, N. *Phys. Rep.* **2016,** *611,* 1–33. doi:10.1016/j.physrep.2015.10.010
48. Büttiker, M.; Harris, E. P.; Landauer, R. *Phys. Rev. B* **1983,** *28,* 1268–1275. doi:10.1103/physrevb.28.1268
49. Martinis, J. M.; Devoret, M. H.; Clarke, J. *Phys. Rev. B* **1987,** *35,* 4682–4698. doi:10.1103/physrevb.35.4682
50. Golubev, D. S.; Il'ichev, E. V.; Kuzmin, L. S. *Phys. Rev. Appl.* **2021,** *16,* 014025. doi:10.1103/physrevapplied.16.014025
51. Devoret, M. H.; Martinis, J. M.; Esteve, D.; Clarke, J. *Phys. Rev. Lett.* **1984,** *53,* 1260–1263. doi:10.1103/physrevlett.53.1260

License and Terms

BEILSTEIN JOURNAL OF NANOTECHNOLOGY

A superconducting adiabatic neuron in a quantum regime

Marina V. Bastrakova[1], Dmitrii S. Pashin[1], Dmitriy A. Rybin[1], Andrey E. Schegolev[2,3], Nikolay V. Klenov[1,4], Igor I. Soloviev[*1], Anastasiya A. Gorchavkina[1,5] and Arkady M. Satanin[5,6]

Full Research Paper

Open Access

Address:
[1]Faculty of Physics, Lobachevsky State University of Nizhni Novgorod, 603950 Nizhny Novgorod, Russia, [2]Skobeltsyn Institute of Nuclear Physics, Lomonosov Moscow State University, 119991 Moscow, Russia, [3]Moscow Technical University of Communication and Informatics (MTUCI), 111024 Moscow, Russia, [4]Faculty of Physics, Lomonosov Moscow State University, 119991 Moscow, Russia, [5]Higher School of Economics, Russia National Research University, 101000 Moscow, Russia and [6]Federal State Unitary Enterprise All-Russia Research Institute of Automatics named after N.L. Dukhov, 101000 Moscow, Russia

Email:
Igor I. Soloviev[*] - igor.soloviev@gmail.com

* Corresponding author

Keywords:
Josephson junction; quantum neuron; quantum-classical neural networks; superconducting quantum interferometer

Beilstein J. Nanotechnol. **2022,** *13,* 653–665.
https://doi.org/10.3762/bjnano.13.57

Received: 20 April 2022
Accepted: 06 July 2022
Published: 14 July 2022

This article is part of the thematic issue "Intrinsic Josephson effect and prospects of superconducting spintronics".

Guest Editor: A. S. Sidorenko

Abstract

We explore the dynamics of an adiabatic neural cell of a perceptron artificial neural network in a quantum regime. This mode of cell operation is assumed for a hybrid system of a classical neural network whose configuration is dynamically adjusted by a quantum co-processor. Analytical and numerical studies take into account non-adiabatic processes as well as dissipation, which leads to smoothing of quantum coherent oscillations. The obtained results indicate the conditions under which the neuron possesses the required sigmoid activation function.

Introduction

The implementation of machine learning algorithms is one of the main applications of modern quantum processors [1-9]. It has been shown that a relatively small quantum circuit may be capable of searching for a large number of synaptic weights of an artificial neural network (ANN) [10-13]. The rate of the weight adjustment is an important parameter that determines the possibility of the ANN dynamic adaptation. Such tunability is required when working with rapidly changing content. The corresponding information flow naturally arises, for example, within the framework of novel telecommunication paradigms, such as software-defined radio [14,15] implying the change of signal frequency and modulation. An efficient architecture of a flexible hybrid system requires a close spatial arrangement of the classical ANN with its control quantum co-processor, see

Figure 1a. Superconductor technology is a promising platform for such a solution since both superconducting quantum machine learning circuits [16-22] and superconducting ANNs [23-37] are rapidly developed nowadays.

Robust implementation of the considered quantum-classical system would benefit from the utilization of a single technology suitable for superconducting qubits. In this case, the classical part can operate in an adiabatic mode ensuring minimal impact on quantum circuits. However, quantum effects, in turn, can significantly affect the operation of neuromorphic elements. In this work, we account for this by considering the neuron cell operation in a quantum regime. We investigate the dynamics of this cell in search of conditions that provide the required sigmoid activation function (conversion of the input magnetic flux into the average output current), suitable for the operation of the ANN as a perceptron [4]. The studied cell is called a quantum neuron or S_Q neuron. Its closest analogue is the flux qubit used by D-Wave Systems in quantum annealers [38-41].

An important incentive for this work are the previously obtained results on classical adiabatic neurons with extremely small energy dissipation [42-45]. We especially note the demonstrated possibility of the adiabatic evolution of the state for a neuron in a multilayer perceptron with Josephson junctions without resistive shunting [46]. It is precisely such a heterostructure without resistive shunting that is used in the implementation of a quantum neuron based on a flux qubit.

The article is organized as follows. First, we present the scheme of the proposed quantum neuron and also investigate the spectrum of the Hamilton operator for such a system. Next, on the basis of the numerical solution of the Schrödinger equation, we investigate dynamic processes in a quantum neuron. We pay special attention to the analysis of the activation function of the cell for two main modes (with one and two minima of the potential energy of the system). We use Wigner functions for a visual interpretation of the dynamics of the neuron. The range of the operating parameters for the proposed neuron circuit under the action of unipolar magnetic flux pulses is found. Finally, the influence of the dissipation on the features of the dynamic processes and characteristics of the cell is revealed.

Methods

Neuron model and basic equations

A single-junction superconducting interferometer with normalized inductance l, a Josephson junction without resistive shunting (JJ), an additional inductance l_a, and an output inductance l_{out} (see Figure 1b) are the basis of the quantum neuron. This circuit has been presented before as a classic superconducting neuron for an adiabatic perceptron [42,46].

The classical dynamics of the system under consideration is described using the equation for the dynamics of the Josephson phase:

$$\omega_p^{-2}\ddot{\varphi}+\omega_c^{-1}\dot{\varphi}+\sin\varphi=b\varphi_{in}(t)-a\varphi, \tag{1}$$

where the coefficients are determined by the expressions

$$a=\frac{l_a+l_{out}}{ll_a+l_{out}(l+l_a)},\ b=\frac{l_a+2l_{out}}{2\left[ll_a+l_{out}(l+l_a)\right]},\ l_a=1+l.$$

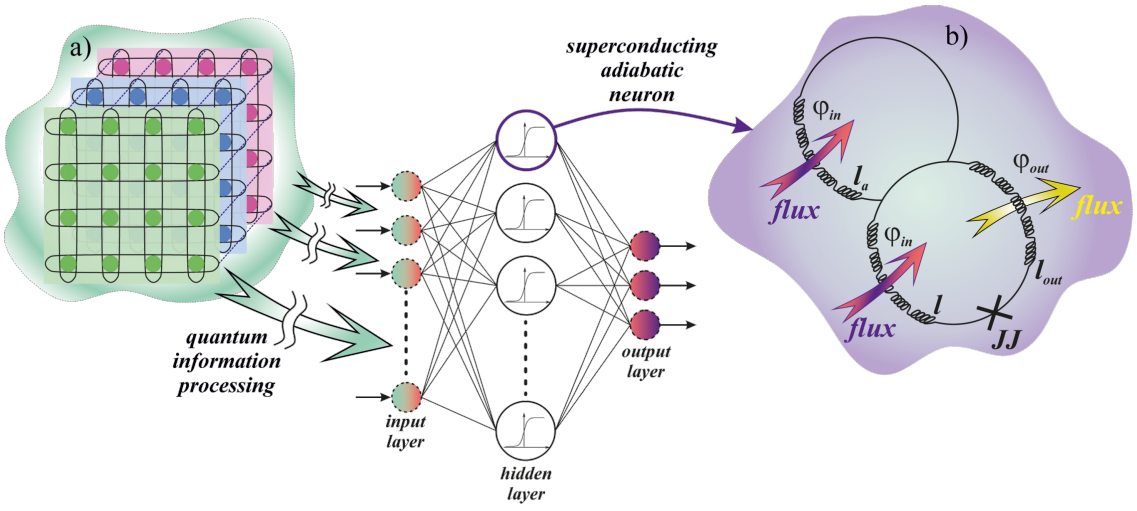

Figure 1: (a) Sketch of a flexible hybrid system consisting of a classical ANN having its configuration (synaptic weights) dynamically adjusted by a quantum co-processor. (b) Schematic representation of the S_Q neuron providing nonlinear magnetic flux transformation.

These coefficients were introduced in [46] when considering the classical mode of this system. Inductances are normalized to $(2\pi I_c/\Phi_0)$, where I_c is the critical current of the Josephson junction and Φ_0 is the magnetic flux quantum. The inertial properties of the system are due to the junction capacitance, which, along with the critical current I_c, determines the plasma frequency of the JJ,

$$\omega_p = \sqrt{\frac{2eI_c}{\hbar C}}.$$

In this case, the dissipative properties of the system are determined by the Josephson characteristic frequency $\omega_c = 2eRI_c\hbar$ (here, R and C are the normal state resistance and capacitance of the Josephson junction, respectively).

Dynamic control of the system states is carried out by a changing external magnetic flux, $\varphi_{in}(t)$, normalized to the magnetic flux quantum Φ_0:

$$\varphi_{in}(t) = A\left[\left(1+e^{-2D(t-t_1)}\right)^{-1} + \left(1+e^{2D(t-t_2)}\right)^{-1}\right] - A, \quad (2)$$

where A is the normalised amplitude of the external action, t_1 and $t_2 = 3t_1$ are the characteristic rise/fall times of the control signal, whose steepness is determined by the parameter D. The phase of the Josephson junction, φ, obeys Equation 1. The activation function of the neuron is determined by the dependence of the output current i_{out} on the input flux φ_{in}:

$$i_{out} = \frac{\varphi_{in} - 2l_a i}{2\left(l_a + l_{out}\right)}, \qquad i = b\varphi_{in} - a\varphi. \quad (3)$$

Spectrum of the neuron Hamiltonian

The quantum regime manifests itself through a discrete spectrum of allowed values for the total energy of the system. The characteristic gaps in the spectrum of the effective Hamiltonian are significantly larger than the thermal smearing in the studied case. Also, the level broadening due to the influence of the environment is relatively small. The described features affect the neuron ability to non-linearly transform the magnetic signal. In order to describe the quantum mechanical behavior of the system (Equation 1), we start from the case of a Josephson junction with a large shunted resistance ($\omega_c^{-1} \to 0$). In this case, Equation 1 can be interpreted as the equation of motion for a particle with mass $M = \hbar^2/2E_c$ (charge energy $E_c = (2e)^2/2C$) in potential

$$U\left[\varphi, \varphi_{in}(t)\right] = E_J \frac{\left[b\varphi_{in}(t) - a\varphi\right]^2}{2a} + E_J\left(1-\cos\varphi\right), \quad \text{with } E_J = \frac{I_c\Phi_0}{2\pi}. \quad (4)$$

The dynamics of the system is governed by the Hamilton function,

$$H\left[p, \varphi, \varphi_{in}(t)\right] = \frac{p^2}{2M} + U\left[\varphi, \varphi_{in}(t)\right].$$

The canonical quantization procedure leads to the Hamiltonian:

$$\hat{H}\left[\hat{p}, \hat{\varphi}, \varphi_{in}(t)\right] = \frac{E_c\hat{p}^2}{\hbar^2} + E_J\left\{\frac{\left[b\varphi_{in}(t) - a\hat{\varphi}\right]^2}{2a} + \left(1-\cos\hat{\varphi}\right)\right\}, \quad (5)$$

where the operators $\hat{p}$ and $\hat{\varphi}$ obey the commutative relation $[\hat{\varphi}, \hat{p}] = i\hbar$.

The form of the potential from Equation 4 in each moment of time, and hence the dynamic behavior of the system, is determined by the physical parameters of the circuit shown in Figure 1. There is a range of inductance values where the potential profile from Equation 4 has a double-well shape under the action of the input flux (Equation 2). Their values can be obtained from solution of the transcendental equation

$$\frac{\partial U(\varphi)}{\partial\varphi} \equiv a\varphi - b\varphi_{in}(t) + \sin\varphi = 0.$$

The potential has more than one extremum in the case that $a < 1$ and ,therefore,

$$l > l^* \equiv \sqrt{l_{out}^2 + 1} - l_{out}.$$

Note that for the classical regime the sigmoidal shape of the activation function is possible only when $l < l^*$ [46].

One of the goals of this work is to determine the parameters of the adiabatic switching of the quantum neuron for $l < l^*$ (single-well mode) and $l > l^*$ (double-well mode). Within the adiabatic approach it is possible to numerically solve the time-independent Schrödinger equation (see Appendix 1) for each moment of time to find "instantaneous energy levels", $E_n(t)$, and "instantaneous wave functions" of the system, $\psi_n(\varphi, t)$:

$$\hat{H}\left[\hat{p}, \hat{\varphi}, \varphi_{in}(t)\right]\psi_n(\varphi, t) = E_n(t)\psi_n(\varphi, t). \quad (6)$$

Figure 2 demonstrates the spectrum of instantaneous energy levels and wave functions of the system at the initial moment of time (Figure 2a,c) and at the moment t_1, when the input magnetic flux (Equation 2) is equal to $\varphi_{in} = 2\pi$ (Figure 2b,d). Note that for the case $l < l^*$ (Figure 2a,b), the form of the potential can be approximated by a parabolic function (single-well mode). The symmetry of the potential under external influence does not change, and only a shift in the energy levels with preservation of the interlevel distance is observed during the rise/fall periods of the signal. A different behavior is observed for $l > l^*$ where during the rise/fall periods of the signal, a double-well potential appears (Figure 2d). Here, the two lowest close energy levels are separated by an energy gap from the rest of the level structure. This resembles the formation of the flux qubit spectrum [47].

Results and Discussion

Dynamics of the quantum neuron without dissipation

The dynamics (evolution of the states of the system, $\Psi(t)$) of the quantum neuron (Equation 5) is associated with the nonlinear transformation of the input magnetic flux (Equation 2). We describe it using the time-dependent Schrödinger equation:

$$i\hbar\frac{\partial}{\partial t}\Psi(t) = \hat{H}\left[\hat{p},\hat{\varphi},\varphi_{in}(t)\right]\Psi(t). \tag{7}$$

Eigenvectors of the system are found by numerical solution of Equation 7 (see details in Appendix 2). Thereafter, from the evolution of average values of the phase and current operators we found the transfer characteristic $i_{out}(\varphi_{in})$ of the S_Q neuron Equation 3, that is, its activation function. Let us explain the idea of our calculations. We assume that the system is initialized at the initial moment of time. At cryogenic temperatures (millikelvin range) the system states are localised at lower energy levels.

According to Equation 3, the dependence of the average value of the output current i_{out} on the input magnetic flux φ_{in} is calculated:

$$\begin{cases}\left\langle\hat{\varphi}(t)\right\rangle = \left\langle\Psi(t)\middle|\hat{\varphi}\middle|\Psi(t)\right\rangle,\\ i_{out} \equiv \left\langle\hat{i}(t)\right\rangle = b\varphi_{in} - a\left\langle\hat{\varphi}(t)\right\rangle.\end{cases} \tag{8}$$

We use the Wigner functions in order to visualize the adiabatic dynamics in the "phase-conjugate momentum" space [48]. This function is determined by the Fourier transform of a bilinear combination of the wave functions:

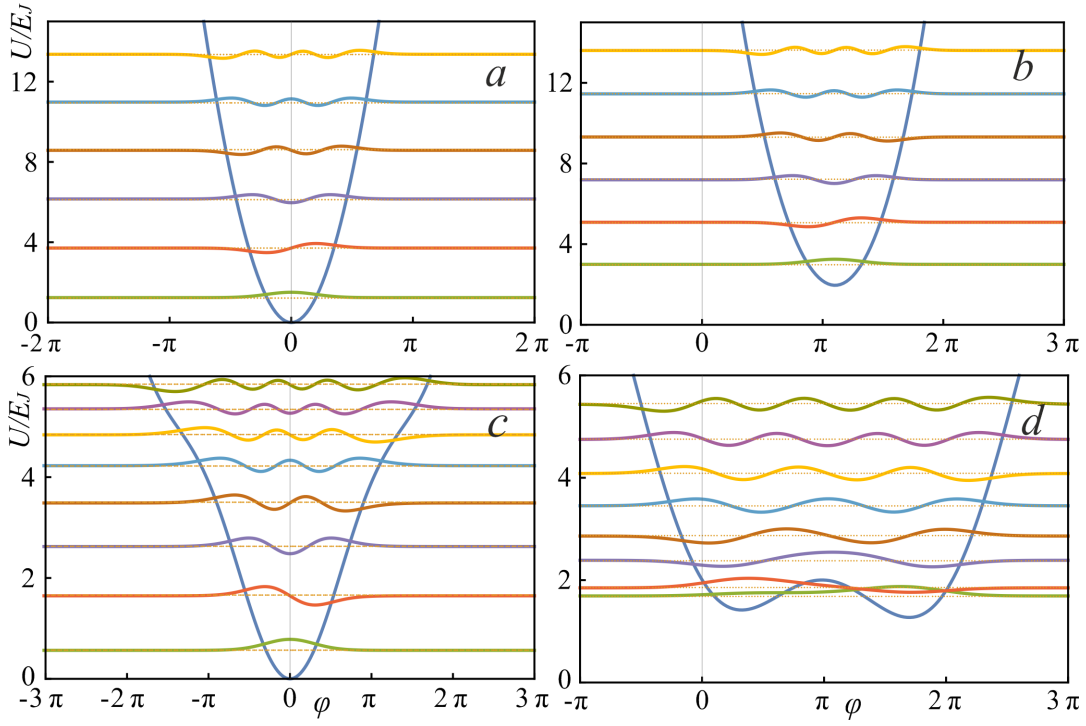

Figure 2: The energy spectrum and adiabatic (instantaneous) wave functions are represented at the initial time $t = 0$ (a, c) and at the rise of the applied flux, $t_1 = 500$ (b, d) for the inductance values $l = 0.1$ (a, b) and $l = 2.5$ (c, d). The parameters of the system and the input magnetic flux are: $E_C = 0.5E_J$, $I_a = I + 1$, $I_{out} = 0.1$, $D = 0.008$, $A = 4\pi$.

$$W(\varphi,p,t)=\frac{1}{2\pi\hbar}\int_{-\infty}^{\infty}\mathrm{d}\xi e^{\frac{ip\xi}{\hbar}}\Psi(\varphi+\xi/2,t)\Psi^{*}(\varphi-\xi/2,t). \quad (9)$$

The wave function $\Psi(\varphi,t)$ can be expanded in terms of the instantaneous eigenvectors $\psi_n(\varphi,t)$:

$$\Psi(\varphi,t)=\sum_n c_n(t)\psi_n(\varphi,t)\exp\left[-\frac{i}{\hbar}\int_0^t E_n(t')\mathrm{d}t'\right], \quad (10)$$

where the coefficients $c_n(0)$ are determined from the initial conditions for the wave function $\Psi(\varphi,0)$. Changes of the coefficients $c_n(t)$ in time are determined by the system of N coupled equations

$$i\frac{\mathrm{d}c_n(t)}{\mathrm{d}t}=\frac{i}{\hbar}\frac{\mathrm{d}\varphi_{\mathrm{in}}(t)}{\mathrm{d}t}\cdot\sum_{m=0}^{N}\left\{\frac{1}{\omega_{n,m}(t)}\left(\frac{\partial\hat{H}}{\partial\varphi_{\mathrm{in}}}\right)_{n,m}c_m(t)\exp\left[i\int_0^t\omega_{n,m}(t')dt'\right]\right\}, \quad (11)$$

where the time-dependent matrix elements appear. Their rate of change is given by $\hbar\omega_{n,m}(t)=E_n(t)-E_m(t)$. Note that if the adiabaticity condition,

$$\left|\frac{1}{\hbar\omega_{n,m}(t)}\left(\frac{\partial\hat{H}}{\partial\varphi_{\mathrm{in}}}\right)_{n,m}\right|\ll 1, \quad (12)$$

is satisfied for pairs of levels, then transitions between them become improbable.

We consider the case where only the two lowest levels are taken into account. In this case, the remaining energy levels lie noticeably higher than the selected doublet. In addition, adiabaticity conditions (Equation 12) should be satisfied. When these conditions are met, the following expression can be written to approximate the wave function:

$$\Psi(\varphi,t)=c_0(t)\psi_0(\varphi,t)\exp\left[-\frac{i}{\hbar}\int_0^t E_0(t')\mathrm{d}t'\right]+c_1(t)\psi_1(\varphi,t)\exp\left[-\frac{i}{\hbar}\int_0^t E_1(t')\mathrm{d}t'\right], \quad (13)$$

and we can get the expression for the Wigner function:

$$W(\varphi,p,t)=|c_0(t)|^2K_{0,0}(\varphi,p,t)+|c_1(t)|^2K_{1,1}(\varphi,p,t)+c_0(t)c_1^{*}(t)K_{0,1}(\varphi,p,t)\exp\left[i\int_0^t\omega_{0,1}(t')\mathrm{d}t'\right]+c_1(t)c_0^{*}(t)K_{1,0}(\varphi,p,t)\exp\left[-i\int_0^t\omega_{0,1}(t')\mathrm{d}t'\right], \quad (14)$$

where

$$K_{n,m}(\varphi,p,t)=\frac{1}{2\pi}\int_{-\infty}^{\infty}\mathrm{d}\xi e^{ip\xi}\psi_n(\varphi+\xi/2,t)\psi_m^{*}(\varphi-\xi/2,t). \quad (15)$$

Further we demonstrate two effects in this approximation: (1) One can construct a superposition of the basis states and observe the manifestation of the interference of quantum states in the oscillations of the output characteristic; (2) there are oscillations of the output characteristic due to the influence of nonadibaticity.

Single-well potential

Figure 3 demonstrates the calculated activation functions of the S_Q neuron operating in the quantum regime in single-well mode ($I < I^{*}$) for three different initial states of the system.

Numerical analysis has shown that the activation functions for the quantum neuron, initialised in the basic states, takes a sigmoidal shape (black and red curves in Figure 3). This is in a good agreement with the classical regime of operation [46].

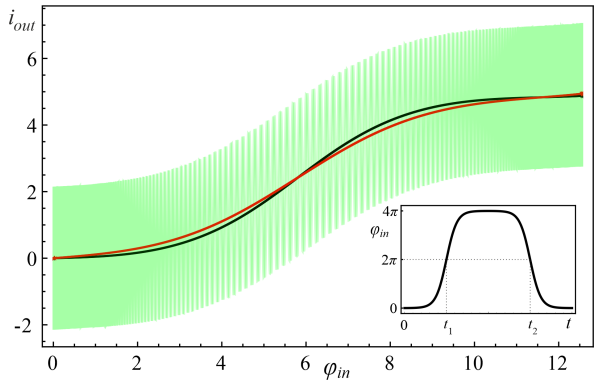

Figure 3: The neuron activation functions for I = 0.1 and different initial states: The black curve corresponds to the ground initial state $\psi_0(\varphi,0)$, the red curve to the first excited state $\psi_1(\varphi,0)$, and green curve corresponds to the superposition of states $([\psi_0(\varphi,0)+\psi_1(\varphi,0)]/\sqrt{2}$. Parameters of the input magnetic flux are D = 0.008, A = 4π, and t_1 = 500.

Note that when the input flux (Equation 2) changes from 0 to 4π, the phase φ on the Josephson junction changes from 0 to 2π and vice versa.

The complete coincidence of the two paths of the system evolution occurs with a significant increase in the rise time " ↑ " (φ = 0→2π) and the fall time " ↓ " (φ = 2π→0) of the input signal. For the superposition of the basic states, as seen in Figure 3, oscillations are observed in the shape of the activation function. In this regard, for clarity of interpretation of the obtained results of the quantum dynamics, we consider the evolution of the system in the phase space.

If the adiabaticity condition (Equation 12) is satisfied and the system was initially at the lowest level $|c_0(0)|^2 = 1$ (see Figure 4a), then the dynamics of the Wigner function reflects the distribution in phase and conjugate momentum related to this level. Similar reasoning can be given for the case when the first excited level (Figure 3b) is populated. Here, the center of the probability density $|\Psi(\varphi,t)|^2$ and the distribution of the Wigner function (Figure 4a,b) shift smoothly, from φ = 0 to 2π, when the cell is exposed to the input magnetic flux. The system remains localized in the initial state, and as a result, the activation function takes a sigmoidal form without any oscillations (black and red curves in Figure 3). If the system is initialised in the superposition of the lowest states (Figure 4c) then the interference term in the Wigner function emerges, see the last two terms in Equation 14. This is expressed as oscillations on the Wigner function between the maximum (red area) and minimum (blue area), see Figure 5. Coherent oscillations on the current–flux dependence are also the evidence of this phenomenon (see the green curve in Figure 3).

Double-well potential

For the double-well potential, when $l > l^*$, the problem of quantum dynamics and the formation of the sigmoidal activation function have also been studied. We start with the parameters of the input flux as presented in Figure 3. Numerical simulations demonstrate a distortion of the sigmoidal form of the activation function even when the S_Q neuron is initialized in the ground state, see Figure 6.

In the process of evolution, a significant rearrangement occurs in the spectrum of energy levels (anti-crossing between the ground and the first excited levels) during the formation of a double-well potential (see Figure 2). This corresponds to the rise period of the signal along the path φ = 0→2π. Note that, in this case, the adiabaticity condition (Equation 12) is violated. This is a consequence of the increase in the input flux φ_{in}, which leads to the excitation of the overlying states. In this

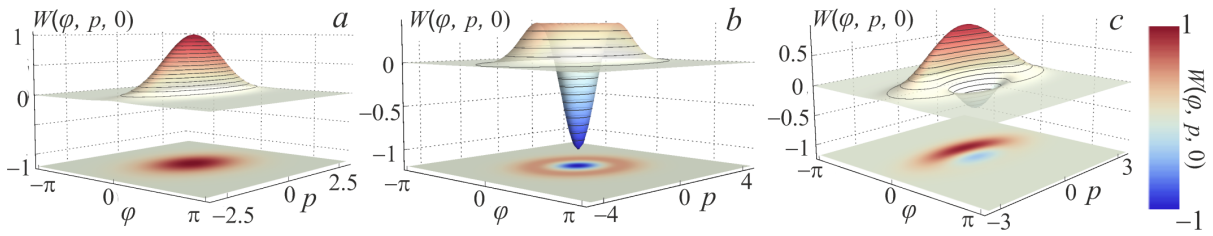

Figure 4: The Wigner functions $W(\varphi, p, t = 0)$ of the considered system initialized at the initial moment of time $t = 0$ (a) in the ground state $\psi_0(\varphi,0)$, (b) in the first excited state $\psi_1(\varphi,0)$ and (c) in the superposition of the lowest states $[\psi_0(\varphi,0)+\psi_1(\varphi,0)]/\sqrt{2}$ for $l = 0.1$. Other parameters are similar to those shown in Figure 3.

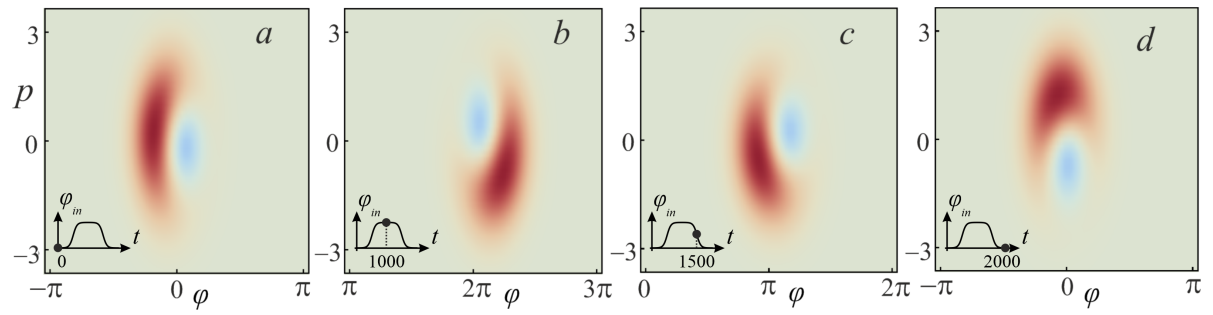

Figure 5: The evolution of the Wigner function under the influence of the input flux φ_{in} for the S_Q neuron initialized in the superposition state $[\psi_0(\varphi,0)+\psi_1(\varphi,0)]/\sqrt{2}$ at the moments $t = 0$ (absence of φ_{in}) (a); $t = 1000$ (the plateau of φ_{in}) (b); $t = 1500$ (the middle of the decreasing branch of φ_{in}) (c); $t = 2000$ (absence of φ_{in}) (d). The remaining parameters are similar to those shown in Figure 3.

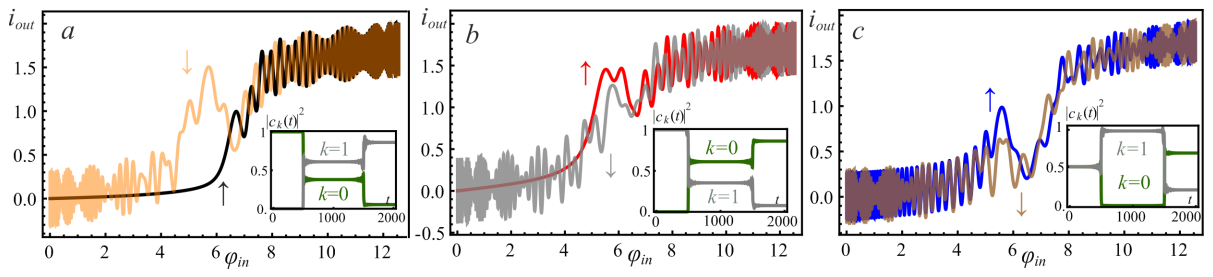

Figure 6: The activation functions of the neuron with I = 2.5 initialized (a) in the ground state, see the black " ↑ " and orange " ↓ " curves; (b) in the first excited state, see the red " ↑ " and gray " ↓ " curves; (c) in the superposition of the basis states, see the blue " ↑ ' and brown " ↓ " curves. Input flux parameters are D = 0.008, A = 4π, t_1 = 500. The symbol " ↑ " corresponds to the rise branch of φ_{in} = 0→4π, the " ↓ " symbol corresponds to the fall branch of φ_{in} = 4π→0. The inserts show the time-dependent evolution of the populations $|c_k(t)|^2$ of the ground state, k = 0, and the first excited, k = 1, state of the system.

case, the system ceases to be localized in the initial state, which is clearly shown in Figure 7 during the evolution of the Wigner function in the phase space. It can be seen that the system evolves adiabatically from the ground state until reaches φ_{in} = 2π, when a double-well potential profile (Equation 4) is formed. In this case, the rate of change of the potential exceeds the rate of state localisation. Due to the tunneling effect, the wave function is redistributed from the left to the right local minimum of the potential profile (see Figure 2). Figure 7b,c clearly shows that the Wigner function has negative values due to the formation of a superposition state during evolution (see also the insets in Figure 6 for the population coefficients $|c_0(t)|^2$ and $|c_1(t)|^2$ for basis levels). Because of this, the activation function in Figure 6 exhibits oscillations associated with the interference of the wave functions. These oscillations are more irregular than the ones in Figure 3 (see the green curve). This is due to the occurrence of interference phase effects of a larger number of states participating in the superposition corresponding to the violation of the adiabaticity condition (Equation 12).

Note that if the rate of the potential changes is less than the rate of the localised state movement and the adiabaticity condition (Equation 12) is satisfied, we can obtain the sigmoidal activation function even in a double-well potential (see Figure 8). In this case, there is a good match between the forward " ↑ " and the backward " ↓ " characteristics of the S_Q neuron.

Activation function of the quantum neuron

We also study the quality of approximation of the neuron activation function by the sigmoidal function for different parame-

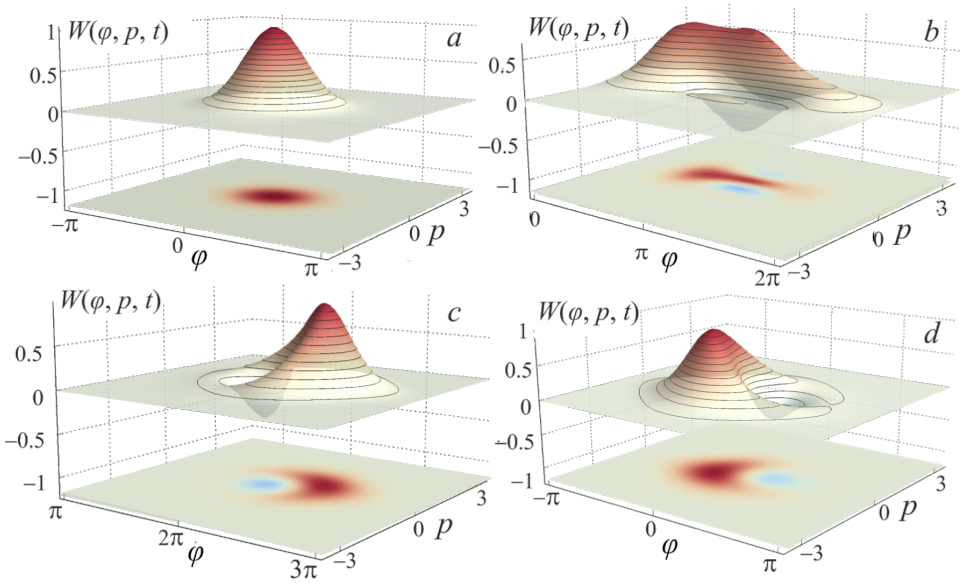

Figure 7: Evolution of the Wigner function of the S_Q neuron with I = 2.5 initialized in the ground state under the action of the input flux φ_{in} at the moments t = 0 (absence of φ_{in}) (a); t = 500 (the middle of the increase of φ_{in}) (b); t = 1000 (the plateau of φ_{in}) (c); t = 2000 (absence of φ_{in}) (d). The input flux parameters are equal to those shown in Figure 6.

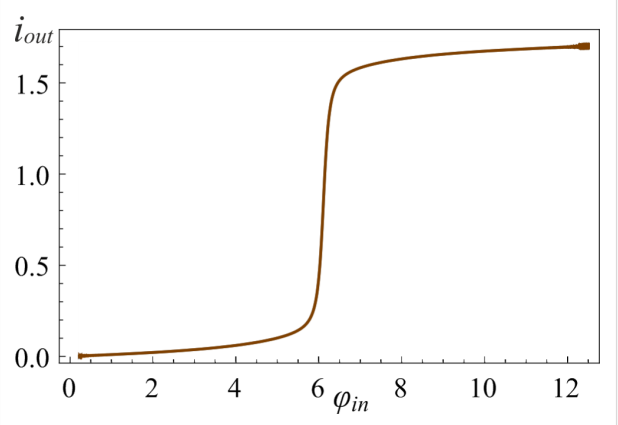

Figure 8: The activation function of the neuron with l = 2.5 initialised at t = 0 in the ground state. Here the parameters are D = 0.0002, A = 4π, and t_1 = 10000.

ters of the cell (in the framework of the adiabaticity conditions). The approximation function is:

$$\sigma(\varphi_{\text{in}}) = \frac{p_1}{1+e^{-p_2\varphi_{\text{in}}+p_3}} + p_4, \tag{16}$$

where p_i are the parameters of the numerical approximation. Our goal is to compare the ideal activation function $\sigma(\varphi_{\text{in}})$ and the activation function of the considered cell $i_{\text{out}}(\varphi_{\text{in}})$. We use the square of the standard deviation, SD, for this purpose:

$$\text{SD} = \text{Dis}\left[\left(\sigma(\varphi_{\text{in}}) - i_{\text{out}}(\varphi_{\text{in}})\right)^2\right], \tag{17}$$

where Dis[(…)] means the dispersion of a data set. Analysis of Figure 6 and Figure 8 allows us to conclude that the parameters affecting the activation function shape are primarily the rise/fall rate of the signal D (see Equation 2) and the inductance value l, which determines the shape of the potential profile. In this regard, we obtain the plane of parameters SD(l, D), presented in Figure 9, where the color indicates the value of the square of the standard deviation from the "ideal sigmoid". The area with SD < 0.0001 (area inside the dark zone in Figure 9) corresponds to the formation of the sigmoid activation function of the required form.

From the analysis of Figure 9, it can be concluded that the higher the value of the inductance l, the slower the process of adiabatic switching of the quantum neuron. For superconducting circuit parameters I_c = 0.35 μA, C =10 fF, $\omega_p \approx 10^{11}$ s^{-1}, the adiabatic switching time is approx. 5 ns for l = 0.1 (see Figure 3, the regime without oscillations) and approx. 100 ns for l = 2.5 (see Figure 8).

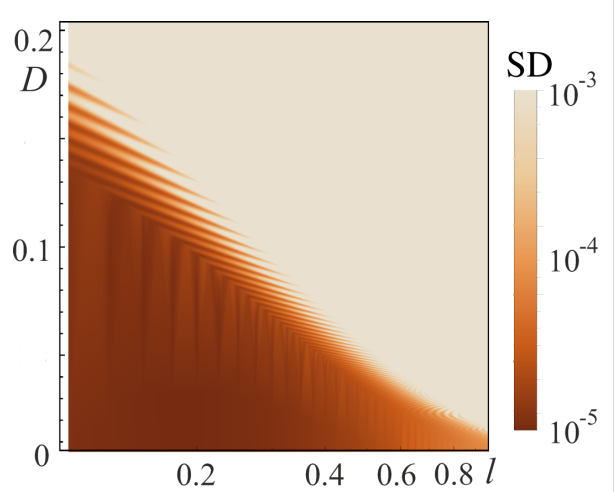

Figure 9: The value of the square of the standard deviation, SD, of the S_Q neuron activation function from the mathematical sigmoid (Equation 16) for different inductance l values and rise/fall rates, D, of the input flux $\varphi_{\text{in}}(t)$. The horizontal axis is in logarithmic scale. At the initial moment, the system was initialized in the ground state. The parameters of the system and the input flux are as follows: A = 4π, $l_a = l + 1$, l_{out} = 0.1.

Influence of dissipation effects on the quantum neuron dynamics

In the classical regime, the dissipation mechanism in the neuron has been considered using the Stewart–McCumber model [49]. To take into account the dissipation in a quantum system, we "place" it in a bosonic bath. For further analysis, we use a linear model of the interaction between the quantum neuron and the bath:

$$\hat{H}_{\text{int}} = k\hat{\varphi}\sum_i\left(\hat{b_i}^{\dagger} + \hat{b_i}\right), \tag{18}$$

where $\hat{b_i}^{\dagger}$ and $\hat{b_i}$ are creation and annihilation operators of the i-th bosonic mode, and k is the coupling constant. With an adiabatic change of the input flux, the S_Q state can be described in terms of the instantaneous eigenbasis $\psi_n(\varphi,t)$, see Equation 6, using a density matrix:

$$\rho(t) = \sum_{m,n}\rho_{mn}(\phi,t)\left|\psi_m(\phi,t)\right\rangle\left\langle\psi_n(\phi,t)\right|. \tag{19}$$

Under the Born–Markov approximation, dissipative dynamics is described by the generalized master equation for the density matrix [50]. Furthermore, by keeping only the secular terms and using the random phase approximation, we reduced it to the Pauli master equation (we present the results of modeling for the generalized master equation with and without the secular approximation in Appendix 3):

$$\dot{\rho}_{mm} = \sum_{n\neq m} \rho_{nn} W_{mn} - \rho_{mm} \sum_{n\neq m} W_{nm}, \tag{20}$$

where the dots denote a differentiation by normalized time, W_{mn} is the transition rate from the state n to m given by the expression

$$W_{mn} = \lambda \left| \left\langle \psi_n \left| \hat{\varphi} \right| \psi_m \right\rangle \right|^2 \cdot \left\{ \theta(\omega_{nm}) \left[\bar{n}(\omega_{nm}) + 1 \right] + \theta(\omega_{mn}) \bar{n}(\omega_{mn}) \right\}. \tag{21}$$

Here $\lambda = (2\pi g k^2)/\hbar^2$ is the renormalized coupling constant, θ is the Heaviside step function,

$$\bar{n}(\omega) = \frac{1}{e^{\hbar\omega/kT} - 1}$$

is the Planck distribution, and g is the density of bosonic modes, which is supposed to be constant. Under adiabatic approximation, the transition rates W_{mn} between the neuron states are calculated in the instantaneous eigenbasis. Numerical simulations are performed for the temperature of the bosonic thermostat at T = 50 mK.

We investigated the relaxation of the excited states for both the single-well ($l < l^*$, Figure 10a,c) and double-well ($l > l^*$, Figure 10b,d) potential shapes. The key result is the suppression of the oscillations of the activation function for the neuron initialized in a superposition of two basic states. The dynamics of changes in the populations $|c_k(t)|^2$ of the energy levels for this case is shown in the insets of Figure 10 (see Figure 6 for comparison). This relaxation takes the full cycle of switching of the input flux ($\varphi_{in} = 0 \Leftrightarrow 4\pi$) due to dissipative processes.

In Figure 10b,c there is an obvious suppression of the oscillations on the activation function, which were observed due to the anti-crossing of the energy levels in the double-well potential. In addition, coherent oscillations on the activation function of the neuron (see Figure 3 and Figure 6c) arising during evolution from the superposition state are also smoothed out. Previously, these oscillations were associated with the interference of the phases of the S_Q states. However, the possible dispersion of the initial phases makes the activation function to be sigmoidal due to the averaging over random phases, see Figure 10c,d.

Conclusion

We have shown that an adiabatic superconducting neuron of a classical perceptron, under certain conditions, retains the sigmoidal shape of the activation function in the quantum regime (when the spectrum of allowed energy values is discrete). Moreover, the sigmoidal transformation of the applied magnetic flux into the average output current can be obtained

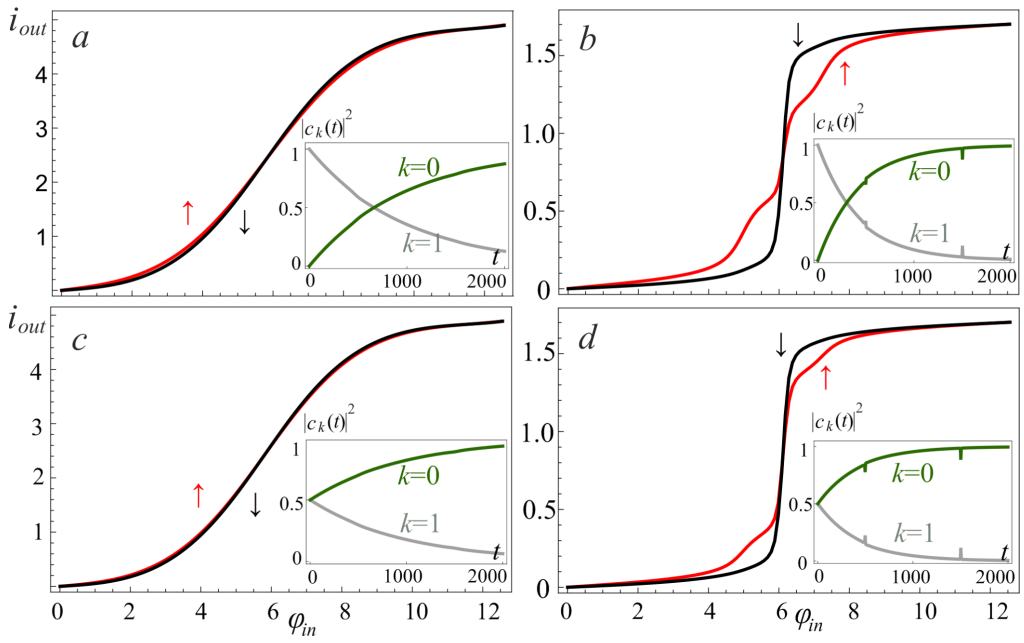

Figure 10: The neuron activation function for l = 0.1 (a, c) and l = 2.5 (b, d) when the cell is initialized in the first excited level (a, b) and in the superposition of two basic states (c, d). The input flux parameters are as follows: D = 0.008, A = 4π, t_1 = 500; the renormalized coupling constant λ = 0.005. The insets present the corresponding populations $|c_k(t)|^2$ of the ground state, k = 0, and the first excited, k = 1, energy levels.

both for single-well and double-well potential energies of the cell. The influence of the initial quantum state of the neuron on the shape of the activation function is especially noticeable for the case of a superposition of basic states. We have also shown how dissipation suppresses "quantum" oscillations on the activation function, just as damping suppresses plasma oscillations in classical Josephson systems. The obtained results pave the way for a classical perceptron and a control quantum co-processor (designed for the rapid search of the perceptron synaptic weights) to work in a single chip in a millikelvin cryogenic stage of a cryocooler. For the practical implementation of such neural networks, we need synapses, which are also based on adiabatic superconducting logic cells with magnetic representation of information [43,45,51]. Fortunately, there are already such elements based on an inductively shunted two-contact interferometer with the ability to adjust parameters. However, their behavior in the quantum mode requires an additional study.

Funding

The S_Q neuron concept was developed with the support of the Russian Science Foundation (project no. 20-12-00130). The numerical simulations were supported by UNN within the framework of the strategic academic leadership program "Priority 2030" of the Ministry of Science and Higher Education of the Russian Federation. The work of AAG and AMS on the section "Dynamics in a quantum neuron without dissipation" was carried out with the support of the RSF project no. 22-21-00586.

Appendix 1

To solve Equation 6, we used the finite difference method [52], where a continuous wave function $\psi(\varphi)$ is transferred to a discrete grid $\phi_n = \phi(\varphi_n)$ with a step $\Delta\varphi$:

$$-\left(\psi_{n+1}+\psi_{n-1}\right)+\left(2+\nu_n\right)\psi_n=\varepsilon_n\psi_n. \tag{22}$$

Here we introduce the following notations:

$$\nu_n = 2M\Delta\varphi^2 V_n/\hbar^2$$

and

$$\varepsilon_n = 2M\Delta\varphi^2 E/\hbar^2 .$$

The boundaries $\psi_0 = \psi_{N+1} = 0$ for Equation 22 are sufficiently removed from the region of actual motion of interest, and the wave functions of localized states are weakly affected by the introduced restrictions.

Appendix 2

We have analyzed the evolution process on the basis of the Cayley algorithm [53]. The evolution operator of the system on a discrete time grid with a step Δt is represented as:

$$\hat{U}\left(\Delta t\right)=e^{-\frac{i\hat{H}\Delta t}{\hbar}}\approx\frac{\hat{I}-i\hat{H}\Delta t/2\hbar}{\hat{I}+i\hat{H}\Delta t/2\hbar}, \tag{23}$$

where $\hat{I}$ is the unit matrix corresponding to the dimensionality of the Hamiltonian of the system (Equation 5), $\hat{H}$, according to

$$t\rightarrow\omega_p\sqrt{\frac{2E_c}{E_J}}t.$$

According to Equation 7, the Schrödinger time-dependent equation, and hence the dynamics of the system, can be found from the following equation:

$$\psi_{n+1}^{j+1}=R_n^{j+1}\psi_n^{j+1}+S_n^{j+1}, \tag{24}$$

where the auxiliary quantities are defined as

$$\begin{aligned}
R_{n-1}^{j+1}&=-\frac{1}{u_n+R_n^{j+1}},\\
S_{n-1}^{j+1}&=-\frac{F_n^{j+1}-S_n^{j+1}}{u_n+R_n^{j+1}}\\
F_n^{j+1}&=-\left(\psi_{n+1}^{j}+\psi_{n-1}^{j}+u_n^{*}\psi_n^{j}\right),\\
u_n&=-2-\frac{2M\Delta\varphi^2V_n}{\hbar^2}+\frac{4iM\Delta\varphi^2}{\hbar\Delta t},
\end{aligned} \tag{25}$$

with boundary conditions

$$\psi_0^{j+1}=\psi_{N+1}^{j+1}=0.$$

Appendix 3

We will use only the Born–Markov approximation and neglect the Lamb shift. Hence, the generalized master equation [50] for the density matrix in terms of the instantaneous eigenbasis in the Schrödinger picture can be written as follows:

$$\begin{aligned}
\dot{\rho}_{mn}=&\,i\frac{E_n(t)-E_m(t)}{\hbar}\rho_{mn}-\sum_{a,b}\rho_{bn}W_{bama}\\
&-\sum_{c,d}\rho_{md}W_{dccn}+\sum_{e,f}\left(\rho_{ef}W_{emfn}+\rho_{fe}W_{enmf}\right),
\end{aligned} \tag{26}$$

where the matrix elements W_{abcd} are defined by

$$W_{abcd} = \frac{\lambda}{2}\langle \psi_a |\hat{\varphi}| \psi_b \rangle \langle \psi_c |\hat{\varphi}| \psi_d \rangle \cdot \left\{ \theta(\omega_{ab}) \left[\overline{n}(\omega_{ab}) + 1 \right] + \theta(\omega_{ba}) \overline{n}(\omega_{ba}) \right\}. \quad (27)$$

It should be noted that for Equation 26 it is necessary that the ground state and the first excited state are not nearly degenerate levels throughout the considered time of system evolution.

The generalized master equation with the secular approximation can be easily obtained from Equation 26 by multiplying the fourth term with the Kronecker delta symbol δ_{mn} and by imposing additional conditions on the indices of summations, that is, $b = m$, $d = n$ and $e = f$. Further, keeping only the diagonal terms of the density matrix, the Pauli master equation can be obtained. For all parameters, we have considered that the secular approximation has a negligibly small effect on the numerical solution of the generalized master equation.

In Figure 11a–d, we present the activation functions obtained by solving the generalized master equation for different values of the inductance l and the renormalized coupling constant λ. Initial conditions are the superposition of states, that is, $[\psi_0(\varphi,0) + \psi_1(\varphi,0)]/\sqrt{2}$. As expected, oscillations arise due to interference between levels, which decrease with increasing the coupling constant.

Note that for small $l < l^*$, and for the neuron initialized either in the ground state or in the excited state, the solution of the generalized master equation is the same as the solution of the Pauli master equation.

ORCID® iDs

Marina V. Bastrakova - https://orcid.org/0000-0002-6597-563X
Andrey E. Schegolev - https://orcid.org/0000-0002-5381-3297
Nikolay V. Klenov - https://orcid.org/0000-0001-6265-3670
Igor I. Soloviev - https://orcid.org/0000-0001-9735-2720
Arkady M. Satanin - https://orcid.org/0000-0001-7613-6535

Preprint

A non-peer-reviewed version of this article has been previously published as a preprint: https://doi.org/10.3762/bxiv.2022.25.v1

References

1. Kak, S. C. *Adv. Imaging Electron Phys.* **1995,** *94,* 259–313. doi:10.1016/s1076-5670(08)70147-2
2. Chrisley, R. L. Quantum learning. *New directions in cognitive science: Proceedings of the international symposium, Saariselka;* 1995; pp 77–89.
3. Kak, S. *Inf. Sci. (N. Y.)* **1995,** *83,* 143–160. doi:10.1016/0020-0255(94)00095-s

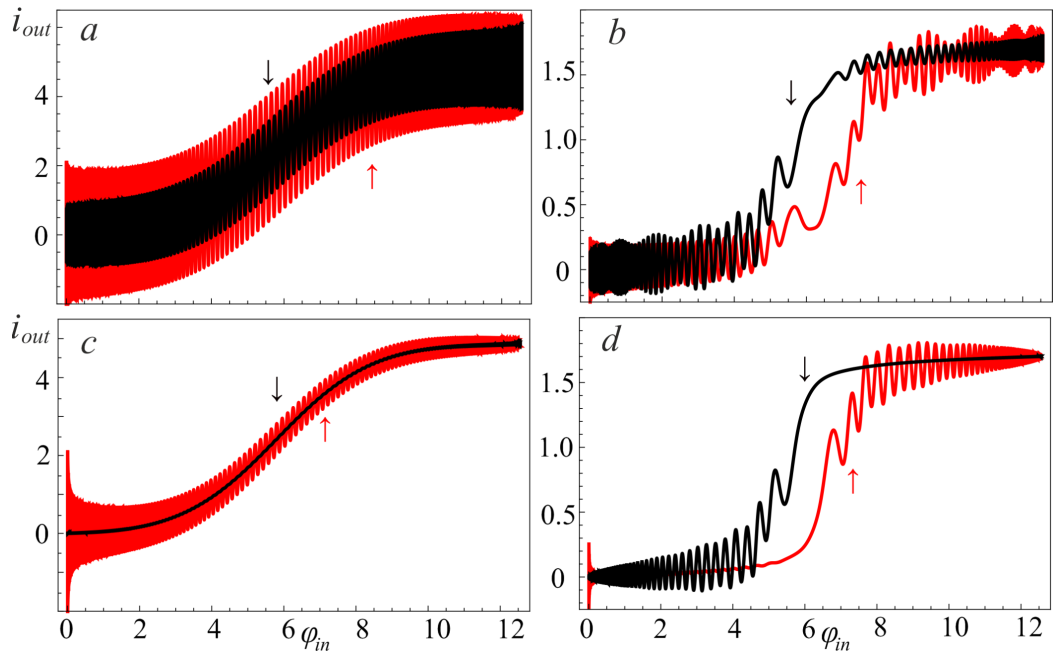

Figure 11: The neuron activation functions for l = 0.1 (a, c) and l = 2.5 (b, d) for different renormalized coupling constants: λ = 0.005 (a, b) and λ = 0.035 (c, d). The input flux parameters are as follows: D = 0.008, A = 4π, t_1 = 500; the temperature of the bosonic thermostat is T = 50 mK; the cell is initialized in the superposition of the two basic states.

4. da Silva, A. J.; Ludermir, T. B.; de Oliveira, W. R. *Neural Networks* **2016,** *76,* 55–64. doi:10.1016/j.neunet.2016.01.002
5. Altaisky, M. V.; Zolnikova, N. N.; Kaputkina, N. E.; Krylov, V. A.; Lozovik, Yu. E.; Dattani, N. S. *Photonics Nanostruct. - Fundam. Appl.* **2017,** *24,* 24–28. doi:10.1016/j.photonics.2017.02.001
6. Cao, Y.; Guerreschi, G. G.; Aspuru-Guzik, A. *arXiv* **2017,** No. 1711.11240. doi:10.48550/arxiv.1711.11240
7. Palmieri, A. M.; Kovlakov, E.; Bianchi, F.; Yudin, D.; Straupe, S.; Biamonte, J. D.; Kulik, S. *npj Quantum Inf.* **2020,** *6,* 20. doi:10.1038/s41534-020-0248-6
8. Torlai, G.; Mazzola, G.; Carrasquilla, J.; Troyer, M.; Melko, R.; Carleo, G. *Nat. Phys.* **2018,** *14,* 447–450. doi:10.1038/s41567-018-0048-5
9. Neugebauer, M.; Fischer, L.; Jäger, A.; Czischek, S.; Jochim, S.; Weidemüller, M.; Gärttner, M. *Phys. Rev. A* **2020,** *102,* 042604. doi:10.1103/physreva.102.042604
10. Adachi, S. H.; Henderson, M. P. *arXiv* **2015,** No. 1510.06356.
11. Benedetti, M.; Realpe-Gómez, J.; Biswas, R.; Perdomo-Ortiz, A. *Phys. Rev. A* **2016,** *94,* 022308. doi:10.1103/physreva.94.022308
12. Albash, T.; Lidar, D. A. *Phys. Rev. X* **2018,** *8,* 031016. doi:10.1103/physrevx.8.031016
13. Ciliberto, C.; Herbster, M.; Ialongo, A. D.; Pontil, M.; Rocchetto, A.; Severini, S.; Wossnig, L. *Proc. R. Soc. A* **2018,** *474,* 20170551. doi:10.1098/rspa.2017.0551
14. Macedo, D. F.; Guedes, D.; Vieira, L. F. M.; Vieira, M. A. M.; Nogueira, M. *IEEE Commun. Surv. Tutorials* **2015,** *17,* 1102–1125. doi:10.1109/comst.2015.2402617
15. Adjemov, S. S.; Klenov, N. V.; Tereshonok, M. V.; Chirov, D. S. *Moscow Univ. Phys. Bull. (Engl. Transl.)* **2015,** *70,* 448–456. doi:10.3103/s0027134915060028
16. Harris, R.; Johnson, M. W.; Lanting, T.; Berkley, A. J.; Johansson, J.; Bunyk, P.; Tolkacheva, E.; Ladizinsky, E.; Ladizinsky, N.; Oh, T.; Cioata, F.; Perminov, I.; Spear, P.; Enderud, C.; Rich, C.; Uchaikin, S.; Thom, M. C.; Chapple, E. M.; Wang, J.; Wilson, B.; Amin, M. H. S.; Dickson, N.; Karimi, K.; Macready, B.; Truncik, C. J. S.; Rose, G. *Phys. Rev. B* **2010,** *82,* 024511. doi:10.1103/physrevb.82.024511
17. Johnson, M. W.; Amin, M. H. S.; Gildert, S.; Lanting, T.; Hamze, F.; Dickson, N.; Harris, R.; Berkley, A. J.; Johansson, J.; Bunyk, P.; Chapple, E. M.; Enderud, C.; Hilton, J. P.; Karimi, K.; Ladizinsky, E.; Ladizinsky, N.; Oh, T.; Perminov, I.; Rich, C.; Thom, M. C.; Tolkacheva, E.; Truncik, C. J. S.; Uchaikin, S.; Wang, J.; Wilson, B.; Rose, G. *Nature* **2011,** *473,* 194–198. doi:10.1038/nature10012
18. Boixo, S.; Rønnow, T. F.; Isakov, S. V.; Wang, Z.; Wecker, D.; Lidar, D. A.; Martinis, J. M.; Troyer, M. *Nat. Phys.* **2014,** *10,* 218–224. doi:10.1038/nphys2900
19. Neill, C.; Roushan, P.; Kechedzhi, K.; Boixo, S.; Isakov, S. V.; Smelyanskiy, V.; Megrant, A.; Chiaro, B.; Dunsworth, A.; Arya, K.; Barends, R.; Burkett, B.; Chen, Y.; Chen, Z.; Fowler, A.; Foxen, B.; Giustina, M.; Graff, R.; Jeffrey, E.; Huang, T.; Kelly, J.; Klimov, P.; Lucero, E.; Mutus, J.; Neeley, M.; Quintana, C.; Sank, D.; Vainsencher, A.; Wenner, J.; White, T. C.; Neven, H.; Martinis, J. M. *Science* **2018,** *360,* 195–199. doi:10.1126/science.aao4309
20. Date, P.; Patton, R.; Schuman, C.; Potok, T. *Quantum Inf. Process.* **2019,** *18,* 117. doi:10.1007/s11128-019-2236-3
21. Kjaergaard, M.; Schwartz, M. E.; Braumüller, J.; Krantz, P.; Wang, J. I.-J.; Gustavsson, S.; Oliver, W. D. *Annu. Rev. Condens. Matter Phys.* **2020,** *11,* 369–395. doi:10.1146/annurev-conmatphys-031119-050605
22. Bastrakova, M.; Klenov, N.; Ruzhickiy, V.; Soloviev, I.; Satanin, A. *Supercond. Sci. Technol.* **2022,** *35,* 055003. doi:10.1088/1361-6668/ac5505
23. Chiarello, F.; Carelli, P.; Castellano, M. G.; Torrioli, G. *Supercond. Sci. Technol.* **2013,** *26,* 125009. doi:10.1088/0953-2048/26/12/125009
24. Schneider, M. L.; Donnelly, C. A.; Russek, S. E.; Baek, B.; Pufall, M. R.; Hopkins, P. F.; Dresselhaus, P. D.; Benz, S. P.; Rippard, W. H. *Sci. Adv.* **2018,** *4,* e1701329. doi:10.1126/sciadv.1701329
25. Schneider, M. L.; Donnelly, C. A.; Russek, S. E. *J. Appl. Phys.* **2018,** *124,* 161102. doi:10.1063/1.5042425
26. Schneider, M. L.; Donnelly, C. A.; Haygood, I. W.; Wynn, A.; Russek, S. E.; Castellanos-Beltran, M. A.; Dresselhaus, P. D.; Hopkins, P. F.; Pufall, M. R.; Rippard, W. H. *Sci. Rep.* **2020,** *10,* 934. doi:10.1038/s41598-020-57892-0
27. Jué, E.; Iankevich, G.; Reisinger, T.; Hahn, H.; Provenzano, V.; Pufall, M. R.; Haygood, I. W.; Rippard, W. H.; Schneider, M. L. *J. Appl. Phys.* **2022,** *131,* 073902. doi:10.1063/5.0080841
28. Segall, K.; LeGro, M.; Kaplan, S.; Svitelskiy, O.; Khadka, S.; Crotty, P.; Schult, D. *Phys. Rev. E* **2017,** *95,* 032220. doi:10.1103/physreve.95.032220
29. Toomey, E.; Segall, K.; Berggren, K. K. *Front. Neurosci.* **2019,** *13,* 933. doi:10.3389/fnins.2019.00933
30. Toomey, E.; Segall, K.; Castellani, M.; Colangelo, M.; Lynch, N.; Berggren, K. K. *Nano Lett.* **2020,** *20,* 8059–8066. doi:10.1021/acs.nanolett.0c03057
31. Mishra, A.; Ghosh, S.; Kumar Dana, S.; Kapitaniak, T.; Hens, C. *Chaos* **2021,** *31,* 052101. doi:10.1063/5.0050526
32. Shainline, J. M.; Buckley, S. M.; McCaughan, A. N.; Chiles, J.; Jafari-Salim, A.; Mirin, R. P.; Nam, S. W. *J. Appl. Phys.* **2018,** *124,* 152130. doi:10.1063/1.5038031
33. Shainline, J. M.; Buckley, S. M.; McCaughan, A. N.; Chiles, J. T.; Jafari Salim, A.; Castellanos-Beltran, M.; Donnelly, C. A.; Schneider, M. L.; Mirin, R. P.; Nam, S. W. *J. Appl. Phys.* **2019,** *126,* 044902. doi:10.1063/1.5096403
34. Cheng, R.; Goteti, U. S.; Hamilton, M. C. *IEEE Trans. Appl. Supercond.* **2019,** *29,* 1–5. doi:10.1109/tasc.2019.2892111
35. Ishida, K.; Byun, I.; Nagaoka, I.; Fukumitsu, K.; Tanaka, M.; Kawakami, S.; Tanimoto, T.; Ono, T.; Kim, J.; Inoue, K. *IEEE Micro* **2021,** *41,* 19–26. doi:10.1109/mm.2021.3070488
36. Feldhoff, F.; Toepfer, H. *IEEE Trans. Appl. Supercond.* **2021,** *31,* 1–5. doi:10.1109/tasc.2021.3063212
37. Klenov, N.; Khaydukov, Y.; Bakurskiy, S.; Morari, R.; Soloviev, I.; Boian, V.; Keller, T.; Kupriyanov, M.; Sidorenko, A.; Keimer, B. *Beilstein J. Nanotechnol.* **2019,** *10,* 833–839. doi:10.3762/bjnano.10.83
38. Dattani, N.; Szalay, S.; Chancellor, N. *arXiv* **2019,** No. 1901.07636. doi:10.48550/arxiv.1901.07636
39. Vyskocil, T.; Djidjev, H. *Algorithms* **2019,** *12,* 77. doi:10.3390/a12040077
40. Boothby, K.; Bunyk, P.; Raymond, J.; Roy, A. *arXiv* **2020,** No. 2003.00133. doi:10.48550/arxiv.2003.00133
41. Boothby, K.; King, A. D.; Raymond, J. *Zephyr Topology of D-Wave Quantum Processors; D-Wave Technical Report Series*; 2021.
42. Schegolev, A. E.; Klenov, N. V.; Soloviev, I. I.; Tereshonok, M. V. *Beilstein J. Nanotechnol.* **2016,** *7,* 1397–1403. doi:10.3762/bjnano.7.130

43. Soloviev, I. I.; Schegolev, A. E.; Klenov, N. V.; Bakurskiy, S. V.; Kupriyanov, M. Y.; Tereshonok, M. V.; Shadrin, A. V.; Stolyarov, V. S.; Golubov, A. A. *J. Appl. Phys.* **2018,** *124,* 152113. doi:10.1063/1.5042147
44. Gorchavkina, A. A.; Bastrakova, M. V.; Klenov, N. V.; Satanin, A. M. *J. Phys.: Conf. Ser.* **2021,** *1740,* 012063. doi:10.1088/1742-6596/1740/1/012063
45. Schegolev, A.; Klenov, N.; Soloviev, I.; Tereshonok, M. *Supercond. Sci. Technol.* **2021,** *34,* 015006. doi:10.1088/1361-6668/abc569
46. Bastrakova, M.; Gorchavkina, A.; Schegolev, A.; Klenov, N.; Soloviev, I.; Satanin, A.; Tereshonok, M. *Symmetry* **2021,** *13,* 1735. doi:10.3390/sym13091735
47. Orlando, T. P.; Mooij, J. E.; Tian, L.; van der Wal, C. H.; Levitov, L. S.; Lloyd, S.; Mazo, J. J. *Phys. Rev. B* **1999,** *60,* 15398–15413. doi:10.1103/physrevb.60.15398
48. Schleich, W. P. *Quantum Optics in Phase Space;* Wiley-VCH: Weinheim, Germany, 2011.
49. Kautz, R. L. *Rep. Prog. Phys.* **1996,** *59,* 935–992. doi:10.1088/0034-4885/59/8/001
50. Albash, T.; Boixo, S.; Lidar, D. A.; Zanardi, P. *New J. Phys.* **2012,** *14,* 123016. doi:10.1088/1367-2630/14/12/123016
51. Soloviev, I. I.; Klenov, N. V.; Bakurskiy, S. V.; Bol'ginov, V. V.; Ryazanov, V. V.; Kupriyanov, M. Y.; Golubov, A. A. *Appl. Phys. Lett.* **2014,** *105,* 242601. doi:10.1063/1.4904012
52. Press, W. H.; Teukolsky, S. A.; Vetterling, W. T.; Flannery, B. P. *Numerical Recipes. The Art of Scientific Computing;* Cambridge University Press: Cambridge, UK, 2007.
53. Goldberg, A.; Schey, H. M.; Schwartz, J. L. *Am. J. Phys.* **1967,** *35,* 177–186. doi:10.1119/1.1973991

License and Terms

BEILSTEIN JOURNAL OF NANOTECHNOLOGY

Experimental and theoretical study of field-dependent spin splitting at ferromagnetic insulator–superconductor interfaces

Peter Machon[1], Michael J. Wolf[2,3], Detlef Beckmann[*4] and Wolfgang Belzig[*1]

Full Research Paper

Open Access

Address:
[1]Department of Physics, University of Konstanz, D-78457 Konstanz, Germany, [2]Institute of Nanotechnology, Karlsruhe Institute of Technology (KIT), D-76021 Karlsruhe, Germany, [3]present address: Institute for Technical Physics, Karlsruhe Institute of Technology (KIT), D-76021 Karlsruhe, Germany and [4]Institute for Quantum Materials and Technologies, Karlsruhe Institute of Technology (KIT), D-76021 Karlsruhe, Germany

Email:
Detlef Beckmann[*] - Detlef.Beckmann@kit.edu; Wolfgang Belzig[*] - Wolfgang.Belzig@uni-konstanz.de

* Corresponding author

Keywords:
circuit theory; magnetism; proximity effect; superconductivity; tunneling

Beilstein J. Nanotechnol. **2022,** *13,* 682–688.
https://doi.org/10.3762/bjnano.13.60

Received: 10 March 2022
Accepted: 08 June 2022
Published: 20 July 2022

This article is part of the thematic issue "Intrinsic Josephson effect and prospects of superconducting spintronics".

Guest Editor: A. S. Sidorenko

Abstract

We present a combined experimental and theoretical work that investigates the magnetic proximity effect at a ferromagnetic insulator–superconductor (FI–S) interface. The calculations are based on the boundary condition for diffusive quasiclassical Green's functions, which accounts for arbitrarily strong spin-dependent effects and spin mixing angles. The resulting phase diagram shows a transition from a first-order to a second-order phase transition for large spin mixing angles. The experimentally found differential conductance of an EuS-Al heterostructure is compared with the theoretical calculation. With the assumption of a uniform spin mixing angle that depends on the externally applied field, we find good agreement between theory and experiment. The theory depends only on very few parameters, mostly specified by the experimental setup. We determine the effective spin of the interface moments as $J \approx 0.74\hbar$.

Introduction

The proximity effect between superconductors and ferromagnets has been investigated intensively in recent years [1,2], giving rise to the field of superconducting spintronics [3,4]. Among the emergent phenomena are π-junctions [5,6], reentrant and multiperiodic reentrant superconductivity [7,8], the triplet proximity effect [9-11], and implementations of superconducting switches and spin valves based on either the singlet or triplet proximity effect [12-18]. Furthermore, the spin-dependent density of states due to the proximity of a magnetic insulator is central for obtaining unprecedentedly high thermoelectric performance at low temperatures [19-23].

Ferromagnetic insulators such as EuO and EuS are interesting materials since they show ferromagnetism (they are almost ideal

Heisenberg ferromagnets) but are electrically insulating at the same time [24-26]. Magnetic insulators have been used successfully, for example, in magnetic Josephson junctions [27], superconducting spin switches [13], and for studying the triplet proximity effect [28]. Ferromagnetic insulators are a good probe of the spin-dependent proximity effect in bilayer structures due to the reduced number of free parameters. This kind of junctions also provides information on the details of the internal magnetization behavior of ferromagnetic insulators in an external field. To be specific, in a simple stacked structure one observes the proximity effect that solely depends on the internal spin-degrees of freedom (spin mixing angles [29]), since the conductance is zero, in contrast to a metallic ferromagnet. The absence of conductance-related parameters (transmission and polarization of each channel) strongly simplifies the boundary condition to a ferromagnetic insulator [30,31], which has been extended meanwhile to insulating antiferromagnets [32]. Thus, one has the opportunity to quantitatively study the microscopic mechanisms that influence the superconducting density of states, in a way that they mainly shift and spin-split the peaks at the superconducting gap edge. Such shifts and following possibility to create of Shiba bands [33,34] have been investigated theoretically also recently in related systems [35,36].

Spin-active scattering in FI–S bilayers has been discussed, for example , in [29] in the clean and in [37] in the dirty limit. Here, we treat the dirty limit appropriate for typical thin film structures. In [37], spin mixing in these systems was described in terms of an expansion for small phase shifts, where the linear order is equivalent to a Zeeman-type spin splitting, and the second order is equivalent to pair breaking by spin-dependent scattering. In contrast, we treat spin mixing of arbitrary strength exactly. The distribution of spin mixing angles ($\delta\varphi_n$, n is the channel index) along the transport channels is the only unknown in the theory. This distribution can be probed directly in a fully electronic experiment, measuring the density of states of the superconducting film by tunnel spectroscopy.

Results and Discussion

Theory

The setup of the underlying experiment is shown in Figure 1a. It consists (bottom-up) of an EuS substrate, a superconducting (Al) film, and a normal metal film that is separated from the superconductor by an oxide layer. The normal layer acts as the tunnel probe to measure the differential conductance of the superconductor and is assumed not to influence the system properties. Since the size of the detector electrode is not small (unlike the tip of a scanning tunneling microscope) and the FI affects the whole superconductor, we assume that the magnetization can be modeled by one magnetization direction that results from averaging over the internal magnetic structure. In the language of the circuit theory [38] this means that we can reproduce the whole system with a single node as depicted in Figure 1b. The superconductor is represented by the node that has a "source" (of coherence) term (marked with Δ) and "leakage" (of coherence) term that is characterized by the Thouless energy of the superconductor ($\varepsilon_{\mathrm{Th}}$) and its normal-state conductance G. Additional pseudo terminals model the spin mixing angles δφ induced by the FI (top), the external field H (right).

To describe the FI–S bilayer as illustrated in Figure 1b within the circuit theory [38], we use the formalism for the boundary conditions for spin-dependent connectors developed in [30],

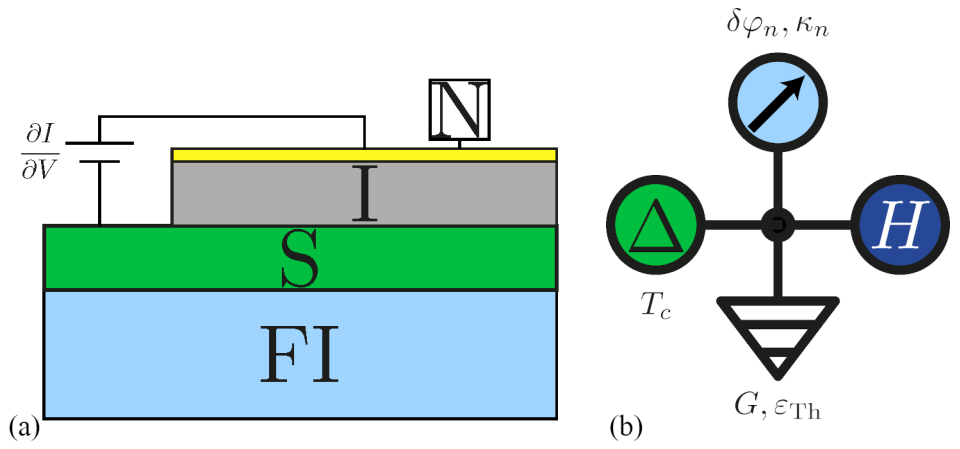

Figure 1: (a) The experimental setup of the FI–S bilayer. The differential conductance is measured with help of the top normal contact (N), which is separated by an insulating barrier (I). (b) Circuit diagram to represent the FI–S bilayer in the quantum circuit theory. The superconductor is represented by the node, the Δ-source term, the $\varepsilon_{\mathrm{Th}}$-leakage term, and its normal-state conductance G. The ferromagnetic insulator adds the $\delta\varphi_n$-term with magnetization directions κ_n for each channel, and in accordance with the experiment an external exchange field is added, here represented by the H-pseudo terminal.

which agrees with the results of [31]. This boundary condition (BC) for the Usadel equation was derived, and it was shown how this BC can be applied to a ferromagnetic insulator–superconductor bilayer system in the limit that the thickness d of the superconducting film is small compared to the coherence length. We define the spin-dependent Green's function of the superconductor as $\hat{G}_\sigma = g_{1,\sigma}\hat{\tau}_1 + g_{3,\sigma}\hat{\tau}_3$. Here, $\sigma = \pm$ denotes the spin index, and $\hat{\tau}_i$ are Pauli matrices in Nambu space. We obtain the following equation that determines the Green's function of the superconductor:

$$\sum_{n=1}^{N} \frac{2i\sigma \sin\left(\delta\varphi_n/2\right) g_{1,\sigma}}{\cos\left(\delta\varphi_n/2\right) - i\sigma g_{3,\sigma} \sin\left(\delta\varphi_n/2\right)} + \frac{G}{G_\mathrm{q}} \frac{i\left(\varepsilon_\sigma + i\delta\right) g_{1,\sigma} + \Delta g_{3,\sigma}}{\varepsilon_\mathrm{Th}} = 0. \tag{1}$$

Here, $\varepsilon_\sigma = \varepsilon + \sigma\mu_\mathrm{B}H$ is the energy including the applied Zeeman field, $\varepsilon_\mathrm{Th} = \hbar D/d^2$ is the Thouless energy, $G_\mathrm{q} = e^2/h$ is the conductance quantum, and $G = \sigma_\mathrm{N}A/d$ is the conductance of the film (in the direction perpendicular to the interface of cross section A). D and σ_N are the diffusion constant and the normal-state conductivity of the film, respectively. Note, that due to the normalization condition for quasiclassical Green's functions one has $g_{1,\sigma} = \sqrt{1 - g_{3,\sigma}^2}$. Due to the small coercivity of EuS the assumption of only one magnetization direction as in [30] is reasonable. This is why the Green's functions decouple in spin space.

In the following, we will only use a single spin mixing angle $\delta\varphi_n = \delta\varphi$ for simplicity to illustrate the results. However, the theory is not restricted to this case. Thus, we replace the sum over the channel index n in the matrix current conservation with the number of channels, that is, $\sum_n \to N$. However, in a phenomenological way we assume that, effectively, only a certain fraction $r \in [0,1]$ of scattering channels contributes to the spin mixing effect. Alternatively, we may say that spin mixing only occurs with a certain probability r. The corresponding equation then reads

$$rN\frac{G_\mathrm{q}}{G}\varepsilon_\mathrm{Th} \frac{2i\sigma \sin\left(\delta\varphi/2\right) g_{1,\sigma}}{\cos\left(\delta\varphi/2\right) - i\sigma g_{3,\sigma} \sin\left(\delta\varphi/2\right)} + \left[i\left(\varepsilon_\sigma + i\delta\right) g_{1,\sigma} + \Delta g_{3,\sigma} \right] = 0. \tag{2}$$

Hence, the strength of the magnetic proximity effect can be expressed by the dimensionless parameter $\varepsilon' = rN(G_\mathrm{q}/G)(\varepsilon_\mathrm{Th}/k_\mathrm{B}T_\mathrm{c})$, where k_B is the Boltzmann constant, and T_c is the critical temperature of the bulk superconductor. Using the conductivity $\sigma_\mathrm{N} = e^2\mathcal{N}_0 D$, the density of states at the Fermi energy $\mathcal{N}_0 = k_\mathrm{F}^2/\pi^2\hbar v_\mathrm{F}$ of the free electron gas, and $N/A = k_\mathrm{F}^2/4\pi$ for the number of channels per area, we can simplify this to $\varepsilon' = rN/2\pi A d\mathcal{N}_0 k_\mathrm{B}T_\mathrm{c} = r\hbar v_\mathrm{F}/8dk_\mathrm{B}T_\mathrm{c}$, where v_F is the Fermi velocity. With the definition $\xi_0 = \hbar v_\mathrm{F}/\pi\Delta(T=0)$ of the superconducting coherence length and the approximation $\Delta(T=0) \approx 1.76\, k_\mathrm{B}T_\mathrm{c}$, one finds $\varepsilon' \approx 0.69 r\xi_0/d$. The parameter ε' becomes smaller for increasing film thickness and decreasing fraction of spin-active channels.

With the above definitions, the BCS self-consistency relation is given by:

$$\Delta = \frac{\lambda}{4\pi} \int_0^{\Omega_\mathrm{BCS}} \mathrm{d}\varepsilon \tanh\left(\frac{\varepsilon}{2T}\right) \mathcal{J}\left[g_{1,+} + g_{1,-} \right]. \tag{3}$$

We defined the cutoff energy Ω_BCS related to the upper limit of the phonon spectrum. In the following, we use $\Omega_\mathrm{BCS} = 100k_\mathrm{B}T_\mathrm{c}$, and the coupling constant λ, which can be eliminated for the bulk superconductor in favor of the critical temperature T_c. After solving the fully self-consistent problem in order to obtain Δ, the differential tunnel conductance (measured as shown in Figure 1a) is found from the standard definition $\frac{\mathrm{d}I}{\mathrm{d}V} = -G_\mathrm{N}\int \mathcal{N}(\varepsilon)\frac{\mathrm{d}f}{\mathrm{d}eV}\mathrm{d}\varepsilon$, with the Fermi distribution f and the normal-state conductance G_N of the tunnel probe. The density of states is given by $\mathcal{N}(\varepsilon) = \mathcal{R}\left(g_{3,+} + g_{3,-}\right)/2$. Note, that the actual total density of states per volume is given as $\mathcal{N}(\varepsilon)\mathcal{N}_0$.

We now discuss the self-consistency relation for different values of the parameter ε'. Figure 2 shows the phase diagram for values $\varepsilon' = [100\text{–}0.1]$, which for a $d = 10$ nm aluminium layer roughly translates into fractions $r = [1\text{–}0.001]$. The plotted curves are the phase boundaries between superconducting and normal state, with the superconducting phase at low temperature and small $\delta\varphi$. In general, the critical value $\delta\varphi_c$ increases with decreasing ε'. For small ε', spin mixing can no longer completely suppress superconductivity for $T = 0$ (note that the boundary conditions are periodic in $\delta\varphi$ and hence the maximum spin mixing is reached at $\delta\varphi = \pi$). For small ε' or high temperature, the phase transition is of second order. For larger ε' and low temperature, the phase transition becomes of first order. In this case, the self-consistency relation becomes multi-valued, and a coexistence region appears. The solid and dashed lines represent the lower and upper boundary of the coexistence region, respectively. The coexistence region becomes larger for larger ε' and correspondingly smaller $\delta\varphi_c$. In this regime, the effect of spin mixing is similar to a Zeeman splitting [39,40].

Now, we discuss the dependence of the density of states on the spin mixing angle $\delta\varphi$ for different values of the parameter ε'. For the sake of clarity, the Zeeman splitting from the external field is ignored at this point. The changes in the density of states

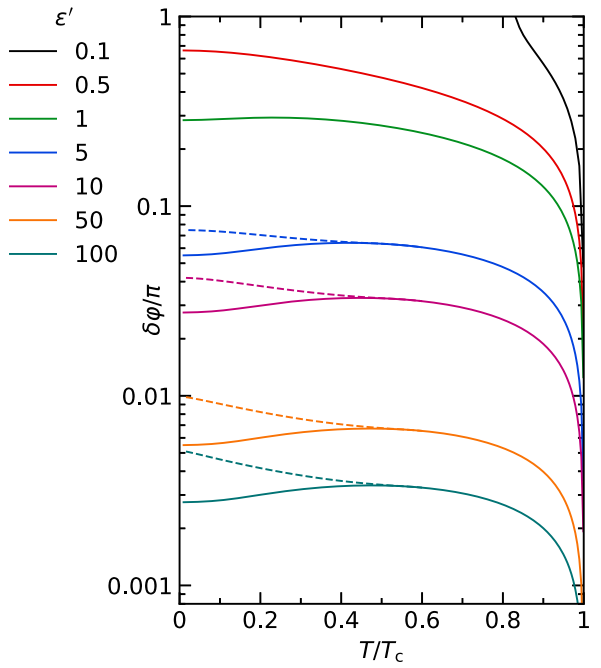

Figure 2: Phase diagram of the spin mixing angle δφ/π as a function of the normalized temperature T/T_c for values of ε' = [100,0.1].

of the superconductor are dominated by two effects. On one hand, the initial peaks at the $T = 0$ superconductor gap Δ_0 are spin-split into two separated peaks, each positioned depending on δφ and Δ. On the other hand, Δ self-consistently also depends on the spin mixing angle.

In Figure 3, we plot the density of states for $T \ll T_c$ with self-consistent Δ. For very thin layers (ε' = 100) the peaks (initially at Δ) symmetrically split into their spin components. This behavior is also is similar to the Zeeman splitting in an applied field, as already measured, for example, in [41]. However, with decreasing ε', the superconductivity persists for larger spin mixing angles and the behavior changes qualitatively until a completely different situation is found at ε' = 0.1. Here, the outer peak position is nearly independent of δφ while only the inner peak moves towards (and across) the Fermi level. Another effect of larger spin mixing angles is that the inner peak is broadened, and finally becomes a wide and flat band. Besides this, the self-consistency relation for thin films produces the typical step-like first-order phase transition at the critical δφ (here always plotted for the upper branch of Figure 2), while especially in the case ε' = 1 a significant shift of the peak positions is visible for larger spin mixing angles. For sufficiently small ε', spin mixing has little effect on Δ.

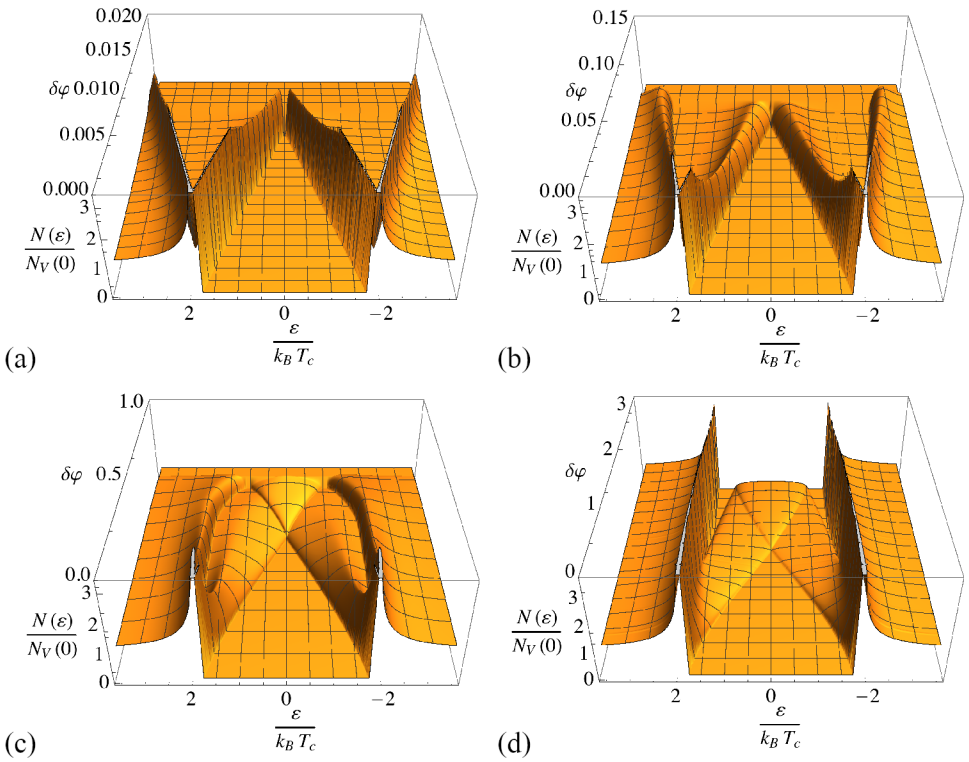

Figure 3: Density of states in a superconductor in proximity to a ferromagnetic insulator indicated by the spin mixing angle δφ, with (from (a) to (d)) ε' = 100,10,1,0.1, while the superconducting order parameter is evaluated self-consistently ($T \ll T_c$).

Comparison of experiment and theory

To illustrate our model, we use it to fit experimental data obtained on a sample made of a superconducting aluminium film on top of the ferromagnetic insulator europium sulfide. Figure 4 shows a false-color scanning electron microscopy image of the sample, together with the experimental scheme. The sample was fabricated in a two-step procedure: First, a EuS film of 44 nm thickness was created by e-beam evaporation of EuS onto a Si(111) substrate heated to 800 °C. In a second fabrication step, aluminium/aluminium oxide/copper tunnel junctions were fabricated on the EuS film using e-beam lithography and shadow evaporation. The nominal aluminium film thickness was d = 10 nm. The differential conductance $g = \mathrm{d}I/\mathrm{d}V$ of the tunnel junctions was measured as a function of the bias voltage V using standard low-frequency lock-in techniques in a dilution refrigerator at base temperatures down to T = 50 mK with an in-plane magnetic field B applied along the direction of the copper wires, as indicated in Figure 4. Details of film fabrication, magnetic properties, and experimental procedures can be found in [42,43].

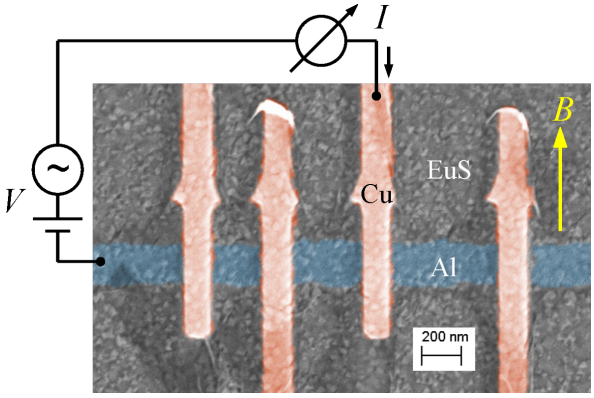

Figure 4: False-color scanning electron microscopy image of the sample and experimental scheme.

Examples of the conductance spectra measured for different applied fields in one of the junctions are shown in Figure 5a. At small fields, the spectra exhibit a well-defined gap with negligible subgap conductance, indicating a defect-free tunnel barrier. Spin splitting of the density of states is clearly visible. The observed splitting greatly exceeds the expected splitting due to the Zeeman energy $\varepsilon_Z = \mu_B B$ (which is about 35 μeV at B = 0.6 T). The solid lines in Figure 5a are fits with our model. We have included orbital depairing in the fits, with an orbital depairing parameter [44]

$$\alpha_{\mathrm{orb}} = \frac{1}{2}\left(\frac{B}{B_{\mathrm{c,orb}}}\right)^2 \tag{4}$$

for a thin film in an in-plane field. From known sample parameters we estimate $B_{\mathrm{c,orb}} \approx 2$ T and $\varepsilon' \approx 70$, which leaves us with Δ and δφ as free parameters. The fits give a good account of the observed spin splitting. The spin mixing angle extracted from the fits is plotted in Figure 5b. It is found to depend on the applied magnetic field over the entire field range. In contrast,

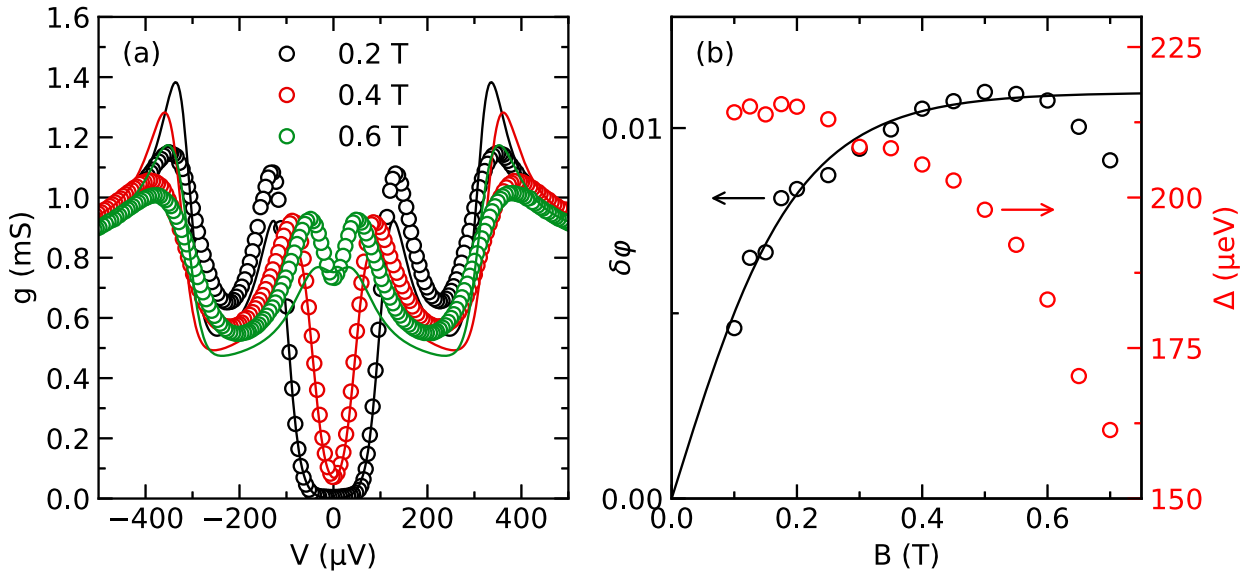

Figure 5: (a) Differential conductance g as a function of the bias V for different applied magnetic fields B (symbols), and fits with our model (lines). (b) Spin mixing angle δφ (left axis) and pair potential Δ (right axis) as functions of the applied field B extracted from the fits (symbols), and fit of the spin mixing angle with a Brillouin function (line).

the EuS magnetization is saturated above a few milliteslas in our film [42]. A similar dependence of the spin splitting on the applied field is commonly observed in EuS/Al structures [45,46], and the microscopic origin is yet unclear. A possible explanation are misaligned spins at the interface, which are nearly free and therefore gradually aligned by the applied field. The misaligned spins might be the result of partial oxidation of the EuS surface during sample transfer between our two fabrication steps. Lacking a microscopic model, we have attempted to fit the field dependence of δφ with a Brillouin function. The fit is shown as a line in Figure 5b. It is in reasonable agreement with the data up to about 0.6 T, with an effective angular momentum $J \approx 0.74\hbar$. While the Eu^{2+} ions in EuS have $J = 7/2$ [47], the stable oxide of Eu is Eu_2O_3 with Eu^{3+} ions and $J = 0$ [48]. Therefore, a reduced effective J at the interface appears reasonable. Above 0.6 T, the data deviate downwards from the fit, and these data points were excluded from the fit. The deviation can be explained by Fermi-liquid renormalization of the effective spin splitting near the critical field [46,49], which is not included in our model.

Conclusion

Based on the general spin-dependent boundary condition [30,31] augmenting the spin-dependent circuit theory [38,50], we investigated FI–S heterostructures in the dirty limit. We discussed the dependence of the density of states (and thus also the differential conductance) on the spin mixing angles for different layer thicknesses observing strong deviations from the typically linear behavior in exchange fields. The model yields a new phase diagram that strongly depends on the spin mixing angle and includes a crossover from a first- to a second-order phase transition.

We applied our theory to our experiment measuring the differential conductance in an EuS–Al bilayer. In the experiment, enhanced spin splitting of the density of states in an external magnetic field was observed. To reproduce the experimental data, we have determined the spin mixing angle as a function of the applied magnetic field, and given an estimate on how to take into account the relation between the external field and the spin mixing angle.

We are thus confident that our theory will in the future provide further motivation for the interesting physics of ferromagnetic insulators and the proximity effect in ferromagnet or antiferromagnet–superconductor heterostructures.

ORCID® iDs

Peter Machon - https://orcid.org/0000-0003-1723-018X
Detlef Beckmann - https://orcid.org/0000-0002-6212-2762
Wolfgang Belzig - https://orcid.org/0000-0002-5109-2203

References

1. Buzdin, A. I. *Rev. Mod. Phys.* **2005,** *77,* 935–976. doi:10.1103/revmodphys.77.935
2. Bergeret, F. S.; Volkov, A. F.; Efetov, K. B. *Rev. Mod. Phys.* **2005,** *77,* 1321–1373. doi:10.1103/revmodphys.77.1321
3. Linder, J.; Robinson, J. W. A. *Nat. Phys.* **2015,** *11,* 307–315. doi:10.1038/nphys3242
4. Eschrig, M. *Rep. Prog. Phys.* **2015,** *78,* 104501. doi:10.1088/0034-4885/78/10/104501
5. Ryazanov, V. V.; Veretennikov, A. V.; Oboznov, V. A.; Rusanov, A. Y.; Larkin, V. A.; Golubov, A. A.; Aarts, J. *Phys. C (Amsterdam, Neth.)* **2000,** *341–348,* 1613–1614. doi:10.1016/s0921-4534(00)01476-3
6. Ryazanov, V. V.; Oboznov, V. A.; Rusanov, A. Y.; Veretennikov, A. V.; Golubov, A. A.; Aarts, J. *Phys. Rev. Lett.* **2001,** *86,* 2427–2430. doi:10.1103/physrevlett.86.2427
7. Zdravkov, V.; Sidorenko, A.; Obermeier, G.; Gsell, S.; Schreck, M.; Müller, C.; Horn, S.; Tidecks, R.; Tagirov, L. R. *Phys. Rev. Lett.* **2006,** *97,* 057004. doi:10.1103/physrevlett.97.057004
8. Sidorenko, A. S.; Zdravkov, V.; Kehrle, J.; Morari, R.; Obermeier, G.; Gsell, S.; Schreck, M.; Müller, C.; Ryazanov, V.; Horn, S.; Tagirov, L. R.; Tidecks, R. *J. Phys.: Conf. Ser.* **2009,** *150,* 052242. doi:10.1088/1742-6596/150/5/052242
9. Keizer, R. S.; Goennenwein, S. T. B.; Klapwijk, T. M.; Miao, G.; Xiao, G.; Gupta, A. *Nature* **2006,** *439,* 825–827. doi:10.1038/nature04499
10. Khaire, T. S.; Khasawneh, M. A.; Pratt, W. P.; Birge, N. O. *Phys. Rev. Lett.* **2010,** *104,* 137002. doi:10.1103/physrevlett.104.137002
11. Robinson, J. W. A.; Witt, J. D. S.; Blamire, M. G. *Science* **2010,** *329,* 59–61. doi:10.1126/science.1189246
12. Gu, J. Y.; You, C.-Y.; Jiang, J. S.; Pearson, J.; Bazaliy, Ya. B.; Bader, S. D. *Phys. Rev. Lett.* **2002,** *89,* 267001. doi:10.1103/physrevlett.89.267001
13. Li, B.; Roschewsky, N.; Assaf, B. A.; Eich, M.; Epstein-Martin, M.; Heiman, D.; Münzenberg, M.; Moodera, J. S. *Phys. Rev. Lett.* **2013,** *110,* 097001. doi:10.1103/physrevlett.110.097001
14. Zdravkov, V. I.; Kehrle, J.; Obermeier, G.; Lenk, D.; Krug von Nidda, H.-A.; Müller, C.; Kupriyanov, M. Y.; Sidorenko, A. S.; Horn, S.; Tidecks, R.; Tagirov, L. R. *Phys. Rev. B* **2013,** *87,* 144507. doi:10.1103/physrevb.87.144507
15. Iovan, A.; Golod, T.; Krasnov, V. M. *Phys. Rev. B* **2014,** *90,* 134514. doi:10.1103/physrevb.90.134514
16. Lenk, D.; Morari, R.; Zdravkov, V. I.; Ullrich, A.; Khaydukov, Y.; Obermeier, G.; Müller, C.; Sidorenko, A. S.; von Nidda, H.-A. K.; Horn, S.; Tagirov, L. R.; Tidecks, R. *Phys. Rev. B* **2017,** *96,* 184521. doi:10.1103/physrevb.96.184521
17. Sidorenko, A. S. *Low Temp. Phys.* **2017,** *43,* 766–771. doi:10.1063/1.4995623
18. Klenov, N.; Khaydukov, Y.; Bakurskiy, S.; Morari, R.; Soloviev, I.; Boian, V.; Keller, T.; Kupriyanov, M.; Sidorenko, A.; Keimer, B. *Beilstein J. Nanotechnol.* **2019,** *10,* 833–839. doi:10.3762/bjnano.10.83
19. Kalenkov, M. S.; Zaikin, A. D.; Kuzmin, L. S. *Phys. Rev. Lett.* **2012,** *109,* 147004. doi:10.1103/physrevlett.109.147004
20. Machon, P.; Eschrig, M.; Belzig, W. *Phys. Rev. Lett.* **2013,** *110,* 047002. doi:10.1103/physrevlett.110.047002
21. Ozaeta, A.; Virtanen, P.; Bergeret, F. S.; Heikkilä, T. T. *Phys. Rev. Lett.* **2014,** *112,* 057001. doi:10.1103/physrevlett.112.057001
22. Kolenda, S.; Wolf, M. J.; Beckmann, D. *Phys. Rev. Lett.* **2016,** *116,* 097001. doi:10.1103/physrevlett.116.097001

23. Kolenda, S.; Machon, P.; Beckmann, D.; Belzig, W. *Beilstein J. Nanotechnol.* **2016,** *7,* 1579–1585. doi:10.3762/bjnano.7.152
24. Matthias, B. T.; Bozorth, R. M.; Van Vleck, J. H. *Phys. Rev. Lett.* **1961,** *7,* 160–161. doi:10.1103/physrevlett.7.160
25. McGuire, T. R.; Argyle, B. E.; Shafer, M. W.; Smart, J. S. *Appl. Phys. Lett.* **1962,** *1,* 17–18. doi:10.1063/1.1777353
26. Mairoser, T.; Mundy, J. A.; Melville, A.; Hodash, D.; Cueva, P.; Held, R.; Glavic, A.; Schubert, J.; Muller, D. A.; Schlom, D. G.; Schmehl, A. *Nat. Commun.* **2015,** *6,* 7716. doi:10.1038/ncomms8716
27. Pal, A.; Barber, Z. H.; Robinson, J. W. A.; Blamire, M. G. *Nat. Commun.* **2014,** *5,* 3340. doi:10.1038/ncomms4340
28. Diesch, S.; Machon, P.; Wolz, M.; Sürgers, C.; Beckmann, D.; Belzig, W.; Scheer, E. *Nat. Commun.* **2018,** *9,* 5248. doi:10.1038/s41467-018-07597-w
29. Tokuyasu, T.; Sauls, J. A.; Rainer, D. *Phys. Rev. B* **1988,** *38,* 8823–8833. doi:10.1103/physrevb.38.8823
30. Machon, P.; Belzig, W. *arXiv* **2015,** 1502.05567. doi:10.48550/arxiv.1502.05567
31. Eschrig, M.; Cottet, A.; Belzig, W.; Linder, J. *New J. Phys.* **2015,** *17,* 083037. doi:10.1088/1367-2630/17/8/083037
32. Kamra, A.; Rezaei, A.; Belzig, W. *Phys. Rev. Lett.* **2018,** *121,* 247702. doi:10.1103/physrevlett.121.247702
33. Shiba, H. *Prog. Theor. Phys.* **1968,** *40,* 435–451. doi:10.1143/ptp.40.435
34. Zittartz, J.; Bringer, A.; Müller-Hartmann, E. *Solid State Commun.* **1972,** *10,* 513–516. doi:10.1016/0038-1098(72)90056-7
35. Ouassou, J. A.; Pal, A.; Blamire, M.; Eschrig, M.; Linder, J. *Sci. Rep.* **2017,** *7,* 1932. doi:10.1038/s41598-017-01330-1
36. Belzig, W.; Beckmann, D. *J. Magn. Magn. Mater.* **2018,** *459,* 276–279. doi:10.1016/j.jmmm.2017.10.062
37. Cottet, A.; Huertas-Hernando, D.; Belzig, W.; Nazarov, Y. V. *Phys. Rev. B* **2009,** *80,* 184511. doi:10.1103/physrevb.80.184511
38. Nazarov, Y. V. *Superlattices Microstruct.* **1999,** *25,* 1221–1231. doi:10.1006/spmi.1999.0738
39. Sarma, G. *J. Phys. Chem. Solids* **1963,** *24,* 1029–1032. doi:10.1016/0022-3697(63)90007-6
40. Maki, K. Gapless Superconductivity. In *Superconductivity;* Parks, R. D., Ed.; Routledge: New York, NY, USA, 1969; Vol. 2, pp 1035–1105. doi:10.1201/9780203737958-6
41. Tedrow, P. M.; Meservey, R. *Phys. Rev. Lett.* **1971,** *26,* 192–195. doi:10.1103/physrevlett.26.192
42. Wolf, M. J.; Sürgers, C.; Fischer, G.; Scherer, T.; Beckmann, D. *J. Magn. Magn. Mater.* **2014,** *368,* 49–53. doi:10.1016/j.jmmm.2014.04.067
43. Wolf, M. J.; Sürgers, C.; Fischer, G.; Beckmann, D. *Phys. Rev. B* **2014,** *90,* 144509. doi:10.1103/physrevb.90.144509
44. Maki, K. *Prog. Theor. Phys.* **1964,** *31,* 731–741. doi:10.1143/ptp.31.731
45. Hao, X.; Moodera, J. S.; Meservey, R. *Phys. Rev. B* **1990,** *42,* 8235–8243. doi:10.1103/physrevb.42.8235
46. Xiong, Y. M.; Stadler, S.; Adams, P. W.; Catelani, G. *Phys. Rev. Lett.* **2011,** *106,* 247001. doi:10.1103/physrevlett.106.247001
47. Zinn, W. *J. Magn. Magn. Mater.* **1976,** *3,* 23–36. doi:10.1016/0304-8853(76)90007-x
48. Huang, N. L.; Van Vleck, J. H. *J. Appl. Phys.* **1969,** *40,* 1144–1146. doi:10.1063/1.1657569
49. Alexander, J. A. X.; Orlando, T. P.; Rainer, D.; Tedrow, P. M. *Phys. Rev. B* **1985,** *31,* 5811–5825. doi:10.1103/physrevb.31.5811
50. Huertas-Hernando, D.; Nazarov, Y. V.; Belzig, W. *Phys. Rev. Lett.* **2002,** *88,* 047003. doi:10.1103/physrevlett.88.047003

License and Terms

BEILSTEIN JOURNAL OF NANOTECHNOLOGY

Ultrafast signatures of magnetic inhomogeneity in $Pd_{1-x}Fe_x$ ($x \leq 0.08$) epitaxial thin films

Andrey V. Petrov[1], Sergey I. Nikitin[1], Lenar R. Tagirov[2], Amir I. Gumarov[1,2], Igor V. Yanilkin[1] and Roman V. Yusupov[*1]

Full Research Paper

Open Access

Address:
[1]Kazan Federal University, Kremlyovskaya 18, Kazan, Russia and [2]Zavoisky Physical-Technical Institute, FRC Kazan Scientific Centre of RAS, Sibirsky trakt 10/7, Kazan, Russia

Email:
Roman V. Yusupov[*] - Roman.Yusupov@kpfu.ru

* Corresponding author

Keywords:
magnetic inhomogeneities; PdFe alloy; thin epitaxial films; time-resolved magneto-optical Kerr effect; time-resolved optical spectroscopy

Beilstein J. Nanotechnol. **2022,** *13,* 836–844.
https://doi.org/10.3762/bjnano.13.74

Received: 31 March 2022
Accepted: 28 July 2022
Published: 25 August 2022

This article is part of the thematic issue "Intrinsic Josephson effect and prospects of superconducting spintronics".

Guest Editor: A. S. Sidorenko

Abstract

A series of $Pd_{1-x}Fe_x$ alloy epitaxial films (x = 0, 0.038, 0.062, and 0.080), a material promising for superconducting spintronics, was prepared and studied with ultrafast optical and magneto-optical laser spectroscopy in a wide temperature range of 4–300 K. It was found that the transition to the ferromagnetic state causes a qualitative change of both the reflectivity and the magneto-optical Kerr effect transients. A nanoscale magnetic inhomogeneity of the ferromagnet/paramagnet type inherent in the palladium-rich $Pd_{1-x}Fe_x$ alloys reveals itself through the occurrence of a relatively slow, 10–25 ps, photoinduced demagnetization component following a subpicosecond one; the former vanishes at low temperatures only in the x = 0.080 sample. We argue that the 10 ps timescale demagnetization originates most probably from the diffusive transport of d electrons under the condition of nanoscale magnetic inhomogeneities. The low-temperature fraction of the residual paramagnetic phase can be deduced from the magnitude of the slow reflectivity relaxation component. It is estimated as ≈30% for x = 0.038 and ≈15% for x = 0.062 films. The minimal iron content ensuring the magnetic homogeneity of the ferromagnetic state in the $Pd_{1-x}Fe_x$ alloy at low temperatures is about 7–8 atom %.

Introduction

Superconductor-based technologies are promising for exaflop-scale supercomputing, big-data processing, artificial intelligence, and neuromorphic computing [1-7]. The highlight features of superconducting data processing techniques, for example, RSFQ logic [1-9], are the high speed and unprecedental energy efficiency [2,3,10-13]. Superconducting spintronics is a branch of superconducting electronics, the key components of which are thin-film magnetic Josephson junctions (MJJs), which include layers of superconductors (S), ferromagnets (F) and insulators (I) [1-3,14,15]. The use of MJJs considerably

reduces the energy consumption, the number of Josephson junctions, and the number of interconnects in superconducting digital circuitries [16], ensuring wide operation margin tolerances and low bit-error rates [17,18].

To realize the full functionality of superconducting digital circuits, several kinds of MJJ-based devices are required, including logic gates [19-23], programmable logics [16], nondissipative biasing [1], and random access and cache memories [17,24-28]. From the fabrication point of view, it is strongly desirable to utilize a universal tunable ferromagnetic material for every application. Among several candidates [1-3], palladium-rich $Pd_{1-x}Fe_x$ alloys look attractive because of the noble-metal base robust against deterioration and the possibility to tune the magnetic properties of $Pd_{1-x}Fe_x$ alloy films by varying the iron content x and the preparation conditions [29,30]. Moreover, attempts have been made to use this material (with low iron concentrations of x = 0.01–0.03) for MJJ memory applications [1,14,15,24,31,32]. However, these studies faced the problems of small critical current and temporal instability of magnetic properties [33]. On the one hand, nanoscale magnetic inhomogeneities are inherent in disordered $Pd_{1-x}Fe_x$ alloys with a high palladium content, on the other hand, these inhomogeneities are extremely undesirable in MJJs. Indeed, within the frame of the percolation model of ferromagnetism in $Pd_{1-x}Fe_x$ alloys with $x < 0.1$ [34,35], magnetic inhomogeneities cause spin-flip and pairing wave function damping, thus, reducing the magnitude of the Josephson critical current. Small-scale inhomogeneities are difficult to detect with either conventional neutron-scattering methods [34] or with the stationary magneto-optical Kerr/Faraday effect and ferromagnetic resonance techniques (the latter two, because of the large scale, yield volume-averaged signals). Resonant magnetic small-angle X-ray scattering applied to $Pd_{1-x}Fe_x$ alloy films with x = 0.03–0.07 revealed static magnetic fluctuations on the lateral scale of about 100 nm attributed to the magnetic domain structures of the films [36]. Smaller-scale fluctuations, due to intrinsic disorder in the alloy composition, still remain unexplored.

Finding a way to achieve magnetic uniformity in $Pd_{1-x}Fe_x$ down to the atomic scale is a challenge. One of the options is the selection of the concentration range of iron at which the alloy would become magnetically homogeneous. This requires a method for detecting magnetic inhomogeneities, preferably with the possibility of being applied to thin films. We propose the use of ultrafast, time-resolved optical and magneto-optical spectroscopy methods for probing magnetic inhomogeneities in thin films. Individual constituents can be characterized by specific relaxation components that can be used to detect magnetic inhomogeneities and track their evolution. In addition, the peculiarities of the magnetization dynamics in magnetically inhomogeneous systems themselves are of interest.

In our recent work, using the example of a thin epitaxial film of $Pd_{0.94}Fe_{0.06}$, it was demonstrated [37] that the dynamics of the reflection coefficient and the angle of rotation of the polarization plane in magneto-optical Kerr effect (MOKE) measurements after a photoexcitation with femtosecond light pulses contain components whose temperature dependence correlates with that of the spontaneous magnetization. It was argued that such responses can serve as a source of information on magnetic inhomogeneities. In this work, we extend the series of $Pd_{1-x}Fe_x$ films to a wider concentration range, confirm the correlation of the ultrafast responses with the magnetic properties of the system, and determine the minimum iron concentration in the alloy that ensures magnetic homogeneity at low temperatures. We discuss the findings in the frame of a model in which ferromagnetic (FM) and paramagnetic (PM) regions coexist, with the latter collapsing upon an increase of the iron content.

Experimental

The samples for the studies were thin epitaxial films of $Pd_{1-x}Fe_x$ with a nominal iron content of x = 0 (pure Pd), 0.038, 0.062, and 0.080 grown on single-crystal MgO(001) substrates by molecular beam epitaxy (MBE). The films were 20 nm thick, continuous, and smooth monocrystalline layers. The MBE equipment provided uniformity of the film thickness within 3% on the 1″ lateral size. The film composition x was measured in situ using X-ray photoelectron spectroscopy (all from SPECS, Berlin) with a nominal accuracy of 0.1%. Details of the synthesis and characterization of the samples used in the work can be found in our previous papers [29,30]. The Curie temperatures for the samples with x = 0.038, 0.062, and 0.080 were ≈120 K, ≈177 K, and ≈210 K, respectively.

The optical experiments were carried out in a pump–probe arrangement with a Legend-USP regenerative amplifier from COHERENT used as a light sourse in a similar way as described in [37]. The pulse repetition rate was 970 Hz, the central wavelength was 800 nm, and the duration was 40 fs. Excitation of the samples was performed by the pump light with a wavelength of 400 nm (second harmonic) and the properties were probed at 800 nm. The pump and probe beams were focused at the sample into the spots with diameters of 0.5 mm and 0.1 mm, respectively. Energy densities of the pump and the probe were 1 mJ/cm^2 and 50 μJ/cm^2, and the incidence angles were ≈2° and ≈18°.

The relaxation of the electronic subsystem was monitored by the relative change in the reflection coefficient ($\Delta R/R$). Ultra-

fast dynamics of the magnetization was analyzed by the deviation of the angle of rotation of the polarization plane of the probing light from the equilibrium in longitudinal MOKE measurements. MOKE reveals itself, in general, in a rotation of the polarization plane and an ellipticity of linearly polarized light on its reflection from a magnetized medium. Macroscopically, it originates from an occurrence of the finite non-diagonal components of the dielectric permittivity tensor of a medium proportional to its magnetization. Therefore, any of the real θ_K (rotation angle) or imaginary η_K (ellipticity) parts of the complex Kerr angle $\Theta_K = \theta_K + i\eta_K$ provide a measure of the magnetization of a medium. An ability to track modifications of these quantities on an ultrafast time scale allows for the study of the magnetization dynamics. In our experiments, the probing light reflected from the sample passed through a Wollaston prism dividing the beam into two orthogonally polarized components. The intensities of these two components were detected by Hamamatsu S2386-5K silicon photodiodes. The difference signal from the output of the photodiodes was used to determine the rotation angle $\Delta\theta = f(\Delta t)$, and the sum signal was used to measure the dynamics of the reflection coefficient $\Delta R/R = g(\Delta t)$. To extract the magnetic contribution $\Delta\theta_K$ to the rotation of the polarization plane $\Delta\theta$, which partially can originate from the pump-induced anisotropy, the responses were measured at two oppositely applied magnetic fields $+H$ and $-H$. In this case, the contribution odd with respect to the sign of the field $\Delta\theta_K = [\Delta\theta(+H) - \Delta\theta(-H)]/2$ has a magnetic nature.

To perform measurements at temperatures from 4.2 to 300 K, the films under study were mounted to the cold finger of the Janis ST-500 helium-flow cryostat. Permanent NdFeB magnets were fixed there, creating a magnetic field directed along the easy axis of the thin film in its plane with a magnitude of 470 Oe at room temperature. This field strength ensures a uniformly magnetized state of the film since the coercive field of the studied samples does not exceed 25 Oe. The sample temperature was set and maintained using a Lakeshore 335 temperature controller with an accuracy of 0.1 K.

Results

Figure 1 shows the dependency of the reflectivity normalized to the equilibrium value on the delay between the pump and the

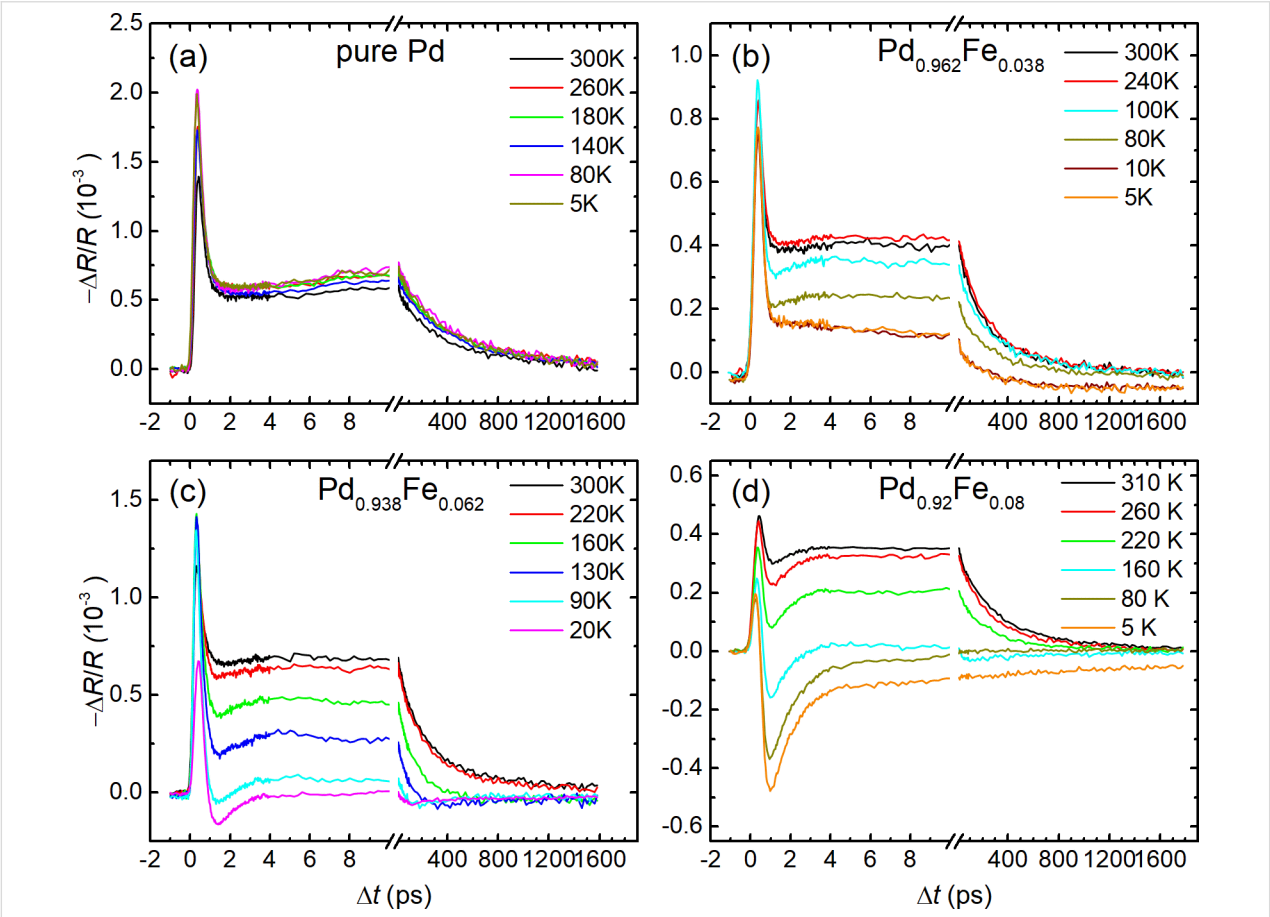

Figure 1: Temperature evolutions of the reflectivity transients of $Pd_{1-x}Fe_x$ alloy thin epitaxial films for compositions with x = 0 (a), 0.038 (b), 0.062 (c), and 0.080 (d).

probe pulses of the four studied samples and its variation with temperature in the range of 5–300 K. In general, the responses of the pure palladium film change very slightly with temperature. The addition of the iron dopant leads to a development of a temperature dependence of $\Delta R/R(\Delta t)$ responses, both qualitative (the appearance of new relaxation components) and quantitative (changes in their amplitudes and time constants). While two decaying exponents are sufficient to describe the relaxation of the reflection coefficient of the Pd and $Pd_{0.962}Fe_{0.038}$ films at the lowest temperature, a minimum of four is required for the $Pd_{0.94}Fe_{0.06}$ film and only three for $Pd_{0.92}Fe_{0.08}$. Thus, with an increase in the iron concentration x in a $Pd_{1-x}Fe_x$ system, the photoinduced dynamics of the electronic subsystem changes from a relatively simple to a much more complex one; subsequently, the character partially simplifies again.

In quantitative terms, in the general case, the relaxation response can be described by the sum of four decaying exponents, two fast and two relatively slow ones, with one positive and one negative amplitude in each pair:

$$-\Delta R/R(\Delta t) = A_f e^{-\Delta t/\tau_f^A} + A_s e^{-\Delta t/\tau_s^A} - B_f e^{-\Delta t/\tau_f^B} - B_s e^{-\Delta t/\tau_s^B}. \quad (1)$$

A significant difference in the values of the characteristic times for the fast and slow components makes it possible to fit them separately, which improves the accuracy of the parameter determination.

To describe the relaxation of the reflectivity of a palladium film, Figure 1a, the first two terms in Equation 1 are sufficient. The fast component with an amplitude A_f has a decay time $\tau_f^A = 0.24 \pm 0.02$ ps. The lifetime of the second, slow component with the amplitude A_s is $\tau_s^A = 410 \pm 10$ ps. Figure 1b–d shows similar dynamics of the reflectance for three films with iron contents of 3.8, 6.2 and 8.0 atom %. At room temperature, the behavior of the responses for the films with 3.8 and 6.2 atom % of iron is similar to the responses obtained from the pure Pd film. The abovementioned fast component for these films has approximately the same lifetime, ≈0.3 ps. The lifetime of the slow component in the samples with 3.8, 6.2, and 8.0 atom % of iron is 240 ± 10, 210 ± 10, and 290 ± 10 ps, respectively. However, with an increase in the iron concentration, at times up to ca. 10 ps, an additional fast exponential decaying component appears. This component is opposite in sign to those given above. The main feature of these responses is their strong temperature dependence. At temperatures above the Curie temperature of the samples, they are not detectable. However, on cooling, starting from the Curie temperature, the $\Delta R/R(\Delta t)$ responses increase sharply. The amplitude of the fast negative component increases in absolute value. Also, both the amplitude and the relaxation time of the slow positive component decrease. At temperatures of 90 and 160 K, another slow negative component appears in the samples with 6 and 8 atom % of iron, respectively. Its relaxation time is about 1 ns. The amplitude of this component is one order of magnitude smaller than the amplitudes of the other components.

Figure 2 shows temperature dependency of the ultrafast dynamics of magnetization. The data are presented here for the films with $x = 0.038$ and $x = 0.080$; for the sample with $x = 0.062$, the responses can be found in [37]. Photoinduced demagnetization and the recovery are observed only at $T < T_C$. One can readily recognize two demagnetization processes that reveal themselves as the rising components and occur at time scales of subpicoseconds and tens of picoseconds. Therefore, the responses in the general case are described by the expression:

$$\Delta\theta_K(\Delta t) = \left[A_{r1}^K\left(1 - e^{-\Delta t/\tau_{r1}^K}\right) + A_{r2}^K\left(1 - e^{-\Delta t/\tau_{r2}^K}\right)\right] \times e^{-\Delta t/\tau_d^K}, \quad (2)$$

where components with amplitudes A_{r1}^K and A_{r2}^K describe the rise (demagnetization), while the factor following the square

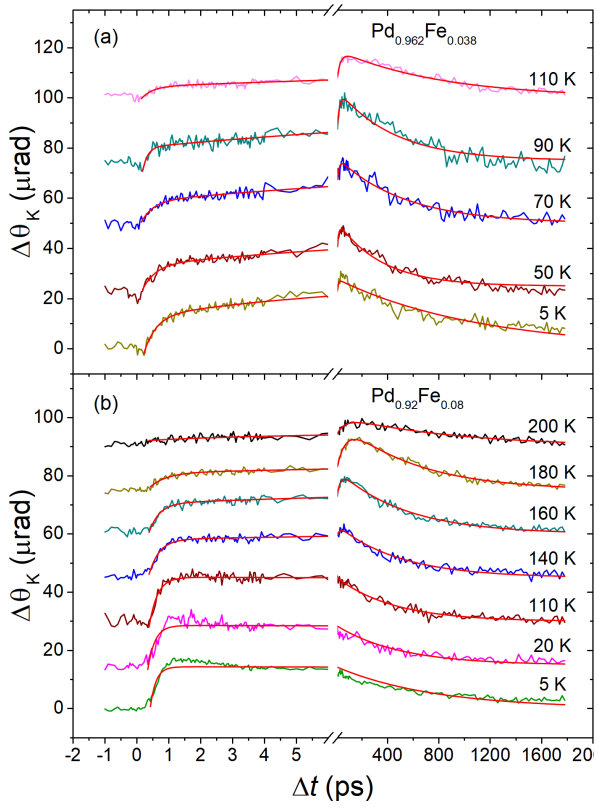

Figure 2: Temperature evolution of the time-resolved magneto-optical Kerr angle transients for the $Pd_{0.962}Fe_{0.038}$ (a) and $Pd_{0.92}Fe_{0.08}$ (b) epitaxial thin films at $T < T_C$; red solid lines are the results of fits with Equation 2.

brackets describes the decay of the signal (magnetization recovery).

Temperature dependences of the amplitudes and the lifetimes of the selected components, obtained from the fit of the experimental data with Equation 1 and Equation 2, are presented in Figure 3 and Figure 4 for the reflectivity and time-resolved MOKE, respectively. We note here the invariance of the amplitude A_s (Figure 3a) and relaxation time τ_s^A (Figure 3b) at $T \geq T_C$, and a kink in their dependences at $T = T_C$ for the films with $x = 0.038$ and 0.062. The evolution of this component is not so obvious for the film with $x = 0.080$: The kink in its temperature dependence and the onset of its suppression take place at a temperature slightly above T_C. Below T_C, all three samples reveal a decrease of A_s and a shortening of τ_s^A. In the samples with 3.8 and 6.2 atom % of iron, the drop of A_s with the temperature decrease slows down and ceases reaching values of ≈15% and ≈30% of its maximum, respectively, at 5 K.

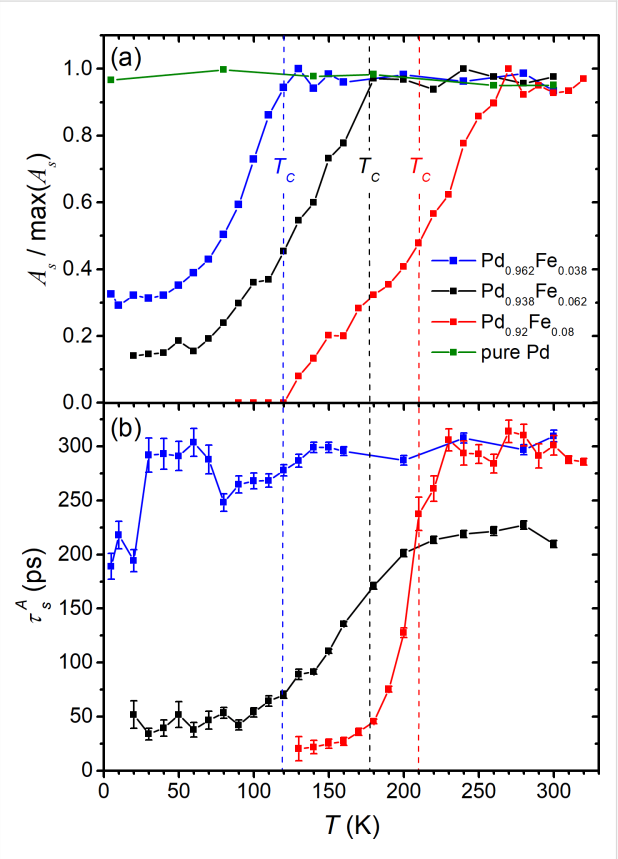

Figure 3: Temperature dependences of the amplitudes (a) and the lifetimes (b) of the slow relaxation components of the reflectivity transients shown in Figure 1. In panel (a) the amplitude A_s for each sample is normalized to its magnitude at room temperature.

Other characteristics, that is, the amplitudes A_f and B_s and the relaxation times τ_f^A and τ_s^B, do not reveal any anomalies in their temperature dependences and therefore are not presented. The amplitude of the fast component B_f for each $Pd_{1-x}Fe_x$ alloy film has a nonzero value practically over the entire temperature range of 5–300 K. It gradually increases with decreasing temperature for samples with 6.2 and 8.0 atom % of iron. For the sample with 3.8 atom % of iron, it has the same behavior down to 150 K, and then decreases to zero at the lowest temperatures. The relaxation time of this component is practically independent of the temperature and is $\tau_f^B = 0.80 \pm 0.10$ ps.

Figure 4a shows the temperature dependences of the amplitudes of the fast demagnetization process. It is observed in the entire temperature range below the Curie temperature of the samples. The average rise time of the fast component of demagnetization for all three samples is ≈0.3 ps and depends only slightly on the temperature. The variation with temperature of the amplitude of the slow demagnetization component A_{r2}^K of the $Pd_{0.962}Fe_{0.038}$ sample, Figure 4c, is similar in character to that of the fast component. In contrast, in the $Pd_{0.938}Fe_{0.062}$ sample, starting from T_C, the amplitude A_{r2}^K increases with lowering the temperature and reaches a maximum at ≈160 K. On further cooling, the amplitude decreases with a tendency to saturate at a small, but still detectable value at the lowest temperatures. In the $Pd_{0.92}Fe_{0.08}$ sample, the slow component is observed only in the range $120\ K < T < T_C$. Here, it also appears at T_C, reaches a maximum at ≈180 K, and drops to zero value at ≈125 K.

Temperature dependences of the characteristic time of the slow demagnetization component are shown in Figure 4d. It has a minimum value for all films at the lowest temperatures of the range of its observation. For the samples with an iron content of 3.8 and 6.2 atom %, the minimum τ_{r2}^K is ≈10 ps, and for a film with 8 atom % of iron, it is ≈20 ps. However, on warming of a sample, the slow demagnetization time increases and becomes several times longer on approaching the Curie temperature.

The magnetization recovery time τ_d^K reveals a similar behavior (see Figure 4b) demonstrating a kind of a critical slowing down characteristic for second-order phase transitions. Starting from a value of ≈0.5 ns at the lowest temperatures, τ_d^K grows rapidly on approaching T_C of the samples, where it gets two to three times longer.

Discussion

In this section, we focus our attention at the components of the ultrafast responses of the electronic (reflectivity) and magnetic (Kerr rotation angle) subsystems, which demonstrate a clear correlation with the establishment of the long-range magnetic order in $Pd_{1-x}Fe_x$ films.

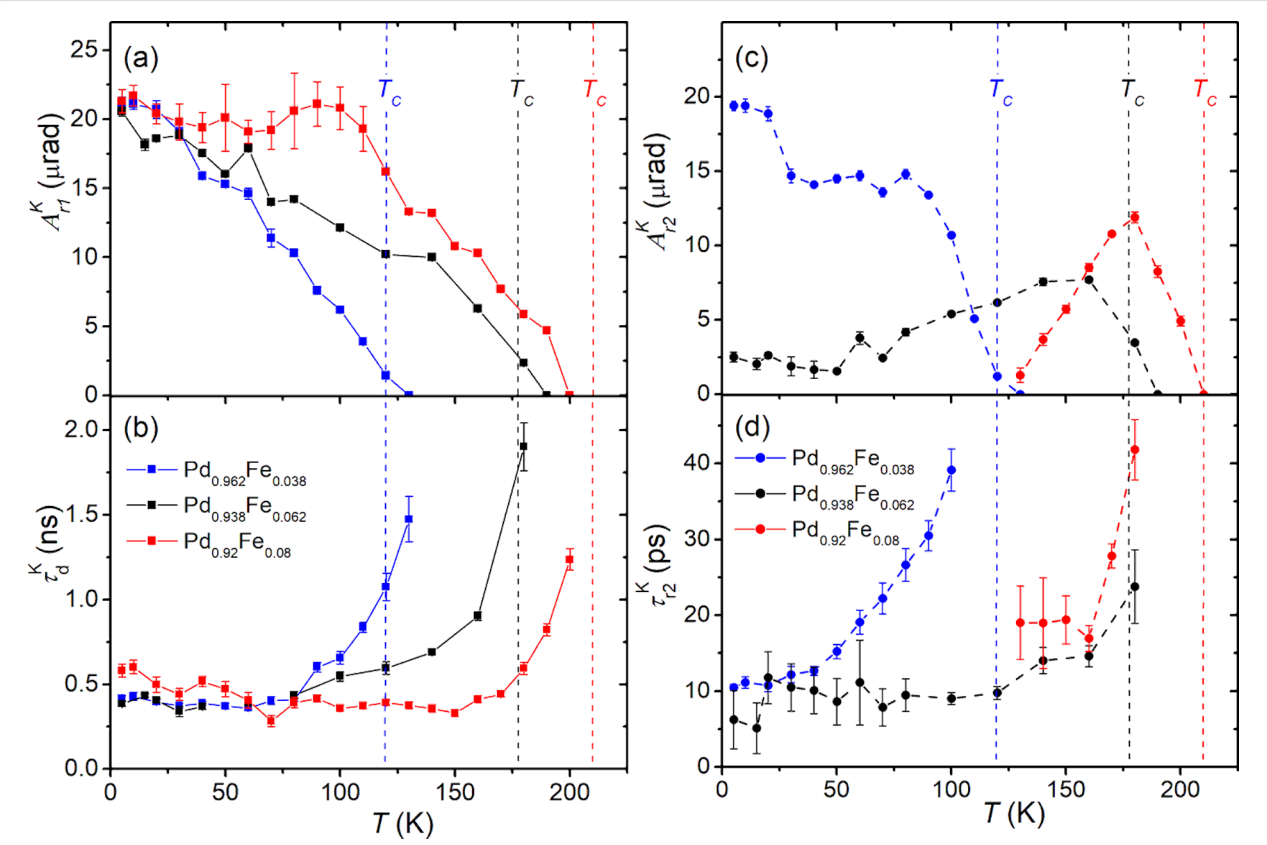

Figure 4: Temperature dependences of the amplitudes of the fast (squares/solid lines) (a) and the slow (circles/dashed lines) (c) photoinduced demagnetization components; characteristic times (b) of the magnetization recovery (squares/solid lines) and (d) of the slow demagnetization (circles/dashed lines) of the $Pd_{0.962}Fe_{0.038}$ (blue), $Pd_{0.938}Fe_{0.062}$ (black), and $Pd_{0.92}Fe_{0.08}$ (red) epitaxial films.

In the $\Delta R/R(\Delta t)$ dependences of the alloys, the slow relaxation component with the amplitude A_s (Figure 3a) follows this trend. While no temperature variation of A_s is observed for a pure palladium film, a sharp kink close to T_C towards its decrease appears for the other three samples. Moreover, for the $Pd_{0.962}Fe_{0.038}$ film, as well as for the $Pd_{0.938}Fe_{0.062}$ film [37], the shape of the properly normalized $A_s(T)$ dependence practically reproduces that for the saturation magnetization $M_s(T)/M_s(0)$ (Figure 5a). In our opinion, within the framework of the magnetic polaron model [34,35], such a situation can be associated with a decrease in the volume of the paramagnetic phase due to the growth of the fraction of magnetic bubbles.

It is worth noting that the A_s amplitude for the $Pd_{0.92}Fe_{0.08}$ sample vanishes below 120 K. Based on the normalized $A_s(T)$ dependences from Figure 3a, one can estimate that in the $Pd_{0.962}Fe_{0.038}$ sample, about 30% of the film volume is left in the paramagnetic state at low temperatures; for the $Pd_{0.938}Fe_{0.062}$ sample, the volume fraction of the paramagnetic phase is ≈15%. The $Pd_{0.92}Fe_{0.08}$ sample is in a homogeneous ferromagnetic state below 120 K. Thus, we associate the slow relaxation of the reflectivity of the $Pd_{1-x}Fe_x$ films with the presence of a residual paramagnetic phase in the sample. We relate its manifestation at temperatures corresponding to the ferromagnetic state of the material to the presence of magnetic inhomogeneities. The latter are most likely formed due to the inhomogeneous distribution of the iron impurities in the palladium host.

As for the Kerr rotation angle dynamics (Figure 2), any detected signals are observed only at temperatures below T_C for each sample. An interesting feature here is the manifestation of two components in the photoinduced demagnetization, that is, the ultrafast component with a characteristic time of ≈0.3 ps, and a noticeably slower one, occurring on a scale of 10–20 ps. The ultrafast process manifests itself at all temperatures below T_C, and its amplitude grows gradually on cooling. The slower demagnetization component reveals a specific temperature dependence of the amplitude A_{r2}^K, which strongly depends on the composition of the film (see Figure 4a).

Going deeper into the details, the amplitude A_{r2}^K for the sample with $x = 0.038$ increases with decreasing temperature in the entire range of 5 K ≤ $T < T_C$. For samples with $x = 0.062$ and 0.080, this amplitude reaches a maximum rather quickly as the

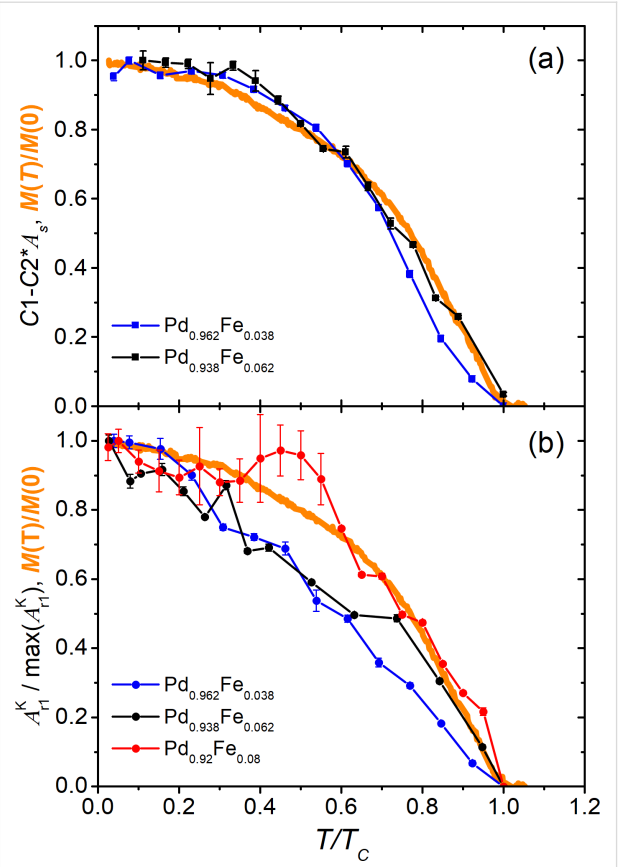

Figure 5: Temperature dependences of the reflectivity slow relaxation amplitudes of the $Pd_{0.962}Fe_{0.038}$ (blue) and $Pd_{0.938}Fe_{0.062}$ (black) samples, transformed and normalized in magnitude for their comparison with the dependence of the saturation magnetization (thick orange line) (a); the same for the Kerr rotation angle dependences (b).

temperature drops below T_C, and then behaves differently for these two samples. In the film with x = 0.062, this component gradually decreases to a level of 25–30% of the maximum, without turning to zero down to a temperature of 5 K. In the film with x = 0.080, on cooling of the sample below T_C, the amplitude A_{r2}^K rapidly decreases after reaching the maximum value. It further approaches zero at 120 K and does not recover at lower temperatures. As we can see from Figure 3a and Figure 4a, the observation of the slow component of the demagnetization correlates with the observation of the slow relaxation of the reflectivity (amplitude A_s). In our opinion, this fact makes it possible to relate the slower component of demagnetization with magnetic inhomogeneities in the sample. The amplitude of this component reaches its maximum, apparently, at temperatures corresponding to the maximum degree of magnetic inhomogeneity of the films. The temperature dependence of the subpicosecond demagnetization component clearly correlates with the course of the saturation magnetization of the film (Figure 4a and Figure 5b), and represents, thus, the response of the ferromagnetic component of the films under study.

The origin of the photoinduced demagnetization specific for a magnetically inhomogeneous ferromagnetic/paramagnetic metallic state is important itself. Therefore, it should be discussed explicitly. First, we note that dilute $Pd_{1-x}Fe_x$ alloys are systems in which magnetism is mainly due to the polarization of palladium 4d electrons. The second distinguishing feature of $Pd_{1-x}Fe_x$ alloys is their small spatial scale of magnetic inhomogeneities, which is of the order of 1 nm.

The subpicosecond component of the photoinduced demagnetization is evidently a result of the photoexcitation of the ferromagnetic fraction as it is. It does not demand any process related to the paramagnetic fraction, and therefore we denote it as “on-site demagnetization”. Indeed, such an ultrafast photoinduced demagnetization is a characteristic feature of the 3d metal ferromagnets that has been a matter of intense discussion in past decades [38-43]. An additional demagnetization component with a characteristic time of ≈10 ps requires the presence of a paramagnetic fraction in the material. However, the transfer of the angular momentum between the paramagnetic and ferromagnetic fractions by highly mobile s and p electrons (which occurs due to the s–d interaction [40]) should only increase the rate of photoinduced demagnetization on a subpicosecond scale. This mechanism was justified to explain the ultrafast (subpicosecond) transfer of the angular momentum in F/N heterostructures with large (tens of nanometer) layer thicknesses [40,44,45].

It is our hypothesis that itinerant electron spin diffusion could bring the PM areas into equilibrium with the FM environment and is an origin of the 10 ps transient. Indeed, the diffusion velocity across the length of ≈1 nm on a time scale of 10 ps can be estimated as 10^{-9} m/10^{-11} s = 100 m/s. For the conventional spin diffusion, the spin memory length is $l_s = \sqrt{D \cdot \tau_s}$, where $D = v_F^2 \tau / 3$ is the diffusion coefficient, τ_s is the Elliott–Yafet spin-relaxation time [46,47], τ is the charge transport relaxation time, and v_F is the Fermi velocity. For the purpose of order-of-magnitude estimation we define the spin-diffusion velocity v_s as $v_s = l_s/\tau_s = \sqrt{D/\tau_s}$, from which $v_s \approx 0.58 v_F \sqrt{\tau/\tau_s}$. Modern band-structure calculations [48,49] show that more than 95% of the electron density of states at the Fermi energy comes from the itinerant 4d electrons. The Fermi velocity of 3d electrons in iron-group ferromagnetic metals was a subject of interest in magnetic nanostructures [50-52] and had a value of about 3×10^5 m/s. Being stronger localized in the narrower 4d bands [44], the itinerant 4d electrons must have a lower velocity, say 10^5 m/s. Then, with the transport time $\tau \approx 10^{-14}$ s and the electron-spin relaxation time $\tau_s \approx 10^{-9}$ s [53] we get $v_s \approx 1.8 \times 10^2$ m/s as an upper bound. An order-of-magnitude matching of the obtained v_s value with the initial guess makes the 4d electron spin diffusion a plausible mechanism of the ob-

served 10–25 ps demagnetization component in a mixed PM/FM state in the palladium-rich PdFe alloys.

Conclusion

Based on the analysis of the experimental data on ultrafast optical and magneto-optical spectroscopy in comparison with the magnetometry data, responses have been identified inherent to the magnetically inhomogeneous state of the epitaxial $Pd_{1-x}Fe_x$ alloy films. The vanishing of these components with decreasing temperature makes it possible to establish a lower limit for the concentration of iron in palladium and the operation temperature that ensures the magnetically homogeneous ferromagnetic state of the films. This is one of the key conditions for their use as weak links in magnetic Josephson junctions and superconducting memory elements based on spin valves.

Funding

This paper (PAV, NSI, GAI, YIV, and YRV) has been supported by the Kazan Federal University Strategic Academic Leadership Program (PRIORITY-2030). LRT thanks the support by a state assignment no. AAAA-A18-118030690040-8 to the Federal Research Center "Kazan Scientific Center of the Russian Academy of Sciences".

ORCID® iDs

Andrey V. Petrov - https://orcid.org/0000-0003-3202-2477
Lenar R. Tagirov - https://orcid.org/0000-0002-1549-7940
Amir I. Gumarov - https://orcid.org/0000-0002-7250-4377
Igor V. Yanilkin - https://orcid.org/0000-0002-8879-8904
Roman V. Yusupov - https://orcid.org/0000-0002-7516-2392

Preprint

A non-peer-reviewed version of this article has been previously published as a preprint: https://doi.org/10.3762/bxiv.2022.22.v1

References

1. Ryazanov, V. V.; Bol'ginov, V. V.; Sobanin, D. S.; Vernik, I. V.; Tolpygo, S. K.; Kadin, A. M.; Mukhanov, O. A. *Phys. Procedia* **2012,** *36,* 35–41. doi:10.1016/j.phpro.2012.06.126
2. Tolpygo, S. K. *Low Temp. Phys.* **2016,** *42,* 361–379. doi:10.1063/1.4948618
3. Soloviev, I. I.; Klenov, N. V.; Bakurskiy, S. V.; Kupriyanov, M. Y.; Gudkov, A. L.; Sidorenko, A. S. *Beilstein J. Nanotechnol.* **2017,** *8,* 2689–2710. doi:10.3762/bjnano.8.269
4. Braginski, A. I. *J. Supercond. Novel Magn.* **2019,** *32,* 23–44. doi:10.1007/s10948-018-4884-4
5. Schneider, M. L.; Donnelly, C. A.; Russek, S. E.; Baek, B.; Pufall, M. R.; Hopkins, P. F.; Dresselhaus, P. D.; Benz, S. P.; Rippard, W. H. *Sci. Adv.* **2018,** *4,* e1701329. doi:10.1126/sciadv.1701329
6. Klenov, N.; Khaydukov, Y.; Bakurskiy, S.; Morari, R.; Soloviev, I.; Boian, V.; Keller, T.; Kupriyanov, M.; Sidorenko, A.; Keimer, B. *Beilstein J. Nanotechnol.* **2019,** *10,* 833–839. doi:10.3762/bjnano.10.83
7. Schegolev, A. E.; Klenov, N. V.; Bakurskiy, S. V.; Soloviev, I. I.; Kupriyanov, M. Yu.; Tereshonok, M. V.; Sidorenko, A. S. *Beilstein J. Nanotechnol.* **2022,** *13,* 444–454. doi:10.3762/bjnano.13.37
8. Mukhanov, O.; Semenov, V.; Likharev, K. *IEEE Trans. Magn.* **1987,** *23,* 759–762. doi:10.1109/tmag.1987.1064951
9. Likharev, K. K. *Phys. C (Amsterdam, Neth.)* **2012,** *482,* 6–18. doi:10.1016/j.physc.2012.05.016
10. Mukhanov, O. A. *IEEE Trans. Appl. Supercond.* **2011,** *21,* 760–769. doi:10.1109/tasc.2010.2096792
11. Herr, Q. P.; Herr, A. Y.; Oberg, O. T.; Ioannidis, A. G. *J. Appl. Phys.* **2011,** *109,* 103903. doi:10.1063/1.3585849
12. Holmes, D. S.; Ripple, A. L.; Manheimer, M. A. *IEEE Trans. Appl. Supercond.* **2013,** *23,* 1701610. doi:10.1109/tasc.2013.2244634
13. Volkmann, M. H.; Sahu, A.; Fourie, C. J.; Mukhanov, O. A. *Supercond. Sci. Technol.* **2013,** *26,* 015002. doi:10.1088/0953-2048/26/1/015002
14. Bakurskiy, S. V.; Klenov, N. V.; Soloviev, I. I.; Bol'ginov, V. V.; Ryazanov, V. V.; Vernik, I. V.; Mukhanov, O. A.; Kupriyanov, M. Y.; Golubov, A. A. *Appl. Phys. Lett.* **2013,** *102,* 192603. doi:10.1063/1.4805032
15. Vernik, I. V.; Bol'ginov, V. V.; Bakurskiy, S. V.; Golubov, A. A.; Kupriyanov, M. Y.; Ryazanov, V. V.; Mukhanov, O. A. *IEEE Trans. Appl. Supercond.* **2013,** *23,* 1701208. doi:10.1109/tasc.2012.2233270
16. Katam, N. K.; Mukhanov, O. A.; Pedram, M. *IEEE Trans. Appl. Supercond.* **2018,** *28,* 1300212. doi:10.1109/tasc.2018.2797262
17. Shafraniuk, S. E.; Nevirkovets, I. P.; Mukhanov, O. A. *Phys. Rev. Appl.* **2019,** *11,* 064018. doi:10.1103/physrevapplied.11.064018
18. Yamanashi, Y.; Nakaishi, S.; Yoshikawa, N. *IEEE Trans. Appl. Supercond.* **2019,** *29,* 1301805. doi:10.1109/tasc.2019.2904700
19. Ortlepp, T.; Ariando; Mielke, O.; Verwijs, C. J. M.; Foo, K. F. K.; Andreski, A.; Rogalla, H.; Uhlmann, F. H.; Hilgenkamp, H. *IEEE Trans. Appl. Supercond.* **2007,** *17,* 659–663. doi:10.1109/tasc.2007.898635
20. Khabipov, M. I.; Balashov, D. V.; Maibaum, F.; Zorin, A. B.; Oboznov, V. A.; Bolginov, V. V.; Rossolenko, A. N.; Ryazanov, V. V. *Supercond. Sci. Technol.* **2010,** *23,* 045032. doi:10.1088/0953-2048/23/4/045032
21. Feofanov, A. K.; Oboznov, V. A.; Bol'ginov, V. V.; Lisenfeld, J.; Poletto, S.; Ryazanov, V. V.; Rossolenko, A. N.; Khabipov, M.; Balashov, D.; Zorin, A. B.; Dmitriev, P. N.; Koshelets, V. P.; Ustinov, A. V. *Nat. Phys.* **2010,** *6,* 593–597. doi:10.1038/nphys1700
22. Nevirkovets, I. P.; Chernyashevskyy, O.; Prokopenko, G. V.; Mukhanov, O. A.; Ketterson, J. B. *IEEE Trans. Appl. Supercond.* **2014,** *24,* 1800506. doi:10.1109/tasc.2014.2318317
23. Yamanashi, Y.; Nakaishi, S.; Sugiyama, A.; Takeuchi, N.; Yoshikawa, N. *Supercond. Sci. Technol.* **2018,** *31,* 105003. doi:10.1088/1361-6668/aad78d
24. Larkin, T. I.; Bol'ginov, V. V.; Stolyarov, V. S.; Ryazanov, V. V.; Vernik, I. V.; Tolpygo, S. K.; Mukhanov, O. A. *Appl. Phys. Lett.* **2012,** *100,* 222601. doi:10.1063/1.4723576
25. Baek, B.; Rippard, W. H.; Benz, S. P.; Russek, S. E.; Dresselhaus, P. D. *Nat. Commun.* **2014,** *5,* 3888. doi:10.1038/ncomms4888

26. Gingrich, E. C.; Niedzielski, B. M.; Glick, J. A.; Wang, Y.; Miller, D. L.; Loloee, R.; Pratt, W. P., Jr.; Birge, N. O. *Nat. Phys.* **2016,** *12,* 564–567. doi:10.1038/nphys3681
27. Nevirkovets, I. P.; Shafraniuk, S. E.; Mukhanov, O. A. *IEEE Trans. Appl. Supercond.* **2018,** *28,* 1800904. doi:10.1109/tasc.2018.2836938
28. Dayton, I. M.; Sage, T.; Gingrich, E. C.; Loving, M. G.; Ambrose, T. F.; Siwak, N. P.; Keebaugh, S.; Kirby, C.; Miller, D. L.; Herr, A. Y.; Herr, Q. P.; Naaman, O. *IEEE Magn. Lett.* **2018,** *9,* 3301905. doi:10.1109/lmag.2018.2801820
29. Esmaeili, A.; Yanilkin, I. V.; Gumarov, A. I.; Vakhitov, I. R.; Gabbasov, B. F.; Kiiamov, A. G.; Rogov, A. M.; Osin, Yu. N.; Denisov, A. E.; Yusupov, R. V.; Tagirov, L. R. *Thin Solid Films* **2019,** *669,* 338–344. doi:10.1016/j.tsf.2018.11.015
30. Esmaeili, A.; Yanilkin, I. V.; Gumarov, A. I.; Vakhitov, I. R.; Gabbasov, B. F.; Yusupov, R. V.; Tatarsky, D. A.; Tagirov, L. R. *Sci. China Mater.* **2021,** *64,* 1246–1255. doi:10.1007/s40843-020-1479-0
31. Niedzielski, B. M.; Diesch, S. G.; Gingrich, E. C.; Wang, Y.; Loloee, R.; Pratt, W. P., Jr.; Birge, N. O. *IEEE Trans. Appl. Supercond.* **2014,** *24,* 1800307. doi:10.1109/tasc.2014.2311442
32. Glick, J. A.; Loloee, R.; Pratt, W. P., Jr.; Birge, N. O. *IEEE Trans. Appl. Supercond.* **2017,** *27,* 1800205. doi:10.1109/tasc.2016.2630024
33. Uspenskaya, L. S.; Khlyustikov, I. N. *J. Exp. Theor. Phys.* **2017,** *125,* 875–878. doi:10.1134/s1063776117100090
34. Nieuwenhuys, G. J. *Adv. Phys.* **1975,** *24,* 515–591. doi:10.1080/00018737500101461
35. Korenblit, I. Y.; Shender, E. F. *Sov. Phys. - Usp.* **1978,** *21,* 832–851. doi:10.1070/pu1978v021n10abeh005686
36. Ewerlin, M.; Pfau, B.; Günther, C. M.; Schaffert, S.; Eisebitt, S.; Abrudan, R.; Zabel, H. *J. Phys.: Condens. Matter* **2013,** *25,* 266001. doi:10.1088/0953-8984/25/26/266001
37. Petrov, A. V.; Yusupov, R. V.; Nikitin, S. I.; Gumarov, A. I.; Yanilkin, I. V.; Kiiamov, A. G.; Tagirov, L. R. *J. Exp. Theor. Phys. Lett.* **2019,** *110,* 217–222. doi:10.1134/s0021364019150104
38. Knorren, R.; Bouzerar, G.; Bennemann, K. H. *J. Phys.: Condens. Matter* **2002,** *14,* R739–R765. doi:10.1088/0953-8984/14/27/201
39. Koopmans, B.; Malinowski, G.; Dalla Longa, F.; Steiauf, D.; Fähnle, M.; Roth, T.; Cinchetti, M.; Aeschlimann, M. *Nat. Mater.* **2010,** *9,* 259–265. doi:10.1038/nmat2593
40. Melnikov, A.; Razdolski, I.; Wehling, T. O.; Papaioannou, E. T.; Roddatis, V.; Fumagalli, P.; Aktsipetrov, O.; Lichtenstein, A. I.; Bovensiepen, U. *Phys. Rev. Lett.* **2011,** *107,* 076601. doi:10.1103/physrevlett.107.076601
41. Fähnle, M.; Illg, C. *J. Phys.: Condens. Matter* **2011,** *23,* 493201. doi:10.1088/0953-8984/23/49/493201
42. Kirilyuk, A.; Kimel, A. V.; Rasing, T. *Rep. Prog. Phys.* **2013,** *76,* 026501. doi:10.1088/0034-4885/76/2/026501
43. Wang, C.; Liu, Y. *Nano Convergence* **2020,** *7,* 35. doi:10.1186/s40580-020-00246-3
44. Alekhin, A.; Razdolski, I.; Berritta, M.; Bürstel, D.; Temnov, V.; Diesing, D.; Bovensiepen, U.; Woltersdorf, G.; Oppeneer, P. M.; Melnikov, A. *J. Phys.: Condens. Matter* **2019,** *31,* 124002. doi:10.1088/1361-648x/aafd06
45. Wieczorek, J.; Eschenlohr, A.; Weidtmann, B.; Rösner, M.; Bergeard, N.; Tarasevitch, A.; Wehling, T. O.; Bovensiepen, U. *Phys. Rev. B* **2015,** *92,* 174410. doi:10.1103/physrevb.92.174410
46. Elliott, R. J. *Phys. Rev.* **1954,** *96,* 266–279. doi:10.1103/physrev.96.266
47. Yafet, Y. *Solid State Phys.* **1963,** *14,* 1–98. doi:10.1016/s0081-1947(08)60259-3
48. Östlin, A.; Appelt, W. H.; Di Marco, I.; Sun, W.; Radonjić, M.; Sekania, M.; Vitos, L.; Tjernberg, O.; Chioncel, L. *Phys. Rev. B* **2016,** *93,* 155152. doi:10.1103/physrevb.93.155152
49. Setayandeh, S. S.; Webb, C. J.; Gray, E. M. *Prog. Solid State Chem.* **2020,** *60,* 100285. doi:10.1016/j.progsolidstchem.2020.100285
50. Petrovykh, D. Y.; Altmann, K. N.; Höchst, H.; Laubscher, M.; Maat, S.; Mankey, G. J.; Himpsel, F. J. *Appl. Phys. Lett.* **1998,** *73,* 3459–3461. doi:10.1063/1.122796
51. Himpsel, F. J.; Altmann, K. N.; Mankey, G. J.; Ortega, J. E.; Petrovykh, D. Y. *J. Magn. Magn. Mater.* **1999,** *200,* 456–469. doi:10.1016/s0304-8853(99)00349-2
52. Altmann, K. N.; Gilman, N.; Hayoz, J.; Willis, R. F.; Himpsel, F. J. *Phys. Rev. Lett.* **2001,** *87,* 137201. doi:10.1103/physrevlett.87.137201
53. Koopmans, B.; Ruigrok, J. J. M.; Dalla Longa, F.; de Jonge, W. J. M. *Phys. Rev. Lett.* **2005,** *95,* 267207. doi:10.1103/physrevlett.95.267207

License and Terms

BEILSTEIN JOURNAL OF NANOTECHNOLOGY

Numerical modeling of a multi-frequency receiving system based on an array of dipole antennas for LSPE-SWIPE

Alexander V. Chiginev[*1,2], Anton V. Blagodatkin[1], Dmitrii A. Pimanov[1,3], Ekaterina A. Matrozova[1], Anna V. Gordeeva[1,2], Andrey L. Pankratov[1,2] and Leonid S. Kuzmin[1,3,§]

Full Research Paper

Open Access

Address:
[1]Nizhny Novgorod State Technical University, Nizhny Novgorod, Minin Street, 24, 603950, Russia, [2]Institute for Physics of Microstructures of the Russian Academy of Sciences, GSP-105, Nizhny Novgorod, 603950, Russia and [3]Chalmers University of Technology, Department of Microtechnology and Nanoscience - MC2, Gothenburg, SE-412 96, Sweden

Email:
Alexander V. Chiginev[*] - chig@ipmras.ru

* Corresponding author
§ deceased

Keywords:
cosmic microwave background (CMB); cold-electron bolometer; dichroic antenna; dipole antenna; LSPE-SWIPE; waveguide horn

Beilstein J. Nanotechnol. **2022,** *13,* 865–872.
https://doi.org/10.3762/bjnano.13.77

Received: 27 June 2022
Accepted: 05 August 2022
Published: 01 September 2022

This article is part of the thematic issue "Intrinsic Josephson effect and prospects of superconducting spintronics".

Guest Editor: A. S. Sidorenko

Abstract

Here we present the results of a numerical modeling of mode composition in the constriction of the Large Scale Polarization Explorer-Short-Wavelength Instrument for the Polarization Explorer (LSPE-SWIPE) back-to-back horn. These results are used for calculating the frequency response of arrays of planar dipole antennas with cold-electron bolometers for 145, 210, and 240 GHz frequencies. For the main frequency channel (i.e., 145 GHz) we have a 45 GHz bandwidth. For the auxiliary frequency channels (i.e., 210 and 240 GHz) placed on the same substrate, we have bandwidths of 26 and 38 GHz, respectively. We performed some optimizations for cold-electron bolometers to achieve a photon noise-equivalent power of 1.1×10^{-16} W/Hz$^{1/2}$. This was achieved by replacing one of two superconductor–insulator–normal tunnel junctions with a superconductor–normal metal contact.

Introduction

The Large Scale Polarization Explorer (LSPE) [1] is an experiment of the Italian Space Agency for observing the polarization pattern of the B-mode of the cosmic microwave background (CMB). These observations can give an important information about primordial gravitational waves. The LSPE project consists of two instruments: Strip and Short-Wavelength Instrument for the Polarization Explorer (SWIPE). LSPE-SWIPE is a balloon-borne radio telescope, which will consist of a main and two auxiliary frequency channels. According to the latest requirements [2], the operating frequency of the LSPE-SWIPE main frequency channel should be 145 GHz with a bandwidth of 30%. The operating frequencies of the auxiliary channels should be equal to 210 and 240 GHz and the bandwidths should be 20% and 10%, respectively. To receive radiation in the indi-

cated frequency ranges, we propose to use arrays of planar dipole antennas located in the opening of a special bidirectional horn that forms the radiation pattern of the receiving system and also serves as a low-frequency filter.

For radiation detection, many bolometer types can be applied. The detectors for this instrument should work at 300 mK, since this is the working temperature of the ^{3}He cryostat used for the LSPE project. One of main candidates for LSPE-SWIPE is a transition-edge sensor (TES) with a spiderweb antenna [2,3]. For the OLIMPO mission, kinetic inductance detectors (KIDs) were used [4]. We propose to use cold-electron bolometers (CEBs) [5,6] integrated into the dipole antennas. The advantages of CEB over other types of bolometers are, in particular, their high sensitivity with background-limited operation [6-8] and a wide dynamic range. These qualities are largely determined by the presence of an internal self-cooling of the electronic subsystem of the CEB absorber [6-8]. Another key advantage for balloon and space missions is the high immunity of CEB against cosmic rays [9] due to a double protection given by the extremely small volume of the absorber and decoupling of electron and phonon systems.

One of the advantages of our implementation is the possibility to make arrays for two auxiliary 210 and 240 GHz channels on the same pixel due to the small size of CEBs. The use of multichroic pixels increases the number of pixels per frequency, at no extra cost per focal plane area, weight, and cryogenic load. Before, the double-frequency system with slot antennas and CEBs for 75 and 105 GHz frequencies for the Cosmic Origins Explorer (COrE) mission has been investigated and a band separation was demonstrated [10]. Now this approach is getting further improvements with arrays of dipole antennas and a voltage-biased mode. To use this mode, the CEBs must be connected in parallel. Superconducting quantum interference devices (SQUIDs) with multiplexing [11] will also be used for readout. Therefore, to match this readout system, the arrays of dipole antennas and CEBs connected in parallel should have a resistance value of 1 Ohm at the working point.

In the present paper, we describe the problems of numerical modeling for double-frequency arrays of dipole antennas connected in parallel on a single substrate with radiation going through the back-to-back horn with predefined parameters.

Results

Calculation of the mode composition in the horn constriction at the incidence plane of a linearly polarized plane wave

The parameters of the back-to-back horn are defined in [3]. They consist of two openings and a constriction connecting them, see the details in [3] and a part of the horn in Figure 1. One of the openings defines the radiation pattern of the receiving system, and the other is facing the receiving antenna array. The constriction of the horn determines the modal composition of the electromagnetic field passing through the horn. For a given constriction diameter, up to 38 modes of a circular waveguide are propagating in the operating frequency range.

For correct numerical modeling of the frequency response of the receiving system, it is necessary to know the distribution of

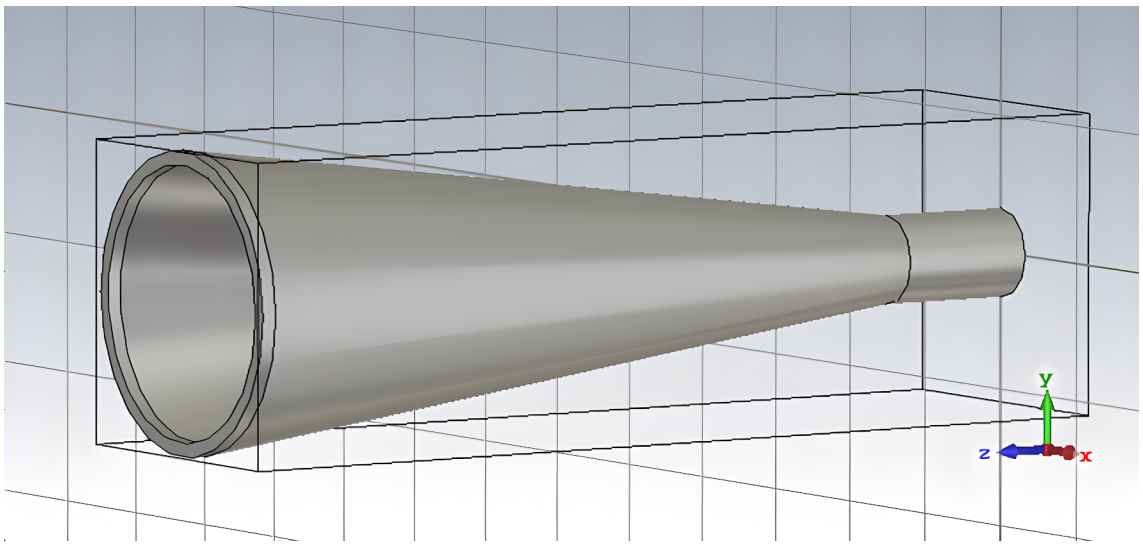

Figure 1: The front part and the constriction of the back-to-back horn of the LSPE-SWIPE receiving system [3] used for the calculation of the mode composition in the constriction.

the field of the incident wave on the matrix of receiving cells. The most consistent would be modeling a back-to-back horn irradiated by a plane electromagnetic wave with a receiving matrix installed in the opposite opening. However, this task requires a lot of computational resources. Therefore, the problem of irradiating the receiving matrix with an incoming radiation was divided into two parts. The first problem was to determine the mode composition of the radiation passing through the constriction of a back-to-back horn when a plane electromagnetic wave falls on it (Figure 1). The second problem was to calculate the power absorbed by the receiving matrix when this matrix is irradiated by the electromagnetic field of a round waveguide port with a calculated mode composition.

The result of the calculation of the mode composition in a back-to-back horn is shown in Figure 2. It can be seen that over the entire operating frequency range of the LSPE-SWIPE, modes with numbers 1 (main), 2, and 4 are present in the horn. Starting from the frequency of 150 GHz, mode 7 appears; amplitudes of modes 7, 9, and 13 are associated with the achievement of the corresponding cutoff frequencies of these modes. The amplitudes of the remaining modes are negligible compared to the amplitudes of the listed modes and can be ignored. The calculated mode amplitudes can be used to calculate the frequency response of antenna arrays with integrated bolometers for the main and auxiliary frequency channels of the LSPE-SWIPE.

Calculation of the frequency response of a planar antenna matrix with integrated cold-electron bolometers

The frequency response of the receiving matrix was calculated as follows. The radiation incident on the matrix is formed by the waveguide port of a circular waveguide with a diameter corresponding to the wide part of the bidirectional horn facing the receiving system (on the right in Figure 1). An RC circuit was used as an equivalent circuit for CEB at high frequencies. In the process of numerical simulation, we calculated the dependence of the power, P_i, released on the active resistance of the i-th RC-chain of the array of receiving cells, on the frequency of the incident radiation, and the total power in all receiving cells:

$$P(f)=\sum_{i=1}^{N}P_i(f). \quad (1)$$

The summation was performed over the cells included in one frequency channel. Thus, as a result of the calculation, the frequency response of the receiving system of one frequency channel was obtained. This calculation principle was used for all types of receiving matrices of the LSPE-SWIPE auxiliary frequency channels.

Main frequency channel of the LSPE-SWIPE

The LSPE-SWIPE 145 GHz main channel receiving system is based on an array of dipole antennas with integrated CEBs

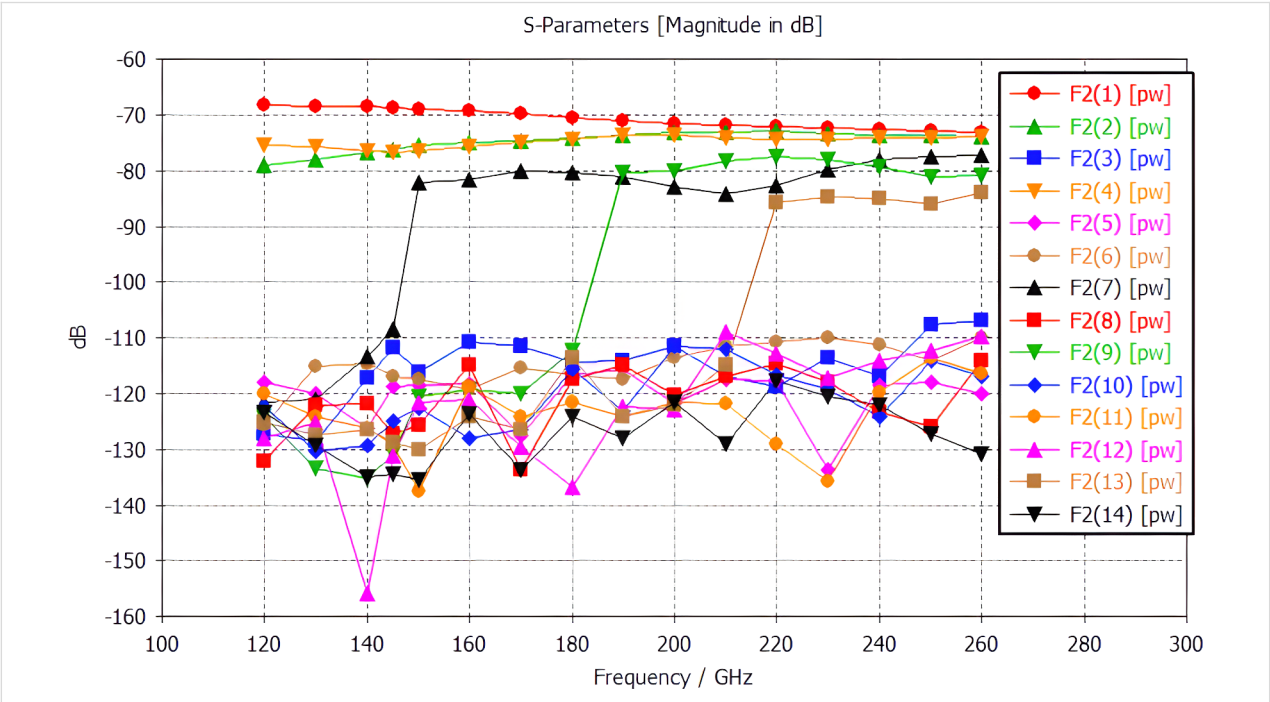

Figure 2: The mode composition of the electromagnetic field in the constriction of a bidirectional horn as a function of frequency.

(Figure 3). The receiving cells are located within a circle under the opening of a bidirectional horn. Its characteristic feature is that the antenna dipoles and wires that provide the CEB DC bias are located in the same layer. This significantly simplifies and reduces the cost of manufacturing such structures.

The frequency response of the LSPE-SWIPE 145 GHz main frequency channel is shown in Figure 4. The received frequency band of the main frequency channel at the level of 0.5 is 45 GHz. At 220 GHz there is a spurious resonance that can be suppressed with a low-pass filter.

Auxiliary frequency channels of the LSPE-SWIPE

The cells are located within a circle with a diameter of 4.5 mm; while one half of the circle is occupied by cells for 210 GHz, the second half is occupied by cells for 240 GHz. Receiving cells with integrated CEBs are located on a 260 μm thick silicon substrate with a silicon dioxide layer. The difficulty of the considered receiving system is the existing specific sample holder, which allows the receiving of the signal from the front side of the pixel only with the back-short placed at the back side of the pixel. Such configuration leads to tougher constraints and less number of free parameters than in [10], where the signal was coming to the antennas through the substrate.

In this work, the receiving system based on a bow-tie dipole antenna was calculated (Figure 5) with the DC bias lines connected to the central parts of the antennas.

The frequency response of the receiving matrix with bow-tie antennas is shown in Figure 6. Rather good band separation is

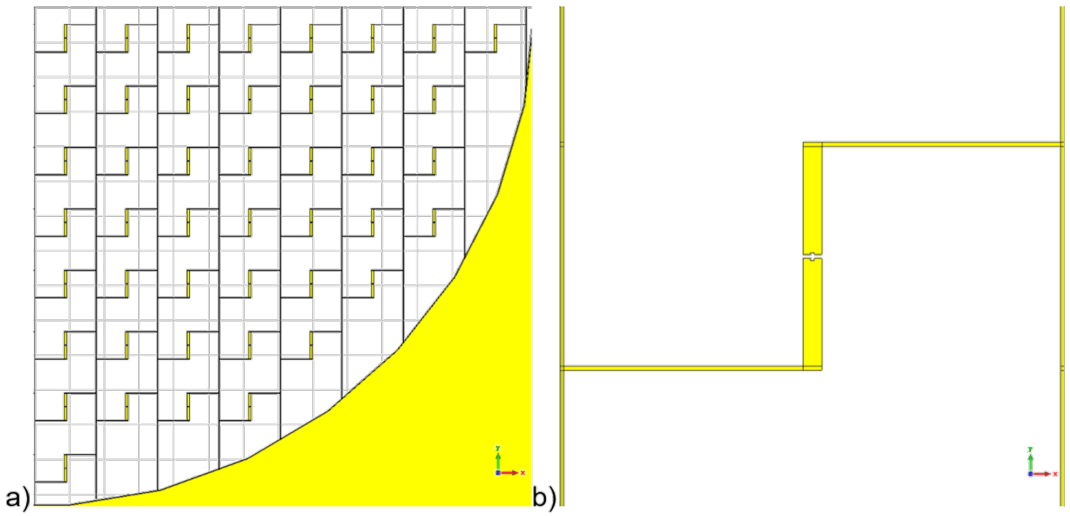

Figure 3: Receiving system of the LSPE-SWIPE145 GHz main channel. a) A quarter of receiving cells matrix on the 14 mm chip. b) A single cell of the receiving system based on a dipole antenna.

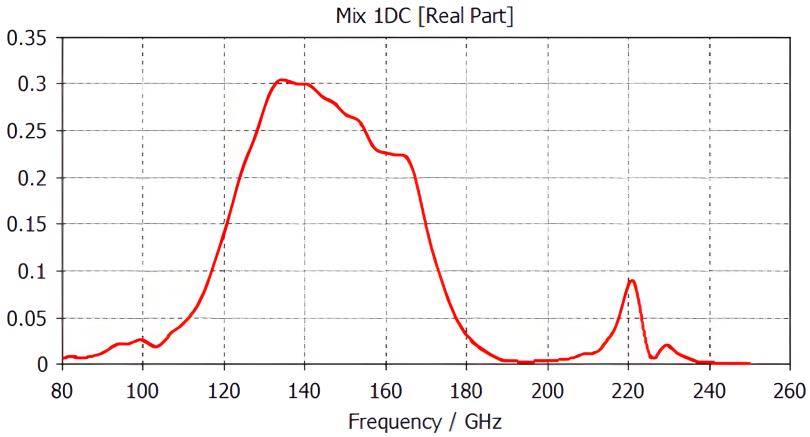

Figure 4: Frequency response of the LSPE-SWIPE 145 GHz main frequency channel.

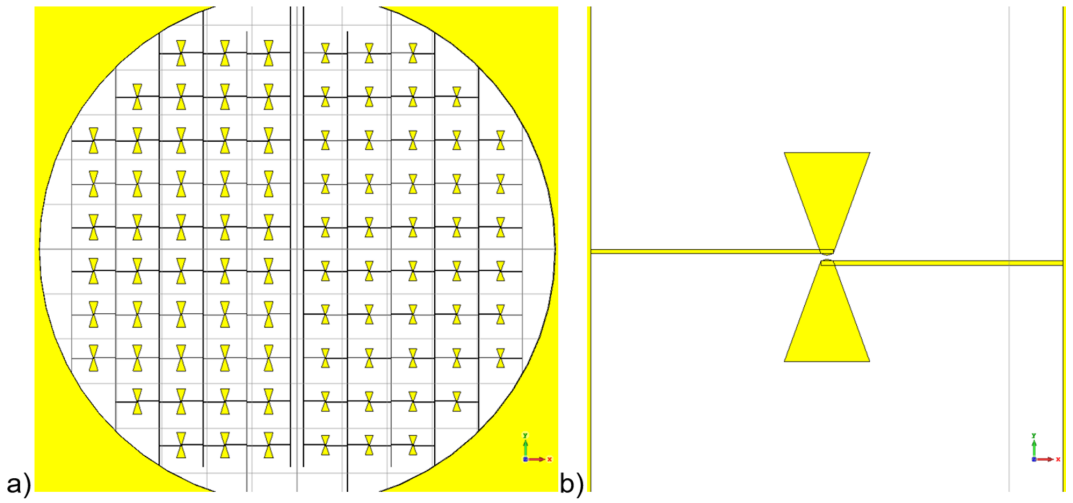

Figure 5: a) Receiving cell array based on bow-tie antennas; half of the 7 mm plate on the left are 210 GHz and on the right 240 GHz frequency channels. b) A receiving system cell based on a bow-tie antenna.

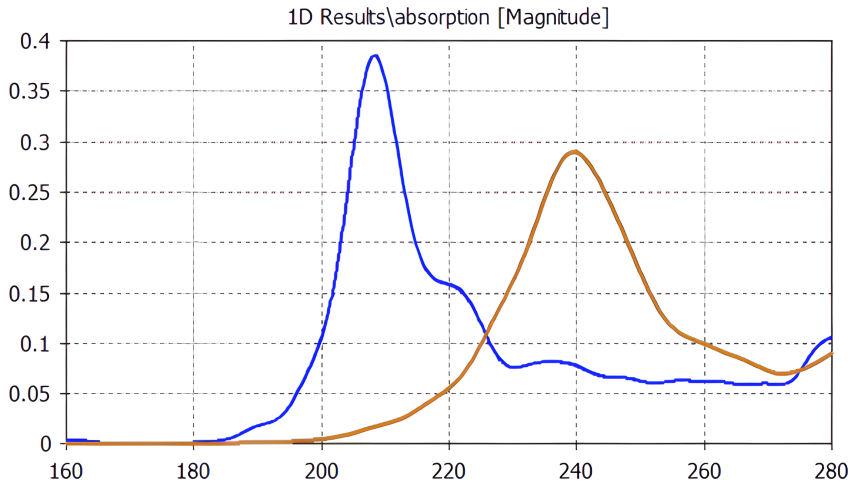

Figure 6: Frequency response of a matrix of receiving cells based on bow-tie antennas for 210 GHz and 240 GHz frequency channels.

visible in spite of a certain cross-talk of the 210 GHz channel. The frequency response width at 50% of the maximum level for the 210 GHz channel is 26 GHz and for the 240 GHz channel is 38 GHz. In addition, the radiofrequency (RF) tails of the 240 GHz channel above 270 GHz are supposed to be suppressed by a band-pass filter.

Noise-equivalent power calculations for the LSPE-SWIPE

The noise-equivalent power (NEP) is a measure of a minimal signal that can be detected, and it qualifies the sensitivity of a detector. The NEP is the ratio of the total system noise (which includes both the internal noise of the detector and the photon noise of the received signal, depending on the signal power) with respect to the responsivity, which can be calculated using the heat balance equations [6].

The power load for the LSPE-SWIPE 145, 210, and 240 GHz frequency channels should be 11, 12.4, and 16 pW, respectively, as stated in Table 4 in [2]. The total NEP level should be approx. 7×10^{-17} W/Hz$^{1/2}$ for the 145 GHz channel, 8.5×10^{-17} W/Hz$^{1/2}$ for the 210 GHz channel, and 1.3×10^{-16} W/Hz$^{1/2}$ for the 240 GHz channel at the working point for a background (photon-noise) limited operation. However, the readout system is based on SQUIDs, and this system has an input current noise of 4–10 pA/Hz$^{1/2}$. To optimize the receiver for better noise characteristics, we consider optimized CEBs with a single superconductor–insulator–normal (SIN)

tunnel junction and a single superconductor–normal (SN) contact [12]. Combined together, they form a SINS structure.

This solution can help reaching better noise characteristics than those of CEBs with two SIN tunnel junctions due to several reasons. First, the responsivity is increased by a factor of two due to hot electrons tunneling only through one SIN junction. Second, the bolometer resistance is decreased twice, which helps in array matching with a SQUID readout (the total resistance of this array should be 1 Ohm). Third, the electron cooling efficiency is increased by a factor of two due to the two-fold increase in the readout for the same power going through the system. Last but not least, the absence of a second SIN tunnel junction suppresses the Coulomb blockade, so the absorber volume can be decreased by a factor of four, leaving the capacitance unchanged.

Therefore, the current responsivity is increased from 40–45 nA/pW to 80–100 nA/pW. Thus, the total NEP for this CEB concept should also be two times better than the total NEP for CEBs with two SIN tunnel junctions and it should be close to the required photon NEP level for the LSPE-SWIPE frequency channels. This comparison for arrays of 66 SINS CEBs with a 6 pW power load is shown in Figure 2 in [12].

For better NEP estimation we should also account for the matching of the CEB array with the SQUID readout system. The mismatching can happen if there is dynamic resistance of the CEB array at the working point with a parasitic resistance of connecting wires higher than 1 Ohm. Then the noise of the SQUID readout system is multiplied by the square root of the ratio of the obtained dynamic resistance of the CEB array and the connecting wires to the required value of 1 Ohm. The NEP estimations for different numbers of CEBs in a parallel array for 145, 210, and 240 GHz frequency channels accounting for possible mismatching with the SQUID readout system are shown below with a SQUID noise of 10 pA/Hz$^{1/2}$.

In Figure 7 and Figure 8 it is seen that the total NEP level (green curves), which includes the NEP of SINS junctions (blue curves) and the NEP of the SQUID readout system (purple curves), nearly approaches the photon NEP level (red line), so the increase in the number of CEBs improves the total NEP. For 200 SINS CEBs of the 240 GHz frequency channel (Figure 9, solid curves), the total NEP curve reaches the photon NEP line at the working point. The minimal value of total NEP in this case is 1.15×10^{-16} W/Hz$^{1/2}$.

These estimations were calculated for an input current noise of the SQUID readout system in the worst case scenario of 10 pA/Hz$^{1/2}$. If this noise is reduced twice (i.e., to 5 pA/Hz$^{1/2}$) the minimal value of the total NEP for 200 SINS CEBs of 240 GHz frequency channel falls below 7×10^{-17} W/Hz$^{1/2}$. In addition, the photon-noise limit can be easily reached for all frequency channels with the use of the Quasiparticle Cascade Amplifier (QCA), which can be added to the SINS CEB. The great benefits of using the QCA are described in detail in [12].

Conclusion

The calculation of the mode composition in the constriction of the LSPE-SWIPE back-to-back horn helps us in modeling the

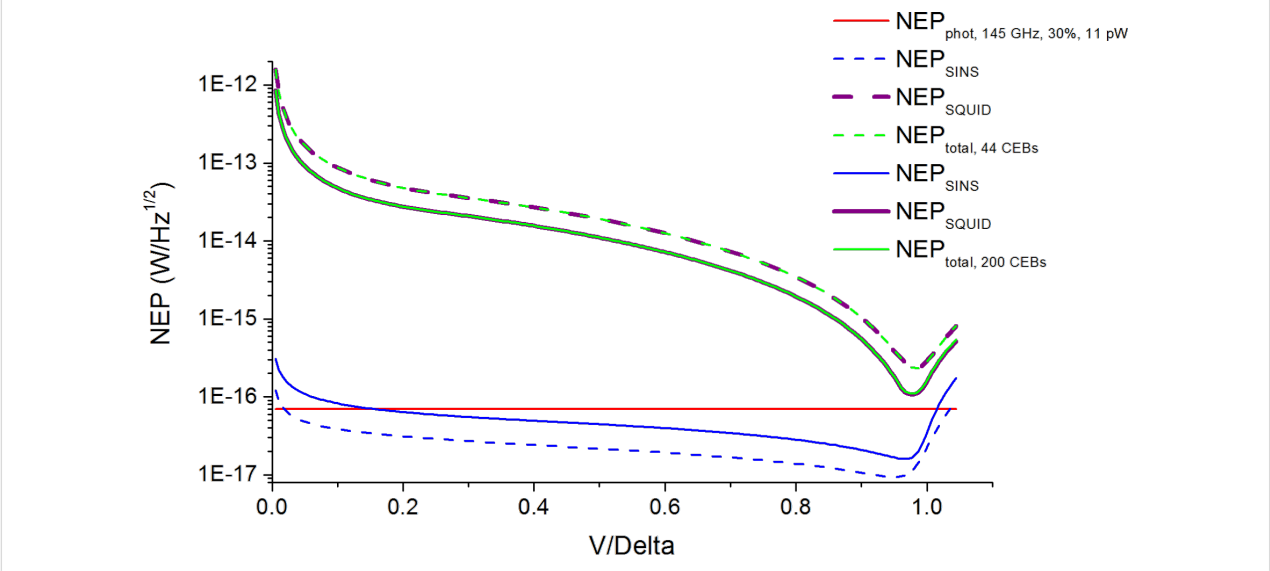

Figure 7: NEP estimations for the 145 GHz channel with 11 pW power load. Dashed curves are for 44 SINS CEBs; solid curves are for 200 SINS CEBs.

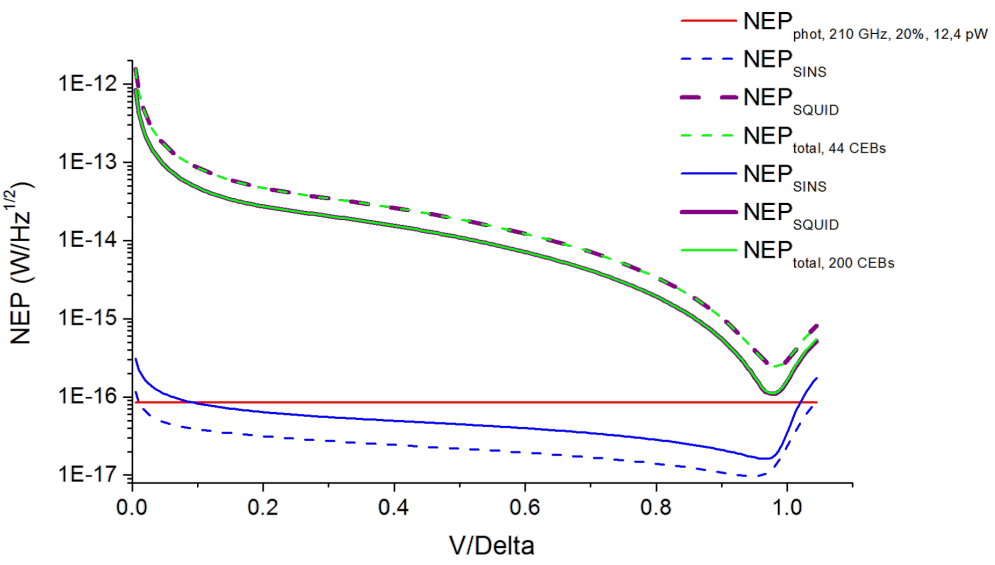

Figure 8: NEP estimations for the 210 GHz channel with 12.4 pW power load. Dashed curves are for 44 SINS CEBs; solid curves are for 200 SINS CEBs.

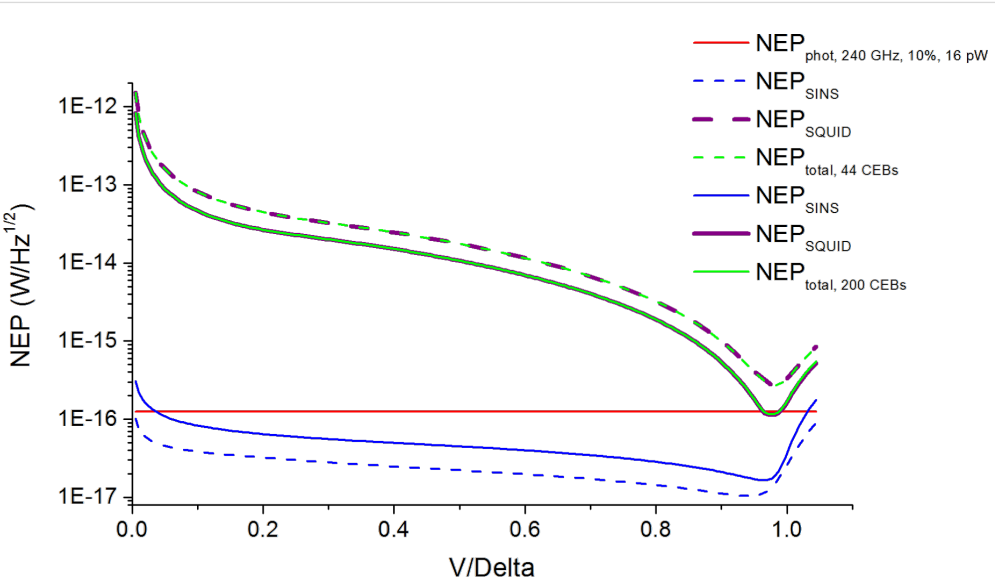

Figure 9: NEP estimations for the 240 GHz channel with 16 pW power load. Dashed curves are for 44 SINS CEBs; solid curves are for 200 SINS CEBs.

frequency response of the receiving systems. We use the calculated mode amplitudes for investigating the frequency response of the arrays of dipole antennas for all frequency channels of the LSPE-SWIPE receiving system.

We have developed a theoretical model of arrays of dipole antennas which can be applicable for all frequency channels of the LSPE-SWIPE. For this purpose, we have used both straight dipole antennas and the bow-tie shaped dipole antennas, which are very useful for meeting the bandwidth requirements for different frequency channels.

To achieve NEP level for photon-noise limited operations, we have performed a very important optimization for cold-electron bolometer design. We changed one of two SIN tunnel junctions to the SN contact, so it became a SINS structure. This change allowed us to increase current responsivity twice and to improve total NEP by the same factor. However, further

improvements can be achieved by the use of the Quasiparticle Cascade Amplifier [12].

Funding

This work has been supported by the Russian Science Foundation (Grant #21-79-20227).

ORCID® iDs

Anton V. Blagodatkin - https://orcid.org/0000-0002-0025-4970
Dmitrii A. Pimanov - https://orcid.org/0000-0002-5323-5642
Ekaterina A. Matrozova - https://orcid.org/0000-0003-1013-1365
Andrey L. Pankratov - https://orcid.org/0000-0003-2661-2745

Preprint

A non-peer-reviewed version of this article has been previously published as a preprint: https://doi.org/10.3762/bxiv.2022.54.v1

References

1. Aiola, S.; Amico, G.; Battaglia, P.; Battistelli, E.; Baù, A.; de Bernardis, P.; Bersanelli, M.; Boscaleri, A.; Cavaliere, F.; Coppolecchia, A.; Cruciani, A.; Cuttaia, F.; D' Addabbo, A.; D' Alessandro, G.; De Gregori, S.; Del Torto, F.; De Petris, M.; Fiorineschi, L.; Franceschet, C.; Franceschi, E.; Gervasi, M.; Goldie, D.; Gregorio, A.; Haynes, V.; Krachmalnicoff, N.; Lamagna, L.; Maffei, B.; Maino, D.; Masi, S.; Mennella, A.; Morgante, G.; Nati, F.; Ng, M. W.; Pagano, L.; Passerini, A.; Peverini, O.; Piacentini, F.; Piccirillo, L.; Pisano, G.; Ricciardi, S.; Rissone, P.; Romeo, G.; Salatino, M.; Sandri, M.; Schillaci, A.; Stringhetti, L.; Tartari, A.; Tascone, R.; Terenzi, L.; Tomasi, M.; Tommasi, E.; Villa, F.; Virone, G.; Withington, S.; Zacchei, A.; Zannoni, M. *Proc. SPIE* **2012,** *8446,* 84467A. doi:10.1117/12.926095
2. Kase, R.; Tsujikawa, S. *J. Cosmol. Astropart. Phys.* **2021,** 008. doi:10.1088/1475-7516/2021/01/008
3. Lamagna, L.; Addamo, G.; Ade, P. A. R.; Baccigalupi, C.; Baldini, A. M.; Battaglia, P. M.; Battistelli, E.; Baù, A.; Bersanelli, M.; Biasotti, M.; Boragno, C.; Boscaleri, A.; Caccianiga, B.; Caprioli, S.; Cavaliere, F.; Cei, F.; Cleary, K. A.; Columbro, F.; Coppi, G.; Coppolecchia, A.; Corsini, D.; Cuttaia, F.; D'Alessandro, G.; de Bernadis, P.; De Gasperis, G.; De Petris, M.; Del Toro, F.; Fafone, V.; Farooqui, Z.; Farsian, F.; Fontanelli, F.; Franceschet, C.; Gaier, T. C.; Gatti, F.; Genova-Santos, R.; Gervasi, M.; Ghigna, T.; Grassi, M.; Grosso, D.; Incardona, F.; Jones, M.; Kangaslahti, P.; Krachmalnicoff, N.; Mainini, R.; Maino, D.; Mandelli, S.; Maris, M.; Masi, S.; Matarrese, S.; May, A.; Mena, P.; Mennella, A.; Molina, R.; Molinari, D.; Morgante, G.; Nati, F.; Natoli, P.; Pagano, L.; Paiella, A.; Paonessa, F.; Passerini, A.; Perez-de-Taoro, M.; Peverini, O. A.; Pezzotta, F.; Piacentini, F.; Piccirillo, L.; Pisano, G.; Polastri, L.; Polenta, G.; Poletti, D.; Presta, G.; Realini, S.; Reyes, N.; Rocchi, A.; Rubino-Martin, J. A.; Sandri, M.; Sartor, S.; Schillaci, A.; Signorelli, G.; Soria, M.; Spinella, F.; Tapia, V.; Tartari, A.; Taylor, A.; Terenzi, L.; Tomasi, M.; Tommasi, E.; Tucker, C.; Vaccaro, D.; Vigano, D. M.; Villa, F.; Virone, G.; Vittorio, N.; Volpe, A.; Watkins, B.; Zacchei, A.; Zannoni, M. *J. Low Temp. Phys.* **2020,** *200,* 374–383. doi:10.1007/s10909-020-02454-x
4. Masi, S.; de Bernardis, P.; Paiella, A.; Piacentini, F.; Lamagna, L.; Coppolecchia, A.; Ade, P. A. R.; Battistelli, E. S.; Castellano, M. G.; Colantoni, I.; Columbro, F.; D'Alessandro, G.; De Petris, M.; Gordon, S.; Magneville, C.; Mauskopf, P.; Pettinari, G.; Pisano, G.; Polenta, G.; Presta, G.; Tommasi, E.; Tucker, C.; Vdovin, V.; Volpe, A.; Yvon, D. *J. Cosmol. Astropart. Phys.* **2019,** 003. doi:10.1088/1475-7516/2019/07/003
5. Kuzmin, L. Optimization of the Hot-Electron Bolometer and A Cascade Quasiparticle Amplifier for Space Astronomy. In *International Workshop on Superconducting Nano-Electronics Devices;* Pekola, J.; Ruggiero, B.; Silvestrini, P., Eds.; Springer: Boston, MA, USA, 2002; pp 145–154. doi:10.1007/978-1-4615-0737-6_16
6. Kuzmin, L. S.; Pankratov, A. L.; Gordeeva, A. V.; Zbrozhek, V. O.; Shamporov, V. A.; Revin, L. S.; Blagodatkin, A. V.; Masi, S.; de Bernardis, P. *Commun. Phys.* **2019,** *2,* 104. doi:10.1038/s42005-019-0206-9
7. Gordeeva, A. V.; Zbrozhek, V. O.; Pankratov, A. L.; Revin, L. S.; Shamporov, V. A.; Gunbina, A. A.; Kuzmin, L. S. *Appl. Phys. Lett.* **2017,** *110,* 162603. doi:10.1063/1.4982031
8. Gordeeva, A. V.; Pankratov, A. L.; Pugach, N. G.; Vasenko, A. S.; Zbrozhek, V. O.; Blagodatkin, A. V.; Pimanov, D. A.; Kuzmin, L. S. *Sci. Rep.* **2020,** *10,* 21961. doi:10.1038/s41598-020-78869-z
9. Salatino, M.; de Bernardis, P.; Kuzmin, L. S.; Mahashabde, S.; Masi, S. *J. Low Temp. Phys.* **2014,** *176,* 323–330. doi:10.1007/s10909-013-1057-5
10. Kuzmin, L. S.; Blagodatkin, A. V.; Mukhin, A. S.; Pimanov, D. A.; Zbrozhek, V. O.; Gordeeva, A. V.; Pankratov, A. L.; Chiginev, A. V. *Supercond. Sci. Technol.* **2019,** *32,* 035009. doi:10.1088/1361-6668/aafeba
11. Heinz, E.; Zakosarenko, V.; May, T.; Meyer, H. G. *Supercond. Sci. Technol.* **2013,** *26,* 045013. doi:10.1088/0953-2048/26/4/045013
12. Kuzmin, L.; Golubev, D. S. *IEEE Trans. Appl. Supercond.* **2022,** *32,* 2300205. doi:10.1109/tasc.2022.3148683

License and Terms

BEILSTEIN JOURNAL OF NANOTECHNOLOGY

Efficiency of electron cooling in cold-electron bolometers with traps

Dmitrii A. Pimanov[1,2], Vladimir A. Frost[1,§], Anton V. Blagodatkin[1,3], Anna V. Gordeeva[1,3], Andrey L. Pankratov[*1,3] and Leonid S. Kuzmin[1,2,§]

Full Research Paper

Open Access

Address:
[1]Nizhny Novgorod State Technical University, Nizhny Novgorod, Minin Street, 24, 603950, Russia, [2]Chalmers University of Technology, Department of Microtechnology and Nanoscience – MC2, Gothenburg, SE-412 96, Sweden and [3]Institute for Physics of Microstructures of the Russian Academy of Sciences, GSP-105, Nizhny Novgorod, 603950, Russia

Email:
Andrey L. Pankratov[*] - alp@ipmras.ru

* Corresponding author
§ deceased

Keywords:
CEB; cold-electron bolometer; electron cooling; noise equivalent power; responsivity

Beilstein J. Nanotechnol. **2022,** *13,* 896–901.
https://doi.org/10.3762/bjnano.13.80

Received: 09 June 2022
Accepted: 11 August 2022
Published: 07 September 2022

This article is part of the thematic issue "Intrinsic Josephson effect and prospects of superconducting spintronics".

Guest Editor: A. S. Sidorenko

Abstract

Electron on-chip cooling from the base temperature of 300 mK is very important for highly sensitive detectors operating in space due to problems of dilution fridges at low gravity. Electron cooling is also important for ground-based telescopes equipped with ^{3}He cryostats being able to function at any operating angle. This work is aimed at the investigation of electron cooling in the low-temperature range. New samples of cold-electron bolometers with traps and hybrid superconducting/ferromagnetic absorbers have shown a temperature reduction of the electrons in the refrigerator junctions from 300 to 82 mK, from 200 to 33 mK, and from 100 to 25 mK in the idle regime without optical power load. The electron temperature was determined by solving heat balance equations with account of the leakage current, sixth power of temperature in the whole temperature range, and the Andreev current using numerical methods and an automatic fit algorithm.

Introduction

Cooling is a key feature to improve the sensitivity of any receiver. Reliable dilution refrigerators providing temperatures below 100 mK have not yet been implemented for operation in space under zero gravity. But ^{3}He cryostats, which provide temperatures down to 250 mK, are widely used for space missions. Another advantage of ^{3}He refrigerators in comparison to dilutions ones is the possibility to work at any operating angle, which is important for ground-based telescopes. Hence, it is an

important task to cool down the detector as much as possible, in a different way than by just a refrigerator. One of the possible solutions of the problem is the on-chip electron cooling, which creates a drain of thermal energy from small detecting elements with the help of tunneling electrons.

Cold-electron bolometers (CEBs) [1-3] have high potential to improve the electron cooling efficiency. This concept is based on negative electrothermal feedback for an incoming signal, which is due to the direct electron cooling of the absorber by the normal metal–insulator–superconductor (NIS) tunnel junctions. Recently, in receivers with cold-electron bolometers [4-6], electron cooling from 300 to 65 mK in the idle mode without optical power load has been shown by our group [7]. Several other research groups also work in the field of electron cooling [8-13]. At present, both systems with single-stage [8-11] and double-stage [12] cooling are being used, as well as hybrid structures with graphene [13]. However, all these experiments were made without useful power load and could not be used for real experiments with detectors. The only experiments with optical power load, demonstrating background-limited operation, were carried out in [5,6,14].

Typical electron cooling in the idle mode is from 300 to 100 mK [11,15]. At low temperatures, electron cooling by a factor of 4.7 has been achieved, cooling from 150 to 32 mK [9] and from 100 to 26 mK [10]. The current record for the electron cooling factor is presented in our previous work [7]. It is 5.3 for cooling from 256 to 48 mK with an unavoidable threshold of 42 mK due to the residual Andreev current. For our measurements, new samples with CEB arrays were deposited, using the equipment of the Center for Quantum Technologies at NNSTU n.a. R.E. Alekseev. These samples have normal metal traps, as well as superconductor/ferromagnet hybrid absorbers based on Al/Fe films, as the previous samples. However, there are different oxidation parameters. This work aims to improve our new fit methodology, which takes into account both leakage and Andreev currents and also uses the sixth power of phonon and electron temperatures.

Results and Discussion

Experimental data fit technique

To determine the electron temperature, the contribution of the Andreev current, as well as the power of black body radiation incoming to the bolometric structure, a program in the programming language C++ has been written. It numerically solves the equations of the stationary CEB theory [16]. We use the approach based on solving the heat balance equation [7]:

$$P_{\mathrm{N}} + P_{e-\mathrm{ph}} + 2P_{\mathrm{cool}} + 2\beta P_{\mathrm{S}} + 2P_{\mathrm{A}} + 2P_{\mathrm{leak}} = 0, \quad (1)$$

where P_{N} is Joule heating in the absorber. $P_{e-\mathrm{ph}} = \Sigma V_{\mathrm{N}}\left(T_{\mathrm{ph}}^6 - T_e^6\right)$ is the heat flux between electron and phonon subsystems, taken with the sixth power [17] due to low electron temperature in our experiments (in our previous calculations we have used the fifth power). Σ is the electron–phonon coupling constant; it has different values, depending on the electron temperature [17]. V_{N} is the absorber volume, P_{cool} is the direct electron cooling power, P_{S} is the net power transferred to the S-electrode, and the coefficient β shows how much of P_{S} comes back to the absorber. $P_{\mathrm{A}} = I_{\mathrm{A}}V$ is the power due to Andreev heating current, V is the voltage drop across the NIS junction, and $P_{\mathrm{leak}} = V^2/R_{\mathrm{leak}}$ is the power associated with the leakage current.

The quasi-particle tunneling current is written as:

$$I_{qp} = \int_{-\infty}^{\infty} \frac{v(\varepsilon)}{eR_{\mathrm{N}}} \cdot \left[\frac{1}{\exp\left(\frac{\varepsilon - eV}{k_{\mathrm{B}}T_{\mathrm{e}}}\right)+1} - \frac{1}{\exp\left(\frac{\varepsilon}{k_{\mathrm{B}}T_{\mathrm{S}}}\right)+1} \right] \mathrm{d}\varepsilon, \quad (2)$$

where V is the NIS junction voltage, T_{e} and T_{s} are the electron temperatures in the normal metal and the superconductor, $v(\varepsilon) = \frac{\varepsilon}{\sqrt{\varepsilon^2 - \Delta^2}}$ is the density of states in the superconductor, Δ is the superconducting gap, and k_{B} is the Boltzmann constant.

Using the integral of the tunneling current through the NIS junction (Equation 2), the electron temperature of an absorber can be obtained [8]. This equation gives correct results if the current consists of a single-particle component only. Otherwise, we have to use a more complex approach based on Equation 1, taking both leakage and Andreev currents into account. These currents may have the same nature, since they both exist due to SN-pinholes in a tunnel barrier. Actually, it is an open question whether these currents are two different components or rather the same current but calculated with different approaches. Here we work with these two currents independently. For the planar geometry at $0 < \varepsilon < \Delta$, the Andreev current is expressed as [7,18]:

$$I_A = -\frac{1}{2eR_{\mathrm{N}}} \int_0^{\Delta} \frac{\Delta d\varepsilon}{\sqrt{\Delta^2 - \varepsilon^2}} \mathrm{Im}(\theta_0) \cdot \left[\begin{array}{c} \tanh\left(\frac{\varepsilon + eV}{2k_{\mathrm{B}}T_{\mathrm{e}}}\right) \\ -\tanh\left(\frac{\varepsilon - eV}{2k_{\mathrm{B}}T_{\mathrm{e}}}\right) \end{array} \right]. \quad (3)$$

The parameterized Green's function,

$$\theta_0 = \frac{2W\Delta}{-ik^2\xi_0^2\sqrt{\Delta^2 - \varepsilon^2} + 2W\varepsilon}, \quad (4)$$

was calculated using the Uzadel equation [19] with Kupriyanov–Lukichev boundary conditions [20], taking into account the decay of a state with a wave vector k due to spin scattering

$$k\xi_0 = \sqrt{\frac{\varepsilon + i/\tau_m}{i\Delta}}. \quad (5)$$

Here, τ_m is the magnetic scattering parameter that is found from the fit. $W = W_0\xi_0/d$ is the effective tunneling parameter for planar tunnel junctions used in our CEB, $W_0 = R(\xi_0)/R_N$ is the tunneling parameter, R_N is the normal resistance of the junction, and $R(\xi_0)$ is the resistance of Al/Fe absorber with the length ξ_0. For aluminium, ξ_0 = 100 nm and, for our samples, d = 14 nm.

Let us take a closer look at the data processing algorithm. The fit program numerically solves the equations of the stationary CEB theory (Equation 1) for a certain set of parameters and material coefficients corresponding to the measured bolometric structure. After the program run, we get the fitted current–voltage characteristics in a numerical form, as well as a set of all parameters that gives the best solution of the equations. In this way, we can determine the parameters of Andreev current and leakage current, as well as the electron temperature, to show the effectiveness of our electron cooling.

Measurements results

The sample OL-G7nn from a new sample series has the same antenna design as in [6,7,21] of a 2D array [22] with four parallel and 48 series connections, and it utilizes the same normal metal traps as in [7]. The current–voltage characteristics of this sample were measured in a Triton 200 dilution cryostat at different phonon temperatures from 100 to 300 mK. According to these characteristics, the electron temperature, as well as the contribution of Andreev and leakage currents, were determined with the use of the heat balance equation (Equation 1). The theoretical current–voltage characteristics show good matching with the experimental ones, as it can be seen in Figure 1a. In Figure 1b we show the plots of differential resistances to demonstrate that the fit agrees well not only for the current–voltage characteristics, but also for its derivatives.

The graphs of the electron temperature of the OL-G7nn sample are shown in Figure 2a for three values of the phonon temperature of 300, 200, and 100 mK. We have started with fitting at 100 mK since Andreev and leakage currents do not change with temperature, and their contribution at lower temperatures becomes more significant, as it is seen in Figure 2b. In particular, the leakage current has been fitted with R_{leak} = 408 MΩ, which was determined from the differential resistance at V = 0 (Figure 1b), W and τ_m are 4.5 × 10^{-5} and 0.8, respectively. After that, we have managed to fit the experimental current–voltage characteristics for 200 and 300 mK with changing only the phonon temperature and Σ, which was 2.25 for 300 mK, 3.35 for 200 mK and 3.57 for 100 mK. The value of Σ depends on the electron temperature [17]. This dependence is clearly seen since the minimal electron temperatures for 100 and 200 mK are quite close, see Figure 2a.

The design of samples C from [7] and OL-G7nn is identical; the only difference is in the normal resistance due to the longer oxidation time of the OL-G7nn sample, which should lead to a thicker tunneling barrier of the NIS junctions and smaller

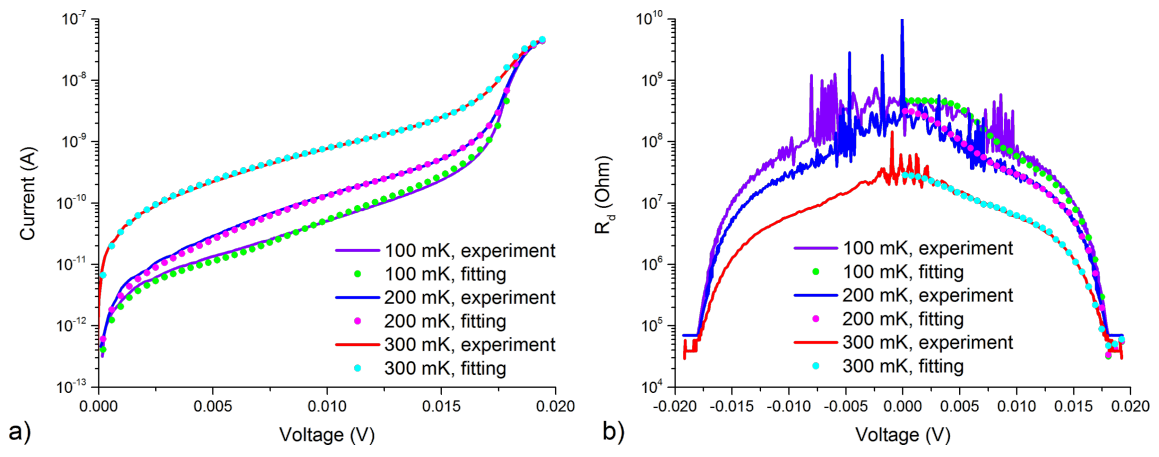

Figure 1: (a) Experimental current–voltage characteristics (solid curves) in comparison with theory (dots) at phonon temperatures of 300, 200, and 100 mK; (b) experimental differential resistances (solid curves) in comparison with theory (dots) at phonon temperatures of 300, 200, and 100 mK.

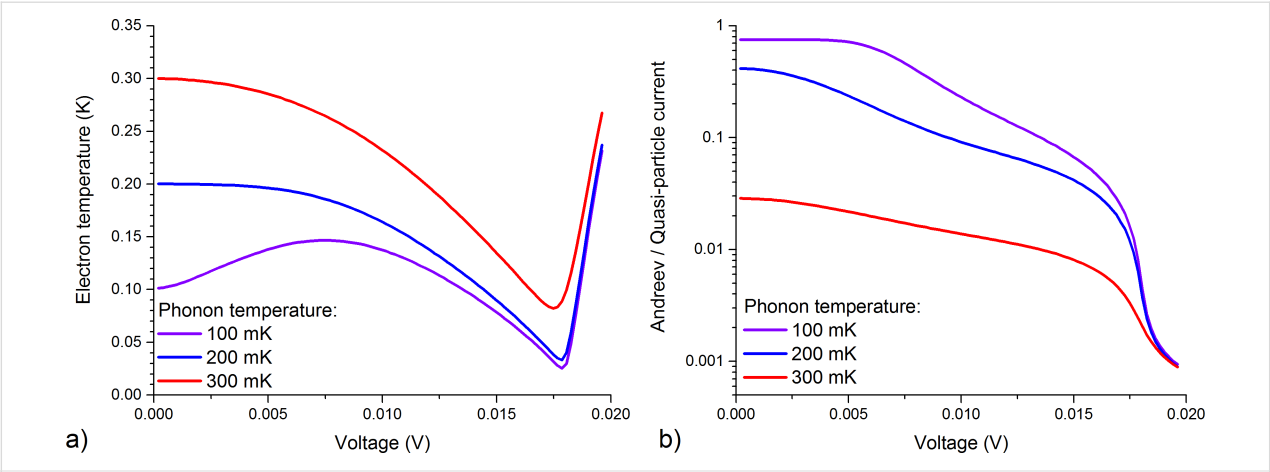

Figure 2: (a) The electron temperature of the absorber determined from the solution of the heat balance equation for sample OL-G7nn; (b) the ratio between Andreev current and quasi-particle current at phonon temperatures of 300, 200, and 100 mK for the same sample.

single-particle and double-particle components of the current. For sample C, the normal resistance per one NIS junction is 1.3 kΩ, and for sample OL-G7nn this resistance is 6.4 kΩ. These differences can be seen in the electron temperature graphs: For the new sample, electron cooling is observed from 300 to 82 mK, from 200 to 33 mK, and from 100 mK to 25 mK. Therefore, cooling from a temperature of 300 mK turned out to be less efficient compared to sample C [7], for which a temperature of 65 mK was achieved. This is related to the smaller transparency of the tunnel barrier (larger resistance) and the corresponding decrease of the single-particle current, which withdraws hot electrons from the absorber. However, due to the lower Andreev heating current, which, when flowing through the normal metal absorber, leads to residual heating and, thus, restricted electron cooling, it was possible to achieve more efficient cooling in the region of low temperatures, that is, down to 25 mK (previously, for sample C, cooling only down to 42 mK was achieved).

The comparison of the sum of the Andreev and leakage currents for sample C from [7] (blue curve) and for sample OL-G7nn (red curve) at a phonon temperature of 200 mK is presented in Figure 3a. It can be seen that, for the new sample, the Andreev and leakage currents are suppressed much stronger, which results in a lower minimal electron temperature down to 33 mK (dashed curves) at 200 mK phonon temperature. Figure 3b shows the ratio of the sum of the Andreev and leakage current components to the quasi-particle current. For the sample OL-G7nn, this sum of currents became lower with respect to the quasi-particle current. But, at the same time, the electron cool-

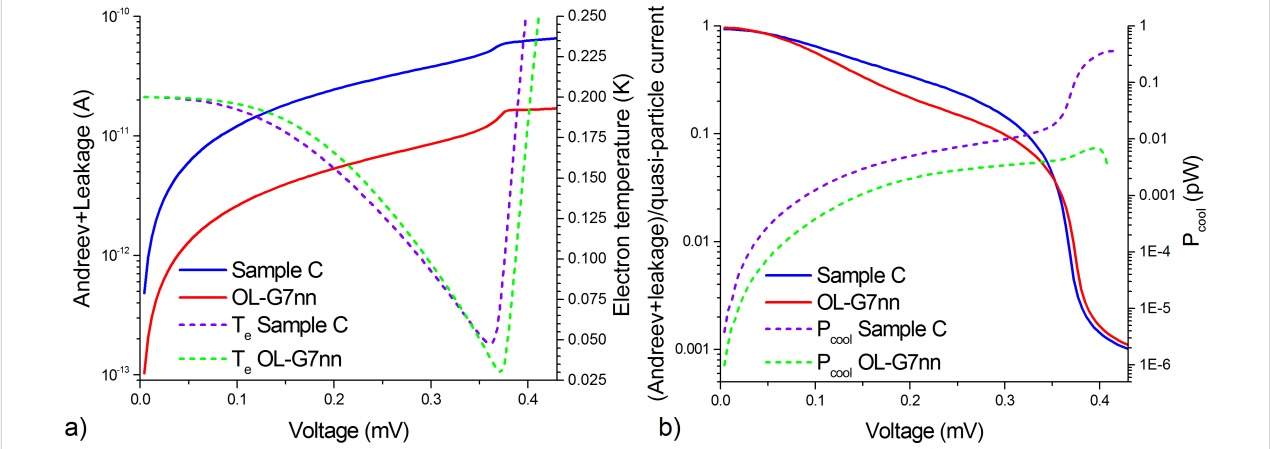

Figure 3: (a) The sum of the Andreev and leakage currents found by solving the heat balance equation for samples C from [7] and OL-G7nn (left axis, solid curves) at 200 mK phonon temperature, recalculated to a single bolometer in the array, and the electron temperatures for samples C and OL-G7nn (right axis, dashed curves); (b) the ratio between the sum of the Andreev and leakage currents and the quasi-particle current of two samples (left axis, solid curves), recalculated to a single bolometer in the array, and the cooling powers for samples C and OL-G7nn (right axis, dashed curves).

ing power (dashed curves) for OL-G7nn is significantly lower, so this sample is not efficient for high background power loads of practical receivers.

Thus, in the future designs of samples, one should select parameters such that the quasi-particle current component remains rather high, but the Andreev and leakage currents are effectively suppressed due to thinner tunneling barriers with higher quality.

Conclusion

Electron cooling is very important for highly sensitive measurements. At modern space applications, it may be the only reliable method to cool down the detector in ^{3}He cryostats to achieve better sensitivity. Cold-electron bolometers are able to show electron self-cooling by a factor of five or even more [7], thus improving sensitivity, so they might be a prospective type of detectors [6].

Although we could not reach a new minimum of electron cooling at 300 mK phonon temperature, we achieved electron cooling from 200 to 33 mK and from 100 to 25 mK due to lower Andreev currents, thus decreasing our previous threshold [7] of 42 mK in the low-temperature range. For a better determination of the parameters, we have improved our fitting algorithm that takes into account both the leakage and Andreev currents and the sixth power of phonon and electron temperatures. The algorithm is able to describe the parameters of the measured sample with high accuracy, as it can be seen from comparison of experimental and theoretical current–voltage characteristics. While the studied sample demonstrates efficient cooling in the low-temperature range, it also shows drawbacks, namely smaller electron cooling power and less efficient electron cooling at 300 mK. Therefore, for practical CEB receivers operating at 300 mK at high power load, the parameters reached in [7] seem to be nearly optimal.

Funding

This work was supported by the Center of Excellence "Center of Photonics" funded by The Ministry of Science and Higher Education of the Russian Federation, contract № 075-15-2022-316.

ORCID® iDs

Dmitrii A. Pimanov - https://orcid.org/0000-0002-5323-5642
Andrey L. Pankratov - https://orcid.org/0000-0003-2661-2745

Preprint

A non-peer-reviewed version of this article has been previously published as a preprint: https://doi.org/10.3762/bxiv.2022.48.v1

References

1. Kuzmin, L. *Proc. SPIE* **2004,** *5498,* 349. doi:10.1117/12.554317
2. Kuzmin, L.; Golubev, D. *Phys. C (Amsterdam, Neth.)* **2002,** *372–376,* 378–382. doi:10.1016/s0921-4534(02)00704-9
3. Kuzmin, L. Optimization of the Hot-Electron Bolometer and A Cascade Quasi-particle Amplifier for Space Astronomy. *International Workshop on Superconducting Nano-Electronics Devices;* Springer: Boston, MA, USA, 2002; pp 145–154. doi:10.1007/978-1-4615-0737-6_16
4. Tarasov, M. A.; Kuzmin, L. S.; Edelman, V. S.; Mahashabde, S.; de Bernardis, P. *IEEE Trans. Appl. Supercond.* **2011,** *21,* 3635–3639. doi:10.1109/tasc.2011.2169793
5. Gordeeva, A. V.; Zbrozhek, V. O.; Pankratov, A. L.; Revin, L. S.; Shamporov, V. A.; Gunbina, A. A.; Kuzmin, L. S. *Appl. Phys. Lett.* **2017,** *110,* 162603. doi:10.1063/1.4982031
6. Kuzmin, L. S.; Pankratov, A. L.; Gordeeva, A. V.; Zbrozhek, V. O.; Shamporov, V. A.; Revin, L. S.; Blagodatkin, A. V.; Masi, S.; de Bernardis, P. *Commun. Phys.* **2019,** *2,* 104. doi:10.1038/s42005-019-0206-9
7. Gordeeva, A. V.; Pankratov, A. L.; Pugach, N. G.; Vasenko, A. S.; Zbrozhek, V. O.; Blagodatkin, A. V.; Pimanov, D. A.; Kuzmin, L. S. *Sci. Rep.* **2020,** *10,* 21961. doi:10.1038/s41598-020-78869-z
8. Rajauria, S.; Gandit, P.; Fournier, T.; Hekking, F. W. J.; Pannetier, B.; Courtois, H. *Phys. Rev. Lett.* **2008,** *100,* 207002. doi:10.1103/physrevlett.100.207002
9. O'Neil, G. C.; Lowell, P. J.; Underwood, J. M.; Ullom, J. N. *Phys. Rev. B* **2012,** *85,* 134504. doi:10.1103/physrevb.85.134504
10. Lowell, P. J.; O'Neil, G. C.; Underwood, J. M.; Zhang, X.; Ullom, J. N. *J. Low Temp. Phys.* **2014,** *176,* 1062–1068. doi:10.1007/s10909-013-1009-0
11. Nguyen, H. Q.; Meschke, M.; Courtois, H.; Pekola, J. P. *Phys. Rev. Appl.* **2014,** *2,* 054001. doi:10.1103/physrevapplied.2.054001
12. Nguyen, H. Q.; Peltonen, J. T.; Meschke, M.; Pekola, J. P. *Phys. Rev. Appl.* **2016,** *6,* 054011. doi:10.1103/physrevapplied.6.054011
13. Vischi, F.; Carrega, M.; Braggio, A.; Paolucci, F.; Bianco, F.; Roddaro, S.; Giazotto, F. *Phys. Rev. Appl.* **2020,** *13,* 054006. doi:10.1103/physrevapplied.13.054006
14. Brien, T. L. R.; Ade, P. A. R.; Barry, P. S.; Dunscombe, C. J.; Leadley, D. R.; Morozov, D. V.; Myronov, M.; Parker, E. H. C.; Prest, M. J.; Prunnila, M.; Sudiwala, R. V.; Whall, T. E.; Mauskopf, P. D. *J. Low Temp. Phys.* **2016,** *184,* 231–237. doi:10.1007/s10909-016-1569-x
15. Kuzmin, L.; Agulo, I.; Fominsky, M.; Savin, A.; Tarasov, M. *Supercond. Sci. Technol.* **2004,** *17,* S400–S405. doi:10.1088/0953-2048/17/5/062
16. Golubev, D.; Kuzmin, L. *J. Appl. Phys.* **2001,** *89,* 6464–6472. doi:10.1063/1.1351002
17. Underwood, J. M.; Lowell, P. J.; O'Neil, G. C.; Ullom, J. N. *Phys. Rev. Lett.* **2011,** *107,* 255504. doi:10.1103/physrevlett.107.255504
18. Vasenko, A. S.; Bezuglyi, E. V.; Courtois, H.; Hekking, F. W. J. *Phys. Rev. B* **2010,** *81,* 094513. doi:10.1103/physrevb.81.094513
19. Vasenko, A. S.; Hekking, F. W. J. *J. Low Temp. Phys.* **2009,** *154,* 221–232. doi:10.1007/s10909-009-9869-z
20. Kuprianov, M. Yu.; Lukichev, V. F. *Sov. Phys. - JETP* **1988,** *67,* 1163–1168.

21. Matrozova, E. A.; Pankratov, A. L.; Gordeeva, A. V.; Chiginev, A. V.; Kuzmin, L. S. *Supercond. Sci. Technol.* **2019,** *32,* 084001. doi:10.1088/1361-6668/ab151d
22. Kuzmin, L. S. *Nanoscale Res. Lett.* **2012,** *7,* 224. doi:10.1186/1556-276x-7-224

License and Terms

BEILSTEIN JOURNAL OF NANOTECHNOLOGY

Nonlinear features of the superconductor–ferromagnet–superconductor φ_0 Josephson junction in the ferromagnetic resonance region

Aliasghar Janalizadeh[1], Ilhom R. Rahmonov[2,3,4], Sara A. Abdelmoneim[5], Yury M. Shukrinov[*2,3,4] and Mohammad R. Kolahchi[1]

Full Research Paper

Open Access

Address:
[1]Department of Physics, Institute for Advanced Studies in Basic Sciences (IASBS), P.O. Box 45137-66731, Zanjan, Iran, [2]BLTP, JINR, Dubna, Moscow Region, 141980, Russia, [3]Dubna State University, Dubna, 141980, Russia, [4]Moscow Institute of Physics and Technology, Dolgoprudny, 141700, Moscow Region, Russia and [5]Physics Department, Menofiya University, Faculty of Science, 32511, Shebin Elkom, Egypt

Email:
Yury M. Shukrinov[*] - shukrinv@theor.jinr.ru

* Corresponding author

Keywords:
Duffing oscillator; Josephson junction; Landau–Lifshitz–Gilbert equation

Beilstein J. Nanotechnol. **2022,** *13,* 1155–1166.
https://doi.org/10.3762/bjnano.13.97

Received: 28 June 2022
Accepted: 26 September 2022
Published: 21 October 2022

This article is part of the thematic issue "Intrinsic Josephson effect and prospects of superconducting spintronics".

Guest Editor: A. S. Sidorenko

Abstract

We demonstrate the manifestations of nonlinear features in magnetic dynamics and *I*–*V* characteristics of a φ_0 Josephson junction in the ferromagnetic resonance region. We show that at small values of the system parameters damping, spin–orbit interaction, and Josephson-to-magnetic energy ratio, the magnetic dynamics is reduced to the dynamics of a scalar Duffing oscillator driven by the Josephson oscillations. The role of the increasing superconducting current in the resonance region is clarified. Shifting of the ferromagnetic resonant frequency and the reversal of its damping dependence due to nonlinearity are demonstrated by the full Landau–Lifshitz–Gilbert–Josephson system of equations and in its different approximations. Finally, we demonstrate the negative differential resistance in the *I*–*V* characteristics and its correlation with the fold-over effect.

Introduction

The coupling of the superconducting phase difference with the magnetic moment of a ferromagnet in a φ_0 junction leads to a number of unique features important for superconducting spintronics and modern information technology [1-5]. It allows one to control the magnetization precession by the superconducting current and affects the current–voltage (*I*–*V*) characteristics by

magnetic dynamics in the ferromagnet, in particular, to create a DC component in the superconducting current [6-8]. A remarkable manifestation of this coupling is the possibility to stimulate a magnetization reversal in the ferromagnetic layer by applying a current pulse through the φ_0 junction [3,9-13].

There are two features of Josephson junctions that come into play in our study. The first one is the broken inversion symmetry in the weak link of the Josephson junction when the link is magnetic, which introduces an extra phase in the current–phase relation, preventing it from being antisymmetric. Such Josephson junctions are named φ_0 junctions [1], and examples, such as MnSi and FeGe, exist. The second one is the nonlinear property of the system, which makes for an anomalous resonance behavior [14].

We couple such a Josephson junction to the model that describes the magnetodynamics in thin films or heterostructures to form the Landau–Lifshitz–Gilbert–Josephson model (LLGJ) [14-16]. It is shown that, for a particular set of parameters, the coupled equations reduce to the dynamics of a Duffing oscillator [14]. The cubic nonlinearity in this oscillator describes several effects in other models, too [17]. One example are the resonance effects in the antiferromagnetic bimeron in response to an alternating current, which has applications in the detection of weak signals [15,18,19].

The Gilbert damping term is added phenomenologically to the Landau–Lifshitz model to reproduce the damping of the precessing magnetic moment. Gilbert damping is also important in modeling other resonance features, as its temperature dependence affects them [20,21], and, in turn, in the superconducting correlations that affect it [22]. The magnetization precession in an ultrathin $Co_{20}Fe_{60}B_{20}$ layer stimulated by microwave voltage under a large angle requires modeling by a Duffing oscillator, too. This is aided by the so-called fold-over features, again due to nonlinearity [16,23,24].

The consequences of the nonlinear nature of the coupled set of the LLGJ system of equations in the weak coupling regime was demonstrated recently in [14]. We showed that, in this regime where the Josephson energy is small compared to the magnetic energy, the φ_0 Josephson junction is equivalently described by a scalar nonlinear Duffing equation. An anomalous dependence of the ferromagnetic resonant frequency (FMR) on the increase of the Gilbert damping was found. We showed that the damped precession of the magnetic moment is dynamically driven by the Josephson supercurrent and the resonance behavior is given by the Duffing spring. The obtained results were based on numerical simulations. The role of the DC superconducting current and the state with negative differential resistance (NDR) in the I–V characteristics were not clarified. Also, the effects of the Josephson-to-magnetic energy ratio and the spin–orbit coupling (SOC) were not investigated at that time.

In the present paper, we study the nonlinear aspects of the magnetic dynamics and I–V characteristics of the φ_0 Josephson junction in the ferromagnetic resonance region. We compare description of the anomalous damping dependence (ADD) exhibited by full LLGJ system of equations with approximated equations and demonstrate the Duffing oscillator features in the small parameter regime. Effects of the Josephson-to-magnetic energy ratio, and the spin–orbit coupling on the ADD, referred to earlier as the α-effect [14] are demonstrated. By deriving the formula that couples the DC superconducting current and maximal amplitude of magnetization we discuss the correlation of superconducting current and the negative differential resistance in the resonance region. Finally, we discuss the experimentally important features by emphasizing the details of the magnetization dynamics and the I–V characteristics of the φ_0 junction.

We have shown that, in the limit of small values for the system parameters Josephson-to-magnetic energy ratio G, damping α, and spin–orbit coupling r, the dynamics is given by a Duffing spring [14]. We focus on the shift in resonance and the effects of nonlinear interactions. We give semi-analytic models to explain our results in various limits.

The paper is organized as follows. In section “Models and Method” we outline the theoretical model and discuss the methods of calculations. The ferromagnetic resonance and the effect of the system parameters on the anomalous damping dependence are considered in subsection A of section “Results and Discussion”. In subsection B we present an analytical description of the dynamics and I–V characteristics of the φ_0 junction at small system parameters. The manifestation of negative differential resistance in the I–V characteristics through the fold-over effect is discussed. We compare the description of the anomalous damping dependence by the full LLGJ system of equations with approximated equations and show how the Duffing oscillator captures the nonlinearities in the regime of parameters with small values in subsection C. We present results on the critical damping and derive a formula that couples the DC superconducting current and the maximal amplitude of magnetization in the ferromagnetic layer. The section “Conclusion” concludes the paper.

Models and Method

The following section is closely related to our work in [13]. The φ_0 junction [6,12,25] that we study is shown in Figure 1. The current–phase relation in the φ_0 junction has the form

$I_s = I_c\sin(\varphi - \varphi_0)$, where $\varphi_0 = rM_y/M_0$, M_y denotes the component of magnetic moment in the $\hat{y}$ direction and M_0 is the modulus of the magnetization. The physics of φ_0 Josephson juncton is determined by a system of equations, which consists of the Landau–Lifshitz–Gilbert (LLG) model, the resistively capacitively shunted junction (RCSJ) model expression with the current–phase relation (I_s) described above, and the Josephson relation between phase difference and voltage.

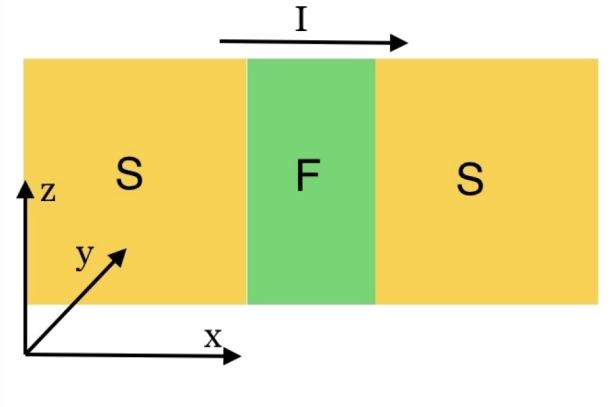

Figure 1: Schematic view of a SFS φ_0 Josephson junction. The external current is applied along the *x* direction. The ferromagnetic easy axis is along *z* direction.

The dynamics of the magnetic moment **M** is described by the LLG equation [26]:

$$\frac{\mathrm{d}\mathbf{M}}{\mathrm{d}t} = -\gamma\mathbf{M}\times\mathbf{H}_{\mathrm{eff}} + \frac{\alpha}{M_0}\left(\mathbf{M}\times\frac{\mathrm{d}\mathbf{M}}{\mathrm{d}t}\right), \tag{1}$$

where **M** is the magnetization vector, γ is the gyromagnetic relation, $\mathbf{H}_{\mathrm{eff}}$ is the effective magnetic field, α is the Gilbert damping parameter, and $M_0 = |\mathbf{M}|$.

In order to find the expression for the effective magnetic field we have used the model developed in [6], where it is assumed that the gradient of the spin–orbit potential is along the easy axis of magnetization taken to be along $\hat{z}$. In this case the total energy of the system can be written as

$$E_{\mathrm{tot}} = -\frac{\Phi_0}{2\pi}\varphi I + E_{\mathrm{s}}(\varphi,\varphi_0) + E_{\mathrm{M}}(\varphi_0), \tag{2}$$

where φ is the phase difference between the superconductors across the junction, I is the external current, $E_s(\varphi,\varphi_0) = E_J[1 - \cos(\varphi - \varphi_0)]$, and $E_J = \Phi_0 I_c/2\pi$ is the Josephson energy. Here Φ_0 is the flux quantum, I_c is the critical current, $r = l\upsilon_{so}/\upsilon_F$, $l = 4hL/\hbar\upsilon_F$, L is the length of the ferromagnetic (F) layer, h is the exchange field of the F layer, $E_M = -K\mathcal{V}M_z^2/\left(2M_0^2\right)$, the parameter υ_{so}/υ_F characterizes a relative strength of spin–orbit interaction, K is the anisotropic constant, and $\mathcal{V}$ is the volume of the F layer.

The effective field for LLG equation is determined by

$$\begin{aligned}\mathbf{H}_{\mathrm{eff}} &= -\frac{1}{V}\frac{\partial E_{\mathrm{tot}}}{\partial\mathbf{M}} \\ &= \frac{\Omega_F}{\gamma}\left[Gr\sin\left(\varphi - r\frac{M_y}{M_0}\right)\hat{\mathbf{y}} + \frac{M_z}{M_0}\hat{\mathbf{z}}\right],\end{aligned} \tag{3}$$

where $\Omega_F = \gamma K/M_0$ is the frequency of the ferromagnetic resonance and $G = E_J/(K\mathcal{V})$ determines the ratio between Josephson energy and magnetic energy.

In order to describe the full dynamics of the φ_0 junction the LLG equations should be supplemented by the equation for the phase difference φ, that is, the equations of the RCSJ model for bias current and the Josephson relation for voltage. According to the extended RCSJ model, which takes into account derivative of φ_0 phase shift, the current flowing through the system in underdamped case is determined by

$$\begin{aligned}I = \frac{\hbar C}{2e}\frac{\mathrm{d}^2\varphi}{\mathrm{d}t^2} + \frac{\hbar}{2eR}\left[\frac{\mathrm{d}\varphi}{\mathrm{d}t} - \frac{r}{M_0}\frac{\mathrm{d}M_y}{\mathrm{d}t}\right] \\ + I_c\sin\left(\varphi - \frac{r}{M_0}M_y\right),\end{aligned} \tag{4}$$

where I is the bias current and C and R are capacitance and resistance of the Josephson junction, respectively. The Josephson relation for the voltage is given by

$$\frac{\hbar}{2e}\frac{\mathrm{d}\varphi}{\mathrm{d}t} = V. \tag{5}$$

We note that, in the framework of the RCSJ model, the displacement current is proportional to the first derivative of the voltage (or the second derivative of the phase difference). The magnetization dynamics plays the role of an external force, and the first order derivative of φ_0 is a source of an external current in the JJ. This was demonstrated in [25,27], where the authors included the first derivative of φ_0 as the source of the electromotive force. The voltage is determined by the phase difference and does not depend on φ_0. From this point of view, in the framework of the RCSJ model, the external current source cannot modify the expression for the displacement current. This is why we do not include the second derivative of φ_0 in our model.

Using Equation 1, Equation 3, Equation 4, and Equation 5 we can write a system of equations, in normalised variables, that describes the dynamics of the φ_0 junction:

$$\begin{aligned}
\dot{m}_x &= \frac{\omega_F}{1+\alpha^2}\left\{-m_y m_z + Grm_z \sin\left(\varphi - rm_y\right)\right. \\
&\left. -\alpha\left[m_x m_z^2 + Grm_x m_y \sin\left(\varphi - rm_y\right)\right]\right\}, \\
\dot{m}_y &= \frac{\omega_F}{1+\alpha^2}\left\{m_x m_z\right. \\
&\left. -\alpha\left[m_y m_z^2 - Gr\left(m_z^2 + m_x^2\right)\sin\left(\varphi - rm_y\right)\right]\right\}, \\
\dot{m}_z &= \frac{\omega_F}{1+\alpha^2}\left\{-Grm_x \sin\left(\varphi - rm_y\right)\right. \\
&\left. -\alpha\left[Grm_y m_z \sin\left(\varphi - rm_y\right) - m_z\left(m_x^2 + m_y^2\right)\right]\right\}, \\
\dot{V} &= \frac{1}{\beta_c}\left[I - V + r\dot{m}_y - \sin\left(\varphi - rm_y\right)\right], \\
\dot{\varphi} &= V
\end{aligned} \tag{6}$$

where $m_{x,y,z} = M_{x,y,z}/M_0$ and satisfy the constraint $\sum_{i=x,y,z} m_i^2(t) = 1$ and $\beta_c = 2eI_cCR^2/\hbar$ is the McCumber parameter. In order to use the same time scale in the LLG and RCSJ equations, in this system of equations we have normalized time to ω_c^{-1}, where $\omega_c = \frac{2eI_cR}{\hbar}$, and $\omega_F = \Omega_F/\omega_c$ is the normalized frequency of ferromagnetic resonance $\Omega_F = \gamma K/M_0$. The bias current is normalized to the critical current I_c and the voltage V is normalized to $V_c = I_cR$. The system in Equation 6 is solved numerically using the fourth-order Runge–Kutta method [14].

Results and Discussion

A. Effect of system parameters on the anomalous damping dependence

ADD of the FMR frequency with increasing α was discussed in [14]. It was found that the resonance curves demonstrate features of a Duffing oscillator, reflecting the nonlinear nature of the LLGJ system of equations. There is a critical damping value at which anomalous dependence comes into play. This critical value depends on the system parameters. Here, we present the details of such a transformation from usual to anomalous dependence with variations in the spin–orbit coupling and the Josephson-to-magnetic energy ratio.

To investigate the effect of damping, we calculate the maximal amplitude of the magnetization component m_y taken at each value of the bias current based on the LLGJ system of equations (Equation 6). In Figure 2 we show the voltage dependence of the maximal amplitude m_y^{max} in the ferromagnetic resonance region at different damping parameters and small values of Josephson-to-magnetic energy ratio, G = 0.05, and spin–orbit coupling, r = 0.05. The ferromagnetic resonance curves exhibit the different forms. An increase in damping shows a nonuniform change in the resonant frequency: It approaches ω_F instead of moving away with increase in α. We emphasize that this happens at small G and r. We consider that such behavior can be explained by the nonlinear nature of the LLGJ system of equations. There is a manifestation of subharmonics of the FMR in Figure 2 at V = 0.25, 0.167, and 0.125.

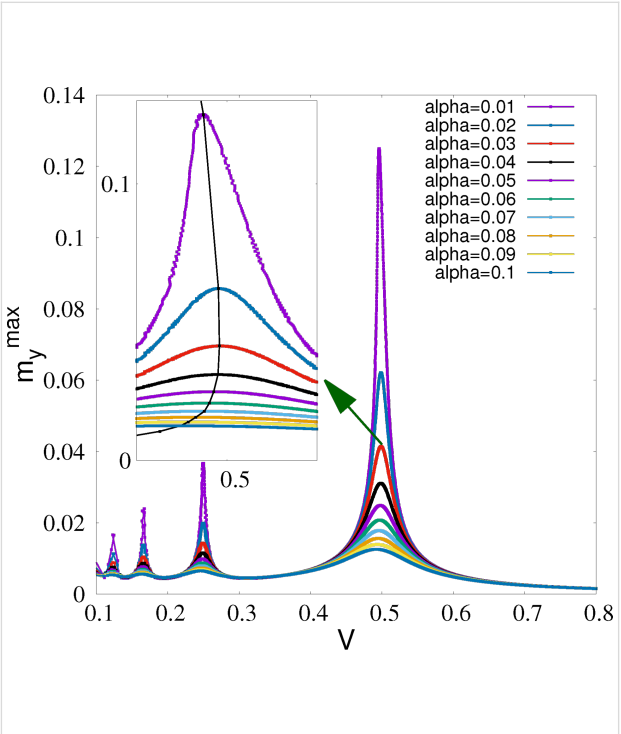

Figure 2: Maximal amplitude of magnetization m_y-component at each value of voltage along the I–V characteristics of the φ_0 junction in the ferromagnetic resonance region for different α. The inset enlarges the main maximum. Parameters: β_c = 25, G = 0.05, r = 0.05, and ω_F = 0.5.

We usually expect the resonance peak to move away from resonance as α increases. Figure 2 shows that this normal effect is accompanied with an anomalous behavior, as can be seen in the inset in this figure, where the resonance peak approaches ω_F as α increases [14].

The manifestation of FMR in the I–V characteristics of the φ_0 junction at three values of the damping parameter is demonstrated in Figure 3. A strong deviation of the I–V curve is observing at α = 0.01, which is a characteristic value for many magnetic materials. This fact indicates that ADD can be observed experimentally by measuring the I–V characteristics in wide interval of the damping parameter.

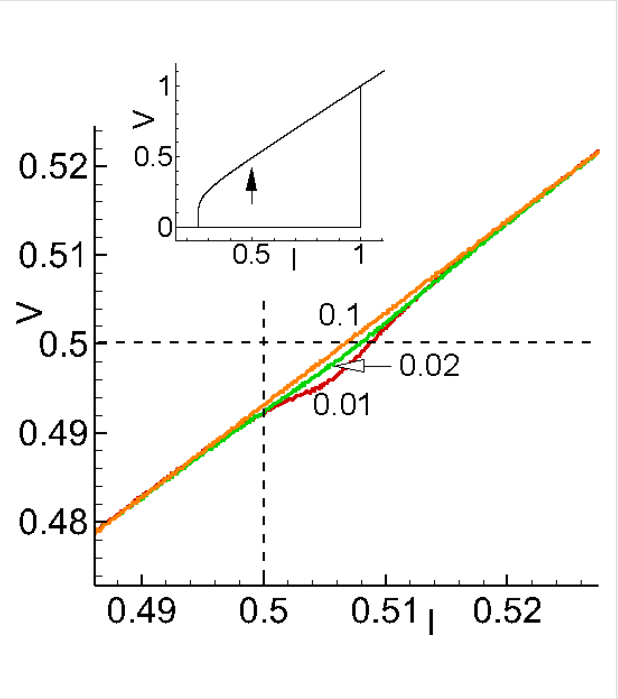

Figure 3: Part of the *I–V* characteristics of the φ_0 junction at $G = 0.05$, $r = 0.05$, and different values of Gilbert damping. The numbers show the α value. The inset shows the total *I–V* characteristics and the arrow indicates the resonance region.

Interesting features of ADD appear through a variation of spin–orbit coupling. As it was demonstrated in [28], an increase in SOC leads to an essential change in *I–V* characteristics and magnetization precession in the ferromagnetic resonance region. The nonlinearity goes stronger and a state with negative differential resistance appears at large SOC.

Figure 4a demonstrates results of numerical simulations of the $m_y^{\max}$ dependence on α at different values of the SOC parameter r.

It shows two specific features of ADD. First, with an increase in r, the critical value of V_{peak} decreases (the curve moves away from ω_F). The second important feature is an increase of α_{crit}, which is indicated by arrows in the figure.

Another model parameter that affects the phenomenon discussed in the present paper is the ratio G between Josephson energy and magnetic energy. Figure 4b demonstrates the results of numerical simulations of the $m_y^{\max}$ dependence on α at different values of G.

Similar to the effect of r, increasing G also causes the value of α_{crit} to increase. By changing the volume of the ferromagnetic layer, the ferromagnetic energy and, consequently, the value of G can be changed [6]. For small values of G, that is, a situation where the magnetic energy is much larger than the Josephson energy, the magnetic layer receives less energy, and its amplitude decreases in the y direction. Also, the maximum value of the oscillation frequency is closer to the magnetic frequency ω_F.

B. Dynamics and *I–V* characteristics of the φ_0 junction at small values of system parameters

As it was discussed in [6,29,30], in the case of G, r and $\alpha \ll 1$, and $m_z \approx 1$, first three equations of the system in Equation 6 can be simplified. Taking into account $\varphi = \omega_J t$ and neglecting quadratic terms of m_x and m_y, we get

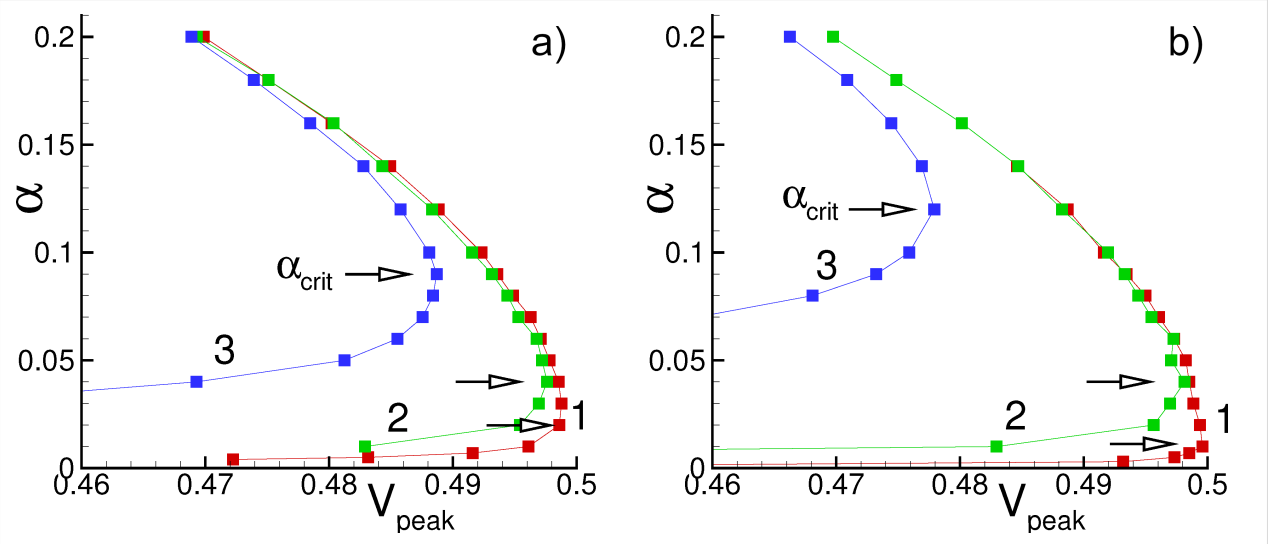

Figure 4: (a) Demonstration of ADD at different values of SOC parameter r at $G = 0.05$. Numbers indicate: 1 – $r = 0.05$; 2 – $r = 0.1$; 3 – $r = 0.5$; Arrows show critical α value, corresponded to the reversal in the α dependence. (b) Demonstration of ADD at different values of the Josephson-to-magnetic energy ratio G at $r = 0.05$. Numbers indicate: 1 – $G = 0.01$; 2 – $G = 0.1$; 3 – $G = 1$.

$$\begin{cases} \dot{m}_x = \omega_F\left[-m_y + Gr\sin\left(\omega_J t\right) - \alpha m_x\right] \\ \dot{m}_y = \omega_F\left[m_x - \alpha m_y\right], \end{cases} \tag{7}$$

This system of equations can be written as the second-order differential equation with respect to m_y,

$$\ddot{m}_y + 2\alpha\omega_F\dot{m}_y + \omega_F^2 m_y = \omega_F^2 Gr\sin\left(\omega_J t\right). \tag{8}$$

The corresponding solution for m_y has the form

$$m_y\left(t\right) = \frac{\omega_+ - \omega_-}{r}\sin\left(\omega_J t\right) - \frac{\gamma_+ - \gamma_-}{r}\cos\left(\omega_J t\right), \tag{9}$$

where

$$\omega_\pm = \frac{Gr^2\omega_F}{2}\frac{\omega_J \pm \omega_F}{\Omega_\pm}, \tag{10}$$

and

$$\gamma_\pm = \frac{Gr^2\omega_F}{2}\frac{\alpha\omega_J}{\Omega_\pm}, \tag{11}$$

with $\Omega_\pm = (\omega_J \pm \omega_F)^2 + (\alpha\omega_J)^2$ (see [6] and the corresponding erratum [31]).

When the Josephson frequency ω_J is approaching the ferromagnetic frequency ω_F, m_y exhibits damped ferromagnetic resonance. The differential resistance in the resonance region decreases, which is manifested in the *I*–*V* characteristics as a resonance branch [7].

Taking into account $rm_y \ll 1$, we rewrite the expression for the superconducting current as

$$\begin{aligned} I_s\left(t\right) &= \sin\left(\omega_J t - r m_y\left(t\right)\right) \\ &= \sin\left(\omega_J t\right) - r m_y\cos\left(\omega_J t\right). \end{aligned} \tag{12}$$

Using Equation 9 we obtain

$$\begin{aligned} I_s\left(t\right) = \sin\left(\omega_J t\right) &- \frac{\omega_+ - \omega_-}{2}\sin\left(2\omega_J t\right) \\ &+ \frac{\gamma_+ + \gamma_-}{2}\cos\left(2\omega_J t\right) + I_0\left(\alpha\right), \end{aligned} \tag{13}$$

where

$$I_0 = \frac{\gamma_+ + \gamma_-}{2}. \tag{14}$$

This superconducting current explains the appearance of the resonance branch in the *I*–*V* characteristics. The generated current I_0 can be expressed through the amplitude of m_y and the SOI parameter r,

$$I_0 = \frac{r}{2}m_y^{\max}\left(\omega_J\right), \tag{15}$$

with $m_y^{\max}(\omega_J)$ being the frequency response of m_y.

At small model parameters $\alpha \ll Gr \ll 1$ of a superconductor-ferromagnet-superconductor (SFS) φ_0 Josephson junction, states with a negative differential resistance appear in the *I*–*V* characteristics in the FMR region. Due to the nonlinearity, the resonance peak is asymmetric. An increase of the nonlinearity leads to bistability (fold-over effect). The question appears if the states with a negative differential resistance are the origin of the fold-over and ADD. In order to clarify this question, we show in Figure 5 a part of the *I*–*V* characteristics of the φ_0 junction together with the *I*–*V* characteristics of a superconductor-insulator-superconductor (SIS) junction in the ferromagnetic resonance region and the numerically calculated superconducting current through the φ_0 junction. The total *I*–*V* characteristics are demonstrated in the inset to this figure.

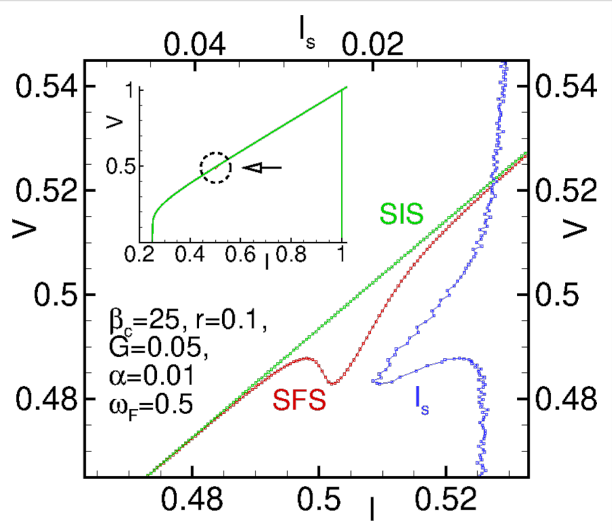

Figure 5: *I*–*V* characteristics of φ_0 and SIS junctions and calculated average superconducting current through the φ_0 junction.

We see the correlation of the fold-over effect in the superconducting current (blue) with the NDR part of the *I*–*V* curve. The

peak in the superconducting current and the minimum of the *I–V* curve are at the same voltage value. So, both effects reflect the nonlinear features of the ferromagnetic resonance in the φ_0 junction. However, in contrast to the fold-over and ADD effects, which begin to appear at relatively small deviations from the linear case, the nonlinearity in case of the NDR plays a more essential role.

We note that, in the resonance region for the considered limit of model parameters, the m_y amplitude is coupled to the value of the superconducting current (see Equation 15). We stress the importance of the performed analysis demonstrating the analytical coupling of time-independent superconducting current and magnetization, reflecting the Duffing oscillator features of the φ_0 junction.

As it is well known, the states with negative differential resistance appear in the *I–V* characteristics of Josephson structures in different physical situations. In particular, nonlinear superconducting structures being driven far from equilibrium exhibit NDR states [32]. The NDR states plays an essential role in applications related to terahertz radiation emission [33]. A detailed explanation of the different types of negative differential resistance in Josephson junctions (i.e., N-shaped and S-shaped) is introduced in [34]. The authors emphasize that the nonlinear behavior of the Josephson junction plays a key role in the NDR feature. In our case, the NDR states appear as a result of the nonlinearity of the system at small values of φ_0 junction parameters, such as SOC, ratio between Josephson energy and magnetic energy, and Gilbert damping. We demonstrate these effects here by presenting results of detailed investigations of the NDR state at different system parameters and discuss the possibility of their control near the ferromagnetic resonance.

Figure 6 shows the effect of the spin–orbit coupling on the *I–V* characteristics at $G = 0.05$ and $\alpha = 0.01$. We see the NDR feature, which is getting more pronounced with an increase in r. A further increase in r leads to a jump down in voltage and then practically linear growth of the *I–V* characteristics.

An interesting question concerns the effect of Gilbert damping. Results of *I–V* characteristics simulations in the resonance region in a certain range of the damping parameter α at $G = 0.05$ and $r = 0.13$ are shown in Figure 7a. In this case, the most pronounced characteristic appears at $\alpha = 0.01$. At $G = 0.05$ and $r = 0.13$, the range of α with pronounced NDR features is $0.01 \leq \alpha < 0.014$.

The maximal amplitude $m_y^{\max}$ as a function of the voltage is shown in Figure 7b. Based on the results presented in Figure 7a and Figure 7b, we came to the important conclusion that the fold-over effect (bistability) and the NDR state have strong correlations and have the same origin related to the nonlinearity at small system parameters.

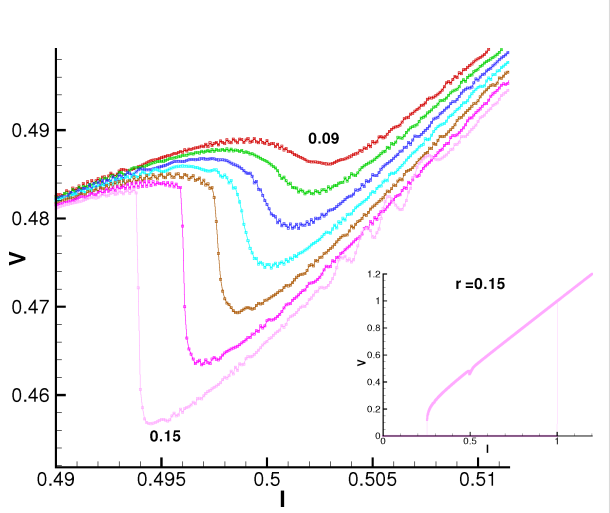

Figure 6: Enlarged parts of the *I–V* curves, in the resonance region at different values of the SOC parameter r, at $\alpha = 0.01$ and $G = 0.05$. The numbers indicate the increase of r from 0.09 to 0.15 with an increment of 0.01. The inset shows the total *I–V* characteristics ar $r = 0.15$.

However, the anomalous damping dependence does not show a one-to-one correlation with either negative differential resistance or fold-over effect. The resonance peak positions of $m_y^{\max}$ in bias current I_{peak} and in voltage V_{peak} as functions of α are demonstrated in Figure 7c. According to our results, we can divide the α interval into two regions (see Figure 7c). Region I includes the values of α where the NDR feature is present, while in region II it disappears. In region II the fold-over effect (bistability) disappears as well, but ADD is realized.

C. Duffing oscillator features of the φ_0 junction and critical damping

The system in Equation 6 is nonlinear and very complex. Hence, in order to provide an analytical study of dynamics of the φ_0 junction, we need to derive an approximated equation for some limited values of model parameters. In [14], it was shown that the resonance curves demonstrate features of a Duffing oscillator, reflecting the nonlinear nature of the LLGJ system of equations. In this section, we present an analytical approach to describe the nonlinear dynamics of the φ_0 junction and compare analytical results obtained from am approximated Duffing equation with numerical simulations of the total system in Equation 6. We show that in the limit of $\alpha \ll G$ and $r \ll 1$, we arrive at the Duffing oscillator. We start with the first three equations of Equation 6 for the magnetization components:

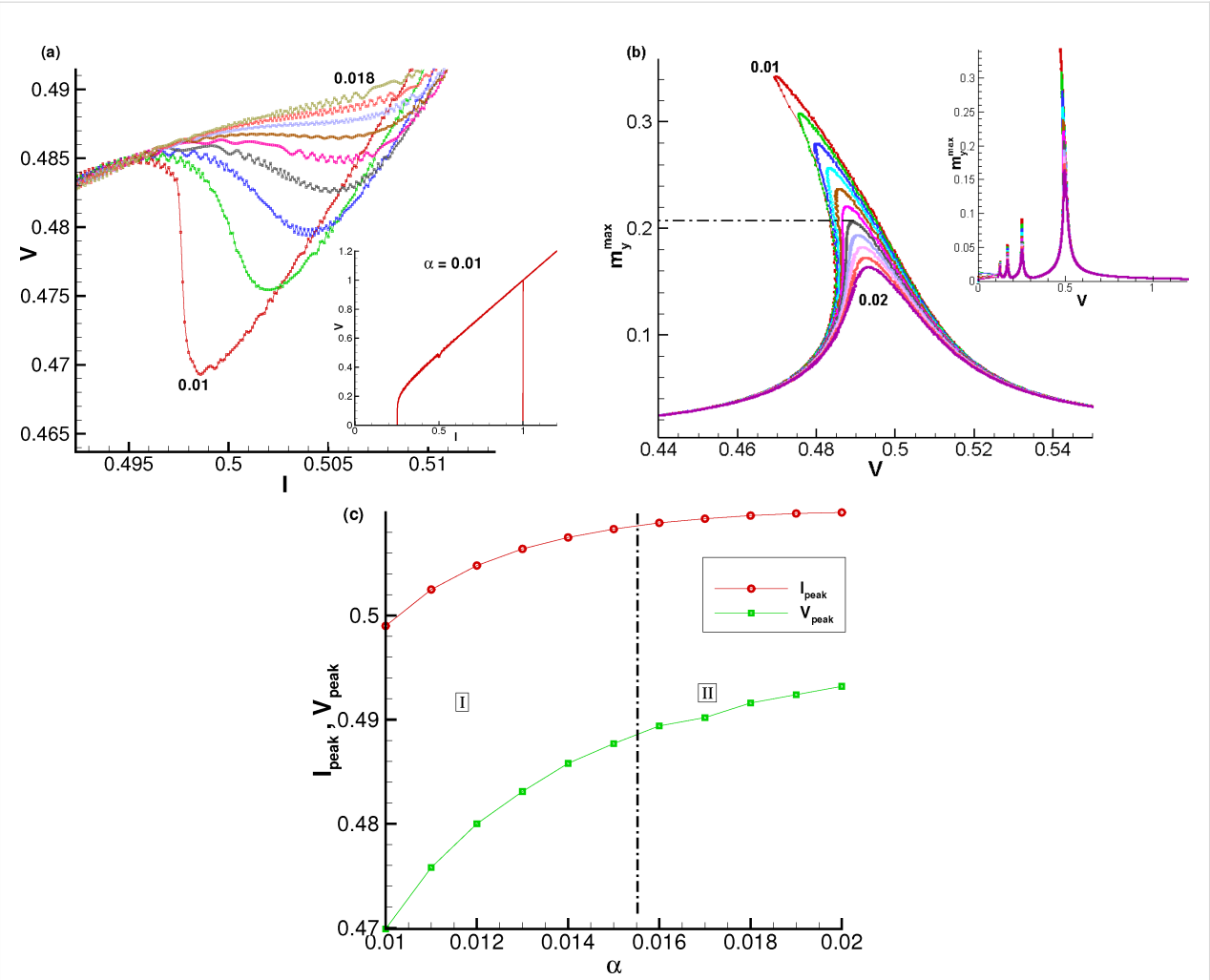

Figure 7: (a) Enlarged parts of the *I*–*V* curves at different values of α. (b) Voltage dependence of m_y^{max} at different α. (c) α-Dependence of the resonance curve maximum in current (I_{peak}) and voltage (V_{peak}). The numbers indicate the value of α from 0.01 to 0.018 in (a) and from 0.01 to 0.02 in (b) by an increment 0.001. Results were obtained at $r = 0.13$ and $G = 0.05$.

$$\begin{aligned}\frac{\dot{m}_x}{\omega_F} &= -m_y m_z + Grm_z \sin\left(\varphi - rm_y\right) - \alpha m_x m_z^2 \\ \frac{\dot{m}_y}{\omega_F} &= m_x m_z - \alpha m_y m_z^2 \\ \frac{\dot{m}_z}{\omega_F} &= -Grm_x \sin\left(\varphi - rm_y\right) + \alpha m_z\left(m_x^2 + m_y^2\right).\end{aligned} \tag{16}$$

Simplifying this system of equations by the same procedure as it was done in [14], we can write equation for m_y as

$$\ddot{m}_y + 2\xi\alpha\dot{m}_y + \xi^2\left(1+\alpha^2\right)m_y - \xi^2\left(1+\alpha^2-\alpha^4\right)m_y^3 = \xi^2 Gr\sin\varphi. \tag{17}$$

Finally, by neglecting the α^2 and α^4 terms, which are much smaller than 1, we come to the well-known Duffing equation,

$$\ddot{m}_y + 2\omega_F\alpha\dot{m}_y + \omega_F^2 m_y - \omega_F^2 m_y^3 = \omega_F^2 Gr\sin\varphi. \tag{18}$$

In the range of small parameter values, this Duffing equation can describe the dynamics of m_y. We will have the full dynamics once we consider the coupling with the Josephson equation,

$$\ddot{\varphi} + \frac{1}{\beta_c}\left[\dot{\varphi} - r\dot{m}_y + \sin\left(\varphi - rm_y\right)\right] = \frac{1}{\beta_c}I. \tag{19}$$

The system of Equation 18 and Equation 19 can replace the LLGJ equations in the limit of G, $r \ll 1$ and G, $r \ll \alpha$.

Taking into account $\varphi = \omega_J t$ we can write the analytically obtained frequency response for Equation 18,

$$\left(m_y^{\max}\right)^2 = \frac{(Gr)^2}{\left[\omega^2 - 1 + \frac{3}{4}\left(m_y^{\max}\right)^2\right]^2 + (2\alpha\omega)^2}, \quad (20)$$

where $\omega = \omega_J/\omega_F$. From Equation 20 we get

$$\left(m_y^{\max}\right)^6 + \frac{8}{3}\left(\omega^2 - 1\right)\left(m_y^{\max}\right)^4 + \left(\frac{4}{3}\right)^2\left[\left(\omega^2 - 1\right)^2 + (2\alpha\omega)^2\right]\left(m_y^{\max}\right)^2 - \left(\frac{4}{3}Gr\right)^2 = 0. \quad (21)$$

This equation allows one to determine analytically the frequency dependence of the $m_y^{\max}$ amplitude. To find it, we solve Equation 21 by the Newton method. Results of the analytical calculations (blue dots), corresponding to Equation 21, and the numerical solution (red dots), corresponding to the full system in Equation 6, are given in Figure 8.

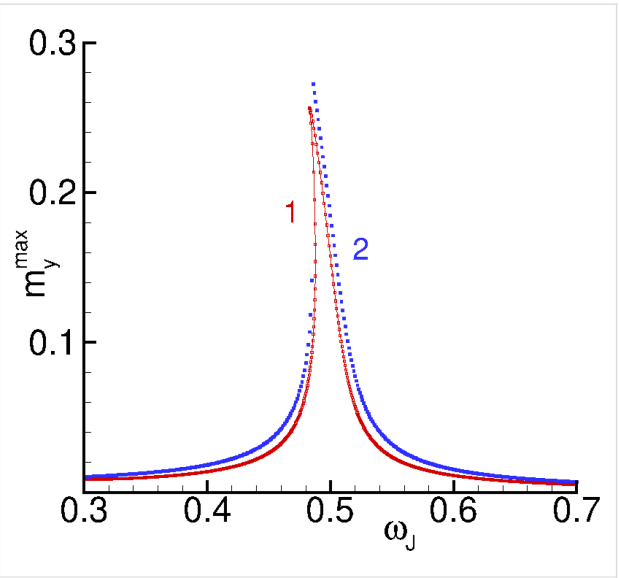

Figure 8: Numerically (red curve) and analytically (blue curve) calculated amplitude dependence of m_y.

We can see that they are close to each other, which proves the correctness of the chosen approximation. Both curves demonstrate an asymmetric resonance peak, which is common for a Duffing oscillator. When the role of the cubic term is getting larger, we observe a bistability of the resonance curve, which is usually called a fold-over effect. Note that the fold-over effect can be also achieved by decreasing the damping. This means that, by decreasing the dissipative term in Equation 18, we can increase the influence of the cubic term in this equation.

The comparison of analytically and numerically calculated superconducting currents as a function of the Josephson frequency is demonstrated in Figure 9. We note that in our normalization $V = \omega_J$.

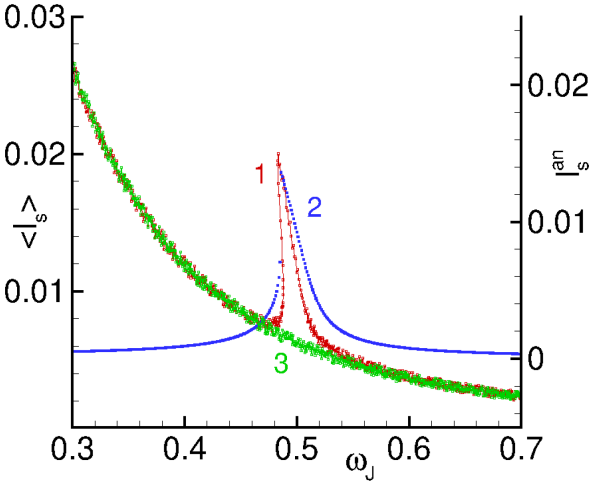

Figure 9: Numerically calculated superconducting current for SFS junction (plot 1) and analytical I_0 (plot 2) and superconducting current for SIS junction (plot 3).

We can see the manifestation of the asymmetric resonance peak in the frequency dependence of the superconducting current. So, the approximated system in Equation 7 reflects one of the main features of a Duffing oscillator.

Figure 10 compares the anomalous damping dependence of the resonance peak of $m_y^{\max}(V)$ calculated numerically according to the full LLGJ system in Equation 6 with the one calculated numerically according to the generalized Duffing model (Equation 17 and Equation 19). We see that in the damping parameter interval [0.001–0.2] the agreement of the dependences is sufficiently good.

Using Equation 18 with $\varphi = \omega_J t$, we can find (see Supporting Information File 1) a relation between the position of the resonance peak in the $m_y^{\max}(V)$ dependence and the damping,

$$\omega_{\text{peak}} = \sqrt{\frac{1-3\alpha^2}{2} + \frac{1}{2}\sqrt{\left(1-\alpha^2\right)^2 - 12\left(\frac{Gr}{4\alpha}\right)^2}}, \quad (22)$$

where $\omega_{\text{peak}} = \frac{\omega_{J,\text{peak}}}{\omega_F}$ determines the position of the resonance peak.

Equation 22 allows one to find the formula for the critical damping α_{crit}, which is an important parameter determining the

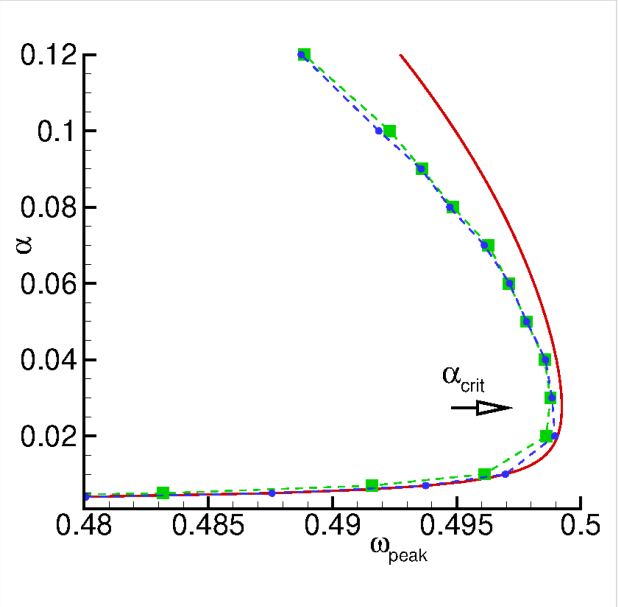

Figure 10: The dependence of the resonance maximum of $m_y^{max}(V)$ on α in the damping parameter interval [0.001–0.12]. Green squares show results calculated numerically according to the full system in Equation 6, blue circles show results calculated numerically according to the generalized Duffing and Josephson equations (Equation 17 and Equation 19). The dashed line connects the symbols to guide the eyes. The solid line show the analytical dependence on α calculated according to Equation 22. All calculations have been carried out with $\beta_c = 25$, $G = 0.05$, $r = 0.05$, and $\omega_F = 0.5$.

reversal point in damping dependence of the resonance peak in $m_y^{max}(V)$.

Taking into account Equation 22 we can write the equation regarding $Gr/(4\alpha)$ (see Supporting Information File 1),

$$9\left(\frac{Gr}{4\alpha_{crit}}\right)^4 + 3\alpha_{crit}^2\left(10\alpha_{crit}^2 - 1\right)\left(\frac{Gr}{4\alpha_{crit}}\right)^2 - 2\alpha_{crit}^4\left(\alpha_{crit}^2 - 1\right)^2 = 0. \quad (23)$$

Using the approximation $10\alpha_{crit}^2 \ll 1$ and $\alpha_{crit}^2 \ll 1$, it gives (see Supporting Information File 1)

$$\alpha_{crit} \approx \frac{1}{2}\sqrt{\sqrt{\frac{3}{2}}Gr}. \quad (24)$$

Figure 11 presents a comparison of numerical and analytical results for α_{crit} as a function of Gr (Table 1).

There is a good agreement between numerical and analytical results of the calculations for small products of Josephson-to-magnetic energy ratio and spin–orbit interaction.

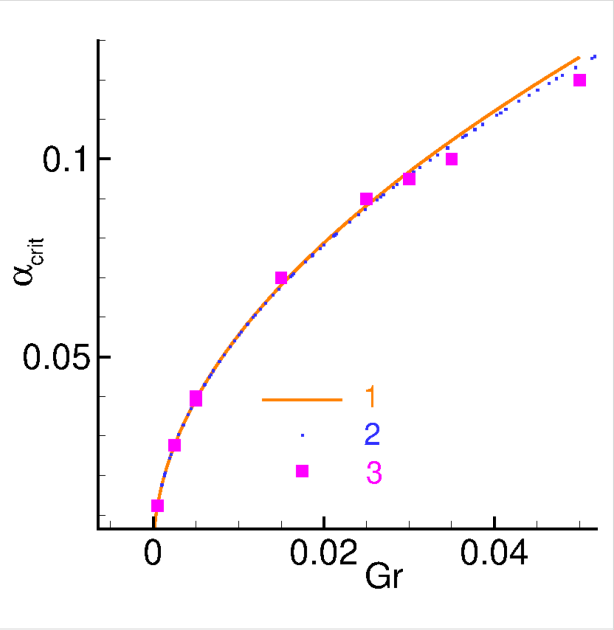

Figure 11: Numerical calculations according to Equation 6 (squares), analytical calculations according to Equation 23 (solid line), and approximated analytical calculations according to Equation 24 (dashed line).

Table 1: A comparison between the numerical and analytical values of α_{crit} at different values of G and r.

G	r	Gr	α_{crit}, numerical	α_{crit}, analytical
0.01	0.05	0.0005	0.0100	0.0123
0.05	0.05	0.0025	0.0300	0.0276
0.05	0.10	0.0050	0.0400	0.0391
0.05	0.30	0.0150	0.0700	0.0677
0.05	0.50	0.0250	0.0900	0.0874
0.10	0.05	0.0050	0.0391	0.0391
0.60	0.05	0.0300	0.0950	0.0958
0.70	0.05	0.0350	0.1000	0.1035
1.00	0.05	0.0500	0.1200	0.1237

Conclusion

The understanding of the nonlinear features of magnetization dynamics in superconductor–ferromagnet–superconductor Josephson junctions and their manifestation in the I–V characteristics has implications for superconductor spintronics and modern information technology. In φ_0 junctions, the nonlinear features can affect the control of magnetization precession by the superconducting current and external electromagnetic radiation [28].

Here, using numerical and analytic approaches, we have demonstrated that at small values of the system parameters

damping, spin–orbit interaction, and Josephson-to-magnetic energy ratio in φ_0 junctions, magnetic dynamics is reduced to the dynamics of the scalar Duffing oscillator driven by the Josephson oscillations. We have clarified the role of the increasing superconducting current in the resonance region leading to the fold-over effect in the ferromagnet magnetization. We have demonstrated the parameter dependence of the anomalous ferromagnetic resonant shifting and the anomalous damping dependence due to the nonlinearity of the full LLGJ system of equations and its different approximations. We have derived an analytical expression for critical damping value. Also, we demonstrated the appearance of negative differential resistance in the *I*–*V* characteristics and the correlation with the occurrence of the fold-over effect in the magnetization of ferromagnet.

We have stressed that the manifestation of negative differential resistance is related to the nonlinear features of the system [34,35]. It was demonstrated that in the case of small model parameter values, the equation for the magnetic subsystem takes the form of the Duffing equation where the nonlinearity manifest itself as the cubic term. We have shown that the appearance of negative differential resistance in the *I*–*V* curve is related to the appearance of the fold-over effect in the $m_y^{\max}$–*V* curve.

We believe that experimentally measured *I*–*V* characteristics of φ_0 junctions with the manifestations discussed in detail here, would allow for close investigations of its nonlinear features important for superconductor electronics and spintronics.

Supporting Information

Supporting Information File 1

Details of calculations for Equation 22 and Equation 24.
[https://www.beilstein-journals.org/bjnano/content/supplementary/2190-4286-13-97-S1.pdf]

Funding

Numerical simulations were funded by Project No. 18-71-10095 of the Russian Science Foundation. The presented results concerning the calculations of DC superconducting current in the Subsection B are supported by the Russian Science Foundation in the framework of project 22-42-04408. A.J. and M.R.K. are grateful to IASBS for financial support.

ORCID® iDs

Ilhom R. Rahmonov - https://orcid.org/0000-0002-8014-9029
Sara A. Abdelmoneim - https://orcid.org/0000-0002-0080-1882
Yury M. Shukrinov - https://orcid.org/0000-0003-2496-0375

References

1. Buzdin, A. *Phys. Rev. Lett.* **2008,** *101,* 107005. doi:10.1103/physrevlett.101.107005
2. Linder, J.; Robinson, J. W. A. *Nat. Phys.* **2015,** *11,* 307–315. doi:10.1038/nphys3242
3. Bobkova, I. V.; Bobkov, A. M.; Silaev, M. A. *Phys. Rev. B* **2018,** *98,* 014521. doi:10.1103/physrevb.98.014521
4. Bobkova, I. V.; Bobkov, A. M.; Rahmonov, I. R.; Mazanik, A. A.; Sengupta, K.; Shukrinov, Y. M. *Phys. Rev. B* **2020,** *102,* 134505. doi:10.1103/physrevb.102.134505
5. Szombati, D. B.; Nadj-Perge, S.; Car, D.; Plissard, S. R.; Bakkers, E. P. A. M.; Kouwenhoven, L. P. *Nat. Phys.* **2016,** *12,* 568–572. doi:10.1038/nphys3742
6. Konschelle, F.; Buzdin, A. *Phys. Rev. Lett.* **2009,** *102,* 017001. doi:10.1103/physrevlett.102.017001
7. Shukrinov, Y. M.; Rahmonov, I. R.; Sengupta, K. *Phys. Rev. B* **2019,** *99,* 224513. doi:10.1103/physrevb.99.224513
8. Shukrinov, Y. M. *Phys.-Usp.* **2022,** *65,* 317–354. doi:10.3367/ufne.2020.11.038894
9. Linder, J.; Yokoyama, T. *Phys. Rev. B* **2011,** *83,* 012501. doi:10.1103/physrevb.83.012501
10. Hoffman, S.; Blanter, Y. M.; Tserkovnyak, Y. *Phys. Rev. B* **2012,** *86,* 054427. doi:10.1103/physrevb.86.054427
11. Eschrig, M. *Rep. Prog. Phys.* **2015,** *78,* 104501. doi:10.1088/0034-4885/78/10/104501
12. Shukrinov, Y. M.; Rahmonov, I. R.; Sengupta, K.; Buzdin, A. *Appl. Phys. Lett.* **2017,** *110,* 182407. doi:10.1063/1.4983090
13. Mazanik, A. A.; Rahmonov, I. R.; Botha, A. E.; Shukrinov, Y. M. *Phys. Rev. Appl.* **2020,** *14,* 014003. doi:10.1103/physrevapplied.14.014003
14. Shukrinov, Y. M.; Rahmonov, I. R.; Janalizadeh, A.; Kolahchi, M. R. *Phys. Rev. B* **2021,** *104,* 224511. doi:10.1103/physrevb.104.224511
15. Shen, L.; Xia, J.; Zhang, X.; Ezawa, M.; Tretiakov, O. A.; Liu, X.; Zhao, G.; Zhou, Y. *Phys. Rev. Lett.* **2020,** *124,* 037202. doi:10.1103/physrevlett.124.037202
16. Azovtsev, A. V.; Nikitchenko, A. I.; Pertsev, N. A. *Phys. Rev. Mater.* **2021,** *5,* 054601. doi:10.1103/physrevmaterials.5.054601
17. Zhu, J.; Zhang, T.; Yang, Y.; Huang, R. *Appl. Phys. Rev.* **2020,** *7,* 011312. doi:10.1063/1.5118217
18. Wang, G.; Chen, D.; Lin, J.; Chen, X. *IEEE Trans. Ind. Electron.* **1999,** *46,* 440–444. doi:10.1109/41.753783
19. Almog, R.; Zaitsev, S.; Shtempluck, O.; Buks, E. *Phys. Rev. Lett.* **2007,** *98,* 078103. doi:10.1103/physrevlett.98.078103
20. Zhao, Y.; Song, Q.; Yang, S.-H.; Su, T.; Yuan, W.; Parkin, S. S. P.; Shi, J.; Han, W. *Sci. Rep.* **2016,** *6,* 22890. doi:10.1038/srep22890
21. Yao, Y.; Song, Q.; Takamura, Y.; Cascales, J. P.; Yuan, W.; Ma, Y.; Yun, Y.; Xie, X. C.; Moodera, J. S.; Han, W. *Phys. Rev. B* **2018,** *97,* 224414. doi:10.1103/physrevb.97.224414
22. Silaev, M. A. *Phys. Rev. B* **2020,** *102,* 144521. doi:10.1103/physrevb.102.144521
23. Nayfeh, A. H.; Mook, D. T. *Nonlinear Oscillations;* John Wiley & Sons Inc.: New York, 1979.
24. Chen, W.; de Loubens, G.; Beaujour, J.-M. L.; Sun, J. Z.; Kent, A. D. *Appl. Phys. Lett.* **2009,** *95,* 172513. doi:10.1063/1.3254242
25. Guarcello, C.; Bergeret, F. S. *Phys. Rev. Appl.* **2020,** *13,* 034012. doi:10.1103/physrevapplied.13.034012
26. Lifshitz, E. M.; Pitaevskii, L. P. *Course of Theoretical Physics, Theory of the Condensed State;* Butterworth Heinemann: Oxford, UK, 1991; Vol. 9.

27. Rabinovich, D. S.; Bobkova, I. V.; Bobkov, A. M.; Silaev, M. A. *Phys. Rev. Lett.* **2019,** *123,* 207001. doi:10.1103/physrevlett.123.207001
28. Abdelmoneim, S. A.; Shukrinov, Y. M.; Kulikov, K. V.; ElSamman, H.; Nashaat, M. *Phys. Rev. B* **2022,** *106,* 014505. doi:10.1103/physrevb.106.014505
29. Shukrinov, Y. M.; Rahmonov, I. R. *Phys. Part. Nucl.* **2020,** *51,* 816–822. doi:10.1134/s1063779620040668
30. Shukrinov, Y. M.; Rahmonov, I. R.; Botha, A. E. *Low Temp. Phys.* **2020,** *46,* 932–938. doi:10.1063/10.0001716
31. Konschelle, F.; Buzdin, A. *Phys. Rev. Lett.* **2019,** *123,* 169901. doi:10.1103/physrevlett.123.169901
32. Pedersen, N. F.; Filatrella, G.; Pierro, V.; Sørensen, M. P. *Phys. C (Amsterdam, Neth.)* **2014,** *503,* 178–182. doi:10.1016/j.physc.2014.02.025
33. Kadowaki, K.; Yamaguchi, H.; Kawamata, K.; Yamamoto, T.; Minami, H.; Kakeya, I.; Welp, U.; Ozyuzer, L.; Koshelev, A.; Kurter, C.; Gray, K. E.; Kwok, W.-K. *Phys. C (Amsterdam, Neth.)* **2008,** *468,* 634–639. doi:10.1016/j.physc.2007.11.090
34. Filatrella, G.; Pierro, V.; Pedersen, N. F.; Sorensen, M. P. *IEEE Trans. Appl. Supercond.* **2014,** *24,* 1–7. doi:10.1109/tasc.2014.2311383
35. Nagel, J.; Speer, D.; Gaber, T.; Sterck, A.; Eichhorn, R.; Reimann, P.; Ilin, K.; Siegel, M.; Koelle, D.; Kleiner, R. *Phys. Rev. Lett.* **2008,** *100,* 217001. doi:10.1103/physrevlett.100.217001

License and Terms

BEILSTEIN JOURNAL OF NANOTECHNOLOGY

Density of states in the presence of spin-dependent scattering in SF bilayers: a numerical and analytical approach

Tairzhan Karabassov[1], Valeriia D. Pashkovskaia[1], Nikita A. Parkhomenko[1], Anastasia V. Guravova[1], Elena A. Kazakova[2], Boris G. Lvov[1], Alexander A. Golubov[3,4] and Andrey S. Vasenko[*1,5]

Full Research Paper

Open Access

Address:
[1]HSE University, 101000 Moscow, Russia, [2]Sechenov First Moscow State Medical University, 119991 Moscow, Russia, [3]Faculty of Science and Technology and MESA Institute for Nanotechnology, University of Twente, 7500 AE Enschede, Netherlands, [4]Moscow Institute of Physics and Technology, 141700 Dolgoprudny, Russia and [5]I. E. Tamm Department of Theoretical Physics, P. N. Lebedev Physical Institute, Russian Academy of Sciences, 119991 Moscow, Russia

Email:
Andrey S. Vasenko[*] - avasenko@hse.ru

* Corresponding author

Keywords:
density of states; Josephson junctions; proximity effect; superconductivity; superconductor/ferromagnet hybrid nanostructures

Beilstein J. Nanotechnol. **2022,** *13,* 1418–1431.
https://doi.org/10.3762/bjnano.13.117

Received: 28 June 2022
Accepted: 07 November 2022
Published: 01 December 2022

This article is part of the thematic issue "Intrinsic Josephson effect and prospects of superconducting spintronics".

Guest Editor: A. S. Sidorenko

Abstract

We present a quantitative study of the density of states (DOS) in SF bilayers (where S is a bulk superconductor and F is a ferromagnetic metal) in the diffusive limit. We solve the quasiclassical Usadel equations in the structure considering the presence of magnetic and spin–orbit scattering. For practical reasons, we propose the analytical solution for the density of states in SF bilayers in the case of a thin ferromagnet and low transparency of the SF interface. This solution is confirmed by numerical calculations using a self-consistent two-step iterative method. The behavior of DOS dependencies on magnetic and spin–orbit scattering times is discussed.

Introduction

It is well-known that superconductivity can be induced in a non-superconducting metal in hybrid structures due to the proximity effect [1-7]. For instance, in NS bilayers (where N denotes a normal metal and S denotes a superconductor), the superconducting correlations penetrate into the normal metal layer over a characteristic decay length $\xi_n = \sqrt{D_n/2\pi T_c}$, where D_n is the diffusion constant in the normal metal and T_c is the transition temperature. When a superconductor S is combined with a ferromagnetic layer F, forming an SF bilayer, the superconductivity leaks into the ferromagnetic region over the characteristic length $\xi_h = \sqrt{D_f/h}$, where D_f is the diffusion constant in F layer and h is the exchange field in the ferromagnetic layer [1]. Not only superconductivity is substantially suppressed due to the exchange field, but also Cooper pairs gain a finite center of

mass momentum, which leads to the oscillatory behavior of the Cooper pair wave function. These oscillations can be described in the diffusive limit in the framework of the so-called Usadel equations, which are written in terms of the quasiclassical Green's functions. This approach proved to be very powerful for the description of the proximity effect in diffusive superconducting hybrids [1-3,8-11].

The scientific community has been examining the proximity effect in SF hybrid structures already for a long while. It has been found that the oscillatory behavior of the superconducting wave function can lead to various interesting phenomena that can be observed experimentally [1,2]. For instance, the superconducting transition temperature shows non-monotonous and, in some cases, oscillatory behavior in multilayered SF structures [12-17]. Recently, it has been shown theoretically that similar behavior can be observed in S/TI structures with non-uniform magnetization patterns on the surface of a 3D topological insulator (TI) [18]. The Josephson critical current demonstrates damped oscillatory behavior as a function of the thickness of the ferromagnetic layer in SFS Josephson junctions [19-47]. Similarly, the density of states (DOS) also demonstrates a damped oscillatory dependence as a function of the F layer thickness in SF systems [48-52].

The density of states is one of the crucial spectral characteristics of the proximity effect in superconducting hybrid structures. For example, the DOS calculation is essential for the quasiparticle current computation in SIFS (where I denotes an insulating layer) [29,51,53-57] or SFIFS tunneling Josephson junctions [58]. Therefore, computation of the DOS is also needed for many actively studied areas of research, including the thermospin [59,60] and thermoelectric [61-66] effects, spin and heat valves [67-75], as well as nanoscale refrigerators [76-78]. Presently, the DOS structure at the free edge of a normal metal layer in NS bilayers is well-known [1-3,79]. It has a so-called mini-gap at the subgap energies $E < \Delta$ (where Δ is the superconducting gap), whose magnitude depends on the NS interface parameters and the thickness of the N layer [79,80]. Replacing the N layer with a ferromagnetic metal F results in a more sophisticated DOS structure since there is a non-zero exchange field, which causes spin-split densities of states for two spin populations of electrons [1-3,81]. More general considerations should also include possible spin-flips as well as spin–orbit scattering processes in the ferromagnetic region [82].

In this work, we consider a diffusive SF bilayer, assuming a relatively low interface transparency and the presence of magnetic and spin–orbit scattering. For this purpose, the Kupriyanov–Lukichev (KL) boundary conditions at the superconductor/ferromagnet interface are perfectly suitable [83]. We build the model employing the Usadel equations. The quasiclassical Usadel equations are based on the Matsubara Green's functions and represent a powerful microscopic tool for the treatment of the diffusive superconducting hybrid structures. This approach is valid as long as the elastic scattering length l is much smaller than the superconducting coherence length $\xi = \sqrt{D_s/2\pi T_c}$, where D_s is the diffusion constant in the superconductor. Previously, the DOS in SF bilayers has been studied numerically [84,85]. We revisit this question and propose an analytical model to describe the influence of spin-flip and spin–orbit scattering on the DOS behavior. Then, we provide a comparison with the exact numerical calculation using a self-consistent two-step iterative method. Furthermore, we briefly discuss the consequences of the different kinds of scattering on the current–voltage characteristics in SFIFS junctions. We do not consider any additional effects in the SF boundary such as spin-dependent interfacial phase shifts (SDIPS). The effect of SDIPS on the DOS behavior in SFIFS junctions has been studied both analytically [86] and numerically [87].

The paper is organized as follows. In the section ("Model") we formulate the theoretical model. In the following sections, the derivation of the analytical results is presented. We discuss the calculations in the section ("Results and Discussion"), and finally we summarize the results in the last section ("Conclusion").

Model

The theoretical model of the SF structure under consideration is depicted in Figure 1. It consists of a ferromagnetic layer with thickness d_f and a superconducting electrode along the x direction. The SF interface is characterized by the dimensionless parameter $\gamma_B = R_B\sigma_n/\xi_f$, where R_B is the resistance of the SF interface in units $\Omega\cdot m^2$, σ_n is the conductivity of the F layer [88,89],

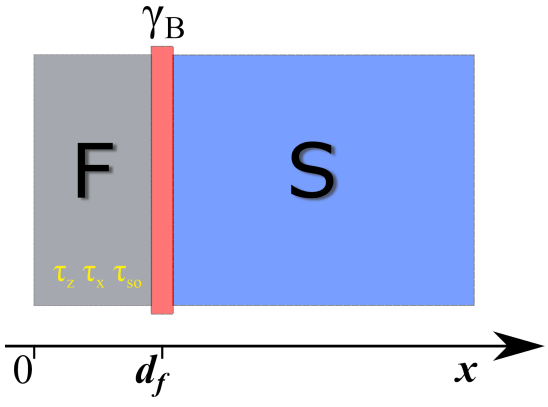

Figure 1: Geometry of the SF bilayer. We consider the SF interface to be a tunnel barrier. Here, γ_B is the interface transparency parameter.

$\xi_f = \sqrt{D_f/2\pi T_c}$, D_f is the diffusion coefficient in the ferromagnetic metal, and T_c is the critical temperature of the superconductor [1,2]. We assume $\hbar = k_B = 1$. We also assume that the SF interface is not magnetically active. We will consider the diffusive limit in this model and neglect the nonequilibrium effects in the structure [90-92].

Our goal is to find the DOS of a single SF bilayer, which can be done by solving the Usadel equations in the ferromagnetic and superconducting layers. We employ the θ parametrization of the normal and anomalous quasiclassical Green's functions, $G = \cos\theta$ and $F = \sin\theta$, respectively. In the spin space, the anomalous functions are parameterized as

$$\hat{F} = \begin{pmatrix} 0 & \sin\theta_{\uparrow} \\ -\sin\theta_{\downarrow} & 0 \end{pmatrix}, \tag{1}$$

and we can write the Usadel equations in the F layer as [4,51,82,84,93]

$$\frac{D_f}{2}\frac{\partial^2\theta_{f\uparrow(\downarrow)}}{\partial x^2} = \left(\omega \pm ih + \frac{1}{\tau_z}\cos\theta_{f\uparrow(\downarrow)}\right)\sin\theta_{f\uparrow(\downarrow)} + \frac{1}{\tau_x}\sin\left(\theta_{f\uparrow} + \theta_{f\downarrow}\right) \pm \frac{1}{\tau_{so}}\sin\left(\theta_{f\uparrow} - \theta_{f\downarrow}\right), \tag{2}$$

where the positive and negative signs correspond to the spin-up (↑) and spin-down (↓) states, respectively. In terms of the electron fermionic operators ψ, the spin-up state corresponds to the anomalous Green's function $F_{\uparrow} \sim \langle \psi_{\uparrow}\psi_{\downarrow}\rangle$, while the spin-down state corresponds to $F_{\downarrow} \sim \langle \psi_{\downarrow}\psi_{\uparrow}\rangle$. We use the Matsubara Green's functions, hence, $\omega = 2\pi T(n + 1/2)$ are the Matsubara frequencies [94]. The exchange field of the ferromagnet is h, and the scattering times are labeled here as τ_z, τ_x and τ_{so}. The parameter $\tau_{z(x)}$ corresponds to the magnetic scattering parallel (perpendicular) to the quantization axis, and τ_{so} is the spin–orbit scattering time [82,84,95].

In the model under consideration, we assume a rotational symmetry around the $\hat{z}$ axis, that is, $\tau_x = \tau_y$. We consider the possibility of anisotropic magnetic scattering times. These can occur in ferromagnetic superconductors where magnetic disorder can be characterized by two scattering times $\tau_x = \tau_y$ and τ_z [82]. The Usadel equations employed in this work are the special case of the more general formalism derived by Ivanov and co-workers [96]. Thus, the equations that we use in our calculations are exactly a quasiclassical limit of the model derived in [96] except that in our model we also include spin–orbit scattering. Ivanov et al. describe the spin-flip scattering via a symmetric matrix of scattering rates Γ_{sf}^{ij}. Depending on the symmetry of the problem, the number of parameters can be different (up to six), for example, in the most symmetric isotropic case, the spin-flip matrix is diagonal and described by one scattering time ($\tau_x = \tau_y = \tau_z$). In the case of a ferromagnetic ordering in which disorder is anisotropic (one axis is special), the spin-flip rates in the directions along the ferromagnetic axis and perpendicular to it may be different. In this case, as we mentioned earlier, two scattering times would be necessary.

In the S layer, the Usadel equation has the following form [93]:

$$\frac{D_s}{2}\frac{\partial^2\theta_s}{\partial x^2} = \omega\sin\theta_s - \Delta(x)\cos\theta_s. \tag{3}$$

Here, D_s is the diffusion coefficient in the superconductor, and $\Delta(x)$ is the superconducting order parameter (pair potential). From the Usadel equations, it can be shown that there is a symmetry relation between $\theta_{\uparrow}$ and $\theta_{\downarrow}$: $\theta_{\uparrow}(E) = \theta^*_{\downarrow}(-E)$, where E is the energy ($\omega_n \rightarrow -iE$) and * is the complex conjugation. Equation 2 and Equation 3 should be supplemented with the self-consistency equation for the coordinate dependence of superconducting order parameter Δ,

$$\Delta(x)\ln\frac{T_c}{T} = \pi T\sum_{\omega>0}\left(\frac{2\Delta(x)}{\omega} - \sin\theta_{s\uparrow} - \sin\theta_{s\downarrow}\right). \tag{4}$$

The resulting system must be complemented by the boundary conditions at the outer boundary of a ferromagnet,

$$\left(\frac{\partial\theta_f}{\partial x}\right)_{x=0} = 0, \tag{5}$$

and the Kupriyanov–Lukichev boundary conditions at the FS interface [83],

$$\xi_f\gamma\left(\frac{\partial\theta_f}{\partial x}\right)_{x=d_f} = \xi_s\left(\frac{\partial\theta_s}{\partial x}\right)_{x=d_f}, \tag{6}$$

$$\xi_f\gamma_B\left(\frac{\partial\theta_f}{\partial x}\right)_{x=d_f} = \sin\left(\theta_s - \theta_f\right)_{x=d_f}. \tag{7}$$

Here $\gamma = \xi_s\sigma_n/\xi_f\sigma_s$, σ_s is the conductivity of the S layer, and $\xi_s = \sqrt{D_s/2\pi T_c}$ is the superconducting coherence length. The indices of the θ-parameterized Green's functions are omitted, since there is no mixing between the components $\theta_{\uparrow}$ and $\theta_{\downarrow}$. In

other words, we are not considering spin-active interfaces. In the case of spin-active barriers, one should use the boundary conditions introduced in [87,97,98], rather than the standard Kupriyanov–Lukichev boundary conditions in Equation 6 and Equation 7. The parameter γ determines the strength of superconductivity suppression in the S layer by the ferromagnet F (inverse proximity effect). For instance, when $\gamma \gg 1$, the inverse proximity effect is very strong, and the order parameter is heavily suppressed near the SF interface compared to its bulk value. On the contrary, when $\gamma = 0$, there is no suppression of the order parameter because there is no inverse proximity effect. In all numerical simulations, we assume that $\gamma \ll 1$, that is, there is almost no superconductivity suppression in the superconductor. The transparency parameter γ_B is proportional to the interface resistance. In the regime of a fully transparent junction, $\gamma_B = 0$, the proximity effect is the strongest, and the θ functions are continuous at the SF interface while $\gamma_B \gg 1$ corresponds to the tunnel junction limit, that is, there is no mutual impact between superconducting layer S and ferromagnetic layer F.

To complete the boundary problem, we also set a boundary condition at $x = +\infty$:

$$\theta_s\left(+\infty\right) = \arctan\left(\frac{\Delta}{\omega}\right), \tag{8}$$

where the Green's functions take the well-known bulk BCS form. The Green's function method allows us to compute the DOS at the outer F boundary by solving the resulting system of equations above.

The DOS at the outer F boundary $N_f(E)$ is normalized to the DOS in the normal state and can be written as

$$N_f\left(E\right) = \left[N_{f\uparrow}\left(E\right) + N_{f\downarrow}\left(E\right)\right]\Big/2, \tag{9}$$

where $N_{f\uparrow(\downarrow)}(E)$ are the spin-resolved DOS written in terms of the spectral angle θ,

$$N_{f\uparrow(\downarrow)}\left(E\right) = \mathrm{Re}\left[\cos\theta_{f\uparrow(\downarrow)}\left(i\omega \to E + i0\right)\right]. \tag{10}$$

To calculate Equation 10, we use a self-consistent two-step iterative method. In the first step, we calculate the pair potential coordinate dependence $\Delta(x)$ using the self-consistency equation (Equation 4) in the S layer. Then, by proceeding to the analytical continuation in Equation 2 and Equation 3 over the quasiparticle energy $i\omega \to E + i0$ and using the $\Delta(x)$ dependence obtained in the previous step, we find the Green's functions by repeating the iterations until convergency is reached.

The DOS in the limit of small F layer thickness

In this section, we obtain the analytical result assuming $d_f \ll \min(\xi_f, \sqrt{D_f/2h})$, which is the case in a thin and weak ferromagnet. Under the condition $\gamma = 0$, we can neglect the suppression of superconductivity in the superconductor. Hence, the problem can be reduced to the rigid boundary condition when the order parameter in the S layer is set to its bulk value Δ_0. We will keep all scattering terms in the solution to obtain a more general result. In this case, we can expand the solution of the Usadel equations up to the second order in small spatial gradients. The θ_f functions can be approximated in the following way:

$$\theta_{f\uparrow} = A_\uparrow + B_\uparrow x + C_\downarrow x^2, \tag{11}$$

$$\theta_{f\downarrow} = A_\downarrow + B_\downarrow x + C_\downarrow x^2, \tag{12}$$

where the coefficients $A_{\uparrow(\downarrow)}$, $B_{\uparrow(\downarrow)}$, $C_{\uparrow(\downarrow)}$ are determined from the boundary conditions.

Inserting the solution in Equation 11 into the Usadel equation in the F layer (Equation 2), we get,

$$\begin{aligned} C_{\uparrow(\downarrow)} = \frac{1}{2}\Bigg[\left(\omega_n \pm ih\right)\sin A_{\uparrow(\downarrow)} + \frac{1}{2}\alpha_z \sin 2A_{\uparrow(\downarrow)}\Bigg] \\ + \frac{1}{2}\Big[\alpha_x \sin\left(A_\uparrow + A_\downarrow\right) \pm \alpha_{so}\sin\left(A_\uparrow - A_\downarrow\right)\Big]. \end{aligned} \tag{13}$$

For convenience, we introduced the scattering rate parameters $\alpha_z = 1/\tau_z\Delta$, $\alpha_x = 1/\tau_x\Delta$, and $\alpha_{so} = 1/\tau_{so}\Delta$. To find the coefficients, we utilize the boundary conditions in Equation 5 and Equation 7,

$$\left(B_{\uparrow(\downarrow)} + 2C_{\uparrow(\downarrow)}x\right)_{x=0} = 0, \tag{14}$$

$$\xi_f\gamma_B\left(B_{\uparrow(\downarrow)} + 2C_{\uparrow(\downarrow)}x\right)_{x=d_f} = \sin\left(\theta_s - A_{\uparrow(\downarrow)}\right)\Big|_{x=d_f}. \tag{15}$$

From the first equation we obtain $B_{\uparrow(\downarrow)} = 0$, while the second equation results in the expression for $A_{\uparrow(\downarrow)}$.

Now, we will discuss a ferromagnet with strong uniaxial anisotropy, in which case the perpendicular fluctuations of the exchange field are suppressed ($\alpha_x \sim 0$). For simplicity, we also assume the ferromagnet with weak spin–orbit interactions and also neglect the spin–orbit scattering time α_{so}. Finally, assuming $\alpha_x = \alpha_{so} = 0$ and keeping the solution to the lowest order, the equation for θ_f takes the form

$$\begin{aligned}&\gamma_B d_f\left(\omega_n \pm ih\right)\tan\theta_{f\uparrow(\downarrow)}\\&+\cos\theta_s\tan\theta_{f\uparrow(\downarrow)}+\alpha_z\gamma_B d_f\sin\theta_{f\uparrow(\downarrow)}=\sin\theta_s,\end{aligned}\tag{16}$$

where $\sin\theta_s = \Delta_0 / \sqrt{\omega_n^2+\Delta_0^2}$ and $\cos\theta_s = \omega_n/\sqrt{\omega_n^2+\Delta_0^2}$. Here, Δ_0 is the bulk value of the pair potential. The equation above can be used for further semi-analytical calculations of the DOS for the case of a thin F layer with the magnetic scattering rate α_z. When $\alpha_z = 0$, Equation 16 reduces to the well-known result (see, for example, [81] or [86]),

$$\tan\theta_{f\uparrow(\downarrow)}=\frac{\sin\theta_s}{\left(\omega_n\pm ih\right)\gamma_B d_f+\cos\theta_s}.\tag{17}$$

Analytical solution in the low proximity limit and small F layer thickness

In this section, we perform further analytical calculations of the anomalous Green's function in the F layer based on the results of the previous section. We then analyze the effect of various scattering rates on the superconducting correlations, including the odd-frequency triplet component, which is generated in the adjacent ferromagnet.

The expression for θ-parameterized Green's functions can be found from the boundary conditions (Equation 14),

$$\begin{aligned}&\gamma_B d_f\left[\left(\omega_n\pm ih\right)+\alpha_z\cos\theta_{f\uparrow(\downarrow)}\right]\sin\theta_{f\uparrow(\downarrow)}\\&+\gamma_B d_f\left[\alpha_x\sin\left(\theta_{f\uparrow}+\theta_{f\downarrow}\right)\pm\alpha_{so}\sin\left(\theta_{f\uparrow}-\theta_{f\downarrow}\right)\right]\\&=\sin\left(\theta_s-\theta_{f\uparrow(\downarrow)}\right).\end{aligned}\tag{18}$$

In order to simplify the calculation and the final form of the solution θ_f, we consider only positive Matsubara frequencies ω_n and perform further linearization of Equation 18, which is justified in the low-proximity limit. Then, we obtain

$$\theta_{f\uparrow(\downarrow)}=\frac{\sin\theta_s\left(\cos\theta_s+\gamma_B d_f\left(\alpha_z+2\alpha_{so}+\omega_n\mp ih\right)\right)}{\gamma_B^2 d_f^2\left[h^2-\left(\alpha_x-\alpha_{so}\right)^2\right]+\left[\cos\theta_s+\gamma_B d_f\left(\sum\alpha_i+\omega_n\right)\right]^2}.\tag{19}$$

Here, $\Sigma\alpha_i$ denotes the sum of all the scattering rates. The above solution is true for thin ferromagnetic layers in the low-proximity limit. A more general analytical solution can be obtained for arbitrary thicknesses using the linearized Usadel equations. In order to find the DOS in the proposed limit, we expand the θ-parametrized normal Green's function around small values of θ_f. In this case, we have

$$N_{f\uparrow(\downarrow)}(E)\approx 1-\frac{1}{2}\mathrm{Re}\left[\theta^2_{f\uparrow(\downarrow)}\left(\omega_n\to -iE\right)\right],\tag{20}$$

and, to calculate the total DOS, we need to sum the contributions from two spin populations using Equation 9.

Results and Discussion

In the present section we outline the main results, including both numerical and analytical calculations. The following parameters are fixed throughout the section: $T = 0.1T_c$, $\gamma = 0.05$, and $d_f = 0.5\xi_f$. First, we discuss general features of the DOS in an SF bilayer in the absence of any scattering. Then the effect of the spin-dependent scattering on the key DOS features in two relevant cases is discussed (see below) and finally, we present the analytical result and compare it with the numerically calculated DOS.

Evolution of the DOS in SF bilayer

It is instructive to discuss the key features of the DOS in an SF bilayer first. That is why, in this section, we briefly discuss the evolution of the DOS for different values of the exchange field h and the barrier transparency γ_B. All the scattering is assumed to be absent for simplicity $\alpha_m = \alpha_x = \alpha_{so} = 0$ in this subsection.

In Figure 2, we observe the influence of an increasing exchange field h on the DOS structure calculated for $\gamma_B = 5$. In particular, we can see the evolution of the DOS peaks. For $h = 0$, that is, for the case of an SN bilayer, we see the well-known DOS structure with the characteristic mini-gap at energies $E < \Delta$ (Figure 2a, black dotted line) [79]. This proximity-induced mini-gap originates from the effective backscattering of the quasiparticles at the SN interface due to a finite interface resistance [99]. As h increases, the DOS splits for the spin-up and spin-down electrons, which results in the mini-gap peak splitting. For a certain value of h, the mini-gap closes, resulting in the DOS enhancement at zero energy as seen from Figure 2b and Figure 2c. This feature known as a zero-energy peak (ZEP)

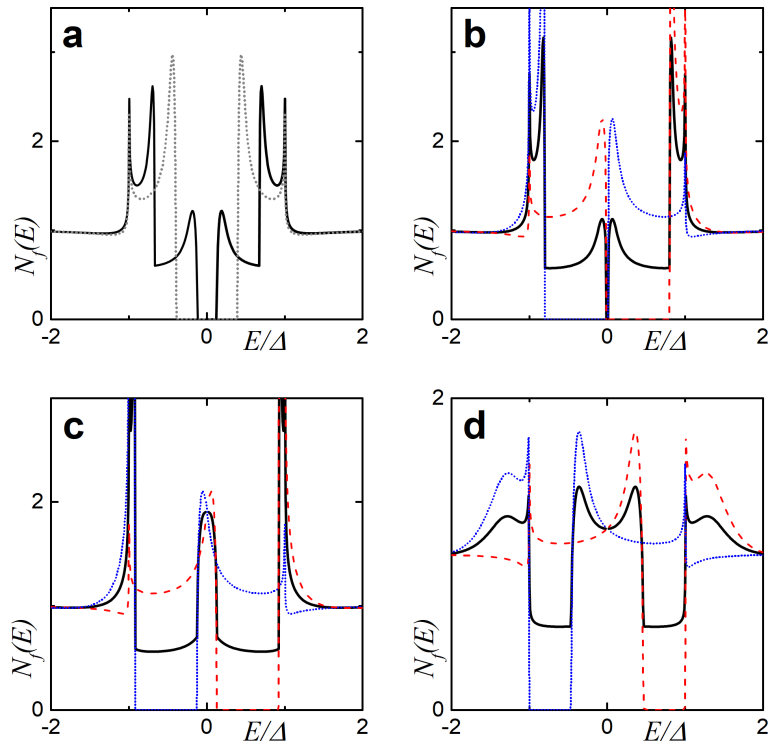

Figure 2: The evolution of the DOS plotted for increasing values of the exchange field h. Here, $\gamma_B = 5$, $d_f = 0.5\xi_f$. In plot (a), the gray dotted line represents the case of $h = 0$ (i.e., the NS bilayer). In plots (a)–(d), black solid lines correspond to the total DOS while red dashed lines show $N_{f\uparrow}(E)$ and blue dash-dotted lines show $N_{f\downarrow}(E)$. (a) Black solid line calculated for $h = 0.4\Delta$, and all lines are calculated for (b) $h = 0.8\Delta$, (c) $h = \Delta$, and (d) $h = 1.6\Delta$.

has been investigated both theoretically [100-103] and experimentally [49]. Another interesting peculiarity of the DOS is the appearance of the characteristic peak at $E = h$, which arises as the exchange field exceeds the superconducting gap $h > \Delta$. Apparently, this peak arises from the evolution of the second spin-split peak due to a non-zero exchange field. The existence of such an effect offers a method of determining relatively small exchange field values in the F layer via DOS measurements [48,51,104].

In Figure 3, the DOS evolution at increasing interface parameter γ_B is shown. The blue solid line corresponds to the subgap exchange field $h = 0.4\Delta$, whereas the black dotted line corresponds to $h = 1.5\Delta$. From the figure we can notice that an increase of γ_B also has a strong influence on the DOS structure. Sufficiently large interface resistance values can close the mini-gap and lead to the emergence of the ZEP (Figure 3c, blue solid line). However, the peak structure is different for the two exchange fields h as seen from the figure.

One can notice that the peak at $E = h$ in Figure 3a is almost absent. The reason that we observe such a behavior is because we consider relatively small values of F layer thickness d_f and transparency parameter γ_B. More detailed analysis can be made in the limiting case of $d_f \gg \xi_f$ and $\gamma_B \gg 1$ and $\gamma = 0$ [51]. In the absence of any scattering, the analytical DOS expression for $E \geq \Delta$ can be written in the following way:

$$N_f(E) = 1 + \sum_{\pm} \frac{16\Delta^2 \cos\left(\frac{2d_f}{\xi_f}\sqrt{\frac{|E\pm h|}{h}}\right)}{(E+\varepsilon)\left(\sqrt{E+\varepsilon}+\sqrt{2\varepsilon}\right)^2} e^{-\frac{2d_f}{\xi_f}\sqrt{\frac{|E\pm h|}{h}}}, \quad (21)$$

where $\varepsilon = \sqrt{E^2-\Delta^2}$. One can clearly see the exponential asymptotic of the peak at $E = h$ from Equation 21. We should not forget that Equation 21 is strictly valid only for large d_f/ξ_f, but nevertheless it may qualitatively explain why we do not see the peak at $E = h$ for small a ratio of d_f/ξ_f. If this factor is relatively small, the variation of the exponent $\{-2(d_f/\xi_f)\sqrt{|E-h|/h}\}$ near the point $E = h$ is also small. The peak is observable only for h of the order of a few Δ. For larger exchange fields, the peak is very difficult to observe since the energy-dependent prefactor of the exponent in Equation 21 decays as E^{-2} for $E \gg \Delta$.

In what follows, we will examine the effect produced by both spin-flip and spin–orbit scattering on the DOS features, mostly focusing on the mini-gap and the DOS peak at $E = h$. Unlike

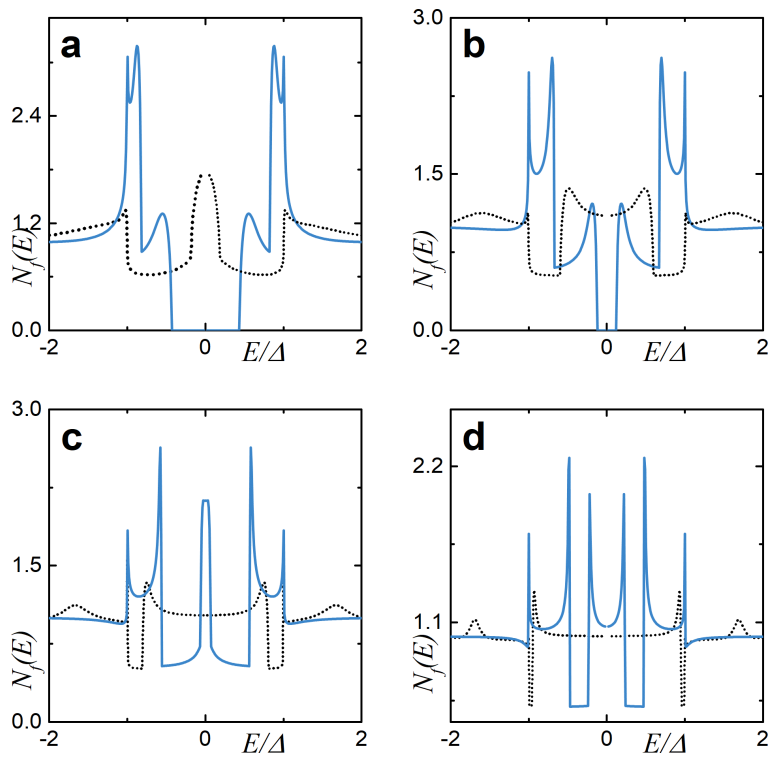

Figure 3: The evolution of the DOS plotted for increasing values of the SF interface transparency γ_B. Here, $d_f = 0.5\xi_f$, the exchange field is $h = 0.4\Delta$ (blue solid line), and $h = 1.7\Delta$ (black dotted line). (a) $\gamma_B = 2$, (b) $\gamma_B = 5$, (c) $\gamma_B = 10$, and (d) $\gamma_B = 25$.

previous results on this topic [84,85], we provide both numerical and analytical results for the DOS calculation. Although the analytical expressions have a rather narrow range of applicability such limiting cases are relevant for experiments.

Effect of scattering on the DOS features

Now we discuss the influence of the finite scattering rates on the DOS features mentioned in the previous section. In this paper we consider two cases of the junction transparency: (i) intermediate interface transparency ($\gamma_B \geq 1$) and (ii) low interface transparency ($\gamma_B \gg 1$). In both cases, we fix the thickness of the F layer to $d_f = 0.5\xi_f$. Focusing on these cases allows us to discuss all major effects on the DOS features utilizing not only numerical solutions of the problem but also some analytical results, which will be presented below.

Intermediate interface transparency ($\gamma_B = 5$)

Figure 4 depicts the DOS dependencies in the case of relatively low interface transparency ($\gamma_B = 5$) in the presence of spin-flip and spin–orbit scattering. It is clearly seen that the decrease of the parallel magnetic scattering time leads to a smearing of the split peaks with the gradual closing of the induced energy gap (mini-gap) in the F layer (Figure 4a). The influence of the perpendicular magnetic scattering can be observed in Figure 4c. While increasing the scattering rate α_x tends to suppress the split peaks, perpendicular magnetic scattering also moves the peaks towards the Fermi energy destroying the mini-gap. This can be explained in terms of the additional effective exchange field in the system, which is due to non-zero perpendicular scattering rates [84]. Summarizing the results of the calculations, it is obvious that the magnetic scattering tends to destroy the proximity-induced superconductivity in the F layer. Such an effect becomes clear from a more detailed analysis of the linearized Usadel equation (Equation 2) in the low-proximity limit. In this case, the anomalous Green's function is dependent on the exchange field h and the magnetic scattering rates, which apparently are pair breaking.

Figure 4b shows that a smaller spin–orbit scattering time leads to the vanishing of the peak splitting in the subgap region. In contrast, though the spin–orbit scattering destroys the double peak structure due to an exchange field smearing them into one peak, it does not produce a destructive effect on the mini-gap magnitude (see below Figure 6b). This feature has been reported previously [85].

Low interface transparency ($\gamma_B = 50$)

Now we focus on the limit of a highly resistive SF interface and investigate the effects of a spin-dependent scattering. As expected, the influence of the adjacent superconducting layer on

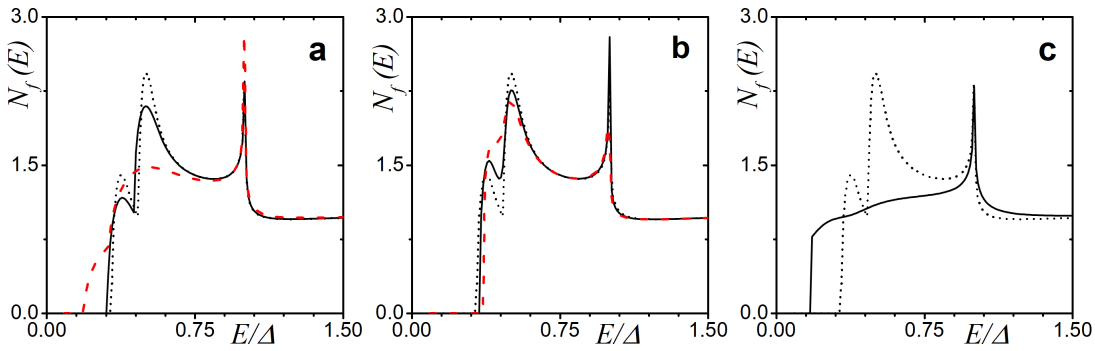

Figure 4: The DOS $N_f(E)$ at the free boundary of the F layer in the SF bilayer in the presence of magnetic and spin–orbit scattering, calculated numerically for different scattering times. The plots correspond to intermediate interface transparency $\gamma_B = 5$, $h = 0.1\Delta$, and $d_f = 0.5\xi_f$. Plot (a) corresponds to $\alpha_z \neq 0$: $\alpha_z = 0.01$ (black solid line) and $\alpha_z = 0.1$ (red dashed line). Plot (b) corresponds to $\alpha_{so} \neq 0$: $\alpha_{so} = 0.05$ (black solid line) and $\alpha_{so} = 0.13$ (red dashed line). Plot (c) corresponds to $\alpha_x \neq 0$: $\alpha_x = 0.2$ (black solid line). The black dotted line represents $N_f(E)$ in the absence of any scattering.

the DOS is rather limited due to low transparency of the interface (Figure 5). It can be seen that the mini-gap is hardly recognizable in the cases of both subgap values of h (Figure 5a,b) and $h > \Delta$ (Figure 5c). From the plots, we can say that the finite scattering rates suppress the DOS features in the case of low interface transparency as well (Figure 5, solid and dashed lines). Even the DOS peak at $E = h$ is suppressed substantially (Figure 5c). However, a closer examination shows that all the scattering rates slightly differ in the way they modify the DOS structure.

We would like to discuss the effect of scattering on the DOS peak located at the exchange energy in more detail. As we have mentioned above, one of the interesting features in the DOS of the considered system is the peak at $E = h$ (Figure 6a). In Figure 6, we demonstrate the influence of different scattering rates on the DOS peak at $E = h$ using the numerically obtained results. The remaining parameters used for calculations here are $\gamma_B = 50$, $d_f = 0.5\xi_f$, and $h = 1.5\Delta$. In Figure 6b, the plot for different values of α_z is shown. It can be noticed that the uniaxial magnetic scattering not only suppresses the peak but also slightly shifts the DOS peak towards $E = 0$. The spin–orbit scattering has a similar effect on the peak, though α_{so} has a stronger effect on the peak height compared to α_z as it can be noticed from Figure 6c. In both cases above, the DOS peak also smears as any of the scattering rates increases. The effect of the perpendicular magnetic scattering α_x is indicated in Figure 6c.

Analytical result for the interfaces with low transparency and qualitative picture

Here, we employ the analytical expression (Equation 20) obtained in the limit of low proximity and thin F layer. Considering the problem in such limit makes it possible to use a simple expression for the qualitative description of the corresponding

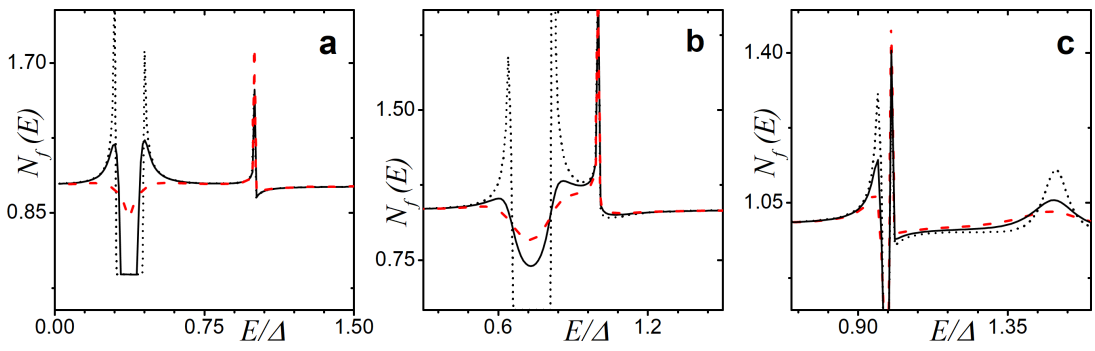

Figure 5: The DOS $N_f(E)$ at the free boundary of the F layer in the SF bilayer in the presence of magnetic scattering, calculated numerically for the low-transparency interface with $\gamma_B = 50$. Plot (a) corresponds to $\alpha_z \neq 0$ and $h = 0.4\Delta$: $\alpha_z = 0.01$ (black solid line) and $\alpha_z = 0.1$ (red dashed line). Plot (b) corresponds to $\alpha_{so} \neq 0$ and $h = 0.8\Delta$: $\alpha_{so} = 0.05$ (black solid line) and $\alpha_{so} = 0.1$ (red dashed line). Plot (c) corresponds to $\alpha_{so} \neq 0$ and $h = 1.5\Delta$: $\alpha_{so} = 0.05$ (black solid line), $\alpha_{so} = 0.1$ (red dashed line). The black dotted line represents $N_f(E)$ in the absence of any scattering.

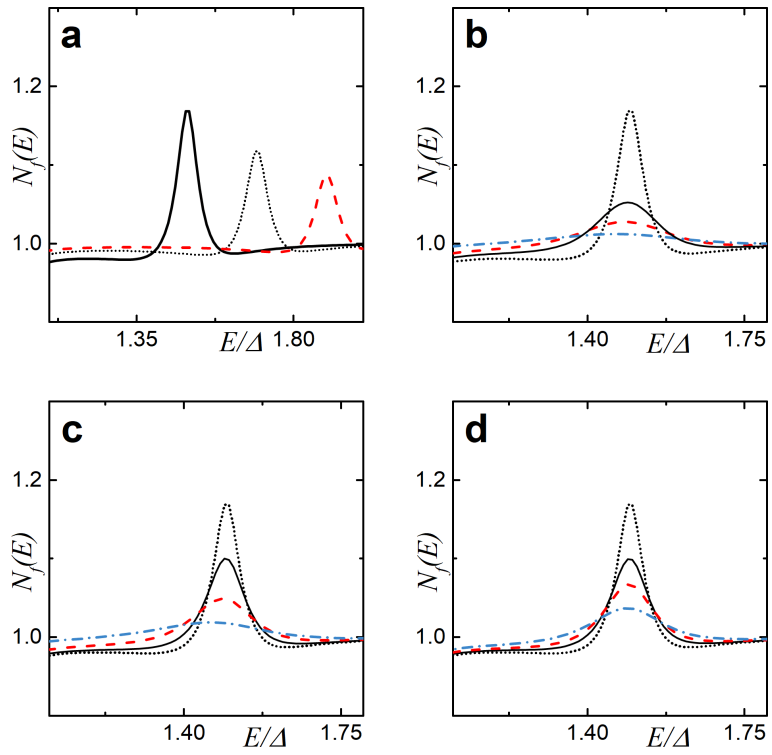

Figure 6: The peak at $E = \Delta$ in the DOS calculated numerically for three different h (a): $h = 1.4\Delta$ (black solid line), $h = 1.6\Delta$ (black dotted line), and $h = 1.9\Delta$ (red dashed line). The influence of different scatterings on the DOS peak at $E = h$ in the SF structure. Here, $\gamma_B = 50$, $d_f = 0.5\xi_f$, and the exchange field is $h = 1.5\Delta$ for plots (b)–(d). In plots (b)–(d), the black dotted line represents the DOS calculated in the absence of any scattering. Plot (b) corresponds to the case of nonzero α_z: $\alpha_z = 0.05$ (black solid line), $\alpha_z = 0.1$ (red dashed line), and $\alpha_z = 0.2$ (blue dash-dotted line). Plot (c) corresponds to the case of nonzero α_{so}: $\alpha_{so} = 0.02$ (black solid line), $\alpha_{so} = 0.06$ (red dashed line), and $\alpha_{so} = 0.15$ (blue dash-dotted line). Plot (d) corresponds to the case of nonzero α_x: $\alpha_x = 0.02$ (black solid line), $\alpha_x = 0.04$ (red dashed line), and $\alpha_x = 0.08$ (blue dash-dotted line).

scattering effects on the DOS structure. It should not be forgotten that the linearized solution of the form in Equation 20 is quite limited in its application. In our case, it is valid when $\gamma_B \gg 1$ and $d_f \ll \min(\xi_f, \sqrt{D_f/h})$, which is true for $\gamma_B = 50$. This tunneling limit is experimentally feasible. Thus, our result could easily be applied.

In Figure 7, the DOS calculated analytically via Equation 20 is illustrated. Here, we focus on the case of zero exchange field $h = 0$ to investigate the impact of each type of scattering on the mini-gap. We plot the analytically obtained DOS for the SN case in the absence of any scattering for comparison (black dotted line) as well. From the figure, one can see that the spin–orbit scattering does not affect the DOS in any way (Figure 7b). This effect has been shown before numerically in [85]. In contrast, both nonzero types magnetic of scattering, α_x and α_z, have a strong effect on the mini-gap, leading to its complete vanishing at some value of α (Figure 7a,c).

Making comparisons with previous results [84,85], we can say that there is a qualitative agreement in the DOS behavior. In the case of large DOS variations and, especially, singularities, the analytical model introduced above may fail. Nevertheless, we can explain major features of $N_f(E)$ in the presence of a spin-dependent scattering. Examining the linearized Usadel equations, we can analyze the anomalous Green's functions by studying even-frequency spin-singlet ($f_s \propto (\theta_{f\uparrow} + \theta_{f\downarrow})/2$) and odd-frequency spin-triplet ($f_t \propto (\theta_{f\uparrow} - \theta_{f\downarrow})/2$) components. When there is an F layer with a relatively high rate of parallel magnetic scattering, we can simplify the linearized Usadel equation and obtain

$$\frac{D_f}{2}\frac{\partial^2\theta_{f\uparrow(\downarrow)}}{\partial x^2} = \frac{1}{\tau_z}\theta_{f\uparrow(\downarrow)}. \tag{22}$$

From this equation, we can find that $\theta_{f\uparrow} = \theta_{f\downarrow} = 0$, leading to supression of both the singlet and triplet components. In the presence of large in-plane magnetic scattering α_x, we obtain $\theta_{f\uparrow} = -\theta_{f\downarrow}$, which leads to $f_s = 0$, whereas the triplet component f_t is nonzero. This can be understood in a similar way from the linearized Usadel equation

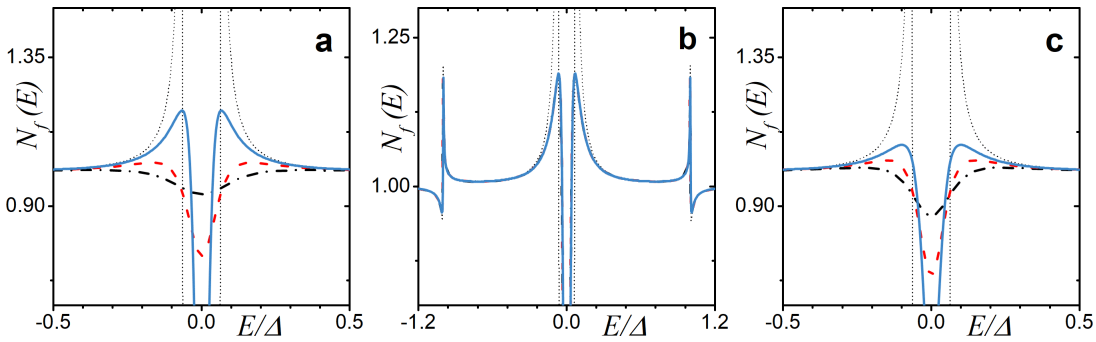

Figure 7: The DOS calculated analytically in the limit of low proximity and thin adjacent normal metal layer $h = 0$ with: (a) finite uniaxial magnetic scattering $\alpha_z > 0$ ($\alpha_x = \alpha_{so} = 0$); (b) spin–orbit scattering $\alpha_{so} > 0$ ($\alpha_z = 0.02$ and $\alpha_x = 0$); and (c) magnetic scattering $\alpha_x > 0$ ($\alpha_z = 0.02$ and $\alpha_{so} = 0$). The curves have been calculated for $\gamma_B = 50$ and $d_f = 0.5\xi_f$. In the plots, the blue solid line corresponds to $\alpha_i = 0.02$, the red dashed line corresponds to $\alpha_i = 0.05$, and the black dash-dotted corresponds to $\alpha_i = 0.1$, where i is the corresponding scattering rate. The faint black dotted line corresponds to the analytical solution of Equation 17.

$$\frac{D_f}{2}\frac{\partial^2\theta_{f\uparrow(\downarrow)}}{\partial x^2} = \frac{1}{\tau_x}\left(\theta_{f\uparrow} + \theta_{f\downarrow}\right). \tag{23}$$

Since the energy gap is defined by the singlet correlations, we observe a detrimental effect of the in-plane scattering on the mini-gap magnitude (Figure 7c). In contrast, in the limit of strong spin–orbit scattering α_{so}, the Usadel equation in F layer reads

$$\frac{D_f}{2}\frac{\partial^2\theta_{f\uparrow(\downarrow)}}{\partial x^2} = \pm\frac{1}{\tau_{so}}\left(\theta_{f\uparrow} - \theta_{f\downarrow}\right), \tag{24}$$

which results in $\theta_{f\uparrow} = \theta_{f\downarrow}$, causing strong suppression of the triplet component and not the singlet one, which in turn explains the robustness of the mini-gap (Figure 7b). It can be demonstrated that the suppression of the triplet component due to spin–orbit scattering can actually lead to the appearance of the mini-gap at finite exchange fields h.

One of the possible ways of observing the DOS features is the examination of the current–voltage characteristics. Utilizing the Werthamer expression for the quasiparticle current in tunneling junctions, we can calculate the I–V curves for an SFIFS junction. The current then reads

$$I = \frac{1}{eR}\int_{-\infty}^{\infty} \mathrm{d}E\, N_{f1}(E - eV) N_{f2}(E)\left[f(E - eV) - f(E)\right]. \tag{25}$$

Here, $N_{f1,2}(E)$ is the density of states (DOS) in the corresponding ferromagnetic layer at $x = 0$, $f(E) = [1 + \mathrm{e}^{E/T}]^{-1}$ is the Fermi–Dirac distribution function, and $R = R_{B0}$ is the resistance across the FIF interface. Both densities of states $N_{f1,2}(E)$ are normalized to their values in the normal state. The abovementioned effects of spin-dependent scattering have a direct influence on the current. Figure 8 demonstrates the current–voltage characteristics of the SFIFS junction calculated in the presence of parallel magnetic (Figure 8a), spin–orbit (Figure 8b), and perpendicular magnetic scattering (Figure 8c). From the plots, we can notice that while a magnetic scattering destroys the mini-gap, the spin–orbit scattering slightly enhances it.

Finally, we compare the analytically derived and numerically calculated DOS in the case of an SF junction with a thin F layer and low-transparency interface. The corresponding result is shown in Figure 9. We can observe a fairly good agreement between the numerical and the analytical calculations. As expected, the analytical expression in Equation 20 cannot describe the features of $N_f(E)$, which are relatively large in scale compared to unity.

Conclusion

We have formulated a model that takes into account magnetic and spin–orbit scattering processes in the framework of the quasiclassical Green's function approach in the diffusive limit. Based on these equations, the local density of states has been calculated numerically. Applying the developed numerical solution, we have studied some previously overlooked features such as the influence of the scattering rates on the peak at $E = h$. Moreover, we provide a relatively simple expression to calculate the DOS analytically in the presence of magnetic scattering α_z for thin F layers. In addition, the analytic solution for the anomalous Green's function has been derived in the limit of low proximity and a thin ferromagnetic layer. Based on this solution, we have been able to present analytical results for the DOS taking into account all spin-dependent scattering. We have demonstrated that the analytical result is in qualitative agree-

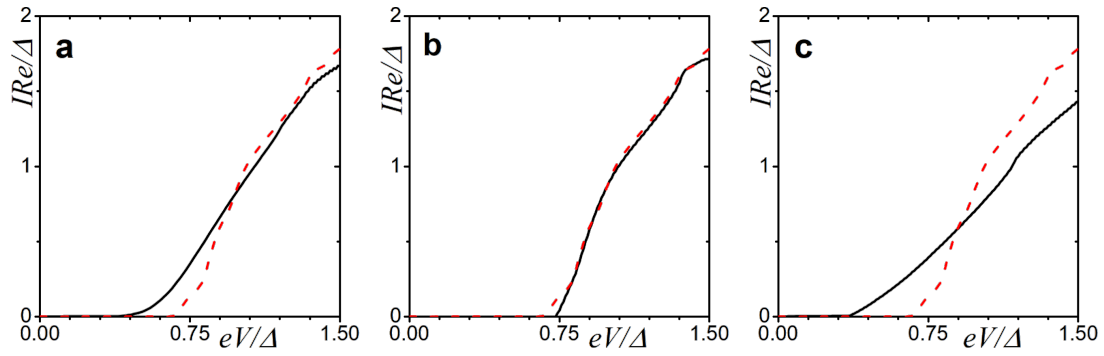

Figure 8: Current–voltage characteristics of a SFIFS junction in the presence of a spin-dependent scattering. The plots correspond to intermediate interface transparency $\gamma_B = 5$, $h = 0.1\Delta$, and $d_f = 0.5\xi_f$. Plot (a) corresponds to $\alpha_z = 0.1$, plot (b) corresponds to $\alpha_{so} = 0.13$, and plot (c) corresponds to $\alpha_x = 0.2$. The red dashed line represents the case of zero scattering.

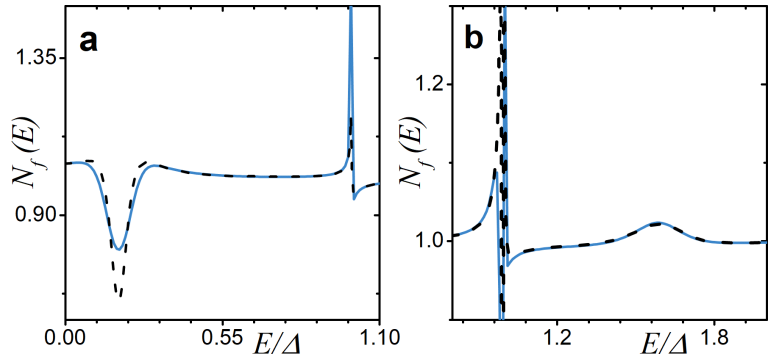

Figure 9: Comparison of the analytical result in the limit of low proximity and a thin adjacent ferromagnetic layer (black dashed line) with the DOS obtained numerically (blue solid line) for two different values of exchange field h. The parameters are $\gamma_B = 50$ and $d_f = 0.5\xi_f$. Plot (a): $h = 0.2\Delta$ and $\alpha_z = \alpha_x = \alpha_{so} = 0.02$. Plot (b): $h = 1.6\Delta$ and $\alpha_z = 0.02$ and $\alpha_{so} = \alpha_x = 0.04$.

ment with the numerical predictions, including previously published findings.

Funding

The numerical calculations of the density of states in S/F bilayers (see Figures 2–6) were supported by the Mirror Laboratories Project of HSE University. The analytical calculations of the density of states in S/F bilayers (see Figure 7 and Figure 9) were supported by the RSF project No. 20-42-09033. The calculations of the current-voltage characteristics of the SFIFS Josephson junctions (see Figure 8) were supported by the Foundation for the Advancement of Theoretical Physics and Mathematics "BASIS".

ORCID® iDs

Tairzhan Karabassov - https://orcid.org/0000-0001-7966-5221
Valeriia D. Pashkovskaia - https://orcid.org/0000-0002-1724-818X
Nikita A. Parkhomenko - https://orcid.org/0000-0003-1176-3989
Andrey S. Vasenko - https://orcid.org/0000-0002-2978-8650

Preprint

A non-peer-reviewed version of this article has been previously published as a preprint: https://doi.org/10.3762/bxiv.2022.55.v1

References

1. Buzdin, A. I. *Rev. Mod. Phys.* **2005,** *77,* 935–976. doi:10.1103/revmodphys.77.935
2. Golubov, A. A.; Kupriyanov, M. Yu.; Il'ichev, E. *Rev. Mod. Phys.* **2004,** *76,* 411–469. doi:10.1103/revmodphys.76.411
3. Bergeret, F. S.; Volkov, A. F.; Efetov, K. B. *Rev. Mod. Phys.* **2005,** *77,* 1321–1373. doi:10.1103/revmodphys.77.1321
4. Demler, E. A.; Arnold, G. B.; Beasley, M. R. *Phys. Rev. B* **1997,** *55,* 15174–15182. doi:10.1103/physrevb.55.15174
5. Ozaeta, A.; Vasenko, A. S.; Hekking, F. W. J.; Bergeret, F. S. *Phys. Rev. B* **2012,** *86,* 060509. doi:10.1103/physrevb.86.060509
6. Bergeret, F. S.; Tokatly, I. V. *Phys. Rev. Lett.* **2013,** *110,* 117003. doi:10.1103/physrevlett.110.117003
7. Khaydukov, Y.; Pütter, S.; Guasco, L.; Morari, R.; Kim, G.; Keller, T.; Sidorenko, A.; Keimer, B. *Beilstein J. Nanotechnol.* **2020,** *11,* 1254–1263. doi:10.3762/bjnano.11.109

8. Fominov, Y. V.; Feigel'man, M. V. *Phys. Rev. B* **2001,** *63,* 094518. doi:10.1103/physrevb.63.094518
9. Klenov, N.; Khaydukov, Y.; Bakurskiy, S.; Morari, R.; Soloviev, I.; Boian, V.; Keller, T.; Kupriyanov, M.; Sidorenko, A.; Keimer, B. *Beilstein J. Nanotechnol.* **2019,** *10,* 833–839. doi:10.3762/bjnano.10.83
10. Bakurskiy, S.; Kupriyanov, M.; Klenov, N. V.; Soloviev, I.; Schegolev, A.; Morari, R.; Khaydukov, Y.; Sidorenko, A. S. *Beilstein J. Nanotechnol.* **2020,** *11,* 1336–1345. doi:10.3762/bjnano.11.118
11. Marychev, P. M.; Vodolazov, D. Y. *Beilstein J. Nanotechnol.* **2020,** *11,* 858–865. doi:10.3762/bjnano.11.71
12. Radović, Z.; Ledvij, M.; Dobrosavljević-Grujić, L.; Buzdin, A. I.; Clem, J. R. *Phys. Rev. B* **1991,** *44,* 759–764. doi:10.1103/physrevb.44.759
13. Jiang, J. S.; Davidović, D.; Reich, D. H.; Chien, C. L. *Phys. Rev. Lett.* **1995,** *74,* 314–317. doi:10.1103/physrevlett.74.314
14. Izyumov, Y. A.; Proshin, Y. N.; Khusainov, M. G. *Phys.-Usp.* **2002,** *45,* 109–148. doi:10.1070/pu2002v045n02abeh001025
15. Fominov, Y. V.; Chtchelkatchev, N. M.; Golubov, A. A. *Phys. Rev. B* **2002,** *66,* 014507. doi:10.1103/physrevb.66.014507
16. Khaydukov, Yu. N.; Vasenko, A. S.; Kravtsov, E. A.; Progliado, V. V.; Zhaketov, V. D.; Csik, A.; Nikitenko, Yu. V.; Petrenko, A. V.; Keller, T.; Golubov, A. A.; Kupriyanov, M. Yu.; Ustinov, V. V.; Aksenov, V. L.; Keimer, B. *Phys. Rev. B* **2018,** *97,* 144511. doi:10.1103/physrevb.97.144511
17. Karabassov, T.; Stolyarov, V. S.; Golubov, A. A.; Silkin, V. M.; Bayazitov, V. M.; Lvov, B. G.; Vasenko, A. S. *Phys. Rev. B* **2019,** *100,* 104502. doi:10.1103/physrevb.100.104502
18. Karabassov, T.; Golubov, A. A.; Silkin, V. M.; Stolyarov, V. S.; Vasenko, A. S. *Phys. Rev. B* **2021,** *103,* 224508. doi:10.1103/physrevb.103.224508
19. Buzdin, A. I.; Bulaevskii, L. N.; Panyukov, S. V. *JETP Lett.* **1982,** *35,* 178.
20. Vdovichev, S. N.; Nozdrin, Y. N.; Pestov, E. E.; Yunin, P. A.; Samokhvalov, A. V. *JETP Lett.* **2016,** *104,* 329–333. doi:10.1134/s0021364016170148
21. Ryazanov, V. V.; Oboznov, V. A.; Rusanov, A. Y.; Veretennikov, A. V.; Golubov, A. A.; Aarts, J. *Phys. Rev. Lett.* **2001,** *86,* 2427–2430. doi:10.1103/physrevlett.86.2427
22. Ryazanov, V. V.; Oboznov, V. A.; Veretennikov, A. V.; Rusanov, A. Y. *Phys. Rev. B* **2001,** *65,* 020501. doi:10.1103/physrevb.65.020501
23. Blum, Y.; Tsukernik, A.; Karpovski, M.; Palevski, A. *Phys. Rev. Lett.* **2002,** *89,* 187004. doi:10.1103/physrevlett.89.187004
24. Sellier, H.; Baraduc, C.; Lefloch, F.; Calemczuk, R. *Phys. Rev. Lett.* **2004,** *92,* 257005. doi:10.1103/physrevlett.92.257005
25. Bauer, A.; Bentner, J.; Aprili, M.; Della Rocca, M. L.; Reinwald, M.; Wegscheider, W.; Strunk, C. *Phys. Rev. Lett.* **2004,** *92,* 217001. doi:10.1103/physrevlett.92.217001
26. Bell, C.; Loloee, R.; Burnell, G.; Blamire, M. G. *Phys. Rev. B* **2005,** *71,* 180501. doi:10.1103/physrevb.71.180501
27. Oboznov, V. A.; Bol'ginov, V. V.; Feofanov, A. K.; Ryazanov, V. V.; Buzdin, A. I. *Phys. Rev. Lett.* **2006,** *96,* 197003. doi:10.1103/physrevlett.96.197003
28. Shelukhin, V.; Tsukernik, A.; Karpovski, M.; Blum, Y.; Efetov, K. B.; Volkov, A. F.; Champel, T.; Eschrig, M.; Löfwander, T.; Schön, G.; Palevski, A. *Phys. Rev. B* **2006,** *73,* 174506. doi:10.1103/physrevb.73.174506
29. Vasenko, A. S.; Golubov, A. A.; Kupriyanov, M. Yu.; Weides, M. *Phys. Rev. B* **2008,** *77,* 134507. doi:10.1103/physrevb.77.134507
30. Anwar, M. S.; Czeschka, F.; Hesselberth, M.; Porcu, M.; Aarts, J. *Phys. Rev. B* **2010,** *82,* 100501. doi:10.1103/physrevb.82.100501
31. Khaire, T. S.; Khasawneh, M. A.; Pratt, W. P.; Birge, N. O. *Phys. Rev. Lett.* **2010,** *104,* 137002. doi:10.1103/physrevlett.104.137002
32. Robinson, J. W. A.; Witt, J. D. S.; Blamire, M. G. *Science* **2010,** *329,* 59–61. doi:10.1126/science.1189246
33. Baker, T. E.; Richie-Halford, A.; Icreverzi, O. E.; Bill, A. *EPL* **2014,** *107,* 17001. doi:10.1209/0295-5075/107/17001
34. Alidoust, M.; Halterman, K. *Phys. Rev. B* **2014,** *89,* 195111. doi:10.1103/physrevb.89.195111
35. Loria, R.; Meneghini, C.; Torokhtii, K.; Tortora, L.; Pompeo, N.; Cirillo, C.; Attanasio, C.; Silva, E. *Phys. Rev. B* **2015,** *92,* 184106. doi:10.1103/physrevb.92.184106
36. Bakurskiy, S. V.; Filippov, V. I.; Ruzhickiy, V. I.; Klenov, N. V.; Soloviev, I. I.; Kupriyanov, M. Yu.; Golubov, A. A. *Phys. Rev. B* **2017,** *95,* 094522. doi:10.1103/physrevb.95.094522
37. Yamashita, T.; Kawakami, A.; Terai, H. *Phys. Rev. Appl.* **2017,** *8,* 054028. doi:10.1103/physrevapplied.8.054028
38. Kontos, T.; Aprili, M.; Lesueur, J.; Genêt, F.; Stephanidis, B.; Boursier, R. *Phys. Rev. Lett.* **2002,** *89,* 137007. doi:10.1103/physrevlett.89.137007
39. Guichard, W.; Aprili, M.; Bourgeois, O.; Kontos, T.; Lesueur, J.; Gandit, P. *Phys. Rev. Lett.* **2003,** *90,* 167001. doi:10.1103/physrevlett.90.167001
40. Born, F.; Siegel, M.; Hollmann, E. K.; Braak, H.; Golubov, A. A.; Gusakova, D. Yu.; Kupriyanov, M. Yu. *Phys. Rev. B* **2006,** *74,* 140501. doi:10.1103/physrevb.74.140501
41. Pepe, G. P.; Latempa, R.; Parlato, L.; Ruotolo, A.; Ausanio, G.; Peluso, G.; Barone, A.; Golubov, A. A.; Fominov, Ya. V.; Kupriyanov, M. Yu. *Phys. Rev. B* **2006,** *73,* 054506. doi:10.1103/physrevb.73.054506
42. Weides, M.; Kemmler, M.; Goldobin, E.; Koelle, D.; Kleiner, R.; Kohlstedt, H.; Buzdin, A. *Appl. Phys. Lett.* **2006,** *89,* 122511. doi:10.1063/1.2356104
43. Weides, M.; Kemmler, M.; Kohlstedt, H.; Waser, R.; Koelle, D.; Kleiner, R.; Goldobin, E. *Phys. Rev. Lett.* **2006,** *97,* 247001. doi:10.1103/physrevlett.97.247001
44. Weides, M.; Schindler, C.; Kohlstedt, H. *J. Appl. Phys.* **2007,** *101,* 063902. doi:10.1063/1.2655487
45. Bannykh, A. A.; Pfeiffer, J.; Stolyarov, V. S.; Batov, I. E.; Ryazanov, V. V.; Weides, M. *Phys. Rev. B* **2009,** *79,* 054501. doi:10.1103/physrevb.79.054501
46. Kemmler, M.; Weides, M.; Weiler, M.; Opel, M.; Goennenwein, S. T. B.; Vasenko, A. S.; Golubov, A. A.; Kohlstedt, H.; Koelle, D.; Kleiner, R.; Goldobin, E. *Phys. Rev. B* **2010,** *81,* 054522. doi:10.1103/physrevb.81.054522
47. Pfeiffer, J.; Kemmler, M.; Koelle, D.; Kleiner, R.; Goldobin, E.; Weides, M.; Feofanov, A. K.; Lisenfeld, J.; Ustinov, A. V. *Phys. Rev. B* **2008,** *77,* 214506. doi:10.1103/physrevb.77.214506
48. Buzdin, A. *Phys. Rev. B* **2000,** *62,* 11377–11379. doi:10.1103/physrevb.62.11377
49. Kontos, T.; Aprili, M.; Lesueur, J.; Grison, X. *Phys. Rev. Lett.* **2001,** *86,* 304–307. doi:10.1103/physrevlett.86.304
50. Halterman, K.; Valls, O. T. *Phys. Rev. B* **2004,** *69,* 014517. doi:10.1103/physrevb.69.014517
51. Vasenko, A. S.; Kawabata, S.; Golubov, A. A.; Kupriyanov, M. Yu.; Lacroix, C.; Bergeret, F. S.; Hekking, F. W. J. *Phys. Rev. B* **2011,** *84,* 024524. doi:10.1103/physrevb.84.024524

52. Kontos, T.; Aprili, M.; Lesueur, J.; Grison, X.; Dumoulin, L. *Phys. Rev. Lett.* **2004,** *93,* 137001. doi:10.1103/physrevlett.93.137001
53. Buzdin, A. *Phys. Rev. Lett.* **2008,** *101,* 107005. doi:10.1103/physrevlett.101.107005
54. Pugach, N. G.; Goldobin, E.; Kleiner, R.; Koelle, D. *Phys. Rev. B* **2010,** *81,* 104513. doi:10.1103/physrevb.81.104513
55. Pugach, N. G.; Kupriyanov, M. Yu.; Vedyayev, A. V.; Lacroix, C.; Goldobin, E.; Koelle, D.; Kleiner, R.; Sidorenko, A. S. *Phys. Rev. B* **2009,** *80,* 134516. doi:10.1103/physrevb.80.134516
56. Volkov, A. F.; Efetov, K. B. *Phys. Rev. Lett.* **2009,** *103,* 037003. doi:10.1103/physrevlett.103.037003
57. Mai, S.; Kandelaki, E.; Volkov, A. F.; Efetov, K. B. *Phys. Rev. B* **2011,** *84,* 144519. doi:10.1103/physrevb.84.144519
58. Karabassov, T.; Guravova, A. V.; Kuzin, A. Y.; Kazakova, E. A.; Kawabata, S.; Lvov, B. G.; Vasenko, A. S. *Beilstein J. Nanotechnol.* **2020,** *11,* 252–262. doi:10.3762/bjnano.11.19
59. Bobkova, I. V.; Bobkov, A. M. *Phys. Rev. B* **2017,** *96,* 104515. doi:10.1103/physrevb.96.104515
60. Linder, J.; Bathen, M. E. *Phys. Rev. B* **2016,** *93,* 224509. doi:10.1103/physrevb.93.224509
61. Machon, P.; Eschrig, M.; Belzig, W. *Phys. Rev. Lett.* **2013,** *110,* 047002. doi:10.1103/physrevlett.110.047002
62. Ozaeta, A.; Virtanen, P.; Bergeret, F. S.; Heikkilä, T. T. *Phys. Rev. Lett.* **2014,** *112,* 057001. doi:10.1103/physrevlett.112.057001
63. Kolenda, S.; Wolf, M. J.; Beckmann, D. *Phys. Rev. Lett.* **2016,** *116,* 097001. doi:10.1103/physrevlett.116.097001
64. Giazotto, F.; Robinson, J. W. A.; Moodera, J. S.; Bergeret, F. S. *Appl. Phys. Lett.* **2014,** *105,* 062602. doi:10.1063/1.4893443
65. Giazotto, F.; Heikkilä, T. T.; Bergeret, F. S. *Phys. Rev. Lett.* **2015,** *114,* 067001. doi:10.1103/physrevlett.114.067001
66. Bobkova, I. V.; Bobkov, A. M.; Belzig, W. *Phys. Rev. B* **2021,** *103,* L020503. doi:10.1103/physrevb.103.l020503
67. Tagirov, L. R. *Phys. Rev. Lett.* **1999,** *83,* 2058–2061. doi:10.1103/physrevlett.83.2058
68. Huertas-Hernando, D.; Nazarov, Y. V.; Belzig, W. *Phys. Rev. Lett.* **2002,** *88,* 047003. doi:10.1103/physrevlett.88.047003
69. Giazotto, F.; Taddei, F. *Phys. Rev. B* **2008,** *77,* 132501. doi:10.1103/physrevb.77.132501
70. Giazotto, F.; Bergeret, F. S. *Appl. Phys. Lett.* **2013,** *102,* 162406. doi:10.1063/1.4802953
71. Alidoust, M.; Halterman, K.; Valls, O. T. *Phys. Rev. B* **2015,** *92,* 014508. doi:10.1103/physrevb.92.014508
72. Halterman, K.; Alidoust, M. *Phys. Rev. B* **2016,** *94,* 064503. doi:10.1103/physrevb.94.064503
73. Halterman, K.; Alidoust, M. *Supercond. Sci. Technol.* **2016,** *29,* 055007. doi:10.1088/0953-2048/29/5/055007
74. Srivastava, A.; Olde Olthof, L. A. B.; Di Bernardo, A.; Komori, S.; Amado, M.; Palomares-Garcia, C.; Alidoust, M.; Halterman, K.; Blamire, M. G.; Robinson, J. W. A. *Phys. Rev. Appl.* **2017,** *8,* 044008. doi:10.1103/physrevapplied.8.044008
75. Halterman, K.; Alidoust, M. *Phys. Rev. B* **2018,** *98,* 134510. doi:10.1103/physrevb.98.134510
76. Ozaeta, A.; Vasenko, A. S.; Hekking, F. W. J.; Bergeret, F. S. *Phys. Rev. B* **2012,** *85,* 174518. doi:10.1103/physrevb.85.174518
77. Kawabata, S.; Ozaeta, A.; Vasenko, A. S.; Hekking, F. W. J.; Sebastián Bergeret, F. *Appl. Phys. Lett.* **2013,** *103,* 032602. doi:10.1063/1.4813599
78. Gordeeva, A. V.; Pankratov, A. L.; Pugach, N. G.; Vasenko, A. S.; Zbrozhek, V. O.; Blagodatkin, A. V.; Pimanov, D. A.; Kuzmin, L. S. *Sci. Rep.* **2020,** *10,* 21961. doi:10.1038/s41598-020-78869-z
79. Golubov, A. A.; Kupriyanov, M. Yu. *J. Low Temp. Phys.* **1988,** *70,* 83–130. doi:10.1007/bf00683247
80. Crouzy, B.; Bascones, E.; Ivanov, D. A. *Phys. Rev. B* **2005,** *72,* 092501. doi:10.1103/physrevb.72.092501
81. Golubov, A. A.; Kupriyanov, M. Yu.; Siegel, M. *JETP Lett.* **2005,** *81,* 180–184. doi:10.1134/1.1914877
82. Houzet, M.; Vinokur, V.; Pistolesi, F. *Phys. Rev. B* **2005,** *72,* 220506. doi:10.1103/physrevb.72.220506
83. Kuprianov, M. Yu.; Lukichev, V. F. *Sov. Phys. JETP* **1988,** *67,* 1163.
84. Gusakova, D. Y.; Golubov, A. A.; Kupriyanov, M. Yu.; Buzdin, A. *J. Exp. Theor. Phys. Lett.* **2006,** *83,* 327–331. doi:10.1134/s0021364006080066
85. Linder, J.; Yokoyama, T.; Sudbø, A. *Phys. Rev. B* **2008,** *77,* 174514. doi:10.1103/physrevb.77.174514
86. Yoshizaki, D.; Golubov, A. A.; Tanaka, Y.; Asano, Y. *Jpn. J. Appl. Phys.* **2012,** *51,* 010108. doi:10.1143/jjap.51.010108
87. Cottet, A.; Linder, J. *Phys. Rev. B* **2009,** *79,* 054518. doi:10.1103/physrevb.79.054518
88. Bezuglyi, E. V.; Vasenko, A. S.; Shumeiko, V. S.; Wendin, G. *Phys. Rev. B* **2005,** *72,* 014501. doi:10.1103/physrevb.72.014501
89. Bezuglyi, E. V.; Vasenko, A. S.; Bratus, E. N.; Shumeiko, V. S.; Wendin, G. *Phys. Rev. B* **2006,** *73,* 220506. doi:10.1103/physrevb.73.220506
90. Vasenko, A. S.; Hekking, F. W. J. *J. Low Temp. Phys.* **2009,** *154,* 221–232. doi:10.1007/s10909-009-9869-z
91. Arutyunov, K. Y.; Auraneva, H.-P.; Vasenko, A. S. *Phys. Rev. B* **2011,** *83,* 104509. doi:10.1103/physrevb.83.104509
92. Arutyunov, K. Y.; Chernyaev, S. A.; Karabassov, T.; Lvov, D. S.; Stolyarov, V. S.; Vasenko, A. S. *J. Phys.: Condens. Matter* **2018,** *30,* 343001. doi:10.1088/1361-648x/aad3ea
93. Usadel, K. D. *Phys. Rev. Lett.* **1970,** *25,* 507–509. doi:10.1103/physrevlett.25.507
94. Belzig, W.; Wilhelm, F. K.; Bruder, C.; Schön, G.; Zaikin, A. D. *Superlattices Microstruct.* **1999,** *25,* 1251–1288. doi:10.1006/spmi.1999.0710
95. Fauré, M.; Buzdin, A. I.; Golubov, A. A.; Kupriyanov, M. Yu. *Phys. Rev. B* **2006,** *73,* 064505. doi:10.1103/physrevb.73.064505
96. Ivanov, D. A.; Fominov, Y. V.; Skvortsov, M. A.; Ostrovsky, P. M. *Phys. Rev. B* **2009,** *80,* 134501. doi:10.1103/physrevb.80.134501
97. Cottet, A. *Phys. Rev. B* **2007,** *76,* 224505. doi:10.1103/physrevb.76.224505
98. Cottet, A.; Huertas-Hernando, D.; Belzig, W.; Nazarov, Y. V. *Phys. Rev. B* **2009,** *80,* 184511. doi:10.1103/physrevb.80.184511
99. McMillan, W. L. *Phys. Rev.* **1968,** *175,* 537–542. doi:10.1103/physrev.175.537
100. Zareyan, M.; Belzig, W.; Nazarov, Y. V. *Phys. Rev. Lett.* **2001,** *86,* 308–311. doi:10.1103/physrevlett.86.308
101. Yokoyama, T.; Tanaka, Y.; Golubov, A. A. *Phys. Rev. B* **2005,** *72,* 052512. doi:10.1103/physrevb.72.052512
102. Yokoyama, T.; Tanaka, Y.; Golubov, A. A. *Phys. Rev. B* **2006,** *73,* 094501. doi:10.1103/physrevb.73.094501
103. Yokoyama, T.; Tanaka, Y.; Golubov, A. A. *Phys. Rev. B* **2007,** *75,* 134510. doi:10.1103/physrevb.75.134510
104. Vasenko, A. S.; Kawabata, S.; Ozaeta, A.; Golubov, A. A.; Stolyarov, V. S.; Bergeret, F. S.; Hekking, F. W. J. *J. Magn. Magn. Mater.* **2015,** *383,* 175–179. doi:10.1016/j.jmmm.2014.11.009

BEILSTEIN JOURNAL OF NANOTECHNOLOGY

Coherent amplification of radiation from two phase-locked Josephson junction arrays

Mikhail A. Galin*[1], Vladimir M. Krasnov[2], Ilya A. Shereshevsky[1], Nadezhda K. Vdovicheva[1] and Vladislav V. Kurin[1]

Full Research Paper

Open Access

Address:
[1]Institute for Physics of Microstructures RAS, 603950 Nizhny Novgorod, Russia and [2]Department of Physics, Stockholm University, AlbaNova University Center, SE-10691 Stockholm, Sweden

Email:
Mikhail A. Galin* - galin@ipmras.ru

* Corresponding author

Keywords:
coherent radiation; Josephson junction arrays; numerical modelling; single-strip line; synchronization

Beilstein J. Nanotechnol. **2022,** *13,* 1445–1457.
https://doi.org/10.3762/bjnano.13.119

Received: 01 July 2022
Accepted: 01 November 2022
Published: 06 December 2022

This article is part of the thematic issue "Intrinsic Josephson effect and prospects of superconducting spintronics".

Guest Editor: A. S. Sidorenko

Abstract

We analyze experimentally and theoretically mutual phase locking and electromagnetic interaction between two linear arrays with a large number of Josephson junctions. Arrays with different separation, either on the same chip or on two separate substrates are studied. We observe a large coherent gain, up to a factor of three, of emitted power from two simultaneously biased arrays, compared to the sum of powers from two individually biased arrays. The phenomenon is attributed to the phase locking of junctions in different arrays via a common electromagnetic field. Remarkably, the gain can exceed the factor of two expected for a simple constructive interference of two oscillators. The larger gain is explained by an additional consequence of mutual interaction between two large arrays. Mutual phase locking of large arrays does not only result in constructive interference outside the arrays, but also improved synchronization of junctions inside each array. Our conclusion is supported by numerical modelling.

Introduction

A Josephson junction (JJ) has the unique ability to transform an applied constant voltage V into electromagnetic (EM) oscillations. The fundamental Josephson frequency, f_J, is connected to V via the ac-Josephson relation, $hf_J = 2eV$, where h is the Planck constant and e is the elementary charge. Josephson generation occurs up to the superconducting gap voltage. Therefore, f_J can be up to about 1 THz for low-T_c JJs [1] and can reach tens of terahertz for high-T_c JJs [2,3]. Thus, a JJ has the potential to be the basis of compact, continuous-wave and tunable terahertz generators, which would facilitate solving the problem of so-called "THz gap" [4].

A single JJ emits only a very small off-chip power, typically in the picowatt range. To enhance it to a practical level of about

1 mW, it is necessary to combine many equivalent junctions in an array [5]. However, synchronization of a large number of radiation sources is a serious electrodynamical problem. This problem can be resolved for a group of JJs that extends in subwavelength dimensions. Such a configuration is realized for intrinsic JJs formed in a BiSCCO crystal where almost 700 JJs are localized within 1 μm [6]. The generation in a wide frequency range of 1–11 THz has been demonstrated from BiSCCO mesas containing up to 250 JJs [2]. A maximal emission of about 1 μW corresponds to in-phase cavity modes in the mesas, indicating the coherent superradiant nature of the emission.

The arrays based on intrinsic JJs suffer from overheating, which impedes a raise of radiation power. This problem manifests considerably less in discrete JJ arrays. Modern lithographic technologies allow for fabricating discrete JJs with dimensions down to the sub-100 nm scale [7]. However, the size of very large arrays with thousands of JJs may exceed the radiation wavelength. For such superwavelength systems, delay effects become dominant for synchronization. To reach the radiation power maximum, JJs should be synchronized with the EM mode excited within the resonator. Such large JJ arrays become similar to a laser where the junctions play the role of atoms in an active medium. The advantage of large JJ arrays working similar to lasers is discussed in more detail in [8]. The resonator can be a cavity of the JJs itself [2], an electrode with embedded JJs [9], or the dielectric substrate on which the JJ array is arranged [10].

Coherent superradiant amplification of emitted power is caused by a constructive interference of EM fields from phase-locked oscillators [11]. For two oscillators, the EM field in the far-field maximally doubles. Hence, the superradiant power, proportional to the square of the EM field, is at most four times larger than that from a single oscillator. For incoherent emission from two unlocked oscillators the power just adds up and is twice the power from a single oscillator. Therefore, the total superradiant power gain for two oscillators, defined as the ratio of coherent-to-incoherent emission, is at most two. For N oscillators, the supperradiant power increase is at most N^2 times the power from one oscillator and the superradiant gain factor is at most N. For large N, this could greatly enhance the emitted power. This is the main motivation for the development of Josephson oscillators based on arrays with many JJs [2,3,6,9,10,12-15].

Resonant modes formed along five straight electrodes with niobium JJs have been directly visualized recently using low-temperature scanning laser microscopy [13]. The scans revealed that the standing waves can provide the global coupling of all junctions in the array, that is, extended parts of the array can interact with each other. This generates the two-dimensional resonant mode that should lead to the increased output power. Therefore, along with the interaction between individual JJs, there is also a mutual coupling between different arrays (including JJs and electrodes) [14]. In the ideal case of two perfectly phase-locked arrays with N JJs each, the total superradiant power is proportional to $4N^2$, which is two times larger than the sum of powers from two incoherent arrays. Therefore, such arrays can be considered as individual oscillators, and the gain factor for two phase-locked arrays equals two. Yet, the physics of inter-array coupling is much more complicated. In reality, synchronization between junctions in each array is not perfect due to the insufficient amplitude of the resonant mode. In this case, resonant coupling of two arrays may improve the state within each array. As we will show, this could increase the gain factor well above a factor of two. The goal of our work is to study inter-array coupling and its manifestations.

In this work we study the interaction between two linear arrays of Nb/NbSi/Nb JJs. The arrays have a single-line geometry with 332 or 380 JJs embedded in a straight electrode. We analyze the mutual interaction between two independently biased arrays oriented parallel to each other. First, we study arrays on the same chip for different distances of 4 and 238 μm between them. Then, we consider two arrays on different chips, stacked on top of each other. We perform simultaneously the measurement of current–voltage characteristic (IVC) and bolometric analysis of the emitted radiation. In all cases, we observe clear signatures of inter-array interaction. They occur when both arrays are biased at the same voltage and oscillate at the same frequency, coinciding with one of the cavity modes in the array electrodes. This leads to a profound enhancement of resonant step amplitudes in the IVCs of the arrays, indicating that the state of one array is strongly affected by oscillations in another array. The inter-array coupling is manifested by a significant amplification of emitted power with a gain factor of up to three. It is well above the factor of two expected in the simple case of bare coherent superposition of oscillations. This result points out that phase locking of oscillations in the two arrays not only leads to coherent amplification of radiation. It also can improve the synchronization inside each array. The latter effect removes the limit of two for the gain factor. Finally, for better understanding, we performed numerical simulations of the inner dynamics for two interacting arrays. Our simulations confirm that two arrays can be phase-locked by a common EM field. They also provide estimation of the resulting superradiant gain. The performed experimental investigations and numerical calculations can give new ideas about the design of discrete JJ arrays that would provide more effective synchronization of JJs in order to get an output power sufficient for practical applications.

Experimental

Samples

We study samples containing one or several straight strips with embedded Nb/NbSi/Nb overlap JJs connected in series. The samples were fabricated by Oliver Kieler (Braunschweig, Germany) and were measured in AlbaNova University Center (Stockholm, Sweden). The fabrication is a self-aligning process using e-beam lithography and reactive ion etching [16,17]. Similar arrays were studied earlier in [9,12,13], where additional information about sample characterization can be found.

Figure 1a,b shows the layout of "sample-1". It has been fabricated on a 1 × 1 cm^2 silicon substrate with the thickness 0.38 mm. It contains three closely located straight strips with a separation of only 4 μm. Each strip has the length L = 5 mm and the width w = 14 μm and contains 332 JJs distributed uniformly along the strip. The junction area is 8 × 8 μm^2. Contact electrodes are connected to each strip, allowing for independent biasing of each of these three arrays. Below, we will analyze the interaction between the leftmost "array-a" biased with a variable dc current and "array-b" in the middle biased with a fixed current (Figure 1b).

Figure 1c shows the layout of "sample-2". It has a significantly larger separation of 238 μm between the adjacent linear arrays. In total, it contains 17 similar lines with 380 JJs and a total length of L = 5.7 mm. The junction area is 6 × 6 μm^2. Below, we will show data for the case when the rightmost "array-a" is biased with a variable dc current and the nearby "array-b" is biased with a fixed current.

Sample-1 and sample-2 were used for on-chip analysis where two linear arrays are placed on the same substrate. We also present data for off-chip synchronization. To this end, two linear arrays were stacked on top of each other.

Radiation detection

An InSb bolometer is used for the detection of Josephson radiation. The detector and measurement procedure are the same as described in [9,12], where additional information can be found. The bolometer is based on a high-purity n-doped InSb crystal with dimension of 2–3 mm, which is placed approximately 0.5 cm above the array. The absorbed radiation causes an increase of charge carriers in the conduction band and leads to a decrease of the dc voltage at a fixed bias current. Therefore, we take the negative change of the dc voltage of the bolometer ΔU as a measure of the absorbed power, that is, $\Delta U = U_0 - U > 0$ where U_0 and U are the voltages on the crystal in absence and in presence of the radiation, respectively. All measurements were performed in a liquid helium dewar at a temperatures

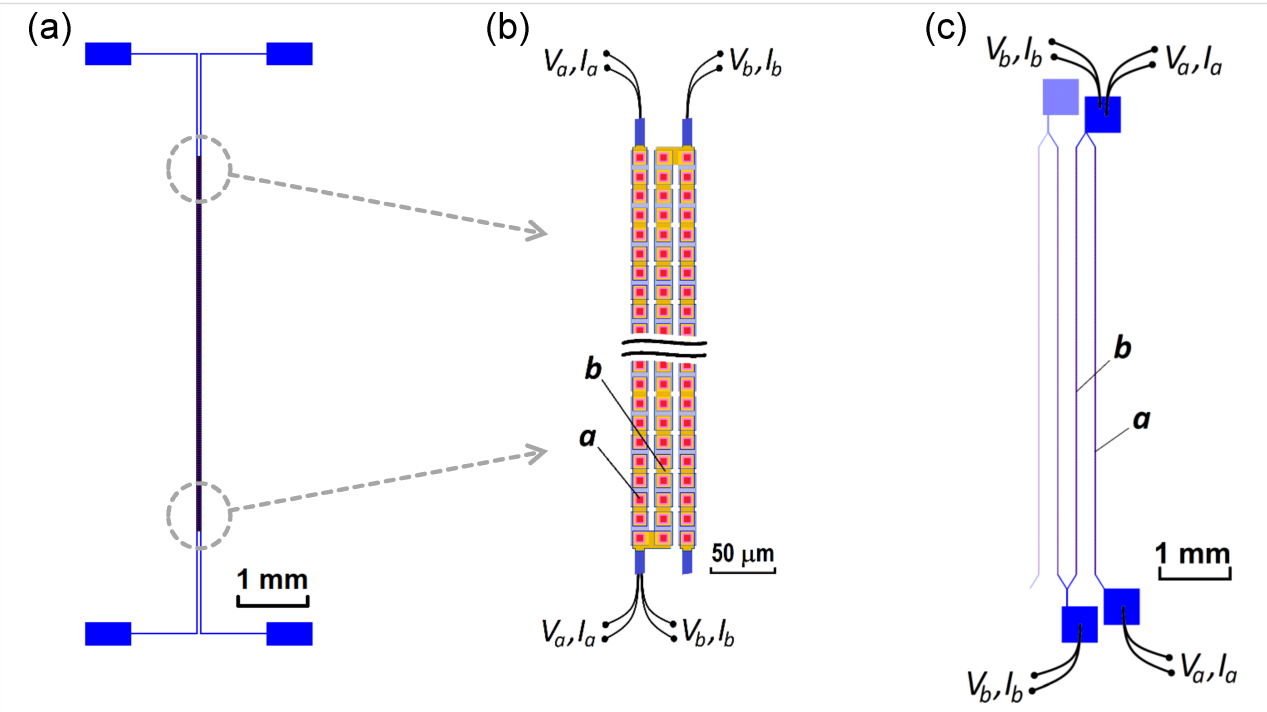

Figure 1: (a) Geometry of sample-1 with 332 JJs in each of the three linear arrays. (b) Two enlarged fragments of sample-1. Red squares represent the JJs, which are between the top (orange rectangles) and the bottom (partly covered blue rectangles) niobium electrodes. (c) Geometry of the right part of sample-2 with 380 JJs in each linear array. In the measurements with either of the samples, the outer array-a was biased by a sweep current (V_a, I_a) while the adjacent inner array-b was biased at fixed voltage V_b and current I_b by another current source. The points of source connections are depicted schematically.

$T \gtrsim 4.2$ K both for the samples and the detector. The calibrated responsivity of the detector at this temperature was estimated as ≃300 V/W.

Results

Figure 2a shows the individually measured IVCs of array-a and array-b of sample-1 (Figure 1a,b). The critical current in both arrays is I_c = 2.0–2.1 mA and the characteristic frequency, estimated within the resistively shunted junction (RSJ) model, is in the range of f_c ~ 100–120 GHz. Figure 2b shows similar data for sample-2. Here, for both arrays, $I_c \approx 2.9$ mA and f_c ~ 80–100 GHz. Although the area of junctions in sample-2 is smaller, the critical current is slightly larger than in sample-1 due to higher doping of the NbSi interlayers. Note that the abrupt transition from a superconductive to a resistive state observed in all IVCs is typical for niobium junctions with medium doping Si interlayer ≲11% [18].

Resonant steps at similar voltages are observed for both pairs of arrays. As shown earlier [9,13], they are caused by standing wave (cavity mode) resonances in the whole length of strips of JJs. However, for both samples the steps are more pronounced in the inner array-b than in the outer array-a. Presumably, this is due to a more beneficial EM environment for the inner strip, which has two adjacent strips on both sides operating as additional single-strip line resonators (see Figure 1).

In Figure 2a, we marked bias points 1–8 in array-b, at which detailed measurements are reported below for sample-1. Using the value of EM wave speed along a single-strip line obtained in [13], we can estimate the corresponding numbers of cavity modes m = 11–18. Similarly, bias points 1–10 in Figure 2b are used for analysis of sample-2. According to our estimation, they correspond to numbers of cavity modes m = 10–19.

Synchronization of two arrays on the same chip

In this work, we aim to study the EM interaction between two independently biased arrays. For the on-chip measurement, the bias current in the outer array-a I_a was varied while the middle/inner array-b was biased at fixed values of current I_b = const. All other arrays remain unbiased and, therefore, inactive. Thus, we measure the dc voltage of array-b V_b and the full IVC of array-a $V_a(I_a)$. Simultaneously, the radiation signal $\Delta U_{ab}(V_a, V_b)$ is detected. The dc bias point of array-b (I_b, V_b) is chosen at one of the resonant steps. These points are marked by numbers in the IVCs of Figure 2.

Synchronization of closely spaced arrays (sample-1)

We start with sample-1, which has the shorter separation between the strips. Figure 3a shows two IVCs of array-a. The green IVC is measured with a passive array-b, V_b = 0, and the red is measured with a fixed bias I_b = 2.98 mA and V_b = 123 mV, corresponding to the bias point 5 in Figure 2a. The inset shows a close-up of the voltage range V_a ~ V_b, which demonstrates that oscillations in array-b lead to a pronounced enhancement of the resonant step in array-a at $V_a \approx V_b$ while other steps are practically unaffected. The differential resistance in the center of this step R_d decreases by a factor of four, from R_d = 16 Ω to R_d = 4 Ω. Since the step amplitude reflects (approximately proportionally) the amplitude of the EM field in the cavity mode, this clearly demonstrates that the active array-b amplifies the EM oscillation amplitude in array-a under the condition $V_a \simeq V_b$. This means almost exact

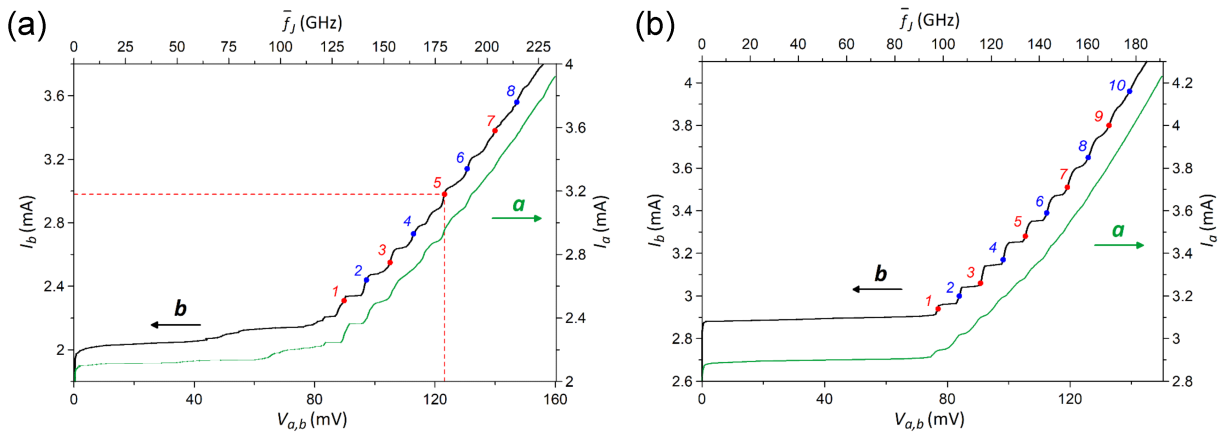

Figure 2: IVCs of outer array-a (rigth axis) and adjacent inner array-b (left axis) of sample-1 (a) and sample-2 (b). The enumerated points correspond to the biasing of the inner array with currents of I_b = 2.31 (1), 2.44 (2), 2.55 (3), 2.73 (4), 2.98 (5), 3.14 (6), 3.38 (7), and 3.56 mA (8) for sample-1 (a) and with currents of I_b = 2.94 (1), 3 (2), 3.06 (3), 3.17 (4), 3.28 (5), 3.39 (6), 3.51 (7), 3.65 (8), 3.8 (9), and 3.96 mA (10) for sample-2 (b). The case of biasing at the indicated point 5 in panel (a) is discussed in Figure 3a,b.

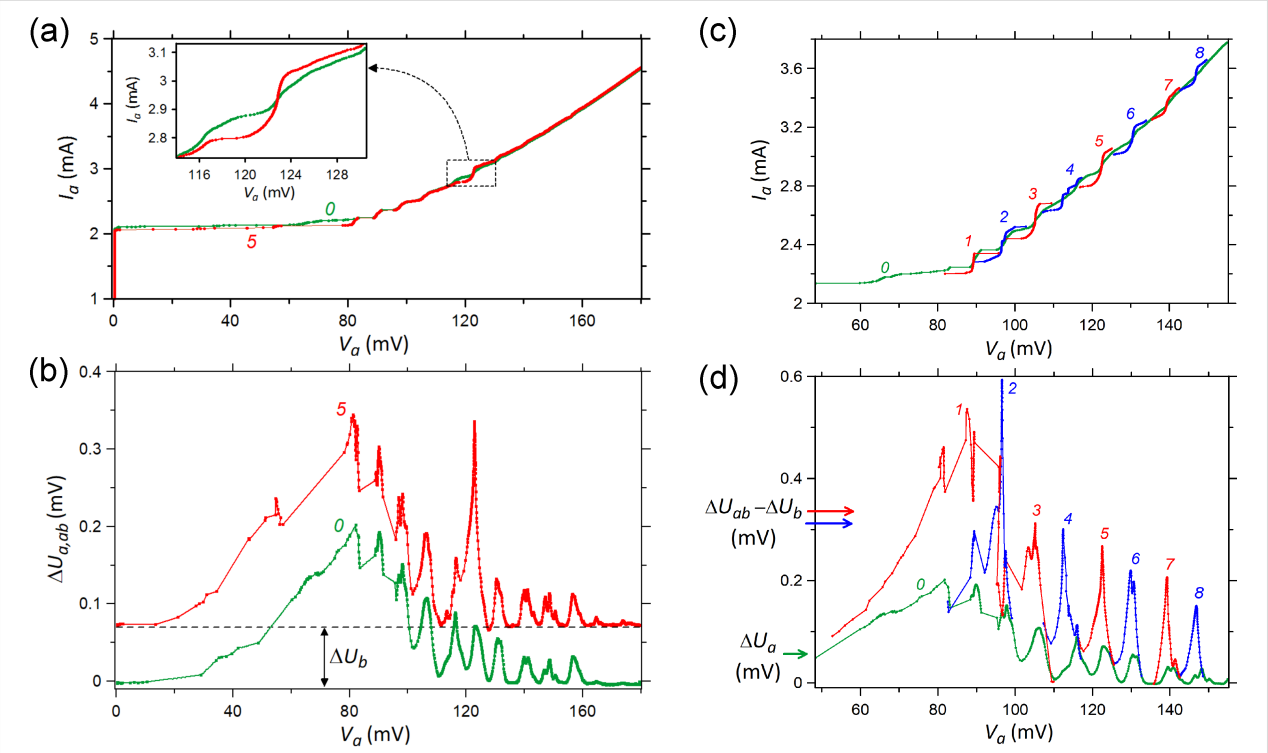

Figure 3: (a, b) IVCs of the outer array-a in sample-1 (a) and corresponding bolometer signal (b) when the inner array-b is unbiased (curves 0) and biased at I_b = 2.98 mA, V_b = 123 mV, which corresponds to point 5 indicated in Figure 2a (curves 5). The inset in panel (a) shows an enlarged fragment of the IVCs at $V_a \sim V_b$ with the current step, which becomes greater and more distinct due to the EM interaction between the two arrays. The value ΔU_b in panel (b) is the radiation signal derived from array-b at unbiased array-a. (c, d) The data set for the IVCs of the outer array-a (c) and for the bolometer signal (d). Curves 0 are derived at an unbiased inner array-b while curves 1–8 correspond to the biasing of array-b at the points indicated in Figure 2a. The curves 1–8 are the fragments of IVCs and bolometer signals in the ranges where significant changes relative to the curves 0 are observed.

equality of the mean Josephson frequencies averaged over all JJs $\overline{f}_a \simeq \overline{f}_b \approx 179$ GHz, which is the necessary condition for phase locking.

In Figure 3b, we present results of the radiation detection measured simultaneously with the IVCs in Figure 3a. The lower green curve shows the detector signal $\Delta U_a(V_a, V_b = 0)$ as a function of the voltage V_a in array-a, for the unbiased array-b, $V_b = 0$. It represents the emission power solely from array-a. The upper red curve shows similar data, $\Delta U_{ab}(V_a, V_b)$, when array-b is biased to the point 5 in Figure 2a. It is seen that here $\Delta U_{ab}(V_a = 0) = 0.07$ mV. This signal offset represents the emission $\Delta U_b(V_b)$ from array-b alone. It can be seen that the shapes of the two curves in Figure 3b are quite similar. At almost all V_a, they simply differ by a constant offset, $\Delta U_{ab}(V_a, V_b = \text{const}) \simeq \Delta U_a(V_a, V_b = 0) + \Delta U_b(V_a = 0, V_b = \text{const})$, as indicated by the dashed horizontal line. This implies that, usually, the powers from the two arrays simply add up, which is typical for the incoherent state. However, a remarkable peak is observed when the voltages of the two arrays practically coincide, $V_a \simeq V_b = 123$ mV. At this point, $\Delta U_{ab}(V_a \simeq V_b) = 0.34$ mV, which is 2.4 times larger than the sum of individual arrays $\Delta U_a(V_b) + \Delta U_b(V_b) \simeq 2\Delta U_b(V_b) = 0.14$ mV. To quantify this effect, we consider the gain factor

$$g = \frac{\Delta U_{ab}(V_a, V_b)}{\Delta U_a(V_a, V_b = 0) + \Delta U_b(V_a = 0, V_b)} \simeq \frac{\Delta U_{ab}(V_a, V_b)}{2\Delta U_a(V_a, V_b = 0)}, \quad (1)$$

which describes the coherent superradiant amplification of the radiation power.

In Figure 3c,d, we show a similar analysis for all explored bias points in array-b. Figure 3c shows the IVC of array-a $I_a(V_a)$ without bias in array-b (green line) and portions of the IVCs at bias points 1–8 of array-b indicated in Figure 2a (red and blue curves). Here, we show eight fragments of separately measured IVCs close to the condition of phase locking $V_a \sim V_b$. It can be seen that at all bias points, V_b, a strong enhancement of the resonant step in array-a occurs compared to the case without bias, $V_b = 0$. This is particularly clear for higher bias points 7

and 8, for which the steps without bias in array-b are barely visible, but with bias they are well developed.

Figure 3d shows the detector response $\Delta U_a(V_a, V_b)$ measured simultaneously with the IVCs from Figure 3c. The lower green curve is measured at an unbiased array-b. The upper red/blue curves correspond to bias points 1–8 in array-b (Figure 2a). At low bias, bias points 1–3, we observe a multimode excitation, that is, some gain occurs even at modes adjacent to V_b. At higher bias, single mode amplification takes place, as for the bias point 5 discussed above (Figure 3b). The gain factors for all eight bias points are given in Table 1. The highest gain is observed at point 7 with $g = 2.9$.

Synchronization of more distant arrays (sample-2)

Next, we consider sample-2 with significantly larger separation between the arrays, namely 238 µm. Figure 4a shows IVCs of the outer array-a. The green curve shows the result without bias in the inner array-b. The blue and red curves show results with bias at points 1–10 indicated in Figure 2b. Comparable to sam-

Table 1: Gain factor from the interaction of outer and inner arrays in sample-1.

No. of step/bias point	1	2	3	4	5	6	7	8
I_b, mA	2.31	2.44	2.55	2.73	2.98	3.14	3.38	3.56
$\bar{f}_j$, GHz	127.5	140.7	153.2	163.7	178.4	189.2	202.9	213.8
g	1.8	1.9	1.9	1.6	2.3	2.1	2.9	2.5

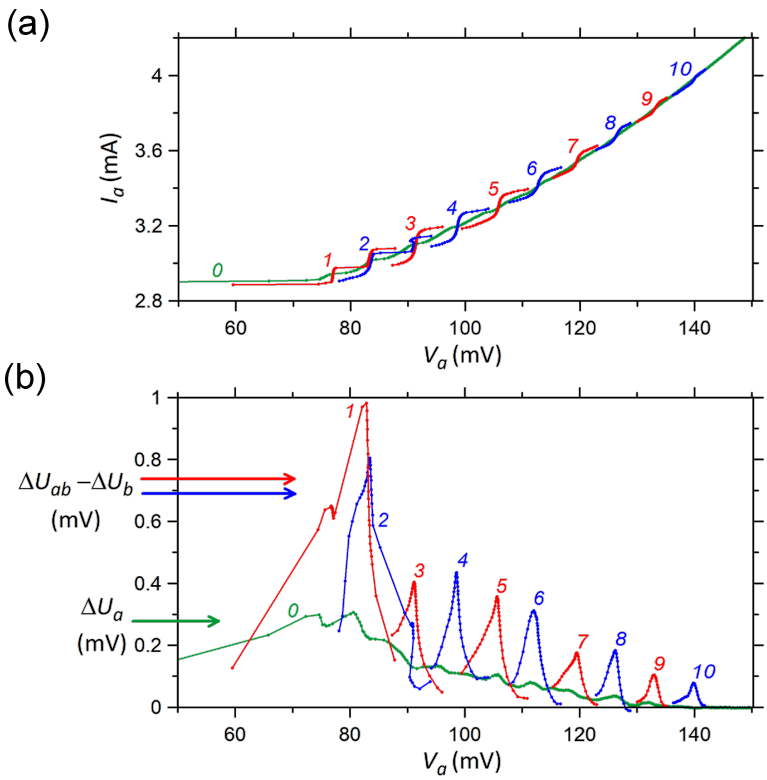

Figure 4: The data set for the IVCs of the outer array-a in sample-2 (a) and for the corresponding bolometer signal (b). Curves 0 are derived at unbiased inner array-b while curves 1–10 correspond to biasing of this array to the points indicated in Figure 2b. The curves 1–10 are the fragments of IVCs and bolometer signals in the ranges where significant changes relative to the curves 0 are observed. The value ΔU_b in panel (b) is the radiation signal derived from array-b at unbiased array-a.

Table 2: Gain factor from the interaction of outer and inner arrays in sample-2.

No. of step	1	2	3	4	5	6	7	8	9	10
I_b, mA	2.94	3	3.06	3.17	3.28	3.39	3.51	3.65	3.8	3.96
$\bar{f}_J$, GHz	97.9	106.8	115.6	124.9	134.1	143.0	151.5	160.2	168.9	177.4
g	1.5	1.8	1.8	1.9	1.8	2.0	1.6	1.9	2.0	2.6

ple-1, Figure 3c, we also can see a significant enhancement of steps in the array at $V_a \approx V_b$. Figure 4b shows the detector response measured simultaneously with the IVCs from Figure 4a. A significant enhancement of emission occurs practically under the condition of phase locking, $V_a \simeq V_b$. The corresponding gain factors are listed in Table 2. They are only slightly smaller than those for sample-1, indicating that the inter-array coupling is not a short-range phenomenon.

Off-chip synchronization

The third series of measurements was performed using arrays at two different substrates. The substrates were stacked on top of each other, as sketched in Figure 5a. To facilitate access to the contact pads of the bottom array, the substrate of the top array was trimmed to a width of about 3 mm. The arrays are similar to those in sample-1, but with a different shape of connecting electrodes (cf. Figure 1a,b and Figure 5a), which does not influence the measurements. The distance between two arrays is approximately equal to the thickness of substrate plus the glue layer and, possibly, a slight misalignment in the lateral direction. Overall, it is about 0.4 mm through the silicon substrate. During measurements, the bottom array-a is biased with a variable dc current and the top array-b is biased with a fixed current. To obtain the most prominent effect, we slightly increased the temperature of the stack to $T = 4.4$ K by placing it above the surface of liquid helium.

Figure 5b shows the IVC of the individually biased top array-b together with the simultaneously measured detector signal. The IVC has the characteristic parameters $I_c = 2.1$ mA and

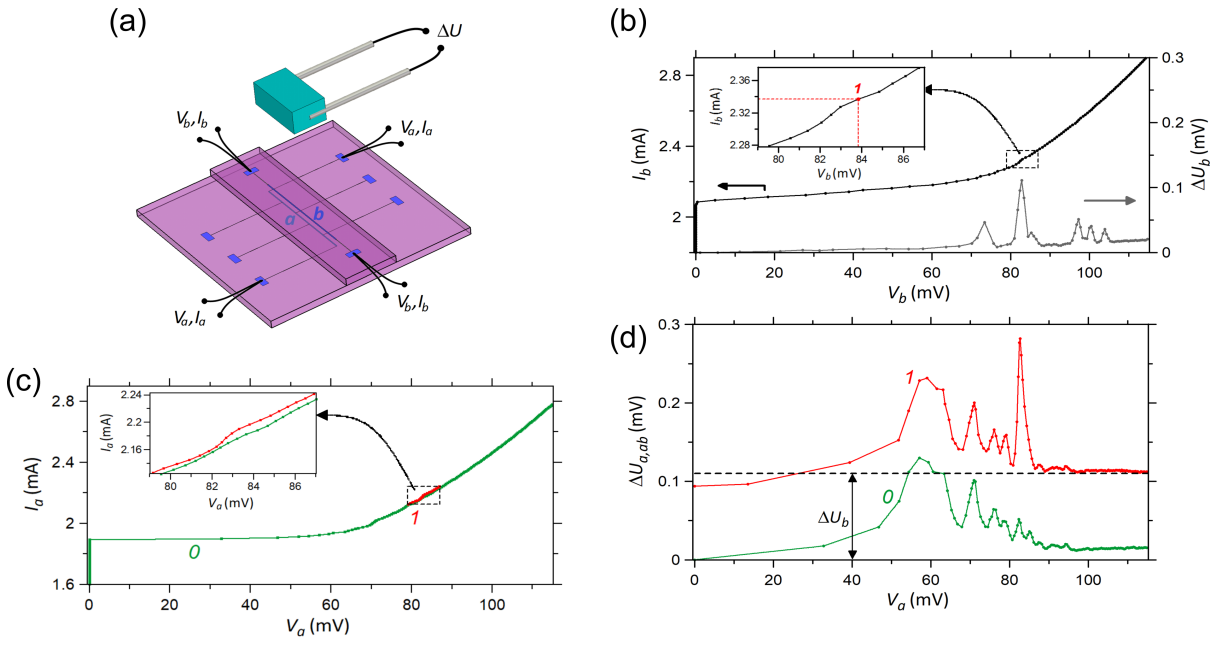

Figure 5: (a) View of the measurement scheme with two JJ arrays on different substrates formed in a stack. Each array is a straight strip with 332 JJs. In the measurements, bottom array-a was biased by a sweep current (V_a, I_a) while top array-b was constantly biased (V_b, I_b) by another current source. Above the stack is the InSb bolometer, in which the signal ΔU caused by the Josephson radiation from the arrays is measured. (b) IVC of array-b (left axis) and corresponding bolometer signal (right axis) when array-a is unbiased. The inset shows the enlarged fragment of the IVC with some weak current step where the indicated bias point $I_b = 2.34$ mA, $V_b = 84$ mV was chosen for the measurement with two biased arrays. (c, d) IVC of the bottom strip (c) and bolometer signal (d) when array-b is unbiased (curves 0) or biased at the point V_b, I_b (curves 1). The inset in panel (c) shows the enlarged fragment of IVCs at $V_a \sim V_b$ with the weak current step that appears due to the EM interaction between two strips. The value ΔU_b in panel (d) is the radiation signal derived from array-b at unbiased array-a.

$f_c \approx 120$ GHz. The maximum radiation signal $\Delta U_b = 0.11$ mV is observed at $I_b = 2.34$ mA, $V_b = 84$ mV, which corresponds to the mean Josephson frequency $\overline{f}_b = 121$ GHz. At this bias point, a weak current step is observed (Figure 5b, inset), which actually is the only one in the whole IVC curve. This bias point is chosen for the subsequent measurements.

In Figure 5c, the green curve represents the individual IVC of array-a without bias in array-b. The red curve shows the part of IVC with bias in array-b at the maximum emission point 1 indicated in the inset in Figure 5b. This IVC has $I_c = 1.9$ mA and $f_c \approx 100$ GHz, which are close to the values for array-b. Figure 5d shows the simultaneously measured detector signal. The lower green curve represents the emission signal from the individual array-a, $\Delta U_a(V_a, V_b = 0)$. Note that it has a clearly different shape compared to $\Delta U_b(V_a = 0, V_b)$ shown in Figure 5b. The upper red curve represents the combined emission, $\Delta U_{ab}(V_a, V_b)$. The general behavior is quite similar to that found in the on-chip experiments. A sharp peak is revealed under the condition of phase locking, $V_a = V_b$, with $\Delta U_{ab} = 0.28$ mV. It is considerably larger than the sum $\Delta U_a + \Delta U_b = 0.17$ mV. The gain factor is $g = 1.7$. Note that, in contrast to on-chip measurements, $\Delta U_a \neq \Delta U_b$, which can depend on the difference in position of the two arrays with respect to the detector, different geometries of substrates and connecting electrodes, and the stacking arrangement of the samples.

The obtained results show that the coupling between JJ arrays can be realized due to EM waves propagating inside the substrate. Note that the distance between the arrays is close to the half wavelength in the substrate, $\lambda_{Si}/2 = c/\left(2f\sqrt{\varepsilon_{Si}}\right)$ ($\varepsilon_{Si} = 11.9$ is the dielectric permittivity of silicon). Under this condition, the fundamental resonant mode can be excited in the substrate between the arrays. This condition is beneficial for inter-array coupling.

Numerical Calculations

The experimental results presented above show that phase locking of two large JJ arrays is a complex phenomenon, which cannot be reduced to a simple constructive interference of two independent sources. For a better understanding of the phase locking dynamics, we perform numerical modelling. Figure 6a demonstrates the general view of the considered model for on-chip synchronization. It contains two identical JJ arrays arranged on a common substrate with a dielectric permittivity of $\varepsilon = 12$, close to that of silicon. The lateral dimensions of the substrate are 2 × 0.6 mm while the thickness is 0.3 mm. We

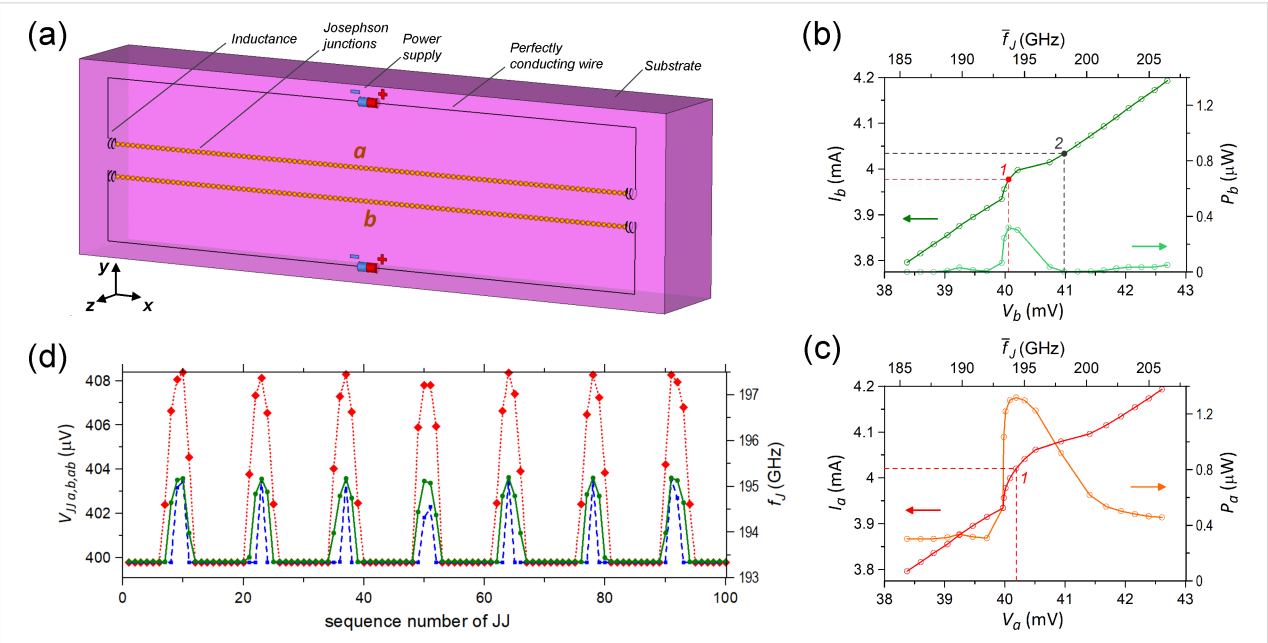

Figure 6: (a) The simulated scheme consisting of two identical JJ arrays on a common substrate. Each array has the form of a line containing 100 JJs. The dimensions of the substrate ($x \times y \times z$) are 2.0 × 0.6 × 0.3 mm, and its dielectric permittivity is $\varepsilon = 12$. The inductances have the value 100 pH while the internal resistance of the power supplies is 90 Ω. The junctions are described in the RSJ model [20] with parameters $I_c = 2.5$ mA, $R_n = 0.1$ Ω, and $\beta = 2$. (b) The IVC (left axis) and radiation power (right axis) of array-b when array-a is unbiased. The radiation power reaches the maximum at point 1, which corresponds to the electromotive force $\mathcal{E}_b = 398$ mV. Point 2 is taken for the analysis in Figure 7a,b. (c) The IVC (left axis) and radiation power (right axis) of array-a when array-b is biased at $\mathcal{E}_b$. At the indicated bias point 1 the radiation power reaches the maximum. (d) Distribution of the dc voltage in the JJs along array-b when array-a is unbiased (green solid line with circles) and along array-b (blue dashed line with squares) and array-a (red dot line with diamonds) when array-a is biased at the bias point 1 indicated in panel (c). In all cases, array-b is biased at point 1 in panel (b).

chose such a narrow substrate to avoid excitation of transverse resonant modes inside the substrate. The substrate is surrounded by vacuum, which is terminated by a perfectly matched layer (PML) to cancel back reflection. The PML conditions, in fact, simulate the walls in an anechoic chamber [19].

The circuit of each JJ array has the form of a rectangle with L = 1.8 mm in length and 0.2 mm in width (Figure 6a). The long side close to the center of substrate contains N = 100 JJs and two identical inductances at the ends. They are needed to electromagnetically decouple the lines with junctions from other parts of the circuits. A power supply of each circuit is located in the middle of the opposite long side. All lumped elements are connected by ideal conductors located at the edges of mesh. The gap between two arrays is 0.1 mm.

The JJs are described by the RSJ model [20]. The corresponding equations of junction dynamics are solved self-consistently with Maxwell equations, which are calculated by the finite-difference time-domain (FDTD) method [21], as described in [8,12,22]. We used the following junction parameters: I_c = 2.5 mA, normal resistance R_n = 0.1 Ω, and McCumber parameter β = 2. These parameters are consistent with experimental data for Nb/NbSi/Nb junctions (Figure 2, Figure 5b,c). The inductances are equal to 100 pH while the internal resistance of the power supplies has the value of 90 Ω. The latter allows for measurements of IVCs close to the regime of constant bias current. However, the electromotive force of the power supply $\mathcal{E}$ is, in fact, the primary source of biasing. The algorithm of the numerical calculations allows one to obtain both transport and radiation characteristics of the lines with JJs. A more detailed description of the model and the calculation procedure can be found in [8,22].

Figure 6b shows a part of the IVC of array-b and the corresponding dependence of the radiation power $P_b(V_b)$ for an inactive array-a. The power P is calculated by integration of the radiation pattern at the specific frequencies where the maximum in the spectrum of the ac current averaged over the JJs is observed [22]. This and subsequent simulations are performed for an upward bias sweep in a range of V that is 1.5–1.7 larger than the characteristic voltage $V_c = I_c R_n N$ = 25 mV. As seen from Figure 6b, in this range the form of the IVC is close to a straight line excluding the range $V \approx$ 40–41 mV, where a current step is observed. The step amplitude is ΔI = 0.08 mA, and the lowest differential resistance is R_d = 2.8 Ω. The radiation power increases abruptly at the step and reaches the maximal value P_b = 0.32 μW at V_b = 40.06 mV, corresponding to an averaged Josephson frequency of $\overline{f}_b$ = 193.7 GHz. The indicated value V_b corresponds to the electromotive force of the power supply $\mathcal{E}_b$ = 398 mV. Array-b was then constantly biased at $\mathcal{E}_b$ for the subsequent analysis of inter-array coupling.

The results of the simulation with two biased arrays are represented in Figure 6c. They show the calculated IVC of array-a at constantly biased array-b as well as the calculated radiation power. It can be seen that, similar to the experimental observations (Figure 3a,c, Figure 4a, and Figure 5c), the step in the IVC becomes more pronounced compared to the previous simulations in Figure 6b. The amplitude has doubled, ΔI = 0.17 mA, and the differential resistance decreased by nearly 5.5 times. The total emitted power $P_{ab}(V_a, V_b)$ has a nonzero offset $P_{ab}(V_a = 0, V_b) \approx 0.32$ μW, corresponding to the power of the individually biased array-b. The maximum total power of P_{ab} = 1.32 μW is observed at V_a = 40.19 mV (point 1 in Figure 6c). The gain factor is $g \simeq 2.1$. This value is consistent with the experimental values reported in Table 1 and Table 2.

Figure 6d shows the distribution of the average dc voltage on the JJs for both simulations. The green line is are for the individually biased array-b and the red/blue line is for the collectively biased array-a and array-b. Here, we can clearly see a signature of standing waves along the arrays. We can see eight flat regions with almost equal junction voltages and frequencies f_J^s = 193.3 GHz. These junctions are in the antinodes of the cavity mode and are synchronized by the EM field of the standing wave oscillating at the frequency f_J^s.

The junctions located at the nodes of the resonant mode are asynchronous. This means that their Josephson frequencies f_J^a differ from the radiation frequency f_J^s, actually $f_J^a > f_J^s$. A similar pattern was obtained in [8], but that inequality was opposite, that is, $f_J^a < f_J^s$. As follows from [8], the latter relation occurs at $\beta \ll 1$. The small value of β also establishes the inverted shape of current steps in the IVC compared to that shown in Figure 6b,c. It can be shown in the same manner as in [8] that the relation between f_J of synchronous and asynchronous junctions as well as the shape of current steps changes to the opposite at $\beta > 1$. Also note that the difference of asynchronous regions for array-a and array-b, which is clearly seen in Figure 6d, is caused by the different biasing sequences and the corresponding history-dependent dynamics.

Discussion

Our experimental data and numerical simulations demonstrate that large JJ arrays can be effectively coupled to each other, resulting in a coherent superradiant enhancement of the emission power. The amplification is observed in the frequency range of 100–200 GHz, both for arrays on a common substrate and for arrays on different substrates formed in a stack. We explain this effect by the interaction between JJ arrays via an EM field.

This field is excited along the surface of the substrate as well as inside the substrate. The amplification tends to grow with an increase of the frequency although the overall radiation power decreases. Similar results were obtained for $Bi_2Sr_2CaCu_2O_{8+x}$ mesa structures in [14,15]. In [14], three simultaneously biased mesas emit a high power of 610 μW while each mesa alone emits a maximum of 120 μW. Following our terminology, this corresponds to a gain factor of $g = 1.7$. In [15], the interaction between two mesas has been revealed via the study of polarization of EM emission. Similar to the present work, the obtained data allows one to conclude that such intrinsic JJ arrays have a mutual coupling through the common substrate.

As described in the Introduction, the simple constructive interference of two oscillators, be it single JJs [23] or arrays, should result in a gain of $g \lesssim 2$. However, in this work, we observe also significantly larger gains. Although this clearly indicates that coherent emission from both arrays takes place, it also indicates that additional more complex phenomena are involved. The clue to understanding is provided by the inset in Figure 3a, which demonstrates that phase locking of the two arrays leads to enhancement of the oscillation amplitude in array-a. From Figure 2, we observe that resonant steps in individually biased arrays are more pronounced in the inner array-b than in the outer array-a. At higher bias, steps in array-a are almost invisible. Let us suppose that, initially, only array-b is synchronized at the cavity mode and emits radiation while array-a is not synchronized and, therefore, practically not emitting. In this case, if inter-array coupling totally synchronizes array-a, then the gain factor would become four. This explanation is consistent with the observation that $g > 2$ is observed for higher steps (Table 1 and Table 2), which are less pronounced in the individually biased array-a. This is also confirmed by numerical simulations where we also observed $g > 2$. Therefore, the gain is caused both by the coherent superradiant effect and by the enhancement of the oscillating EM field in each array. The latter is an additional factor that explains why/how the gain factor could be larger than two. The key is that, in our case, the interaction takes place between large arrays with many oscillating junctions. This is a much more complex phenomenon than locking of two oscillators. Here, a mutual synchronization of the two arrays assists also in better internal synchronization within each of the arrays.

The simulated voltage profile in Figure 6d clearly indicates that the cavity mode is playing a decisive role for synchronization of the array. Junctions in the antinodal regions are phase-locked by the driving EM field of the cavity mode. In the nodal regions, the driving force is very small, and, therefore, JJs are unsynchronized there. These asynchronous nodal regions make a vanishingly small contribution to the radiation power (see Appendix). Therefore, the overall emission spectrum remains very sharp and is practically not influenced by the voltage/frequency deviation at nodal JJs. In fact, it is the cavity mode in the electrode, rather than individual junctions, that is causing the emission. The role of the JJs is just to excite and pump energy into the mode.

We have observed similar coherent gains for the on-chip case with small, 4 μm (sample-1), and significantly larger, 238 μm (sample-2), separation between the arrays as well as for off-chip measurements on different chips with even larger separation ~400 μm. This demonstrates that arrays can effectively interact at a fairly long range. It would be interesting to study in more detail how the amplification depends on the separation between arrays. We have already access to a suitable Nb array consisting of several subarrays with different distances between each. Hence, the corresponding measurements may be carried out in close future.

In the simulations, we see the same effect of amplification for the total power radiated by JJ arrays at frequencies near 190 GHz. The amplification is comparable to that from the measurements. We present in the Appendix the distribution of power generated by each junction and of the phase shift between ac voltage and ac current. This analysis gives a visual pattern of the considered effect of amplification as well as of the synchronization of JJs.

Conclusion

We explored experimentally and numerically the EM interaction between large JJ arrays containing more than 300 JJs and having superwavelength dimensions. The studied Nb/NbSi/Nb JJ arrays exhibit strong cavity mode resonances, caused by the formation of standing waves along the whole length of the array [13]. We observed mutual coupling between the arrays both on the same chip and on different chips and at different separations between the arrays. We reported significant coherent amplification of radiation emission when both arrays are brought to the same cavity mode resonance. A coherent gain factor, that is, the ratio of the joint emission power from the two arrays to the sum of powers from individually biased arrays, as large as 2.9 was observed. This is well beyond the limit of two, characteristic for the bare constructive interference of two oscillators. The large gain factor indicates that additional effects are taking place. The key is that, in our case, the interaction takes place between large arrays with many oscillating junctions. This is a much more complex phenomenon than locking of two oscillators. Here, a mutual synchronization of the two arrays assists also in better internal synchronization within each of the arrays. This facilitates gains larger than two. This conclusion has been supported by the performed numerical simulations.

Finally, we note that the effect of coherent amplification of radiation from several coupled JJ arrays depends on a number of geometrical factors and material parameters. Those should be accounted for in the design and fabrication of large JJ arrays. Proper design, in which this effect is maximally manifested, allows for increasing the output radiation power, which will facilitate the implementation of JJ arrays in practical applications.

Appendix: Additional Information about Numerical Simulations

The numerical algorithm allows for calculating also the energy parameters for all JJs that can facilitate the study of synchronization of junctions in the arrays (Figure 6a). We can define the work of the n-th JJ under an EM field per unit time, or the generated power, as $P_n = -\mathrm{Re}(\tilde{I}_n\tilde{V}_n^*)/2 = -\left|\tilde{I}_n\right|\left|\tilde{V}_n\right|/2\times\cos\varphi_n$, where φ_n is the phase shift between $\tilde{I}_n$ and $\tilde{V}_n$, that is, $\varphi_n = \arg(\tilde{I}_n) - \arg(\tilde{V}_n)$. As well as for the radiation power P, these amplitudes are taken at the frequency corresponding to the maximum of $\sum_{n=1}^{N}\left|\tilde{I}_n\right|$.

As seen from Figure 7a, if array-a is inactive and array-b is biased to the point 2 in Figure 6b, out of the current step, then P_n is distributed along array-b rather chaotically taking values of both signs. Almost half of the junctions have a negative sign of P_n. This means that the field does a positive work under these junctions. Hence, these junctions operate as consumers, not as generators. The total generated power in the array is only $P = \sum_{n=1}^{N} P_n = 0.3$ nW. As seen from Figure 6b the radiation power in point 2 is also practically zero on the scale of microwatts. The phase shift φ_n also has a chaotic character taking values in a wide range (Figure 7b). For 77 junctions, φ_n ranges from 180° to 360°. Thus, the differential impedance Z of most of the junctions acquires a capacitive character.

When array-b is biased within the current step, and array-a is inactive (point 1 in Figure 6b), the distributions P_n and φ_n along array-b become structured. As seen from Figure 7c,d, they have an oscillation form similar to the distribution of the dc voltage in JJs (Figure 6d). Therefore, P_n and φ_n exhibit, here, the resonant mode excited in the array. As seen from Figure 7c, the junctions in the nodes do a significantly smaller work under the field compared to the junctions in the antinodes, which generate a power of P_n = 4–6 nW. Regarding the phase shift, the junctions in the antinodes have $\varphi_n \gtrsim 180°$ (Figure 7d), which is characteristic for a generator with small capacitance. However, when moving towards the nodes, φ_n decreases down to 110–120°, that is, the differential impedance Z of the JJs acquires an inductive character.

Similar patterns of P_n and φ_n are observed for both arrays when array-b is biased within the current step (point 1 in Figure 6c). However, the junctions in the antinodes of the resonant mode now generate a larger power: P_n = 7–9 nW for array-b and P_n = 9–11 nW for array-a (Figure 7c). Moreover, the range of junctions that do a large work under the field slightly widens in each antinode. This is in agreement with the conclusion made from the radiative analysis about the amplification of Josephson radiation when two arrays are biased (Figure 6b,c). Each array does a larger work under the field when two arrays are simultaneously biased compared to the case in which only one array is active. Calculating the total generated power P for all three cases in Figure 7c, we obtain 0.4 μW from array-b with inactive array-a and 1.35 μW from the arrays when they are both

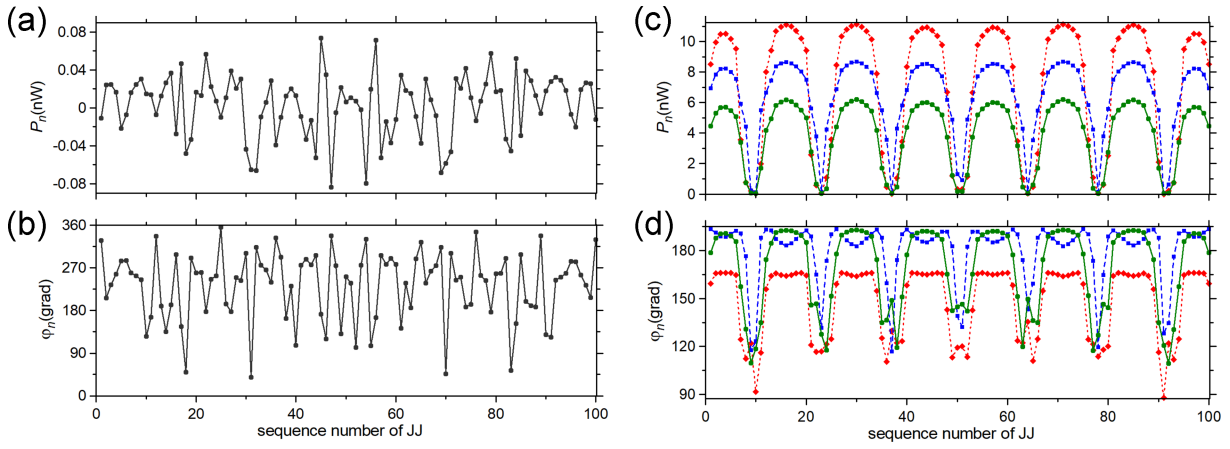

Figure 7: (a, b) Distribution of work of JJs under the EM field (a) and of the phase shift between ac voltage and ac current in the junctions (b) along array-b when array-a is unbiased, and when array-b is out of the current step (point 2 in Figure 6b). (c, d) Distribution of work of JJs under the EM field (c) and of the phase shift between ac voltage and ac current in the junctions (d) along array-b when array-a is unbiased (green solid line with circles) and along array-b (blue dashed line with squares) and array-a (red dot line with diamonds) when array-a is biased. The bias points for the arrays are within the current steps of the IVCs (points 1 in Figure 6b,c).

biased. These values are slightly less than those of the radiation power P_b and P_{ab} (Figure 6b,c) calculated by the integration of radiation pattern. This decrease can be caused by dissipations of the radiation in the active loads of the power supplies (Figure 6a).

The phase shift φ_n in the arrays undergoes slight changes when two arrays are biased instead of one (Figure 7d). In each antinode of the mode of array-b, φ_n has two local maxima instead of one with the widening of range where $\varphi_n \gtrsim 180°$. For array-a, the phase shift in the antinodes decreases to $\varphi_n \approx 160–170°$, that is, Z of the effectively generating JJs acquires an inductive character.

Keep in mind that I_n is determined by the resonant mode. Thus, it has an equal oscillation frequency throughout each array [8]. Moreover, when the active arrays are coupled, the common resonant mode is formed. Therefore, the data presented in Figure 6d and Figure 7c,d allow one to conclude that the JJs in antinodes of the resonant mode become phase-locked via the common EM field. Such phase locking is fully constructive, that is, all junctions in the antinodes do a positive work under the field. This is what essentially provides the amplification of the Josephson radiation. The present conclusion is in accordance with the data of direct visualisation of the modes presented in [13], in which the global synchronization of the whole JJ array was indicated.

Acknowledgements

The authors are grateful to Oliver Kieler for sample fabrication.

Funding

The work was supported by Center of Excellence "Center of Photonics" funded by The Ministry of Science and Higher Education of the Russian Federation, contract No. 075-15-2022-316.

ORCID® iDs

Mikhail A. Galin - https://orcid.org/0000-0002-7214-6522
Vladimir M. Krasnov - https://orcid.org/0000-0002-3131-8658
Ilya A. Shereshevsky - https://orcid.org/0000-0001-6134-8391
Nadezhda K. Vdovicheva - https://orcid.org/0000-0003-4704-7597
Vladislav V. Kurin - https://orcid.org/0000-0001-7019-1074

References

1. Villegier, J.-C. Refractory Niobium Nitride NbN Josephson Junctions and Applications. In *Josephson Junctions: History, Devices, and Applications;* Wolf, E. L.; Arnold, G. B.; Gurvitch, M. A.; Zasadzinski, J. F., Eds.; Pan Stanford Publishing: Singapore, 2017; pp 147–183.
2. Borodianskyi, E. A.; Krasnov, V. M. *Nat. Commun.* **2017,** *8,* 1742. doi:10.1038/s41467-017-01888-4
3. Kleiner, R.; Wang, H. *J. Appl. Phys.* **2019,** *126,* 171101. doi:10.1063/1.5116660
4. Tonouchi, M. *Nat. Photonics* **2007,** *1,* 97–105. doi:10.1038/nphoton.2007.3
5. Darula, M.; Doderer, T.; Beuven, S. *Supercond. Sci. Technol.* **1999,** *12,* R1–R25. doi:10.1088/0953-2048/12/1/001
6. Kakeya, I.; Wang, H. *Supercond. Sci. Technol.* **2016,** *29,* 073001. doi:10.1088/0953-2048/29/7/073001
7. Morosh, V.; Linek, J.; Müller, B.; Martínez-Pérez, M. J.; Wolter, S.; Weimann, T.; Beyer, J.; Schurig, T.; Kieler, O.; Zorin, A. B.; Kleiner, R.; Koelle, D. *Phys. Rev. Appl.* **2020,** *14,* 054072. doi:10.1103/physrevapplied.14.054072
8. Galin, M. A.; Shereshevsky, I. A.; Vdovicheva, N. K.; Kurin, V. V. *Supercond. Sci. Technol.* **2021,** *34,* 075005. doi:10.1088/1361-6668/abfd0b
9. Galin, M. A.; Klushin, A. M.; Kurin, V. V.; Seliverstov, S. V.; Finkel, M. I.; Goltsman, G. N.; Müller, F.; Scheller, T.; Semenov, A. D. *Supercond. Sci. Technol.* **2015,** *28,* 055002. doi:10.1088/0953-2048/28/5/055002
10. Song, F.; Müller, F.; Scheller, T.; Semenov, A.; He, M.; Fang, L.; Hübers, H.-W.; Klushin, A. M. *Appl. Phys. Lett.* **2011,** *98,* 142506. doi:10.1063/1.3576910
11. Rabinovich, M. I.; Trubetskov, D. I. Self-Excited Oscillations in Multifrequency Systems. In *Oscillations and Waves in Linear and Nonlinear Systems;* Hazewinkel, M., Ed.; Kluwer Academic Publishers: Dordrecht, Netherlands, 1989; pp 329–352. doi:10.1007/978-94-009-1033-1_16
12. Galin, M. A.; Borodianskyi, E. A.; Kurin, V. V.; Shereshevskiy, I. A.; Vdovicheva, N. K.; Krasnov, V. M.; Klushin, A. M. *Phys. Rev. Appl.* **2018,** *9,* 054032. doi:10.1103/physrevapplied.9.054032
13. Galin, M. A.; Rudau, F.; Borodianskyi, E. A.; Kurin, V. V.; Koelle, D.; Kleiner, R.; Krasnov, V. M.; Klushin, A. M. *Phys. Rev. Appl.* **2020,** *14,* 024051. doi:10.1103/physrevapplied.14.024051
14. Benseman, T. M.; Gray, K. E.; Koshelev, A. E.; Kwok, W.-K.; Welp, U.; Minami, H.; Kadowaki, K.; Yamamoto, T. *Appl. Phys. Lett.* **2013,** *103,* 022602. doi:10.1063/1.4813536
15. Kobayashi, R.; Hayama, K.; Fujita, S.; Tsujimoto, M.; Kakeya, I. *Phys. Rev. Appl.* **2022,** *17,* 054043. doi:10.1103/physrevapplied.17.054043
16. Mueller, F.; Behr, R.; Weimann, T.; Palafox, L.; Olaya, D.; Dresselhaus, P. D.; Benz, S. P. *IEEE Trans. Appl. Supercond.* **2009,** *19,* 981–986. doi:10.1109/tasc.2009.2017911
17. Kieler, O.; Wendisch, R.; Gerdau, R.-W.; Weimann, T.; Kohlmann, J.; Behr, R. *IEEE Trans. Appl. Supercond.* **2021,** *31,* 1100705. doi:10.1109/tasc.2021.3060678
18. Gudkov, A. L.; Kupriyanov, M. Y.; Samus', A. N. *J. Exp. Theor. Phys.* **2012,** *114,* 818–829. doi:10.1134/s1063776112030144
19. Taflove, A.; Hagness, S. C. Perfectly Matched Layer Absorbing Boundary Conditions. *Computational Electrodynamics: The Finite-Difference Time-Domain Method;* Artech House Inc.: Boston/London, 2005; pp 273–328.
20. Likharev, K. K. The Josephson effect. *Dynamics of Josephson Junctions and Circuits;* Gordon and Breach Science Publishers: Paris, France, 1986; pp 1–26.
21. Yee, K. *IEEE Trans. Antennas Propag.* **1966,** *14,* 302–307. doi:10.1109/tap.1966.1138693

22. Kurin, V. V.; Vdovicheva, N. K.; Shereshevskii, I. A. *Radiophys. Quantum Electron. (Engl. Transl.)* **2017,** *59,* 922–936. doi:10.1007/s11141-017-9762-6
23. Finnegan, T. F.; Wahlsten, S. *Appl. Phys. Lett.* **1972,** *21,* 541–544. doi:10.1063/1.1654250

License and Terms

BEILSTEIN JOURNAL OF NANOTECHNOLOGY

Induced electric conductivity in organic polymers

Konstantin Y. Arutyunov*[1,2], Anatoli S. Gurski[1], Vladimir V. Artemov[3], Alexander L. Vasiliev[3,4,5], Azat R. Yusupov[6], Danfis D. Karamov[7] and Alexei N. Lachinov[6,7]

Full Research Paper

Open Access

Address:
[1]National Research University Higher School of Economics, 101000, Moscow, Russia, [2]P. L. Kapitza Institute for Physical Problems RAS,119334, Moscow, Russia, [3]Federal research center "Crystallography and photonics" RAS, 119333, Moscow, Russia, [4]National research center "Kurchatov institute", 123182, Moscow, Russia, [5]Moscow Institute of Physics and Technology (State University), MIPT, 141701 Moscow Region, Russia, [6]Bashkir State Pedagogical University n.a. M. Akmulla, 450008, Ufa, Russia and [7]Institute of Molecule and Crystal Physics UFRC RAS, 450054, Ufa, Russia

Email:
Konstantin Y. Arutyunov* - karutyunov@hse.ru

* Corresponding author

Keywords:
conducting polymer; superconductivity; thin films

Beilstein J. Nanotechnol. **2022,** *13,* 1551–1557.
https://doi.org/10.3762/bjnano.13.128

Received: 23 September 2022
Accepted: 29 November 2022
Published: 19 December 2022

This article is part of the thematic issue "Intrinsic Josephson effect and prospects of superconducting spintronics".

Guest Editor: A. S. Sidorenko

Abstract

Poly(diphenylene phthalide) (PDP) belongs to the class of carbocyclic organic electroactive polymers, which exhibits electric conductive properties when an external electric field and/or mechanical stress is applied. In this work, the transport properties of thin-film layered lead–PDP–lead structures were experimentally studied in a wide temperature range. At sufficiently high temperatures, the current voltage characteristics are satisfactorily described in terms of the injection model of currents limited by the space charge. At temperatures below ≈8 K, a number of samples exhibit features that can be explained by the effect of induced superconductivity in a thin film of conducting polymer enclosed between two massive superconductors (lead).

Introduction

Most polymers can be classified as organic dielectrics. However, there exists a specific class of polymers, typically characterized by the existence of conjugated π-bonds, which enable delocalization of electrons leading to electric conductivity in the ground state of the system. Relatively recently it was found that finite electric current can pass also through non-conjugated polymers. In the ground state they are wide-band dielectrics, but can exhibit high electric conductivity under the influence of such external parameters as mechanical stress and/or electric field [1]. The effect is interpreted as stimulation of metallic state [2].

Poly(diphenylene phthalide) (PDP) was chosen as the object of study being a representative electro-active polymer demon-

strating induced electric conductivity. PDP is a carbocyclic polymer with high chemical and thermal stability, transparency in the visible spectrum, and high mechanical strength [3,4]. PDP has an amorphous structure with a degree of crystallinity not exceeding 15%. It is characterized by unusually high chemical resistance. The conditions for the selective production of PDP with a molecular weight of more than (50–60) × 10^3 without the formation of a gel fraction have been found. A model image of the structural unit of the PDP polymer is shown in Figure 1a. Polymers of this class are soluble in organic solvents and have exceptional film-forming properties [5,6]. According to these results, continuous homogeneous films can be obtained by centrifugation from a solution in cyclohexanone on a metal surface with a thickness from several nanometers up to micrometers. High homogeneity and defect-free surfaces on nanoscopic scales have been repeatedly confirmed by various methods, including scanning tunneling and atomic force microscopy. In some cases, it was possible to observe regions with surface macromolecular (quasicrystalline) ordering [7].

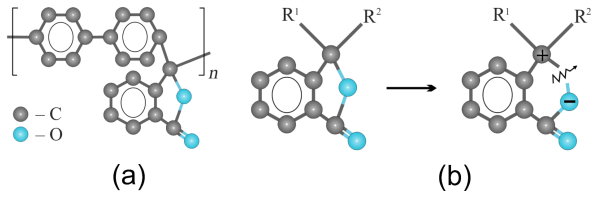

Figure 1: (a) Structural unit of poly(diphenylene phthalide) (PDP) molecule. (b) Schematics of C–O bond break leading to C^+ and O^- ionization of the corresponding atoms, which enables effective charge transfer along the polymer chain [2].

The remarkable property of PDP is that, depending on the length of certain atomic bonds, its molecule can exist in several spatial configurations. Under normal conditions, PDP is a wide-gap dielectric material and is characterized by the following parameters: band gap ≈4.3 eV, electronic work function ≈4.2 eV, electron affinity ≈2 eV, first ionization potential ≈6.2 eV. Experimental evaluations of the electronic parameters of PDP have been made earlier by various methods [8,9]. Quantum chemical studies of PDP [10] have shown that its molecular structure is unstable with regard to interaction with an excess (thermal) electron and can result in a transition to a metastable state. However, in that state, e.g. induced by external electric field, the system is characterized by non-zero density of electronic states within the energy gap. The depth of such states increases if the system accepts an extra electron (Figure 1b), thus indirectly enabling electric conductivity along the polymer chain [11]. Later the validity of this model was supported experimentally and further elaborated [12-14].

The purpose of this work was to study this interesting phenomenon in a wide temperature range: from 4.2 K to room temperature.

Experimental

Layered Pb–PDP–Pb heterostructures were fabricated in a glove box in nitrogen atmosphere with minimum moisture and oxygen content without exposure to room atmosphere between cycles of formation of different layers. Glass or oxidized silicon were used as substrates. The substrates were preliminarily cleaned in ethanol and distilled water in an ultrasonic bath. The surfaces were hydrophilized by treating the substrates with cyclohexanone immediately before applying the polymer solution. The electrodes consisted of two mutually perpendicular lead strips with a width of ≈1 mm, between which the PDP polymer film was 'sandwiched' (Figure 2a). Lead was chosen as fairly low-melting metal exhibiting superconducting properties. Formation of thin-film lead electrodes with thicknesses from 50 nm to 200 nm was carried out by thermal evaporation in vacuum. The critical temperature of bulk lead is $T_c(Pb_{3D})$ = 7.2 K. However, in the form of a thin film, the critical temperature of a superconductor can differ significantly from the tabulated value [15,16]. In our samples, the critical temperature of lead electrodes varied from 7.8 K < $T_c(Pb_{film})$ < 8.2 K. Submicron PDP films were prepared by centrifuging the polymer from a solution in cyclohexanone on a solid substrate. When preparing the solution, the polymer was first soaked in a small amount of solvent until complete dissolution, then the solvent was added in the required amount, and the solution was kept for another day in the dark. For fabrication of films of various thicknesses, solutions of polymers in cyclohexanone with concentrations of 0.1–15 wt % were used. The polymer solution of specified concentration was applied onto the dielectric substrate fixed on a centrifuge holder. The rotation speed was typically 2000 rpm. The resulting polymer film was dried in air for about 45–60 min at room temperature. Then the final drying was carried out to remove solvent residues at a temperature of 150–200 °C for 45 min. Depending on the concentration of the solutions, it was possible to obtain films of various thicknesses from several nm to several μm. The formation of films from dilute solutions occurs according to the mechanism of linear or loop adsorption, when macromolecules at the interface are completely or partially elongated. Also, film formation at such low concentrations strongly depends on the energy interaction of macromolecules with the substrate surface, which explains the weak dependence of the film thickness on the solution concentration. With an increase in concentration, associates of macromolecules are formed in the solution, and the influence of adhesion processes decreases, but the cohesive forces increase. In the entire thickness range from 3 nm to 1 μm, the films are solid, without significant defects and/or pin holes. The polymer films

were studied by atomic force microscopy (AFM) using an earlier described methodology [5]. The study of the film morphology showed that they are homogeneous, and within the entire thickness range from 3 nm to 1 μm the films are solid, without significant defects and/or pin holes. The observation confirms the good film-forming properties of the PDP polymer solutions. For example, Figure 2b shows the topography of the polymer film 0.1 wt % on Si substrate. The plot at the bottom demonstrates the variation of the structure along the line, depicted at the upper panel. The distance between the measuring lines is of the order of the polymer film thickness, which is just 3 nm.

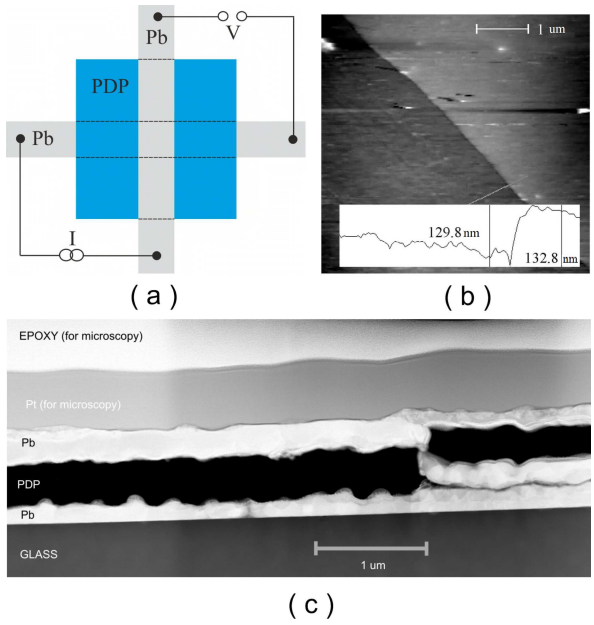

Figure 2: (a) Schematics of a Pb (grey)–PDP (blue)–Pb (grey) three layer heterostructure on insulating substrate (not indicated for simplicity). The layout enables electron transport measurements of each lead strip and the whole sandwich itself. (b) Atomic force microscope scan of a PDP film 0.1 wt % on Si substrate. The plot at the bottom illustrates the roughness of the surface along the indicated line. (c) Side view of a Pb–PDP–Pb structure on glass with solitary defect (lead shortcut) obtained by transmission electron microscopy.

After electric measurements, a number of heterostructures was sent for analysis by high resolution transmission electron microscopy and/or scanning electron microscopy. None of the studied samples showed a systematic 'sticking' of lead electrodes through the thickness of the polymer or formation of multiple metallic dendrites. However, a number of microphotographs showed some defects in the form of shortcuts (Figure 2c). The origin of these artifacts is not entirely clear: they could be initially present in heterostructures, or they could have appeared during the preparation of a sample for electron microscopy.

Results and Discussion

The experiment was carried out in a four-contact configuration at direct or alternating currents. Both $R(T)$ and $V(I)$ dependences of the Pb–PDP–Pb sandwich could be measured, as shown in Figure 2a, and the transport characteristics of each lead electrode separately. To measure differential characteristics $dI/dV(V)$, modulation technique and phase-sensitive lock-in detection were used. To suppress the negative effect of stray electromagnetic pickups, a multistage RLC filter system was used [17]. While $R(T)$ measurements at cryogenic temperatures, the current value from 0.1 to 100 μA was chosen so that its increase by an order of magnitude would not lead to a noticeable shift in the temperature of the superconducting phase transition. All experiments were carried out in a ^{4}He direct pumped cryostat. The semiconducting thermosensors were calibrated by the ^{4}He vapor pressure and by the reference points of superconducting transitions in pure bulk superconductors (Al, In, Sn, Pb). The resulting absolute error in determining the temperature was ≈10 mK, while the relative error was less than 1 mK. Repeated measurements of T_c of the same sample coincided with an accuracy of several mK. An analysis was made of the degradation of samples over time. The difference between two measurements of the same sample was 3 months, while the shift in the beginning of the phase transition was minimal $\delta T_c \approx 0.01$ K.

It has been established that in the measured Pb–PDP–Pb structure, the shape of the current–voltage characteristics strongly depends on temperature. At 300 K the I–V dependencies have a nonlinear character $j \approx kU^n$, typical for organic dielectrics. At temperatures ≈77 K and below, the dependence $j = f(U)$ is also nonlinear, but is significantly different. In particular, as the voltage increases, there is the tendency for the current flowing through the heterostructure to saturate. Previously [2], it was found that at high temperatures, the mechanism of overcoming the barrier at the metal/polymer contact is satisfactorily described in terms of the injection current model limited by the space charge. At low temperatures, the tunneling mechanism is the predominant mechanism.

Figure 3 shows the current–voltage characteristics of Pb–PDP–Pb structures with different PDP film thicknesses. With increase of the polymer film thickness, the current decreases. Therefore, they were measured over a wide voltage range. The shape of the I–V characteristics depends on the energy spectrum. Several regimes could be distinguished on the I–V plots: (a) ohmic mode at low voltages: thermally generated charge carriers prevail; (b) mode with a predominance of traps: trapped charge carriers in small traps limit the current; (c) the limit of trap filling: the quasi-Fermi level reaches the energy of the trap E_t, the traps are filled and there is a steep increase in

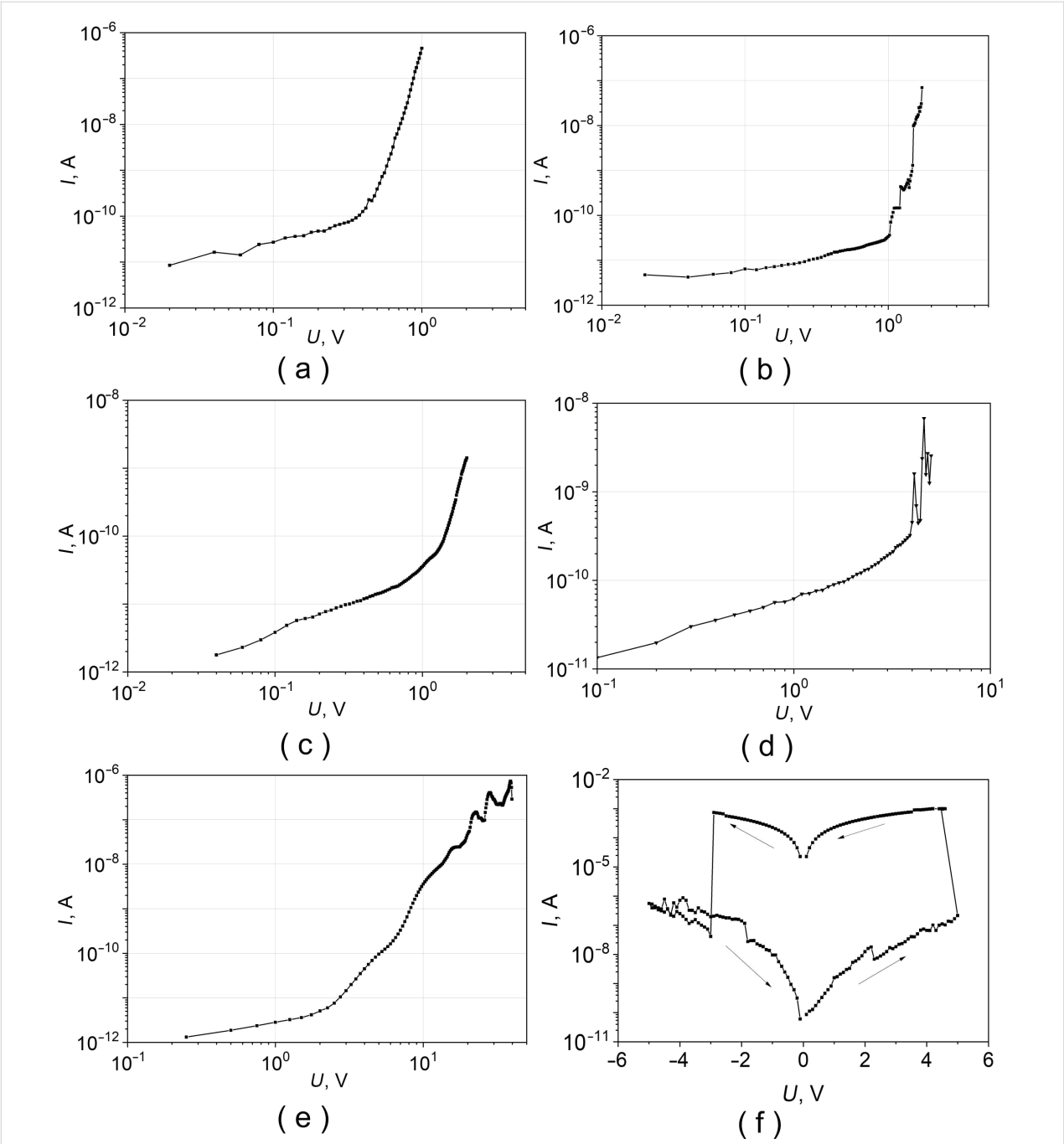

Figure 3: Current–voltage characteristics, measured at room temperature, of several Pb–PDP–Pb sandwiches with different thicknesses of the polymer film: (a) 10 nm, (b) 25 nm, (c) 45 nm, (d) 150 nm, (e) 360 nm; (f) is the same structure as in (c) and with 2 kOhm load resistance in the electric circuit; (f) demonstrates the switching phenomenon of the thin PDP film from insulating to metal state. Thickness of Pb electrodes is about 200 nm.

current. It should be noted that in a circuit with finite load resistance the effect of electronic switching to a highly conductive state can be observed (Figure 3f). Such a bi-stable switching is often used in practice to create non-volatile memory elements.

Presented in Figure 3 *I–V* characteristics do not contradict the presented above model considerations. In this regard, to analyze the *I–V* at 300 K, one can apply the formalism of the theory of injection currents, which makes it possible to estimate the concentration of intrinsic charge carriers (n_0) and their minimum mobility (μ) [18]:

$$n_0 = \frac{\varepsilon\varepsilon_0 U_n}{eL^2} \quad (1)$$

$$\mu = \frac{jL^3}{\varepsilon\varepsilon_0 U_n^2} \quad (2)$$

where, j is the current density, L is the distance between the electrodes, U_n is the voltage corresponding to the transition point from linear to parabolic dependency of the I–V's, n_0 is the equilibrium concentration of charge carriers, ε and ε_0 dielectric constants of the polymer and vacuum, respectively, and μ is the maximum mobility of charge carriers.

According to this model, the ohmic behavior of the I–V characteristics at low voltages is due to intrinsic charge carriers. If, however, the concentration of injected carriers begins to exceed the concentration of intrinsic carriers, then the transition to a sublinear regime is observed. The corresponding estimations give the following values $n_0 = 10^{21}$–10^{23} m^{-3}, $\mu = 10^{-15}$ to 10^{-17} m^2/Vs.

The analysis of the I–V characteristics within the framework of Schottky barrier formation makes it possible to estimate the height of potential barriers at the metal/polymer interfaces utilizing the Richardson expression [18]:

$$\varphi = \frac{kT}{e}\ln\left(\frac{AA^*T^2}{I_s}\right) \quad (3)$$

where T is the temperature, k is the Boltzmann constant, e is the electron charge, A is the contact area, A^* is the Richardson constant, I_s the saturation current. To proceed, it is important to determine the saturation current using, e.g., the semi-logarithmic dependence of the current on applied voltage. This is the so-called current at zero voltage. In addition, it is necessary to take into account the non-ideality coefficient of the barrier. We chose the value of the latter from previous measurements. As the result, the value of the potential barrier calculated using Equation 3 is equal to 0.7. As expected, the transport characteristics of thin-film lead electrodes demonstrated the metallic behavior: in normal state, the resistance of the films decreased linearly with decreasing temperature, and the I–V characteristics exhibit ohmic behavior. At temperatures of the order of $T_c(Pb_{film}) \approx 8$ K, a sharp superconducting transition was observed.

Perhaps the most interesting are the results of transport measurements of Pb–PDP–Pb sandwiches at temperatures below the critical temperature of the superconducting transition of lead electrodes. In a number of samples, with a polymer film thickness of less than 350 nm, features are observed that unambiguously indicate the presence of a superconducting state: a sharp drop in resistance to instrumental zero ≈5 nV (Figure 4a) and presence of supercurrent in the I–V's (Figure 4b,c and d). A trivial explanation may be the occurrence of shortcuts between the lead plates: either macroscopic 'pinholes' or formation of multiple thin dendrites. The second possibility seems unlikely: neither the previous studies, nor the selective microscopic analysis of several samples by scanning and transmission electron microscopy revealed signs of the presence of dendrites. While the side view microphotographs made by high-resolution transmission electron microscopy occasionally reveal some macroscopic features such as lead electrode shortcuts through the polymer film (Figure 2c). These defects are episodic, and their character does not resemble the 'melting through' of the PDP film during the thermal deposition of lead. Moreover, the PDP decomposition starts at 440 °C, which is significantly higher than the melting point of lead, 327 °C. Moreover, it cannot be ruled out that such defects as 'collapse' of lead electrodes (Figure 2c) are not intrinsic, and could have appeared only during the process of sample preparation for transmission microscopy. The sufficiently high critical current (Figure 4b–d) also indicates the large area of the conductive channel, which does not correspond to the scenario of the occurrence of single point short circuits. The I–V dependencies of the Pb–PDP–Pb sandwiches above the superconducting temperature of the lead electrodes are essentially non-ohmic (Figure 3), which supports the claim about the absence of trivial metal-to-metal shortcuts.

The second alternative explanation of the dependencies in Figure 4 may be the Josephson effect: the flow of supercurrent between two superconductors separated by a dielectric barrier. However, the correlation of the order parameters of two spatially separated superconductors is a subtle quantum mechanical effect, which in all practical cases is observed at dielectric thicknesses of the order of several nm, while in our case superconductivity in Pb–PDP–Pb sandwiches manifests itself at polymer thicknesses up to 350 nm. Hence, it can be assumed that the dependencies in Figure 4 can be explained by the effect of induced superconductivity in a thin film of conducting polymer enclosed between two massive superconductors (lead). The substantiation of this assertion requires further verification. In the near future, experiments are planned on planar heterostructures, where superconductivity, if observed, cannot be explained by trivial metallic shortcuts.

Conclusion

$R(T)$, $V(I)$ and $dV/dI(V)$ dependences of thin-film layered structures lead–PDP–lead were experimentally studied in a wide temperature range. At sufficiently high temperatures, the I–V dependences are satisfactorily described in terms of the currents

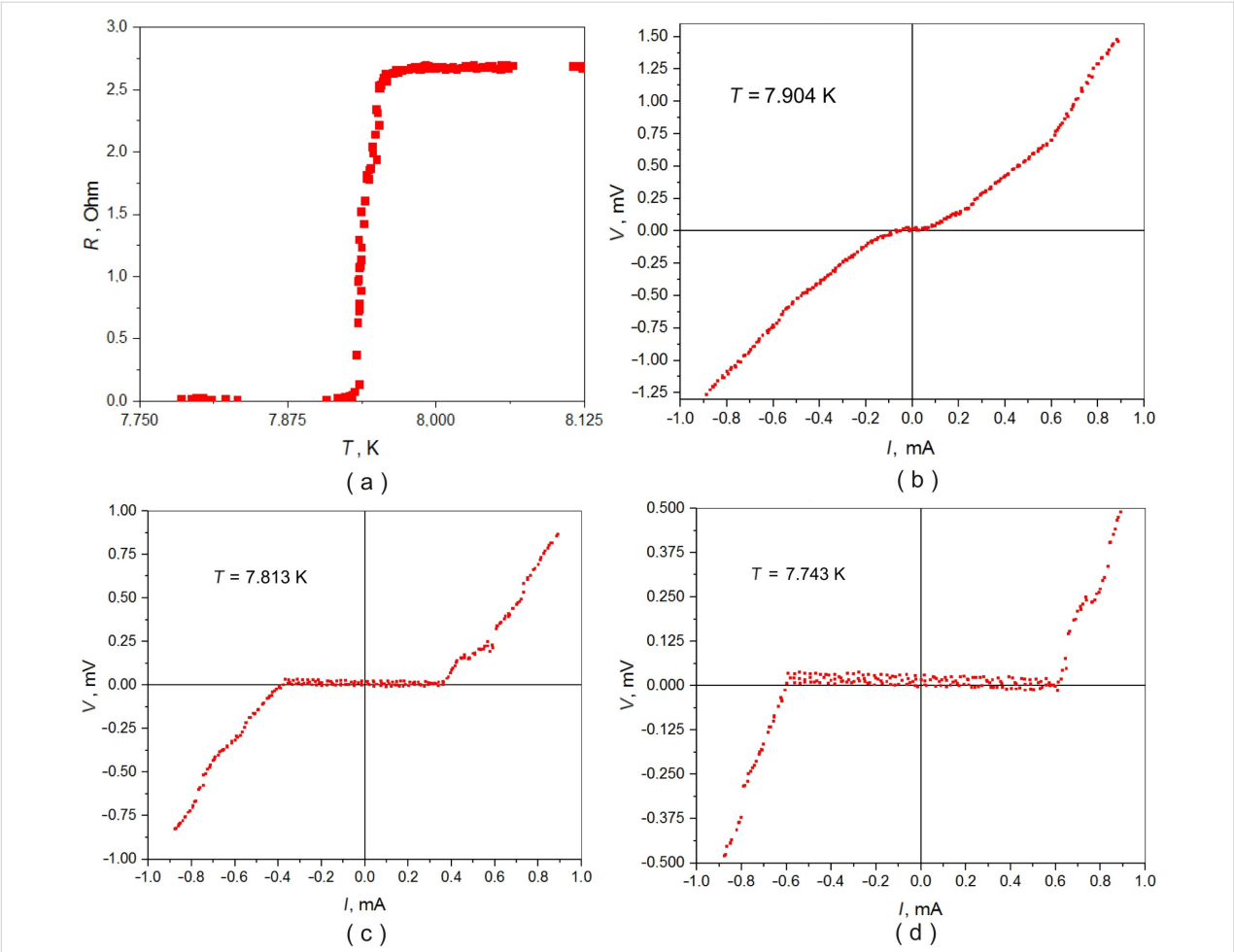

Figure 4: Sandwich structure Pb–PDP–Pb–0.4-GLASS, thickness of polymer is about 350 nm, both Pb electrodes are ≈200 nm thick. (a) Resistance vs temperature $R(T)$ dependence; (b), (c), and (d) voltage vs current $V(I)$ characteristics measured at various temperatures.

injection model limited by the space charge. At temperatures below ≈8 K, a number of samples exhibit features that can be explained by the effect of induced superconductivity in a thin film of a conducting polymer enclosed between two massive superconductors (lead).

Acknowledgements

The samples were fabricated using equipment of the Center for Collective Use "Agidel" of the UFRC RAS. Electron microscopy studies were performed with the eqipment of Shared Research Center FSRC “Crystallography and Photonics” RAS, and were partly supported by the Ministry of Science and Higher Education of the Russian Federation within the State assignment FSRC “Crystallography and Photonics” RAS in the part of SEM and TEM measurements.

Funding

The work was supported by the Mirror Lab project between HSE University and Bashkir state pedagogic University. The activity of A.S.G. was supported by the Basic Research program of HSE University.

ORCID® iDs

Konstantin Y. Arutyunov - https://orcid.org/0000-0001-9373-5185
Vladimir V. Artemov - https://orcid.org/0000-0002-5253-8481
Alexander L. Vasiliev - https://orcid.org/0000-0001-7884-4180
Danfis D. Karamov - https://orcid.org/0000-0002-7081-1947

Preprint

A non-peer-reviewed version of this article has been previously published as a preprint: https://doi.org/10.3762/bxiv.2022.77.v1

References

1. Lachinov, A. N.; Kornilov, V. M.; Zagurenko, T. G.; Zherebov, A. Y. *J. Exp. Theor. Phys.* **2006,** *102,* 640–645. doi:10.1134/s1063776106040133
2. Lachinov, A. N.; Vorob'eva, N. V. *Phys.-Usp.* **2006,** *49,* 1223–1238. doi:10.1070/pu2006v049n12abeh006176

3. Salazkin, S. N.; Zolotukhin, M. G.; Kovardakov, V. A.; Rafikov, S. R.; Dubrovina, L. V.; Gladkova, Y. A.; Pavlova, S.-S. A. *Polym. Sci. USSR* **1987,** *29,* 1572–1578. doi:10.1016/0032-3950(87)90419-9
4. Salazkin, S. N. *Polym. Sci., Ser. B* **2004,** *46,* 203–223.
5. Karamov, D. D.; Kornilov, V. M.; Lachinov, A. N.; Kraikin, V. A.; Ionova, I. A. *Tech. Phys.* **2016,** *61,* 1085–1090. doi:10.1134/s106378421607015x
6. Lachinov, A. N.; Tameev, A. R.; Yusupov, A. R.; Vannikov, A. V. *Russ. J. Electrochem.* **2012,** *48,* 316–319. doi:10.1134/s1023193512020097
7. Kornilov, V. M.; Lachinov, A. N. *J. Exp. Theor. Phys. Lett.* **1995,** *61,* 520–523.
8. Zykov, B. G.; Baydin, V. N.; Bayburina, Z. S.; Timoshenko, M. M.; Lachinov, A. N.; Zolotuchin, M. G. *J. Electron Spectrosc. Relat. Phenom.* **1992,** *61,* 123–129. doi:10.1016/0368-2048(92)80055-d
9. Wu, C. R.; Lachinov, A.; Johansson, N.; Stafström, S.; Kugler, T.; Rasmusson, J.; Salaneck, W. R. *Synth. Met.* **1994,** *67,* 125–128. doi:10.1016/0379-6779(94)90024-8
10. Johansson, N.; Lachinov, A.; Stafström, S.; Kugler, T.; Salaneck, W. R. *Synth. Met.* **1994,** *67,* 319–322. doi:10.1016/0379-6779(94)90064-7
11. Zykov, B. G.; Vasil'ev, Y. V.; Fal'ko, V. S.; Lachinov, A. N.; Khvostenko, V. I.; Gileva, N. G. *J. Exp. Theor. Phys. Lett.* **1996,** *64,* 439–443. doi:10.1134/1.567237
12. Komolov, A. S.; Lazneva, E. F.; Gerasimova, N. B.; Sobolev, V. S.; Pshenichnyuk, S. A.; Asfandiarov, N. L.; Kraikin, V. A.; Handke, B. *Phys. Solid State* **2019,** *61,* 1922–1926. doi:10.1134/s1063783419100214
13. Komolov, A. S.; Lazneva, E. F.; Gerasimova, N. B.; Sobolev, V. S.; Pshenichnyuk, S. A.; Asfandiarov, N. L.; Kraikin, V. A.; Handke, B. *Phys. Solid State* **2021,** *63,* 362–367. doi:10.1134/s1063783421020104
14. Pshenichnyuk, S. A.; Modelli, A.; Asfandiarov, N. L.; Lazneva, E. F.; Komolov, A. S. *J. Chem. Phys.* **2019,** *151,* 214309. doi:10.1063/1.5130152
15. Arutyunov, K. Y.; Zavialov, V. V.; Sedov, E. A.; Golokolenov, I. A.; Zarudneva, A. A.; Shein, K. V.; Trun'kin, I. N.; Vasiliev, A. L.; Konstantinidis, G.; Stavrinidis, A.; Stavrinidis, G.; Croitoru, M. D.; Shanenko, A. A. *Phys. Status Solidi RRL* **2019,** *13,* 1800317. doi:10.1002/pssr.201800317
16. Arutyunov, K. Y.; Sedov, E. A.; Golokolenov, I. A.; Zav'yalov, V. V.; Konstantinidis, G.; Stavrinidis, A.; Stavrinidis, G.; Vasiliadis, I.; Kekhagias, T.; Dimitrakopulos, G. P.; Komninu, F.; Kroitoru, M. D.; Shanenko, A. A. *Phys. Solid State* **2019,** *61,* 1559–1562. doi:10.1134/s1063783419090038
17. Zavyalov, V. V.; Chernyaev, S. A.; Shein, K. V.; Shukaleva, A. G.; Arutyunov, K. Y. *J. Phys.: Conf. Ser.* **2018,** *969,* 012086. doi:10.1088/1742-6596/969/1/012086
18. Yusupov, A. R.; Gadiev, R. M.; Lachinov, A. N.; Kornilov, V. M.; Kalimullina, L. R.; Galiev, A. F.; Kian, M.; Salazkin, S. N. *Synth. Met.* **2021,** *274,* 116733. doi:10.1016/j.synthmet.2021.116733

License and Terms

BEILSTEIN JOURNAL OF NANOTECHNOLOGY

Observation of collective excitation of surface plasmon resonances in large Josephson junction arrays

Roger Cattaneo[1], Mikhail A. Galin[2] and Vladimir M. Krasnov[*1]

Full Research Paper

Open Access

Address:
[1]Stockholm University, Physics Department, SE-10691 Stockholm, Sweden and [2]Institute for Physics of Microstructures RAS, 603950 Nizhny Novgorod, Russia

Email:
Vladimir M. Krasnov[*] - vladimir.krasnov@fysik.su.se

* Corresponding author

Keywords:
cavity modes; Josephson junctions; synchronization mechanism; THz radiation

Beilstein J. Nanotechnol. **2022,** *13,* 1578–1588.
https://doi.org/10.3762/bjnano.13.132

Received: 18 August 2022
Accepted: 29 November 2022
Published: 28 December 2022

This article is part of the thematic issue "Intrinsic Josephson effect and prospects of superconducting spintronics".

Associate Editor: A. J. Meixner

Abstract

Josephson junctions can be used as sources of microwave radiation. However, synchronization of many junctions is required for achieving a coherent amplification of the emitted power. In this work we present an experimental study of large arrays containing up to one thousand Nb/Nb_xSi_{1-x}/Nb junctions. The arrays exhibit profound cavity mode resonances, corresponding to the formation of standing waves at the electrode/substrate interface. We observe that resonant steps in the current–voltage characteristics appear above some threshold number of junctions, $N_{th} \approx 100$, and then progressively enhance in amplitude with further increment of the number of junctions in the resistive oscillating state. We use an external detector to measure the emission of electromagnetic waves. The emission power correlates with the step amplitude. Our results indicate that the emission is facilitated by the cavity modes in the electrodes. The modes are collectively excited by active junctions. In turn, the standing wave imprints its order on the array, facilitating mutual phase-locking of junctions. This provides an indirect coupling mechanism, allowing for the synchronization of junctions, which do not directly interact with each other. Our results demonstrate that electrodes can effectively work as a common external resonator, facilitating long-range phase-locking of large junction arrays with sizes larger than the emitted wavelength.

Introduction

Terahertz sources of electromagnetic waves (EMWs) in the range of 0.1–10 THz are characterized by a low power efficiency [1-6]. Josephson junctions (JJs) can generate tunable terahertz radiation in a broad frequency range, from sub-terahertz in low-T_c superconductors [7-9], to tens of terahertz in high-T_c superconductors [10-18]. The performance of Josephson oscillators is limited by impedance mismatch [18,19] and self-heating [13,17,20,21]. Proper device engineering can obviate these obstacles and improve the performance [18]. A single JJ is able to emit EMWs, but with a low power [22].

Therefore, synchronization of many JJs is required for coherent superradiant amplification of the emitted power [7-10,19,23-25].

Synchronization of many oscillators is a difficult task. It requires their mutual coupling, which can be either direct or indirect. The direct coupling is caused by interjunction interaction via shared electromagnetic fields and currents [26]. For conventional overlap JJs the scale of such interaction is short (nanoscale) because it is limited by the corresponding screening lengths in superconducting electrodes [27]. However, for planar JJs the direct interaction can be of long range due to the presence of long-range stray fields [28]. Indirect coupling is caused by interaction of JJs with a common external resonator [7,8,29-35]. The resonator imprints the phase order onto the junction array and, thus, can synchronize JJs without direct interjunction coupling. The scale of such indirect coupling is not limited by screening lengths and can be truly of long range. For example, in [9,34], the successful indirect synchronization of up to 9000 JJs in a large array (≈1 cm) was demonstrated. The indirect coupling via a common resonator is the most promising way for the synchronization of very large arrays with sizes significantly larger than the emitted wave length.

In this work, we study experimentally large JJ arrays containing up to 1000 Nb/Nb_xSi_{1-x}/Nb junctions. The arrays exhibit strong cavity mode resonances resulting in the appearance of a profound step structure in the current–voltage (*I*–*V*) characteristics. The resonances are caused by the formation of surface plasmon-type standing waves at the electrode–substrate interface [34]. Thus, the electrodes themselves act as a common external resonator, facilitating the effective indirect coupling between JJs and the long-range phase-locking of the arrays. Our main result is the observation of a gradual development of collective resonances upon sequential switching of JJs into the oscillating resistive state. We show that a threshold number of JJs, $N_{th} \approx 100$, is required for excitation of the collective cavity modes. Above the threshold, the amplitude of resonant steps grows in a quasi-linear manner with the number of active JJs. We employ an external microwave detector for measuring EMW emission from the arrays. It is observed that the emitted power is correlated with the amplitude of the resonant step in the *I*–*V*s, implying that the emission is facilitated by the cavity modes [9,32-34]. We conclude that the long electrodes in the studied arrays are acting both as external resonators and microwave antennas. The large length (approx. 1 cm) of the electrodes facilitates good impedance matching with free space and improves the radiation power efficiency. The cavity modes in the electrodes are excited collectively by the JJs, which are, in turn, mutually phase-locked by the modes. This provides a positive feedback mechanism allowing for the synchronization of large arrays without direct interjunction interaction.

Samples

We study arrays of Nb/Nb_xSi_{1-x}/Nb JJs fabricated on oxidized Si substrates and connected in series by Nb electrodes. The Nb_xSi_{1-x} interlayer with the composition $x \simeq 0.14$ was deposited by co-sputtering from Nb and Si sources. Details about the fabrication procedure can be found in [36]. Figure 1a and Figure 1c show layouts of the two studied arrays, which we refer to as (a) "meander" and (c) "linear", respectively. The arrays are similar to those studied in [9,34,37], but have smaller JJ areas. Additional information about transport properties of such arrays can be found in [9,34,36,37].

The meander array (Figure 1a) has seven identical (vertical) sections with $N = 1000$ JJs in each and with an overall size in the vertical direction of 6.25 mm. Each section consists of 125 horizontal segments with a length of 230 μm, a width of 10 μm, and a separation of 40 μm. Each segment contains eight overlap-type JJs with the area 6×6 μm^2. This can be seen from the close-up shown in the left panel of Figure 1a. The distance between nearby junction centers is 12 μm. A cross section of the junctions is sketched in the bottom-left panel of Figure 1c.

The linear array (Figure 1c) contains five straight sections (lines) with $N = 332$ JJs in each. The spacing between the lines is 6 μm. Sizes and separation of the JJs is the same as for the meander array.

The two outermost lines in the linear array and all seven sections of the meander array can be measured independently. We tested all of them, and they show similar characteristics. Below we will show data for one of the sections of each array, marked by the red bands in Figure 1a and Figure 1c. The meander array does not contain any specific resonator. In this case, collective cavity modes originate solely from interconnecting Nb electrodes, acting as a travelling wave antenna for surface plasmons at the electrode–substrate interface [9,34]. The linear array contains also two extra Nb lines (without JJs) on each side of the array forming a slot waveguide, which may act as an additional external resonator. However, comparison with similar arrays without such lines [9,34] does not reveal any significant influence of these lines, implying that even for the linear array the electrodes are playing the dominant role in array dynamics.

Results

Measurements were performed in a closed-cycle ^{4}He cryostat (sample in gas) with rotatable sample holder. The magnetic

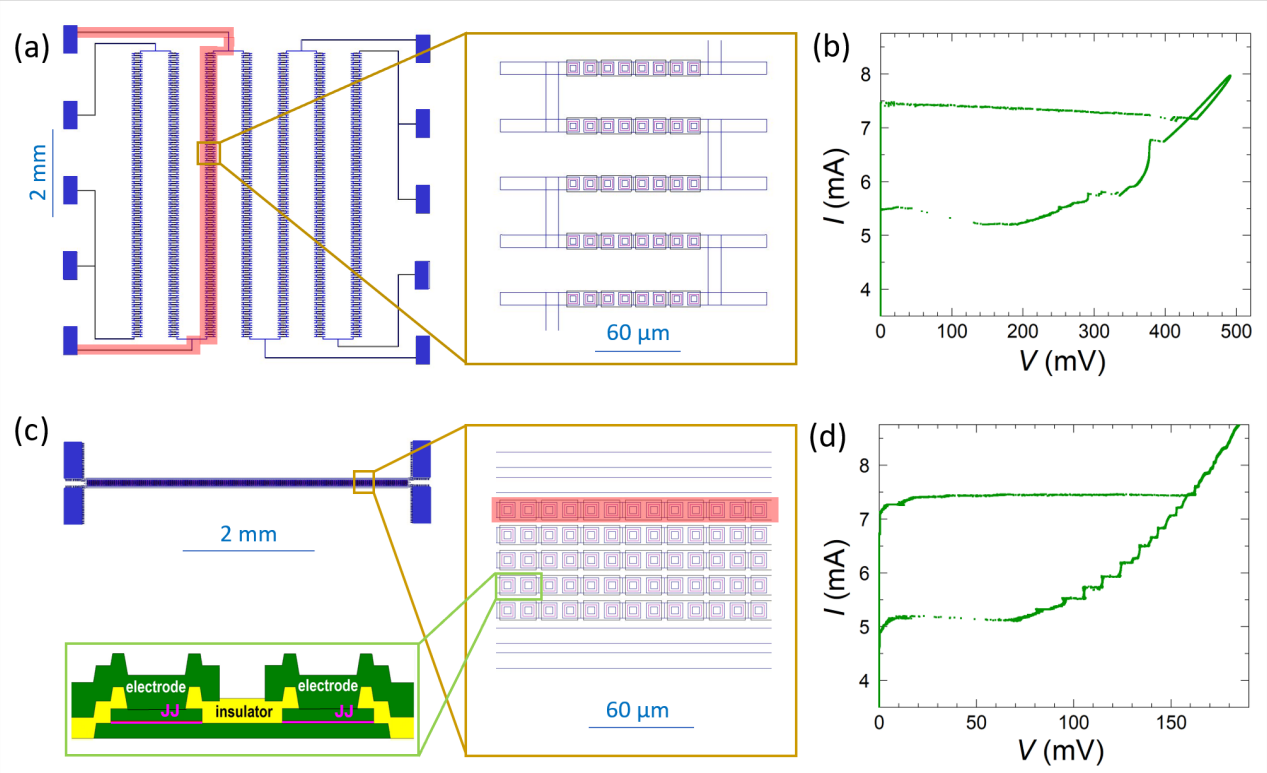

Figure 1: (a, c) Layouts of the studied meander and linear arrays. The meander array in (a) contains seven meandering sections with N = 1000 JJs in each. The linear array in (c) contains five straight lines with N = 332 JJs in each. The right panels represent corresponding closeups (top view). The bottom-left part in (c) shows a sketch of the junction cross section with Nb in green, SiO_2 in yellow, and the junction interlayer in magenta (from [36]). Red bands in (a) and (c) mark one of the sections in each array, which was used for detailed studies. Panels (b) and (d) show the I–V characteristics of the marked sections in the meander (b) and linear (d) arrays. Measurements are done in zero magnetic field at $T \simeq 2.6$ K. Appearance of profound steps in the I–Vs due to excitation of cavity resonances in electrodes is clearly seen for both arrays.

field is supplied by a superconducting solenoid. Figure 1b and Figure 1d show the I–V curves (up and down bias swipes) for meander and linear arrays, respectively, at zero magnetic field and $T \simeq 2.6$ K. For both arrays, all JJs switch simultaneously from the superconducting to the resistive state, at similar critical currents, $I_c \simeq 7.5$ mA. This indicates good reproducibility of the fabrication procedure with almost identical JJs. The characteristic voltage per JJ is quite large, $I_cR_n \simeq 0.5$ mV. As seen from Figure 1b and Figure 1d, well-defined vertical steps appear in the reverse branch of the I–V characteristics for both arrays. As shown in [9,34], they are caused by propagation of surface plasmon-type EMWs along the Nb electrode–Si substrate interface. These steps appear when the Josephson frequency coincides with one of the cavity mode frequencies, corresponding to formation of standing waves along the whole length (approx. 1 cm) of the electrodes [34]. Cavity modes depend on the array geometry. Therefore, the step structure is different for the two arrays. The meander array, Figure 1b, exhibits a single large step at high voltage and many low-amplitude steps with small separation in voltage. The linear array, Figure 1d, exhibits several evenly spaced steps. The I–V characteristics are hysteretic, with the retrapping current being significantly smaller than the switching current. The hysteresis leads to a metastability, which allows for the observation of different voltage states at the same current. This will be exploited for accessing a larger variety of states with different number of active junctions in the oscillating resistive state.

Figure 2a shows the modulation, $I_c(H)$, of the critical current versus the in-plane magnetic field for the linear array. The period of modulation agrees well with the expected value for a single JJ. However, the shape of $I_c(H)$ with sharp peaks deviates from the standard Fraunhofer pattern, characteristic for a single JJ. The reason is that the measured I_c represents the smallest I_c for all JJs in the array. As discussed below, a magnetic field causes a spread in the modulations I_c for different JJs. Therefore, the measured $I_c(H)$ is lower than the Fraunhofer modulation for an individual JJ. Presumably, the spread of the modulations I_c is caused by the uneven distribution of fluxon numbers in JJs when the flux per junction is not equal to integer and half-integer numbers of flux quanta.

Figure 2b–d shows the I–Vs measured at different magnetic fields indicated by vertical lines with the corresponding color in

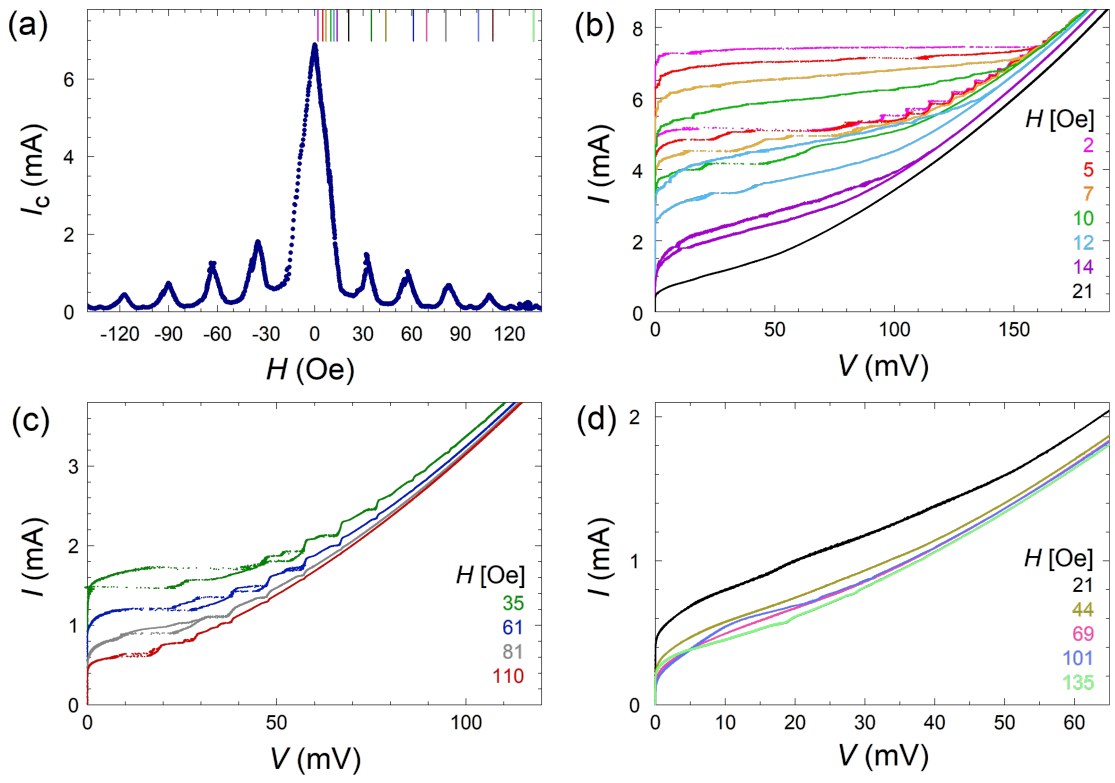

Figure 2: (a) Fraunhofer-type modulation of the critical current as a function of in-plane magnetic field for the linear array. Panels (b–d) show the *I*–*V* characteristics at different magnetic fields indicated by the same-color vertical lines in (a). Panel (b) represents the *I*–*V*s at the central lobe. Panels (c) and (d) show the *I*–*V*s close to (c) maxima and (d) minima of $I_c(H)$ at different lobes. A correlation between I_c and the step amplitudes can be seen.

Figure 2a. The step amplitude, ΔI, modulates in a correlated manner with $I_c(H)$. ΔI is large at maxima of $I_c(H)$, see Figure 2c, and vanishes when $I_c(H) \to 0$, see Figure 2d. The correlation between ΔI and I_c reflects the cavity mode–junction interaction. The mechanism for appearance of resonant steps is similar to that for the formation of Shapiro steps upon external microwave (MW) irradiation. The steps appear via rectification of the cavity-mode-induced MW current in the electrodes and the amplitude of the rectified current is proportional to I_c of the JJs [38].

Dynamic states with different number of active junctions

We want to emphasize that the discussed cavity resonances represent a collective behavior of the arrays. A single JJ does not exhibit such steps [36]. To analyze the collective behavior, it is necessary to switch junctions one-by-one into the oscillating resistive state. Since the JJs are almost identical, at $H = 0$, they all simultaneously switch together, as seen in Figure 1b and Figure 1d. However, application of a small magnetic field introduces a spread in critical currents, as can be seen from Figure 2b. In combination with the hysteresis in the *I*–*V* characteristics, this makes it possible to reach a large variety of dynamic states with different numbers of active JJs.

Figure 3a and Figure 3b show thus obtained *I*–*V*s of the meander array with different number of active JJs. Here, each *I*–*V* curve is measured in a single swipe while sequentially increasing the current amplitude. Figure 3a and Figure 3b represent the *I*–*V*s for small and large ranges of *N*, respectively. The voltage at a given current scales linearly with the number of JJs, which allows for an unambiguous determination of *N*. In Figure 3a, $N = 46$, 63, 90, 107, 122, 140, 155, 172, 184, and 207 (from left to right). In Figure 3b $N = 140$, 172, 184, 207, 224, 243, 271, 284, 304, 328, 365, 380, 422, 444, 478, 521, 560, 591, 632, 671, and 1000 (all JJs). The number of active junctions for some curves is indicated by the corresponding color. As can be seen from Figure 3a, the *I*–*V* characteristics for a small number of JJs in the resistive state do not exhibit resonant steps. In Figure 3b, the steps are gradually developing above some threshold number of JJs, N_{th}. Figure 3c represents an integrating oscillogram measured during repetitively sweeping the bias up and down with slowly changing amplitude. It allows for an almost complete mapping of the *I*–*V* evolution with changing

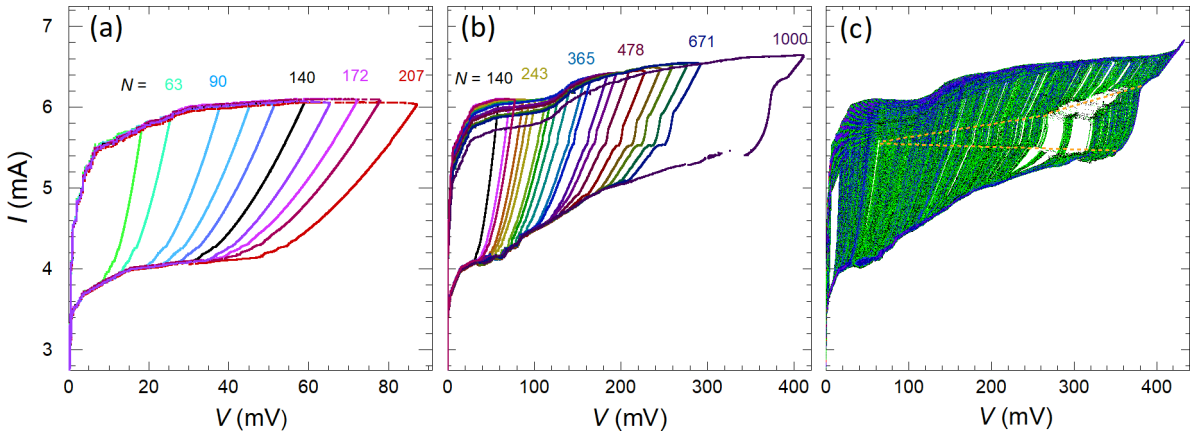

Figure 3: Ensembles of the *I*–*V* characteristics with different numbers of active JJs for the meander array at T = 2.4 K and for an in-plane field of H = 7 Oe. (a, b) The *I*–*V*s obtained in a single swipe (a) for a small number of JJs, $N \leq 207$ and (b) at larger N = 140–1000. The number of active JJs, N, is indicated for some *I*–*V*s using the same color. A gradual development of the main resonant step at $I \simeq 5.5$ mA with increasing N can be seen. (c) An integrated oscillogram accumulated during many current swipes with varying amplitudes. It demonstrates a large variety of achievable states with different numbers of active JJs. Dashed orange lines indicate a quasi-linear increase of the step amplitude with increasing N for $N > N_{th} \simeq 150$.

the number of active JJs. Dashed orange lines indicate edges of the main resonance step. They reveal a quasi-linear increase of the step amplitude with increasing N, for $N > N_{th} \simeq 150$.

Figure 4 shows similar data for the linear array. Figure 4a shows the integrating oscillogram of the *I*–*V* obtained at $H \simeq 7$ Oe. Figure 4b shows a close-up of the step structure. Dashed green lines in Figure 4b mark edges of three distinct cavity modes. The general behavior is the same as for the meander array. We observe the appearance and the gradual increase of the step amplitudes at $N > N_{th}$. The threshold numbers for the three highlighted steps are $N_{th} \simeq 88$, 113, and 120 for the low-, middle-, and high-voltage resonances, respectively. Due to the presence of many closely spaced resonant steps in the *I*–*V* of the linear array, it is difficult to identify and analyze specific modes. Therefore, in what follows, we will perform a quantitative analysis only on the meander array.

In Figure 5a, we show portions of the *I*–*V* curves for the meander array with different number of active JJs in the bias range corresponding to the main resonance. The resonant step is large for N = 671 (red), distinct for N = 330 (orange), barely

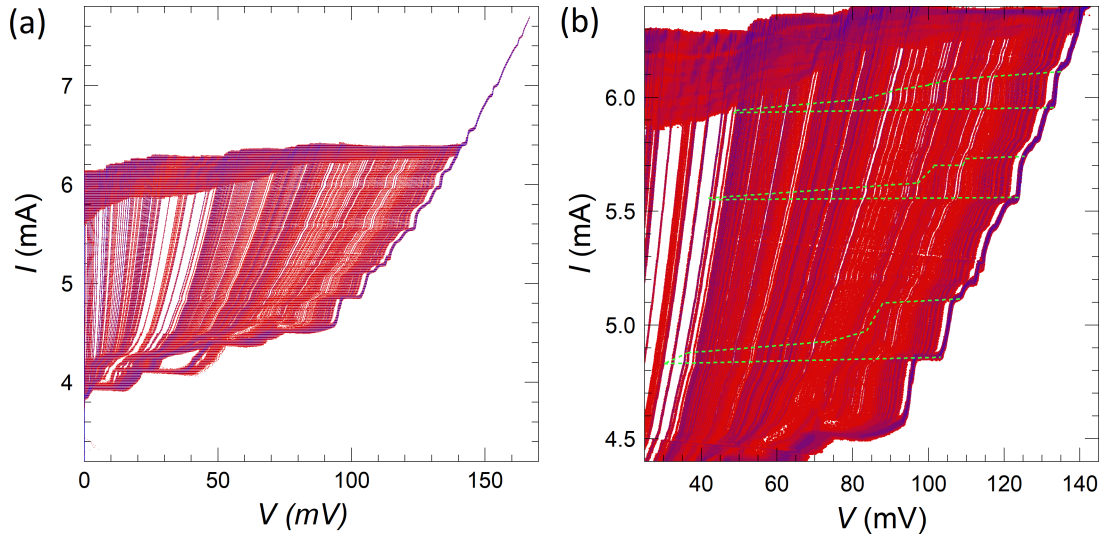

Figure 4: (a) An integrated oscillogram for the linear array at T = 2.4 K and for an in-plane field H = 7 Oe. Panel (b) shows a closeup view, which illustrates appearance and gradual evolution of several steps with increasing N. Edges of three distinct resonant steps are indicated by dashed green lines.

visible for N = 207 (violet), and not seen for smaller N. To quantify the step amplitude, ΔI, at small N we plot the differential conductance, dI/dV. Figure 5b shows the dI/dV(I) curves for the I–Vs from Figure 5a, normalized by the resonant voltage V_{step}. This quantity does not depend on the number of active JJs. A current step in the I–V is represented by a peak in V_{step} dI/dV. The height of the peak reflects the sharpness of the step and the width is equal to the step amplitude, ΔI. For the well-developed step, N = 671, both the height and the width of the peak are large. From Figure 5b, it can be seen that with decreasing N both the height and the width of the peak decrease. For N = 153 (blue) a small peak is still visible, but for N = 106 (olive) we can not distinguish any signature of the resonant step. This observation clearly shows that the observed steps are not inherent to individual Nb/Nb$_x$Si$_{1-x}$/Nb JJs but are the consequence of collective surface-plasmon resonances. The finite threshold number is the consequence of the collective excitation of the cavity mode [32,33].

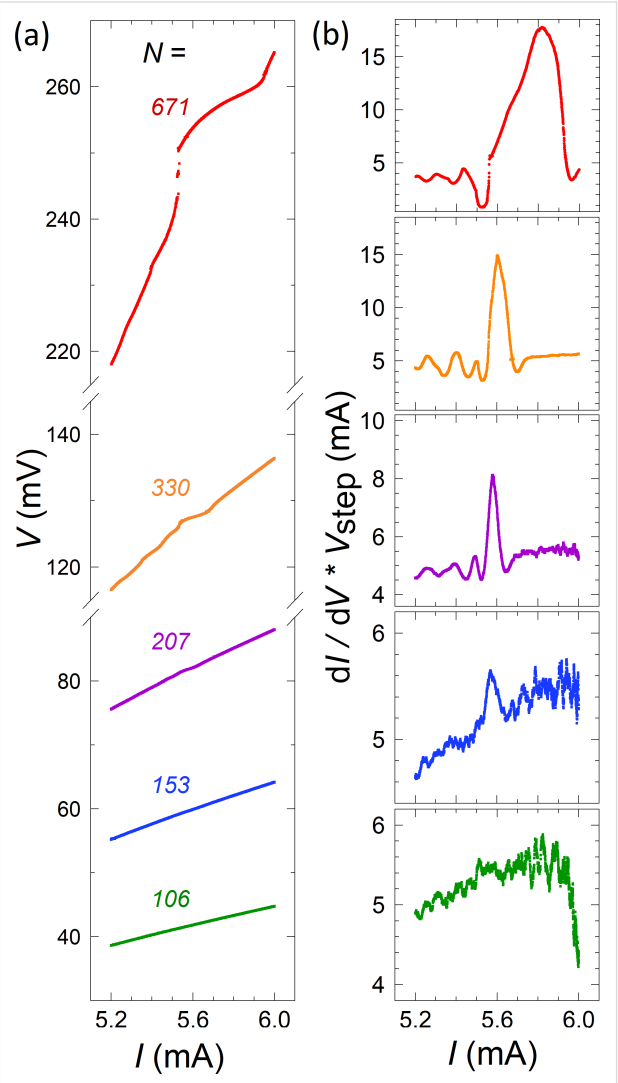

Figure 5: (a) Parts of the V–I curves near the main resonance for the meander array with different number of active JJs, N. (b) Normalized differential conductance for the I–V characteristics from (a). The peak represents the resonant step. It reduces with decreasing N and is not visible for N = 106 (lower panel) below the threshold number of JJs.

Radiation detection

For detection of EMW emission we use a superconducting microwave detector. Figure 6a shows an optical image of the detector. It consists of a log-periodic microwave antenna [39] with a broad frequency range of ca. 15–700 GHz. In the center, there is a nanoscale JJ sensor, shown in Figure 6b. The detector is made of a Nb film (70 nm thick), using a fabrication technique similar to that described in [28]. The antenna is patterned using photolithography and reactive ion etching. The JJ sensor with variable thickness and a width of ≈100 nm is made by Ga^+ focused ion beam etching. The JJ is made small in order to increase its resistance R_n to approx. 50 Ω, which is needed for a good impedance matching with the antenna.

In order to calibrate the detector, we use a MW source with f = 74.5 GHz. Figure 6c represents a sketch of the calibration setup. The detector is placed in an optical cryostat and the gigahertz signal is guided through an optical window using two high-density polyethylene lenses. The gigahertz source is linearly polarized. To tune the incoming microwave power, P_{MW}, we use a wire-grid polarizer with adjustable angle θ. The blue curve in Figure 6d represents the I–V of the detector without MW power. It is seen that the detector JJ has a very large $I_cR_n \simeq 2$ mV, enabling large readout signal and broad operation frequency up to $f \approx 1$ THz. Olive and pink curves in Figure 6d show the I–Vs with attenuated and full MW power, respectively. The detector operates as a Josephson switching current detector [15]. The incoming MW signal suppresses the switching current, I_s, of the detector JJ. At high MW power, it is fully suppressed and the I–V is Ohmic with a normal resistance R_n = 42.8 Ω, as seen from the pink I–V from Figure 6d.

To quantify the suppression of I_s, we measure the ac resistance at a fixed current amplitude, I_{ac}, corresponding to the bias range in Figure 6d (without dc bias offset). As shown in [40], $R_{ac}/R_n \simeq 1 - (I_s/I_{ac})^2$. Figure 6e shows the thus obtained detector resistance, R_d, versus $\cos^2\theta$ of the polarizer, which is proportional to the incoming MW power. With increasing P_{MW}, R_d decreases due to suppression of I_s. At high MW power, when $I_s \to 0$, $R_d \to R_n$ = 42.8 Ω. As discussed in [15], the complete suppression of I_s corresponds to the absorbed MW power, $P_a \simeq \left(2\sqrt{2}/3\pi\right) I_{c0}^2 R_n \simeq 30$ nW. Thus, we can perform an absolute calibration of the absorbed power as a function of the detector resistance, as shown in Figure 6f. The absorbed power depends on the absorption efficiency, γ, the antenna area, A_a, and the power density, P_{MW}/A_{MW}, where A_{MW} is the micro-

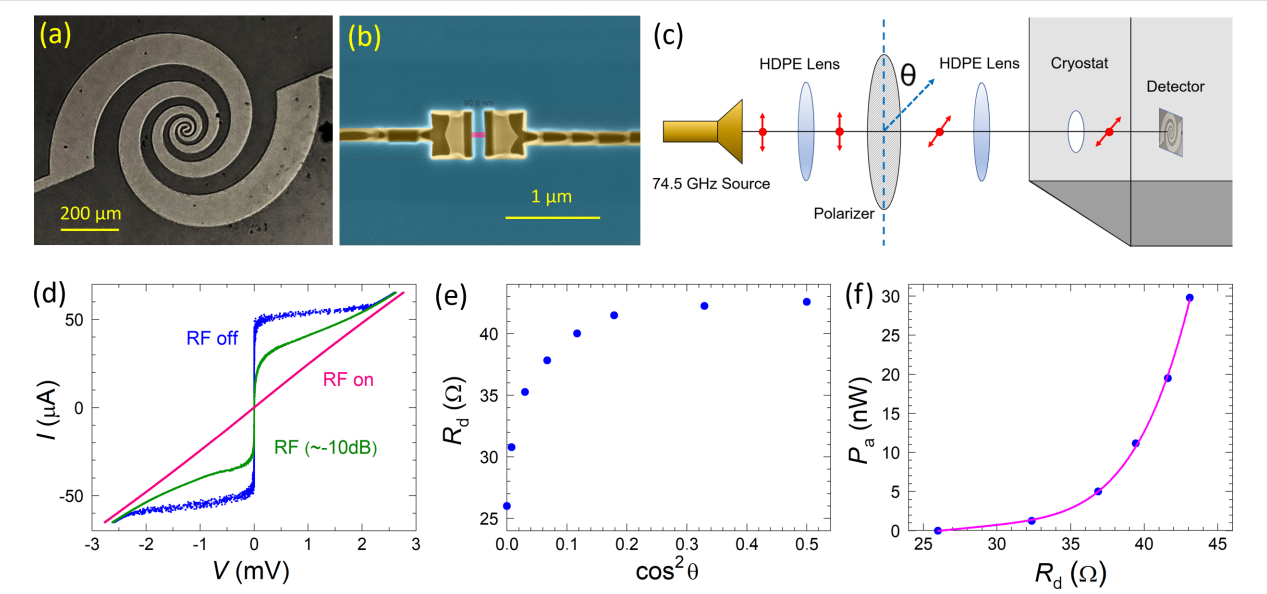

Figure 6: (a) Optical image of a superconducting detector with a log-periodic microwave antenna. (b) SEM image of a nanoscale sensor junction (false color). (c) Schematics of the calibration setup using a microwave source with f = 74.5 GHz. (d) The I–V characteristics of the sensor junction at T = 2.4 K without (blue) and with attenuated (olive) and full (pink) microwave power. (e) The ac resistance of the detector, R_d, as a function of $\cos^2\theta$ of the polarizer angle, proportional to the transmitted power. (f) Obtained calibration curve of the detector, that is, absorbed microwave power, P_a, as a function of R_d.

wave spot area, $P_a = \gamma P_{MW}(A_a/A_{MW})$. Taking an optimal $\gamma = 0.5$ [19,41] and an antenna radius of $r_a \simeq 0.5$ mm while also assuming a MW spot radius of $r_{MW} \approx 1$ cm, we can estimate the total incoming power, $P_{MW} = \gamma^{-1}P_a(r_{MW}/r_a)^2 \simeq 24$ μW. It is consistent with the total power of the source of approx. 100 μW, taking into account losses on the way to the detector via diffraction on optical windows and a set of low-temperature MW filters (Zitex). Such an estimation indicates that the absorption efficiency γ of our detector is indeed not far from the optimal. However, the overall detection efficiency, $P_a/P_{MW} \approx 10^{-3}$, is small because of geometrical constraints, $(r_a/r_{MW})^2 \ll 1$.

For the analysis of EMW emission, the detector is placed face-to-face at about 1.5 cm distance from the array. The sample/detector arrangement is similar to that described in [9]. The detector position is fixed, but the sample is placed on a rotatable sample holder, facilitating adjustment of the angle α between the normals of the detector and the array. As discussed in [9], emission from such arrays has a strong angular dependence. Below we show measurements for the meander array at $\alpha = 45°$, which corresponds to the emission maximum.

Figure 7 represents simultaneous measurements of the I–V characteristics and the detector response (represented by the color scale) for the meander array. Figure 7a and Figure 7b show two integrated oscillograms acquired in external fields of 8 and 15 Oe, respectively. Figure 7c shows the I–Vs (single sweeps at the returning branch) for fields from 0 to 20 Oe at an angle of 45° with respect to the normal of the JJs. It is seen that the magnetic field strongly affects the emission. For example, at H = 8 Oe in Figure 7a, the main resonance is dominating, but, at H = 15 Oe in Figure 7b, many more smaller steps appear. The main resonance is not shown in Figure 7b in order to show details of the smaller steps, but it is still there, as can be seen from Figure 7c. The I–Vs from Figure 7 reveal several emitting resonances, for which the emission power grows in a correlated manner with the step amplitude upon increasing the number of active JJs.

The linear array exhibits a qualitatively similar behavior, as reported in [9,34] and as shown in Figure 4. However, the presence of many nearby steps complicates unambiguous identification and analysis of specific cavity modes.

Discussion

Figure 8 summarizes our main results, that is, the observation of collective excitation of surface plasmon resonances by large Josephson junction arrays and the correlated enhancement of EMW emission. Figure 8a shows a close-up on the I–V characteristics from Figure 3b for the meander array at the main resonance. Figure 8b shows the step amplitude as a function of the number of active JJs for this resonance. Blue symbols represent ΔI measured directly from the I–V characteristics. Orange symbols are obtained by integration of the areas of the peak in differential conductance, $\int(dI/dV)dV$, taken from Figure 5b. The latter data set was multiplied with a calibration factor of

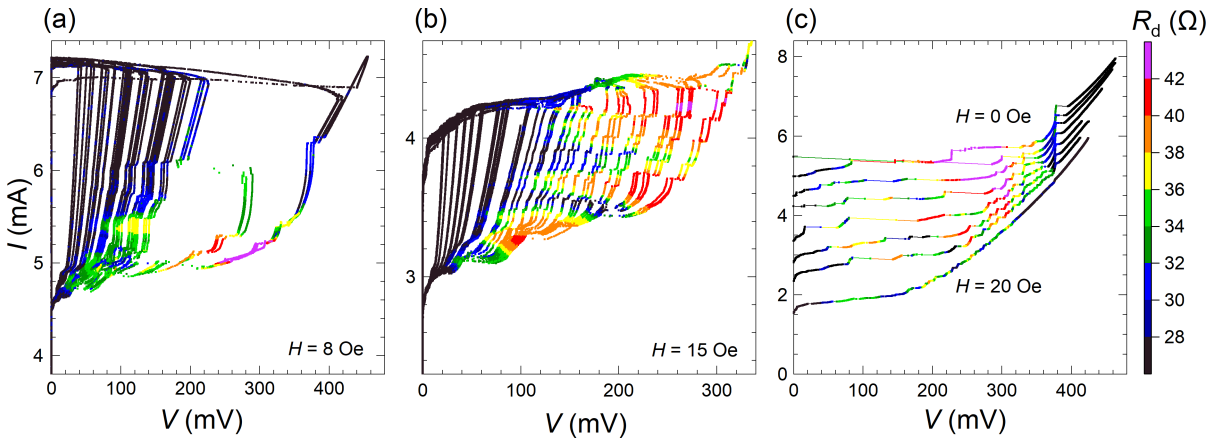

Figure 7: (a, b) The *I*–*V* characteristics (integrated oscillograms) of the meander array acquired at (a) H = 8 Oe and (b) 15 Oe at an angle of 45° with respect to the normal of the JJs. Panel (c) shows the return branch of the *I*–*V* characteristics (single swipe) at H = 0, 7, 9, 11, 13, 15, 17, and 20 Oe (from top to bottom). All *I*–*V* curves are color-coded by the simultaneously measured detector resistance R_d with the scale shown on the right side of panel (c). A correlated development of resonant step amplitude and the emitted power can be seen. Measurements are done at T = 2.4 K at the angle α = 45° between array and detector.

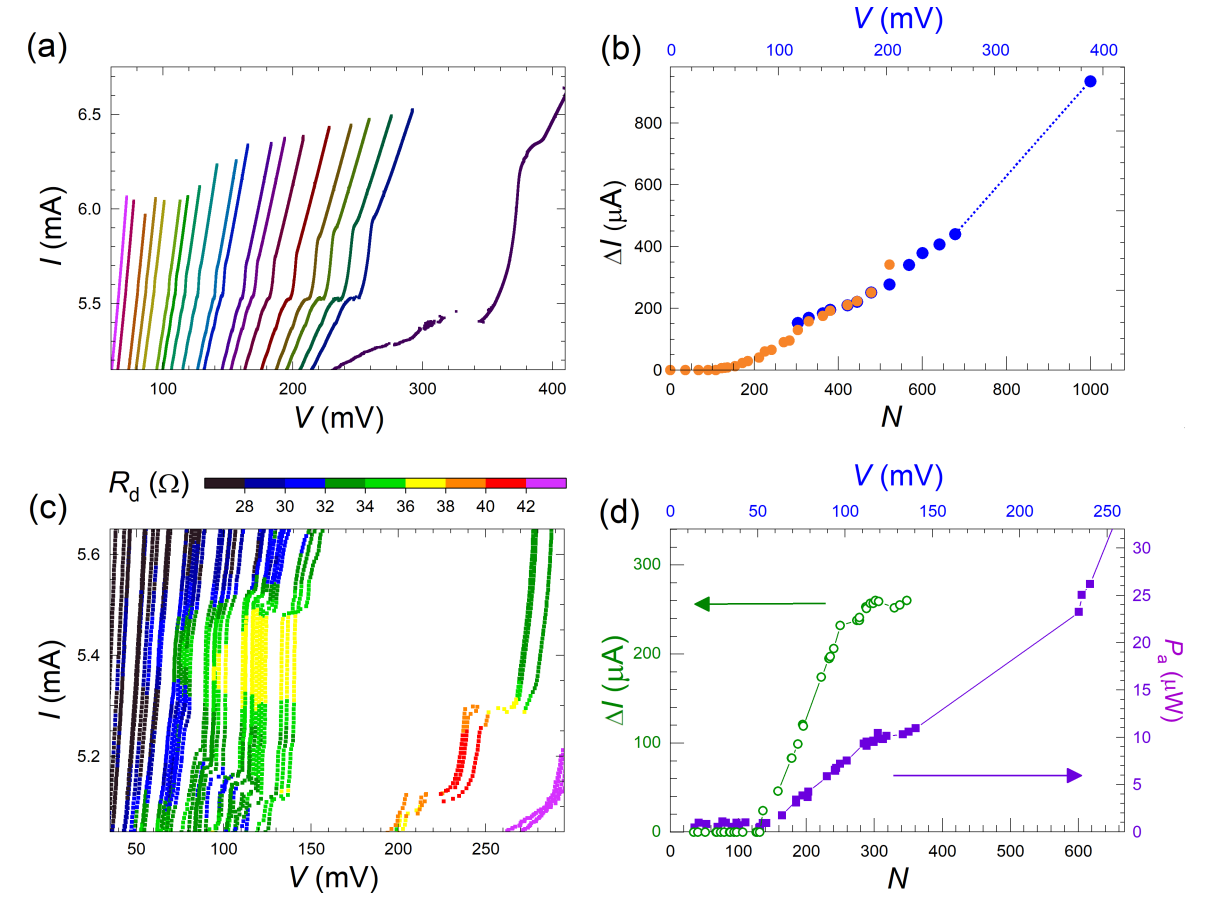

Figure 8: (a) Parts of the *I*–*V* characteristics of the meander array near the main resonance. (b) The main step amplitude, ΔI, as a function of the number of active junctions, N. Blue symbols are measured directly from the *I*–*V* characteristics, and orange symbols are obtained by integration of the resonant peak area in d*I*/d*V*. (c) Simultaneous transport and detection measurements of a secondary resonance from Figure 7a. (d) Step amplitude, ΔI, (olive open circles) and the detected (absorbed) power, P_a, (purple solid squares) as a function of N for the secondary step from (c).

2.63 in order to merge it with direct measurements of ΔI in the range $300 < N < 500$ where both methods are working well. A quasi-linear growth in $\Delta I(N)$ starting from the threshold number $N_{th} \simeq 150$ is observed. However, as can be seen from Figure 7a and Figure 7c, there is practically no emission at this most prominent step with $V(N = 1000) = 389$ mV, which corresponds to $f_J \simeq 188$ GHz, even when all $N = 1000$ JJs are active. This is not surprising because a non-emitting cavity mode is expected to have the highest quality factor due to the lack of radiative losses [19]. Therefore, this step is large because it is non-emitting.

Figure 8c shows the data for a secondary resonance from Figure 7a with a lower voltage and $f_J \simeq 182$ GHz. In Figure 8d, we plot the step amplitude, ΔI (olive, left axis), and the detected (absorbed) MW power, P_a (violet, right axis), as a function of N for the secondary mode from Figure 8c. The general behavior is similar, that is, a quasi-linear growth from a threshold number $N_{th} \simeq 160$. Up to $N = 350$, there is a direct correlation, $P_a \propto \Delta I$. However, at larger $N > 600$ we observe a superlinear upturn in the emission power, consistent with [9]. This is a likely indication of the global synchronization of the array, which leads to the coherent superradiant emission, for which P_{MW} should be proportional to ΔI^2. The emitted power at $N > 700$ becomes so large that it saturates our detector. Therefore, unfortunately we can not confidently analyze further development of the mode.

Generally, we observe that all cavity modes are behaving similarly, that is, ΔI and P_a increase in a quasi-linear manner with N, above some threshold number N_{th}. This clearly shows a collective nature of the excited resonance. Yet, there are some differences. For example, some modes emit strongly and some do not emit at all. Such behavior is characteristic for constructively and destructively interfering coherent states [19]. Also, the threshold number is individual for each mode. The large variety of modes and their differences can be seen in Figure 7b. In Figure 9, we analyze the detected power vs N for the two most distinct emitting modes from Figure 7b at different biases $I = 3.7$ mA (down triangles) $I =$ and 4.2 mA (circles). Here, the threshold number is significantly larger, $N_{th} \simeq 380$, and the power does not grow linearly but increases abruptly for $N > N_{th}$.

The results presented here are consistent with several previous works. A linear increase of a resonant step amplitude with increasing junction number has been observed in [30,31]. A threshold behavior for excitation of a common resonance has been reported in [8,15]. However, the ability to individually switch JJs in very large arrays allows us to observe those effects with an unprecedented clarity. This facilitates unambiguous interpretation of synchronization and emission mechanisms

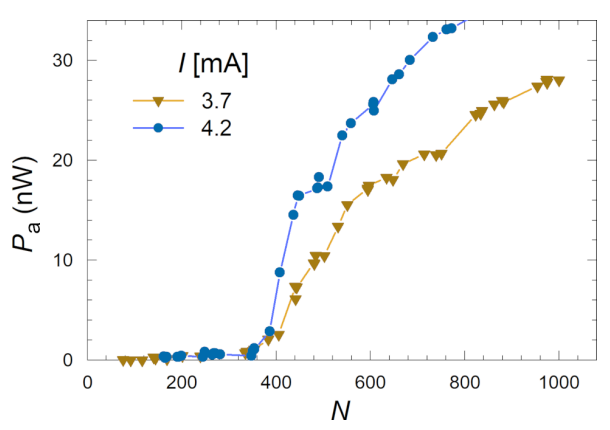

Figure 9: Detected power as a function of the number of active junctions for two modes from Figure 7b at bias currents of $I = 3.7$ mA (down triangles) and $I = 4.2$ mA (circles).

from such arrays, in which JJs are indirectly coupled via a common resonator. Combining our results with earlier observations, we can make the following conclusions on the mechanisms of formation of collective resonant steps, emission, and synchronization in large JJ arrays:

(I) The mechanism for the formation of resonant steps in the I–V is similar to that behind Shapiro steps with the only difference that the corresponding MW current, I_{MW}, originates from the cavity mode in the array rather than from an external source. Therefore, the amplitude of the step, ΔI, is proportional to the critical current and modulates together with it as a function of magnetic field, as demonstrated in Figure 2. At small step amplitudes, $\Delta I \ll I_{c0}$, the cavity mode current is directly proportional to the step amplitude, $I_{MW} \simeq a\Delta I$ with $a \approx 1$ (see section 11.3 in [38]).

(II) The absence of emission at $N < N_{th}$ shows that the emission in this case is not caused by direct interference of electromagnetic fields from individual JJs. The JJs in our study have an overlap (parallel-plate capacitor) geometry. They are characterized by a large impedance mismatch and a very low emission efficiency [19]. The emission is facilitated by the long (approx. 1 cm) electrode, which acts as a matching travelling wave antenna [9]. The role of the JJs is just to pump oscillations, I_{MW}, in the antenna. Therefore, the quadratic increase of the emission power as a function of the number of active JJs [8,30,42] in this case is not due to direct interference of radiation fields from individual JJs (which are negligible due impedance mismatch) but is the consequence of the linear $I_{MW}(N) \propto \Delta I(N) \propto N$ dependence. The emission power from the antenna in this case remains quadratic: $P(N) = I_{MW}^2(N)/Z \propto N^2$, where Z is the corresponding microwave impedance. However, generally $I_{MW}(N)$ can be nonlinear, in which case $P(N)$ is non-

quadratic. Indeed, the nonlinear $I_{MW}(N)$ dependence often appears in corresponding numerical simulations [33]. Furthermore, the simple analysis above assumes a perfect phase-locking of the array to a single cavity mode, which is not always the case. During the experiments we observed switching between nearby modes, which prevents us from a straightforward analysis of the linear array. Presumably, such instability and incomplete phase-locking leads to a linear dependence $P_a(N) \propto \Delta I(N)$, which is shown in Figure 8d up to $N \simeq 430$. An improvement of phase-locking at larger N leads to the boost in the emission power, as also reported in [9]. Yet, for JJs coupled via a cavity mode, even a perfect parabolic dependence $P \propto N^2$ is not the consequence of direct superradiant emission from N JJs. It should rather be referred to as a collective cavity mode emission (emission by a cavity mode pumped collectively by a phase-locked array of oscillators). This is still a coherent phenomenon, but the emission occurs from a single source, namely the antenna formed by the electrode.

(III) The synchronization: the overlap-type JJs in the studied arrays are separated by 12 μm, which is much larger than the London penetration depth. This precludes direct interaction between the JJs [28]. Therefore, JJs are coupled only indirectly via common cavity modes, corresponding to the formation of standing surface plasmon waves along the electrode [34]. The standing wave imprints its order on Josephson junctions in the array. This requires a critical amplitude, which translates into a threshold number of active JJs for excitation of the cavity resonance [32,33].

Conclusion

We have studied large arrays containing up to 1000 Nb/Nb_xSi_{1-x}/Nb Josephson junctions. By applying a small magnetic field, we managed to acquire a large variety of dynamic states with different numbers of active junctions in the oscillating resistive state. This allowed for a detailed analysis of the collective phenomena that take place in the arrays. We reported a gradual development of cavity mode resonances in the arrays upon sequential switching of JJs into the oscillating state. We show that a threshold number of JJs, $N_{th} \approx 100$, is required for excitation of such resonances. Above the threshold, the amplitude of resonant steps in the I–V characteristics grows in a quasi-linear manner with the number of active JJs. We employ an external microwave detector to measure the electromagnetic wave emission from the arrays. It is observed that the emission power is correlated with the amplitude of the resonant steps in the I–V characteristics.

Our observations clearly reveal the collective, indirect mechanism of interjunction coupling. Studied junctions are of the overlap type and are separated by a distance of 12 μm, that is, one hundred times larger than the London penetration depth in Nb. This precludes direct interactions between them. Nevertheless, they can be effectively synchronized via the indirect coupling mechanism mediated by the extended centimeter-long electrodes in the arrays, which act as transmission lines for surface plasmon-type electromagnetic waves. Therefore, they both support collective cavity resonances and act as matching antennas for microwave emission.

Our observations imply that cavity modes in the electrodes are pumped collectively by the junctions, which are in turn mutually phase-locked by the modes. This provides a positive feedback mechanism, which allows for the synchronization of large arrays without direct interjunction interaction. The electromagnetic wave emission in this case is facilitated by the cavity modes in the large resonator outside the junctions formed by the electrodes, rather than by direct emission from the junctions. We conclude that such indirect coupling is effective for the synchronization of very large arrays.

Acknowledgements

The authors are grateful to Oliver Kieler for sample fabrication.

Funding

M.A.G. acknowledges support from the Russian Science Foundation Grant 20-42-04415.

ORCID® iDs

Roger Cattaneo - https://orcid.org/0000-0002-5935-7165
Mikhail A. Galin - https://orcid.org/0000-0002-7214-6522
Vladimir M. Krasnov - https://orcid.org/0000-0002-3131-8658

References

1. Tonouchi, M. *Nat. Photonics* **2007,** *1,* 97–105. doi:10.1038/nphoton.2007.3
2. Razeghi, M.; Lu, Q. Y.; Bandyopadhyay, N.; Zhou, W.; Heydari, D.; Bai, Y.; Slivken, S. *Opt. Express* **2015,** *23,* 8462–8475. doi:10.1364/oe.23.008462
3. Wang, X.; Shen, C.; Jiang, T.; Zhan, Z.; Deng, Q.; Li, W.; Wu, W.; Yang, N.; Chu, W.; Duan, S. *AIP Adv.* **2016,** *6,* 075210. doi:10.1063/1.4959195
4. Gmachl, C.; Capasso, F.; Sivco, D. L.; Cho, A. Y. *Rep. Prog. Phys.* **2001,** *64,* 1533–1601. doi:10.1088/0034-4885/64/11/204
5. Ferguson, B.; Zhang, X.-C. *Nat. Mater.* **2002,** *1,* 26–33. doi:10.1038/nmat708
6. Walther, C.; Fischer, M.; Scalari, G.; Terazzi, R.; Hoyler, N.; Faist, J. *Appl. Phys. Lett.* **2007,** *91,* 131122. doi:10.1063/1.2793177
7. Han, S.; Bi, B.; Zhang, W.; Lukens, J. E. *Appl. Phys. Lett.* **1994,** *64,* 1424–1426. doi:10.1063/1.111904
8. Barbara, P.; Cawthorne, A. B.; Shitov, S. V.; Lobb, C. J. *Phys. Rev. Lett.* **1999,** *82,* 1963–1966. doi:10.1103/physrevlett.82.1963
9. Galin, M. A.; Borodianskyi, E. A.; Kurin, V. V.; Shereshevskiy, I. A.; Vdovicheva, N. K.; Krasnov, V. M.; Klushin, A. M. *Phys. Rev. Appl.* **2018,** *9,* 054032. doi:10.1103/physrevapplied.9.054032

10. Ozyuzer, L.; Koshelev, A. E.; Kurter, C.; Gopalsami, N.; Li, Q.; Tachiki, M.; Kadowaki, K.; Yamamoto, T.; Minami, H.; Yamaguchi, H.; Tachiki, T.; Gray, K. E.; Kwok, W.-K.; Welp, U. *Science* **2007,** *318,* 1291–1293. doi:10.1126/science.1149802
11. Katterwe, S.-O.; Motzkau, H.; Rydh, A.; Krasnov, V. M. *Phys. Rev. B* **2011,** *83,* 100510(R). doi:10.1103/physrevb.83.100510
12. Welp, U.; Kadowaki, K.; Kleiner, R. *Nat. Photonics* **2013,** *7,* 702–710. doi:10.1038/nphoton.2013.216
13. Kashiwagi, T.; Yamamoto, T.; Kitamura, T.; Asanuma, K.; Watanabe, C.; Nakade, K.; Yasui, T.; Saiwai, Y.; Shibano, Y.; Kubo, H.; Sakamoto, K.; Katsuragawa, T.; Tsujimoto, M.; Delfanazari, K.; Yoshizaki, R.; Minami, H.; Klemm, R. A.; Kadowaki, K. *Appl. Phys. Lett.* **2015,** *106,* 092601. doi:10.1063/1.4914083
14. Kakeya, I.; Wang, H. *Supercond. Sci. Technol.* **2016,** *29,* 073001. doi:10.1088/0953-2048/29/7/073001
15. Borodianskyi, E. A.; Krasnov, V. M. *Nat. Commun.* **2017,** *8,* 1742. doi:10.1038/s41467-017-01888-4
16. Delfanazari, K.; Klemm, R. A.; Joyce, H. J.; Ritchie, D. A.; Kadowaki, K. *Proc. IEEE* **2020,** *108,* 721–734. doi:10.1109/jproc.2019.2958810
17. Cattaneo, R.; Borodianskyi, E. A.; Kalenyuk, A. A.; Krasnov, V. M. *Phys. Rev. Appl.* **2021,** *16,* L061001. doi:10.1103/physrevapplied.16.l061001
18. Krasnov, M. M.; Novikova, N. D.; Cattaneo, R.; Kalenyuk, A. A.; Krasnov, V. M. *Beilstein J. Nanotechnol.* **2021,** *12,* 1392–1403. doi:10.3762/bjnano.12.103
19. Krasnov, V. M. *Phys. Rev. B* **2010,** *82,* 134524. doi:10.1103/physrevb.82.134524
20. Krasnov, V. M.; Sandberg, M.; Zogaj, I. *Phys. Rev. Lett.* **2005,** *94,* 077003. doi:10.1103/physrevlett.94.077003
21. Wang, H. B.; Guénon, S.; Gross, B.; Yuan, J.; Jiang, Z. G.; Zhong, Y. Y.; Grünzweig, M.; Iishi, A.; Wu, P. H.; Hatano, T.; Koelle, D.; Kleiner, R. *Phys. Rev. Lett.* **2010,** *105,* 057002. doi:10.1103/physrevlett.105.057002
22. Koshelets, V. P.; Shitov, S. V. *Supercond. Sci. Technol.* **2000,** *13,* R53–R69. doi:10.1088/0953-2048/13/5/201
23. Koshelev, A. E. *Phys. Rev. B* **2010,** *82,* 174512. doi:10.1103/physrevb.82.174512
24. Benseman, T. M.; Gray, K. E.; Koshelev, A. E.; Kwok, W.-K.; Welp, U.; Minami, H.; Kadowaki, K.; Yamamoto, T. *Appl. Phys. Lett.* **2013,** *103,* 022602. doi:10.1063/1.4813536
25. Kashiwagi, T.; Yuasa, T.; Tanabe, Y.; Imai, T.; Kuwano, G.; Ota, R.; Nakamura, K.; Ono, Y.; Kaneko, Y.; Tsujimoto, M.; Minami, H.; Yamamoto, T.; Klemm, R. A.; Kadowaki, K. *J. Appl. Phys.* **2018,** *124,* 033901. doi:10.1063/1.5033914
26. Filatrella, G.; Pedersen, N. F.; Wiesenfeld, K. *Phys. C (Amsterdam, Neth.)* **2006,** *437–438,* 65–68. doi:10.1016/j.physc.2005.12.020
27. Sakai, N.; Maeda, T.; Yamauchi, H.; Tanaka, S. *Phys. C (Amsterdam, Neth.)* **1993,** *212,* 75–80. doi:10.1016/0921-4534(93)90487-b
28. Grebenchuk, S. Y.; Cattaneo, R.; Krasnov, V. M. *Phys. Rev. Appl.* **2022,** *17,* 064032. doi:10.1103/physrevapplied.17.064032
29. Ngai, K. L. *Phys. Rev.* **1969,** *182,* 555–568. doi:10.1103/physrev.182.555
30. Monaco, R.; Grønbech-Jensen, N.; Parmentier, R. D. *Phys. Lett. A* **1990,** *151,* 195–201. doi:10.1016/0375-9601(90)90191-p
31. Davidson, A.; Pedersen, N. F. *Appl. Phys. Lett.* **1992,** *60,* 2017–2019. doi:10.1063/1.107129
32. Filatrella, G.; Pedersen, N. F.; Wiesenfeld, K. *Phys. Rev. E* **2000,** *61,* 2513–2518. doi:10.1103/physreve.61.2513
33. Almaas, E.; Stroud, D. *Phys. Rev. B* **2002,** *65,* 134502. doi:10.1103/physrevb.65.134502
34. Galin, M. A.; Rudau, F.; Borodianskyi, E. A.; Kurin, V. V.; Koelle, D.; Kleiner, R.; Krasnov, V. M.; Klushin, A. M. *Phys. Rev. Appl.* **2020,** *14,* 024051. doi:10.1103/physrevapplied.14.024051
35. Ono, Y.; Minami, H.; Kuwano, G.; Kashiwagi, T.; Tsujimoto, M.; Kadowaki, K.; Klemm, R. A. *Phys. Rev. Appl.* **2020,** *13,* 064026. doi:10.1103/physrevapplied.13.064026
36. Mueller, F.; Behr, R.; Weimann, T.; Palafox, L.; Olaya, D.; Dresselhaus, P. D.; Benz, S. P. *IEEE Trans. Appl. Supercond.* **2009,** *19,* 981–986. doi:10.1109/tasc.2009.2017911
37. Galin, M. A.; Klushin, A. M.; Kurin, V. V.; Seliverstov, S. V.; Finkel, M. I.; Goltsman, G. N.; Müller, F.; Scheller, T.; Semenov, A. D. *Supercond. Sci. Technol.* **2015,** *28,* 055002. doi:10.1088/0953-2048/28/5/055002
38. Barone, A.; Paternò, G. *Physics and Applications of the Josephson Effect;* John Wiley & Sons, 1982. doi:10.1002/352760278x
39. Hinostroza, I. Design of wideband arrays of spiral antenna. Ph.D. Thesis, École supérieure d'électricité, 2013.
40. Hovhannisyan, R. A.; Kapran, O. M.; Golod, T.; Krasnov, V. M. *Nanomaterials* **2021,** *11,* 2058. doi:10.3390/nano11082058
41. Krasnov, V. M. *Phys. Rev. B* **2011,** *83,* 174517. doi:10.1103/physrevb.83.174517
42. Jain, A. K.; Likharev, K. K.; Lukens, J. E.; Sauvageau, J. E. *Phys. Rep.* **1984,** *109,* 309–426. doi:10.1016/0370-1573(84)90002-4

License and Terms

BEILSTEIN JOURNAL OF NANOTECHNOLOGY

The influence of structure and local structural defects on the magnetic properties of cobalt nanofilms

Alexander Vakhrushev*[1,2], Aleksey Fedotov[1,2,3], Olesya Severyukhina[1,2,3] and Anatolie Sidorenko[2,4]

Full Research Paper

Open Access

Address:
[1]Modeling and Synthesis of Technological Structures Department, Institute of Mechanics, Udmurt Federal Research Centre, Ural Division, Russian Academy of Sciences, Baramzinoy 34, Izhevsk 426067, Russia, [2]Orel State University named after I.S. Turgenev, Komsomolskaya Str. 95, 302026, Orel, Russia, [3]Nanotechnology and Microsystems Department, Kalashnikov Izhevsk State Technical University, Studencheskaya 7, Izhevsk 426069, Russia and [4]Institute of Electronic Engineering and Nanotechnologies of Technical University of Moldova, Academiei 3/3, Chisinau 2028, Moldova

Email:
Alexander Vakhrushev* - Vakhrushev-a@yandex.ru

* Corresponding author

Keywords:
LAMMPS; magnetic materials; molecular dynamics; nanocomposites; nanofilms; spintronics

Beilstein J. Nanotechnol. **2023,** *14,* 23–33.
https://doi.org/10.3762/bjnano.14.3

Received: 21 July 2022
Accepted: 07 December 2022
Published: 04 January 2023

This article is part of the thematic issue "Intrinsic Josephson effect and prospects of superconducting spintronics".

Associate Editor: E. Meyer

Abstract

The present paper considers a mathematical model describing the time evolution of spin states and magnetic properties of a nanomaterial. We present the results of two variants of nanosystem simulations. In the first variant, cobalt with a structure close to the hexagonal close-packed crystal lattice was considered. In the second case, a cobalt nanofilm formed in the previously obtained numerical experiment of multilayer niobium–cobalt nanocomposite deposition was investigated. The sizes of the systems were the same in both cases. For both simulations, after pre-correction in the initial time stages, the value of spin temperature stabilized and tended to the average value. Also, the change in spin temperature occurred near the average value. The system with a real structure had a variable spin temperature compared to that of a system with an ideal structure. In all cases of calculations for cobalt, the ferromagnetic behavior was preserved. Defects in the structure and local arrangement of the atoms cause a deterioration in the magnetic macroscopic parameters, such as a decrease in the magnetization modulus.

Introduction

The analysis of phase transitions and related critical phenomena in condensed media is a complex, time-consuming, and often a high-cost process from a technological point of view [1-3]. On the one hand, this is due to the need to use a comprehensive approach in theoretical studies, since the behavior of different phases is often described by different models or state equations

[4]. Another reason is that phase transformation mechanisms originate at the nanoscale and atomic levels [5,6], where observation and experiments require modern and expensive equipments. In this regard, precision experimental studies in critical regions are fraught with significant difficulties due to both temporal and spatial scales of object behavior [4].

Despite the existing difficulties, the interest in the study of phase transitions is not decreasing. Evolutionary analysis of the structural transformations of substances finds wide application in many areas of science and technology, including physics of multicomponent systems. One promising application of multicomponent systems is the development of phase-transition heat-storage materials [7,8], in which heat storage and accumulation occur due to phase transformations. The functioning of such storage media is based on energy fluctuations in the process of crystallization or melting of the media. In contrast to traditional media, thermal storage does not require sealing of the working volume during change of aggregate states, and is actively implemented as a highly efficient and energy-saving technology in the field of construction [9] and solar energy [10].

Phase transformations occupy an important position in the theories of superconductivity and ferromagnetic alloys. These theories actively consider composites with shape memory [11,12]. Such composites are also called intelligent materials of the future [13] due to their unique functional properties and the possibility of restoring the original parameters under certain external conditions. Both thermodynamic conditions [14] and magnetoelectric fields [15] can act as external perturbations affecting the internal state and phase transitions of the samples. It has been shown in [11,12,16] that structural phase transitions in shape memory materials are in close relationship with external static and induction fields. Studying the role of magnetism on the structural features of composites opens up promising possibilities, since it allows predicting and creating new materials with controllable properties.

The idea of mutual correlation between material structure and its magnetic properties is being developed in the field of spintronics. Modern computing devices face a number of difficulties during production, including those related to arrangement of nanoscale computing elements on integrated circuits and their subsequent cooling during operation [17,18]. Problems related to excessive heat dissipation and performance improvement can be solved with the help of spintronics devices, which are currently presented in a fairly wide variety of valuable effects: spin valves and valves in thin films and heterostructures [19,20], sensors based on the anomalous Hall effect [21], spin injection and magnetism detection [22,23], giant magnetic resistance effects in data storage items and hard drives [24,25], ultrafast magneto-optical switches and optically induced ferromagnetic materials [26]. The discovery and implementation of topological insulators in Josephson contacts make spintronics devices excellent candidates for applications in quantum computing [27,28] as well as in quantum cryptography [29].

The extensive influence of phase transitions and critical phenomena on the working properties of the samples testifies the importance of a detailed study of structural transformations and possible stable states. Morphological analysis enables the identification of local defects in the crystal structure, which form different scale aggregates that can further serve as causes of deterioration of the target material functional characteristics [30,31]. Comprehensive studies in this area not only allow to establish the presence of structural heterogeneities and features, but also to formulate the main laws of their origin and development.

This work is devoted to solving an important problem regarding the relationship between the magnetic properties of multilayer nanocomposites and their structure. The problem of studying the influence of structure on the materials magnetic properties is not new and has been previously solved by other authors [4,32-34]. For example, in [4], to describe the thermodynamic equilibrium and nonequilibrium properties of magnetic materials, a multiscale approach of a mathematical model is used. This approach includes methods of first principles, spin models based on the stochastic Landau–Lifshitz–Gilbert equation, and a submodel of micromagnetism, described by the Landau–Lifshitz–Bloch equation. The reference [32] is also devoted to the development of modeling methods in the field of materials phase transitions, but with the help of classical and quantum Monte Carlo approaches. The main emphasis of the work is placed on studies of the statistical lattice model, including a high-precision calculation of the critical indices.

The intermetallic magnetic compound FeRh is discussed in [33]. In the considered material, the thermodynamic first-order phase transition is observed near room temperature. Heating the material above the transition temperature changes its magnetic behavior from antiferromagnetic to ferromagnetic and is accompanied by a significant change in the crystal lattice structure and an increase in electrical conductivity. The material is promising for applied research and development of new spintronics devices, energy management sensors, and magnetic recording media.

Research focused on specific application devices based on phase-transition memory state is discussed in detail in [34]. Phase-transition memory technology is among actively developing and promising technologies since it enables the design of

small devices with high performance, durability, and cost-effectiveness. The authors of [34] review how the characteristics of phase transition memory combine with various potential applications, addressing some of the problems of this technology, including those related to cell design, negative structural features, and changes in nanomaterials that can occur during fabrication.

Thus, the evaluation and elaboration of structural changes in a nanomaterial arising from its production are important tasks, often closely related to the composition of the sample in question. In this paper, we propose one mathematical model to investigate the relationship between the material structure and its magnetic properties. Mathematical modeling is used to estimate the influence of the disturbances in the atomic arrangement inside the crystal lattice, in the destruction and fragmentation zones of spin orientation inside the material, and overall magnetization of the sample.

Description and Conditions of the Numerical Experiment

The structure and magnetic properties of the nanomaterial were investigated in this work using a promising nanocomposite formed by alternating layers of cobalt and niobium. The proposed composite has potentially promising functional properties and can be used in magnetic systems with controlled effective energy exchange in Josephson contacts [35], which are successfully implemented in memory and information storage devices. A similar layered heterostructure, but with the addition of a thin platinum film necessary for the generation of spin–orbit bonds, is also described in [36].

Comprehensive research on new promising materials is a complex multistage process. The general scheme of the problem-oriented analysis of a multilayer composite of niobium and cobalt is presented in Figure 1. At the preparation stage of the conceptual model, the expected requirements to the main properties of the predicted material are formulated, a manufacturing method, and an approximate composition are proposed on the basis of already existing technologies. The conceptual model for our study is based on a sample whose structure and composition is shown in the upper right part of Figure 1.

At the next development stage, the technological processes of nanocomposite manufacturing were simulated and system-

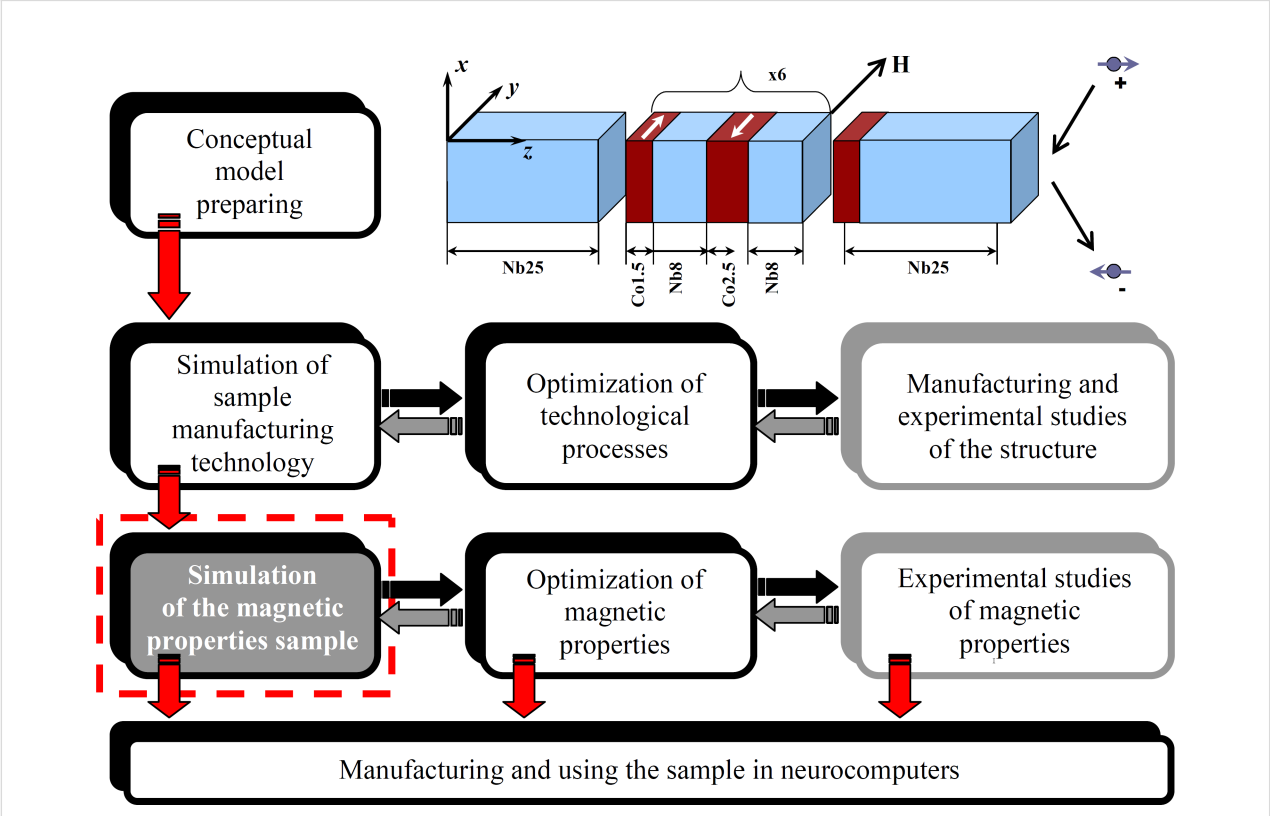

Figure 1: Problem statement for the complex study of cobalt and niobium heterostructures. The sketch of the Nb/Co spin-valve nanosystem was reproduced from [37] (© 2020 A. Vakhrushev et al., distributed under the terms of the Creative Commons Attribution License (http://creativecommons.org/licenses/by/4.0)).

atized. This was done to establish the dependence of the structure and characteristics of the nanocomposites on the production parameters, to check the presence of target functional aspects, and to determine controllable properties (i.e., those properties that are influenced and corrected in the manufacturing process). The previously conducted studies considered the influence of sample parameters (e.g., temperature of the substrate on which the magnetron sputtering of nanofilms takes place, the intensity and deposition direction) on the final properties of the sample. The results of numerical experiments are described in the literature [37-39].

The next stage of sample study involved the optimization of the nanofilm interface. The basic magnetic properties of the nanocomposite depend on the quality of the interface between the layers, so the problem of obtaining clearly separated contact layers is highly relevant. Using simulations, it was demonstrated that optimization of the nanofilm interface can be obtained either by introducing additional intermediate thin layers neutral to the original composition, such as aluminum oxide, or by additional processing means, such as mechanical alignment and intensive substrate cooling. The stage of experimental studies of the sample structure is necessary to identify the real structure of the nanocomposite and to compare the data with previously obtained simulation results.

This current work is aimed at modeling the magnetic properties of the nanomaterial heterostructure under study. In Figure 1, the block of modeling magnetic properties is highlighted by a red dashed line. As noted earlier, the formed nanofilms have a nonideal structure. Consequently, the influence of the real structure and local order of atoms on parameters with considerable practical interest (e.g., magnetization, different types of energies, spin temperatures, and particle orientations) remains open.

The last two steps of the analysis, which include the optimization of magnetic properties and experimental study of magnetic properties, are the subject of future research and are cited in this work for a complete understanding of the complex task of developing new promising nanomaterials.

A Mathematical Model for Studying the Magnetic Properties of Nanomaterials

When describing the magnetic properties of a nanosystem, simultaneous equations of classical molecular dynamics are used, which are supplemented by considering the spin vectors $\mathbf{s}_i$ for each atom. The motion equation for atoms and spins is written in the following form:

$$\frac{\mathrm{d}\mathbf{r}_i}{\mathrm{d}t} = \frac{\mathbf{p}_i}{m_i}, \tag{1}$$

$$\frac{\mathrm{d}\mathbf{p}_i}{\mathrm{d}t} = \sum_{i\neq j}^{N}\left[-\frac{\mathrm{d}U\left(\left|\mathbf{r}_{ij}\right|\right)}{\mathrm{d}\left|\mathbf{r}_{ij}\right|}+\frac{\mathrm{d}J\left(\left|\mathbf{r}_{ij}\right|\right)}{\mathrm{d}\left|\mathbf{r}_{ij}\right|}\mathbf{s}_i\cdot\mathbf{s}_j\right]e_{ij}, \tag{2}$$

$$\frac{\mathrm{d}\mathbf{s}_i}{\mathrm{d}t} = \mathbf{f}_i\times\mathbf{s}_i, \tag{3}$$

where $\mathbf{r}_i$ is the vector characterizing the position of the particle i; $\mathbf{s}_i$,and $\mathbf{s}_j$ are the spin vectors; $\mathbf{p}_i$ is the momentum; $\mathbf{e}_{ij}$ is the unit vector along $\mathbf{r}_{ij}$; $\mathbf{f}_i$ is the analogue of the force applied to spin; and U is the potential energy.

The general form of the expression for describing the total energy of magnetic systems can be written in the following form:

$$H = H_{\mathrm{z}} + H_{\mathrm{ex}} + H_{\mathrm{an}} + H_{\mathrm{Neel}} + H_{\mathrm{dm}} + H_{\mathrm{me}} + H_{\mathrm{di}}, \tag{4}$$

where the first two terms in the right-hand side are the Zeeman and exchange interactions, respectively, the next two terms describe magnetic anisotropy, followed by the terms responsible for the Dzialoshinsky–Moriya, magnetoelectric, and dipole interactions, respectively. The consideration of different types of interactions in a model depends on the structure of the systems considered, as well as on problems that are solved in the simulation. The determination of parameters used to describe different types of interactions in modeling magnetic systems requires additional numerical and experimental investigations. For this reason, the emphasis at this stage was placed on the pairwise anisotropy model of Neel.

The exchange interaction provides a natural connection between the spin and lattice degrees of freedom due to the dependence of the function J on the interatomic distance. This function determines the intensity of the interaction. As noted in [40], the function J is a symmetric radial function. Due to its symmetrical representation, only isotropic phenomena and processes in materials can be described using the J function. At the same time, anisotropic effects are of great interest, since they often affect the most prospective and promising magnetic nanomaterials. Magnetic crystallographic anisotropy arises on spin–orbit interaction of atoms. As a consequence, this type of interaction should be separately taken into account when constructing theoretical models and conducting numerical experiments.

The type and parameters of the crystal lattice of magnets largely determine the type and shape of the resulting magnetic

anisotropy. In ferromagnets, magnetic anisotropy is characterized by the magnitude and orientation of the magnetization, as well as by the change in the magnetic energy of the material. The main causes of magnetic anisotropy are temperature changes, dipole interactions, mechanical deformations, or other external factors. If external influences are absent, then due to spin–orbit interactions of atoms inside the nanomaterial, magnetic crystallographic anisotropy can occur, which is caused by a change in the internal energy and by the symmetry or asymmetry of the crystal structure of ferromagnets.

The dipole–dipole interaction does not make a significant contribution to the anisotropy energy and its value is insignificant. Only in a number of rare-earth metals the contribution of the dipole–dipole interaction can be significant due to large magnetic moments of the atoms and small values of the crystal lattice parameters.

Approximations for modeling spin–orbit coupling have been proposed in [41,42]. In particular, the functions proposed by Neel [41] for modeling the bulk magnetostriction and surface anisotropy in cobalt were used in [43]. The model proposed by Neel considers magnetocrystalline anisotropy in more complex forms as compared to uniaxial anisotropy. This model is used to describe magnetocrystalline anisotropy between pairs of magnetic spins:

$$H_{\text{Neel}} = -\sum_{i,j=1,i\neq j}^{N} g_1(r_{ij})\left((\mathbf{e}_{ij}\cdot\mathbf{s}_i)(\mathbf{e}_{ij}\cdot\mathbf{s}_j)-\frac{\mathbf{s}_i\cdot\mathbf{s}_j}{3}\right)+ \\ +q_1(r_{ij})\left((\mathbf{e}_{ij}\cdot\mathbf{s}_i)^2-\frac{\mathbf{s}_i\cdot\mathbf{s}_j}{3}\right)\left((\mathbf{e}_{ij}\cdot\mathbf{s}_j)^2-\frac{\mathbf{s}_i\cdot\mathbf{s}_j}{3}\right)+ \\ +q_2(r_{ij})\left((\mathbf{e}_{ij}\cdot\mathbf{s}_i)(\mathbf{e}_{ij}\cdot\mathbf{s}_j)^3+(\mathbf{e}_{ij}\cdot\mathbf{s}_j)(\mathbf{e}_{ij}\cdot\mathbf{s}_i)^3\right), \quad (5)$$

where the intensity of the dipole and quadrupole contributions are described using the functions g_1,q_1,q_2:

$$g_1(r_{ij}) = g(r_{ij}) + \frac{12}{35}q(r_{ij}), \quad (6)$$

$$q_1(r_{ij}) = \frac{9}{5}q(r_{ij}), \quad (7)$$

$$q_2(r_{ij}) = -\frac{2}{5}q(r_{ij}). \quad (8)$$

When modeling, it is convenient to describe the functions $q(r_{ij})$ and $g(r_{ij})$ with the Bethe–Slater curve:

$$f(r_{ij}) = 4\alpha\left(\frac{r_{ij}}{\delta}\right)^2\left(1-\gamma\left(\frac{r_{ij}}{\delta}\right)^2\right)e^{-\left(\frac{r_{ij}}{\delta}\right)^2}\Theta(R_c - r_{ij}), \quad (9)$$

where α (in eV), δ (in Å), and γ (dimensionless value) are constant coefficients that depend on the structure of the sample under study and $\Theta(R_c - r_{ij})$ is the Heaviside function. The coefficients α, δ, and γ must be chosen so that the aforementioned function corresponds to the values of the magnetoelastic constant of the materials under consideration.

The following equation is used to calculate the spin temperature:

$$T_s = \frac{\hbar}{2k_{\text{B}}}\frac{\sum_{i=1}^{N}|\mathbf{s}_i\times\boldsymbol{\omega}_i|^2}{\sum_{i=1}^{N}\mathbf{s}_i\times\boldsymbol{\omega}_i}, \quad (10)$$

where $\mathbf{s}_i$ is vector representing the magnetic spin of the particle, ω_i is the magnetic moment, and $\hbar$ is the Planck constant. This approach to calculate spin temperature was proposed in [44].

The approach described in this paper and originally proposed by the authors [40] is implemented using direct simulation methods. At each time point, we do not know the assumed spin location, but we know its computed value, which is calculated based on empirical parameters or other previously obtained data. Therefore, an additional advantage is that systems of arbitrary size, including small ones, can be considered for calculating magnetic properties based on the combined model of molecular dynamics and magnetization dynamics.

The technique used includes simulations of atomic magnetic spins associated with lattice vibrations. The dynamics of these magnetic spins can be used to simulate a wide range of phenomena related to magnetoelasticity or to study the influence of defects on the magnetic properties of materials.

Results and Discussion

As numerical experiments at the stage of modeling technological processes of niobium and cobalt sample manufacturing showed, the structure of the formed layers is not ideal. Visually, noticeable crystallization zones are observed in the formed nanofilms. In addition, there are areas of mixed structures, where the amorphous atomic structure most likely prevails. Quantitatively, the structure of nanofilms can be estimated, for example, by calculating the lattice ideality parameter [45]. This

parameter is close to zero in ideal crystal lattices and has a positive value where the structure of the material differs from the reference one, and the higher the value of the parameter, the higher the degree of discrepancy.

For the sample under study, the change in the ideality parameter, averaged over thin horizontal layers, is shown in Figure 2. The legend to the figure provides information about the temperature of the substrate on which nanofilms were deposited in the numerical experiments.

Niobium is known as one of the most actively used superconductors [46,47] with a superconducting transition temperature for pure metal equal to 9.25 K. In superconductors, including niobium, due to the Meissner effect, the phenomenon of complete or partial ejection of the magnetic field from the material volume occurs [48,49]. In the superconductivity mode, which is the mode of greatest interest for the magnetic behavior of the target film heterostructure, the absence of a magnetic field is observed inside the metal, which is predominantly concentrated near the surface. For the reasons previously described, niobium nanofilms were excluded from explicit consideration in numerical experiments to investigate the magnetic properties of the spin nanocomposite, whose appearance and structure are demonstrated in Figure 3a.

To investigate the magnetic properties of nanomaterials, the substrate temperature was set in the range of niobium nanofilm superconductivity mode operation at 5 K. Regarding the problem of nanofilm deposition and structure formation, we considered three substrate temperatures on which the deposition took place: 300 , 500, and 800 K. These temperatures are determined by process features of niobium and cobalt-based nanocomposite fabrication and can be seen in the legend shown in Figure 2. For both studies of magnetic properties and nanofilm deposition mechanisms, the substrate temperature was maintained using a Nose–Hoover thermostat.

Thus, at the initial stage of studying magnetic characteristics, the spin behavior of only cobalt atoms was analyzed for two calculation variants. In the first case, the cobalt atoms were located near the nodes of the hexagonal close-packed (HCP) crystal lattice, since this cobalt modification is more stable at temperatures up to 700 K. The functional features of the nanocomposite involve its superconducting niobium nanolayers, so the simulation was performed at a nanosystem temperature of 5 K. For the first version of the numerical experiment, a $2 \times 2 \times 2$ unit crystal cell of HCP cobalt, bounded on all sides by periodic boundary conditions, was considered. The size of such a system (i.e., 0.5 nm × 0.87 nm × 0.82 nm) is relatively small.

For the second variant of the numerical experiment, the real structure of cobalt nanofilms obtained earlier by simulating their deposition processes was considered. In order to preserve the structure of the cobalt nanofilm, a small volume was cut out from it, shown in Figure 3a as a white rectangle. This volume had strictly the same dimensions as the ideal HCP structure in the first numerical experiment. A group of cobalt atoms with structural defects acquired as a result of film sputtering in an enlarged form is shown in Figure 3b. Henceforward, to simplify the formulation, the nanosystem of cobalt atoms from the numerical experiment with nanofilm deposition will be referred to as the real one.

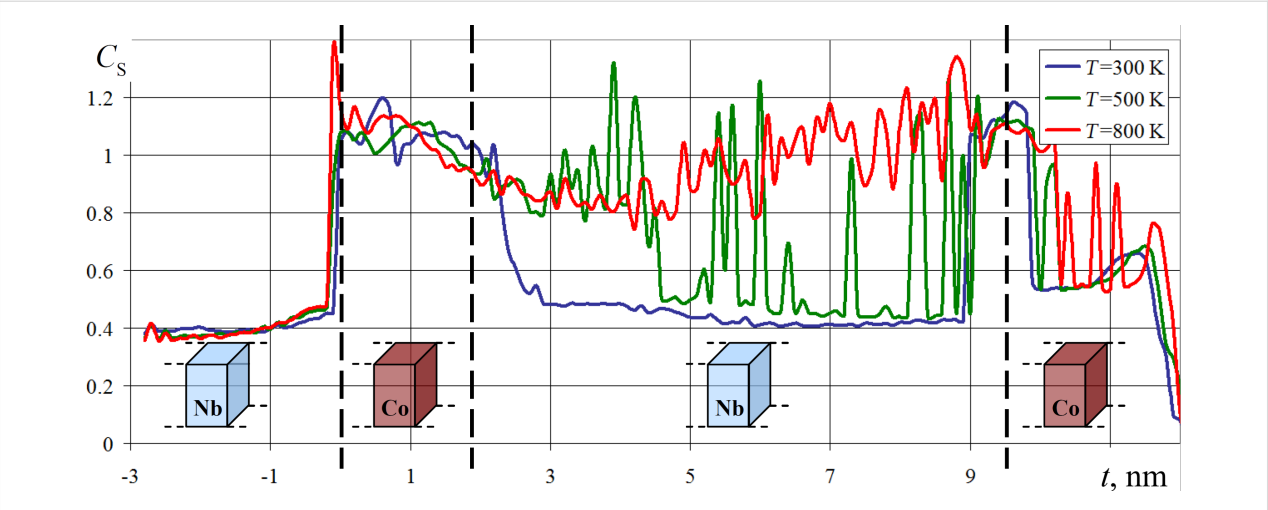

Figure 2: Variation of the average value of the crystal lattice ideality parameter in horizontal layers of a niobium and cobalt nanocomposite. Image reproduced from [37] (© 2020 A. Vakhrushev et al., distributed under Creative Commons Attribution License (http://creativecommons.org/licenses/by/4.0)).

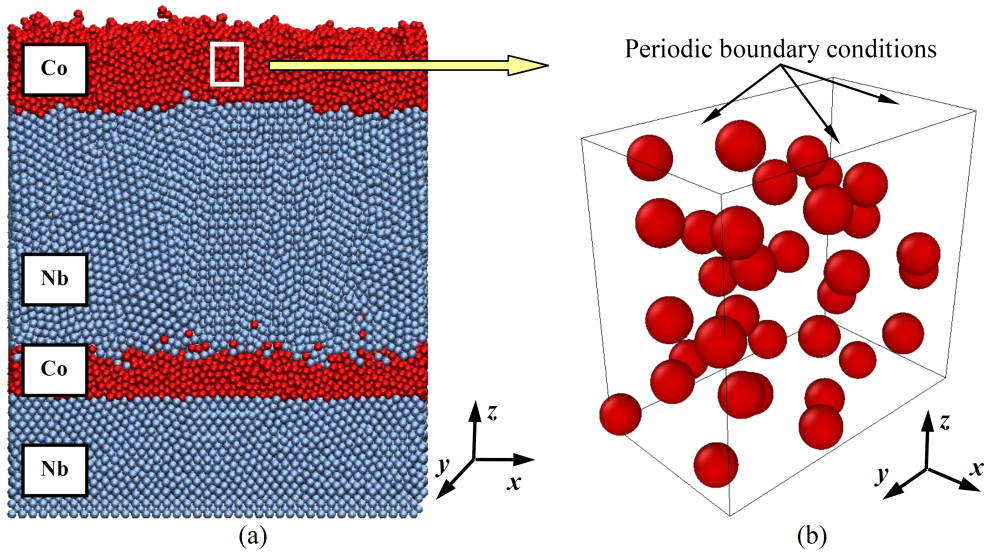

Figure 3: Multilayer nanocomposite of niobium and cobalt (a) formed in a numerical experiment during deposition on a 300 K substrate and a group of cobalt atoms was cut out to simulate the magnetic properties (b). The image shown in (a) was adapted from [37] (© 2020 A. Vakhrushev et al., distributed under the terms of the Creative Commons Attribution License (http://creativecommons.org/licenses/by/4.0)).

The small size of the system in question was chosen for several reasons. First, the actual produced nanofilms in composites of cobalt and niobium have a small thickness, reaching 1–2 nm in some layers. Of practical interest are structural defects and their influence on the magnetic properties of thin films. Therefore, in our studies, a small volume in the cobalt nanofilm is cut out and the simulation results were compared to that of the corresponding volume with an ideal structure.

In addition, the periodic boundary conditions used in molecular dynamics enables one to balance the influence of direct boundary effects by symmetrically continuing identical computational volumes along those space directions where they are used, in our case along all three *x, y, z* directions. Lastly, the small computational cell in this work was used for clarity, so that the orientation of individual atom spins could be easily traced.

Subsequently, the two selected systems were exposed to an external magnetic field with induction $\mathbf{B}_{ext}$ = 1.0 T in the *ox* axis direction (along the nanofilm surface for the real structure variant) for 100 ps. The result of the spin distribution at the final moment is shown in Figure 4. The time for the spin distributions of the atoms are shown in Figure 4 corresponds to 100 ps.

In order to catch the smallest changes in the spin behavior of the material and to take them into account, an integration step of 0.1 fs was chosen. The normal and spin temperatures were maintained at the initial value of 5 K. The coordinates of the atoms changed insignificantly, which is associated with small thermal fluctuations and their linear velocities. As for the spin rearrangement, at the initial times, corresponding to the interval of 0–5 ps, the change in the spin direction of atomic spins was active. At the initial time, a chaotic spin distribution regulated only by their initial spin temperature, was set for the atoms. Later, the direction of spins was influenced by the external magnetic field, as well as by their mutual arrangement and force behavior, which caused their reorientation.

Analysis of Figure 4 shows that there are significant differences in the spin distributions of an ideal crystalline hexagonal close-packed cobalt (letters (a), (b), (c)) and the nanofilm with structural defects formed as a result of the numerical experiment (letters (d), (e), (f)). Crystalline cobalt is characterized by small changes in spin states at finite times, with atomic spins set in the direction of external magnetic field induction, (i.e., *ox* axis). Nanofilms with structural defects and deviations from crystal lattice nodes are subject to higher randomness with respect to the direction of spins. The disordered orientation of spins is related to the enhanced influence of magnetic characteristics and forces of neighboring atoms. In the case of lattice distortions and defects in the material, zones of anomalies arise, which also bring about a stable magnetic state in the form of a local minimum of energy.

Internally, the behavior of atomic spins can be evaluated by calculating the spin temperature of the material. The spin temperature is equal to the normal temperature but reflects the degrees of freedom of the atoms responsible for the magnetic

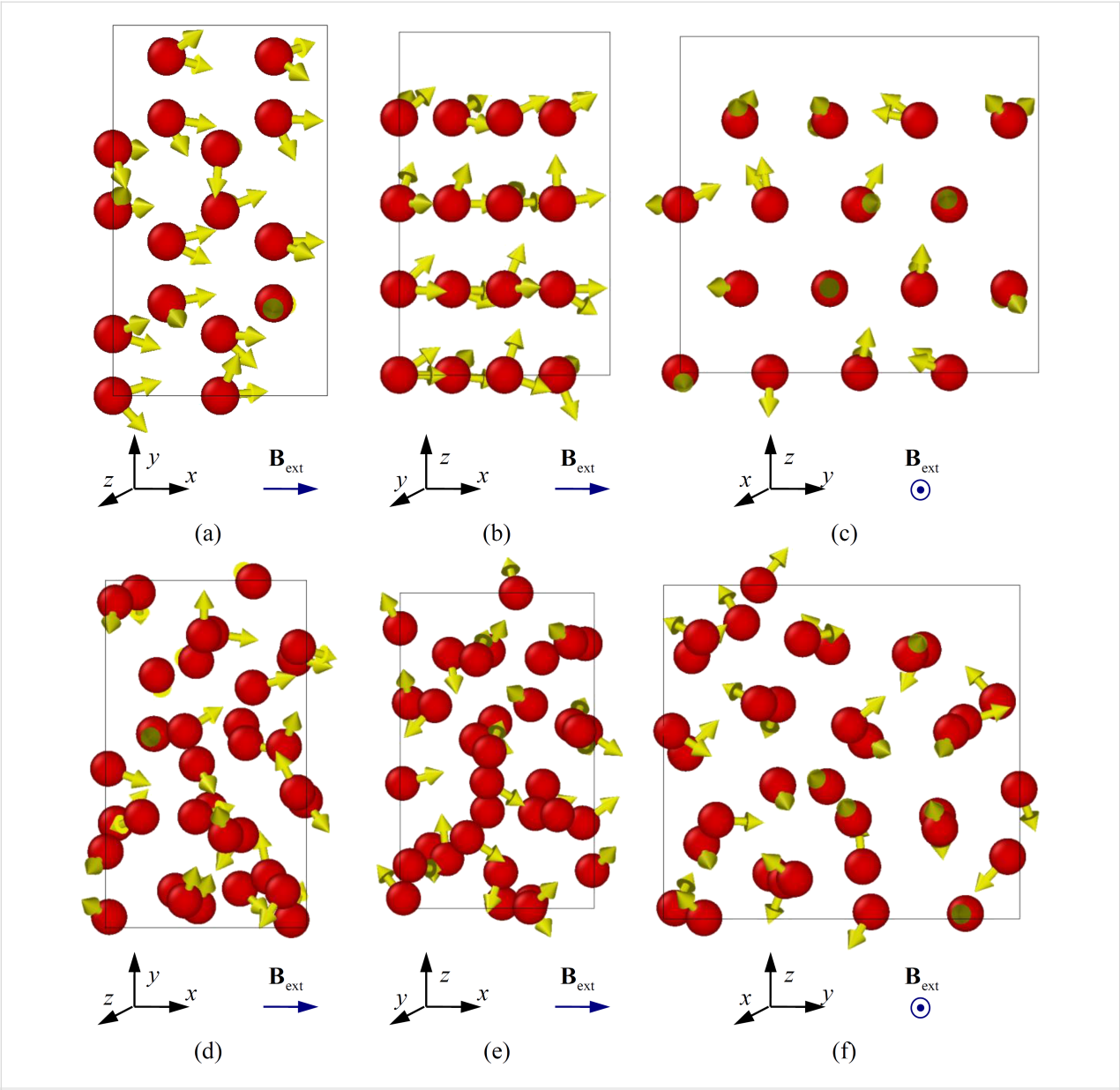

Figure 4: Spatial distribution of cobalt atom spins for ideal crystal hexagonal close-packed lattice (a), (b), (c) and nanofilm structure (d), (e), (f) formed in the numerical experiment at a deposition temperature of 300 K, spin relaxation time 100 ps, and external magnetic field value of 1.0 T.

energy fluxes. A graph of spin temperature variations for the two versions of ideal and real nanosystems under consideration is shown in Figure 5.

As it can be seen from Figure 5, at initial time intervals (0–3 ps) the spin temperature for both simulation variants is subject to considerable changes. In the graph of Figure 5, this time period is marked by the letter (a) and is shown in an enlarged form. The jumps in the spin temperature transformation at 0–3 ps correspond to an active rearrangement of the atomic spin directions, which were unstable in the initial state due to stochastic allocation. Subsequently, the spin temperature fluctuations decrease, and its fluctuations occur near the thermostat target value of 5 K. For an interval of 5–100 ps, the reorientation of spins is slow and mutually consistent, which is reflected in a small change in spin temperature. The system with a real structure has a less stable spin temperature behavior. The variation of this parameter in the range of 3–25 K indicates greater scattering and amplified oscillations of instantaneous values compared to those of the ideal structure case.

Another macroscopic, but dependent on each atom, characteristic of the material is its magnetization. The magnetization determines the effect of partial or complete ordering of magnetic

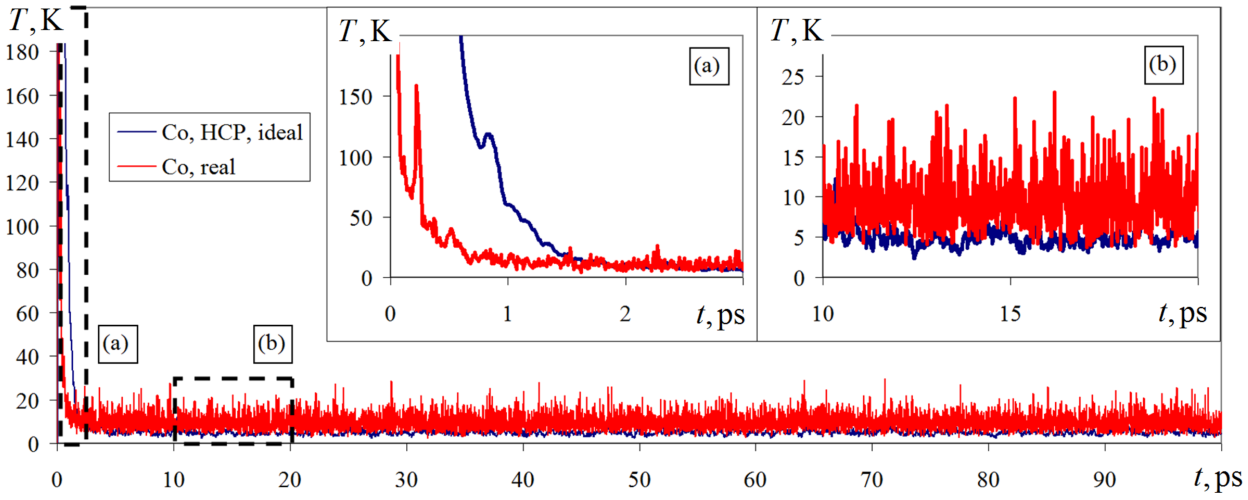

Figure 5: Changes in spin temperature under a constant external magnetic field of 1.0 T for ideal hexagonally close-packed cobalt and cobalt from the deposited nanofilm obtained in a numerical experiment.

moments of a set of atoms under the influence of an external magnetic field, which allows the use of this value to evaluate the response of nanocomposites to external factors, considering its structure and internal features. Dynamics of the vector modulus of the investigated sample during simulation for two variants of the investigated structure under a constant external magnetic field of 1.0 T is presented in Figure 6.

The change in the modulus of the magnetization vector at the initial times (0–7 ps) is also characterized (e.g., spin temperature) by an increased variability. The gradual rearrangement of atomic spin states does not allow us to instantly find a stable energy state. The length of the initial section of the magnetization graph with high volatility has a longer length compared to the same value for the spin temperature.

For an interval of 7–100 ps, the magnetization modulus value is set near the mean value, which is 0.7 $e{\cdot}Å^{-1}{\cdot}ps^{-1}$ for the case of an ideal crystal structure and 0.47 $e{\cdot}Å^{-1}{\cdot}ps^{-1}$ for the real structure variant, where e is the notation of the electron charge. Such nanomaterial behavior is associated with the ordering of magnetic moments and is typical for ferromagnetic materials (e.g., cobalt [50,51]). Thus, from the analysis of the graphs in Figure 6 we can conclude that, despite the defects in the struc-

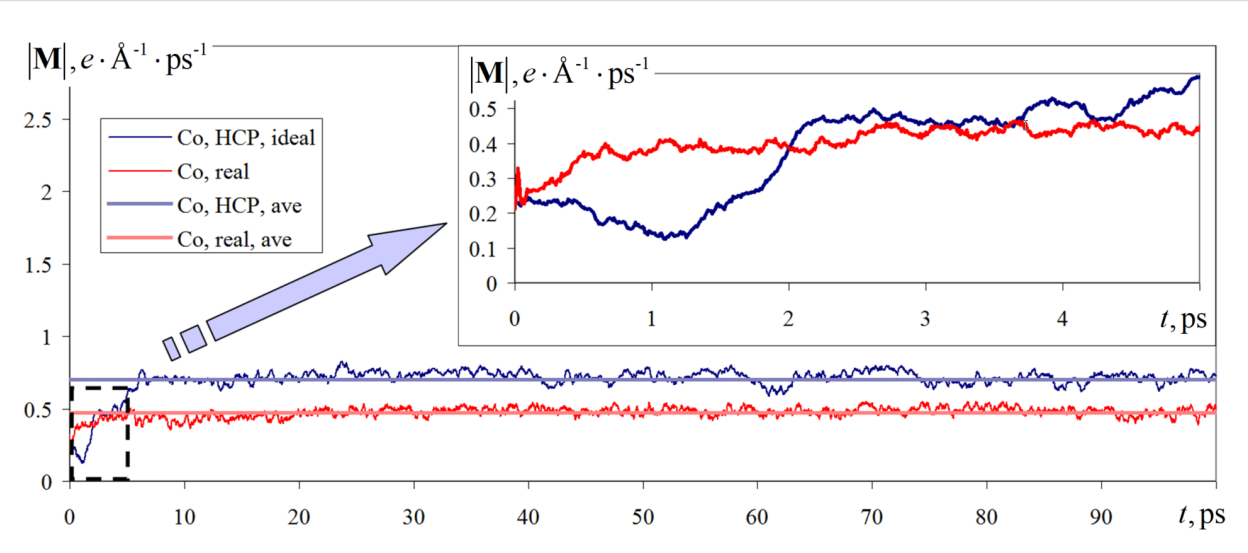

Figure 6: Changes in the magnetization vector modulus under a constant external magnetic field with an induction of 1.0 T for ideal hexagonally dense-packed cobalt and cobalt from the deposited nanofilm obtained in the numerical experiment.

ture and the local arrangement of the atoms, cobalt retains its ferromagnetic character. However, there may be a decrease or deterioration of the magnetic macroscopic parameters, such as the magnetization modulus.

Conclusion

A mathematical model capable of reproducing the time evolution of spin states and magnetic properties of a nanomaterial is proposed. This model reflects the response of an external magnetic field on the behavior of individual atoms, and considers the internal structure and features of structural defects at the nanoscale when calculating the macroscopic magnetic characteristics of a material.

The spatial distribution of cobalt atom spins for an ideal crystalline hexagonal close-packed lattice was studied. The structure of the nanofilm formed in a numerical experiment during deposition on a substrate maintained at a constant temperature of 300 K shows that the spin directions are significantly dependent on the material structure. Under an external magnetic field with an induction of 1.0 T, a reorientation of spins along the external magnetic field is observed for crystalline ordered cobalt. Conversely, for cobalt from the nanofilm a more chaotic distribution of spins is characteristic, but also with a predominant direction parallel to the vector of induction of the external magnetic field.

In numerical experiments, for the ideal and real structure it is obtained that after preliminary adjustment and significant jumps in the initial time intervals, the change of spin temperature occurs in a small range of values near the average thermostat target value. The system with the real structure has a less stable behavior of the spin temperature and a larger scattering of instantaneous values, which may indicate a less energetically stable state of the nanomaterial.

Analyses of simulation results show that for both calculation variants, with ideal hexagonal close-packed and with real structure, the ferromagnetic behavior is preserved for cobalt. Defects in the structure and local arrangement of atoms can be the cause of the deterioration of magnetic macroscopic parameters. For example, the magnetization modulus for the considered nanosystem in the case of the real structure decreased by 30–50%.

The mathematical model used in this work serves as a predictive tool, allowing to correct nanocomposite manufacturing processes and to reveal their weak points (e.g., the influence of indistinctly separated interfaces of nanofilms on the magnetic properties). Experimental studies on the subject of work are associated with a number of difficulties, and related results are planned to be published in following papers.

Funding

The research was supported by the Russian Science Foundation project 20-62-47009, "Physical and Engineering Foundations of Non-Von Neumann Architecture Computers Based on Superconductor Spintronics".

ORCID® iDs

Alexander Vakhrushev - https://orcid.org/0000-0001-7901-8745
Aleksey Fedotov - https://orcid.org/0000-0002-0463-3089
Anatolie Sidorenko - https://orcid.org/0000-0001-7433-4140

Preprint

A non-peer-reviewed version of this article has been previously published as a preprint: https://doi.org/10.3762/bxiv.2022.64.v1

References

1. Markov, S. I.; Shurina, E. P.; Itkina, N. B. *J. Phys.: Conf. Ser.* **2019,** *1333,* No. 032052. doi:10.1088/1742-6596/1333/3/032052
2. Hardtdegen, H.; Mikulics, M.; Rieß, S.; Schuck, M.; Saltzmann, T.; Simon, U.; Longo, M. *Prog. Cryst. Growth Charact. Mater.* **2015,** *61,* 27–45. doi:10.1016/j.pcrysgrow.2015.10.001
3. Pasupathy, A.; Velraj, R.; Seeniraj, R. V. *Renewable Sustainable Energy Rev.* **2008,** *12,* 39–64. doi:10.1016/j.rser.2006.05.010
4. Kazantseva, N.; Hinzke, D.; Nowak, U.; Chantrell, R. W.; Atxitia, U.; Chubykalo-Fesenko, O. *Phys. Rev. B* **2008,** *77,* No. 184428. doi:10.1103/physrevb.77.184428
5. Wang, Z.; Wei, J.; Morse, P.; Dash, J. G.; Vilches, O. E.; Cobden, D. H. *Science* **2010,** *327,* 552–555. doi:10.1126/science.1182507
6. Lin, Y.-C.; Dumcenco, D. O.; Huang, Y.-S.; Suenaga, K. *Nat. Nanotechnol.* **2014,** *9,* 391–396. doi:10.1038/nnano.2014.64
7. Chen, H.; Li, J.; Li, Y.; Cheng, X. *J. Alloys Compd.* **2020,** *829,* No. 154574. doi:10.1016/j.jallcom.2020.154574
8. Wang, Y.; Tang, B.; Zhang, S. *J. Mater. Chem.* **2012,** *22,* 18145–18150. doi:10.1039/c2jm33289b
9. Barrio, M.; Font, J.; López, D. O.; Muntasell, J.; Tamarit, J. L. *Sol. Energy Mater. Sol. Cells* **1992,** *27,* 127–133. doi:10.1016/0927-0248(92)90115-6
10. Bie, Y.; Li, M.; Malekian, R.; Chen, F.; Feng, Z.; Li, Z. *Appl. Therm. Eng.* **2018,** *135,* 218–227. doi:10.1016/j.applthermaleng.2018.02.036
11. Oikawa, K.; Ota, T.; Ohmori, T.; Tanaka, Y.; Morito, H.; Fujita, A.; Kainuma, R.; Fukamichi, K.; Ishida, K. *Appl. Phys. Lett.* **2002,** *81,* 5201–5203. doi:10.1063/1.1532105
12. Sutou, Y.; Imano, Y.; Koeda, N.; Omori, T.; Kainuma, R.; Ishida, K.; Oikawa, K. *Appl. Phys. Lett.* **2004,** *85,* 4358–4360. doi:10.1063/1.1808879
13. Hager, M. D.; Bode, S.; Weber, C.; Schubert, U. S. *Prog. Polym. Sci.* **2015,** *49-50,* 3–33. doi:10.1016/j.progpolymsci.2015.04.002
14. Müller, I.; Seelecke, S. *Math. Comput. Modell.* **2001,** *34,* 1307–1355. doi:10.1016/s0895-7177(01)00134-0
15. Ullakko, K.; Huang, J. K.; Kantner, C.; O'Handley, R. C.; Kokorin, V. V. *Appl. Phys. Lett.* **1996,** *69,* 1966–1968. doi:10.1063/1.117637
16. Owerre, S. A. *J. Phys.: Condens. Matter* **2018,** *30,* No. 245803. doi:10.1088/1361-648x/aac365
17. Paul, S.; Chatterjee, N.; Ghosal, P. *J. Syst. Archit.* **2019,** *98,* 271–288. doi:10.1016/j.sysarc.2019.08.002

18. Najam, S.; Ahmed, J.; Masood, S.; Ahmed, C. M. *IEEE Access* **2019,** *7,* 25493–25505. doi:10.1109/access.2019.2901010
19. Zahnd, G.; Vila, L.; Pham, V. T.; Cosset-Cheneau, M.; Lim, W.; Brenac, A.; Laczkowski, P.; Marty, A.; Attané, J. P. *Phys. Rev. B* **2018,** *98,* No. 174414. doi:10.1103/physrevb.98.174414
20. Zhou, T.; Mohanta, N.; Han, J. E.; Matos-Abiague, A.; Žutić, I. *Phys. Rev. B* **2019,** *99,* No. 134505. doi:10.1103/physrevb.99.134505
21. Serlin, M.; Tschirhart, C. L.; Polshyn, H.; Zhang, Y.; Zhu, J.; Watanabe, K.; Taniguchi, T.; Balents, L.; Young, A. F. *Science* **2020,** *367,* 900–903. doi:10.1126/science.aay5533
22. Das, K. S.; Liu, J.; van Wees, B. J.; Vera-Marun, I. J. *Nano Lett.* **2018,** *18,* 5633–5639. doi:10.1021/acs.nanolett.8b02114
23. Gurram, M.; Omar, S.; van Wees, B. J. *2D Mater.* **2018,** *5,* No. 032004. doi:10.1088/2053-1583/aac34d
24. Abert, C. *Eur. Phys. J. B* **2019,** *92,* 120. doi:10.1140/epjb/e2019-90599-6
25. Shen, R. L.; Zhong, J. *Proc. Inst. Mech. Eng., Part J* **2009,** *223,* 735–737. doi:10.1243/13506501jet526
26. Yamamoto, S.; Taguchi, M.; Someya, T.; Kubota, Y.; Ito, S.; Wadati, H.; Fujisawa, M.; Capotondi, F.; Pedersoli, E.; Manfredda, M.; Raimondi, L.; Kiskinova, M.; Fujii, J.; Moras, P.; Tsuyama, T.; Nakamura, T.; Kato, T.; Higashide, T.; Iwata, S.; Yamamoto, S.; Shin, S.; Matsuda, I. *Rev. Sci. Instrum.* **2015,** *86,* No. 083901. doi:10.1063/1.4927828
27. Meier, F.; Levy, J.; Loss, D. *Phys. Rev. Lett.* **2003,** *90,* No. 047901. doi:10.1103/physrevlett.90.047901
28. Lehmann, J.; Gaita-Ariño, A.; Coronado, E.; Loss, D. *J. Mater. Chem.* **2009,** *19,* 1672–1677. doi:10.1039/b810634g
29. Kłobus, W.; Grudka, A.; Baumgartner, A.; Tomaszewski, D.; Schönenberger, C.; Martinek, J. *Phys. Rev. B* **2014,** *89,* No. 125404. doi:10.1103/physrevb.89.125404
30. Amigo, N. *Mol. Simul.* **2019,** *45,* 951–957. doi:10.1080/08927022.2019.1616293
31. Zong, B.; Phuoc, N. N.; Wu, Y.; Ho, P.; Ma, F.; Han, G.; Yang, Y.; Li, Z.; He, S.; Wu, Y. *ChemElectroChem* **2015,** *2,* 1760–1767. doi:10.1002/celc.201500230
32. Kamilov, I. K.; Murtazaev, A. K.; Aliev, K. K. *Phys.-Usp.* **1999,** *42,* 689–709. doi:10.1070/pu1999v042n07abeh000498
33. Lewis, L. H.; Marrows, C. H.; Langridge, S. *J. Phys. D: Appl. Phys.* **2016,** *49,* No. 323002. doi:10.1088/0022-3727/49/32/323002
34. Burr, G. W.; Breitwisch, M. J.; Franceschini, M.; Garetto, D.; Gopalakrishnan, K.; Jackson, B.; Kurdi, B.; Lam, C.; Lastras, L. A.; Padilla, A.; Rajendran, B.; Raoux, S.; Shenoy, R. S. *J. Vac. Sci. Technol., B: Microelectron. Nanometer Struct.–Process., Meas., Phenom.* **2010,** *28,* 223–262. doi:10.1116/1.3301579
35. Klenov, N.; Khaydukov, Y.; Bakurskiy, S.; Morari, R.; Soloviev, I.; Boian, V.; Keller, T.; Kupriyanov, M.; Sidorenko, A.; Keimer, B. *Beilstein J. Nanotechnol.* **2019,** *10,* 833–839. doi:10.3762/bjnano.10.83
36. Banerjee, N.; Ouassou, J. A.; Zhu, Y.; Stelmashenko, N. A.; Linder, J.; Blamire, M. G. *Phys. Rev. B* **2018,** *97,* No. 184521. doi:10.1103/physrevb.97.184521
37. Vakhrushev, A.; Fedotov, A.; Boian, V.; Morari, R.; Sidorenko, A. *Beilstein J. Nanotechnol.* **2020,** *11,* 1776–1788. doi:10.3762/bjnano.11.160
38. Sidorenko, A. S.; Morari, R. A.; Boian, V.; Prepelitsa, A. A.; Antropov, E. I.; Savva, Y. B.; Fedotov, A. Y.; Sevryukhina, O. Y.; Vakhrushev, A. V. *J. Phys.: Conf. Ser.* **2021,** *1758,* No. 012037. doi:10.1088/1742-6596/1758/1/012037
39. Vakhrushev, A.; Fedotov, A.; Sidorenko, A. *Key Eng. Mater.* **2021,** *888,* 57–65. doi:10.4028/www.scientific.net/kem.888.57
40. Tranchida, J.; Plimpton, S. J.; Thibaudeau, P.; Thompson, A. P. *J. Comput. Phys.* **2018,** *372,* 406–425. doi:10.1016/j.jcp.2018.06.042
41. Beaujouan, D.; Thibaudeau, P.; Barreteau, C. *Phys. Rev. B* **2012,** *86,* No. 174409. doi:10.1103/physrevb.86.174409
42. Perera, D.; Eisenbach, M.; Nicholson, D. M.; Stocks, G. M.; Landau, D. P. *Phys. Rev. B* **2016,** *93,* No. 060402. doi:10.1103/physrevb.93.060402
43. Neel, L. *J. Phys. Radium* **1954,** *15,* 376–378. doi:10.1051/jphysrad:01954001505037601
44. Nurdin, W. B.; Schotte, K.-D. *Phys. Rev. E* **2000,** *61,* 3579–3582. doi:10.1103/physreve.61.3579
45. Kelchner, C. L.; Plimpton, S. J.; Hamilton, J. C. *Phys. Rev. B* **1998,** *58,* 11085–11088. doi:10.1103/physrevb.58.11085
46. Finnemore, D. K.; Stromberg, T. F.; Swenson, C. A. *Phys. Rev.* **1966,** *149,* 231–243. doi:10.1103/physrev.149.231
47. Casalbuoni, S.; Knabbe, E. A.; Kötzler, J.; Lilje, L.; von Sawilski, L.; Schmüser, P.; Steffen, B. *Nucl. Instrum. Methods Phys. Res., Sect. A* **2005,** *538,* 45–64. doi:10.1016/j.nima.2004.09.003
48. Aull, S.; Kugeler, O.; Knobloch, J. *Phys. Rev. Spec. Top.–Accel. Beams* **2012,** *15,* 062001. doi:10.1103/physrevstab.15.062001
49. Thompson, D. J.; Minhaj, M. S. M.; Wenger, L. E.; Chen, J. T. *Phys. Rev. Lett.* **1995,** *75,* 529–532. doi:10.1103/physrevlett.75.529
50. Moragues-Canovás, M.; Talbot-Eeckelaers, C. E.; Catala, L.; Lloret, F.; Wernsdorfer, W.; Brechin, E. K.; Mallah, T. *Inorg. Chem.* **2006,** *45,* 7038–7040. doi:10.1021/ic0605773
51. Batallan, F.; Rosenman, I.; Sommers, C. B. *Phys. Rev. B* **1975,** *11,* 545–557. doi:10.1103/physrevb.11.545

License and Terms

BEILSTEIN JOURNAL OF NANOTECHNOLOGY

Upper critical magnetic field in NbRe and NbReN micrometric strips

Zahra Makhdoumi Kakhaki[1], Antonio Leo[1,2], Federico Chianese[3], Loredana Parlato[3], Giovanni Piero Pepe[3], Angela Nigro[1,2], Carla Cirillo[2] and Carmine Attanasio[*1]

Full Research Paper

Open Access

Address:
[1]Dipartimento di Fisica “E. R. Caianiello”, Università degli Studi di Salerno, I-84084 Fisciano (Sa), Italy, [2]CNR-SPIN, c/o Università degli Studi di Salerno, I-84084 Fisciano (Sa), Italy and [3]Dipartimento di Fisica “E. Pancini”, Università degli Studi di Napoli Federico II, I-80125 Napoli, Italy

Email:
Carmine Attanasio[*] - cattanasio@unisa.it

* Corresponding author

Keywords:
non-centrosymmetric superconductors; Pauli and orbital contribution; upper critical fields; Werthamer–Helfand–Hohenberg theory

Beilstein J. Nanotechnol. **2023,** *14,* 45–51.
https://doi.org/10.3762/bjnano.14.5

Received: 10 October 2022
Accepted: 19 December 2022
Published: 05 January 2023

This article is part of the thematic issue "Intrinsic Josephson effect and prospects of superconducting spintronics".

Guest Editor: A. S. Sidorenko

Abstract

Non-centrosymmetric superconductors have recently received significant interest due to their intriguing physical properties such as multigap and nodal superconductivity, helical vortex states, as well as non-trivial topological effects. Moreover, large values of the upper critical magnetic field have been reported in these materials. Here, we focus on the study of the temperature dependence of the perpendicular magnetic field of NbRe and NbReN films patterned in micrometric strips. The experimental data are studied within the Werthamer–Helfand–Hohenberg theory, which considers both orbital and Zeeman pair breaking. The analysis of the results shows different behavior for the two materials with a Pauli contribution relevant only in the case of NbReN.

Introduction

Superconducting films of NbRe and NbReN have recently received great attention in the field of low-temperature electronics as suitable candidates for the realization of fast superconducting nanowire single-photon detectors (SNSPDs) [1-4]. Apart from the reduced values of the superconducting gap and short quasi-particle relaxation times [5], the property that makes these materials appropriate to be used as SNSPDs is the high value of the electrical resistivity [6]. This feature is related to the polycrystalline or amorphous nature of these materials when deposited in a thin-film form [4,7,8]. In addition to the applicative interest, the study of these materials is relevant from a fundamental point of view. Nb_xRe_{1-x} (NbRe) for $0.13 \leq x \leq 0.38$ crystallizes in the non-centrosymmetric Ti_5Re_{24}-type structure with the space group $I\bar{4}3m$ (No. 217) [9-12]. This non-centrosymmetric nature of the material leads to intriguing and unconventional physical properties such as the

time-reversal symmetry breaking observed with muon-spin rotation and relaxation studies [13] and large values of the upper critical magnetic fields [11,14], which are above the Pauli paramagnetic limit [15,16]. In the case of thin films, the structure of NbRe is polycrystalline with grains of small dimensions, typically of the order of 2–3 nm [7,8,17]. NbReN films also present a polycrystalline nature with a moderate texture. In this case, it was possible to interpret the results of the structural characterization only by assuming for NbReN the same unit cell as that of NbRe [4]. However, detailed knowledge of its structural and microscopic properties is still lacking. Finally, while the morphological properties are similar to those of NbRe films [18], the values of the electrical resistivity stand slightly higher with respect to NbRe films [4,7,18].

The value of the upper critical magnetic field is a fundamental quantity that gives a measure of the robustness of the superconductivity in a specific material. For a standard BCS *s*-wave type-II superconductor, Werthamer, Helfand, and Hohenberg (WHH) have calculated the temperature dependence of the critical field [19]. In this model, two mechanisms are responsible for the breaking of the superconductivity and both contribute to the behavior of $H_{c2}(T)$, namely the orbital and the paramagnetic effect. While the former is due to the Lorentz force acting on electrons of the Cooper pairs with opposite momentum, the latter is related to splitting of the spin-singlet pairs because of the Zeeman effect. Accordingly, paramagnetic pair-breaking effects are absent in spin-triplet superconductors. The Pauli limiting field is given by $H_{\mathrm{p}}(0) = \Delta(0)/\left(2\sqrt{2}\mu_{\mathrm{B}}\right)$, where $\Delta(0)$ is the superconducting energy gap at zero temperature and μ_{B} is the Bohr magneton [15]. For weakly coupled BCS superconductors it is $H_{\mathrm{p}}(0)$ [T] ≈ $1.84T_{\mathrm{c}}$ [K]. In the dirty limit, the orbital limit at zero temperature is given by $H_{\mathrm{c2}}^{\mathrm{orb}}(0) = 0.69T_{\mathrm{c}}\left(\mathrm{d}H_{\mathrm{c2}}/\mathrm{d}T\right)_{T=T_{\mathrm{c}}}$ [19]. Close to the critical temperature, T_{c}, the contribution of the orbital term dominates in determining the value of H_{c2}, at low temperatures and high fields, the Pauli term is predominant [20,21]. In general, the relative weight of the two effects is given in the theory by the Maki parameter $\alpha = H_{\mathrm{c2}}^{\mathrm{orb}}(0)/\sqrt{2}H_{\mathrm{p}}(0)$ [19,22]. Alternatively, it could be convenient to express α in terms of normal-state properties [19,22,23]. In this case, $\alpha = 3/(2k_{\mathrm{F}}\ell)$ [24] where k_{F} is the Fermi wave vector and ℓ is the mean free path. If spin–orbit scattering is also taken into account, another quantity, λ_{so} (the spin–orbit parameter), is introduced in the theory [19]. The effect of λ_{so} is to soften the role of α in determining the values of $H_{\mathrm{c2}}(T)$ [19]. When $\lambda_{\mathrm{so}} = 0$, it is $H_{\mathrm{c2}}(0) = H_{\mathrm{c2}}^{\mathrm{orb}}(0)/\sqrt{1+\alpha^2}$ [23]. The WHH theory has been used to interpret the temperature dependence of the critical fields of several superconductors [20,24-36], including non-centrosymmetric materials for which experiments give contradictory results [14,37-43]. In particular, values of the critical field larger than $H_{\mathrm{p}}(0)$ have been experimentally observed. These results, which cannot be described by the WHH model, are interpreted as an indication of the presence of an unconventional superconducting pairing in the material.

In this paper, we measure the temperature dependence of the perperpendicular, $H_{\mathrm{c2}\perp}(T)$, and parallel, $H_{\mathrm{c2}\parallel}(T)$, critical field of NbRe and NbReN microstrips. The behavior of $H_{\mathrm{c2}\perp}(T)$ is analyzed in the framework of the WHH theory. We find that while for NbRe the value of the critical field is purely orbital-limited, in the case of NbReN, the effect of the Pauli contribution plays a relevant role in the temperature dependence of $H_{\mathrm{c2}\perp}$. We have not observed a positive curvature of $H_{\mathrm{c2}\perp}(T)$ near T_{c} as it was in the case of two-band superconductivity [44] or proximity-coupled superconducting systems [45,46].

Experimental

NbRe and NbReN films were sputtered on oxidized Si substrates in a UHV dc magnetron system with base pressure of 1×10^{-8} mbar. The films were deposited at room temperature from a stoichiometric NbRe ($Nb_{0.18}Re_{0.82}$) 99.95% pure target of 5 cm diameter at a power of 350 W. NbRe films, 8 nm thick, were grown at a Ar pressure of 4 μbar, which resulted in a deposition rate of 0.3 nm/s. NbReN films, 10 nm thick, were reactively sputtered in a mixture of inert Ar (85%) and reactive N_2 (15%) gas at a total pressure of 3.5 μbar at a rate of 0.36 nm/s. NbRe films were patterned by standard optical lithography and lift-off procedures to realize a Hall bar geometry of width w = 10 μm and a distance between the voltage contacts of L = 90 μm. The NbReN films were structured by using direct laser writer exposure followed by argon ion etching into constriction-type bridges with w = 2 μm and L = 700 μm. Further details on the fabrication procedure of the films are reported elsewhere [4,8].

The superconducting properties have been analyzed by electrical resistance measurements using a standard four-probe technique in a Cryogenic Ltd. CFM9T cryogen-free system. The microstrips were biased with a current of I_{b} = 10 μA. During the measurements, the error on the temperature value was less than 10 mK. The superconducting H–T phase diagrams were obtained by measuring the resistive transitions in the presence of the magnetic field applied perpendicularly or parallely to the surface of the samples. For each field, the value of T_{c} was determined using the 50% R_{N} criterion, where R_{N} is the value of the normal-state resistance at 10 K.

Results and Discussion

Figure 1 displays the normalized resistive transitions in zero magnetic field of the NbRe and NbReN microstrips. The critical temperature, the low-temperature resistivity, and the residual

resistivity ratio (RRR) are reported for both microstrips in Table 1. The RRR is defined as the ratio of the resistivity at room temperature and at 10 K, that is, RRR = ρ_{300K}/ρ_{10K} = R_{300K}/R_{10K}. The values of T_c are not significantly smaller than the values measured on unpatterned films of the same thickness [4,8]. The rounding present at the onset of both the curves is due to the paraconductivity phenomenon, whose nature has been analyzed in detail in the case of unstructured NbReN films of different thickness [4].

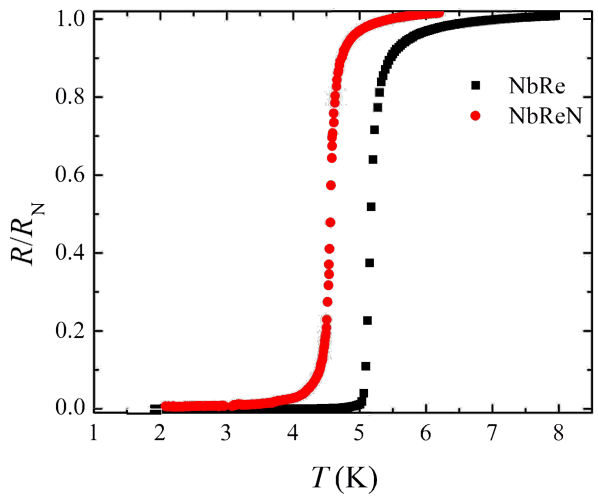

Figure 1: Resistive transition in zero magnetic field of the NbRe (black squares) and NbReN (red circles) microstrips.

Table 1: Parameter values of NbRe and NbReN microstrips.

Parameters	NbRe	NbReN
Film thickness (nm)	8	10
ρ (μΩ·cm)	248	220
RRR	0.92	0.94
D (× 10^{-4} m^2/s)	0.49	0.48
T_c (K)	5.31	4.61
$\lvert dH_{c2}/dT\rvert_{T_c}$ (T/K)	2.23	2.27
$\alpha = 3/(2k_F\ell)$	0.51	0.51
$\mu_0 H_p(0)$ (T)	9.78	8.48
$\mu_0 H_{c2}^{orb}(0)$ (T)	8.09	7.17
$\mu_0 H_{c2}(0)$ (T)	8.12	6.38

In Figure 2, the resistive curves of NbRe are shown for various values of H with the microstrip placed perpendicularly (Figure 2a) or parallely (Figure 2b) to the external field. The same quantities measured for NbReN are shown in Figure 2c and Figure 2d. In Figure 2e and Figure 2f, the field dependence of the width of the resistive transitions, ΔT_c, is reported for NbRe and NbReN, respectively. We define $\Delta T_c = T_c^{90\%} - T_c^{10\%}$, where $T_c^{90\%}$ ($T_c^{10\%}$) is the critical temperature obtained with the 90% (10%) R_N criterion. As it can be seen, when the samples are placed perpendicularly to the field the curves significantly broaden at high fields due to the entering of the vortices. However, the value of ΔT_c is similar for both materials. In contrast, in a parallel field, ΔT_c is almost constant in both cases.

The temperature dependence of H_{c2} for NbRe and NbReN is displayed, respectively, in Figure 3a and Figure 3b, where both $H_{c2\perp}(T)$ and $H_{c2\parallel}(T)$ are reported. In the insets of Figure 3a and Figure 3b, the temperature dependence of the anisotropy coefficient $\gamma(T) = H_{c2\parallel}(T)/H_{c2\perp}(T)$ is given for NbRe and NbReN, respectively. For both the materials, γ shows a nonmonotonic behavior with a fast increase followed by a smooth decrease when the temperature is lowered. However, for NbReN, γ is larger by a factor of almost two than for NbRe. We will comment on this point later on.

In the dirty limit and assuming that spin–orbit scattering is negligible with respect to spin-independent scattering, the temperature dependence of H_{c2} is given by the implicit equation [19]

$$\ln\frac{1}{t} = \sum_{\nu=-\infty}^{\infty}\left\{\frac{1}{|2\nu+1|} - \left[|2\nu+1| + \frac{\bar{h}}{t} + \frac{\left(\alpha\bar{h}/t\right)^2}{|2\nu+1| + \left(\bar{h}+\lambda_{so}\right)/t}\right]^{-1}\right\}, \quad (1)$$

where $t = T/T_c$, $\bar{h} = \frac{4}{\pi^2}H_{c2}(T)\frac{1}{T_c\lvert dH_{c2}/dT\rvert_{T_c}}$. $\lambda_{so} = \hbar/(3\pi k_B T_c \tau_{so})$ with τ_{so} being the mean free time for spin–orbit scattering. We have used Equation 1 with $\lambda_{so} = 0$ to describe the experimental data for both materials using the measured values of T_c and the slope of $H_{c2\perp}$ close to T_c, which can be accurately determined via the many transition curves measured at very low fields. Moreover, the values of α for both materials have been obtained from the normal-state properties. Therefore, the WHH curves obtained from Equation 1 do not contain any fitting parameter [19,40]. All these quantities together with other superconducting and normal-state properties of the two materials are summarized in Table 1. In Figure 4 the perpendicular H–T phase diagram is reported for NbRe (Figure 4a) and NbReN (Figure 4b) microstrips together with the prediction given by the WHH theory. As far as NbRe is concerned, the experimental data are not described by the WHH theory considering $\alpha = 0.51$, the value obtained from the normal-state properties (see solid line in Figure 4a). In fact, $k_F\ell = 3Dm/\hbar$ [47], where $D = \left(4k_B/\pi e\right)\times\lvert\mu_0 dH_{c2}/dT\rvert_{T_c}^{-1}$ [48] is the quasiparticle diffusion coefficient and m is the mass of the electron. From the value of D reported in Table 1, we get $k_F\ell \approx 1.3$ and then $\alpha = 0.51$. In contrast, data are very well reproduced by the

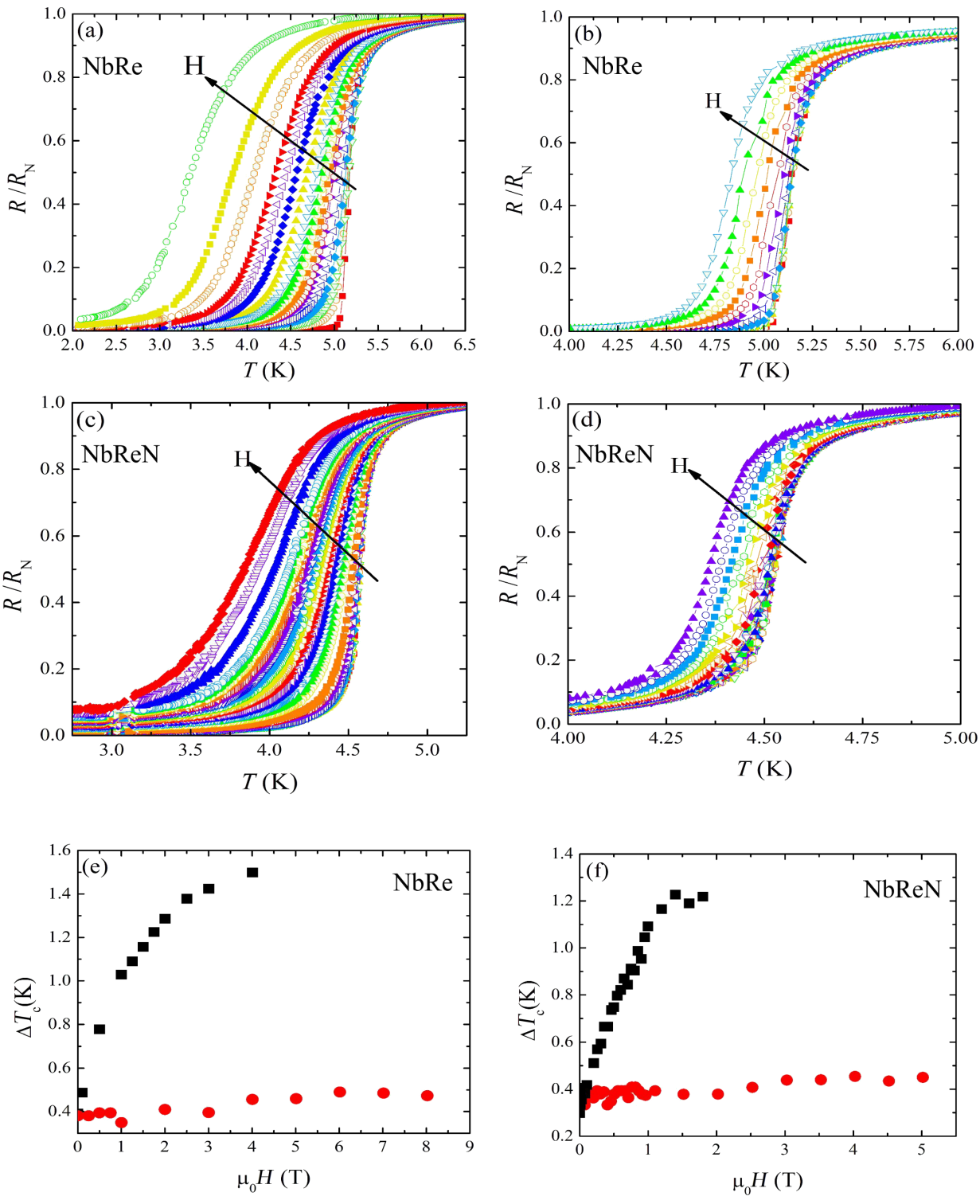

Figure 2: (a) Temperature dependence of the resistance of the NbRe microstrip in various magnetic fields in the perpendicular geometry. The curves have been measured for increasing magnetic fields (as indicated by the arrow) from $\mu_0 H$ = 0.003 to 4 T. (b) The same as panel (a) but in the parallel geometry. The field increases from $\mu_0 H$ = 0.003 to 8 T. (c) Temperature dependence of the resistance of the NbReN microstrip in various magnetic fields in the perpendicular geometry. The curves have been measured for increasing magnetic fields from $\mu_0 H$ = 0.001 to 3 T. (d) The same as panel (c) but in the parallel geometry. The field increases from $\mu_0 H$ = 0.007 to 5 T. (e, f) ΔT_c field dependence of (e) the NbRe and (f) the NbReN microstrip for the perpendicular (black squares) and parallel (red circles) geometries.

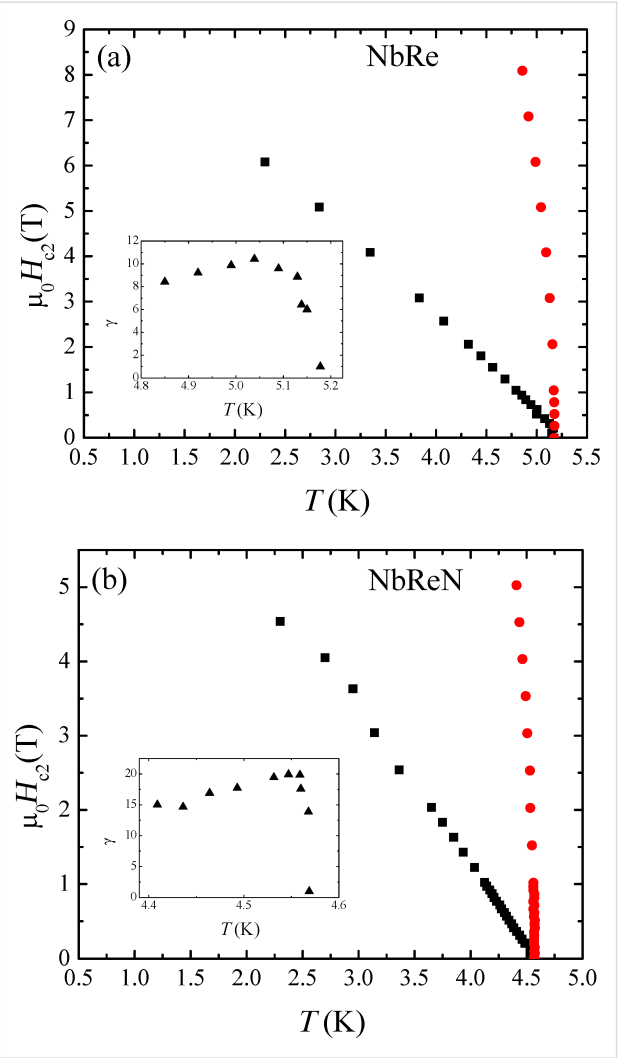

Figure 3: (a, b) *H*–*T* phase diagram of (a) the NbRe and (b) the NbReN microstrip. Black squares and red circles indicate the temperature dependence of $H_{c2\perp}$ and $H_{c2\parallel}$, respectively. The insets show the behavior of the anisotropy coefficient γ as a function of the temperature.

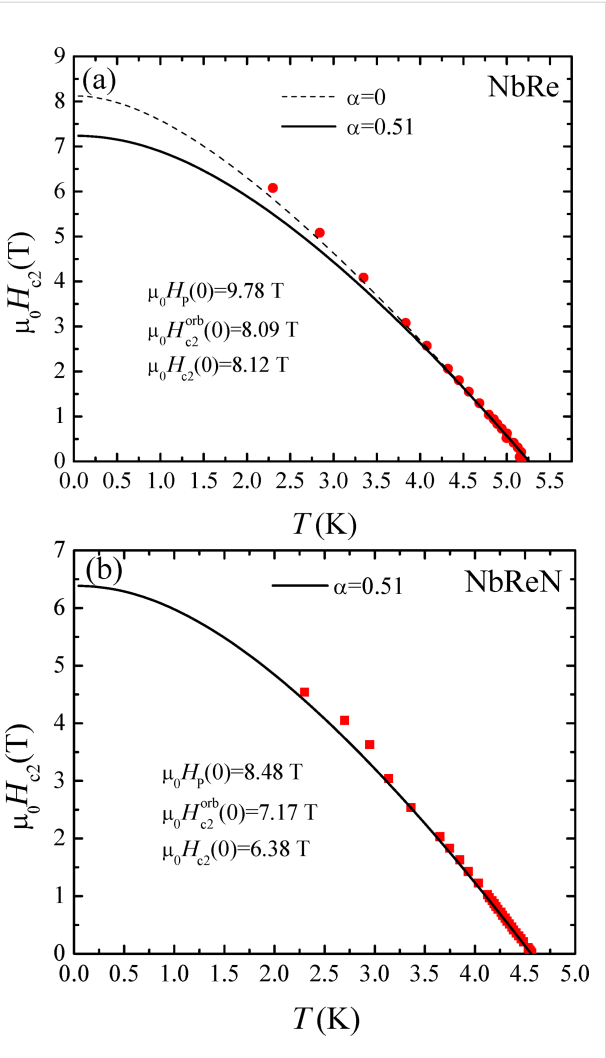

Figure 4: (a, b) Temperature dependence of the perpendicular upper critical field of (a) the NbRe and (b) the NbReN microstrip. The lines represent the WHH calculations. Details of the procedure are given in the text.

WHH theory with α = 0, even though the points at the lowest temperature lay above the curve (see dashed line in Figure 4a). The value of the zero-temperature critical magnetic field [$H_{c2\perp}(0)$ = 8.12 T] is below $H_p(0)$ = 9.78 T, and since α = 0, the orbital limiting to $H_{c2\perp}$ is the only contribution that should be considered. Our result, which is in line with other studies on $H_{c2\perp}(T)$ made on non-centrosymmetric materials in bulk forms [37,39,41], may suggest the presence of a triplet component of the order parameter. This result was even more evident in the case of polycrystalline NbRe samples, for which the experimental points in the *H*–*T* phase diagram stand well above the WHH line with α = 0 [14]. This result, interpreted in [14] as an indication of unconventional superconducting pairing, may be weakened in our case due to the poorer crystal quality of our disordered films. In the case of NbReN, the data are well described by the WHH theory with α = 0.51, as shown by the solid line in Figure 4b. In this case, the critical field is paramagnetically limited with the Pauli contribution that lowers the value of the critical field with respect to the pure orbital-limited case (α = 0). This suppression of the perpendicular critical field in conjunction with the steepest behavior of $H_{c2\parallel}$ in the studied temperature range could also be the cause of the larger value of γ measured on the NbReN microstrip. Again, we ascribe this effect to the crystallographic properties of the films. Indeed, it is reasonable to suppose that the presence of the N atoms in the atomic cell may break the non-centrosymmetricity of the system, thus depressing the spin-triplet component of the order parameter. For this reason, $H_{c2\perp}$ becomes paramagnetically limited [24,35]. In order to confirm these results, we are currently working on different experiments that may give more

direct access to the order parameter in these systems. Regarding the aforementioned purpose, while in the case of NbRe it is now even more evident that films with larger crystallites are mandatory [7,8,12], detailed analyses of the NbReN crystal structure are still lacking and need to be performed.

Conclusion

We have studied the H–T phase diagram for NbRe and NbReN microstrips. Despite the fact that the two materials show very similar morphological, normal-state, and superconducting properties, different results are obtained for the $H_{c2\perp}(T)$ behavior. In particular, while for NbRe the critical magnetic field is related to the orbital contribution, the Pauli limitation plays a relevant role in the case of NbReN. We correlate this result to the different microscopic properties of the two materials.

ORCID® iDs

Zahra Makhdoumi Kakhaki - https://orcid.org/0000-0003-0330-8943
Antonio Leo - https://orcid.org/0000-0002-9137-2111
Loredana Parlato - https://orcid.org/0000-0002-1646-3435
Angela Nigro - https://orcid.org/0000-0001-8326-5781
Carla Cirillo - https://orcid.org/0000-0001-8755-4484
Carmine Attanasio - https://orcid.org/0000-0002-3848-9169

References

1. Caputo, M.; Cirillo, C.; Attanasio, C. *Appl. Phys. Lett.* **2017,** *111,* 192601. doi:10.1063/1.4997675
2. Cirillo, C.; Chang, J.; Caputo, M.; Los, J. W. N.; Dorenbos, S.; Esmaeil Zadeh, I.; Attanasio, C. *Appl. Phys. Lett.* **2020,** *117,* 172602. doi:10.1063/5.0021487
3. Esmaeil Zadeh, I.; Chang, J.; Los, J. W. N.; Gyger, S.; Elshaari, A. W.; Steinhauer, S.; Dorenbos, S. N.; Zwiller, V. *Appl. Phys. Lett.* **2021,** *118,* 190502. doi:10.1063/5.0045990
4. Cirillo, C.; Granata, V.; Spuri, A.; Di Bernardo, A.; Attanasio, C. *Phys. Rev. Mater.* **2021,** *5,* 085004. doi:10.1103/physrevmaterials.5.085004
5. Dobrovolskiy, O. V.; Vodolazov, D. Y.; Porrati, F.; Sachser, R.; Bevz, V. M.; Mikhailov, M. Y.; Chumak, A. V.; Huth, M. *Nat. Commun.* **2020,** *11,* 3291. doi:10.1038/s41467-020-16987-y
6. Holzman, I.; Ivry, Y. *Adv. Quantum Technol.* **2019,** *2,* 1800058. doi:10.1002/qute.201800058
7. Cirillo, C.; Carapella, G.; Salvato, M.; Arpaia, R.; Caputo, M.; Attanasio, C. *Phys. Rev. B* **2016,** *94,* 104512. doi:10.1103/physrevb.94.104512
8. Cirillo, C.; Caputo, M.; Divitini, G.; Robinson, J. W. A.; Attanasio, C. *Thin Solid Films* **2022,** *758,* 139450. doi:10.1016/j.tsf.2022.139450
9. Lue, C. S.; Su, T. H.; Liu, H. F.; Young, B.-L. *Phys. Rev. B* **2011,** *84,* 052509. doi:10.1103/physrevb.84.052509
10. Singh, R. P.; Smidman, M.; Lees, M. R.; Paul, D. M.; Balakrishnan, G. *J. Cryst. Growth* **2012,** *361,* 129–131. doi:10.1016/j.jcrysgro.2012.09.013
11. Chen, J.; Jiao, L.; Zhang, J. L.; Chen, Y.; Yang, L.; Nicklas, M.; Steglich, F.; Yuan, H. Q. *Phys. Rev. B* **2013,** *88,* 144510. doi:10.1103/physrevb.88.144510
12. Cirillo, C.; Fittipaldi, R.; Smidman, M.; Carapella, G.; Attanasio, C.; Vecchione, A.; Singh, R. P.; Lees, M. R.; Balakrishnan, G.; Cuoco, M. *Phys. Rev. B* **2015,** *91,* 134508. doi:10.1103/physrevb.91.134508
13. Shang, T.; Smidman, M.; Ghosh, S. K.; Baines, C.; Chang, L. J.; Gawryluk, D. J.; Barker, J. A. T.; Singh, R. P.; Paul, D. M.; Balakrishnan, G.; Pomjakushina, E.; Shi, M.; Medarde, M.; Hillier, A. D.; Yuan, H. Q.; Quintanilla, J.; Mesot, J.; Shiroka, T. *Phys. Rev. Lett.* **2018,** *121,* 257002. doi:10.1103/physrevlett.121.257002
14. Sundar, S.; Salem-Sugui, S., Jr.; Chattopadhyay, M. K.; Roy, S. B.; Sharath Chandra, L. S.; Cohen, L. F.; Ghivelder, L. *Supercond. Sci. Technol.* **2019,** *32,* 055003. doi:10.1088/1361-6668/ab06a5
15. Clogston, A. M. *Phys. Rev. Lett.* **1962,** *9,* 266–267. doi:10.1103/physrevlett.9.266
16. Chandrasekhar, B. S. *Appl. Phys. Lett.* **1962,** *1,* 7–8. doi:10.1063/1.1777362
17. Periyasamy, M.; Bradshaw, H.; Sukenik, N.; Alpern, H.; Yochelis, S.; Robinson, J. W. A.; Millo, O.; Paltiel, Y. *Appl. Phys. Lett.* **2020,** *117,* 242601. doi:10.1063/5.0030892
18. Barone, C.; Cirillo, C.; Carapella, G.; Granata, V.; Santoro, D.; Attanasio, C.; Pagano, S. *Sci. Rep.* **2022,** *12,* 1573. doi:10.1038/s41598-022-05511-5
19. Werthamer, N. R.; Helfand, E.; Hohenberg, P. C. *Phys. Rev.* **1966,** *147,* 295–302. doi:10.1103/physrev.147.295
20. Fuchs, G.; Drechsler, S.-L.; Kozlova, N.; Bartkowiak, M.; Hamann-Borrero, J. E.; Behr, G.; Nenkov, K.; Klauss, H.-H.; Maeter, H.; Amato, A.; Luetkens, H.; Kwadrin, A.; Khasanov, R.; Freudenberger, J.; Köhler, A.; Knupfer, M.; Arushanov, E.; Rosner, H.; Büchner, B.; Schultz, L. *New J. Phys.* **2009,** *11,* 075007. doi:10.1088/1367-2630/11/7/075007
21. Ma, K.; Gornicka, K.; Lefèvre, R.; Yang, Y.; Rønnow, H. M.; Jeschke, H. O.; Klimczuk, T.; von Rohr, F. O. *ACS Mater. Au* **2021,** *1,* 55–61. doi:10.1021/acsmaterialsau.1c00011
22. Maki, K. *Physics* **1964,** *1,* 127–143. doi:10.1103/physicsphysiquefizika.1.127
23. Maki, K. *Phys. Rev.* **1966,** *148,* 362–369. doi:10.1103/physrev.148.362
24. Glezer Moshe, A.; Farber, E.; Deutscher, G. *Phys. Rev. Res.* **2020,** *2,* 043354. doi:10.1103/physrevresearch.2.043354
25. Angrisani Armenio, A.; Mercaldo, L. V.; Prischepa, S. L.; Salvato, M.; Attanasio, C.; Maritato, L. *J. Supercond.* **2001,** *14,* 411–414. doi:10.1023/a:1011138808751
26. Hunte, F.; Jaroszynski, J.; Gurevich, A.; Larbalestier, D. C.; Jin, R.; Sefat, A. S.; McGuire, M. A.; Sales, B. C.; Christen, D. K.; Mandrus, D. *Nature* **2008,** *453,* 903–905. doi:10.1038/nature07058
27. Bose, S.; Raychaudhuri, P.; Banerjee, R.; Ayyub, P. *Phys. Rev. B* **2006,** *74,* 224502. doi:10.1103/physrevb.74.224502
28. Lei, H.; Graf, D.; Hu, R.; Ryu, H.; Choi, E. S.; Tozer, S. W.; Petrovic, C. *Phys. Rev. B* **2012,** *85,* 094515. doi:10.1103/physrevb.85.094515
29. Lu, Y.; Takayama, T.; Bangura, A. F.; Katsura, Y.; Hashizume, D.; Takagi, H. *J. Phys. Soc. Jpn.* **2014,** *83,* 023702. doi:10.7566/jpsj.83.023702
30. Hänisch, J.; Iida, K.; Kurth, F.; Reich, E.; Tarantini, C.; Jaroszynski, J.; Förster, T.; Fuchs, G.; Hühne, R.; Grinenko, V.; Schultz, L.; Holzapfel, B. *Sci. Rep.* **2015,** *5,* 17363. doi:10.1038/srep17363
31. Sultana, R.; Rani, P.; Hafiz, A. K.; Goyal, R.; Awana, V. P. S. *J. Supercond. Novel Magn.* **2016,** *29,* 1399–1404. doi:10.1007/s10948-016-3507-1
32. Xing, X.; Zhou, W.; Wang, J.; Zhu, Z.; Zhang, Y.; Zhou, N.; Qian, B.; Xu, X.; Shi, Z. *Sci. Rep.* **2017,** *7,* 45943. doi:10.1038/srep45943

33. Solenov, D.; Nikolo, M.; Singleton, J.; Jiang, J.; Weiss, J.; Hellstrom, E. *AIP Conf. Proc.* **2017,** *1895,* 060004. doi:10.1063/1.5007389
34. Nakamura, D.; Adachi, T.; Omori, K.; Koike, Y.; Takeyama, S. *Sci. Rep.* **2019,** *9,* 16949. doi:10.1038/s41598-019-52973-1
35. Zaytseva, I.; Abaloszew, A.; Camargo, B. C.; Syryanyy, Y.; Cieplak, M. Z. *Sci. Rep.* **2020,** *10,* 19062. doi:10.1038/s41598-020-75968-9
36. Bristow, M.; Knafo, W.; Reiss, P.; Meier, W.; Canfield, P. C.; Blundell, S. J.; Coldea, A. I. *Phys. Rev. B* **2020,** *101,* 134502. doi:10.1103/physrevb.101.134502
37. Fang, L.; Yang, H.; Zhu, X.; Mu, G.; Wang, Z.-S.; Shan, L.; Ren, C.; Wen, H.-H. *Phys. Rev. B* **2009,** *79,* 144509. doi:10.1103/physrevb.79.144509
38. Kase, N.; Akimitsu, J. *J. Phys. Soc. Jpn.* **2009,** *78,* 044710. doi:10.1143/jpsj.78.044710
39. Isobe, M.; Arai, M.; Shirakawa, N. *Phys. Rev. B* **2016,** *93,* 054519. doi:10.1103/physrevb.93.054519
40. Mayoh, D. A.; Barker, J. A. T.; Singh, R. P.; Balakrishnan, G.; Paul, D. M.; Lees, M. R. *Phys. Rev. B* **2017,** *96,* 064521. doi:10.1103/physrevb.96.064521
41. Barker, J. A. T.; Breen, B. D.; Hanson, R.; Hillier, A. D.; Lees, M. R.; Balakrishnan, G.; Paul, D. M.; Singh, R. P. *Phys. Rev. B* **2018,** *98,* 104506. doi:10.1103/physrevb.98.104506
42. Su, H.; Shang, T.; Du, F.; Chen, C. F.; Ye, H. Q.; Lu, X.; Cao, C.; Smidman, M.; Yuan, H. Q. *Phys. Rev. Mater.* **2021,** *5,* 114802. doi:10.1103/physrevmaterials.5.114802
43. Hoshi, K.; Kurihara, R.; Goto, Y.; Tokunaga, M.; Mizuguchi, Y. *Sci. Rep.* **2022,** *12,* 288. doi:10.1038/s41598-021-04393-3
44. Palistrant, M.; Surdu, A.; Ursu, V.; Petrenko, P.; Sidorenko, A. *Low Temp. Phys.* **2011,** *37,* 451–458. doi:10.1063/1.3610174
45. Sidorenko, A. S.; Sürgers, C.; v. Löhneysen, H. *Phys. C (Amsterdam, Neth.)* **2002,** *370,* 197–204. doi:10.1016/s0921-4534(01)00929-7
46. Antropov, E.; Kalenkov, M. S.; Kehrle, J.; Zdravkov, V. I.; Morari, R.; Socrovisciuc, A.; Lenk, D.; Horn, S.; Tagirov, L. R.; Zaikin, A. D.; Sidorenko, A. S.; Hahn, H.; Tidecks, R. *Supercond. Sci. Technol.* **2013,** *26,* 085003. doi:10.1088/0953-2048/26/8/085003
47. Ioffe, A. F.; Regel, A. R. *Prog. Semicond.* **1960,** *4,* 239.
48. Guimpel, J.; de la Cruz, M. E.; de la Cruz, F.; Fink, H. J.; Laborde, O.; Villegier, J. C. *J. Low Temp. Phys.* **1986,** *63,* 151–165. doi:10.1007/bf00682068

License and Terms

BEILSTEIN JOURNAL OF NANOTECHNOLOGY

Cooper pair splitting controlled by a temperature gradient

Dmitry S. Golubev[1] and Andrei D. Zaikin[*2,3]

Full Research Paper

Open Access

Address:
[1]QTF Centre of Excellence, Department of Applied Physics, Aalto University, FI-00076 Aalto, Finland, [2]I.E. Tamm Department of Theoretical Physics, P.N. Lebedev Physical Institute, 119991 Moscow, Russia and [3]National Research University Higher School of Economics, 101000 Moscow, Russia

Email:
Andrei D. Zaikin[*] - andrei.zaikin@kit.edu

* Corresponding author

Keywords:
Cooper pair splitting; entanglement; quantum shot noise; superconducting hybrid nanostructures

Beilstein J. Nanotechnol. **2023,** *14,* 61–67.
https://doi.org/10.3762/bjnano.14.7

Received: 01 October 2022
Accepted: 23 December 2022
Published: 09 January 2023

This article is part of the thematic issue "Intrinsic Josephson effect and prospects of superconducting spintronics".

Guest Editor: A. S. Sidorenko

Abstract

Electrons in two different normal metallic electrodes attached to a sufficiently thin superconducting island may become entangled due to the effect of Cooper pair splitting. This phenomenon is of fundamental importance and may also have serious implications for developing quantum communication technologies. One way to identify Cooper pair splitting is to analyze long-range cross correlations of fluctuating currents in three-terminal hybrid normal–superconducting–normal nanostructures. Here, we theoretically investigate non-trivial behavior of cross-correlated non-local shot noise in the presence of a temperature gradient. We suggest that applying a temperature gradient may serve as an extra tool to control the phenomenon of Cooper pair splitting.

Introduction

Normal metals connected to a superconductor exhibit a variety of non-trivial phenomena associated with the existence of proximity-induced superconducting correlations spreading over long distances at sufficiently low temperatures [1]. One of these phenomena is the so-called crossed Andreev reflection (CAR): A Cooper pair may split into two electrons [2] (see Figure 1a), thereby generating pairs of entangled electrons in different metallic electrodes [3]. This phenomenon and its effect on electron transport in normal metal–superconductor–normal metal (NSN) hybrid structures were intensively investigated both theoretically [4-10] and experimentally [11-18] over the past decades.

The process competing with CAR is the so-called elastic cotunneling (EC), where an electron is transferred from one normal metal to another across an effective barrier created by the energy gap inside the superconductor, see Figure 1b. Unlike CAR, EC does not produce entangled electrons. In the zero-temperature limit, CAR and EC contributions to the low-bias non-local conductance of an NSN device cancel each other in the limit of low-transparency barriers [4]. In contrast, at high transmissions, the CAR contribution vanishes [6,7]. These observations make an unambiguous identification of CAR in transport experiments a non-trivial task.

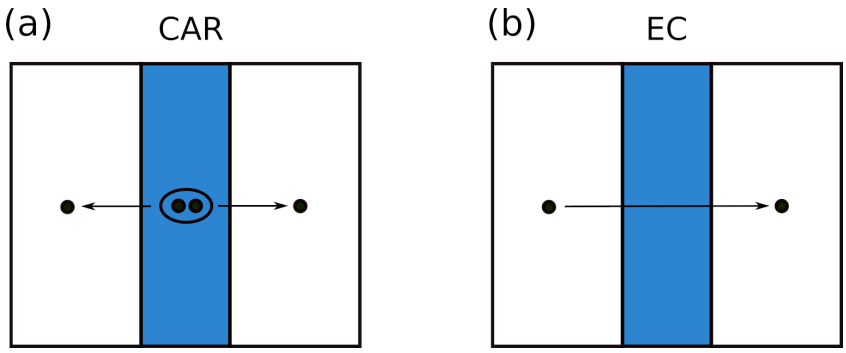

Figure 1: Schematics of the processes of crossed Andreev reflection (a) and elastic cotunneling (b). These schemes are redrawn from [25].

The way out is to investigate fluctuations of electric currents passing through both NS boundaries of an NSN structure. While in non-superconducting multiterminal structures cross correlations of current noise in different terminals always remain negative [19], such cross correlations may become positive in the presence of superconductivity due to the process of CAR. This conclusion was initially reached theoretically in the limit of low-transparency barriers at NS interfaces [20,21] and later extended to the case of arbitrary barrier transmissions [22-25]. Positively cross-correlated non-local shot noise was indeed observed in a number of experiments [26,27]. Real-time observation of Cooper pair splitting was also reported in a recent work [28].

Usually, an interplay between positive and negative cross correlations of current noise in NSN devices can be controlled and tuned by applying external bias voltages. In this work we suggest another way of controlling Cooper pair splitting: We predict and investigate non-trivial behavior of cross-correlated non-local shot noise in the presence of a temperature gradient. Note that, previously, this so-called “delta-T” noise was studied in normal atomic-scale junctions [29]. Here, we demonstrate that such kind of noise can also manifest itself in subtle non-local properties of hybrid NSN structures associated with the phenomena of crossed Andreev reflection and Cooper pair splitting.

Results and Discussion

Let us consider the NSN structure depicted in Figure 2. Normal metallic leads are attached to a bulk superconductor with the aid of two junctions described by a set of conducting channel transmissions $\tau_{1,n}$ and $\tau_{2,n}$ with n being the integer number enumerating all conducting channels. The two junctions are located at a distance considerably shorter than the superconducting coherence length ξ. Normal electrodes are kept at different temperatures T_1 and T_2, thus creating a temperature gradient across our device. In addition, voltages V_1 and V_2 can be applied to two normal leads, as shown in Figure 2.

The Hamiltonian of this structure can be chosen in the form

$$\hat{H} = \sum_{r=1,2} \left(\hat{H}_r + \hat{H}_{T,r} \right) + \hat{H}_S, \tag{1}$$

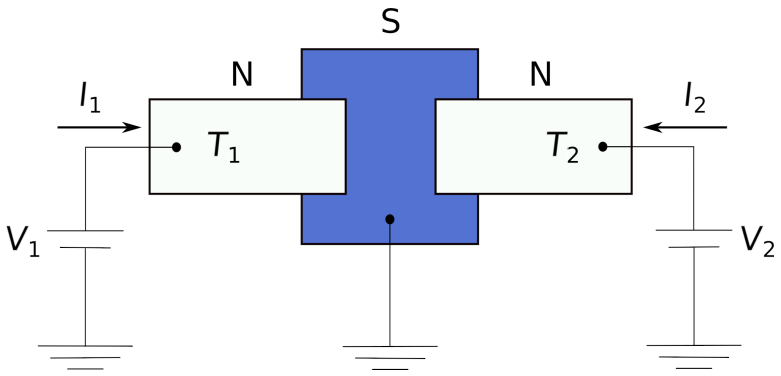

Figure 2: Schematics of the NSN structure under consideration. Normal electrodes are biased by external voltages V_1 and V_2 and are kept at different temperatures T_1 and T_2. The superconducting electrode is assumed to be thinner than the superconducting coherence length ξ.

where

$$\hat{H}_r = \sum_{\alpha=\uparrow,\downarrow} \int \mathrm{d}\mathbf{x} \hat{\Psi}^{\dagger}_{r,\alpha}(\mathbf{x}) \left(-\frac{\nabla^2}{2m} - \mu - eV_r \right) \hat{\Psi}_{r,\alpha}(\mathbf{x}), \quad (2)$$

are the Hamiltonians of two normal leads, $\hat{\Psi}^{\dagger}_{r,\alpha}(\mathbf{x}), \hat{\Psi}_{r,\alpha}(\mathbf{x})$ denote creation and annihilation operators for an electron with a spin projection α at a point **x**, m is the electron mass, and μ is the chemical potential,

$$\hat{H}_S = \int \mathrm{d}\mathbf{x} \left[\sum_{\alpha} \hat{\Psi}^{\dagger}_{S,\alpha}(\mathbf{x}) \left(-\frac{\nabla^2}{2m} - \mu \right) \hat{\Psi}_{S,\alpha}(\mathbf{x}) + \Delta \hat{\Psi}^{\dagger}_{S,\uparrow}(\mathbf{x}) \hat{\Psi}^{\dagger}_{S,\downarrow}(\mathbf{x}) + \Delta^* \hat{\Psi}_{S,\downarrow}(\mathbf{x}) \hat{\Psi}_{S,\uparrow}(\mathbf{x}) \right] \quad (3)$$

is the Hamiltonian of a superconducting electrode with the order parameter Δ and the terms

$$\hat{H}_{T,r} = \int_{\mathcal{A}_r} \mathrm{d}^2\mathbf{x} \sum_{\alpha=\uparrow,\downarrow} \left[t_r(\mathbf{x}) \hat{\Psi}^{\dagger}_{r,\alpha}(\mathbf{x}) \hat{\Psi}_{S,\alpha}(\mathbf{x}) + t^*_r(\mathbf{x}) \hat{\Psi}^{\dagger}_{S,\alpha}(\mathbf{x}) \hat{\Psi}_{r,\alpha}(\mathbf{x}) \right] \quad (4)$$

account for electron transfer through the junctions between the superconductor and the normal leads. In Equation 4, the surface integrals are taken over the contact areas $\mathcal{A}_r$, and $t_r(\mathbf{x})$ denote coordinate- and spin-independent tunneling amplitudes.

Let us denote the probability for N_1 and N_2 electrons to be transferred, respectively, through the junctions 1 and 2 during the observation time t as $P_t(N_1,N_2)$. Introducing the so-called cumulant generating function $\mathcal{F}(\chi_1,\chi_2)$ by means of the formula

$$e^{\mathcal{F}(\chi_1,\chi_2)} = \sum_{N_1,N_2} e^{-iN_1\chi_1 - iN_2\chi_2} P_t(N_1,N_2) \quad (5)$$

with $\chi_{1,2}$ being the counting fields, one can express the average currents through the junctions $I_r = \langle \hat{I}_r(t) \rangle$, and the current–current correlation functions

$$S_{rr'} = \frac{1}{2} \int \mathrm{d}t \left[\left\langle \hat{I}_r(t_0+t) \hat{I}_{r'}(t_0) + \hat{I}_{r'}(t_0) \hat{I}_r(t_0+t) \right\rangle - 2 \left\langle I_r(t_0) \right\rangle \left\langle I_{r'}(t_0) \right\rangle \right] \quad (6)$$

in the following form

$$I_r = \lim_{t\to 0} \frac{ie}{t} \frac{\partial \mathcal{F}}{\partial \chi_r}\bigg|_{\chi_r=0}, \quad S_{rr'} = -\lim_{t\to 0} \frac{e^2}{t} \frac{\partial^2 \mathcal{F}}{\partial \chi_r \partial \chi_{r'}}\bigg|_{\chi_r=0}. \quad (7)$$

The cumulant generating function $\mathcal{F}$ in Equation 5 be evaluated in a general form with the aid of the path integral technique [22,25], which yields

$$\mathcal{F}(\chi_1,\chi_2) = \mathrm{tr}\left[\ln \hat{\mathcal{G}}^{-1}(\chi_1,\chi_2) \right], \quad (8)$$

where $\hat{\mathcal{G}}^{-1}$ is the Keldysh Green function of our system

$$\mathcal{G}^{-1}(\chi_1,\chi_2) = \begin{pmatrix} \check{G}_1^{-1} & \check{t}_1(\chi_1) & 0 \\ \check{t}_1^{\dagger}(\chi_1) & \check{G}_S^{-1} & \check{t}_2(\chi_2) \\ 0 & \check{t}_2^{\dagger}(\chi_2) & \check{G}_2^{-1} \end{pmatrix}, \quad (9)$$

the 4 × 4 matrices $\check{G}_j^{-1}$ represent the inverse Keldysh Green functions of isolated normal and superconducting leads and $\check{t}_r$ is the diagonal 4 × 4 matrix in the Nambu–Keldysh space describing tunneling between the leads,

$$\check{t}_r(\chi_r) = \begin{pmatrix} -t_r e^{-i\frac{\chi_r}{2}} & 0 & 0 & 0 \\ 0 & t_r e^{i\frac{\chi_r}{2}} & 0 & 0 \\ 0 & 0 & t_r e^{i\frac{\chi_r}{2}} & 0 \\ 0 & 0 & 0 & -t_r e^{-i\frac{\chi_r}{2}} \end{pmatrix}. \quad (10)$$

Further analysis of the general expression for the function $\mathcal{F}$ (Equation 8) is essentially identical to that already carried out in [25]. Therefore, it is not necessary to go into details here. Employing Equation 7 and making use of the results [25], we recover general expressions for both the currents I_r across the junctions and the cross-correlated current noise S_{12} in the presence of a temperature gradient between two normal terminals.

In what follows we will be particularly interested in the limit of low voltages and temperatures $eV_{1,2}, T_{1,2} \ll \Delta$. In this case, I_r (containing both local and non-local components) is practically insensitive to temperature and matches with the results [6,7,10] derived earlier in the corresponding limit.

For the non-local current noise in the same limit $eV_{1,2}, T_{1,2} \ll \Delta$ we obtain

$$
\begin{aligned}
S_{12} = & \frac{e^4 R_0^S}{\pi^2 \hbar^2} \sum_{n,m} \int \mathrm{d}E A_{1,n} A_{2,m} \\
& \times \Bigg\{ \frac{\left(1-2A_{1,n}\right)\left(1-2A_{2,m}\right)}{\sqrt{A_{1,n}A_{2,m}}} \Big[w\left(n_1^-, n_2^+\right) + w\left(n_1^+, n_2^-\right) - w\left(n_1^-, n_2^-\right) - w\left(n_1^+, n_2^+\right) \Big] \\
& + w\left(n_1^-, n_2^+\right) + w\left(n_1^+, n_2^-\right) + w\left(n_1^-, n_2^-\right) - w\left(n_1^+, n_2^+\right) \\
& - 4\Big[\left(1-A_{1,n}\right) w\left(n_1^-, n_1^+\right) + \left(1-A_{2,m}\right) w\left(n_2^-, n_2^+\right) \Big] \\
& - 2A_{1,n}\left(w\left(n_1^-, n_1^-\right) + w\left(n_1^+, n_1^+\right) \right) - 2A_{2,m}\left(w\left(n_2^-, n_2^-\right) + w\left(n_2^+, n_2^+\right) \right) \Bigg\},
\end{aligned}
\tag{11}
$$

where we defined the Andreev reflection probabilities per conducting channel in both junctions

$$
A_{1,n} = \frac{\tau_{1,n}^2}{\left(2-\tau_{1,n}\right)^2}, \quad A_{2,m} = \frac{\tau_{2,m}^2}{\left(2-\tau_{2,m}\right)^2}, \tag{12}
$$

introduced the function

$$
w\left(n_r, n_{r'}\right) = n_r\left(1-n_{r'}\right) + \left(1-n_r\right) n_{r'}. \tag{13}
$$

and employed Fermi distribution functions for electrons and holes in the normal leads

$$
n_r^{\pm} = \frac{1}{1+e^{\left(E \pm eV_r\right)/T_r}}. \tag{14}
$$

Equation 11 defines the low-energy cross-correlated current noise in the presence of a temperature gradient and represents the main general result of the present work.

The expression (Equation 11) contains the integrals of the type $\int \mathrm{d}E\, w\left(n_1^{\pm}, n_2^{\pm}\right)$, which cannot be handled analytically except in some special limits, i.e.,

$$
\int \mathrm{d}E\, w\left(n_1^{\pm}, n_2^{\pm}\right) = e\left(V_1 - V_2\right) \coth \frac{e\left(V_1 - V_2\right)}{2T} \tag{15}
$$

for $T_1 = T_2 = T$ and

$$
\int \mathrm{d}E\, w\left(n_1^{\pm}, n_2^{\pm}\right) = T_1 \ln\left(2 + 2\coth \frac{e\left(V_1 - V_2\right)}{T_1} \right) \tag{16}
$$

for $T_1 \gg T_2$. In the opposite limit $T_2 \gg T_1$ in Equation 16 one should simply interchange $T_1 \leftrightarrow T_2$.

In order to proceed, we note that there exists a very accurate interpolation formula between the above limits. It reads

$$
\int \mathrm{d}E\, w\left(n_1^{\pm}, n_2^{\pm}\right) \simeq T_{\mathrm{eff}} \ln\left(2 + 2\coth \frac{e\left(V_1 - V_2\right)}{T_{\mathrm{eff}}} \right), \tag{17}
$$

where we defined an effective temperature

$$
T_{\mathrm{eff}} = \frac{T}{\ln 2} \sqrt{1 + \frac{\left(\delta T\right)^2}{T^2}\left(\ln^2 2 - 1/4\right)} \tag{18}
$$

and introduced the notations $T = (T_1 + T_2)/2$ and $\delta T = T_1 - T_2$.

With the aid of this interpolation, the non-local noise (Equation 11) can be reduced to a much simpler form

$$
\begin{aligned}
S_{12} \simeq & G_{12} T_{\mathrm{eff}} \Bigg[\gamma_+ \ln\left(2 + 2\cosh \frac{e\left(V_1 + V_2\right)}{T_{\mathrm{eff}}} \right) \\
& - \gamma_- \ln\left(2 + 2\cosh \frac{e\left(V_1 - V_2\right)}{T_{\mathrm{eff}}} \right) \\
& - 4G_{12} \Bigg[\beta_1 eV_1 \coth \frac{eV_1}{T_1} + \left(1-\beta_1\right) T_1 \\
& + \beta_2 eV_2 \coth \frac{eV_2}{T_2} + \left(1-\beta_2\right) T_2 \Bigg] \Bigg].
\end{aligned}
\tag{19}
$$

Here we have introduced the non-local conductance in the limit of zero temperature and zero bias voltage,

$$G_{12} = \frac{2e^4 R_0^S}{\pi^2}\left(\sum_n A_{1,n}\right)\left(\sum_m A_{2,m}\right), \tag{20}$$

R_0^S being the normal state resistance of a superconducting island [25], as well as the parameters

$$\gamma_\pm = \frac{\sum_{n,m} A_{1,n}A_{2,m}\left(\dfrac{\left(1-2A_{1,n}\right)\left(1-2A_{2,m}\right)}{\sqrt{A_{1,n}A_{2,m}}} \pm 1\right)}{\sum_{n,m} A_{1,n}A_{2,m}}, \tag{21}$$

and the local Fano factors for two barriers in the Andreev reflection regime

$$\beta_1 = \frac{\sum_n A_{1,n}\left(1-A_{1,n}\right)}{\sum_n A_{1,n}}, \quad \beta_2 = \frac{\sum_m A_{2,m}\left(1-A_{2,m}\right)}{\sum_m A_{2,m}}. \tag{22}$$

At zero bias voltages $V_1 = V_2 = 0$, we obtain the noise in the form

$$S_{12} \simeq 4G_{12}\left(T_{\text{eff}} \ln 2 - 2T\right). \tag{23}$$

Hence, for the excess non-local noise $\delta S_{12} = S_{12}(T,\delta T) - S_{12}(T,0)$ induced by the temperature gradient we get

$$\delta S_{12} = 4G_{12}T\left(\sqrt{1+\frac{(\delta T)^2}{T^2}\left(\ln^2 2 - 1/4\right)} - 1\right). \tag{24}$$

This contribution is positive and reaches its maximum $\delta S_{12} \simeq 0.44 G_{12} T$ at $|\delta T| = T$.

The effect of the temperature gradient on cross-correlated non-local noise remains appreciable also at non-zero bias voltages $V_{1,2}$, in which case it essentially depends on transmission distributions in both junctions.

We start from the tunneling limit $A_{1,n}, A_{2,m} \ll 1$, where one has

$$\gamma_+ = \gamma_- \equiv \gamma = \frac{\sum_{n,m}\sqrt{A_{1,n}A_{2,m}}}{\sum_{n,m} A_{1,n}A_{2,m}} \gg 1. \tag{25}$$

Keeping only the terms $\propto \gamma_\pm$ in the expression (Equation 19), we obtain

$$S_{12} \simeq G_{12}T_{\text{eff}}\gamma\left[\ln\left(2+2\cosh\frac{e\left(V_1+V_2\right)}{T_{\text{eff}}}\right) - \ln\left(2+2\cosh\frac{e\left(V_1-V_2\right)}{T_{\text{eff}}}\right)\right]. \tag{26}$$

The first and the second terms on the right-hand side of this formula are attributed, respectively, to CAR and EC processes. We observe that, similarly to the limit $\delta T = 0$, the noise cross correlations remain positive, $S_{12} > 0$, provided V_1 and V_2 have the same sign, and they turn negative, $S_{12} < 0$, should V_1 and V_2 have different signs. The result is also illustrated in Figure 3.

In the opposite limit of perfectly conducting channels in both junctions with $\tau_{1,n} = \tau_{2,m} = 1$ one gets $\gamma_+ = 2$, $\gamma_- = 0$, $\beta_1 = \beta_2 = 0$. Hence, in this case, Equation 19 yields

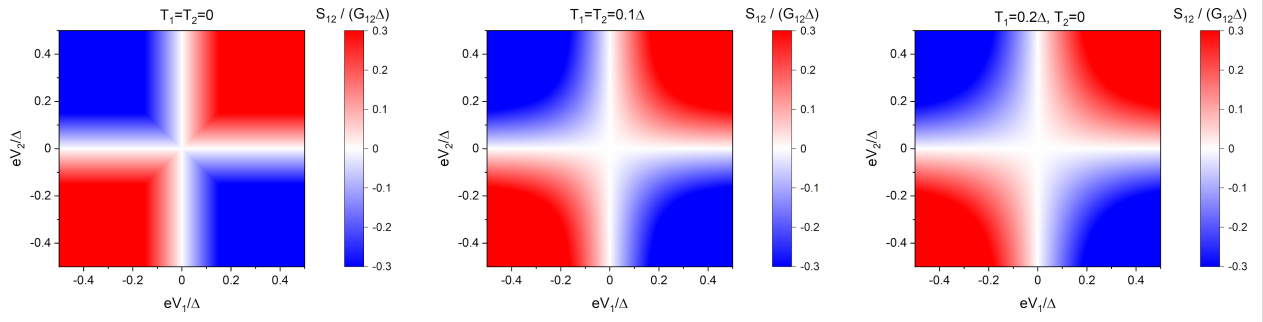

Figure 3: Non-local noise S_{12} (Equation 26) in the tunneling limit (Equation 25). Left panel: $T = 0$; middle panel: $T = 0.1\Delta$, $\delta T = 0$; right panel: $|\delta T| = T = 0.1\Delta$.

$$S_{12} \simeq 2G_{12}\left[T_{\text{eff}} \ln\left(2+2\cosh\frac{e\left(V_1+V_2\right)}{T_{\text{eff}}}\right)-4T\right]. \quad (27)$$

This result is always positive at non-zero bias and sufficiently low temperatures, indicating the importance of CAR processes in this limit, see also Figure 4.

Yet another important physical limit is realized provided the contact has the form of a short diffusive wire with the corresponding Thouless energy exceeding the superconducting gap Δ. In this diffusive limit the transmission probability distributions in both junctions are defined by the well-known formula

$$P_r\left(\tau_r\right)=\frac{\pi}{2e^2R_r^N}\frac{1}{\tau_r\sqrt{1-\tau_r}}, \quad r=1,2 \quad (28)$$

with R_r^N being the resistances of diffusive contacts in the normal state. Making use of this formula, one readily finds $\gamma_\pm = \pm 1$ and $\beta_1 = \beta_2 = 1/3$. Then Equation 19 reduces to

$$S_{12} \simeq G_{12}T_{\text{eff}}\sum_{\pm}\ln\left(2+2\cosh\frac{e\left(V_1\pm V_2\right)}{T_{\text{eff}}}\right) -\frac{4}{3}G_{12}\left(4T+\sum_{r=1,2}eV_r\coth\frac{eV_r}{T_r}\right). \quad (29)$$

This result is also displayed in Figure 5.

Conclusion

Comparing the non-local shot noise pattern in all the above limits, we can make several important conclusions. First, in full accordance with our previous results [22,25], this pattern turns out to be markedly different depending on particular transmission distributions for intermetallic barriers, thus emphasizing different roles played by CAR and EC processes. Second, relative contributions of the latter processes can be reliably controlled by applied external bias voltages V_1 and V_2 as well as by varying temperature T. Third, we observe that the non-local shot noise patterns undergoes additional modifications provided a temperature gradient is applied to our structure. Hence, the temperature gradient, along with other parameters, can also serve as a possible extra tool to control and tune the process of

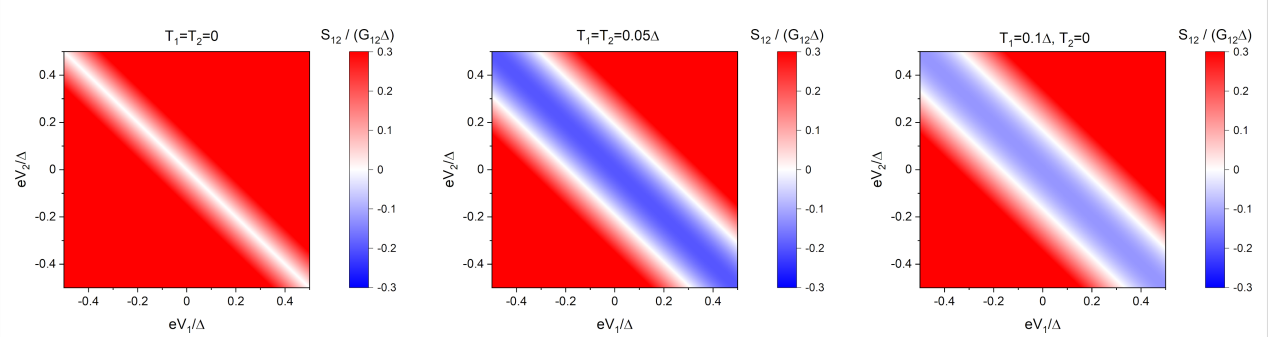

Figure 4: Non-local noise S_{12} (Equation 27) in the case of fully transparent junctions. Left panel: $T = 0$; middle panel: $T = 0.05\Delta$, $\delta T = 0$; right panel: $|\delta T| = T = 0.05\Delta$.

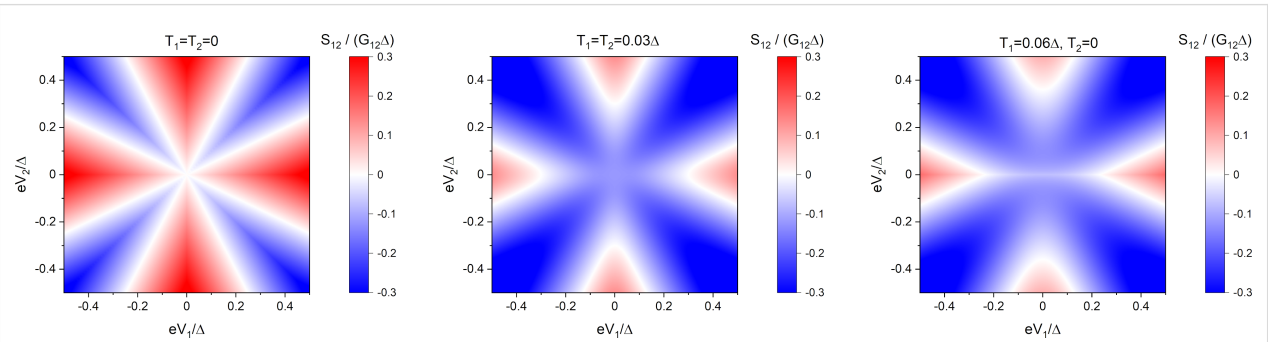

Figure 5: Non-local noise S_{12} (Equation 29) in the case of diffusive barriers. Left panel: $T = 0$; middle panel: $T = 0.03\Delta$, $\delta T = 0$; right panel: $|\delta T| = T = 0.03\Delta$.

Cooper pair splitting in multiterminal hybrid normal–superconducting metallic structures.

References

1. Belzig, W.; Wilhelm, F. K.; Bruder, C.; Schön, G.; Zaikin, A. D. *Superlattices Microstruct.* **1999,** *25,* 1251–1288. doi:10.1006/spmi.1999.0710
2. Deutscher, G.; Feinberg, D. *Appl. Phys. Lett.* **2000,** *76,* 487–489. doi:10.1063/1.125796
3. Lesovik, G. B.; Martin, T.; Blatter, G. *Eur. Phys. J. B* **2001,** *24,* 287–290. doi:10.1007/s10051-001-8675-4
4. Falci, G.; Feinberg, D.; Hekking, F. W. J. *Europhys. Lett.* **2001,** *54,* 255–261. doi:10.1209/epl/i2001-00303-0
5. Brinkman, A.; Golubov, A. A. *Phys. Rev. B* **2006,** *74,* 214512. doi:10.1103/physrevb.74.214512
6. Kalenkov, M. S.; Zaikin, A. D. *Phys. Rev. B* **2007,** *75,* 172503. doi:10.1103/physrevb.75.172503
7. Kalenkov, M. S.; Zaikin, A. D. *Phys. Rev. B* **2007,** *76,* 224506. doi:10.1103/physrevb.76.224506
8. Morten, J. P.; Brataas, A.; Belzig, W. *Phys. Rev. B* **2006,** *74,* 214510. doi:10.1103/physrevb.74.214510
9. Golubev, D. S.; Zaikin, A. D. *Phys. Rev. B* **2007,** *76,* 184510. doi:10.1103/physrevb.76.184510
10. Golubev, D. S.; Kalenkov, M. S.; Zaikin, A. D. *Phys. Rev. Lett.* **2009,** *103,* 067006. doi:10.1103/physrevlett.103.067006
11. Beckmann, D.; Weber, H. B.; v. Löhneysen, H. *Phys. Rev. Lett.* **2004,** *93,* 197003. doi:10.1103/physrevlett.93.197003
12. Russo, S.; Kroug, M.; Klapwijk, T. M.; Morpurgo, A. F. *Phys. Rev. Lett.* **2005,** *95,* 027002. doi:10.1103/physrevlett.95.027002
13. Cadden-Zimansky, P.; Chandrasekhar, V. *Phys. Rev. Lett.* **2006,** *97,* 237003. doi:10.1103/physrevlett.97.237003
14. Hofstetter, L.; Csonka, S.; Nygård, J.; Schönenberger, C. *Nature* **2009,** *461,* 960–963. doi:10.1038/nature08432
15. Kleine, A.; Baumgartner, A.; Trbovic, J.; Golubev, D. S.; Zaikin, A. D.; Schönenberger, C. *Nanotechnology* **2010,** *21,* 274002. doi:10.1088/0957-4484/21/27/274002
16. Brauer, J.; Hübler, F.; Smetanin, M.; Beckmann, D.; v. Löhneysen, H. *Phys. Rev. B* **2010,** *81,* 024515. doi:10.1103/physrevb.81.024515
17. Schindele, J.; Baumgartner, A.; Schönenberger, C. *Phys. Rev. Lett.* **2012,** *109,* 157002. doi:10.1103/physrevlett.109.157002
18. Kolenda, S.; Wolf, M. J.; Golubev, D. S.; Zaikin, A. D.; Beckmann, D. *Phys. Rev. B* **2013,** *88,* 174509. doi:10.1103/physrevb.88.174509
19. Blanter, Y. M.; Büttiker, M. *Phys. Rep.* **2000,** *336,* 1–166. doi:10.1016/s0370-1573(99)00123-4
20. Börlin, J.; Belzig, W.; Bruder, C. *Phys. Rev. Lett.* **2002,** *88,* 197001. doi:10.1103/physrevlett.88.197001
21. Bignon, G.; Houzet, M.; Pistolesi, F.; Hekking, F. W. J. *Europhys. Lett.* **2004,** *67,* 110–116. doi:10.1209/epl/i2003-10293-9
22. Golubev, D. S.; Zaikin, A. D. *Phys. Rev. B* **2010,** *82,* 134508. doi:10.1103/physrevb.82.134508
23. Freyn, A.; Flöser, M.; Mélin, R. *Phys. Rev. B* **2010,** *82,* 014510. doi:10.1103/physrevb.82.014510
24. Flöser, M.; Feinberg, D.; Mélin, R. *Phys. Rev. B* **2013,** *88,* 094517. doi:10.1103/physrevb.88.094517
25. Golubev, D. S.; Zaikin, A. D. *Phys. Rev. B* **2019,** *99,* 144504. doi:10.1103/physrevb.99.144504
26. Wei, J.; Chandrasekhar, V. *Nat. Phys.* **2010,** *6,* 494–498. doi:10.1038/nphys1669
27. Das, A.; Ronen, Y.; Heiblum, M.; Mahalu, D.; Kretinin, A. V.; Shtrikman, H. *Nat. Commun.* **2012,** *3,* 1165. doi:10.1038/ncomms2169
28. Ranni, A.; Brange, F.; Mannila, E. T.; Flindt, C.; Maisi, V. F. *Nat. Commun.* **2021,** *12,* 6358. doi:10.1038/s41467-021-26627-8
29. Lumbroso, O. S.; Simine, L.; Nitzan, A.; Segal, D.; Tal, O. *Nature* **2018,** *562,* 240–244. doi:10.1038/s41586-018-0592-2

License and Terms

BEILSTEIN JOURNAL OF NANOTECHNOLOGY

A distributed active patch antenna model of a Josephson oscillator

Vladimir M. Krasnov

Full Research Paper

Open Access

Address:
Department of Physics, Stockholm University, AlbaNova University Center, SE-10691 Stockholm, Sweden

Email:
Vladimir M. Krasnov - Vladimir.Krasnov@fysik.su.se

Keywords:
antenna theory; cavity modes; Josephson effect; terahertz radiation

Beilstein J. Nanotechnol. **2023,** *14,* 151–164.
https://doi.org/10.3762/bjnano.14.16

Received: 11 November 2022
Accepted: 13 January 2023
Published: 26 January 2023

This article is part of the thematic issue "Intrinsic Josephson effect and prospects of superconducting spintronics".

Associate Editor: J. M. van Ruitenbeek

Abstract

Optimization of Josephson oscillators requires a quantitative understanding of their microwave properties. A Josephson junction has a geometry similar to a microstrip patch antenna. However, it is biased by a dc current distributed over the whole area of the junction. The oscillating electric field is generated internally via the ac-Josephson effect. In this work, I present a distributed, active patch antenna model of a Josephson oscillator. It takes into account the internal Josephson electrodynamics and allows for the determination of the effective input resistance, which couples the Josephson current to cavity modes in the transmission line formed by the junction. The model provides full characterization of Josephson oscillators and explains the origin of the low radiative power efficiency. Finally, I discuss the design of an optimized Josephson patch oscillator capable of reaching high efficiency and radiation power for emission into free space.

Introduction

A flux-flow oscillator (FFO) is the most extensively studied Josephson source of high-frequency electromagnetic waves (EMW) [1-12]. A FFO was used in the first direct demonstration of Josephson emission by Yanson et al., back in 1965 [13,14]. State of the art FFOs, developed by Koshelets and co-workers show a remarkable performance in terms of tunability and linewidth [6,9,12]. However, they emit very little power into free space [11,13,15,16]. The low radiation power efficiency, that is, the ratio of radiated to dissipated power, is commonly attributed to a large impedance mismatch between a Josephson junction (JJ) and free space [10,16,17]. But there is no consensus about the value of the junction impedance: Is it very small [16] or, in contrast, very large [10]? At present, there is no clear understanding about what causes the impedance mismatch and which geometrical parameters should be changed for solving the problem. The discovery of significant terahertz emission from stacked intrinsic JJs in layered high-T_c cuprates [18-27] further emphasizes the necessity of a quantitative understanding of microwave emission from Josephson oscillators.

Figure 1a shows a sketch of a typical FFO. It is based on a sandwich-type (overlap) JJ with the length, $a \gg \lambda_J$, much larger than the Josephson penetration depth, and both in-plane sizes much larger than the thickness of the junction interface, $d \ll b \ll a$. The in-plane magnetic field, H_y, introduces a chain of Josephson vortices (fluxons) in the JJ. The dc bias current, I_b, exerts a Lorentz force, F_L, and causes a unidirectional fluxon motion. Upon collision with the junction edge, the fluxons annihilate. The released energy produces an EMW pulse, which is partially emitted but mostly reflected backwards in the JJ. Propagation and reflection of FFO pulses in the transmission line (TL) formed by the JJ leads to the formation of standing waves. The corresponding cavity mode resonances are manifested by Fiske steps in the current–voltage (I–V) characteristics [16,28-32]. FFOs exhibit sharp emission maxima at the Fiske steps [9,12,13]. Such a conditional emission indicates that several additional and equally important phenomena (apart from the ac-Josephson effect) are involved in FFO operation [10]. The excitation of high-quality factor, $Q \gg 1$, cavity modes is one of them.

Geometry is playing a decisive role for characteristics of microwave devices. Although calculations of radiative impedances of JJs do exist [33], they were not made for the FFO geometry. From the outside, the overlap JJ looks like a well-known microstrip patch antenna [34-36]. The difference, however, is inside. A standard patch antenna has a point-like feed-in port, while in a JJ the bias current is distributed over the whole area of the JJ. Furthermore, the oscillating component of the current is actively generated inside the JJ by means of the ac-Josephson effect and the flux-flow phenomenon. Therefore, a JJ can be considered as an actively pumped patch antenna with a distributed feed-in current.

In this work, I present a distributed, active patch antenna model of a Josephson oscillator. It expands the TL model of a patch antenna [36], taking into account the spatial distribution of the input current density in a JJ, described by the perturbed sine-Gordon equation. In the presence of a magnetic field and fluxons, the oscillating current is distributed nonuniformly within the junction. This nonuniformity is essential for the FFO operation. It determines the variable input resistance, which enables the coupling of the Josephson current to cavity mode resonances in the junction. The presented model allows for the application of many of patch antenna results and facilitates full characterization of Josephson oscillators, including the emission power, directivity, and power efficiency. The model explains the origin of the low power efficiency for emission in free space and clarifies which parameters can be changed to improve the FFO characteristics. Finally, I discuss the design of a Josephson patch oscillator that can reach high power for emission in free space with the optimal power efficiency of approx. 50%.

Results

The spatial-temporal distribution of voltage in a JJ is described by the equation (see chapter 9 in [31]):

$$\frac{\partial^2 V}{\partial x^2}+\frac{\partial^2 V}{\partial y^2}-\frac{1}{c_0^2}\frac{\partial^2 V}{\partial t^2}=L_{\square}\frac{\partial J_z}{\partial t}, \tag{1}$$

where c_0 is the (Swihart) velocity of EMWs in the TL formed by the JJ and $L_{\square}$ is the inductance of JJ per square. J_z is the current density through the JJ, which has Cooper pair and quasiparticle (QP) components,

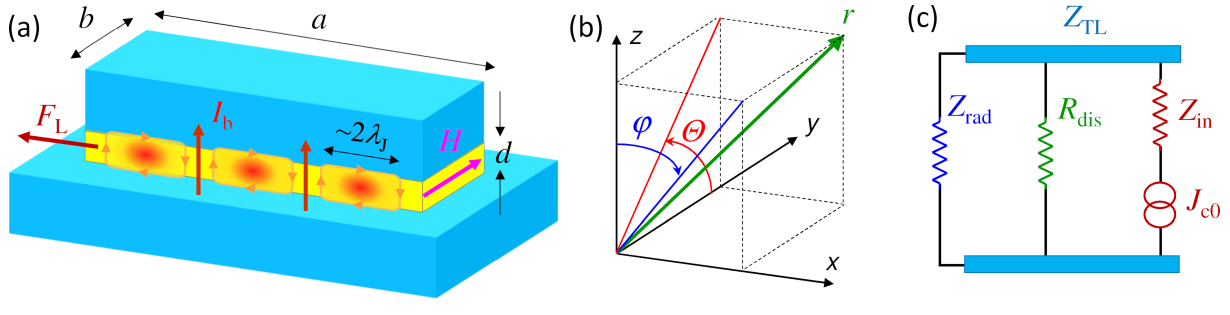

Figure 1: (a) A sketch of the Josephson flux-flow oscillator. It is based on a sandwich-type junction with two superconducting electrodes (light blue) separated by a dielectric interlayer (yellow). Red ovals represent Josephson vortices that are driven by the Lorentz force, F_L, exerted by the dc bias current, I_b. From the outside, the junction has a patch antenna geometry. However, inside it is driven by a distributed dc current, and the oscillating voltage is generated internally by a combination of the ac-Josephson effect and the flux-flow phenomenon. (b) Clarification of spatial and angular coordinates. (c) An equivalent circuit of the Josephson junction. The ac-Josephson effect provides a source of the high-frequency alternating current with the fixed amplitude of current density, J_{c0}. The oscillating voltage at the junction edges is generated by means of the input junction impedance, Z_{in}, and is distributed between the internal dissipative resistance, R_{dis}, and the external radiative impedence, Z_{rad}, connected by the transmission line impedance Z_{TL}.

$$J_z = J_{c0}\sin\eta + \frac{V}{r_{QP}}. \quad (2)$$

Here, J_{c0} is the Josephson critical current density, η is the Josephson phase difference, and $r_{QP} = R_{QP}ab$ is the QP resistance per unit area.

Active patch antenna model of a junction

Equation 1 is the equation for an active TL [37] with a distributed feed-in current density J_z. Therefore, a JJ has many similarities with the microstrip patch antenna. However, there are three main differences:

(i) The feed-in geometry. A patch antenna has a point-like feed-in port, through which the oscillating current is applied [34-36]. The FFO is biased by a dc current distributed over the whole JJ area.

(ii) The excitation scheme. A patch antenna is a linear oscillator pumped by a harmonic signal. In contrast, a JJ is biased by a dc-current and the oscillatory component is generated inside the JJ via the ac-Josephson effect and the flux-flow phenomenon.

(iii) The slow propagation speed of EMWs inside the JJ, $c_0 \ll c$. This is caused by a large kinetic inductance of superconducting electrodes. For Nb-based JJs, $c/c_0 \approx 40$ (see the estimation in section Discussion). For atomic-scale intrinsic JJs in layered cuprates, c_0 can be almost 1000 times slower than c [32]. Because of that, the wavelength inside the JJ is much smaller than in free space, $\lambda \ll \lambda_0$. Therefore, a JJ corresponds to a patch antenna with an extraordinary large effective permittivity, $\varepsilon_r^* = (c/c_0)^2$.

The dynamics of a JJ is described by a nonlinear perturbed sine-Gordon equation,

$$\frac{\partial^2\eta}{\partial\tilde{x}^2} - \frac{\partial^2\eta}{\partial\tilde{t}^2} - \alpha\frac{\partial\eta}{\partial\tilde{t}} = \sin\eta - \tilde{J}_b. \quad (3)$$

It follows from Equation 1 and Equation 2, taking into account the ac-Josephson relation, $V = (\Phi_0/2\pi)\partial\eta/\partial t$. Equation 3 is written in a dimensionless form with space, $\tilde{x} = x/\lambda_J$, normalized by λ_J,and time, $\tilde{t} = \omega_p t$, by the Josephson plasma frequency, ω_p. Here α is the QP damping factor, and $\tilde{J}_b = J_b/J_{c0}$ is the normalized bias current density, which originates from the $\partial^2 V/\partial y^2$ term in Equation 1 [38]. In what follows, "tilde" will indicate dimensionless variables, $\tilde{\omega} = \omega/\omega_p$ and $\tilde{k} = \lambda_J k$. The definition of and the interconnection between different variables are clarified in the Appendix section.

Radiative resistance of a patch antenna

A rectangular patch antenna has two radiating slots, which correspond to the left and right edges of the JJ in Figure 1a. The slots can be considered as magnetic current lines (magnetic dipoles) [39]. Radiation from the antenna is determined by the radiative impedance, Zrad. For a patch with a very thin insulator (as is the case for a tunnel JJ), the radiative admittance of one slot, $1/Z_{rad1} = G_1 + iB_1$, contains a large imaginary part B_1, caused by the large capacitance. However, at the cavity mode resonance the imaginary contributions from the two slots cancel out [34,36,39] and the radiative impedance becomes real. Therefore, at the resonance the radiation power from one slot is

$$P_1 = G_1\frac{|v(0,a)|^2}{2}, \quad (4)$$

where $|v(0,a)|$ is the amplitude of voltage oscillations at the slot ($x = 0,a$) and G_1 is the radiative conductance of the single slot. Low-T_c JJs are operating at sub-terahertz frequencies, for which the wavelength in free space is large, $\lambda_0 \gg b \gg d$. In this limit [36,39],

$$G_1 = \frac{4\pi}{3Z_0}\left[\frac{b}{\lambda_0}\right]^2, \quad (b \ll \lambda_0) \quad (5)$$

where $Z_0 = \sqrt{\mu_0/\varepsilon_0} \simeq 376.73$ (Ω) is the impedance of free space.

To calculate the total radiation power from both slots one has to take into account the mutual radiative conductance, G_{12}, and the array factor AF [36]. G_{12} is originating from a cross product of electric and magnetic fields generated by different slots. For $\lambda_0 \gg b \gg d$ it is equal to [36,40]

$$G_{12} = \frac{\pi}{Z_0}\left[\frac{b}{\lambda_0}\right]^2\int_0^\pi J_0\left(k_0 a\sin\Theta\right)\sin^3\Theta d\Theta. \quad (6)$$

Here, J_0 is the zeroth-order Bessel function, $k_0 = 2\pi/\lambda_0$ is the wave number in free space, and the angle Θ is defined in Figure 1b. For the n-th cavity mode,

$$k_n = \frac{\pi}{a}n, \quad \omega_n = c_0 k_n, \quad (7)$$

the argument of J_0 becomes $(c_0/c)\pi n\sin\Theta$. Since $c_0 \ll c$, k_0a is small. Expanding in Equation 6, $J_0(x) \simeq 1 - x^2/4$ (for $x \ll 1$), we obtain:

$$G_{12} \simeq G_1\left[1-\frac{2}{5}\left(\frac{c_0}{c}\pi n\right)^2\right], \quad \left(\frac{c_0}{c}\pi n \ll 1\right). \tag{8}$$

It is seen that the mutual conductance for a JJ with thin electrodes (slow c_0) is not negligible and can be as big as the single-slot conductance G_1, Equation 5.

The array factor takes into account the interference of electromagnetic fields from the two slots in the far field. It depends on the separation between the slots, a, the relative phase shift, β, and the direction (φ,Θ). Since radiation from a patch antenna is induced by magnetic current lines, it is more intuitive to consider the interference of magnetic fields, $H_1 + H_2 = \mathrm{AF}H_1$. For the geometry of Figure 1a and Figure 1b, it can be written as [36,40]

$$\mathrm{AF} = 2\cos\left[\frac{1}{2}\left(k_0 a\sin\Theta\sin\varphi+\beta\right)\right]. \tag{9}$$

Odd-number cavity modes have antisymmetric voltage oscillations but symmetric magnetic currents, $\beta = 0$. This leads to a constructive interference with the maximum AF = 2 perpendicular to the patch along the z-axis. For even modes its vice versa, $\beta = \pi$, and a destructive interference leads to a node, AF = 0, along the z-axis.

The total emission power is

$$P_{\mathrm{rad}} = \frac{\left(\left|v(0)\right|^2+\left|v(a)\right|^2\right)G_1 \pm 2\left|v(0)\right|\left|v(a)\right|G_{12}}{2}, \tag{10}$$

where the plus/minus signs are for odd/even modes, respectively. For equal amplitudes, $|v(0)| = |v(a)|$,

$$P_{\mathrm{rad}} = \frac{\left|v(0)\right|^2}{2R_{\mathrm{rad}}}, \tag{11}$$

with the effective radiative resistance

$$P_{\mathrm{rad}} = \frac{1}{1\pm G_{12}/G_1}\frac{3Z_0}{8\pi}\left[\frac{\lambda_0}{b}\right]^2. \tag{12}$$

Determination of voltage amplitudes

To calculate P_{rad}, we need voltage amplitudes at the JJ edges. Within the TL model of patch antennas, $v(x)$ is obtained by decomposition into a sum of cavity eigenmodes [34]. For JJs, a similar approach is used for the analysis of Fiske steps [16,29-31]. To separate dc and ac components, we write

$$\eta(x,t) = kx + \omega t + \phi(x,t). \tag{13}$$

Here, $k = 2\pi(\Phi/\Phi_0)/a$ is the phase gradient induced by the external field, where Φ is the flux in the JJ. $\omega = 2\pi\Phi_0 V_{\mathrm{dc}}$ is the angular Josephson frequency proportional to the dc voltage V_{dc}. The last term, ϕ, represents the oscillatory component induced by cavity modes and fluxons. This term generates the ac voltage, which we aim to determine:

$$v(x,t) = \frac{\Phi_0}{2\pi}\frac{\partial\phi}{\partial t}. \tag{14}$$

Small-amplitude, multimode analysis

In the small-amplitude limit, $\phi \ll 1$, a perturbation approach can be used. A linear expansion of Equation 3 yields [16,29,31],

$$\frac{\partial^2\phi}{\partial\tilde{x}^2}-\frac{\partial^2\phi}{\partial\tilde{t}^2}-\alpha\frac{\partial\phi}{\partial\tilde{t}} = \sin(kx+\omega t)+\cos(kx+\omega t)\phi-\Delta\tilde{J}_{\mathrm{b}}. \tag{15}$$

Here, $\Delta\tilde{J}_{\mathrm{b}} = \tilde{J}_{\mathrm{b}} - \alpha\tilde{\omega}$ is the excess dc current with respect to the ohmic QP line. It is caused by the second term on the right-hand side, which enables nonlinear rectification of the Josephson current. The excess dc current is defined as

$$\Delta I = I_{\mathrm{c0}}\lim_{T\to\infty}\frac{1}{T}\int_0^T \mathrm{d}t\frac{1}{a}\int_0^a \cos(kx+\omega t)\phi\,\mathrm{d}x. \tag{16}$$

The oscillatory part is described by the equation

$$\frac{\partial^2\phi}{\partial\tilde{x}^2}-\frac{\partial^2\phi}{\partial\tilde{t}^2}-\alpha\frac{\partial\phi}{\partial\tilde{t}} = \sin(kx+\omega t). \tag{17}$$

A comparison with Equation 1 shows that this is the active TL equation in which the supercurrent wave, $\sin(kx + \omega t)$, acts as a distributed (x,t)-dependent drive.

To obtain ϕ, a decomposition into cavity eigenmodes is made [15,16,29,31], similar to the TL analysis of patch antennas [34-36]:

$$\phi(x,t) = -ie^{i\omega t}\sum_{n=1}^{\infty} g_n \cos(k_n x). \tag{18}$$

Note that Equation 18 does not include the dc term, $n = 0$, which is accounted for in $\Delta\tilde{J}_b$ instead, so that ϕ generates solely ac voltage, as described by Equation 14. Substituting Equation 18 in Equation 17 and taking into account the orthogonality of eigenfunctions, one obtains

$$g_n = \frac{B_n + iC_n}{\tilde{\omega}^2 - \tilde{k}_n^2 - i\alpha\tilde{\omega}}, \tag{19}$$

$$B_n = \frac{\sin(k-k_n)a}{(k-k_n)a} + \frac{\sin(k+k_n)a}{(k+k_n)a}, \tag{20}$$

$$C_n = -\frac{1-\cos(k-k_n)a}{(k-k_n)a} + \frac{1-\cos(k+k_n)a}{(k+k_n)a}. \tag{21}$$

From Equation 14, voltage amplitudes at radiating slots are:

$$v(0) = \frac{\Phi_0\omega}{2\pi} e^{i\omega t}\sum_{n=1}^{\infty} g_n, \tag{22}$$

$$v(a) = \frac{\Phi_0\omega}{2\pi} e^{i\omega t}\sum_{n=1}^{\infty} (-1)^n g_n. \tag{23}$$

Excess current

Without geometrical resonances, the dc current, well above the field-dependent critical current, $I \gg I_c(H)$, is determined by the QP resistance, $I = V/R_{QP}$. In dimensionless units, $I/I_{c0} = \alpha V/V_p$, where $V_p = \Phi_0\omega_p/2\pi$ is the voltage at plasma frequency. At resonances, a partial rectification of the oscillating supercurrent occurs, leading to the appearance of Fiske steps in the I–V curves. The excess dc current, obtained from Equation 16, is [16,29,31]

$$\Delta I = \frac{I_{c0}}{4}\sum_{n=1}^{\infty}\left[B_n \operatorname{Im}(g_n) - C_n \operatorname{Re}(g_n)\right] \tag{24}$$

Figure 2a shows calculated I–V characteristics of a JJ with $a = 5\lambda_J$, $\alpha = 0.1$ and at a magnetic field corresponding to $\Phi = 5\Phi_0$ in the JJ. Blue symbols represent the direct numerical simulation of the sine-Gordon Equation 3 for up and down current sweep. The red line shows the analytic solution with the excess current given by Equation 24. The agreement between exact (without linearization) numeric and (approximate) analytic solutions is quite good. It is seen that a series of Fiske steps appear in the I–V. Vertical grid lines mark positions of cavity mode resonances, $\omega/c_0 = k_n$. Fiske steps appear at this condition because of the vanishing of $\tilde{\omega}^2 - \tilde{k}_n^2$ term in the denomi-

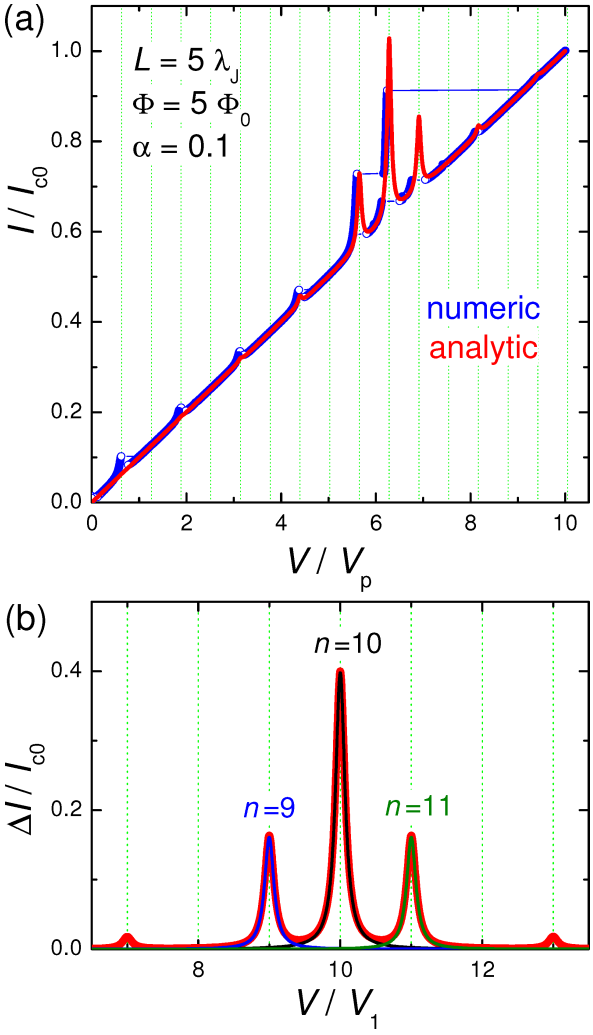

Figure 2: (a) Simulated current–voltage characteristics of a junction with $L = 5\lambda_J$, $\Phi/\Phi_0 = 5$ and $\alpha = 0.1$. Blue symbols represent the full numeric solution of the sine-Gordon equation (up and down current sweep). The red line represents the approximate (perturbative) analytic solution, $I = V/R_{QP} + \Delta I$. (b) Excess dc current, $\Delta I(V)$, at Fiske steps. The thick red line represents the multimode analytic solution, Equation 24. Thin blue, black, and olive lines show single-mode solutions for $n = 9$, 10, and 11, respectively. Vertical grid lines in (a) and (b) mark Fiske step voltages. Voltages are normalized by (a) the plasma frequency voltage, V_p, and (b) the lowest Fiske step voltage, V_1.

nator of g_n, Equation 19. The main step occurs at the double resonance condition, $\omega/c_0 = k_n = k$. It happens at $n = 2\Phi/\Phi_0$ and leads to the vanishing of $(k - k_n)$ in the denominators of Equation 20 and Equation 21. The condition, $\omega/c_0 = k$, is referred to as the velocity matching because at this point the velocity of the fluxon chain (or phase velocity of the current wave in Equation 17) reaches c_0 [16].

Single-mode analysis

Figure 2b shows the excess current, $\Delta I/I_{c0}$ versus V, normalized by the $n = 1$ Fiske step voltage, $V_1 = \Phi_0 c_0/2a$. Such normalization clearly shows that the main resonance occurs at $n = 2\Phi/\Phi_0 = 10$. The thick red line represents the full multimode solution, Equation 24. Thin blue, black, and olive lines represent a single eigenmode contribution for $n = 9$, 10, and 11, respectively. A perfect coincidence with the red line indicates that for underdamped JJs, $\alpha \ll 1$, it is sufficient to consider just a single mode. This greatly simplifies the analysis.

For a resonance at mode n,

$$g_n\left(\tilde{\omega} = \tilde{k}_n\right) = \frac{iB_n - C_n}{\alpha \tilde{k}_n}, \tag{25}$$

and

$$\left|v_n(0,a)\right| = \frac{\Phi_0 \omega}{2\pi}\left|g_n\right| = \frac{\Phi_0 \omega_p}{2\pi\alpha} F_n, \tag{26}$$

$$\Delta I = \frac{F_n^2}{4\alpha \tilde{k}_n} I_{c0}, \tag{27}$$

where

$$F_n = \sqrt{B_n^2 + C_n^2}. \tag{28}$$

Large-amplitude case

The described above perturbative approach is valid only for small amplitudes. Simulations in Figure 2a are made for an underdamped JJ, $\alpha = 0.1$. In this case the quality factor of high-order cavity modes is large,

$$Q_n = \omega_n R_{QP} C = \frac{\tilde{\omega}_n}{\alpha} \gg 1,$$

and $|g_n|$ is not small. Since ϕ appears within the sin η term in Equation 3, the maximum possible amplitude of $|g_n|$ is π. This reflects one of the key differences between FFO and patch antenna. The patch antenna is a linear element in which the voltage amplitude is directly proportional to the feed current. A FFO is essentially nonlinear. The amplitude of Josephson phase oscillations will not grow beyond $|g_n| = \pi$. Instead, higher harmonic generation will occur.

Full numerical simulations of the sine-Gordon equation (Equation 3), shown by blue symbols in Figure 2a, reveal that the amplitude of oscillations reach π at the end of the velocity-matching step. This causes a premature switching out of the resonance before reaching the resonant frequency. It is somewhat miraculous that the agreement with the perturbative solution (red line in Figure 2a) is so good. Apparently, it works remarkably well far beyond the range of its formal applicability, $|g_n| \ll 1$.

A general single-mode solution for an arbitrary amplitude was obtained by Kulik [30]. The amplitude at the resonance, $\tilde{\omega} = \tilde{k}_n$, is given by the first solution of the implicit equation [31],

$$J_0\left(\frac{\left|g_n\right|}{2}\right) = \frac{\alpha \tilde{k}_n}{F_n}\left|g_n\right|, \tag{29}$$

where J_0 is the zeroth-order Bessel function. This equation can be easily solved numerically. It is also possible to obtain an approximate analytic solution by expanding $J_0(x) \simeq 1 - x^2/4$ for small x. With such expansion, Equation 29 is reduced to a quadratic equation with the solution

$$\left|g_n\right| = \sqrt{16 + \left(\frac{8\alpha \tilde{k}_n}{F_n}\right)^2} - \frac{8\alpha \tilde{k}_n}{F_n}. \tag{30}$$

For overdamped JJs, $\alpha \gg 1$, it reduces to the small-amplitude result of Equation 25, $|g_n| = F_n/\alpha \tilde{k}_n$. For underdamped JJs, it qualitatively correctly predicts saturation of the amplitude for $\alpha \to 0$, although at a value of 4 instead of π. Thus, Equation 30 provides a simple and sufficiently good approximation for a significantly broader range of damping parameters than Equation 25.

Input resistance

For the practically most important velocity matching mode, $k_n = k$, from Equations 19–21 it follows, $B_n = 1$, $C_n = 0$, $F_n = 1$, leading to a remarkably simple result,

$$\left|v(0,a)\right| = \frac{\Phi_0 \omega_p}{2\pi\alpha} = I_{c0} R_{QP}. \tag{31}$$

This equation has a straightforward meaning illustrated by the equivalent circuit in Figure 1c. A JJ is a source of a spatially

distributed oscillating current, $J_z = J_{c0}\sin(\omega t + kx)$, with a fixed amplitude, J_{c0}, but spatially dependent phase, kx. It couples to the cavity mode via some effective input impedance Z_{in}. Z_{in} depends on ω, k_n and k and is, in general, complex. However, since the phase of the current wave is strongly varying along the junction, it is hard to define the phase shift between current and voltage. Therefore, in what follows, I will be talking about the input resistance, $R_{in} = |Z_{in}|$, defined via the relation

$$\left|v(0,a)\right| = I_{c0}R_{in}. \tag{32}$$

From Equation 26 it follows,

$$R_{in} = R_{QP}F_n. \tag{33}$$

Figure 3a–c shows, respectively, B_n, C_n, and $R_{in}/R_{QP} = F_n$ versus n for the case from Figure 2. Lines are obtained for continuous variation of n in Equation 20 and Equation 21, and circles represent the actual cavity modes with integer n. From Figure 3c, it is seen that R_{in} has a distinct maximum at the velocity matching condition $n = 2\Phi/\Phi_0 = 10$. At this point, $\tilde{\omega} = \tilde{k}_n = \tilde{k}$, the wave numbers of the cavity mode and the current wave coincide, leading to a perfect coupling along the whole length of the JJ. Therefore, $R_{in} = R_{QP}$ and $v = I_{c0}R_{QP}$. For other modes, $k_n \neq k$, the coupling with Josephson current oscillations is much weaker. As seen from Figure 3c, it is oscillating with n. For the particular case with integer Φ/Φ_0, R_{in} vanishes for all even modes. This leads to the absence of corresponding Fiske steps in Figure 2a.

The coupling of a cavity mode to the current wave in the JJ depends on magnetic field and flux in the JJ (via the parameter k). This is illustrated in Figure 3d for $\Phi/\Phi_0 = 5$ (olive line, the same as in Figure 3c), 5.25 (blue), and 5.5 (red). Although the oscillatory behavior of Fiske step amplitudes is well known [16,29,31], the interpretation of such behavior in terms of the input resistance makes a clear connection to the analysis of patch antennas, for which R_{in} is one of the most important parameters. From this point of view, geometrical resonances with large voltage amplitudes appear only for modes coupled to the current source (Josephson oscillations) via a large input resistance, Equation 32. As seen from Figure 3d, the best coupling with maximum, $R_{in} = R_{QP}$, occurs for the velocity-matching step, $n = 2\Phi/\Phi_0$. Modes with $R_{in} = 0$ are not coupled to Josephson oscillations and, therefore, are not excited at all. In particular, there is no coupling to any mode in the absence of an applied field, $R_{in}(H = 0) = 0$. This is why Fiske steps do not appear at zero field.

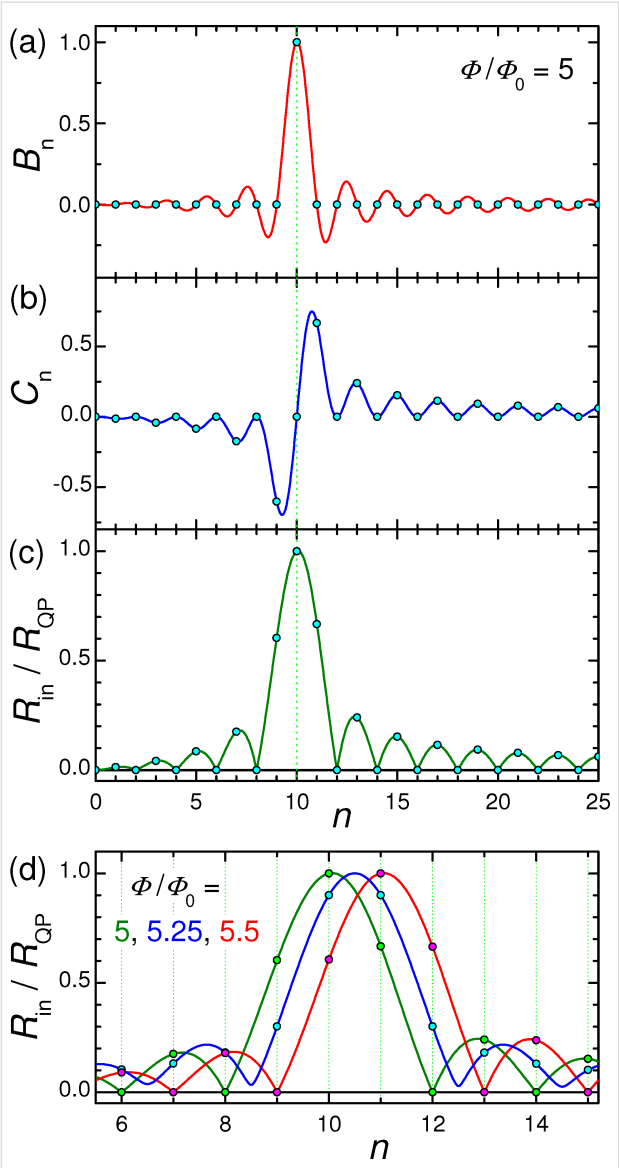

Figure 3: Panels (a) and (b) show mode-number dependence of coefficients B_n and C_n, given by Equation 20 and Equation 21, for the case from Figure 2 with $\Phi/\Phi_0 = 5$. Panel (c) shows the corresponding oscillatory dependence of the input resistance, Equation 28 and Equation 33. (d) Input resistance for $\Phi/\Phi_0 = 5$ (olive), 5.25 (blue) and 5.5 (red). The large R_{in} enables good coupling of the cavity mode to the Josephson current.

Inclusion of radiative losses in a cavity mode analysis

Finally, in order to calculate radiative characteristics, we need to take into consideration radiative losses. In the previous section, only QP losses in a pure cavity eigenmode were considered. Yet, pure eigenmodes, $E_n \propto \cos(k_n x)$, $H_n \propto \sin(k_n x)$, do not emit any radiation because they do not produce ac magnetic fields at the edges $H_n(0,L) = 0$ [36]. Consequently, the Pointing vector is zero. In other words, eigenmodes have infinite radiative impedance, $Z_{rad}(0,L) = E(0,L)/H(0,L) = \infty$. Therefore,

despite large electric fields, the radiated power $P_{\rm rad} \propto E^2/Z_{\rm rad}$ is zero [10].

Radiative losses can be included using the equivalent circuit sketched in Figure 1c. Voltage oscillations at the JJ edges are produced by the oscillating supercurrent via the input resistance, Equation 32. The generated electromagnetic power is distributed between internal losses, characterized by the dissipative resistance, $R_{\rm dis}$, and radiative losses to free space, characterized by the radiative resistance $R_{\rm rad}$. They are connected by the transmission line impedance,

$$Z_{\rm TL} = \sqrt{\frac{\bar{Z}_{\rm surf} + i\omega\bar{L}}{\bar{G}_{\rm QP} + i\omega\bar{C}}}. \tag{34}$$

Here $Z_{\rm surf}$ is the surface impedance of the electrodes, $G_{\rm QP} = 1/R_{\rm QP}$ is the quasiparticle conductance, L is the inductance, and C is the capacitance of the JJ. The bars indicate that the quantities are taken per unit length. For not very high frequencies and temperatures, the surface resistance of Nb electrodes is small (as will be discussed below). For tunnel JJs, $G_{\rm QP}$ is also small. In this case,

$$R_{\rm TL} \simeq \sqrt{\frac{\bar{L}}{\bar{C}}} = Z_0\sqrt{\frac{\Lambda d}{\varepsilon_{\rm r} b^2}}. \tag{35}$$

It is very small because $b \gg \Lambda \gg d$ and can be neglected for all practical cases. Therefore, in Figure 1c we may consider that the dissipative and radiative resistances are connected in parallel. Analysis of patch antennas [36] and numerical calculations for JJs with radiative boundary conditions [10] show that radiative losses can be simply included in the cavity mode analysis by introducing the total quality factor, $Q_{\rm tot}$, of the cavity mode with parallel dissipative and radiative channels,

$$\frac{1}{Q_{\rm tot}} = \frac{1}{Q_{\rm dis}} + \frac{1}{Q_{\rm rad}}. \tag{36}$$

Here, $Q_{\rm dis}$ is associated with all possible dissipative losses, such as QP resistance in the JJ as well as surface resistance in electrodes and dielectric losses while $Q_{\rm rad}$ represents radiative losses,

$$Q_{\rm dis,rad} = \omega C R_{\rm dis,rad}. \tag{37}$$

Using definitions of α and Q, we can introduce a total damping factor

$$\alpha_{\rm tot} = \frac{\omega}{\omega_{\rm p}}\frac{1}{Q_{\rm tot}} = \frac{1}{\omega_{\rm p} C R_{\rm tot}}, \tag{38}$$

where the total resistance is

$$R_{\rm tot} = \frac{R_{\rm dis}R_{\rm rad}}{R_{\rm dis} + R_{\rm rad}}. \tag{39}$$

Thus, to include radiative losses, α and $R_{\rm QP}$ in the equations above should be replaced by $\alpha_{\rm tot}$ and $R_{\rm tot}$. For the n-th cavity mode resonance we obtain,

$$P_{{\rm rad},n} = \frac{I_{\rm c0}^2 R_{\rm tot}^2}{2R_{\rm rad}} F_n^2. \tag{40}$$

For the most important velocity matching resonance from Equation 31, we obtain

$$P_{{\rm rad},k} = \frac{I_{\rm c0}^2 R_{\rm tot}^2}{2R_{\rm rad}}, \tag{41}$$

with $R_{\rm rad}$ and $R_{\rm tot}$ defined in Equation 12 and Equation 39.

Power efficiency

The total power dissipated in a JJ is given by the product of dc voltage and dc current,

$$P_{\rm tot} = VI = \frac{\Phi_0\omega}{2\pi}\left[\alpha_{\rm dis}\tilde{\omega} + \frac{F_n^2}{4\alpha_{\rm dis}\tilde{\omega}}\right] I_{\rm c0}. \tag{42}$$

Here, the left factor is the dc voltage, and the right one is the total dc current. It contains the QP current (first term) and the rectified excess current, ΔI, (second term). The latter is written using Equation 27 at the resonance condition $\tilde{\omega} = \tilde{k}_n$. It is important to note that the nonlinear rectification occurs only inside the JJ. Therefore, the damping parameter $\alpha_{\rm dis}$ within the JJ is used for both terms. The first term in Equation 42 describes dissipative dc losses, which generate only heat, $P_{\rm heat} = V^2/2R_{\rm dis}$. The second term in Equation 42 describes the total power consumed by the cavity mode, $P_{\rm cav} = V\Delta I$. Only this term is participating in radiation. From Equation 39 and Equation 40, we obtain a well-known connection between the radiated power and the power consumed solely by the cavity mode,

$$\frac{P_{\rm rad}}{P_{\rm cav}} = \frac{2R_{\rm dis}R_{\rm rad}}{\left(R_{\rm dis} + R_{\rm rad}\right)^2}. \tag{43}$$

As usual, the maximum emission power is achieved at the matching condition $R_{rad} = R_{dis}$. In this case, exactly one half of the cavity mode power is emitted and another half is dissipated. This is typical for antennas [36] and is consistent with direct simulations for JJs with radiative boundary conditions [10]. Yet, the overall power efficiency is reduced by the "leakage" QP current in Equation 42, which just produces heat. For the I–V curves in Figure 2a, the ohmic QP current is more than twice ΔI at the velocity matching step. Therefore, the total power efficiency, P_{rad}/P_{tot}, for such moderately underdamped JJ will not exceed 50/3 ≃ 17%. Since the leakage current decreases with increasing R_{QP}, strongly underdamped JJs are necessary for reaching a power efficiency of approx. 50%. This is the case for Nb tunnel JJs [9] and for high-quality intrinsic JJs in Bi-2212 high-T_c cuprates, for which the quality factor may exceed several hundreds [32] and ΔI can be several times larger than the leakage QP current [9,32].

Discussion

Estimation of parameters

Let us estimate characteristic impedances for the case of Nb/AlO_x/Nb tunnel JJs, which are used in state-of-the-art FFOs [9,11]. I assume that a = 100 μm, b = 10 μm, d = 2 nm, ε_r = 10, $d_1 = d_2$ = 100 nm, the zero-temperature London penetration depth λ_{L0} = 100 nm, $J_{c0} = 5 \times 10^3$ (A/cm^2), $I_{c0} = J_{c0}ab$ = 50 mA, and the characteristic voltage $I_{c0}R_n$ = 1 mV. This yields, R_n = 20 mΩ, C = 44.25 pF, Λ = 272.6 nm, inductance $L^* = \mu_0 \Lambda a/b$ = 3.43 pH, and $c_0/c = 2.71 \times 10^{-2}$.

Surface resistance

Within the two-fluid model, the surface resistance of two superconducting electrodes can be written as [41]:

$$R_{surf} \simeq \frac{a}{b}\mu_0^2\omega^2\lambda_{L0}^3\sigma_n \frac{\left(T/T_c\right)^4}{\left(1-\left(T/T_c\right)^4\right)^{3/2}}. \tag{44}$$

Here, σ_n is the normal state conductivity. This approximation is valid for not very high temperatures, $T/T_c < 0.8$. Using typical parameters for sputtered Nb films, $\sigma_n \simeq 1.75 \times 10^5$ (Ω·cm)$^{-1}$ [42], frequency f = 400 GHz, and $T/T_c = 0.5$, we obtain: $R_{surf} \simeq 0.12$ Ω.

Transmission line impedance

The TL impedance is given by Equation 34 where $G_{QP} = 1/R_{QP}$. For tunnel JJs, $R_{QP} \gg R_n$ at sub-gap voltages. I will assume $R_{QP} = 25R_n$, typical for Nb tunnel JJs [9,11]. This gives R_{QP} = 0.5 Ω and G_{QP} = 2 Ω^{-1}. At f = 400 GHz, ωL^* = 8.61 Ω, ωC = 111.2 Ω^{-1}, and $Z_{TL} \simeq 0.278 + i0.0015$ Ω. It practically coincides with the resistance of an ideal TL, Equation 35. The value of Z_{TL} is only slightly affected by an ill-defined QP resistance and remains practically the same even if we use the upper limit, $G_{QP} = 1/R_n$. Importantly, Z_{TL} is small because of very small d.

Dissipative resistance

The effective dissipative resistance is affected by all sources of dissipation, including QP and dielectric losses in the junction barrier and surface resistance in electrodes. According to Equation 37, R_{dis} is defined via the effective quality factor, Q_{dis}, which can be written as:

$$\frac{1}{Q_{dis}} = \frac{1}{Q_{QP}} + \frac{1}{Q_{surf}} + \frac{1}{Q_{diel}}, \tag{45}$$

where Q_{QP}, Q_{surf} and Q_{diel} are determined by QP, surface, and dielectric losses, respectively. QP and surface resistance contribution can be accounted for using the TL analysis. The quality factor of a TL is determined by the relation

$$Q_{TL} = k_1/2k_2,$$

where k_1 and k_2 are real and imaginary parts of the wave number in the TL, $k = k_1 - ik_2$. They are obtained from the TL dispersion relation,

$$k^2 = -\left(R_{surf} + i\omega L^*\right)\left(G_{QP} + i\omega C\right).$$

Taking into account that $G_{QP} = 1/R_{QP} \ll \omega C$, $R_{surf} \ll \omega L^*$, and $Q_{TL}^{-1} = Q_{QP}^{-1} + Q_{surf}^{-1}$, we obtain

$$Q_{QP} = \omega R_{QP} C \simeq 55.6, \tag{46}$$

$$Q_{surf} = \frac{\omega L^*}{R_{surf}} \simeq 71.7. \tag{47}$$

Dielectric losses in the AlO_x barrier of a JJ were estimated in [43]. At $f \simeq 10$ GHz, $Q_{diel} \approx 10^4$. Although it should decrease at f = 400 GHz, we anticipate that it is still in the range of ca. 10^3. Therefore, dielectric losses are negligible, compared to QP and surface loses. Assuming Q_{diel} = 500, we obtain, from Equations 45–47, Q_{dis} = 29.48 and $R_{dis} \simeq 0.265$ Ω. It is close to the effective dissipative resistance of the TL,

$$R_{dis} \simeq \frac{Q_{TL}}{\omega C} = \frac{R_{QP}}{1 + R_{QP}R_{surf}C/L^*} \tag{48}$$

Radiative and total resistances

From Equation 12 and Equation 8, taking into account the smallness of c_0/c, we can write,

$$R_{\rm rad} \simeq \frac{3Z_0}{16\pi}\left[\frac{\lambda_0}{b}\right]^2. \quad (49)$$

Substituting $\lambda_0 = 750$ μm for $f = 400$ GHz, we obtain a very large value, $R_{\rm rad} \simeq 126.5$ kΩ. Since $R_{\rm rad} \gg R_{\rm dis}$, the total resistance, Equation 39, is $R_{\rm tot} = 0.265\ \Omega \simeq R_{\rm dis}$.

Table 1 summarizes characteristic resistances.

Radiation power

From Equation 41, we get the maximum radiation power at the velocity matching condition, $P_{{\rm rad},k} \simeq 0.7$ nW. It is much smaller than the total dc power at the velocity matching step, approx. $\Phi_0 f I_{\rm c0} \simeq 40$ μW. The corresponding power efficiency of approx. 10^{-5} reflects the key problem for using FFO as a free-space oscillator.

Whom to blame?

The very low radiation power efficiency of a JJ is colloquially attributed to "impedance mismatch". However, so far, there was no clear understanding of what mismatches with what. A long-living misconception is that the mismatch is between the TL and free-space impedances, $Z_{\rm TL} \ll Z_0$ [16]. However, this is not the source of the poor performance. On the contrary, it is beneficial to have a small TL impedance, connecting two radiating slots in a patch antenna [36]. The small $Z_{\rm TL}$ does not affect antenna performance and can be neglected.

The real source of the problem becomes apparent from Equation 41. It is associated with the more than five orders of magnitude mismatch between the total and radiative resistances, $R_{\rm tot} \ll R_{\rm rad}$, see Table 1. There are two main reasons for the mismatch: (i) The smallness of the junction width with respect to the free-space wavelength. The factor $(\lambda_0/b)^2$ in Equation 12 and Equation 49 leads to a very large $R_{\rm rad} \gg Z_0$. (ii) The smallness of the junction resistance, $R_{\rm QP} \ll Z_0$. The huge mismatch indicates that a JJ alone does not work as a free-space oscillator.

What to do?

Accurate matching between radiative and junction resistances is necessary for efficient emission into free space. Therefore, $R_{\rm QP}$ should be increased and $R_{\rm rad}$ decreased to a fraction of Z_0. However, this is not possible for the standard FFO geometry as sketched in Figure 1a. Indeed, increasing $R_{\rm QP}$ would require the reduction of junction sizes, which would lead to even faster increase of $R_{\rm rad}$. Alternatively, $R_{\rm QP}$ can be increased by decreasing $J_{\rm c0}$, but this will not reduce $R_{\rm rad}$. Therefore, the impedance matching requires modification of the oscillator geometry.

There are many ways of coupling a Josephson oscillator to free space. First, I note that biasing electrodes that are attached to the junction, significantly affect the net impedance. Since the total length of the electrodes (few millimeters) is larger than λ_0, the electrodes will reduce the net impedance and, thus, improve impedance matching with free space [17]. Analysis of large JJ arrays demonstrated that long electrodes may act as a traveling wave antenna, facilitating a power efficiency of several percent at $f = 0.1$–0.2 THz [44,45], which is much better than approx. 10^{-5} estimated above for the bare junction without electrodes. In [11], a free-space oscillator based on an FFO, coupled to a double-slot antenna, was demonstrated. Although the power efficiency was not specified, a detected off-chip signal up to 55 dB higher than the background noise was reported at $f = 0.5$ THz. In [27], a mesa structure containing several hundreds of stacked $Bi_2Sr_2CaCu_2O_{8+\delta}$ intrinsic JJs was implemented in a turnstile antenna. A radiation power efficiency up to 12% at $f \simeq 4$ THz was reported. The record high efficiency was attributed to a good impedance matching with free space [17]. In [24], a $Bi_2Sr_2CaCu_2O_{8+\delta}$ mesa was implemented into a patch antenna and far-field emission at $f = 1.5$ THz was reported.

Common for all mentioned approaches is that the junctions, which are small compared to λ_0 and, according to Equation 49, have poor coupling to free space, are coupled to large passive elements, comparable with λ_0. These elements act as microwave antennas, enabling good impedance matching and enhancing the power efficiency for emission in free space. The target parameters for such oscillators are $f \approx 1$–10 THz, a high power-efficiency of approx. 50% and a sufficiently high off-cryostat power above 1 mW.

Table 1: Estimation of characteristic resistances (in ohms) for a Nb/AlO_x/Nb tunnel junction with sizes $a = 100$ μm, $b = 10$ μm, $d = 2$ nm, $d_1 = d_2 = 100$ nm, $J_{\rm c0} = 5000$ (A/cm^2), at $T/T_{\rm c} = 0.5$ and $f = 400$ GHz.

R_n	$R_{\rm QP}$	$R_{\rm surf}$	$R_{\rm TL}$	ωL^*	$(\omega C)^{-1}$	$R_{\rm dis}$	$R_{\rm rad}$	$R_{\rm tot}$
0.02	0.5	0.12	0.28	8.6	0.009	0.265	126.5k	0.265

Josephson patch oscillator

Since in this work I consider patch antennas, below I will dwell on the patch antenna approach, discussed by Ono and co-workers [24]. Figure 4 shows a design of a Josephson patch oscillator (JPO). Here, small junctions (red) are acting as an excitation source for a superconducting patch antenna. The bottom junction electrode (blue) forms the ground plane, and the top electrode (cyan) creates the patch antenna with sizes (a, b), comparable to λ_0. In principle, the JPO can be driven by a single JJ. However, as follows from the estimation above (see Table 1), raising the junction resistance to the desired Z_0 level would require a drastic (100 times) reduction of the junction area. This will also lead to a proportional reduction of I_{c0} and the net available power. Therefore, a better strategy is to use a stack of JJs with large-enough area, enabling high-enough I_{c0}. The number of JJs, N, is an additional controllable parameter, allowing for fine-tuning of R_n and R_{tot}. Furthermore, in-phase synchronization of N JJs would provide the N-fold increment of the oscillating voltage $v(0,L)$, leading to a superradiant amplification of the emission power, $P_{rad} \propto N^2$ [10].

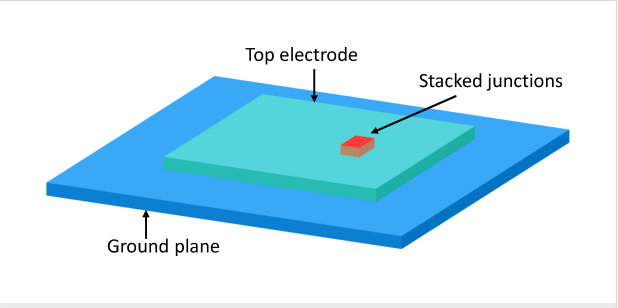

Figure 4: A proposed design of the impedance-matched free-space Josephson oscillator. Here, a small stack of Josephson junctions (red) is sandwiched between two large superconducting electrodes, namely the ground plane (blue) and the top electrode (light blue). The stack is acting as a source of microwave current (feed-in) for the patch antenna formed by the electrodes.

Moderate-size (approx. 10 μm) $Bi_2Sr_2CaCu_2O_{8+\delta}$ mesa structures are optimal for JPOs. The R_n of such mesas can be easily raised to several hundred ohms, while maintaining I_{c0} of a few milliamperes. This facilitates the optimal net power level $\approx I^2R_n$ of several milliwatts [24,27]. It is small enough for obviation of catastrophic self-heating, which is one of the major limiting factors for superconducting devices [17,27]. Simultaneously, it is large enough to enable emission above 1 mW, provided the radiation power efficiency is close to the optimal approx. 50%.

The operation frequency should be aligned with the Josephson frequency at the characteristics voltage, $I_{c0}R_n$, of JJs. For operation at the primary TM^x_{100} mode, one side of the patch should be $a \simeq \lambda/2$, where $\lambda = \lambda_0/\sqrt{\varepsilon_r}$ is the wavelength inside the patch and ε_r is the relative dielectric permittivity of the insulation layer between the patch electrodes. The other size, b, is adjustable and strongly affects the patch antenna performance. For $b \ll \lambda_0$, the radiative conductance per slot is given by Equation 5. In the opposite limit, it becomes [36]

$$G_1 = \frac{\pi}{Z_0}\left(\frac{b}{\lambda_0}\right). \quad (b \ll \lambda_0) \tag{50}$$

One of the most important parameters of the emitting antenna is the directivity, D, of the radiation pattern. A rectangular patch at the TM^x_{100} mode has the main lobe directed perpendicular to the patch (in the z-axis direction) with [36]

$$D = 6.6, \quad (b \ll \lambda_0)$$
$$D = 8\left(\frac{b}{\lambda_0}\right). \quad (b \gg \lambda_0)$$

A good free-space emitter should have a value for D as large as possible. From this point of view, it is preferable to have fairly wide antennas $b \sim \lambda_0$.

Finally, the position (x, y) of the stack plays an important role in the selection of the excited cavity mode. To excite solely the TM^x_{100} mode, the stack should be placed at x close to one of the radiating slots, that is, $x \sim a$ and $y = b/2$. The position x of the stack affects the effective input resistance of the antenna and provides another adjustable parameter for patch antenna operation, along with the shape of the top electrode [35,36,46]. The FFO input resistance, Equation 33, is not relevant for JPOs, because it describes coupling to an internal cavity mode within the JJ. In JPOs, the Josephson current is coupled to an external cavity mode in the patch. Since the patch is much larger than the JJ, the feed-in of the JPO is not distributed (in contrast to a FFO). Consequently, there is no need for a magnetic field. The best coupling occurs at $H = 0$, corresponding to the homogeneous distribution of the Josephson current. Generally, operation of JPOs is described by the standard patch antenna theory [36]. The only interesting physics is associated with synchronization of JJs in the stack [10], which can be forced by the high-quality cavity mode in the antenna [47].

Conclusion

I described a distributed, active patch antenna model of a Josephson oscillator. It expands the standard transmission line model of a patch antenna, taking into account the spatial-temporal distribution of the input Josephson current density in a Josephson junction. In the presence of a magnetic field and fluxons, the distribution of the oscillatory component of current

is nonuniform. This nonuniformity is essential for operation of a Josephson flux-flow oscillator and determines the effective input resistance, which enables the coupling between the Josephson current and the cavity modes in the junction. The presented model allows for the explicit application of many patch antenna results and facilitates full characterization of the device, including emission power, directivity, and power efficiency. The model explains the low power efficiency for emission in free space. It is primarily caused by the smallness of the junction width compared to the free-space wavelength and the corresponding mismatch between very large radiative and small junction resistances. The model clarifies which parameters can be changed to improve FFO characteristics. Finally, I discussed the design of a Josephson patch oscillator that can reach high power for emission in free space with the optimal power efficiency of approx. 50%.

Appendix

Definition of variables (Table 2).

ORCID® iDs

Vladimir M. Krasnov - https://orcid.org/0000-0002-3131-8658

Preprint

A non-peer-reviewed version of this article has been previously published as a preprint: https://doi.org/10.3762/bxiv.2022.86.v1

References

1. Soerensen, M. P.; Parmentier, R. D.; Christiansen, P. L.; Skovgaard, O.; Dueholm, B.; Joergensen, E.; Koshelets, V. P.; Levring, O. A.; Monaco, R.; Mygind, J.; Pedersen, N. F.; Samuelsen, M. R. *Phys. Rev. B* **1984,** *30,* 2640–2648. doi:10.1103/physrevb.30.2640

Table 2: Definition of variables.

Variable	Definition	Properties
a, b	junction length and width in (x, y) plane	$a \gg \lambda_J$, $b \sim \lambda_J$
α	quasiparticle damping factor	$\alpha = 1/\omega_p R_{QP} C = 1/Q_{QP}(\omega_p)$
C	junction capacitance	$C = \varepsilon_0 \varepsilon_r ab/d$
c_0	Swihart velocity	$c_0 = c\sqrt{d/\varepsilon_r \Lambda} = a/\sqrt{L^* C}$
$d, d_{1,2}$	thicknesses of JJ interlayer and the two electrodes	$d \ll b \ll a$
Φ	flux in the junction	$\Phi = H_y \Lambda^* a$
Φ_0	flux quantum	$\Phi_0 = h/2e$
J_{c0}, I_{c0}	maximum critical current density and critical current	$I_{c0} = J_{c0} ab$
k	field-induced phase gradient	$k = 2\pi\Phi/\Phi_0 a$
k_n	wave number of a cavity mode	$k_n = (\pi/a)n$
$L^*, L_\square$	inductance of JJ and inductance per square	$L^* = \mu_0 \Lambda a/b$, $L_\square = \mu_0 \Lambda$
$\lambda_{L1,2}$	London penetration depths of the two JJ electrodes	–
λ_0	wavelength in free space	–
λ	wavelength in the patch antenna	$\lambda = \lambda_0/\sqrt{\varepsilon_r}$
λ_J	Josephson penetration depth	$\lambda_J = [\Phi_0/2\pi\mu_0 J_{c0}\Lambda]^{1/2} = c_0/\omega_p$
Λ	characteristic length associated with JJ inductance	$\Lambda = d + \lambda_{L1}\coth(d_1/\lambda_{L1}) + \lambda_{L2}\coth(d_2/\lambda_{L2})$
Λ^*	effective magnetic thickness of the JJ	$\Lambda^* = d + \lambda_{L1}\tanh(d_1/2\lambda_{L1}) + \lambda_{L2}\tanh(d_2/2\lambda_{L2})$
η	Josephson phase difference	–
ω_p	Josephson plasma frequency	$\omega_p = [2\pi I_{c0}/\Phi_0 C]^{1/2}$
ω_J	angular Josephson frequency	$\omega_J = \partial\eta/\partial t = 2\pi V_{dc}/\Phi_0$
ω_n	cavity mode angular frequency	$\omega_n = c_0 k_n$
R_{QP}, (r_{QP})	subgap quasiparticle resistance, (per unit area)	$r_{QP} = R_{QP} ab$
R_{dis}	net dissipative resistance	–
R_{surf}	surface resistance of electrodes	–
R_n	normal state resistance of the JJ	–
R_{TL}	transmission line resistance	–
R_{rad}	radiative resistance	–
R_{in}	effective input resistance of the JJ	–
R_{tot}	total load resistance of the JJ	–

2. Nagatsuma, T.; Enpuku, K.; Sueoka, K.; Yoshida, K.; Irie, F. *J. Appl. Phys.* **1985,** *58,* 441–449. doi:10.1063/1.335643
3. Qin, J.; Enpuku, K.; Yoshida, K. *J. Appl. Phys.* **1988,** *63,* 1130–1135. doi:10.1063/1.340019
4. Zhang, Y. M.; Winkler, D.; Claeson, T. *Appl. Phys. Lett.* **1993,** *62,* 3195–3197. doi:10.1063/1.109127
5. Golubov, A. A.; Malomed, B. A.; Ustinov, A. V. *Phys. Rev. B* **1996,** *54,* 3047–3050. doi:10.1103/physrevb.54.3047
6. Koshelets, V. P.; Shitov, S. V.; Shchukin, A. V.; Filippenko, L. V.; Mygind, J.; Ustinov, A. V. *Phys. Rev. B* **1997,** *56,* 5572–5577. doi:10.1103/physrevb.56.5572
7. Ustinov, A. V. *Phys. D (Amsterdam, Neth.)* **1998,** *123,* 315–329. doi:10.1016/s0167-2789(98)00131-6
8. Cirillo, M.; Grønbech-Jensen, N.; Samuelsen, M. R.; Salerno, M.; Rinati, G. V. *Phys. Rev. B* **1998,** *58,* 12377–12384. doi:10.1103/physrevb.58.12377
9. Koshelets, V. P.; Shitov, S. V. *Supercond. Sci. Technol.* **2000,** *13,* R53–R69. doi:10.1088/0953-2048/13/5/201
10. Krasnov, V. M. *Phys. Rev. B* **2010,** *82,* 134524. doi:10.1103/physrevb.82.134524
11. Kinev, N. V.; Rudakov, K. I.; Filippenko, L. V.; Baryshev, A. M.; Koshelets, V. P. *IEEE Trans. Terahertz Sci. Technol.* **2019,** *9,* 557–564. doi:10.1109/tthz.2019.2941401
12. Paramonov, M. E.; Filippenko, L. V.; Khan, F. V.; Kiselev, O. S.; Koshelets, V. P. *Appl. Sci.* **2022,** *12,* 8904. doi:10.3390/app12178904
13. Yanson, I. K.; Svistunov, V. M.; Dmitrenko, I. M. *Sov. Phys. - JETP* **1965,** *21,* 650.
14. Yanson, I. K. *Low Temp. Phys.* **2004,** *30,* 515–521. doi:10.1063/1.1789911
15. Langenberg, D. N.; Scalapino, D. J.; Taylor, B. N.; Eck, R. E. *Phys. Rev. Lett.* **1965,** *15,* 294–297. doi:10.1103/physrevlett.15.294
16. Langenberg, D. N.; Scalapino, D. J.; Taylor, B. N. *Proc. IEEE* **1966,** *54,* 560–575. doi:10.1109/proc.1966.4776
17. Krasnov, M. M.; Novikova, N. D.; Cattaneo, R.; Kalenyuk, A. A.; Krasnov, V. M. *Beilstein J. Nanotechnol.* **2021,** *12,* 1392–1403. doi:10.3762/bjnano.12.103
18. Ozyuzer, L.; Koshelev, A. E.; Kurter, C.; Gopalsami, N.; Li, Q.; Tachiki, M.; Kadowaki, K.; Yamamoto, T.; Minami, H.; Yamaguchi, H.; Tachiki, T.; Gray, K. E.; Kwok, W.-K.; Welp, U. *Science* **2007,** *318,* 1291–1293. doi:10.1126/science.1149802
19. Wang, H. B.; Guénon, S.; Yuan, J.; Iishi, A.; Arisawa, S.; Hatano, T.; Yamashita, T.; Koelle, D.; Kleiner, R. *Phys. Rev. Lett.* **2009,** *102,* 017006. doi:10.1103/physrevlett.102.017006
20. Kakeya, I.; Omukai, Y.; Yamamoto, T.; Kadowaki, K.; Suzuki, M. *Appl. Phys. Lett.* **2012,** *100,* 242603. doi:10.1063/1.4727899
21. Benseman, T. M.; Gray, K. E.; Koshelev, A. E.; Kwok, W.-K.; Welp, U.; Minami, H.; Kadowaki, K.; Yamamoto, T. *Appl. Phys. Lett.* **2013,** *103,* 022602. doi:10.1063/1.4813536
22. Zhang, H.; Wieland, R.; Chen, W.; Kizilaslan, O.; Ishida, S.; Han, C.; Tian, W.; Xu, Z.; Qi, Z.; Qing, T.; Lv, Y.; Zhou, X.; Kinev, N.; Ermakov, A. B.; Dorsch, E.; Ziegele, M.; Koelle, D.; Eisaki, H.; Yoshida, Y.; Koshelets, V. P.; Kleiner, R.; Wang, H.; Wu, P. *Phys. Rev. Appl.* **2019,** *11,* 044004. doi:10.1103/physrevapplied.11.044004
23. Borodianskyi, E. A.; Krasnov, V. M. *Nat. Commun.* **2017,** *8,* 1742. doi:10.1038/s41467-017-01888-4
24. Ono, Y.; Minami, H.; Kuwano, G.; Kashiwagi, T.; Tsujimoto, M.; Kadowaki, K.; Klemm, R. A. *Phys. Rev. Appl.* **2020,** *13,* 064026. doi:10.1103/physrevapplied.13.064026
25. Delfanazari, K.; Klemm, R. A.; Joyce, H. J.; Ritchie, D. A.; Kadowaki, K. *Proc. IEEE* **2020,** *108,* 721–734. doi:10.1109/jproc.2019.2958810
26. Tsujimoto, M.; Fujita, S.; Kuwano, G.; Maeda, K.; Elarabi, A.; Hawecker, J.; Tignon, J.; Mangeney, J.; Dhillon, S. S.; Kakeya, I. *Phys. Rev. Appl.* **2020,** *13,* 051001. doi:10.1103/physrevapplied.13.051001
27. Cattaneo, R.; Borodianskyi, E. A.; Kalenyuk, A. A.; Krasnov, V. M. *Phys. Rev. Appl.* **2021,** *16,* L061001. doi:10.1103/physrevapplied.16.l061001
28. Coon, D. D.; Fiske, M. D. *Phys. Rev.* **1965,** *138,* A744–A746. doi:10.1103/physrev.138.a744
29. Kulik, I. O. *JETP Lett.* **1965,** *2,* 84.
30. Kulik, I. O. *Sov. Phys. Tech. Phys.* **1967,** *12,* 111.
31. Barone, A.; Paternò, C. *Physics and Applications of the Josephson Effect;* John Wiley & Sons, Inc.: New York, USA, 1982.
32. Katterwe, S. O.; Rydh, A.; Motzkau, H.; Kulakov, A. B.; Krasnov, V. M. *Phys. Rev. B* **2010,** *82,* 024517. doi:10.1103/physrevb.82.024517
33. Bulaevskii, L. N.; Koshelev, A. E. *J. Supercond. Novel Magn.* **2006,** *19,* 349–367. doi:10.1007/s10948-006-0176-5
34. Carver, K. R.; Mink, J. W. *IEEE Trans. Antennas Propag.* **1981,** *29,* 2–24. doi:10.1109/tap.1981.1142523
35. Okoshi, T. *Planar Circuits for Microwaves and Lightwaves;* Springer-Verlag: Berlin Heidelberg New York Tokyo, 1985. doi:10.1007/978-3-642-70083-5
36. Balanis, C. A. *Antenna Theory: Analysis and Design,* 3rd ed.; John Wiley & Sons, Inc., Publ.: Hoboken, New Jersey, 2005.
37. Lindquist, C. S. *J. Franklin Inst.* **1971,** *291,* 1–17. doi:10.1016/0016-0032(71)90258-4
38. Krasnov, V. M. *Phys. Rev. B* **2020,** *101,* 144507. doi:10.1103/physrevb.101.144507
39. Derneryd, A. *IEEE Trans. Antennas Propag.* **1976,** *24,* 846–851. doi:10.1109/tap.1976.1141445
40. Derneryd, A. *IEEE Trans. Antennas Propag.* **1978,** *26,* 532–535. doi:10.1109/tap.1978.1141890
41. Schmidt, V. V.; Müller, P.; Ustinov, A. V. *The Physics of Superconductors: Introduction to Fundamentals and Applications,* 3rd ed.; Springer Berlin: Berlin, Germany, 1997. doi:10.1007/978-3-662-03501-6
42. Krasnov, V. M.; Oboznov, V. A.; Ryazanov, V. V. *Phys. C (Amsterdam, Neth.)* **1992,** *196,* 335–339. doi:10.1016/0921-4534(92)90455-l
43. Gunnarsson, D.; Pirkkalainen, J.-M.; Li, J.; Paraoanu, G. S.; Hakonen, P.; Sillanpää, M.; Prunnila, M. *Supercond. Sci. Technol.* **2013,** *26,* 085010. doi:10.1088/0953-2048/26/8/085010
44. Galin, M. A.; Borodianskyi, E. A.; Kurin, V. V.; Shereshevskiy, I. A.; Vdovicheva, N. K.; Krasnov, V. M.; Klushin, A. M. *Phys. Rev. Appl.* **2018,** *9,* 054032. doi:10.1103/physrevapplied.9.054032
45. Galin, M. A.; Rudau, F.; Borodianskyi, E. A.; Kurin, V. V.; Koelle, D.; Kleiner, R.; Krasnov, V. M.; Klushin, A. M. *Phys. Rev. Appl.* **2020,** *14,* 024051. doi:10.1103/physrevapplied.14.024051
46. Delfanazari, K.; Asai, H.; Tsujimoto, M.; Kashiwagi, T.; Kitamura, T.; Yamamoto, T.; Wilson, W.; Klemm, R. A.; Hattori, T.; Kadowaki, K. *IEEE Trans. Terahertz Sci. Technol.* **2015,** *5,* 505–511. doi:10.1109/tthz.2015.2409552
47. Cattaneo, R.; Galin, M. A.; Krasnov, V. M. *Beilstein J. Nanotechnol.* **2022,** *13,* 1578–1588. doi:10.3762/bjnano.13.132

BEILSTEIN JOURNAL OF NANOTECHNOLOGY

Spin dynamics in superconductor/ferromagnetic insulator hybrid structures with precessing magnetization

Yaroslav V. Turkin*[1,2] and Nataliya Pugach[1]

Full Research Paper

Open Access

Address:
[1]HSE University, Moscow 101000, Russia and [2]Vernadsky Crimean Federal University, Simferopol 295007

Email:
Yaroslav V. Turkin* - yturkin@hse.ru

* Corresponding author

Keywords:
ferromagnetic resonance; proximity effect; superconducting spintronics

Beilstein J. Nanotechnol. **2023,** *14,* 233–239.
https://doi.org/10.3762/bjnano.14.22

Received: 12 December 2022
Accepted: 06 February 2023
Published: 21 February 2023

This article is part of the thematic issue "Intrinsic Josephson effect and prospects of superconducting spintronics".

Guest Editor: A. S. Sidorenko

Abstract

The main goal of the present work is the description of the dynamics of spin current and induced magnetization inside a superconducting film S that is in contact with a ferromagnetic insulator layer FI. Spin current and induced magnetization are calculated not only at the interface of the S/FI hybrid structure, but also inside the superconducting film. The new and interesting predicted effect is the frequency dependence of the induced magnetization with a maximum appearing at high temperatures. It is also shown that the increase of the magnetization precession frequency can drastically change the spin distribution of quasiparticles at the S/FI interface.

Introduction

Creation and manipulation of spin flows in superconducting hybrid systems have become a very active research area during the last decade because of the possibility to create spin supercurrents with much larger relaxation lengths and spin lifetimes [1]. The creation of persistent spin currents in superconductors opens new ways for the development of prospective spintronic devices such as magnon transistors [2,3] and superconducting magnon crystals [4]. In this context, the challenge of superconducting spin injection is one of the central problems in modern superconducting spintronics. There are several ways of spin current injection into a superconductor, for example, the spin Hall effect [5], the spin Seebek effect [6], and ferromagnetic resonance spin pumping [7,8]. The spin pumping technique in hybrid structures consisting of a ferromagnetic insulator and a superconductor is considered to be the most preferable way to inject spin currents because of the absence of Joule heating. Moreover, proximity coupling between magnetic excitations plays a crucial role in ferromagnetic Josephson junctions [9-12] and mesoscopic structures [13]. Recent experimental research [5,8,14] shows that the interaction between the supercon-

ducting correlations and spin waves influences the dynamics of both superconducting and magnetic films. Interfacial exchange interaction between Cooper pairs and magnons results in a nonstationary induced magnetization and spin currents in the superconducting film and changes the magnetic excitation spectrum inside the ferromagnetic insulator [15]. Despite the large number of discussions in experimental works, there is no clear understanding of the interplay between superconducting and magnetic excitations inside proximity-coupled hybrid structures. That is why developing a consistent theory of the inverse proximity effect is one of the central topics of modern superconducting spintronics. There is a series of theoretical papers [7,16-19] describing spin current injection and induced magnetization generation in microscopic [7,16] and quasiclassical [17-19] frameworks. However, the main subject of these works is the magnetic excitation spectrum in hybrid structures. Most of the works ignore the dynamics of nonuniform distributions of induced magnetization and spin current inside the superconducting film, which can be called the "dynamic inverse proximity effect". Distributions of spin current and induced magnetization were calculated in recent works [20,21], where the authors investigate spin current flow through Josephson-like trilayer structures.

The proximity effect is the penetration of superconducting correlations in an adjacent nonsuperconducting layer, which serves as an origin of the Josephson effect, for example. While the reverse influence of a magnetic layer on a superconducting condensate is called the inverse proximity effect. Both spin current and induced magnetization in the superconductor originate from singlet–triplet Cooper pair conversion, which is the main mechanism of the inverse proximity effect. The magnetization in a superconductor is induced by the proximity in a stationary case, and the spin current is pumped only via magnetic dynamics in the adjacent layer. The quasiclassical theory of proximity effect in superconductor/ferromagnetic insulator hybrid structures was applied to describe nonstationary phenomena, such as generation of spin transfer torques, nonuniform thermoelectric effects, and domain wall movement. The theoretical description of the dynamic proximity effect is the more complex task because of the double time structure of the nonstationary Usadel equation. The recent successes in the theory of boundary conditions for quasiclassical approximations [22,23] enabled the development of adequate models of the proximity effect in different types of superconducting hybrid structures. Quasiclassical boundary conditions can successfully describe the interfaces between, among other things, a superconductor and weak or strong ferromagnets [22-24], normal metals [25-27], and half-metals [28]. The first attempts to implement nonstationary, adiabatic, quasiclassical boundary conditions were made in [18,19]. In these works, calculations based on Usadel equations combined with adiabatic, nonstationary boundary conditions were made. We show that the adiabatic approximation is useful in a wide range of magnetization precession frequencies. The main goal of our theory is to describe the dynamic perturbations produced by the spin current and induced magnetization inside the superconducting film in contact with a ferromagnetic insulator layer with precessing magnetization. Distributions of spin current and induced magnetization originating from the dynamic proximity effect in aluminium were recently calculated [29]. Another important problem that occurs during consideration of the dynamic inverse proximity effect is the nonequilibrium behavior of quasiparticles at the S/FI interface. In this work, we present our new results that prove that adiabatic dynamics of quasiparticles into the superconducting layer can be changed by spin pumping from the adjacent ferromagnetic insulating layer.

Model

The investigated structure is schematically presented in Figure 1. The spin current is injected from the ferromagnetic insulator (FI) to the superconducting film (SC). The thickness of the ferromagnetic insulator does not matter, because the superconducting correlations do not penetrate into the insulating material. Uniform magnetization periodically precesses in the ferromagnetic insulator with a cyclic frequency Ω. To describe the nonstationary state of the superconducting conden-

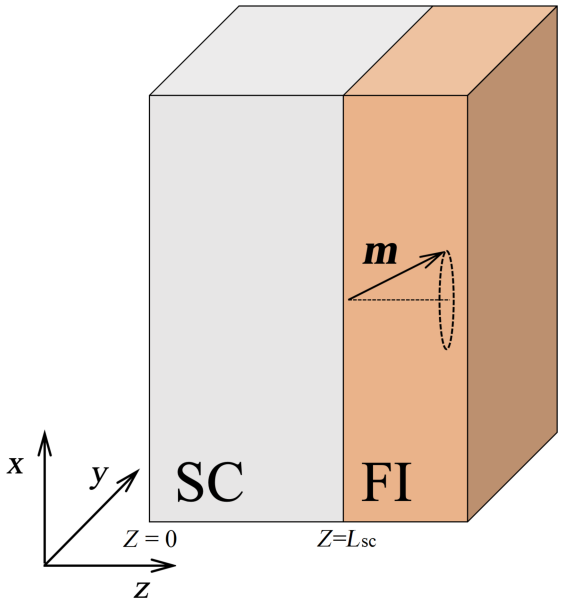

Figure 1: The investigated hybrid superconducting structure consisting of a ferromagnetic insulator (FI) adjacent to a superconductor (SC). The interface between the superconducting layer and free space is located at $z = 0$; the interface between the superconducting layer and the ferromagnetic insulator is located at $z = L_{sc}$. The magnetization **m** in the ferromagnetic insulator layer is uniform and precesses with the cyclic frequency Ω.

sate, we use the formalism of two-time quasiclassical Green's functions in Nambu–spin-Keldysh space [28]. We expand the Green's function assuming a weak proximity effect [28] with the ferromagnetic insulator: $\check{g}(t_1,t_2) \approx \check{g}^{(0)} + \check{g}^{(1)}$. To handle the expansion of the order parameter correctly, we should cancel the odd orders of the perturbation, because the triplet Green's function components do not contribute to the order parameter. Only even orders of the perturbation series determine its correction. Thus, the superconducting order parameter in the linear regime, has only a zero-order term in expansion.

The resulting dynamics of the superconducting condensate in the weak proximity effect regime can be described via the nonstationary Usadel equation [18,19,30]:

$$\hbar\left\{\check{\rho}_4\,\partial_t, \check{g}\right\}_t - \hbar D\partial_z\left(\check{g}\circ\partial_z\,\check{g}\right) = i\left[\check{\Delta}^{(0)}, \check{g}\right], \qquad (1)$$

where $\check{\Delta}^{(0)}$ is the stationary BCS superconducting order parameter matrix [28], D is the diffusion constant, $\check{\rho}_4 = \sigma_0 \otimes \sigma_x \otimes i\sigma_y$ is the auxiliary matrix in Nambu–spin-Keldysh space, $\circ$ is the time convolution operator, and the anticommutator $\{f, g\}_t = f(t_1)g(t_1, t_2) + g(t_1, t_2)f(t_2)$. We have dropped the coordinate dependence of the Green's functions for simplicity of notation. We consider the time-dependent magnetization at the interface as an adiabatic perturbation that changes slowly compared to the timescale of the superconducting system: $\hbar\Omega \ll \Delta$. A similar approach was used in our recent work [29].

In general, the equation can be solved numerically within the mixed representation formalism [31]. Sometimes, the Usadel equation (Equation 1) can be solved analytically, for example, in the case of weak superconductivity, as it has been done in the pioneering work by Houzet [32]. Two-time quasiclassical Green's functions have the following structure [28]:

$$\hat{g}^{R/A} = \begin{bmatrix} g^{R/A} & f^{R/A} \\ -\tilde{f}^{R/A} & -\tilde{g}^{R/A} \end{bmatrix}, \qquad (2)$$

$$\hat{g}^{K} = \begin{bmatrix} g^{K} & f^{K} \\ \tilde{f}^{K} & \tilde{g}^{K} \end{bmatrix}. \qquad (3)$$

The time-periodicity condition allows for the representation of spin current and induced magnetization as time-harmonic variables:

$$\mathbf{j}_z^s(z,t) = \mathbf{j}_z^s(z)e^{i\Omega t}, \qquad (4)$$

$$\mathbf{M}(z,t) = \mathbf{M}(z)e^{i\Omega t}, \qquad (5)$$

where $t = (t_1 + t_2)/2$ is the center-of-mass time argument. To form a closed set of equations, we should add the equation for the normalization condition [30] in mixed representation. The amplitudes of the observables in Equation 4 and Equation 5 can be calculated from the Fourier components of quasiclassical Green's functions using a standard procedure [29]:

$$\mathbf{M}(z) = \frac{\hbar g\mu_B N_0}{8}\int_{-\infty}^{+\infty} d\omega\ \mathrm{Tr}\left[\hat{\boldsymbol{\kappa}}\hat{g}^K(\omega)\right], \qquad (6)$$

where $\hat{\boldsymbol{\kappa}} = \mathrm{diag}(\boldsymbol{\sigma}, \boldsymbol{\sigma}^*)$ is the spin operator in electron–hole–spin space, g is the gyromagnetic ratio for free electrons, μ_B is the Bohr magneton, N_0 is the density of states at the Fermi level, and $\hat{g}^K(\omega)$ is the Fourier–Winger transform of the Green's function [29,30] The expression for the spin current takes the following form [29]:

$$\mathbf{j}_z^s(z) = \frac{\hbar^2 N_0 D}{8}\int_{-\infty}^{+\infty} d\omega\ \mathrm{Tr}\left[\hat{\rho}_4\hat{\boldsymbol{\kappa}}\left(\check{g}^{(0)}\circ\partial_z\,\check{g}^{(1)}\right)^K(\omega)\right], \qquad (7)$$

where K is the Keldysh component.

Using the normalization condition, Keldysh Green's function can be written through the distribution function $\hat{\psi}$: $\hat{g}^K = \hat{g}^R\circ\hat{\psi} - \hat{\psi}\circ\hat{g}^A$. In thermal equilibrium, the distribution matrix reduces to a function $\tanh(\beta\hbar\omega/2)$, $\beta = 1/kT$, which corresponds to the Fermi distribution function.

Results and Discussion

For the numerical calculations, we have considered niobium as a superconducting metal with the following parameters: $T_c = 9.2$ K, $\Delta^{(0)} \approx 1.76k_B\cdot T_c = 1.4$ meV, $D = 0.8\cdot10^{-3}$ m$^2\cdot$s^{-1}, and $\varepsilon_F \approx 5.32$ eV. We approximate the DOS on the Fermi level with the free electron gas value $N_0 \approx 4.9\cdot10^{46}$ J$^{-1}\cdot$m^{-3}. The coherence length has been estimated using $\xi_0 = \sqrt{\hbar D / 2\pi k_B T_c}$, where k_B is the Boltzmann constant and $\xi_0 \approx 11$ nm. We numerically solve Equation 1 in mixed representation with the normalization condition. To obtain physical observables from the quasiclassical Green's functions, one should find the harmonic coefficients in Equation 6 and Equation 7 and directly calculate observable values at the space-time points. In this work, we are interested in the calculation of spin current distributions along the thickness of the superconducting film, as well as the influence of induced magnetization dynamics on the electron perturbations in the S film. The dynamics of any observ-

able will be periodic and can be characterized by its amplitude value. Thus, we only need to calculate the doubled absolute value of the coefficients in Equation 6 and Equation 7, which are exactly the amplitudes of the spin current and magnetization in the linear regime. Nonadiabatic processes are unlikely because the ratio $\Delta/\hbar\Omega \gg 1$ for the $Nb/Y_3Fe_5O_{12}$ (YIG) hybrid structure. However, the superconducting order parameter may be partially reduced near the S/FI interface because of the inverse proximity effect. It gives rise to the spin distribution of quasiparticles with energies close to the spectrum gap near the interface.

Both spin current and induced magnetization in the superconductor originate from the singlet–triplet Cooper pair conversion mechanism, which is the main origin of the inverse proximity effect. The spin current can be induced only by the nonstationary flow of triplet Cooper pairs, just as in a conventional spin-pumping bilayer structure with a normal metal [33]. Thus, spin currents cannot emerge when the magnetization is stationary inside the ferromagnetic insulator layer. However, there is a possibility to induce stationary pure spin currents inside trilayer superconducting structures [1].

The distributions of spin current amplitudes into the S layer are depicted in Figure 2. The amplitudes are normalized by the factor $j_{s0} = (\hbar/2e)j_{e0}$. The charge current density normalization factor is $j_{e0} = 2eN_0D\Delta^{(0)}/\xi = 6.262\cdot10^6$ A·cm^{-2}.

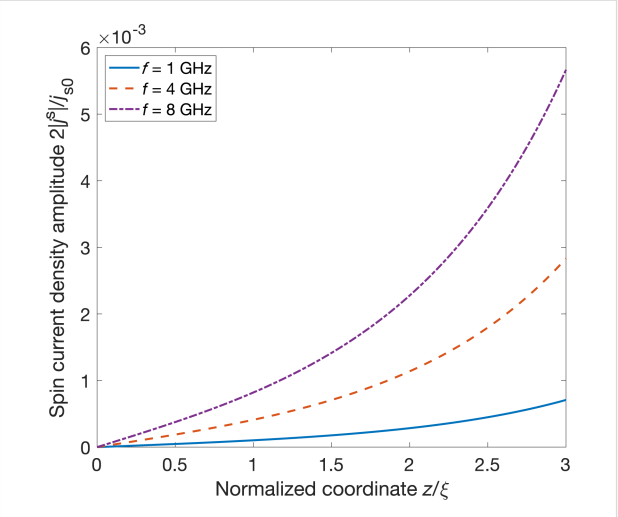

Figure 2: Distributions of the spin current density inside the superconducting layer at different frequencies of the magnetization precession. The interface between the superconducting layer and ferromagnetic insulator is located at $z = 3\xi$

Distributions of spin current and induced magnetization for aluminum were calculated in our previous work [29]. One can see that the spin current amplitudes decay at a distance of the coherence length, similarly to the induced magnetization. However, the amplitude of the spin current strongly depends on the frequency of the magnetization precession. This effect is similar to ferromagnetic resonance spin pumping in normal metal/ferromagnetic insulator structures. In the last case (normal metal), the decay of the spin current is a consequence of spin relaxation processes, but we do not take into account any spin relaxation mechanisms within our model for a superconductor. We should mention that both spin pumping mechanisms in superconductors and normal metals are determined by the penetration of nonequillibrium spin density from the interface. In metals, such a penetration is limited by the spin flip scattering, while inside the superconductor, the spin relaxation time is usually much longer. Thus, induced magnetization and spin current in our problem are determined mainly by the competition between spin singlet and spin triplet orders [34] Therefore, we conclude that the main mechanism of the spin current decay is similar to that for the induced magnetization. It corresponds to the lowering of the triplet pair density away from the magnetic interface where the singlet–triplet conversion occurs. Moreover, we should point out that the decrease of spin current inside the superconducting layer completely agrees with the boundary condition of the zero matrix current at the interface between the free space and superconducting layer at $z = 0$.

Now let us consider the Fourier coefficients for the induced magnetization. Earlier, we have shown that the induced magnetization almost does not depend on the precession frequency [29]. This is because the absolute value of the projection of the magnetization vector to the interface plane does not change with a change of the precession frequency and may be given by the stationary component of the induced magnetization [35].

However, more precise results presented in Figure 3 show that the induced magnetization at the interface depends nonmonotonically on the precession frequency. Moreover, a maximum becomes obvious with increasing temperature, even if we do not take into account the thermal suppression of the superconducting order parameter. The competition between two different spin pumping mechanisms can explain this interesting behavior. The first mechanism is the adiabatic spin pumping of the superconducting condensate, and the second one is the spin pumping of the thermally generated quasiparticles, for example, unpaired electrons and holes. The competition of these two spin pumping mechanisms gives rise to the nonmonotonous frequency dependence of the induced magnetization, which is the sum of the quasiparticle spin density and the triplet correlations component.

The interplay between magnetization precession and proximity effect can suppress superconductivity at the interface causing an

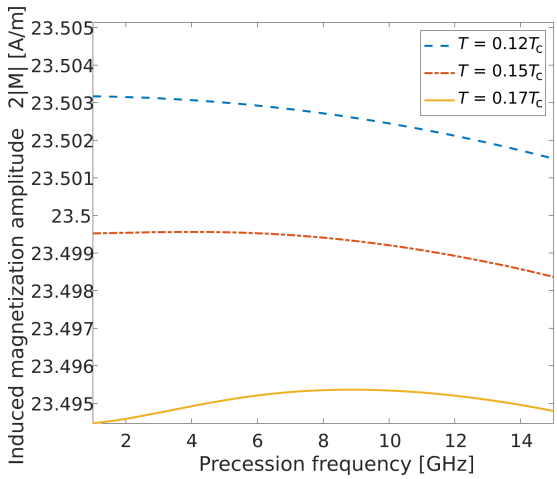

Figure 3: In-plane component of the induced magnetization at the S/FI interface as a function of the magnetic precession frequency at different temperatures.

increasing number of quasiparticles. To explore the spin dynamics of the quasiparticles more deeply, let us investigate spin components of the electron block of the distribution function. Spin polarization of quasiparticles can be obtained by applying a spin polarization operator to the distribution function matrix. Due to the block-diagonal structure of the spin operator in electron–hole space, the spin distribution of quasiparticles can be represented as a superposition of electron-like and hole-like spin distributions $\mathrm{Tr}[\hat{\boldsymbol{\kappa}}\hat{\psi}] = \mathrm{Tr}[\boldsymbol{\sigma}\psi_{\mathrm{el}}] + \mathrm{Tr}[\boldsymbol{\sigma}^{*}\psi_{\mathrm{hl}}]$. The first term in this expression corresponds to the spin polarization of electron-like quasiparticles and is mathematically equivalent to the trace of the product of Pauli matrix and the left upper block of the distribution matrix. Figure 4 illustrates the dynamics of the quasiparticle distribution function at magnetization precession frequencies of 1 and 8 GHz. The color maps for quasiparticles with x and y spin component evolution $S_{x,y}(z, \varepsilon, t) = \mathrm{Tr}[\sigma_{x,y}\psi_{\mathrm{el}}]$ are presented in Figure 4. The spin distribution function splits into two almost symmetric peaks around the spectrum gap value with increasing frequency (Figure 5). The asymmetry of the electron spin distribution is very small but visible in Figure 5, where two peaks emerge twice during one period of magnetization oscillation. This picture is similar for hole excitations due to the electron–hole symmetry. It should be noticed that a fraction of the spin distribution is lying inside the gap and should not be taken into account. But in the time-dependent case, there is always an energy shift equal to $\pm\hbar\Omega/2$. This energy shift appears in every time convolution. The real consequences of these undergap states may be found if one takes into account also the density of states correction, which is beyond the scope of the current paper. Thus, the effect of spin distribution func-

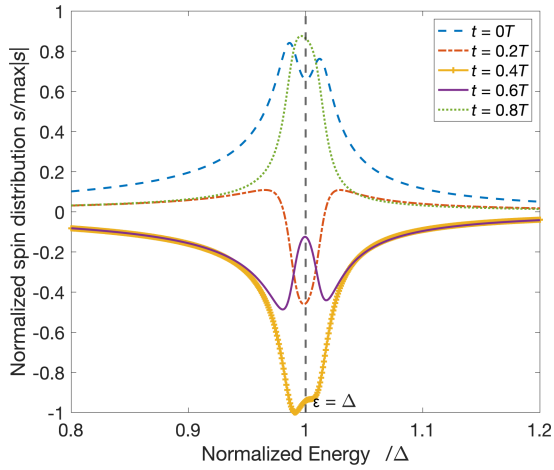

Figure 5: Snapshots of the spin distribution function at different moments of the precession period at a frequency of 8 GHz.

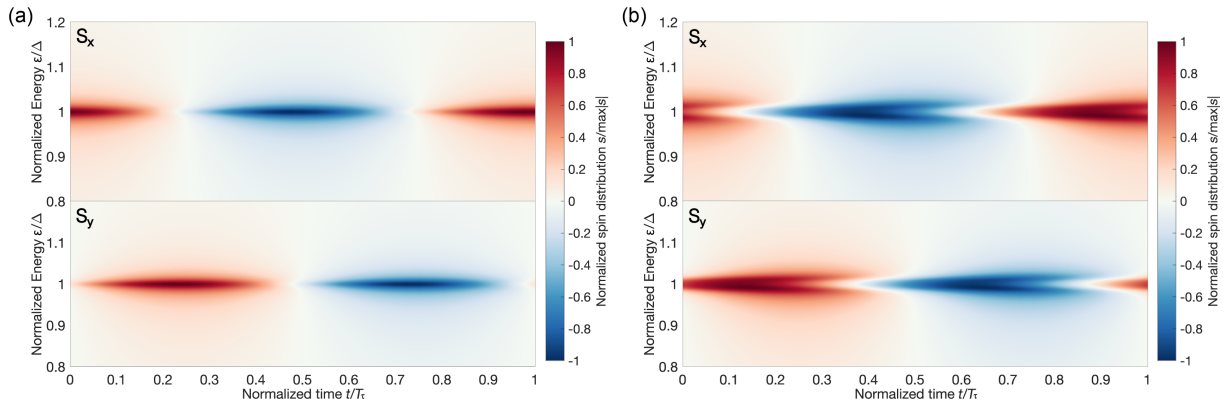

Figure 4: Evolution of the spin-resolved distribution function at the S/FI interface (S_x component in the upper panels and S_y component in the lower panels) at magnetization precession frequencies of (a) 1 GHz and (b) 8 GHz. The normalized time is equal to t/T_{τ}, where $T_{\tau} = 2\pi/\Omega$ is the period of magnetization precession.

tion splitting can be revealed in superconducting hybrid systems with nonequilibrium electron–hole distributions such as superconductor/normal metal contacts [36]. This is one more evidence of the significant role of quasiparticles in the spin dynamics of hybrid superconducting structures.

Conclusion

In this work, we have investigated the simplest case of the linear adiabatic dynamics of spin current and spin polarization of quasiparticles caused by the proximity of a superconductor to a ferromagnetic insulator. It was found that the spin current density amplitude is proportional to the frequency of the magnetization precession. Spin supercurrent distributions are similar to those of the spin pumping in normal metal/ferromagnetic insulator hybrid structures. But the spin current penetrates into the superconducting film to distances much longer than in normal metals. This behavior is a result of the adiabatic singlet–triplet Cooper pair conversion process at the interface, that is, the inverse proximity effect. We have found that the induced magnetization at the interface has a weakly nonmonotonous dependence on the magnetization precession frequency with a maximum appearing at increasing temperatures. We suppose that this effect originates from spin pumping of quasiparticles, which can be generated at the interface. There is also a dynamical effect of spin splitting of the quasiparticle distribution. This effect can have some nontrivial consequences in superconducting systems with broken electron–hole symmetry. All these effects emerge in the adiabatic regime. The results demonstrate the rich potential of the dynamic inverse proximity effect in hybrid superconductor/ferromagnetic insulator structures, making them promising candidates for novel spintronic devices.

Funding

The induced magnetization calculation was financially supported by the Ministry of Science and Higher Education of the Russian Federation, Megagrant project N 075-15-2022-1108. The calculations of the non-equilibrium spin current were supported by the Russian Science Foundation project 23-72-00018 “Study of non-equilibrium and boundary phenomena in superconducting hybrid nanostructures”. Investigation of the quasiparticle distribution and dynamics was supported by the Basic Research Program of HSE.

ORCID® iDs

Yaroslav V. Turkin - https://orcid.org/0000-0003-1714-5735

Preprint

A non-peer-reviewed version of this article has been previously published as a preprint: https://doi.org/10.3762/bxiv.2022.85.v1

References

1. Linder, J.; Robinson, J. W. A. *Nat. Phys.* **2015,** *11,* 307–315. doi:10.1038/nphys3242
2. Chumak, A. V.; Serga, A. A.; Hillebrands, B. *Nat. Commun.* **2014,** *5,* 4700. doi:10.1038/ncomms5700
3. Cornelissen, L. J.; Liu, J.; van Wees, B. J.; Duine, R. A. *Phys. Rev. Lett.* **2018,** *120,* 097702. doi:10.1103/physrevlett.120.097702
4. Golovchanskiy, I. A.; Abramov, N. N.; Stolyarov, V. S.; Bolginov, V. V.; Ryazanov, V. V.; Golubov, A. A.; Ustinov, A. V. *Adv. Funct. Mater.* **2018,** *28,* 1802375. doi:10.1002/adfm.201802375
5. Jeon, K.-R.; Ciccarelli, C.; Kurebayashi, H.; Wunderlich, J.; Cohen, L. F.; Komori, S.; Robinson, J. W. A.; Blamire, M. G. *Phys. Rev. Appl.* **2018,** *10,* 014029. doi:10.1103/physrevapplied.10.014029
6. Ozaeta, A.; Virtanen, P.; Bergeret, F. S.; Heikkilä, T. T. *Phys. Rev. Lett.* **2014,** *112,* 057001. doi:10.1103/physrevlett.112.057001
7. Inoue, M.; Ichioka, M.; Adachi, H. *Phys. Rev. B* **2017,** *96,* 024414. doi:10.1103/physrevb.96.024414
8. Yao, Y.; Song, Q.; Takamura, Y.; Cascales, J. P.; Yuan, W.; Ma, Y.; Yun, Y.; Xie, X. C.; Moodera, J. S.; Han, W. *Phys. Rev. B* **2018,** *97,* 224414. doi:10.1103/physrevb.97.224414
9. Stoutimore, M. J. A.; Rossolenko, A. N.; Bolginov, V. V.; Oboznov, V. A.; Rusanov, A. Y.; Baranov, D. S.; Pugach, N.; Frolov, S. M.; Ryazanov, V. V.; Van Harlingen, D. J. *Phys. Rev. Lett.* **2018,** *121,* 177702. doi:10.1103/physrevlett.121.177702
10. Heim, D. M.; Pugach, N. G.; Kupriyanov, M. Y.; Goldobin, E.; Koelle, D.; Kleiner, R.; Ruppelt, N.; Weides, M.; Kohlstedt, H. *New J. Phys.* **2015,** *17,* 113022. doi:10.1088/1367-2630/17/11/113022
11. Heim, D. M.; Pugach, N. G.; Kupriyanov, M. Y.; Goldobin, E.; Koelle, D.; Kleiner, R. *J. Phys.: Condens. Matter* **2013,** *25,* 215701. doi:10.1088/0953-8984/25/21/215701
12. Pugach, N. G.; Kupriyanov, M. Y.; Vedyayev, A. V.; Lacroix, C.; Goldobin, E.; Koelle, D.; Kleiner, R.; Sidorenko, A. S. *Phys. Rev. B* **2009,** *80,* 134516. doi:10.1103/physrevb.80.134516
13. Holmqvist, C.; Fogelström, M.; Belzig, W. *Phys. Rev. B* **2014,** *90,* 014516. doi:10.1103/physrevb.90.014516
14. Jeon, K.-R.; Ciccarelli, C.; Kurebayashi, H.; Cohen, L. F.; Montiel, X.; Eschrig, M.; Wagner, T.; Komori, S.; Srivastava, A.; Robinson, J. W. A.; Blamire, M. G. *Phys. Rev. Appl.* **2019,** *11,* 014061. doi:10.1103/physrevapplied.11.014061
15. Golovchanskiy, I. A.; Abramov, N. N.; Stolyarov, V. S.; Golubov, A. A.; Ryazanov, V. V.; Ustinov, A. V. *J. Appl. Phys.* **2020,** *127,* 093903. doi:10.1063/1.5141793
16. Kato, T.; Ohnuma, Y.; Matsuo, M.; Rech, J.; Jonckheere, T.; Martin, T. *Phys. Rev. B* **2019,** *99,* 144411. doi:10.1103/physrevb.99.144411
17. Ojajärvi, R.; Heikkilä, T. T.; Virtanen, P.; Silaev, M. A. *Phys. Rev. B* **2021,** *103,* 224524. doi:10.1103/physrevb.103.224524
18. Silaev, M. A. *Phys. Rev. B* **2020,** *102,* 144521. doi:10.1103/physrevb.102.144521
19. Silaev, M. A. *Phys. Rev. B* **2020,** *102,* 180502. doi:10.1103/physrevb.102.180502
20. Simensen, H. T.; Johnsen, L. G.; Linder, J.; Brataas, A. *Phys. Rev. B* **2021,** *103,* 024524. doi:10.1103/physrevb.103.024524
21. Ojajärvi, R.; Bergeret, F. S.; Silaev, M. A.; Heikkilä, T. T. *Phys. Rev. Lett.* **2022,** *128,* 167701. doi:10.1103/physrevlett.128.167701
22. Cottet, A.; Huertas-Hernando, D.; Belzig, W.; Nazarov, Y. V. *Phys. Rev. B* **2009,** *80,* 184511. doi:10.1103/physrevb.80.184511

23. Eschrig, M.; Cottet, A.; Belzig, W.; Linder, J. *New J. Phys.* **2015,** *17,* 083037. doi:10.1088/1367-2630/17/8/083037
24. Tokuyasu, T.; Sauls, J. A.; Rainer, D. *Phys. Rev. B* **1988,** *38,* 8823–8833. doi:10.1103/physrevb.38.8823
25. Zaitsev, A. V. *Zh. Eksp. Teor. Fiz.* **1984,** *86,* 1742–1758.
26. Kuprianov, M. Y.; Lukichev, V. F. *Zh. Eksp. Teor. Fiz.* **1988,** *94,* 149.
27. Nazarov, Y. V. *Superlattices Microstruct.* **1999,** *25,* 1221–1231. doi:10.1006/spmi.1999.0738
28. Fyhn, E. H.; Linder, J. *Phys. Rev. B* **2019,** *100,* 224508. doi:10.1103/physrevb.100.224508
29. Turkin, Y. V.; Pugach, N. G.; Ekomasov, E. G.; Lvov, B. G. *Phys. Met. Metallogr.* **2023,** *124,* in press.
30. Brinkman, A.; Golubov, A. A.; Rogalla, H.; Wilhelm, F. K.; Kupriyanov, M. Y. *Phys. Rev. B* **2003,** *68,* 224513. doi:10.1103/physrevb.68.224513
31. Larkin, A. I.; Ovchinnikov, Y. N. Vortex Motion in Superconductors. In *Nonequilibrium superconductivity;* Langenberg, D.; Larkin, A. I., Eds.; Elsevier: Amsterdam, Netherlands, 1986.
32. Houzet, M. *Phys. Rev. Lett.* **2008,** *101,* 057009. doi:10.1103/physrevlett.101.057009
33. Xu, Y.; Awschalom, D. D.; Nitta, J., Eds. *Handbook of Spintronics;* Springer: Dordrecht, Netherlands, 2016. doi:10.1007/978-94-007-6892-5
34. Pugach, N. G.; Safonchik, M.; Champel, T.; Zhitomirsky, M. E.; Lähderanta, E.; Eschrig, M.; Lacroix, C. *Appl. Phys. Lett.* **2017,** *111,* 162601. doi:10.1063/1.5000315
35. Yagovtsev, V. O.; Gusev, N. A.; Pugach, N. G.; Eschrig, M. *Supercond. Sci. Technol.* **2021,** *34,* 025003. doi:10.1088/1361-6668/abc7f5
36. Gordeeva, A. V.; Pankratov, A. L.; Pugach, N. G.; Vasenko, A. S.; Zbrozhek, V. O.; Blagodatkin, A. V.; Pimanov, D. A.; Kuzmin, L. S. *Sci. Rep.* **2020,** *10,* 21961. doi:10.1038/s41598-020-78869-z

License and Terms